Development, Installation and Operation of a Container-based Mass Testing System for 20-inch Photomultiplier Tubes for JUNO

Dissertation

der Mathematisch-Naturwissenschaftlichen Fakultät
der Eberhard Karls Universität Tübingen
zur Erlangung des Grades eines
Doktors der Naturwissenschaften
(Dr. rer. nat.)

vorgelegt von

Alexander Felix Tietzsch
aus Tübingen

Tübingen
2020

Gedruckt mit Genehmigung der Mathematisch-Naturwissenschaftlichen Fakultät der Eberhard Karls Universität Tübingen.

Tag der mündlichen Qualifikation:	09. Oktober 2020
Stellvertretender Dekan:	Prof. Dr. József Fortágh
1. Berichterstatter:	Prof. Dr. Tobias Lachenmaier
2. Berichterstatter:	Prof. Dr. Josef Jochum

Sometimes science is more art than science, Morty. Lot of people don't get that.

– Rick Sanchez [1]

[1] from: *Rick and Morty*, created by Justin Roiland and Dan Harmon (Adult Swim), 2014 (S1E06).

Abstract

One of the big unanswered questions in neutrino physics is the ordering of the neutrino masses. This will be addressed by the **J**iangmen **U**nderground **N**eutrino **O**bservatory (JUNO), a large liquid-scintillator neutrino oscillation experiment currently under construction in China. To reach its primary goal of determining the neutrino mass ordering (as part of a broad physics program), JUNO requires an unprecedented energy resolution of at least $3\,\%/\sqrt{E_{\mathrm{vis}}[\mathrm{MeV}]}$, which is realized i.e. by a high optical coverage consisting of about 18'000 20-inch photomultiplier tubes (PMTs). All parts deployed in the JUNO experiment further need to fulfill dedicated quality criteria; this is relevant in particular for the 20-inch PMTs regarding several key characteristics (such as dark rate, photo-detection efficiency, charge and timing resolution etc.). Consequently, each of the 20-inch PMTs needs to be tested and characterized separately before being mounted into the detector.

In the scope of this thesis, a specially designed multi-channel PMT mass testing facility within four commercial shipping containers has been developed and assembled in collaboration with colleagues from University of Hamburg. These four *container systems* include a dedicated light system, commercial read-out electronics and a custom-made data acquisition software for fully automated control of the PMT characterization. This PMT mass testing facility aims to measurement several key characteristics in a stable and comparable way and assessed according to the requirements of JUNO. The system has been set up close to the JUNO site and has been running successfully for almost three years now.

This thesis will present design and setup of the mass testing facility, including measurements investigating the performance, accuracies and systematics of the developed systems as well as an exemplary data analysis of more than one thousand 20-inch PMTs, proving the capability of the facility. This work is supported by the Deutsche Forschungsgemeinschaft.

Keywords: photomultiplier tubes, test systems, neutrinos, neutrino oscillations, astroparticle physics, photon detectors, mass testing, container

Zusammenfassung

Die Neutrinomassenordnung ist nach wie vor eine der großen ungeklärten Fragen in der Neutrinophysik. Diesem Problem soll im **J**iangmen **U**nderground **N**eutrino **O**bservatory (JUNO) nachgegangen werden, einem großen, Flüssigszintillator-basierten Neutrinooszillationsexperiment, das zurzeit in China aufgebaut wird. Zur Bestimmung der Massenordnung, die das Hauptziel von JUNO (in einem breiten Physikprogramm) darstellt, ist eine bisher unerreichte Energieauflösung von mindestens $3\,\%/\sqrt{E_{\mathrm{vis}}[\mathrm{MeV}]}$ erforderlich. Diese soll insbesondere durch eine große optische Abdeckung des Detektorvolumens, bestehend u.a. aus ca. 18'000 20-Zoll-Photomultipliern (PMTs), erreicht werden. Alle Teile, die in JUNO eingesetzt werden, müssen außerdem strenge Qualitätskriterien erfüllen, was insbesondere auch die Eigenschaften der PMTs betrifft (z.B. hinsichtlich Dunkelrate, Photon-Nachweiswahrscheinlichkeit, Zeit- und Ladungsauflösung). Deshalb müssen sämtliche 20-Zoll-PMTs vor dem Einbau in den Detektor getestet und charakterisiert werden.
Im Rahmen dieser Arbeit wurde dafür in Zusammenarbeit mit Kollegen der Universität Hamburg ein spezielles Testsystem für diese PMTs entwickelt und in vier kommerziellen Schiffscontainern aufgebaut. Diese *Container-Systeme* beinhalten u.a. eine spezielle Auswahl an Lichtquellen, kommerzieller Datennahme-Elektronik und eine eigens entwickelte Datennahme-Software, welche die PMT-Charakterisierungen vollautomatisiert steuert. Mit diesem Massentestsystem können die Eigenschaften der PMTs in einer stabilen und reproduzierbaren Art und Weise bestimmt und auf die Anforderungen von JUNO hin überprüft werden. Das System wurde in China in der Nähe des JUNO-Experiments aufgebaut und läuft dort erfolgreich seit mittlerweile fast drei Jahren.
In dieser Arbeit werden neben Design und Aufbau auch begleitende Messungen zu Systemeigenschaften, Genauigkeit und Systematiken vorgestellt, ebenso wie eine exemplarische Datenanalyse von mehr als eintausend 20-Zoll-PMTs, um das Leistungsvermögen des entwickelten Systems zu demonstrieren. Diese Arbeit wurde gefördert von der Deutschen Forschungsgemeinschaft.

Keywords: Photoelektronenvervielfacher, Testsysteme, Neutrinos, Neutrinooszillationen, Astroteilchenpyhsik, Photondetektoren, Massentests, Container

Contents

Introduction

In the past few decades, neutrinos have become one of the most active fields in (astro)particle physics. However, more than sixty years after the first detection of neutrinos by Cowan and Reines [1] there is still much to discover about their actual nature. This situation originates from an extraordinary low interaction cross-section: since neutrinos are only weakly interacting, they typically pass through matter unimpeded and thus undetected [2]. Nonetheless, various particle physics experiments have observed neutrinos from natural sources since then, see e.g. [3–11]. These days neutrino physics has evolved from the mere detection of neutrinos to a discipline performing high-precision measurements, investigating on one side even small effects and contributing on the other side to astrophysical multi-messenger observations and so heading towards the beginning of neutrino astronomy. A set of new experiments is currently in development or already under construction (see e.g. [12–16]) to further unveil the actual nature of the neutrino and answer remaining yet fundamental open questions. Exiting new results are expected to come in the 2020s, pushing forward the frontiers in neutrino physics. With continuously increasing demands on precision and energy resolution leading to larger and more complex experimental setups, also the technical requirements and needed accurateness are increasing; hence, this progress necessitates in particular high standards for the individual performance and reliability of all components.

One of the remaining open questions in neutrino physics is the ordering of the neutrino masses, which has various implications on fundamental questions in astroparticle physics and beyond [17, 18]. Due to the unknown sign of the large squared mass difference Δm^2_{3x}, two possibilities could be realized in nature, the so called *normal mass ordering* or the *inverted mass ordering*. To examine this, the **J**iangmen **U**ndergroud **N**eutrino **O**bservatory (JUNO) experiment has been proposed, a large volume liquid-scintillator detector currently under construction in the Jiangmen prefecture in southern China. Its primary goal is to determine the neutrino mass ordering with a significance of $3-4\,\sigma$ after approximately six years of data taking using antineutrinos from two nearby nuclear power plants. In addition, JUNO will also contribute to many other topics such as a high precision measurement of the neutrino oscillation parameters, geo-neutrinos, supernova neutrinos or even rare event searches like proton decay or indirect dark matter detection via annihilation [17]. To detect the sub-dominant effects in the oscillation pattern, which depend on the mass ordering, JUNO requires an unprecedented energy resolution of at least $3\,\%/\sqrt{E_{\text{vis}}\,[\text{MeV}]}$. This

is both challenging and absolutely essential for the success of JUNO. A key to realize such a high-performing experimental setup is the definition of strict quality criteria for all components deployed in JUNO, especially those which are related to the final energy resolution of the detector. Since the energy resolution is mainly driven by photon statistics, maximizing the light yield has motivated most decisions for design and choice of components. As a consequence, alongside optimal optical properties of the liquid scintillator target, a high optical coverage of the detector volume with impeccably performing photo-sensors is crucial. In special focus is here the performance of the about 18'000 20-inch photomultiplier tubes (PMTs) in the setup, which add the overwhelming majority to the optical coverage of the central detector (additional 2'000 PMT will be placed in the veto around the central detector). Following these considerations, a well performing PMT system satisfying dedicated requirements in performance and individual properties is indispensable; this condenses in a high quantum efficiency at the corresponding wavelength, a good resolution in charge and timing and a low noise level. Since ensuring these requirements is essential for the success of JUNO, it is therefore vital to identify PMTs, which cannot provide an adequate performance, and discard them before they are being mounted into the detector. In face of the huge number of PMTs that JUNO will be instrumented with, a dedicated system will be necessary which has to be able to perform individual quality tests providing reliable and comparable results for every single PMT, whilst still maintaining the overall schedule of JUNO.
To achieve this, a mass testing facility for JUNO PMTs was set up aiming to perform a large number of PMT qualification tests in parallel. Therefore, operation and organization of these tests rely on a well-structured work flow, a high level of automation and stable conditions within the system, while a specific measurement program for the full characterization process considers all relevant PMT parameters. The individual PMT characteristics can be determined then from the acquired data; furthermore, it allows to study PMT peculiarities as well as performance of the used mass testing facility with high statistics.

This work has contributed major parts to the development and setup of the mentioned PMT mass testing system. The thesis is structured as follows: In chapter 1, a short introduction to neutrino physics is given. In chapter 2, the JUNO experiment is presented, while the PMTs to be used in JUNO are described separately in chapter 3. In the following chapters the PMT mass testing setup developed in the scope of this thesis is presented, with a full description of the setup in chapter 4, its measurement program and operating software in chapter 5, as well as accompanying measurements to examine its performance and calibrate the system in chapter 6. In chapter 7, the analysis methods for the acquired raw data are shown, followed by an exemplary analysis of a selected raw data sample in chapter 8 to further prove the capability of the system and estimate its accuracies and systematics. This thesis will conclude with a short outlook on further plans and possibilities for the container system and its contribution to JUNO.

Chapter 1

Neutrino Physics

This first chapter will give a short introduction to the field of neutrino physics. It describes the role of neutrinos in the standard model of particle physics (in section 1.1) and introduces important concepts like neutrino oscillations (in section 1.2) and the question of neutrino mass ordering (in section 1.3), that are of special interest for the experimental collaboration in which this work has been set up.

1.1. Neutrinos in the Standard Model

In the Standard Model of Particle Physics (SM), neutrinos are elementary Dirac fermions without electric charge [19–21], interacting only via the weak interaction. They are observed in three different flavors (electron neutrino ν_e, muon neutrino ν_μ and tau neutrino ν_τ, plus anti particles $\overline{\nu}_e$, $\overline{\nu}_\mu$, $\overline{\nu}_\tau$) associated to the corresponding charged lepton, see Figure 1.1. Due to violation of parity symmetry in the weak interaction, neutrinos (antineutrinos) occur only in left-handed (right-handed) chirality [22, 23] and thus are introduced in the standard model as only left-handed doublets together with their associated charged leptons [19]; right-handed charged leptons however are introduced as singlets without a counterpart [1]. Neutrinos are produced in many naturally occurring nuclear reactions under participation of weak interaction, like radioactive beta decay, nuclear fusion or core collapse supernovae, but also in artificial neutrino sources like particle accelerators.
Although neutrinos were introduced as massless, they have been proven to have a finite mass (see section 1.2), which however is surprisingly small compared to the other massive fermions in the standard model [19, 24]. The smallness of the neutrino masses thus is questioning the mechanism of mass generation in the neutrino sector to be the same as for the other particles of the SM. As an explanation, additional generic models like the "seesaw" mechanism have already been developed, amending the existing neutrino standard model in order to better understand the relative sizes

[1] In the Goldhaber experiment [22], the helicity of neutrinos has been measured, which is identical to the chirality for massless fermions. Though neutrinos are found to have finite mass and helicity is not invariant under Lorentz transformation, the chirality of neutrinos was named instead here due to its implications in the V-A theory of weak interaction in general [23].

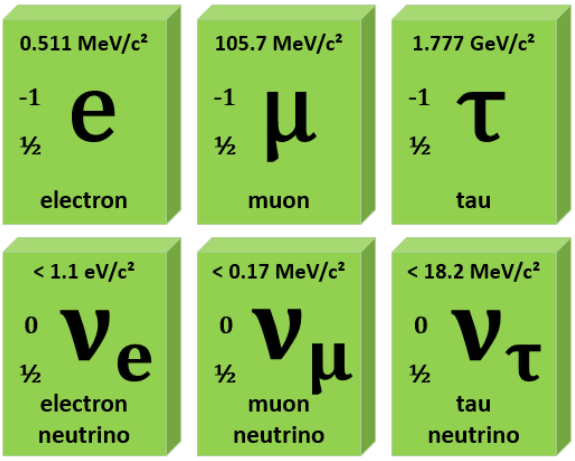

Figure 1.1.: Table of leptons in the Standard Model of Particle Physics. Numbers in boxes (from top to bottom) indicate the mass or upper mass limit, electric charge and spin of the respective particle. Box columns further indicate the particle "families" or "generations", which also define the "lepton flavor" number, which is conserved in a SM with massless neutrinos (i.e. no neutrino oscillations). Values from [19].

of neutrino masses, see e.g. [25–28] for more information. Current upper limits for neutrino masses are $m_\nu < 1.1\,\text{eV}$ (90 % C.L.) for the electron (anti)neutrino from direct measurement in the KATRIN experiment [29], as well as $\sum_\nu m_\nu < 230\,\text{meV}$ (95 % C.L.) for the sum of all neutrino masses from indirect cosmological observations [2] with the Planck CMB mission [30].

Since neutrinos are only weakly interacting and thus have only tiny interaction cross-sections [3] [31], neutrino experiments are challenging and usually demand large and complex experimental setups, all the more for performing high precision measurements of e.g. energy spectrum, absolute mass or flux etc. As such experiments are expensive and usually are scheduled to run for a long time in order to gain suitable statistics, many fundamental questions in neutrino physics still remain open to date (the following exemplary list is based on [17]):

- The **total number of neutrino flavors** is not finally ascertained, as the investigation of a possible existence of additional heavy, sterile [4] neutrino flavors is ongoing. Experiments for the sterile neutrino search are e.g. the MiniBooNE [32, 33] and STEREO [34] experiment.
- Neutrinos are suitable candidates for being Majorana particles, meaning that neutrinos and antineutrinos are the same particle but with different helicity. The **unknown Dirac or Majorana character** of massive neutrinos – which

[2] Limit depending on the used model, see [30] for more detailed information.

[3] Compared to all other fermions of the SM.

[4] "Sterile" means, that these neutrinos do not participate on the weak interaction.

is also a question of a possible lepton number violation – can be probed via observation of neutrinoless double beta decay, which is moreover the only experimentally feasible way at present. Running or planned experiments in this field are e.g. GERDA [35], LEGEND [16] or nEXO [36].

- The **absolute mass scale** of neutrinos is still not clear, and only upper limits of the neutrino masses can be given at the moment. The absolute neutrino mass can be probed via neutrinoless double beta decay, as the lifetime of such decays depends on the effective neutrino mass $m_{\beta\beta}$ (see also section 1.3), or can be investigated in direct neutrino mass measurements via β-endpoint spectroscopy [37]. Present experiments for a such direct mass measurements are e.g. KATRIN [38, 39] and ECHo [40, 41].

- Beside the absolute masses, also the **ordering of neutrino masses** is not fully determined. This will be discussed in section 1.3. Since the mass ordering has influence on several different processes in particle physics, astrophysics and cosmology, it can also be probed in many different ways and experiments, like e.g. JUNO, NOνA [42, 43], DUNE [13, 44], HyperK [15] or IceCube-PINGU [14, 45] (for more details about the JUNO experiment, see also chapter 2).

- The existence of **CP violation in the neutrino sector**, like it is already observed in the quark sector [5], cannot be excluded, but is also not yet proven to date. A few more details will be discussed in section 1.2 as well. Experiments looking for CP violation are e.g. NOνA, DUNE, HyperK or T2K [51].

- At last, some open questions are also connected to neutrino oscillation, which is a well-investigated behavior of neutrinos (and discussed in the next section), but not all of the related parameters are fully determined yet. Open questions here are the **octant of** θ_{23} e.g. investigated by NOνA, DUNE, IceCube-PINGU and T2K [52], or the **unitarity of the mixing matrix** e.g. investigated by JUNO, DUNE, HyperK and IceCube-PINGU, which can probe for non-standard or heavy sterile neutrinos (see first bullet point again). As the neutrino mass ordering has an impact on the neutrino oscillation, it can be investigated by some kinds of neutrino oscillation experiments as well (using atmospheric, long-baseline accelerator, reactor or supernova neutrinos).

1.2. Neutrino Oscillations

First indications for a need to extend the "neutrino standard model" have been given by Davis et al. [53] as they observed a significant deficit in the flux of solar neutrinos compared to predictions from the solar standard model (SSM) [54]. The experiment,

[5] CP violation in the quark sector has been observed in decay of neutral kaons, e.g. by Cronin and Fitch et al. [46], and in decay of B and D mesons in the experiments BaBar [47], Belle [48] and LHCb [49, 50].

located deep underground in the Homestake mine in South Dakota, measured the solar neutrino flux for a period of more than 20 years, using a tank with 615 t of perchloroethylene as neutrino target. The detection of solar electron neutrinos was realized by a neutrino capture process on the chlorine nuclei in the target, from which the produced argon atoms have been extracted and counted in an elaborated way [3]. The measured neutrino flux covered only around a third of what was expected from the SSM, and could neither be explained by any statistical or systematical effect from his setup nor with modifications of the SSM [6] [56, 57]. This deficit was further confirmed by following solar neutrino experiments like GALLEX/GNO [5, 58] and SAGE [6] and was denoted long time as "solar neutrino puzzle / problem", see e.g. [56, 59, 60]. The apparent anomaly finally turned out to be attributed to *neutrino oscillation*, a spontaneous and periodic change from one neutrino flavor to another, requiring neutrinos having finite masses and lepton flavors being mixed [17].
The existence of neutrino oscillation was finally proven by the experiments Super-Kamiokande [61, 62] and SNO [7, 63] as they could provide a model-independent test of neutrino flavor changes [7] and total flux of solar neutrinos and thus direct evidence for existence of non-ν_e components in the solar neutrino flux [19]. Today, neutrino oscillation has been observed in various other experiments and for almost all kinds of flavor transitions, see e.g. KamLAND [8], T2K [52], K2K [64], NOνA [43], MINOS [65], Double Chooz [66], DayaBay [67], RENO [68] or OPERA [69]. Since neutrino oscillation requires non-vanishing neutrino mass differences (and therefore at least one massive neutrino) and violates lepton flavor conservation, the evidence for neutrino mixing further constituted new physics beyond the (original) standard model [17].

The formalism of neutrino oscillation can be built analogously to the Cabbibo-Kobayashi-Maskawa (CKM) formalism of flavor mixing in the quark sector [19, 70]. Flavor transitions in the quark sector were introduced to preserve the universality of weak interaction [71] as well as to include CP violation in the charged current Lagrangian [72]. Although a standard theory for the origin of neutrino masses has not been established yet, one may expect a straightforward extension of the SM in which the phenomena of lepton flavor (and so neutrino) mixing and CP violation emerges for a similar reason [17].
Both the eigenstates of the weak interaction (flavor eigenstates) as well as its mass eigenstates form a complete, orthonormal basis of the neutrino within the SM [19]. The flavor eigenstates couple to the $W^{\pm}$ vector boson in the weak interaction, while the mass eigenstates diagonalize the neutrino's free-particle Hamiltonian and so describe its evolution in time (or propagation, respectively). The relation between both

[6] The SSM was used as reference model for the sun and its physical processes. It considers constraints from the total luminosity of the sun, as well as properties of atomic nuclei including cross-sections for nuclear reactions like fusion processes, measured precisely in lab experiments and connected to the production of neutrinos. Changes of parameters within the model thus still have to be compatible with the lab measurement results [55].

[7] Super-Kamiokande initially detected the flavor changes only using atmospheric neutrino.

neutrino bases is given by the Pontecorvo-Maki-Nakagawa-Sakata (PMNS) matrix U (or U_{PMNS}) [73–75], which fully describes a unitary transformation connecting the mass and flavor eigenstates of the neutrino. In general, each flavor eigenstate can be written as a superposition of mass eigenstates, and vice versa:

$$|\nu_\alpha\rangle = \sum_k U^*_{\alpha k} |\nu_k\rangle \ , \tag{1.1}$$

$$|\nu_k\rangle = \sum_\alpha U_{\alpha k} |\nu_\alpha\rangle \ . \tag{1.2}$$

with the mass eigenstates ν_k ($k = 1, 2, 3, ...$), the flavor eigenstates ν_α ($\alpha = e, \mu, \tau, ...$) and the respective matrix element $U^{(*)}_{\alpha k}$ (or its complex conjugated) from the PMNS matrix:

$$\begin{pmatrix} \nu_e \\ \nu_\mu \\ \nu_\tau \\ \vdots \end{pmatrix} = \underbrace{\begin{pmatrix} U_{e1} & U_{e2} & U_{e3} & \cdots \\ U_{\mu 1} & U_{\mu 2} & U_{\mu 3} & \cdots \\ U_{\tau 1} & U_{\tau 2} & U_{\tau 3} & \cdots \\ \vdots & \vdots & \vdots & \ddots \end{pmatrix}}_{U_{\mathrm{PMNS}}} \begin{pmatrix} \nu_1 \\ \nu_2 \\ \nu_3 \\ \vdots \end{pmatrix} \ . \tag{1.3}$$

If standard three-neutrino theory is considered (as done in section 1.1), U_{PMNS} reduces to a 3×3 unitary matrix. If unitarity could not be proven for this three-dimensional matrix, this would strongly hint at additional, possibly sterile neutrino flavors not yet observed [8]. If the PMNS matrix was equal to the identity matrix, mass and flavor eigenstates would equate; however, experiments show that this is not the case.
In the most common parametrization [9] of the PMNS matrix, three parameters are covered by rotary or "mixing" angles θ_{ij} (with $i, j = 1, 2, 3$ and $i < j$), and one complex phase δ_{CP} as remaining parameter, which describes CP violation for $\delta \neq 0$:

$$\begin{aligned} U &= \begin{pmatrix} U_{e1} & U_{e2} & U_{e3} \\ U_{\mu 1} & U_{\mu 2} & U_{\mu 3} \\ U_{\tau 1} & U_{\tau 2} & U_{\tau 3} \end{pmatrix} \\ &= \begin{pmatrix} 1 & 0 & 0 \\ 0 & c_{23} & s_{23} \\ 0 & -s_{23} & c_{23} \end{pmatrix} \begin{pmatrix} c_{13} & 0 & s_{13} e^{-i\delta} \\ 0 & 1 & 0 \\ -s_{13} e^{i\delta} & 0 & c_{13} \end{pmatrix} \begin{pmatrix} c_{12} & s_{12} & 0 \\ -s_{12} & c_{12} & 0 \\ 0 & 0 & 1 \end{pmatrix} \end{aligned}$$

[8] Unitarity of the PMNS matrix depends not only on the number of light neutrino, but could also depend on the mechanism of neutrino mass generation, see e.g. [25–27] again. As constraint from the experimental data, any possible deviation of U from unitarity must be small [17, 76–78].

[9] In general, there are N^2 degrees of freedom in any unitary matrix of dimension N. In the case of the 3×3 PMNS matrix, five of those real parameters can be absorbed as phases of the lepton fields. Thus the PMNS matrix can be parametrized by four free parameters only [28]. In case of Majorana neutrinos, this is not valid anymore as their mass term is not invariant under re-phasing of neutrino fields [28]. This leads to two additional Majorana phases ρ and σ, which have to be added via $U' = U \times diag(e^{i\rho}, e^{i\sigma}, 1)$ [17]. However, as this is of minor interest in this work, only the Dirac case will be described here.

$$= \begin{pmatrix} c_{12}c_{13} & s_{12}c_{13} & s_{13}e^{-i\delta} \\ -s_{12}c_{23} - c_{12}s_{23}s_{13}e^{i\delta} & c_{12}c_{23} - s_{12}s_{23}s_{13}e^{i\delta} & s_{23}c_{13} \\ s_{12}s_{23} - c_{12}c_{23}s_{13}e^{i\delta} & -c_{12}s_{23} - s_{12}c_{23}s_{13}e^{i\delta} & c_{23}c_{13} \end{pmatrix} \tag{1.4}$$

using $s_{ij} = \sin\theta_{ij}$ and $c_{ij} = \cos\theta_{ij}$ [19, 28]. Assuming CPT symmetry, the PMNS matrix is identical for the mixing of antineutrinos [79].

Since $U \neq \mathbb{1}_{3\times3}$, if a free neutrino is produced in an eigenstate of the weak interaction, it is automatically in a superposition of its mass eigenstates (see Equation 1.1). This superposition now slightly de-phases during propagation, since each mass eigenstate advances individually. This directly leads to changes in the flavor contribution. Because the phases appear periodically, the original neutrino state recovers periodically as well [10] and so produces an oscillating pattern in the neutrino flavor contributions over the distance [11].
The propagation of neutrinos in their mass eigenstates $|\nu_k\rangle$ can be described with the standard Hamiltonian, which leads to (using the plane wave solution):

$$|\nu_k(t)\rangle = e^{-i\boldsymbol{p_k}\cdot\boldsymbol{x}} |\nu_k(0)\rangle \ , \tag{1.5}$$

where quantities are expressed in natural units ($c = 1$, $\hbar = 1$) and with $\boldsymbol{p_k}$, $\boldsymbol{x}$ the relativistic momentum and position vectors of the particle relative to its source. If the neutrino was produced in a weak eigenstate $|\nu_\alpha\rangle$, there is an overlap with a new eigenstate $|\nu_\beta\rangle$ after traveling a distance L. Hence, a transition probability from flavor α to β can be given as:

$$P_{\alpha\to\beta} = |\langle\nu_\beta|\nu_\alpha(L)\rangle|^2 = \left|\sum_k \sum_l U^*_{\alpha k} U_{\beta l} e^{-i\frac{m_k^2 L}{2E}} \langle\nu_l|\nu_k\rangle\right|^2 = \left|\sum_k U^*_{\alpha k} U_{\beta k} e^{-i\frac{m_k^2 L}{2E}}\right|^2 \ . \tag{1.6}$$

This can be written more conveniently as

$$\begin{aligned} P_{\alpha\to\beta} = \delta_{\alpha\beta} &- 4\sum_{k>j} \mathfrak{Re}\left(U^*_{\alpha k} U_{\beta k} U_{\alpha j} U^*_{\beta j}\right) \sin^2\left(\frac{\Delta m^2_{kj} L}{4E}\right) \\ &+ 2\sum_{k>j} \mathfrak{Im}\left(U^*_{\alpha k} U_{\beta k} U_{\alpha j} U^*_{\beta j}\right) \sin\left(\frac{\Delta m^2_{kj} L}{2E}\right) , \end{aligned} \tag{1.7}$$

where $\Delta m^2_{kj} \equiv m^2_k - m^2_j$. With c and $\hbar$ restored, the phase of the squared sin-function is defined as

$$\frac{\Delta m^2\, c^3\, L}{4\hbar\, E} = \frac{\mathrm{GeV\,fm}}{4\hbar c} \times \frac{\Delta m^2}{\mathrm{eV}^2} \frac{L}{\mathrm{m}} \frac{\mathrm{MeV}}{E} \approx 1.27 \times \frac{\Delta m^2}{\mathrm{eV}^2} \frac{L/E}{\mathrm{m/MeV}} \ , \tag{1.8}$$

[10] Only valid as long as the full quantum mechanical state maintains coherence, which usually is the case since the neutrino masses are almost negligible compared to their kinetic energy.

[11] Neutrinos transformed into pure mass eigenstates do not oscillate but keep their flavor content respective to the actual mixing of flavor eigenstates within the mass eigenstate of production.

see also [19]. As example, the transition probability for an exemplary case of a certain initial and final state will be given, which shall be the survival probability of electron antineutrinos (conservation of initial $\overline{\nu}_e$ state) here:

$$P_{\overline{\nu}_e \to \overline{\nu}_e} = 1 - \sin^2(2\theta_{12})\,\cos^4(\theta_{13})\,\sin^2(\Delta_{21}) \\ - \sin^2(2\theta_{13}) \cdot \left(\sin^2(\theta_{12})\,\sin^2(\Delta_{32}) + \cos^2(\theta_{12})\,\sin^2(\Delta_{31})\right) \ , \tag{1.9}$$

using $\Delta_{ij} = \Delta m^2_{ij} L/4E$ (with $i, j = 1, 2, 3$ and $i > j$). This probability is displayed in Figure 1.2 for selected ranges of L, E and for L/E combined, using values from [80].

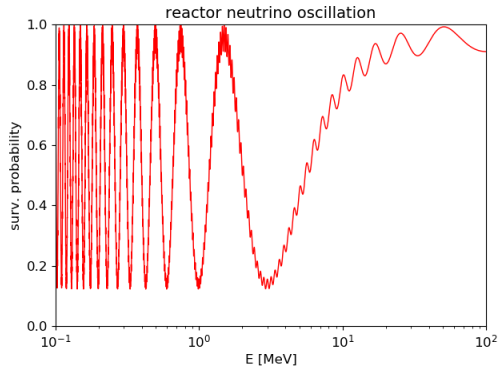

(a) $L = 50\,\text{km}$ fixed, $E = [0.1, 100]\,\text{MeV}$

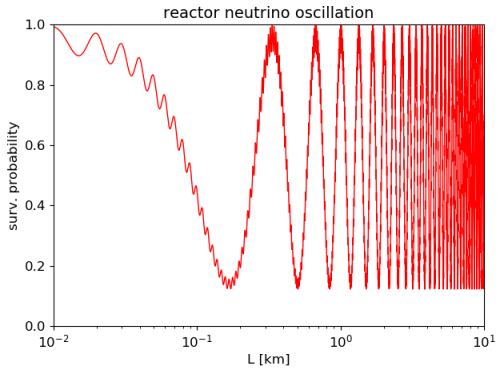

(b) $L = [0.1, 100]\,\text{km}$, $E = 10\,\text{MeV}$ fixed

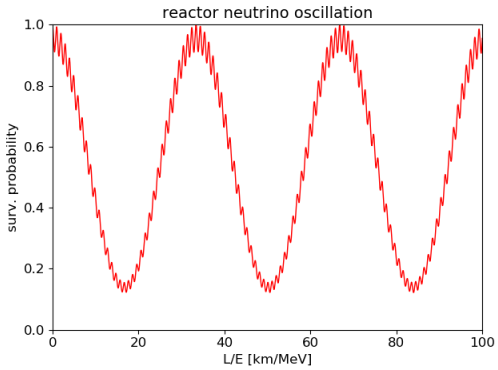

(c) $L/E = [0, 100]\,\text{km/MeV}$

Figure 1.2.: Survival probability of electron (anti)neutrinos at fixed distance (panel **(a)**), fixed energy (panel **(b)**) and L/E combined (panel **(c)**), assuming three-neutrino case and normal mass ordering, using parameter values from [80].

Current best fit values for all oscillation parameters as derived from available experimental data are listed in Table 1.1 [80, 81], introducing already the differentiation of neutrino mass orderings, explained in detail in the next section. The sign of Δm^2_{3l}, which is the largest absolute neutrino mass difference, and the octant of θ_{23} are still unclear, although values above 45° are slightly favored at the moment (even $\theta_{23} = 45°$

Table 1.1.: Three-flavor oscillation parameters from fit to global data as of November 2018. The shown results are obtained including the tabulated χ^2 data on atmospheric neutrinos provided by the Super-Kamiokande collaboration, see [81] for details. The numbers in the 1st (2nd) column are obtained assuming normal ordering (NO) (inverted ordering, IO) and relative to the respective local $\Delta\chi^2$ minimum (best fit point (bfp)). Note that Δm^2_{3l} defines the largest mass difference, with $\Delta m^2_{3l} = \Delta m^2_{31} > 0$ for NO and $\Delta m^2_{3l} = \Delta m^2_{32} < 0$ for IO. Values taken from: [80].

	Normal Ordering (best fit)		Inverted Ordering ($\Delta\chi^2 = 10.4$)	
	bfp $\pm 1\sigma$	3σ range	bfp $\pm 1\sigma$	3σ range
$\sin^2\theta_{12}$	$0.310^{+0.013}_{-0.012}$	$0.275 \to 0.350$	$0.310^{+0.013}_{-0.012}$	$0.275 \to 0.350$
$\theta_{12}/^\circ$	$33.82^{+0.78}_{-0.76}$	$31.61 \to 36.27$	$33.82^{+0.78}_{-0.75}$	$31.61 \to 36.27$
$\sin^2\theta_{23}$	$0.563^{+0.018}_{-0.024}$	$0.433 \to 0.609$	$0.565^{+0.017}_{-0.022}$	$0.436 \to 0.610$
$\theta_{23}/^\circ$	$48.6^{+1.0}_{-1.4}$	$41.1 \to 51.3$	$48.8^{+1.0}_{-1.2}$	$41.4 \to 51.3$
$\sin^2\theta_{13}$	$0.02237^{+0.00066}_{-0.00065}$	$0.02044 \to 0.02435$	$0.02259^{+0.00065}_{-0.00065}$	$0.02064 \to 0.02457$
$\theta_{13}/^\circ$	$8.60^{+0.13}_{-0.13}$	$8.22 \to 8.98$	$8.64^{+0.12}_{-0.13}$	$8.26 \to 9.02$
$\delta_{CP}/^\circ$	221^{+39}_{-28}	$144 \to 357$	282^{+23}_{-25}	$205 \to 348$
$\frac{\Delta m^2_{21}}{10^{-5}\,\mathrm{eV}^2}$	$7.39^{+0.21}_{-0.20}$	$6.79 \to 8.01$	$7.39^{+0.21}_{-0.20}$	$6.79 \to 8.01$
$\frac{\Delta m^2_{3l}}{10^{-3}\,\mathrm{eV}^2}$	$+2.528^{+0.029}_{-0.031}$	$+2.436 \to +2.618$	$-2.510^{+0.030}_{-0.031}$	$-2.601 \to -2.419$

is possible). For the CP violating phase, certain non-zero values are favored, however, CP conservation still cannot be excluded at the moment.

1.3. Neutrino Mass Ordering

One of the major remaining open questions connected to neutrino oscillation parameters is the ordering of the neutrino masses (also known as "neutrino mass hierarchy" (NMH)) [18]. As it was indicated in section 1.1 and already noticed in Table 1.1, there are two possible ways the neutrino masses can be sorted: $m_1 < m_2 < m_3$ (following $|U_{e1}|^2 > |U_{e2}|^2 > |U_{e3}|^2$) [12], which is called the "*normal mass ordering*" (NO) and $m_3 < m_1 < m_2$, which is called the "*inverted mass ordering*" (IO). Since the absolute value of Δm^2_{31} differs only a little in both NO and IO and the uncertainty in previous neutrino oscillation experiments was larger that this difference, the sign of the large (atmospheric) mass squared difference could not be determined yet. In contrast to that, the sign of Δm^2_{21} could be determined in solar neutrino experiments by the MSW effect [82, 83] to be $\Delta m^2_{21} > 0$.

[12] This identifies the m_1 mass eigenstate as the one with highest flavor contribution of ν_e.

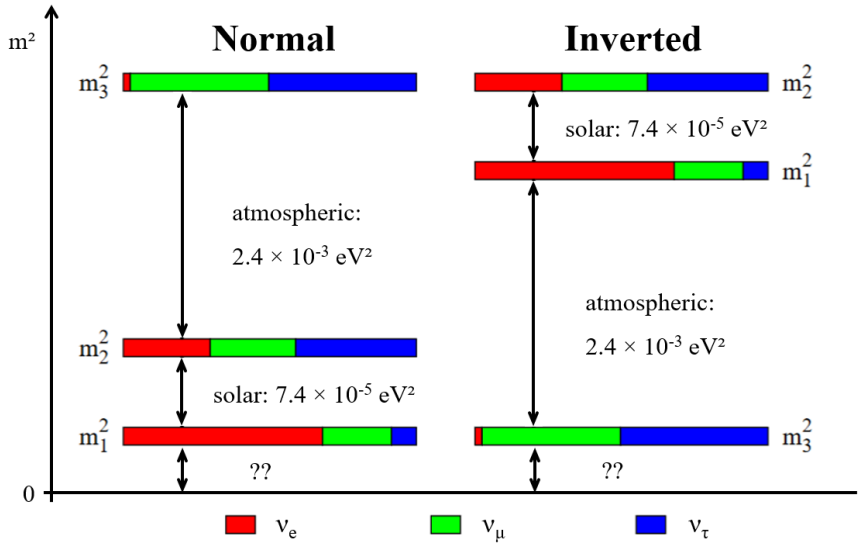

Figure 1.3.: Illustration of neutrino mass eigenstates in normal and inverted ordering, with colors indicating the flavor content of the mass eigenstates [17]. Mass eigenstate m_1 is quoted as the one with highest ν_e contribution.

The two possible orderings are also illustrated in Figure 1.3. Current experimental results of e.g. the T2K [51], NOνA [84] or Super-Kamiokande [85] experiment show a mild preference towards a normal mass ordering, with a combined significance in the order of $2-3\,\sigma$ [81, 86, 87], but also depending on the assumed value of δ_{CP}.

The neutrino mass ordering has various implications for other questions in neutrino physics [17, 18]. So are the output values of other oscillation parameters such as θ_{13}, θ_{23} and δ_{CP} in global fits sensitive to the sign of Δm^2_{31}, which is an important information for the data analysis in atmospheric, long-baseline accelerator or supernova neutrino experiments. There are also different parameter spaces for measuring the absolute neutrino mass (see Figure 1.4) or searching for $0\nu\beta\beta$ decays (see Figure 1.5) with respect to the neutrino mass ordering. Beyond that, the mass ordering might also play a role in understanding the origin of neutrino masses and mixing [17].
Determining the neutrino mass ordering thus can be achieved by measuring such effects that are sensitive to the sign of Δm^2_{31}. The most direct approach is a neutrino oscillation measurement with an energy resolution good enough to resolve features in the neutrino spectrum that are related to the mass ordering, as it is illustrated in Figure 1.6 for both NO and IO. Such an experimental setup has been discussed intensively already, see e.g. [89–93].
The JUNO experiment was designed to meet or even exceed the necessary requirements for e.g. energy resolution and a low background for the purpose of determining the neutrino mass ordering. As this thesis was written in the scope of the JUNO experiment, its physics program, experimental setup and more details about the energy resolution will be discussed in chapter 2.

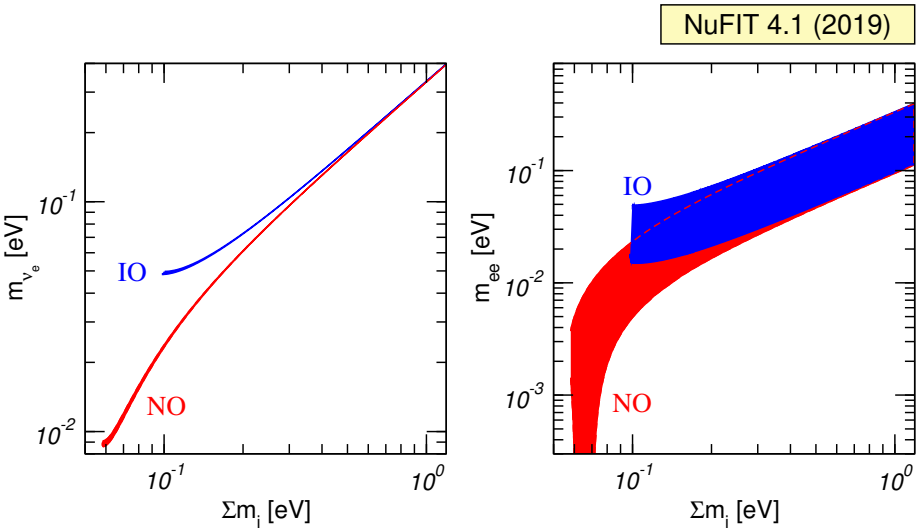

Figure 1.4.: Allowed regions of neutrino masses at 2σ depending on the mass ordering, obtained by projecting the results of the global analysis of oscillation data in the planes $(\sum_i m_i, m_{\nu_e} = \sqrt{\sum_i m_i^2 |U_{ei}|^2})$ and $(\sum_i m_i, m_{ee} = |\sum_i m_i U_{ei}^2|)$. The region for each ordering is defined with respect to its local minimum. Image credit: [80, 81].

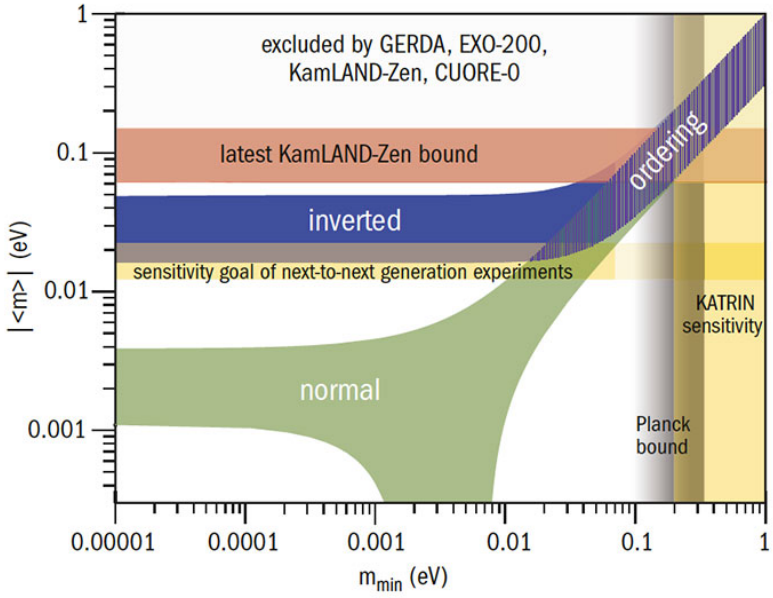

Figure 1.5.: The search for neutrinoless double-beta decay depends critically on the ordering of the neutrino masses, as illustrated by the predicted two-sigma values of the effective Majorana mass parameter $|< m >| = \sum_i m_i |U_{ei}|^2$, which controls the decay rate, versus the mass of the lightest neutrino (here m_{min}), with $m_{\text{min}} = m_1$ for NO and $m_{\text{min}} = m_3$ for IO. Image credit: [88].

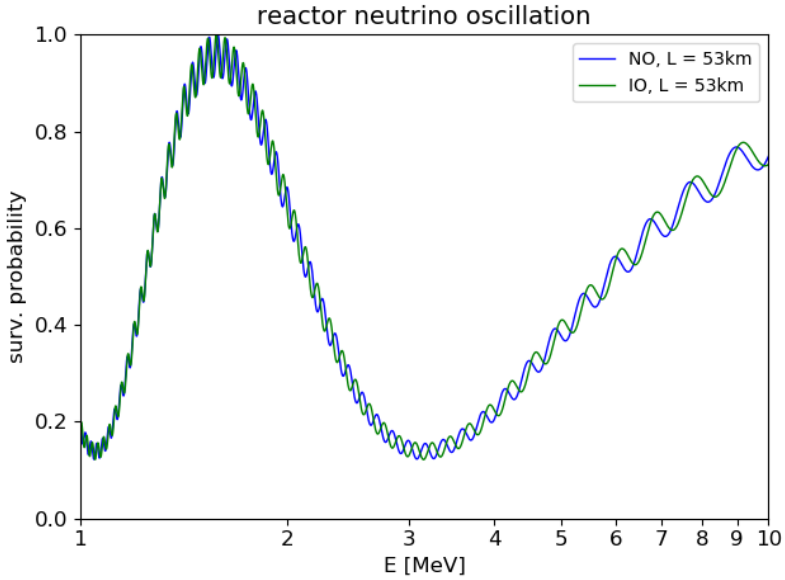

Figure 1.6.: Neutrino oscillation spectra (electron (anti)neutrino survival probability) at distance $L = 53\,\text{km}$ (similar to the one in Figure 1.2a) assuming NO and IO, using oscillation parameters from Table 1.1. The position of the small wiggles depends mainly on the neutrino mass ordering. Effect is the clearest around 3 MeV.

Another way to determine the mass ordering is the use of matter effects in long-baseline accelerator experiments [94], as it is planned (or already realized) by NOνA and DUNE, or using a terrestrial MSW effect influencing atmospheric neutrinos traveling through Earth [95], which is of interest e.g. for PINGU, HyperK or DUNE. More complete reviews about the determination of the neutrino mass ordering can be found in [18, 96, 97].

The expected sensitivity of each of these experiments is below the $5\,\sigma$ threshold for a full determination of the mass ordering (most of them expect a sensitivity in the order of $3-4\,\sigma$, see Figure 1.7), which is mainly due to the extraordinary energy resolution required for a good measurement in neutrino oscillation experiments, as well as the low electron density along the tracks for experiments using matter effects [13]. However due to the complementary approach of vacuum oscillation and matter effects, a much higher sensitivity can be gained from combining results of both kinds of experiments, like it was estimated for JUNO and PINGU in [99, 100], see also Figure 1.8.

[13] Compared with electron density in Sun's center, where the MSW effect plays a relevant role.

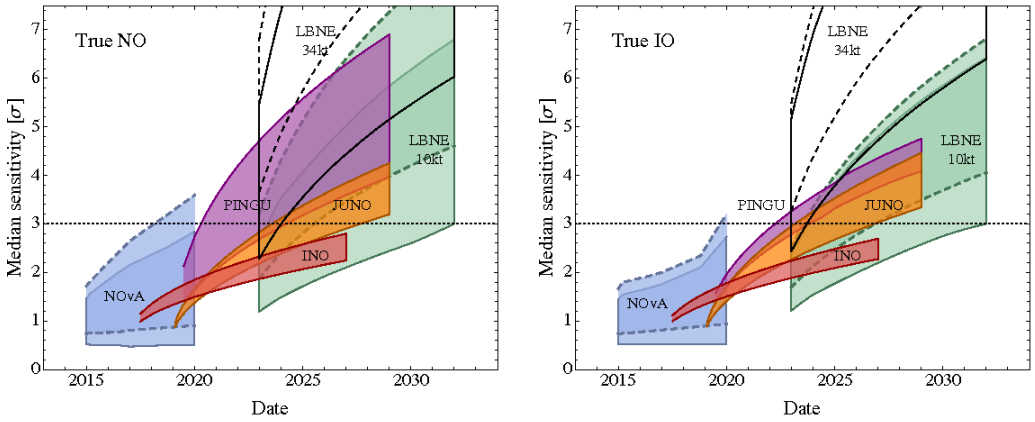

(a) σ to rule out IO, if NO is true **(b)** σ to rule out NO, if IO is true

Figure 1.7.: Predicted sensitivities of neutrino mass ordering measurements. The left (right) panel shows the median sensitivity in number of sigmas for rejecting the IO (NO) if the NO (IO) is true for different facilities as a function of the date (as of 2014). The width of the bands correspond to different true values of the CP phase δ for NOνA and LBNE (now DUNE [44]), different true values of θ_{23} between 40° and 50° for INO and PINGU, and energy resolutions between $3\%/\sqrt{E\,[\mathrm{MeV}]}$ and $3.5\%/\sqrt{E\,[\mathrm{MeV}]}$ for JUNO. For the long baseline experiments, the bands with solid (dashed) contours correspond to a true value for θ_{23} of 40° (50°). Image taken from [98].

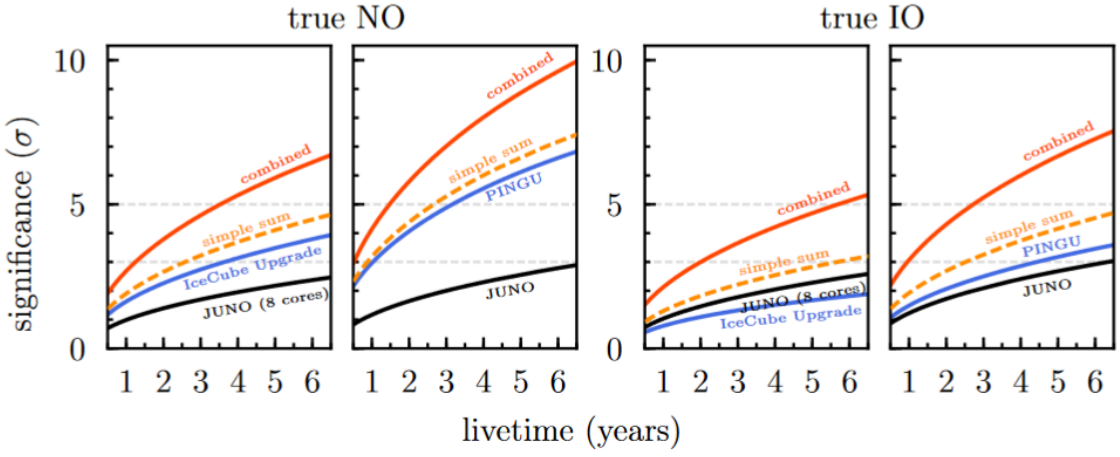

Figure 1.8.: Livetime evolution of the neutrino mass ordering sensitivity of stand-alone, simple (quadratic) sum and combination of considered experiments JUNO and PINGU. Results for the nominal JUNO configuration and PINGU are shown side-by-side with the 8-core JUNO configuration (labeled as "JUNO (8 cores)") and the IceCube Upgrade. The two panels on the left assume true NO, while the two panels on the right assume true IO. Image credit: [100].

Chapter 2

The Jiangmen Underground Neutrino Observatory

In this chapter, one of the major experiments investigating the neutrino mass ordering in the coming decade shall be introduced: the JUNO experiment.
This chapter presents the basic conditions of JUNO (see section 2.1), points out its manifold physics program (see section 2.2), described neutrino detection signal and background (see section 2.3), focuses on the energy resolution as crucial parameter for a successful and significant measurement of the neutrino mass ordering (see section 2.4), and concludes with a detailed overview on the experimental setup and design of the JUNO detector (see section 2.5). The chapter is based mostly on [17] and [12], where also more detailed information can be found.

2.1. Introduction and Setting

The Jiangmen Underground Neutrino Observatory (JUNO) experiment is a large liquid scintillator based medium-baseline reactor neutrino experiment, currently under construction in Guangdong province in southern China, next to the city of Kaiping in the Jiangmen prefecture, see Figure 2.1. Originally planned as follow-up experiment to Daya Bay [90–92, 101], a new collaboration was established in July 2014 to realize this experiment. In contrast to Daya Bay, which has focused on the direct measurement of the θ_{13} mixing angle from neutrino oscillation [67, 102] using several liquid-scintillator targets at short baselines from nuclear reactors, JUNO mainly focuses on the unanswered question of the neutrino mass ordering. Therefore, a large fiducial detector volume at medium baseline and an excellent energy resolution will be necessary, which in parallel also offers opportunities for addressing plenty of other interesting topics in neutrino and astroparticle physics [17].
The JUNO collaboration consists of around 640 members from 77 institutes in 17 countries [1] in Asia, Europe, North and South America, see Figure 2.2. The whole project is mainly funded by the Institute of High Energy Physics (IHEP) in Beijing

[1] Status of January 2020.

and the Chinese Academy of Science. Start of regular data taking with JUNO is currently scheduled to mid of 2022 (construction completed by 2021).

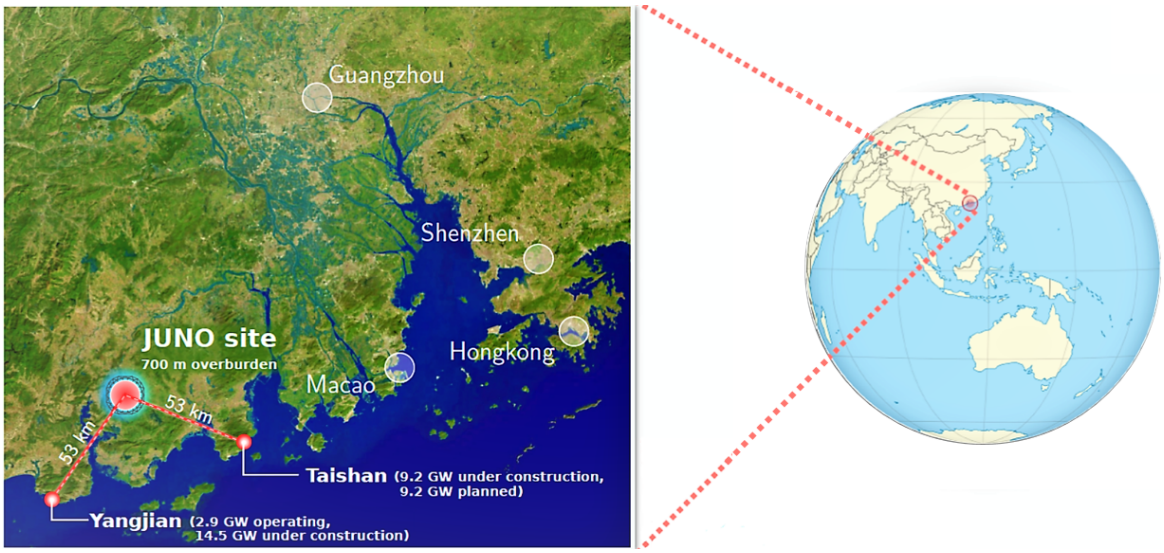

Figure 2.1.: Location of the JUNO experiment site in southern China. Image credit: JUNO Collaboration, taken from [103].

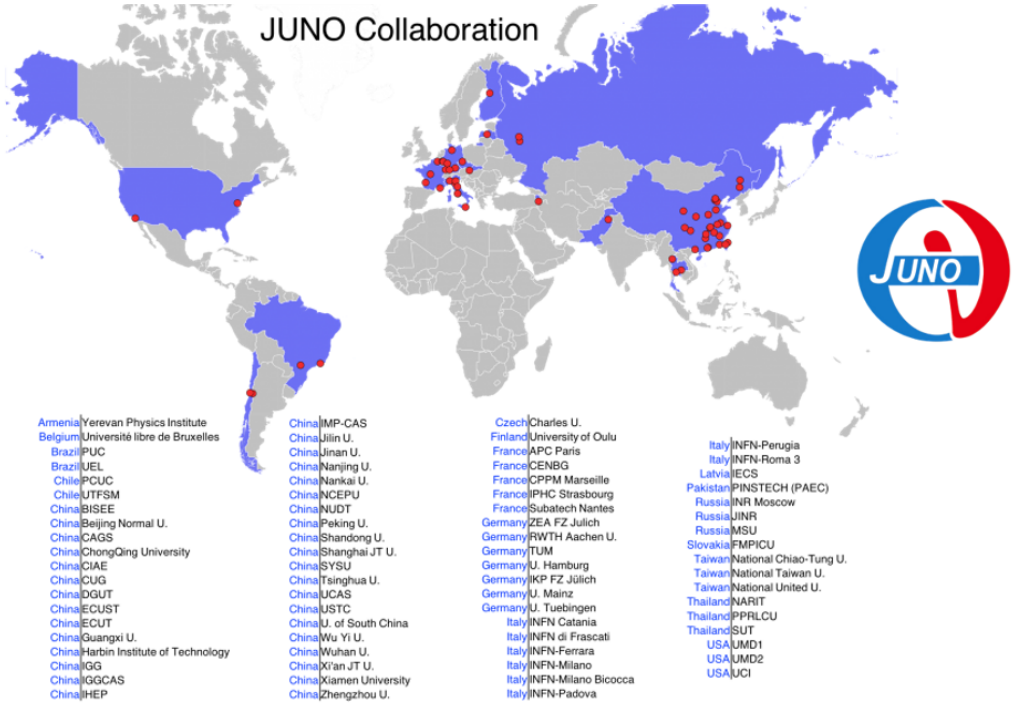

Figure 2.2.: Map of all members of the JUNO collaboration (status of January 2019) and JUNO logo. Image credit: JUNO Collaboration.

Main sources of electron antineutrinos [2] for this experiment and used for the determination of the neutrino mass ordering are two strong nuclear power plants (NPP) at medium distance to the experimental site, named Taishan NPP and Yangjiang NPP, with a combined thermal power of around 36 GW. Both NPPs are located at a distance of 53 km each to the detector, see Figure 2.1 again. Details about the power plants are presented in Table 2.1.

Table 2.1.: Summary of thermal power and baseline to the JUNO detector of all nearby reactor cores, including Yangjiang NPP (YJ) and Taishan NPP (TS) currently under construction and the remote NPPs Daya Bay (DYB) and Huizhou (HZ) at larger distances. Total thermal power at distance of around 53 km is 35.8 GW, with approx. 26.6 GW ready by 2020. Source: [12].

Cores	YJ-C1	YJ-C2	YJ-C3	YJ-C4	YJ-C5	YJ-C6
Power (GW_{th})	2.9	2.9	2.9	2.9	2.9	2.9
Baseline (km)	52.75	52.84	52.42	52.51	52.12	52.21
Cores	TS-C1	TS-C2	TS-C3	TS-C4	DYB	HZ
Power (GW_{th})	4.6	4.6	4.6	4.6	17.4	17.4
Baseline (km)	52.76	52.63	52.32	52.20	215	265

All six reactor cores of Yangjiang NPP are planned to be running in commercial operation at scheduled start of data taking. At Taishan NPP, only two reactor cores were scheduled to be ready in 2020, when the construction of JUNO was started. If only two cores will be realized at Taishan NPP in time, the full power of all reactor cores combined at start of data taking would shrink to 26.6 GW_{th} in total. Both NPPs are constructed and operated by the Chinese General Nuclear Power Group [17].
In Figure 2.3, a typical reactor neutrino spectrum is depicted, including the inverse beta decay (IBD) cross-section for neutrinos in the respective energy range and expected (yet un-oscillated) neutrino spectrum as it would be measured by a detector.

2.2. Physics Potential and Goals

JUNO aims to measure the neutrino mass ordering with a significance of $3-4\,\sigma$ after six years of data taking [17, 92, 112]. Since the JUNO experiment is intended as an observatory for multiple neutrino sources, also other terrestrial and astrophysical neutrino sources are of interest in JUNO.

2.2.1. Determination of the Neutrino Mass Ordering

The neutrino mass ordering can be derived from the observed reactor neutrino spectrum by resolving the features depending on the oscillation frequencies Δm^2_{21} and

[2] In the following also simply denoted as "reactor neutrinos".

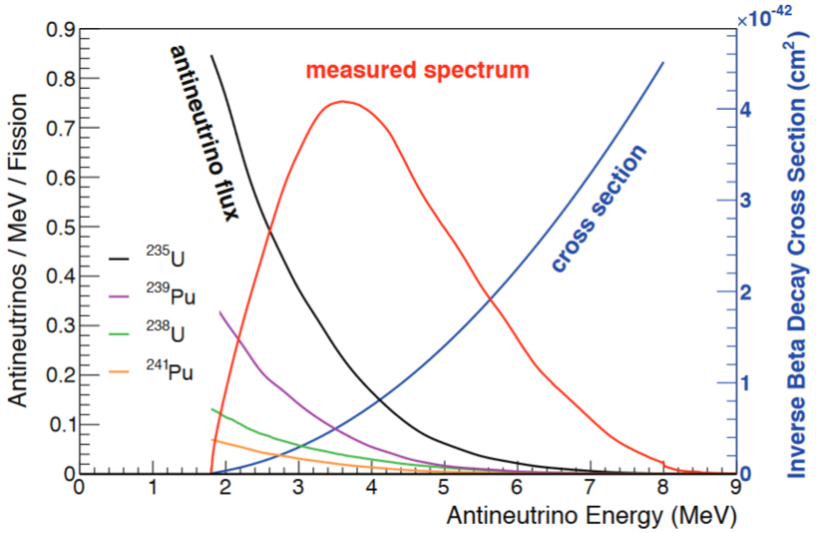

Figure 2.3.: Plot of typical antineutrino flux from a U/Pu reactor core (black) and inverse beta decay (IBD) cross-section (main neutrino detection reaction – blue). Unoscillated neutrino spectrum (convolution of both) is shown in red. A calculation of IBD cross-section can be found in [104], reactor neutrino spectra can be computed by inversion of measured β-spectra of fission products, see [105–110]. Image credit: [111].

Δm^2_{ee}. This leads to slightly different spectra depending on whether normal or inverted mass ordering is true, as already shown in Figure 1.6 and illustrated again in Figure 2.4.
The observed spectrum can be fitted to expectations from neutrino oscillation patterns, using Equation 1.9. By defining a phase ϕ following [115–117], with

$$\sin\phi = \frac{\cos^2\theta_{12}\,\sin\left(2\sin^2\theta_{12}\,\Delta_{21}\right) - \sin^2\theta_{12}\,\sin\left(2\cos^2\theta_{12}\,\Delta_{21}\right)}{\sqrt{1-\sin^2 2\theta_{12}\,\sin^2\Delta_{21}}}\,, \tag{2.1}$$

the survival probability can be transformed into

$$\begin{aligned} P_{\overline{\nu}_e\to\overline{\nu}_e} = 1 &- \cos^4\theta_{13}\,\sin^2\theta_{12}\,\sin^2\Delta_{21} \\ &- \frac{1}{2}\sin^2 2\theta_{13}\left[1-\sqrt{1-\sin^2 2\theta_{12}\,\sin^2\Delta_{21}}\cdot\cos\left(2\,|\Delta_{ee}|\pm\phi\right)\right] \end{aligned} \tag{2.2}$$

introducing the effective squared mass difference

$$\Delta m^2_{ee} = \cos^2\theta_{12}\cdot\Delta m^2_{31} + \sin^2\theta_{12}\cdot\Delta m^2_{32}\,. \tag{2.3}$$

Hereby, the mass ordering becomes manifest in the $\pm$ sign of the phase ϕ in Equation 2.2, which can be determined by a frequency analysis of the observed neutrino spectrum, see also [17]. This leads to a preference towards a certain sign of ϕ, with a positive phase corresponding to normal mass ordering, a negative to inverted mass ordering, respectively.

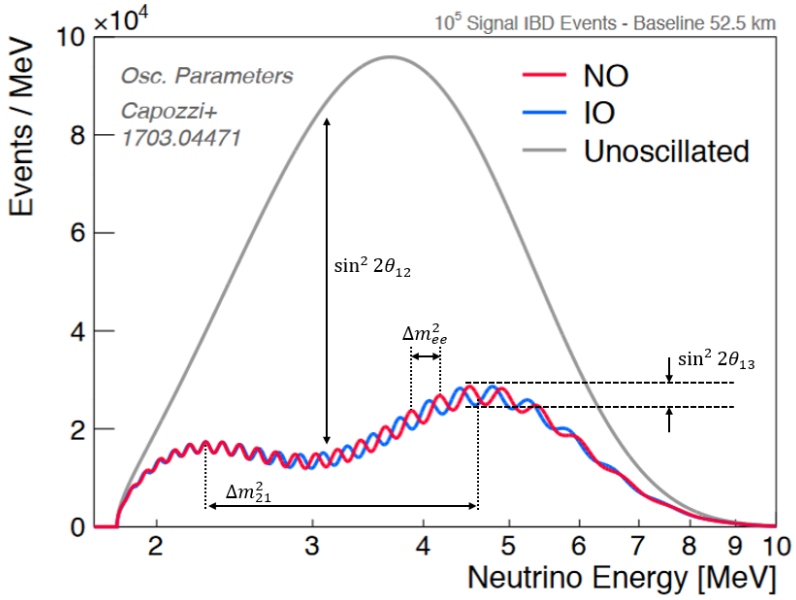

Figure 2.4.: Spectrum of reactor antineutrino flux at baseline $L = 52.5\,\text{km}$. As illustrated, the oscillation amplitudes are defined by mixing angles, oscillation frequencies depend on squared mass differences. Expected neutrino spectrum without any oscillation (grey) and with full oscillation assuming different mass orderings (red: normal mass ordering, blue: inverted mass ordering) are drawn in this plot. Oscillation parameters for plot from [113], image credit: [114].

The location of the JUNO site is optimized to provide the highest significance for a determination of the neutrino mass ordering. In the typical energy range of reactor antineutrinos from 1 to around 8 MeV (see Figure 2.3 again), the location of such an experiment should fit into the first solar oscillation minimum, see Figure 2.5. At this distance, the experiment benefits the most from a superposition effect of both the short baseline ("reactor") oscillation, driven by the large squared mass differences Δm^2_{31} and Δm^2_{32} (in Figure 2.4 indicated by the effective squared mass difference Δm^2_{ee}), and the medium baseline ("solar") oscillation frequencies, driven by the small squared mass difference Δm^2_{21} [90–92, 116, 117]. Furthermore, an equal distance to all sources is crucial to avoid negative interference in the oscillation pattern by dephasing of the neutrino fluxes from different reactor cores [17]. The impact of the total distance to and the differences in distances of multiple neutrino sources on the significance for the mass ordering is illustrated in Figure 2.6. The location of JUNO relative to both NPPs was chosen accordingly, leading to the previously noted distance of around 53 km to each NPP. As noted in Table 2.1, with the actual reactor core distribution, the maximum ΔL between two cores is only around 0.5 km.
In order to resolve the neutrino spectrum and thus the participating frequencies for a determination of the neutrino mass ordering, high requirements to the energy resolution have to be met in JUNO to finally achieve the aimed significance, see also section 2.4.

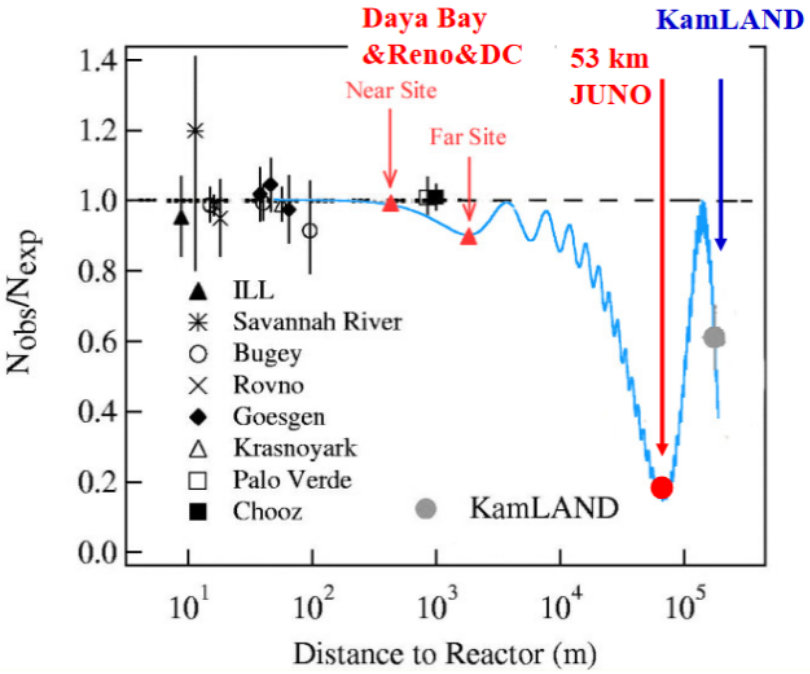

Figure 2.5.: Neutrino oscillation spectrum (electron antineutrino survival probability) assuming normal mass ordering, with baselines of various experiments marked inside (for JUNO, supposing $E_\nu = 4\,\mathrm{MeV}$ and $\sin^2 2\theta_{13} = 0.1$ in this plot). Image based on [118], taken from [119].

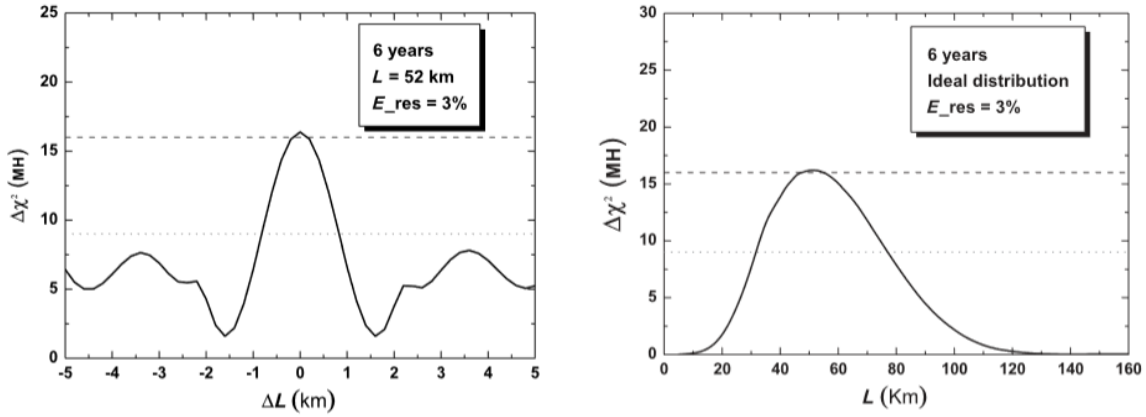

Figure 2.6.: Effects of different distances of neutrino sources to detector on NMO significance. *Left panel:* Effects of distance differences between two neutrino sources (reactor cores). De-phasing effect is strongest for $\Delta L \sim 1.7\,\mathrm{km}$. *Right panel:* Significance depending of the averaged baseline from source to detector. Maximum is around $L \sim 53\,\mathrm{km}$. Image credit: [92].

2.2.2. More Physics with JUNO

In addition to the determination of the neutrino mass ordering, JUNO has the chance to contribute to numerous questions in neutrino physics, making it a multi-purpose experiment.

JUNO will be the first experiment to simultaneously observe neutrino oscillations driven by both the solar and atmospheric squared mass differences in one spectrum and from a single source, combined with an unprecedented energy resolution. This enables JUNO to study **neutrino oscillation parameters with high precision**. Using the medium baseline and nonetheless high statistics in neutrino detection, precise measurements of the solar parameters θ_{12} and Δm^2_{21} as well as of the effective mass difference $|\Delta m^2_{ee}|$ with uncertainties of less than 1 % aimed after ten years of measurement will be possible [17]. Table 2.2 shows the current precision of relevant oscillation parameters and the expected precision achievable with JUNO.

Table 2.2.: Current and expected precision for several neutrino oscillation parameters, with individual $1\,\sigma$ uncertainties from experiments. MINOS and global value in second column describe $|\Delta m^2_{31}|$ while expected JUNO precision is given here for $|\Delta m^2_{ee}|$. The θ_{13} uncertainty is the lowest in short baseline experiments like Daya Bay and not in focus of JUNO, thus no expected uncertainty value is given here. θ_{23} is not measurable with reactor neutrinos, therefore it's not mentioned here at all; see e.g. results from T2K [51, 52] and NOνA [84] for information. Global values taken from [81], values for JUNO from [17]. Systematic effects with influence on the precision in JUNO are bin-to-bin energy uncertainty, energy scale and non-linearity uncertainties as well as background influences [17], with all single effects summed up to denoted final value.

	Δm^2_{21}	$\lvert\Delta m^2_{31}\rvert$ or $\lvert\Delta m^2_{ee}\rvert$	$\sin^2\theta_{12}$	$\sin^2\theta_{13}$
Individual $1\,\sigma$	2.4 % [120]	4.1 % [65]	6.7 % [121]	3.4 % [67]
Leading Experiment	KamLAND	MINOS	SNO	Daya Bay
Global $1\,\sigma$	2.8 %	1.4 %	4.1 %	2.9 %
JUNO Nominal [3]	0.24 %	0.27 %	0.54 %	–
JUNO + Syst.	0.59 %	0.44 %	0.67 %	–

The high precision measurement of the oscillation parameters can also probe for new physics beyond the standard model, as it could give better constraints on the unitarity of the PMNS oscillation matrix and probably hint for more (yet hidden) neutrino flavors if the unitarity of the PMNS matrix would not be confirmed (see section 1.2 again). Together with short baseline oscillation experiments like Daya Bay [102, 122] and solar neutrino experiments like SNO [121], a first direct unitarity test of the PMNS matrix will be possible reaching a precision around 2.5 %, mainly limited by the solar oscillation parameter precision (see also [77, 123, 124] for more details).

[3] Nominal setup considers 2000 effective days of measurement, normal mass ordering, $3\,\%/\sqrt{E\,[\mathrm{MeV}]}$ energy resolution and 73 % IBD efficiency, see [17, 92] and section 2.4 for details.

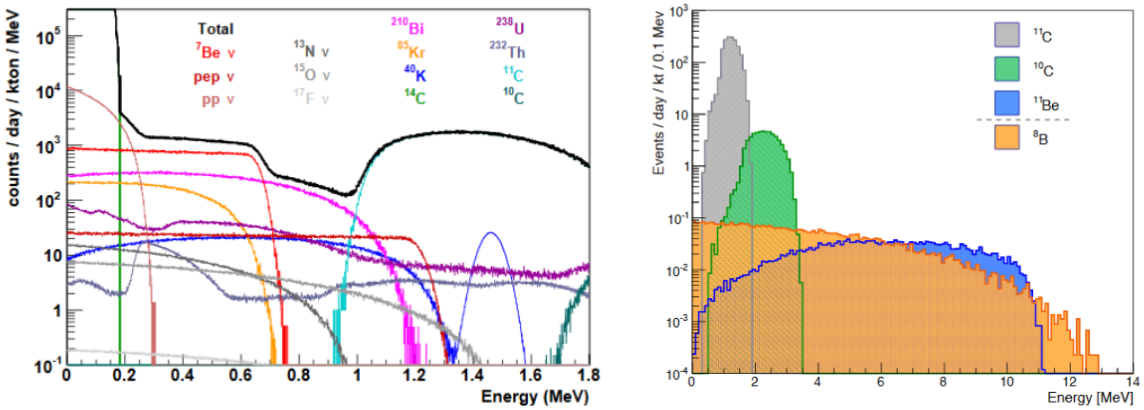

Figure 2.7.: Simulated solar neutrino fluxes in JUNO compared to main background contributors. *Left:* Different solar neutrino spectra compared to background contributions from remaining radioactivity in the scintillator. For the plot, ideal radio-purity (U/Th $< 10^{-16}$ g/g, ^{40}K/^{14}C $< 10^{-17}$ g/g) was assumed. *Right*: ^{8}B-ν's compared to simulated cosmogenic backgrounds from spallation (rates estimated and scaled from KamLAND and Borexino data, see [128, 129] for details). Image credit: [17].

Not only precision measurements of the reactor neutrino flux can help to precisely measure oscillation parameters, also specifically looking for **solar and atmospheric neutrinos** can contribute to improve the uncertainties from Table 2.2. Here again, JUNO benefits from its instrumentation and high energy resolution (see section 2.4 and section 2.5), enabling low thresholds for the detection of elastic scattering events of all types of neutrinos in the detector, which is helpful to observe solar and atmospheric neutrinos. In doing so, JUNO could contribute to improve models for metallicity and flux composition [125–127] as well as for the MSW transition region by resolving flux and spectral shape of ^{7}Be- and ^{8}B-neutrinos from the sun, combined with a measurement of CNO neutrinos [12]. The solar neutrino event rates though compete with low energy backgrounds from residual radioactivity in the scintillator (mainly ^{40}K and isotopes from the uranium/thorium chains) or with backgrounds from spallation of cosmic muons on nuclei in the target volume. The requirements on radio-purity for these measurements are challengingly high, in particular compared to the ones necessary for the reactor neutrino measurement [17], see also in subsection 2.5.4. The estimated signal in JUNO as well as main backgrounds are shown in Figure 2.7.

Measuring **supernova neutrinos** is another prominent goal for JUNO's prospects in being a neutrino observatory and playing a future key role in neutrino astrophysics. Due to its size, JUNO would be able to detect high rates of supernova burst neutrinos from a supernova in the Milky Way, and thus can be used as alert [4] for a possible

[4]Multiple neutrino experiments worldwide are connected together to a Supernova Early Warning System (SNEWS), see e.g. [130]. The lead of neutrinos with respect to the light burst detection can be used for an observatory alert for optical telescopes.

direct observation by other telescopes in multiple wavelengths. The expected large statistics could furthermore contribute to a first determination of a supernova neutrino energy spectrum with complete flavor information [17].
Assuming a core-collapse supernova at a typical galactic distance of 10 kpc, JUNO could register about 5000 related IBD events and around 3000 events from all-flavor elastic neutrino scattering [17]. This requires a highly efficient trigger and data acquisition system able to handle the large data stream for such a big number of events, distributed over the relatively short time of the neutrino burst [5].
Aside from burst neutrinos, JUNO could also look for the **diffuse supernova neutrino background (DSNB)**, which is formed by the integrated flux of all past core-collapse supernovae in the visible universe. The DSNB could hold information about star formation and death rates in the universe as part of an average core-collapse neutrino spectrum. Although DSNB neutrinos are very hard to distinguish from various backgrounds, a positive signal at up to the $3\,\sigma$ level could be conceivable with JUNO after 10 years of measurement, assuming typical DSNB parameters [12, 17]. Current DSNB limits can be found in [134], ongoing studies on these topic for JUNO can be found in [135, 136].

JUNO will also be capable of measuring **geo-neutrinos** from decay chains of ^{232}Th and ^{238}U as well as ^{40}K in Earth's inner parts, due to its low energy threshold and background (more information about this in section 2.3).
Geo-neutrinos are an interesting tool to learn about the chemical composition of the Earth and its mantle and crust. For geo-neutrinos, only a few liquid-scintillator based experiments like KamLAND [137, 138] and Borexino [139, 140] were able to measure geo-neutrinos and provide estimations about radioactive contributions to the terrestrial heat production so far. Combined surveys from these experiments estimate radio-nuclides to account for approximately the half of Earth's total surface heat flux of 47 ± 2 TW [141, 142].
Using models for U/Th distribution in different reservoirs in Earth's mantle and crust like from [143], the integrated geo-neutrino flux in JUNO can be predicted: assuming a chondritic U/Th ratio, JUNO is expected to detect a geo-neutrino signal of $S_{\mathrm{tot}} = 39.7^{+6.5}_{-5.2}$ TNU [6] in an energy range of a few MeV [144], despite of the huge reactor antineutrino background in this energy region, see Figure 2.8. Due to the size of JUNO, the detection of an unprecedented number of geo-neutrinos in total is possible. Moreover, the statistical power of the geo-neutrino signal at JUNO enables a measurement of the Th/U ratio, which could provide valuable insights into Earth's origin and evolution [17].
To improve accuracy and precision of this estimate, future studies of JUNO will necessarily require input from geological, geochemical and geophysical studies of the surrounding area of JUNO [17].

[5] In case of supernova SN1987A, neutrino events have been detected in a time window of only around 10 s [131–133].

[6] TNU: terrestrial neutrino unit, with 1 TNU = 1 event/yr/10^{32} target protons.

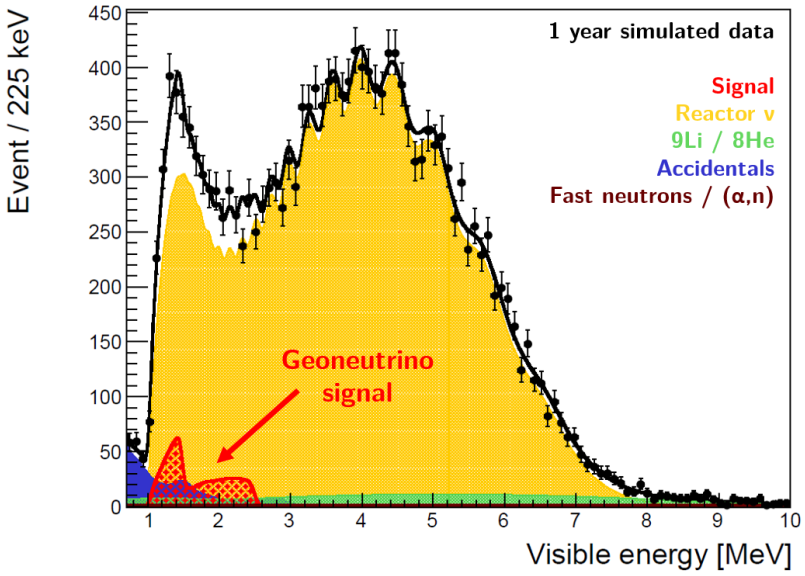

Figure 2.8.: Plot about the expected geo-neutrino spectrum (red area) in one year simulated data with fixed chondritic Th/U mass ratio, and compared with backgrounds at same energy window (see description in plot). The data points show all simulated candidates passing the selection cuts (see section 2.3), the black line shows the sum for the best fit. Image credit: [17].

Last, having a large active detector volume with an estimated overall runtime of more than 20 years in total, JUNO could be able to also observe very rare events like **nucleon decay** in the detector volume. Baryon number violation is predicted in many GUT theories (see e.g. [145–147], among many others) with expected very long lifetimes. Possible decay branches are

$$p \to K^+ + \overline{\nu} \quad (\text{with } \overline{\nu} = \sum_{e,\mu,\tau} \overline{\nu}_i),$$

for a SUSY-favored GUT or

$$p \to \pi^0 + e^+$$

for a non-SUSY GUT with best current limits of $\tau(p \to K^+\overline{\nu}) > 5.9 \times 10^{33}$ yrs and $\tau(p \to \pi^0 e^+) > 1.4 \times 10^{34}$ yrs at 90 % C.L. [148, 149].
In the search for a possible proton decay, JUNO has advantages compared to experiments like Super-Kamiokande (SK) or HyperK by its use of liquid scintillator, which provides a quick and direct light emission and allows a high accuracy in energy reconstruction. Hence, it's possible to resolve the initial proton decay as well as subsequent decay of the daughter particles as a three-fold coincidence signal, in order to get a clear signal identification [17, 149]. For example, a signal for the $p \to K^+\overline{\nu}$ decay channel is identifiable by a discrimination of the prompt signal from the K^+ recoil and the delayed signal from the kaon decay via $K^+ \to \mu^+\nu_\mu$. The delayed signal is coincident within an average time of 12 ns (lifetime of the charged kaon) and followed

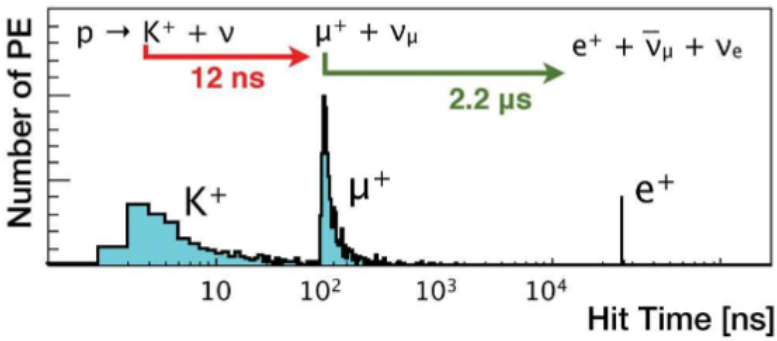

Figure 2.9.: Simulated hit time distribution of photoelectrons (PE) from a proton decay event and subsequent decays in JUNO. Image credit: [17].

by light emission from a starting muon in the detector, then followed again by a single positron signal after around 2.2 μs from the decay of the started muon, all with well-defined energies. This combined gives a highly efficient measurement mode and could help to surpass the current SK limits after already three years of data taking, with taken the atmospheric background already into account [12, 17] and despite having less target mass than the other (competitive) experiments. Such a coincident signal is also illustrated in Figure 2.9.

Some more topics of JUNO's physics program like sterile neutrino search or the search for neutrinos from dark matter self-annihilation can be found in [17], where also more detailed information about the aforementioned physics program is given.

2.3. Signal and Background

As mentioned in Figure 2.3, the detection of reactor antineutrinos is achieved via a coincident inverse beta decay (IBD) signal [17]: the incoming electron antineutrino interacts with a free proton inside the target volume, producing a neutron and a positron,

$$p + \overline{\nu}_e \;\rightarrow\; n + e^+ \;. \tag{2.4}$$

Since the neutron is around 2000 times heavier than the positron, the latter carries the major part of the kinetic energy of the incident neutrino, apart from the positron rest mass, the proton-neutron mass difference and a small recoil energy taken away by the neutron [7]. The energy threshold for this reaction is

$$E_{\text{thr,IBD}} = (m_n - m_p + m_e)c^2 \simeq 1.8\,\text{MeV} \;.$$

[7] The kinetic energy of the incident proton is negligible here.

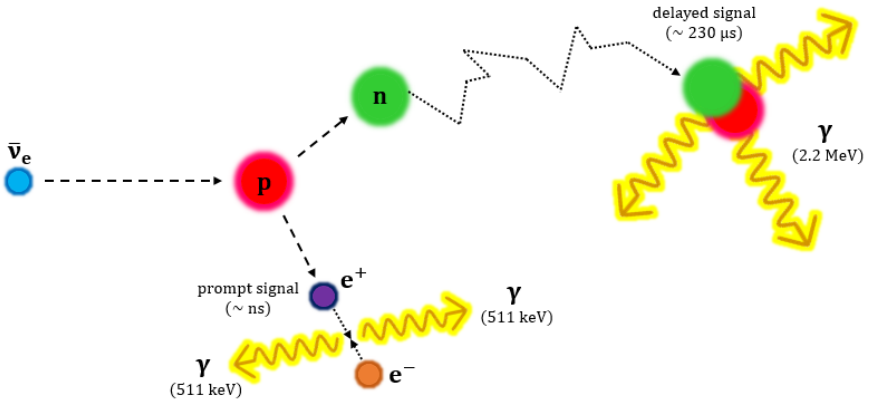

Figure 2.10.: Sketch of inverse beta decay signal, like it will be used for antineutrino detection in JUNO. After the IBD, the positron is annihilating with one of the surrounding electrons, whilst the neutron thermalizes first and then got captured by a hydrogen nucleus. Both processes release photons with distinct energies and can be separated by time into prompt and delayed signal.

The positron annihilates within a few nanoseconds releasing two 511 keV photons, thus the visible energy of the *prompt signal* is

$$E_{vis} \simeq E_\nu - 0.8\,\text{MeV} \ . \tag{2.5}$$

The neutron thermalizes in the medium before being captured on a hydrogen [8] nucleus from the scintillator and releasing a 2.2 MeV γ-ray, corresponding to the released deuteron's binding energy. Since thermalization of the neutron in the medium and the capture process takes some time (exponential distribution with $\langle t \rangle \sim 230\,\mu$s), the neutron capture signal on hydrogen can be observed as *delayed signal* like illustrated in Figure 2.10, giving a distinct coincidence and thus a clear detection signal [17].

With a total reactor power of 36 GW at 53 km distance, a spherical 20 kt liquid scintillator detector will observe approximately 83 IBD events per day from reactor neutrinos [17], considering disappearance by oscillation, IBD cross-section for respective energies [31] and usual models for reactor antineutrino spectra [105–110].
In order to count only IBD events from reactor neutrinos, all other physical processes depositing energy in the detector have to be sorted out. This is important especially for IBD-like events, which falsely could get counted as neutrino events, if not treated carefully. These are the main backgrounds for a detection of reactor neutrinos:

- accidental coincidences of unrelated processes, like radioactive decays of impurities in the LS, (in)elastic scattering of nuclei with cosmic muons or from radiation entering the detector from outside and thermalization and/or decay of energetic (instable) particles produced in spallation processes with cosmic radiation,

[8] Neutron capture on carbon nuclei is also possible, but with a lower cross-section [150].

- fast neutrons from cosmic spallation outside of the detector, which cannot be tagged and so can enter the detector volume,
- (α, n) processes (like e.g. $^{13}\mathrm{C}(\alpha, n)^{16}\mathrm{O}$) induced by α particles from the U/Th decay chains,
- cosmogenic isotopes like ^{8}He and ^{9}Li produced in spallation processes on carbon by energetic cosmic muons inside the detector,
- and geo-ν's, which are indistinguishable from reactor neutrinos due to their low energy, but have a different energy spectrum.

To still collect a large number of neutrino events in a manageable time, an intelligent background reduction is necessary, aiming to increase the total exposure of the detector and help to reach the aimed event number of $\mathcal{O}(100\mathrm{k})$ events within the scheduled period of six years. This can be realized by applying several cuts to the data in order to identify and dismiss the mentioned background events from the neutrino signals: Cuts on energy as well as differences in time and space (vertex cut) can help to reduce the number of accidental coincidences significantly. Of eminent importance is the identification and subtraction of background events from cosmogenic isotopes like ^{9}Li and ^{8}He, since their rates are at the same level like the neutrino signal. They both have a "long" lifetime ($\tau \sim \mathcal{O}(100\,\mathrm{ms})$) and can mimic an IBD signal by their βn-decay. This makes it hard to distinguish such events from "real" neutrino events. Since cosmogenic isotopes are correlated in time and space with their parent muon, a reduction of these background events can be achieved with help of sophisticated muon track reconstruction in the detector, see e.g. [151, 152]. With use of these methods, only a distinct region around the muon track can be vetoed after a through-going muon, which already cuts away most of the cosmogenic background events, but avoids introducing large detector dead times from vetoing the whole detector.
In Table 2.3 the estimated rates of expected IBD events in JUNO compared to the main backgrounds are listed. With the final selection, still about 60 IBD events per day can be observed with JUNO, accompanied by only around 4 background events per day [17]. More details about this can be found in [12].

2.4. Energy Resolution and Significance

The physics potential of JUNO is closely connected to the question how well the detector is able to resolve the features in the observed neutrino spectrum.
Assuming 73 % IBD efficiency, aforementioned reactor antineutrino flux models (see Figure 2.3 again) and oscillation parameters including accuracies from the latest global fits [81] as "nominal setup" [9], a significance of better than $3\,\sigma$ for identifying the correct neutrino mass ordering after a period of six years (2000 effective days of measurement) is aimed with JUNO [17, 92, 112].

[9] Terrestrial matter effects for θ_{12} and Δm^2_{21} are equally considered.

Table 2.3.: Expected rates for $\overline{\nu_e}$ induced IBD signals and backgrounds in JUNO, before and after cuts [17]. IBD efficiency is noted with respect to value in the first line (100 %). Absolute rates in events/day, estimated from simulations. After full application of selection cuts, S/B ratio is ~ 15.

Selection	IBD eff.	IBD	Geo-νs	Accidental	^{9}Li/^{8}He	Fast n	(α, n)
–	100 %	83	1.5	$\sim 5.7 \cdot 10^4$	84	–	–
Fiducial volume	91.8 %	76	1.4		77		
Energy cut	97.8 %			410			
Time cut	99.1 %	73	1.3		71	0.1	0.05
Vertex cut	98.7 %			1.1			
Muon veto	83 %	60	1.1	0.9	1.6		
Combined	73 %	60			3.8		

In order to resolve the mass ordering with the aimed significance, the energy resolution of the detector needs to be better or equal to the size of the ratio between the two participating frequencies [17, 153], meaning

$$\frac{\Delta m^2_{12}}{|\Delta m^2_{ee}|} \sim \frac{7.4 \cdot 10^{-5}\,\mathrm{eV}^2}{2.5 \cdot 10^{-3}\,\mathrm{eV}^2} \sim 3\,\% \ , \tag{2.6}$$

using values from [80]. The detector's final energy resolution has direct influence on the significance of determining the correct neutrino mass ordering with JUNO. Consequently considering the estimate in Equation 2.6, an energy resolution of $3\,\%/\sqrt{E\,[\mathrm{MeV}]}$ or better (with E the visible energy of the positron from the IBD event) becomes the key performance criteria for JUNO [12, 92]. A worse energy resolution would smear out the oscillation fine structure in the spectrum related to the mass ordering (so depicted for an energy resolution of 6 % in Figure 2.11) and thus would lower the determination significance [154]. The combined influence of both statistics and energy resolution on the significance for the determination of the neutrino mass ordering is displayed in Figure 2.12.
Using further external constrains for $\left|\Delta m^2_{\mu\mu}\right|$ from complementary long-baseline neutrino beam experiment like NOνA [43] or DUNE [44] or atmospheric neutrino oscillation experiments like IceCube-PINGU [14] or HyperK [155], additional information about the mass ordering could be revealed [10]. Hence, the mass ordering could be resolved to even a level of more than $4\,\sigma$ significance in JUNO after six years, assuming a precision of 1 % for $\left|\Delta m^2_{\mu\mu}\right|$ [17, 156].

[10] Combinations of different effective squared mass differences can include information about the mass ordering, so for example is $\left|\Delta m^2_{ee}\right| - \left|\Delta m^2_{\mu\mu}\right| = \pm\Delta m^2_{21}\,(\cos 2\theta_{12} - \sin 2\theta_{12} \sin\theta_{13} \tan\theta_{23} \cos\delta)$ with the $\pm$ sign denoting the mass ordering [153]. This can be included as additional pull term to the neutrino spectrum fit and thus increase significance for JUNO. See also [92, 153] for more information about these effective squared mass difference synergy effects.

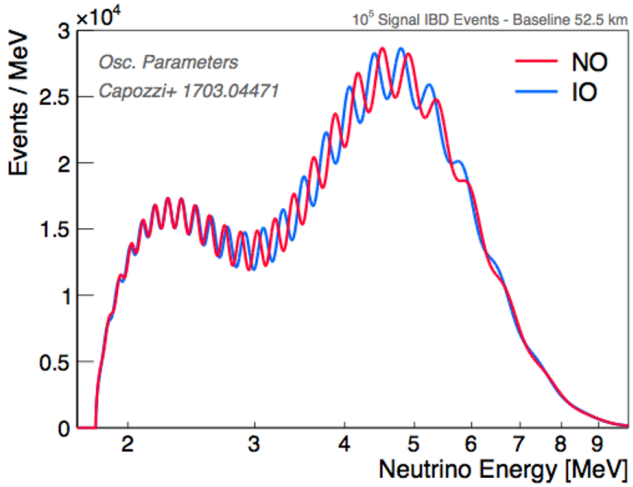

(a) $\sigma_E = 0$

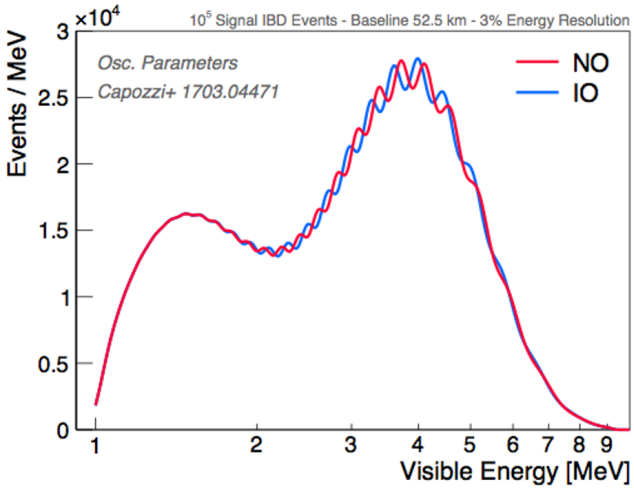

(b) $\sigma_E = 3\,\%/\sqrt{E}$

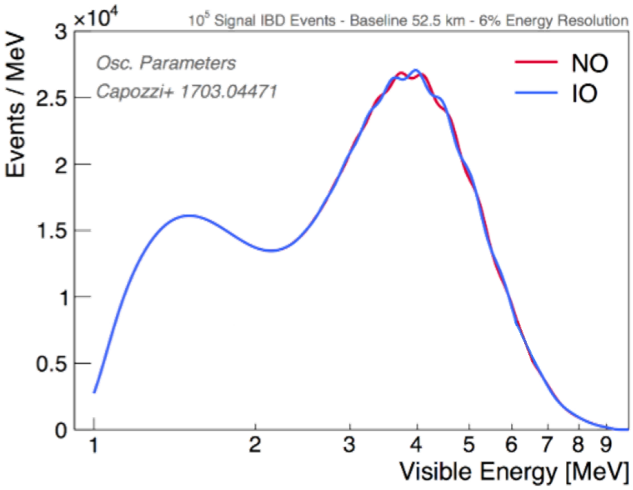

(c) $\sigma_E = 6\,\%/\sqrt{E}$

Figure 2.11.: Expected neutrino oscillation spectra in JUNO (similar to Figure 2.4), assuming a baseline of 52.5 km and different energy resolutions. Oscillation parameters for plots from [113]. Image credit: [114].

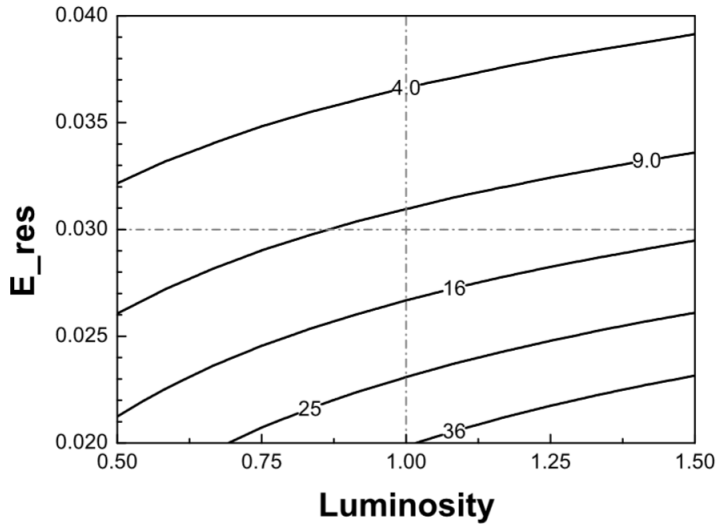

Figure 2.12.: Iso-$\Delta\chi^2_{\mathrm{MO}}$ (significance) contour plot for JUNO as function of energy resolution and event statistics (luminosity). A luminosity of 1 equals a running period of six years with nominal setup (see text for more information). Significance in correct MO determination is $\sigma = \sqrt{\Delta\chi^2_{\mathrm{MO}}}$. Image credit: [17].

Following the consideration about the energy resolution, the $3\,\%/\sqrt{E}$ goal was defined as major criterion in the design and development of the JUNO detector. The detector performance though can be influenced deliberately not only by the design, but also the choice of materials (e.g. liquid scintillator) and components (e.g. photomultiplier tubes) integrated in JUNO, and also depends on how well the detector performance is understood. Using a generic parametrization, the detector's energy resolution can be defined as

$$\frac{\sigma_E}{E} = \sqrt{\left(\frac{a}{\sqrt{E}}\right)^2 + b^2 + \left(\frac{c}{E}\right)^2} \tag{2.7}$$

with E again the visible energy in MeV. The final value for energy resolution σ_E depends on photon statistics (parametrized by factor a), non-stochastic terms (from Cherenkov light contribution, light quenching, detector non-uniformity and vertex-reconstruction, parametrized by b) and noise, including dark count rates of the used photomultiplier tubes (parametrized by c). All three parameters can be estimated with calibration sources and studied via Monte Carlo simulations [17].
The aimed energy resolution can then be achieved with following major specifications and assuming a total light yield of ~ 1200 p.e./MeV deposited energy [12, 17]:

- an optical coverage of the central detector volume of more than 75 %,
- a high photocathode quantum efficiency of the used photomultiplier tubes (PMTs) in the order of 30 %, with minimum collection efficiency of 90 % and only moderate dark count rate,

- and an attenuation length of the used liquid scintillator in the central detector volume of more than 20 m at 430 nm wavelength.

The JUNO detector further has to be large enough to gain sufficiently large statistics of neutrino events (for the mentioned significance of $> 3\,\sigma$, $\mathcal{O}(100\text{k})$ inverse beta decay events are required [12, 17]) and has to ensure highest performance of all its components and subsystems (to assure to a low failure rate of components). The design of JUNO is following these criteria and will be described in section 2.5 in detail.
To optimize the material- or component-related parameters of the parametrization in Equation 2.7, major efforts in quality assurance are necessary: all detector components should fulfill dedicated quality criteria, so for example the PMTs in case of photo-detection efficiency, charge resolution, timing and dark noise. In order to guarantee the desired, but thoroughly challenging energy resolution of $3\,\%/\sqrt{E\,[\text{MeV}]}$ in JUNO, testing all components for their individual characteristics becomes crucial for the success of JUNO. As a contribution to this, a large-scaled PMT quality examination setup was developed in the scope of this thesis, see chapter 4 and following.

But not only the energy resolution has influence on the final sensitivity for the true mass ordering, however it is the key criteria for design and instrumentation of JUNO. The achievable significance in reality is limited by several systematic uncertainties: such from the reactor spectrum (absolute and relative rates), from the spectral shape of the reactor neutrino flux, as well as detector related uncertainties that depend on the achieved accuracy in the calibration of energy response non-linearities [11] and residual non-linearities between measured and expected antineutrino spectrum, which are connected to the actual knowledge of Δm^2_{ee}. The uncertainty in energy response (or energy scale) should be better that 1 %, which demands a meticulous calibration of the whole detector system. This is challenging, but was shown to be possible already at Daya Bay [157, 158] and Double Chooz [66], and shall be realized in JUNO by using several complementary calibration systems [159]. Also a good understanding of the various, physical backgrounds is important, as otherwise their influence on the observed spectrum and a possible decrease in exposure (due to applied cuts or introduced, long dead times, see section 2.3) could push down the significance for a determination of the neutrino mass ordering as well [12, 17, 117].

All together, the final significance for the nominal setup under real conditions is estimated to $\Delta\chi^2_{\text{MH, real}} \simeq 9.6$ (compared to $\Delta\chi^2_{\text{MH, ideal}} \simeq 16$ in an ideal and background-free world [12]), which corresponds to the already mentioned $\gtrsim 3\,\sigma$ [17]. The expected sensitivity for JUNO under ideal and real conditions is plotted in Figure 2.13. More information about the mentioned systematics in JUNO can be found in [17] as well.

[11] Correlation between light output / overall number of detected photons in the detector to actual particle (e^+) energy.

[12] Biggest effect of this reduction is coming from the slightly deviant distances of the single reactor cores to the JUNO detector and the irreducible reactor neutrino background from DYB and HZ reactors (see Table 2.1 again) [17].

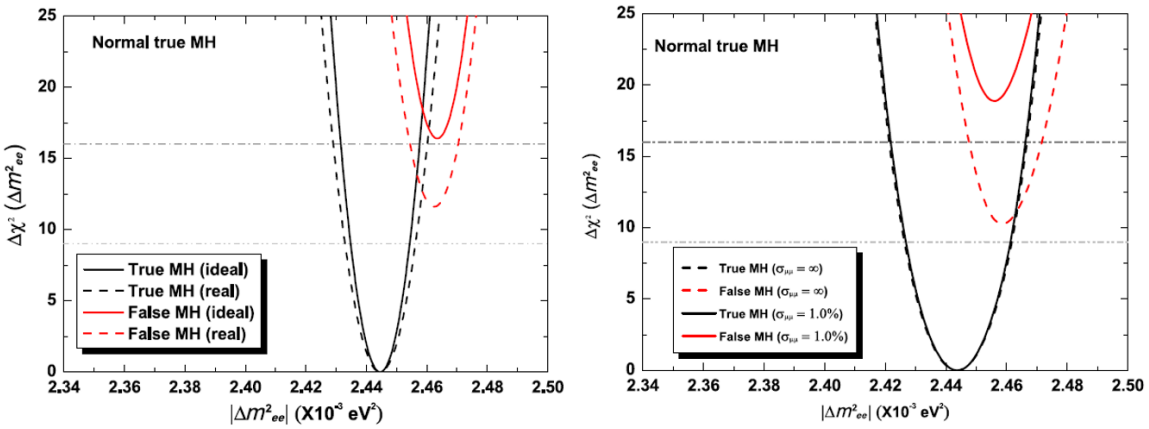

Figure 2.13.: Comparison of neutrino mass ordering or hierarchy (MH) sensitivity in different scenarios. *Left panel:* under ideal conditions (JUNO nominal setting with 2000 days data taking at 73 % IBD efficiency, $3\,\%/\sqrt{E\,[\mathrm{MeV}]}$ energy resolution, oscillation parameters from [81]) and realistic conditions, considering the actual reactor core distribution. *Right panel:* reactor-only and combined distributions of $\Delta\chi^2_{\mathrm{MH}}$, assuming 1 % relative error on $\Delta m^2_{\mu\mu}$ (with CP-violating phase δ is assigned to be $90°/270°$ ($\cos\delta = 0$)). Fitting with the wrong mass ordering (drawn in red) leads to higher values in $\Delta\chi^2_{\mathrm{MH}}$ w.r.t. the true ordering (assuming NO as true in this models). Image credit: [17, 92].

2.5. Experimental Setup

This section finally focuses on the JUNO setup and describes the JUNO detector system as well as its accompanying setups OSIRIS and TAO. The design of the JUNO detector follows the goal of reaching an energy resolution of $3\,\%/\sqrt{E\,[\mathrm{MeV}]}$, as described in section 2.4. The detector description presented in the following is mainly based on [12].

The JUNO experiment will be placed in an underground lab with roughly 700 m of granite rock overburden ($\sim$ 1900 m.w.e.) to shield the detector against backgrounds from cosmic radiation. Due to the massive overburden, the rate of cosmic muons in the detector is reduced to around $3.0\,\mathrm{mHz/m^2}$ with an average muon energy of 215 GeV, estimated by simulations based on the surveyed mountain profile [17, 160]. Aside from the JUNO detector in the main cavern, the lab provides space for support facilities and back-end electronics, as well as separated halls for liquid scintillator purification and monitoring.

2.5.1. Overall Detector Design

The **central detector** (CD) of JUNO, which is depicted in Figure 2.14, consists of a large, spheric acrylic vessel with diameter of 35.4 m and a wall thickness of 12 cm. The central detector volume will be filled with 20 kilo-tonnes of liquid scintillator (LS), based on linear alkyl-benzene, which represents the target material. The acrylic vessel itself will be hold by a shell-like stainless steel support structure (SSS – **stainless steel**

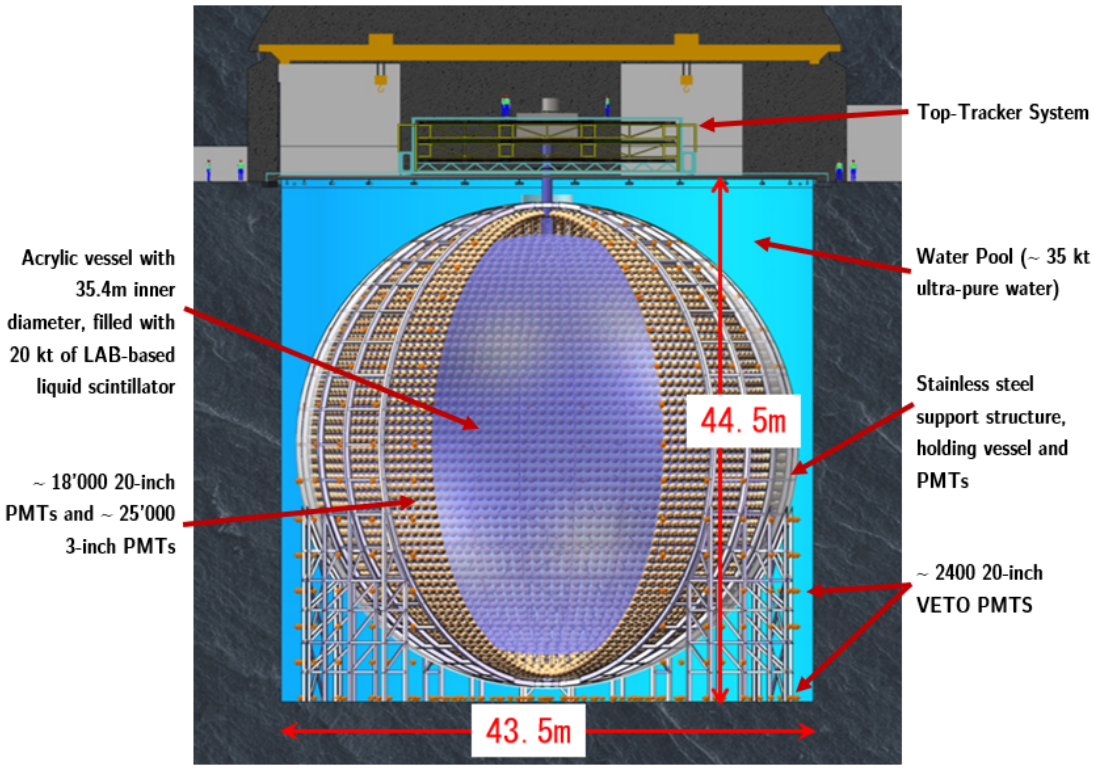

Figure 2.14.: Overview about the JUNO detector. Main components are marked inside the picture. Acrylic vessel with liquid scintillator inside is embedded into water pool, same as steel support structure and mounted PMTs. Distance of PMT surfaces to detector center is $\sim 19.5\,\mathrm{m}$. Image credit: JUNO Collaboration, taken from [161].

lattice shell) with a diameter of 40.1 m, which will also carry around 18'000 20-inch photomultiplier tubes (PMTs) and additional 25'000 3-inch PMTs, both looking inside in direction of the detector's center. Since the large PMTs are of special interest in this thesis, more detailed information about design and working principle of the chosen 20-inch PMT types as well as a dedicated list of requirements in performance needed for JUNO is given in chapter 3.
CD and SSS are embedded into a larger, cylindrical buffer volume excavated from the surrounding rock and called the **water pool** (WP). It will be filled with ultra-pure water and instrumented with additional more than 2000 20-inch PMTs, enabling the water pool to work as active Cherenkov veto system for through-going muons. The whole detector complex is further partially covered by another veto system, the **top tracker** (TT) system, which is also used for muon detection and track reconstruction.

2.5.2. Target Material

Liquid scintillator mostly consists of organic molecules featuring benzene rings, that can be excited by ionizing particles traversing the solvent. De-excitation can occur essentially via emission of fluorescence light, typically in the near UV wavelength

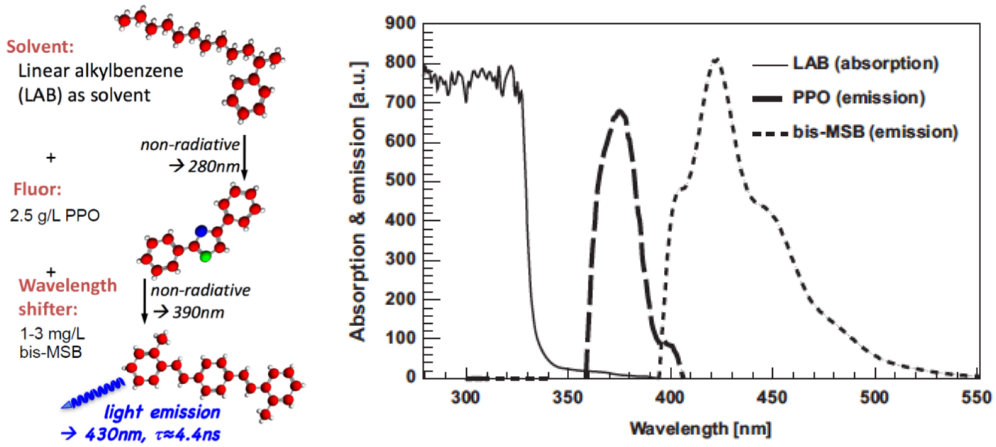

Figure 2.15.: *Left:* sketch drawing of the liquid scintillator components and the mechanism of shifting the excitation between the molecules and thus the output wavelength to around 430 nm. Image taken from [169]. *Right:* wavelength dependence of light absorption by LAB, compared to emission spectra of PPO and bis-MSB. It shows, that LAB is highly transparent for light emitted by the wavelength-shifters. Image credit: [170].

regime, or by non-radiative energy transfer to another molecule [162, 163]. Time profile and emitted wavelength spectrum depends on the decay constants and internal de-excitation mechanisms in the used organic material.
For JUNO, linear alkylbenzene (LAB) has been chosen as solvent and forms the bulk of the target material [12]. It can provide an excellent transparency when purified, a high light yield of around 10^4 photons per MeV of deposited energy and low chemical reactivity combined with a low toxicity, which makes it a natural choice for such an experiment with large detector volume [17, 164–166]. Due to the expected total runtime of JUNO of 20 to 30 years, also aging effects of the liquid scintillator have been considered in the choice for LAB [167]. Further, the decay time of the scintillator's excitation is only a few nanoseconds [168] providing a more or less instantaneous light output to an energy deposit in the target, which is helpful in event reconstruction and for applying cuts in order to reduce background.
Since the aromatic solvent is not transparent for its own fluorescence light, the excitation is passed non-radiatively to a two-component system, the JUNO detector liquid is doted with [12]. It consists of around 2.5 g/l of 2,5-diphenyloxazole (PPO) as scintillating flour and $1 - 3$ mg/l of p-bis-(o-methylstyryl)-benzene (bis-MSB) as secondary wavelength-shifter, with main absorption bands in the wavelength region of the LAB emission. Hence, the emitted photon wavelength is increased by Stokes shift to around 430 nm at peak [162, 171]. The so emitted output light spectrum also matches better to the wavelength-dependent quantum efficiency of the employed photomultiplier tubes [12, 166, 172, 173] and moreover avoids spectral self-absorption by the solvent. Figure 2.15 shows the absorption respective emission spectra of the different scintillator components.
At the final wavelength of $\sim$ 430 nm, the full liquid scintillator must provide a high

transparency with more than 20 m of attenuation length, corresponding to an absorption length of around 60 m and a Rayleigh scattering length of around 30 m [17], so that enough photons from events in the detector's center reach the PMTs placed outside the central volume and thus to ensure a good energy and spatial resolution over the full detector volume. To ensure the high transparency and further a very high radio-purity in order to reduce internal background sources, the liquid scintillator has to pass complex purification and cleaning steps beforehand, including Al_2O_3 purification columns, fractional distillation, water extraction and steam stripping [12, 164]. An attenuation length of LAB in the order of up to 25 m was already achieved in the lab and at pilot experiments at Daya Bay [174, 175]. More information about the liquid scintillator purification can be found in [12, 176].

2.5.3. Veto Systems

SSS and PMTs are placed in a larger cylindrical volume, the water pool (WP). The WP has a diameter of 43.5 m and height of 44 m, see Figure 2.14 again, and will be filled with around 35 kt of ultra-pure water. Continuously performed filtration by a dedicated water processing system will keep the internal radon contamination on a level of $< 0.2\,\mathrm{Bq/m^3}$ [177, 178]. The WP shields the CD from the surrounding rock with a buffer thickness of at least 3.2 m at any point from fast neutrons, which are produced in cosmic spallation processes in the rock material and then enter the detector. The water also acts as a buffer between CD and PMTs for unavoidable remaining radio-impurities, in particular ^{40}K as well as U and Th contaminations, mostly sitting in the PMT glass [17, 179].
By instrumenting the WP with around 2'400 20-inch PMTs, see Figure 2.16, it can be used as active Cherenkov veto for detecting cosmic muons or other charged particles entering the detector and possibly penetrate the inner detector volume. The efficiency in muon tagging with the veto systems is expected to be in the 95 percentile [160, 180, 181], see also section 2.3 again.

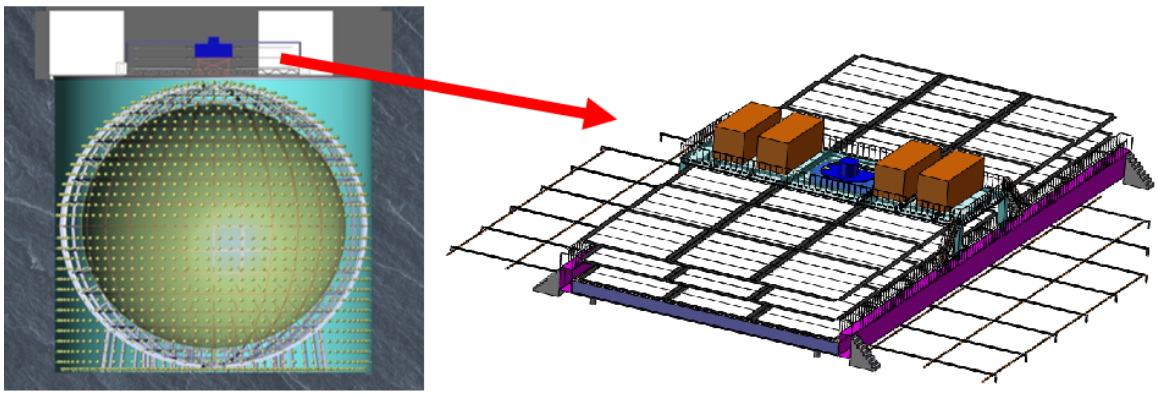

Figure 2.16.: Sketches of JUNO detector (concrete: water pool with Cherenkov veto) with position of veto PMTs in the water pool (left panel) and top tracker system (right panel). Image credit: JUNO Collaboration, taken from [161, 181].

Additionally, an area of around 60 % of the top of the JUNO detector will be covered by a three-layer top-tracker (TT) system, consisting of plastic-scintillator panels recycled from the target tracker modules of the OPERA experiment [182] and adapted to match the JUNO requirements, see also Figure 2.16. This allows a high precision tracking of particles traversing the TT and so the detector from above [12, 183]. Information about traversing cosmic muons from both the Cherenkov veto and the TT system combined can be used as input for highly sophisticated track reconstruction algorithms [151, 152], offering efficient background reduction and allowing to increase the detector's exposure.

2.5.4. OSIRIS Pre-Detector

The radio-purity of the LS will be essential for the success of the JUNO experiment [184]. In order to avoid internal background inside the CD as good as possible, minimal requirements for the scintillator's radio-purity are set to 10^{-15} g/g of residual contaminations from the uranium / thorium decay chains and 10^{-16} g/g of residual ^{40}K contamination in the solvent. Since these background sources directly compete with rare event searches like the solar neutrino program of JUNO (see subsection 2.2.2 again), especially for this goal even more restrict levels for the remaining contaminations down to 10^{-17} g/g for U/Th and 10^{-18} g/g for ^{40}K are highly desirable [13] [12]. Since the aimed radio-activity levels are too low to be checked via mass spectroscopy, a companion setup of JUNO called OSIRIS (Online Scintillator Internal Radioactivity Investigation System), set up next to the scintillator purification plants and acting as a 20-ton stand-alone pre-detector close to the JUNO experiment, will be in charge of monitoring the scintillator's radio-purity during filling and reprocessing as well as providing radio-purity data during the commissioning of the LS purification system. Further, OSIRIS can also work as test bed for JUNO detector subsystems [185, 186].
OSIRIS consists of a 3×3 m cylindrical acrylic vessel holding around 20 tons of LS, monitored by 76 20-inch PMTs from the same type as used in the JUNO detector, see Figure 2.17. The acrylic vessel is embedded into a 9×9 m cylindrical carbon steel tank filled with water as buffer for radiation background from the detector hall and the surroundings. The PMTs will be mounted on a scaffolding surrounding the acrylic vessel and deployed into the water as well, so that the water also buffers the monitored LS from radioactive contaminations in the PMT glass and housings, similar as it's the case at the JUNO main detector. 64 of these PMTs are monitoring the LS inside of the acrylic vessel, while 12 PMT are observing the buffer tank for muon detection, similar to the WP of JUNO. In contrast to JUNO, where the PMT electronics are housed in underwater boxes (see section 3.2 for details), OSIRIS will use so-called iPMTs (see e.g. [188] for more information) with the full-readout electronics sealed together with the base directly to the PMT. The optical coverage of the acrylic vessel by PMTs will be around 13 %, leading to an energy resolution of $\sim 5 - 6$ % at 1 MeV

[13] Also contaminations with several other radio-nuclides like ^{14}C, ^{210}Bi, ^{210}Po or ^{85}Kr should be minimized and thus monitored.

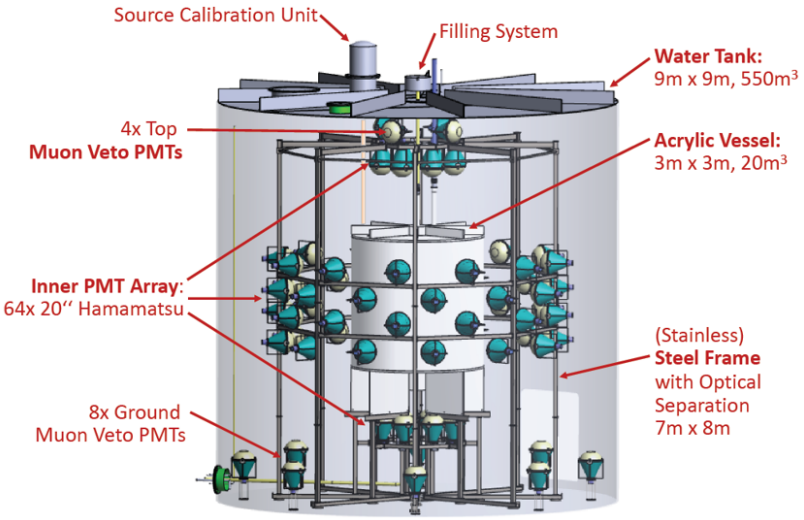

Figure 2.17.: Sketch drawing of the OSIRIS pre-detector. Image credit: OSIRIS Working Group of JUNO Collaboration, taken from [187].

deposited energy, which is sufficient for the tasks of OSIRIS [189]. The system is aimed and optimized to reach a sensitivity to the baseline radio-purity of $\sim 10^{-16}$ g/g for U/Th within 1 day of measurement [184].
For more information about OSIRIS, see [176, 185, 186, 189] for instance.

2.5.5. JUNO-TAO

To exclude remaining known and unknown features and uncertainties in the reactor spectrum [190, 191] and thus reduce one source of systematic errors in the reactor neutrino flux measurement, it was decided to add a near detector setup to JUNO [192]. The significance of the JUNO experiment will benefit from a direct antineutrino spectrum measurement close to one of the reactor cores [193], despite it appears that spectral distortions in the neutrino flux play only little role for the determination of the neutrino mass ordering [194]. This principle was used before in the θ_{13}-experiments Double Chooz [195], Daya Bay [102, 196] and RENO [68] where also near-detector systems were set up in close distance to the neutrino sources, but with focus on the actual, unoscillated neutrino flux. Such a near detector system is going to be constructed in the very vicinity of Taishan NPP, with only 30 - 40 m distance to one reactor core, and was named JUNO-TAO (Taishan Antineutrino Observatory).
The design of JUNO-TAO is different to the main JUNO detector to guarantee a very high energy resolution at least comparable to JUNO even though this near detector will be much smaller than JUNO. The 2.6 tons of liquid scintillator used in JUNO-TAO will be doted with gadolinium like in Daya Bay [102] and Double Chooz [66], to increase significance in neutron capture detection after inverse beta decay events, because Gd has a significantly higher cross-section for a capture of thermal neutrons, as well as a higher de-excitation energy after the capture [197]. The detector will be

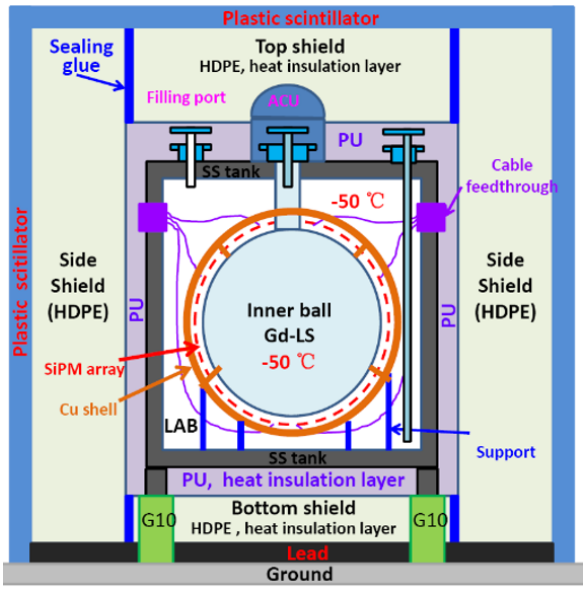

Figure 2.18.: Scheme of the Taishan Antineutrino Observatory (JUNO-TAO), which acts as a near detector for JUNO. TAO will be placed close to one of the Taishan NPP reactor cores and consists of a 2.6 ton Gd-doted liquid-scintillator target, surrounded by roughly $10\,\mathrm{m}^2$ SiPM, running at $-50°\,\mathrm{C}$, and thus providing an energy resolution of up to $\sim 1.5\,\%/\sqrt{E\,[\mathrm{MeV}]}$. Image credit: JUNO Collaboration, taken from [184].

instrumented with $10\,\mathrm{m}^2$ of silicon photomultipliers (SiPM) around the target volume, providing a very high photo-detection efficiency in the order of 50 % and thus resulting in a light yield of up to 4500 p.e./MeV deposited energy. For reducing dark noise in the SiPMs, the whole detector system will be operated at $-50°\,\mathrm{C}$. This combination of a high performing light detection system together with the small distance to the reactor neutrino source enables JUNO-TAO to collect up to 20 times the event number of JUNO in half the time of detector operation, with an outstanding energy resolution of $\sim 1.5\,\%/\sqrt{E\,[\mathrm{MeV}]}$. Such a high-resolution system could not only help to investigate reactor spectrum anomalies in benefit for JUNO, like for example the 5 MeV distortion in the reactor spectrum reported by Double Chooz [195], Daya Bay [198] and RENO [199], but could also act as benchmark for testing nuclear database information from reactors at a high precision level [200]. Because of the vicinity to the reactor core and the lack of a massive overburden like present for JUNO, a good shielding against neutrons and other radiation from outside is necessary. In order to do so, the central detector part of JUNO-TAO will be buffered by non-doped LAB to enable a good detection of background radiation entering the detector, and shielded by thick layers of high density polyethylene (HDPE) and polyurethane (PU).
A simple sketch of JUNO-TAO is depicted in Figure 2.18. For more details, see [192, 200] for instance.

Chapter 3

Photomultiplier Tubes in JUNO

Photomultiplier tubes (PMTs) are the main instrument for the detection of particle interactions in the central detector of the JUNO experiment. The PMTs detect the light which is released by the liquid scintillator in the CD or by Cherenkov radiation in the WP and thereby enable JUNO to detect neutrinos and other particle interactions in the first place. The energy resolution as well as the spatial and timing resolution of the JUNO detector directly depends on the efficiency of the PMTs, thus making them a vital element for the physics program in the setup of JUNO.
Three different PMT types are used in JUNO [201]: 20-inch dynode PMTs type R12860 HQE from Japanese company Hamamatsu, newly developed 20-inch microchannel plate PMTs (MCP-PMTs) from Chinese company Northern Night Vision Technology Ltd. (NNVT), as well as 3-inch dynode PMTs type XP72B22 from Chinese company HZC Photonics. While the small PMTs will be mounted only around the CD, the large PMTs will be part of both the CD and the Cherenkov veto for cosmic muons in the WP of JUNO.

This chapter is based mainly on [202, 203] and focuses on the functionality of the different PMT types of interest (see section 3.1), describes how the PMTs are integrated into JUNO (see section 3.2) and explains key characteristics of PMTs and lists their requirements in performance (see section 3.3), which are set as precondition for a use in the JUNO experiment in order to achieve the aimed energy resolution described before in section 2.4.
Since the performance of the 3-inch PMTs is not as crucial for the success of JUNO as it is the case for the 20-inch PMTs, and the 3-inch PMTs were not objects of the mass testing setup described in chapter 4 and following either, they therefore are of minor interest in this thesis; so this chapter mainly focuses on the large PMTs, while the small PMT system will only be mentioned shortly in subsection 3.1.1 and section 3.2.

3.1. Basic Principles of PMTs

Photomultiplier tubes are extremely sensitive light detectors with exceptionally fast time response and the ability to detect even diminutive amounts of light down to single

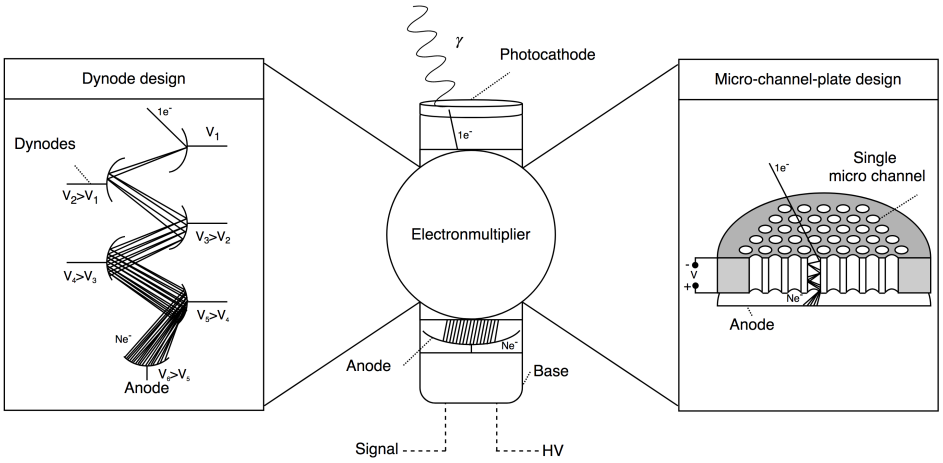

Figure 3.1.: Working principles for different PMT types: an incoming photon releases an electron via photoelectric effect on the photocathode, which is then focused to and multiplied in an amplification system (e.g. dynode system or micro-channel plate), resulting in a charge avalanche at the anode. At the base, where also the operating high voltage for the amplification system is applied, the charge cloud is output as measurable signal. Image credit: [204].

photons [202]. This is achieved by converting the incoming light into a measurable, electric signal [203], which can be read out at the end. The working principle of the different PMT types is depicted in a first sketch in Figure 3.1.

A PMT usually consists of an evacuated glass bulb (bare or encapsulated) with a photocathode vapor-deposited inside on top or front window of the PMT (depending on the actual form of the tube). The photocathode is sensitive to photons of certain wavelengths depending on the photocathode's material to undergo a photoelectric effect with a particular quantum efficiency (QE) and to release an electron into the vacuum tube. The quantum efficiency is defined as ratio of the number of released photo-electrons N_{pe} to the number of incident photons N_{ph},

$$QE\,(\lambda, \vec{r}) = N_{pe}/N_{ph}\ , \tag{3.1}$$

and can depend both on the wavelength of the incoming photon, and the point of interaction $\vec{r}$ on the photocathode [1].
When a high voltage (HV) is applied to the PMT (more precisely the PMT base, see also Figure 3.1), the released electrons will be accelerated towards a multiplication system, which can consist of multiple stages or just a single work piece. The PMT base, which is connected to pins on the back and thereby to the inner structure of

[1] This accommodates small, local deviations in the QE over the photocathode, due to unavoidable differences in thickness of the photo-sensitive material or other non-uniformities. For an ideal PMT, the QE would be independent from the point of interaction on the photocathode (same as for the collection efficiency).

the PMT, distributes the applied voltage to the stages of the multiplication system in an optimized way, so that the released charges from the photocathode are collected, focused and multiplied, ending in a charge avalanche which finally is collected again at the anode. The collection efficiency (CE) defines the ratio of the number of released photo-electrons at the photocathode N_{pe} to the number of down-going charge avalanches leading to a photo-detection signal N_{det},

$$CE\left(\vec{r}\right) = N_{det}/N_{pe} \ , \tag{3.2}$$

which can also depend on the point $\vec{r}$ on the photocathode where the incident charge has been released, but also on geometry and properties of the focusing electrodes [2]. Modern PMTs can reach collection efficiencies of more than 90 %, see [202, 205, 206] for instance.
QE and CE are tied together to the photo-detection efficiency PDE of the PMT, via

$$PDE\left(\lambda, \vec{r}\right) = \frac{1}{S_n} \int_{S_{pc}} QE\left(\lambda, \vec{r}\right) \cdot CE\left(\vec{r}\right) \, dS = \frac{N_{det}}{N_{ph}} \ , \tag{3.3}$$

with λ the wavelength on the incoming (detected) photon, $\vec{r}$ the position of the photon interaction with the photocathode, S_n (S_{pc}) the nominal PMT surface (photocathode area) [3] and N_{ph} (N_{det}) the number of incoming (detected) photons [201].
The total charge finally reaching the anode can be measured as voltage signal over a resistor at the signal output of the PMT base. Since the amplification process is feasible for electrons released by a single incident photon, PMTs are perfect instruments to detect diminutive amounts of light, while the generated signals are easy to measure.

For the JUNO experiment, PMTs of two different types have been chosen: one with a dynode system (PMTs from Hamamatsu) and one using a micro-channel plate (PMTs from NNVT) as multiplication system.

3.1.1. Dynode PMTs

Photomultiplier tubes with a dynode system have been used in many established neutrino experiments, e.g. KamLAND [8], Double Chooz [207], Daya Bay [208], RENO [209], SNO [210], BoreXino [211], Super-Kamiokande [212] and others.
The multiplication system of a dynode PMTs consists of several stages of secondary-emissive electrodes, realized by thin metal plates in the center or back of the PMT and set to consecutively increasing potentials from a divided external supply voltage applied via the PMT base. The accelerated electrons released at the photocathode are

[2] The focusing electrode generates the electric field inside the tube, so that the maximum number of electrons are focused onto the first dynode regardless of their initial velocity and (ideally) of their release position on the photocathode [203].

[3] Nominal area S_n is defined by diameter of PMT's glass bulb, which does not necessarily match the photocathode area S_{pc} [201].

focused by a collection grid and guided towards the dynode system, where they strike the first stage releasing secondary electrons by impact ionization. These secondary electrons then are accelerated themselves towards the next dynode to release more secondary electrons. This ends up after several stages in a charge avalanche focused on the anode in the back of the PMT, which is then output over a resistor creating a measurable voltage signal on the PMT output. The working principle of a dynode PMT is also depicted in Figure 3.2.
The ratio between incoming charge Q_{in} hitting the first dynode stage and outgoing charge Q_{out} measured at the anode stage defines the amplification of the signal by the PMT and is called *gain* G. The gain of the amplification system can be calculated also from the secondary emission coefficients δ_i, which depend on the dynode material, the applied voltage (potential difference between respective stage and stages before) and describe the average number of emitted secondary electrons per hit (and thus the individual amplification factor of a single stage) [213, 214],

$$G = \frac{Q_{out}}{Q_{in}} = \prod_{i=1}^{n} \delta_i(V) \ , \tag{3.4}$$

with n the number of amplification stages in the PMT. Dynode PMTs are usually running with voltages between 1 and 3 kV, generating a gain in the order of 10^7 depending on number of dynode stages and applied voltage.

For JUNO, 20-inch dynode PMTs of Hamamatsu type R12860 HQE [214] are used; in total, 5000 of these PMTs will be deployed in JUNO. The Hamamatsu dynode PMTs have a bulb shape and a relatively broad neck, see Figure 3.3. The dynode system consists of a box-and-linear-focused [4] type structure with ten stages. A bialkali [5] layer vapor-deposited on the inside of the PMT front glass is working as photocathode, providing a high QE with a maximum of typically 30–35 % at around 390 nm [6] [12, 172]. Using a focusing grid in front of the first dynode, a high CE of around 95 % or better can be achieved, ending with a typical PDE in the order of around 27 % using individual supply voltages between $\sim$ 1500 and $\sim$ 2350 V [172, 214]. Despite its large size, the Hamamatsu PMT provides a good timing and charge resolution.
More information about this PMT type can be found e.g. in [172, 219, 220], for information about the used PMT bases, see e.g. [179].

In addition to the large PMTs, around 25'000 3-inch PMTs of type XP72B22 from

[4] Describes the way the dynodes are arranged inside the PMT, optimized under various aspects like high collection efficiency in all stages, minimized electron transit time spread and to prevent ion or light feedback from the latter stages. For more information, see also [202].

[5] Typical bialkali photocathodes are metallic compounds like Sb-K-Cs or Sb-Rb-Cs with a high sensitivity (respectively quantum efficiency) in the near-UV and blue wavelength regime; more information can be found in [203, 218] for instance.

[6] At 420 nm, which is the reference wavelength in the PMT tests and also the peak output wavelength of the liquid scintillator, the QE is usually reduced by a few percentage points.

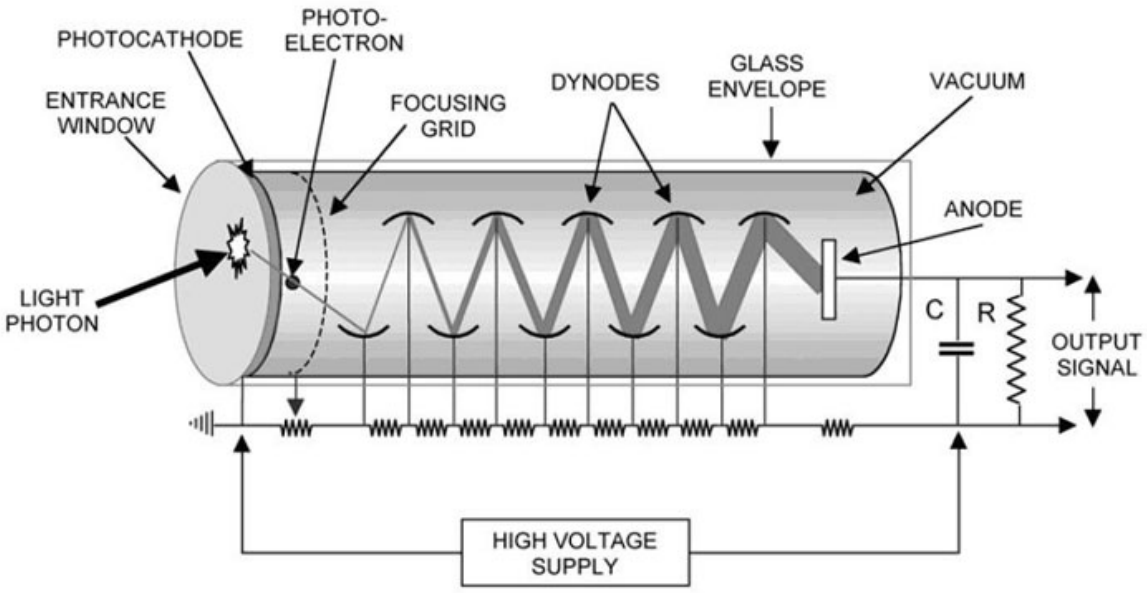

Figure 3.2.: Working principle of a dynode PMT. An incoming photon traverses the entrance window and releases a photo-electron at the photocathode, which is then accelerated by the focusing grid towards a dynode system, consisting of multiple stages with different potentials, defined by the PMT base. Here, the evolving charge cloud is amplified by subsequent impact ionization on the stages and finally directed onto the anode. Image credit: [215].

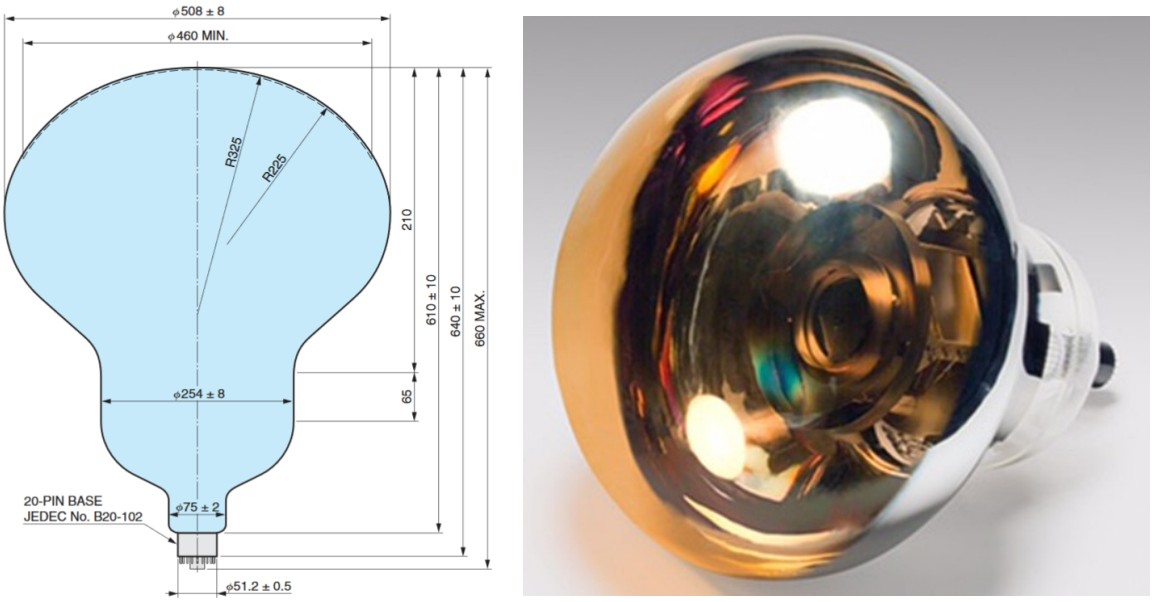

(a) design of a R12860 PMT

(b) picture of a real R12860 PMT

Figure 3.3.: Sketch of the design and size (panel **(a)**) and picture of a real 20-inch PMT type R12860 from Hamamatsu (panel **(b)**), like used in JUNO. Image credits: [216, 217].

company HZC Photonics are used in JUNO. These PMTs have a bulb shaped head on a cylindrical tube and are using a box-and-linear-focused dynode configuration, as well as a bialkali photocathode like the large dynode PMTs [221]. While QE and supply voltage (and also the amplification gain) usually are slightly lower for these PMTs compared to the Hamamatsu ones (see e.g. [222, 223]), the dark count rate is drastically decreased due to their small size. Despite the differences in size, the timing performance of the 3-inch PMTs is comparable to the 20-inch ones.
More information about the small PMTs can be found e.g. in [221, 222].

3.1.2. MCP-PMTs

Micro-channel plate PMTs (MCP-PMTs) are using a different principle for charge collection and signal amplification. In contrast to the dynode PMTs, there is no system with multiple separated stages, but a micro-channel element instead. This element is a piece of a Ni-Cr compound with tiny holes (capillaries with pore sizes between 5 and 50 μm) [224] and set under high voltage. Electrons from the photocathode are accelerated towards this element to hit the openings of the micro-channels. Inside the channels (which often are inclined), these electrons strike the channel walls releasing secondary electrons into the channels. Because of the potential difference between top and bottom of the plate, the electrons are continuously accelerated, strike the walls again and thereby induce the known avalanche effect, like depicted in Figure 3.4. After leaving the channel at the bottom, the charge avalanche is directed towards the anode, where a voltage signal can be read out. Since the interaction of incoming photons via photo-electric effect and the ability of detecting even diminutive amounts of light is the same as for the dynode PMTs, MCP-PMTs aren't principally inferior compared to dynode PMTs (however the performance in some PMT characteristics can differ). The gain of the MCP is defined as ratio between incoming charge entering the micro-channel plate and outgoing charge measured at the anode, similar to Equation 3.4.

For JUNO, in total around 15'000 20-inch MCP-PMTs from NNVT (type N6201) will be deployed in central detector and water pool of JUNO [226]. This PMT type is a very new development from scratch, which was pushed together with the JUNO project by IHEP Beijing and the Chinese company NNVT, located in Nanjing [12, 227–229]. The NNVT PMTs have a more ellipsoidal bulb and a smaller neck than the Hamamatsu PMTs, see Figure 3.5. The micro-channel plate used for charge amplification has a thickness of around 0.5 mm and a channel size of around 12 μm [224]. NNVT also uses bialkali photocathodes for their MCP-PMTs, providing up to $\sim$ 30 % QE at 420 nm wavelength [7] [231, 232]. To increase the overall PDE, the photocathode is not only deposited on the top, but spread on the whole PMT bulb, separated into a transition

[7] In the first batches, NNVT could deliver PMTs with only around 27 % QE in average [173, 230]. During the mass production of MCP-PMTs for JUNO, NNVT improved the PMT performance and established a version with high QE of their tubes, providing average QE values of around 30 % [231]. Around half of the total MCP-PMT sample for JUNO will be of those "HighQE MCP-PMTs" with average PDE values of up to 30 %.

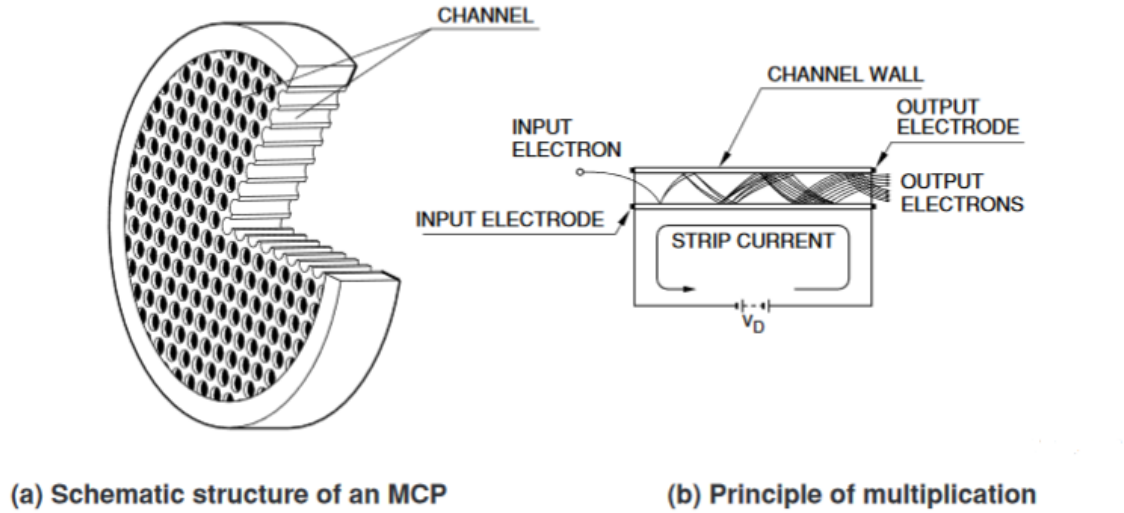

Figure 3.4.: Working principle of a micro-channel plate amplification. In panel **(a)**, a sketch of a micro-channel plate is shown. In panel **(b)**, the multiplication principle is illustrated in a side view of a channel. The incoming electron is scattered multiple times on the channel walls, releasing secondary electrons. An applied voltage on the plate accelerates the electron cloud towards the end of the channels, releasing a charge avalanche in direction of the output electrode (anode). Image credit: [202].

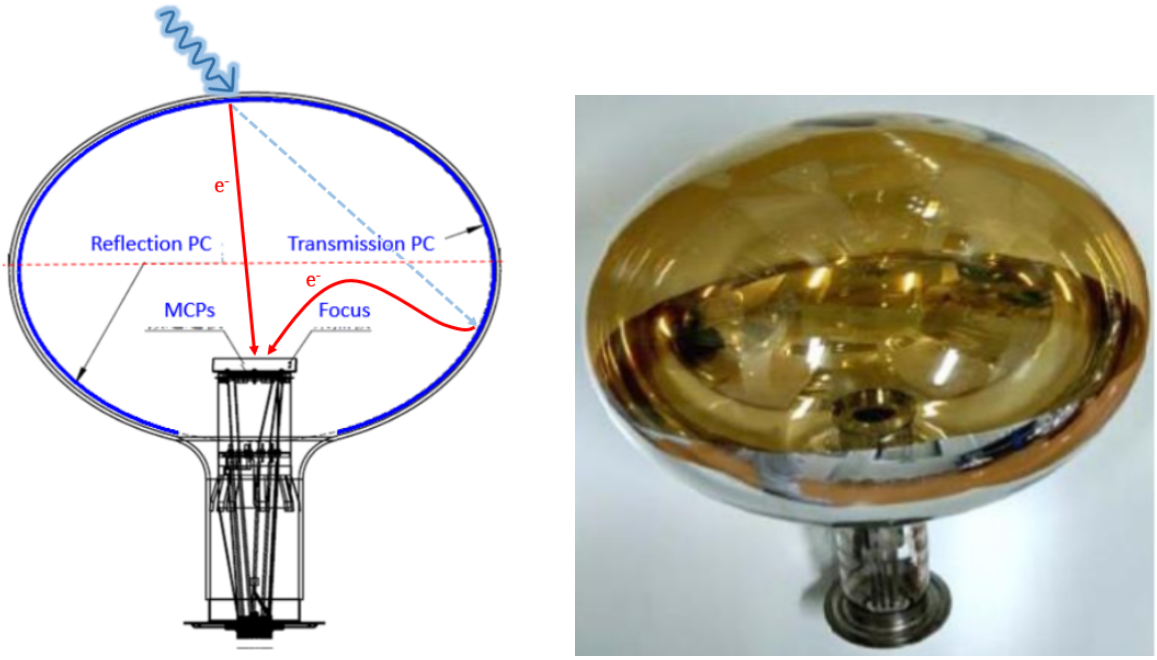

(a) design of a NNVT PMT (N6201) **(b)** picture of a real NNVT PMT (N6201)

Figure 3.5.: Sketch of the design (panel **(a)**) and picture of a real MCP-PMT from NNVT (panel **(b)**) type N6201, like used in JUNO. Transmission photocathode is reaching from top to the PMT equator, the reflection photocathode is reaching from the equator to the PMT neck. Images taken from: [179, 225].

part from top to the equator, and a reflection part from the equator to the neck, where the photocathode on the inside is applied onto a reflective aluminum layer to increase the photo-effect likelihood in this part [173], see also Figure 3.5 again. Further, a specified electric field is applied in order to recollect electrons which didn't hit the micro-channels in first try but rather hit the spacings in between; with this, a high CE of almost 100 % could be achieved using individual supply voltages of 1.5 to 2.5 kV (to provide a gain in the order of 10^7), but at costs in timing performance [231, 233]. More information about this PMT type can be found e.g. in [173, 179, 231, 234].

3.2. PMT System in JUNO

The light detection and so the PMT system is the essential part of the JUNO detector for a successful energy and event reconstruction. It consists of two independent PMT systems, the large (20-inch) and the small (3-inch) PMT system, arranged in a way to collect as much light as possible from events inside the target. For reaching an optical coverage of more than 75 % as noted in section 2.4, the central detector will be instrumented with around 17'600 20-inch PMTs of both types, supplemented by the 25'000 3-inch PMTs placed in the gaps between the large PMTs, see Figure 3.6, providing the necessary coverage of the inner volume [223, 235].

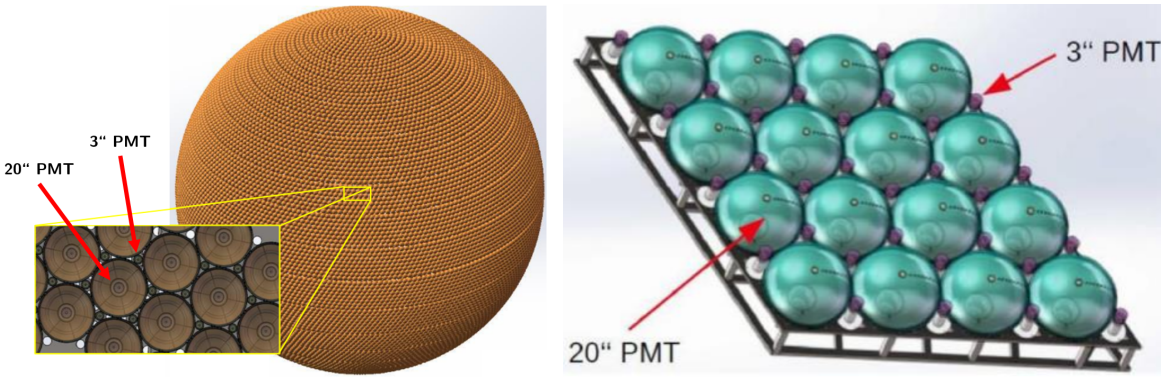

Figure 3.6.: Illustrations of way to group the large and small PMTs together into JUNO. *Left panel:* Simulation of PMTs placed around the CD, with the 20-inch (large circles) and 3-inch PMTs (small circles) stacked closely together, placing the small PMTs within the gaps between the large PMTs. *Right panel:* possible solution of how to mount the PMTs around the CD by grouping them on substructures or panels (in blocks). Image credit: JUNO Collaboration, taken from [169, 187].

All PMTs will be mounted onto the SSS inside the WP of JUNO, facing the central detector volume with around 1.5 m distance as buffer (water and vessel) to the liquid scintillator in the CD (see Figure 2.14 again). The total photocathode coverage of the target volume then sums up to around 78 % [235].
Additional 2'400 20-inch PMTs will be placed in the WP as instrumentation for the water Cherenkov veto. Since the Hamamatsu PMTs have a better timing resolution

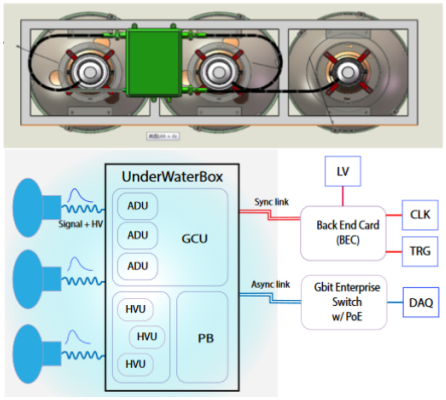

(a) 20-inch PMT (LPMT) UW box design

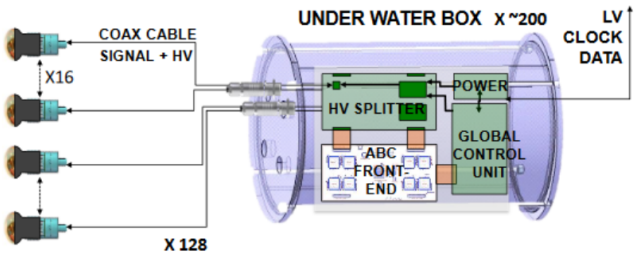

(b) 3-inch PMT (sPMT) UW box design

Figure 3.7.: Underwater electronics systems for the operation of the JUNO PMTs. Large PMTs are connected in triplets to one underwater (UW) box (panel **(a)**), which is housing the digitization and HV units for the PMTs. The small PMTs are grouped in 16, with eight sPMT groups connected to another UW box (panel **(b)**) keeping the respective front-end electronics similar to the UW box of the large PMTs. All UW boxes further are connected with long CAT-5e cables to the back-end electronics, placed outside of the detector. Image credits: JUNO Collaboration, taken from [103, 223].

than the MCP-PMT (see e.g. [231]) [8], all available PMTs of this type will be used around the central detector volume [9].
Due to their size, the 20-inch PMTs (sometimes also denoted as 'LPMT's) form the main light collection system of JUNO, as they contribute the vast majority to the optical coverage of the CD. These "inner" PMTs are connected in triplets with short cables inside of stainless steel bellows and water-tight connectors to underwater boxes, housing most of the operating and digitizing electronics (like HV, trigger organization, ADC units etc.) for the PMTs, see Figure 3.7a. The underwater boxes finally are connected via long CAT-5e cables with a length up to 100 m to the back-end electronics outside the detector [235–237]. All 20-inch PMTs will also become potted (with the PMT base sealed to its neck) and protected by implosion covers, see Figure 3.8, to suppress possible shock-waves in the water tank, if one of the PMTs would burst under the water pressure or by accident (see e.g. [179, 238] for more information). Further, a high radio-purity for the PMT glass must be ensured for all PMTs (see also section 3.3), same as a high reliability for a total failure rate of $< 0.5\,\%$ in the first six years of operation (to avoid negative influences on energy reconstruction and resolution from failing PMTs) [179, 188, 225] and a long lifetime for an expected total operation time of JUNO of around 20 years [17].

[8] Essential parameter here is the transit time spread (TTS), see also section 3.3 for details.

[9] The CD will be instrumented with 5'000 Hamamatsu PMTs and around 12'600 NNVT MCP-PMTs, while the veto will be instrumented with around 2'400 MCP-PMTs only. Position of Hamamatsu and NNVT PMTs around the CD will be randomly / uniformly distributed.

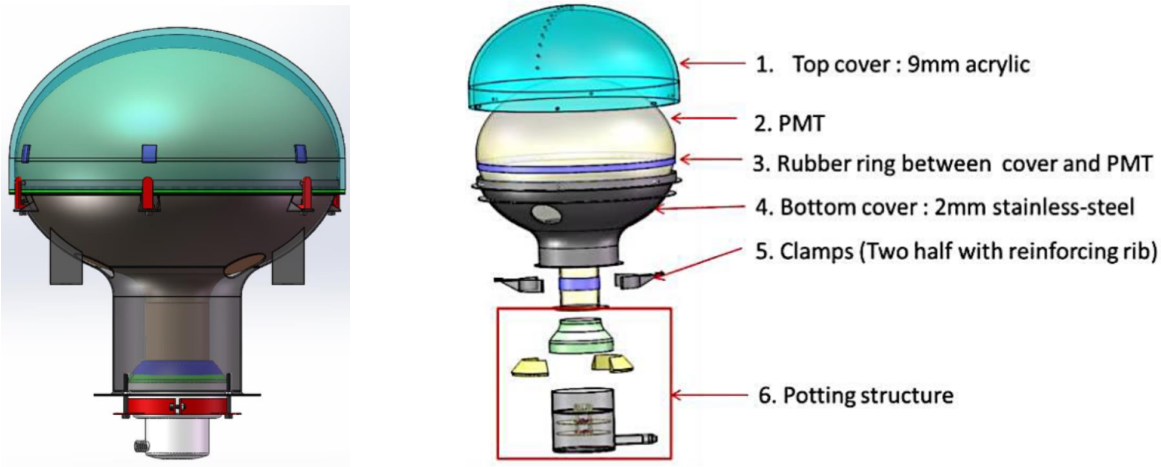

Figure 3.8.: Sketch drawings of PMT protection cover and potting of JUNO PMTs. All large PMTs mounted into JUNO will get such a protection housing to avoid creation of shock-waves in the surrounding liquid in case of a tube breaking. The PMT base will be waterproof encapsulated in the potting structure and glued to the PMT pins. Image credit: JUNO Collaboration, taken from: [179, 225].

The 3-inch type XP72B22 PMTs (sometimes denoted as 'sPMT's) from HZC Photonics contribute around three percentage points to the total optical coverage of the CD. They are connected in groups of 128 to a different set of underwater boxes, see Figure 3.7b, providing HV to the PMTs and processing the PMT signals before guiding to the back-end electronics [222, 223, 239]. The small PMTs are only used for the CD instrumentation, but not for the water Cherenkov veto system.
Since both LPMT and sPMT systems are grouped and operated separately, they can be used as a double-calorimetric system [240, 241]. This will be beneficial especially in luminous events like cosmic muon or supernova events [10], or for a better control of systematics by a cross-calibration of the LPMT system, which will reduce nonlinearities and will give the detector a greater dynamic range and granularity [242].

Since external magnetic fields, in particular the Earth's magnetic field (EMF), could influence the performance of the PMTs, all PMTs need to be placed in a sufficiently field-free environment. Due to their large size, the 20-inch PMTs would be affected the most by the EMF, so an effective magnetic field compensation is inevitable to guarantee a good performance and maximum possible PDE [12, 243, 244]. To provide this, the whole inner detector including all PMTs around the acrylic sphere will be surrounded by a large coil compensating the EMF inside to a level of less than 10 % (w.r.t. the uncompensated field strength), see [244] for instance. The central axis of the coils must match the field vector of the magnetic field for best compensation.

[10] The small PMTs run almost always in single p.e. counting mode (also for higher energetic events), due to their small size [223, 240].

3.3. Characteristic PMT Parameters and Quality Requirements in JUNO

For neutrino detectors using PMTs like JUNO, their performance is driving the accuracy and resolution of energy, position or tracking and time measurements, which are critical factors for the physics potential [201]. Consequently, in order to ensure that JUNO will achieve the aimed energy resolution with the just presented PMTs, the definition of detailed performance requirements and quality criteria for both PMT types is necessary.

In the following, short physical descriptions of all PMT parameters of interest are given based on [202, 203, 214]. This shall serve to establish a basic understanding, which PMT parameters are important and have influence on the performance of the JUNO detector and why there is a need for checking all PMTs for their actual capability before installing them into the JUNO detector. Hence, it also motivates the development of a testing system for the large PMTs, which was main topic of this thesis and will be presented in the subsequent chapters. Another, detailed description based on how these parameters can be determined is examined later in chapter 7, also including illustrations defining the respective parameters based on real PMT raw data samples.

- The **Photon Detection Efficiency (PDE)** determines the PMT's ability to detect photons and is the product of collection and photocathode quantum efficiency, see Equation 3.3. The PDE value represents the integrated efficiency for photon detection via release of photo-electrons over the whole PMT photocathode and collection by successfully accelerating it towards the multiplication system. Together with the dark count rate, the PDE is the most important PMT parameter for a quality examination, as it can have direct impact on the energy resolution of JUNO [201], see also section 2.4 again.

- The **Dark Count Rate (DCR)** is the rate of signal events not originating from photon interactions at the photocathode (meaning photon-induced release of electrons) and thus being background to the real signal. In intermediate operating voltage regime, these events mostly are randomly generated electrons from thermal excitations in the photocathode following Richardson's law. Thus, the DCR strongly depends on the temperature during the measurement [11] [245]. Besides thermionic emission, dark count events can also be produced by leakage currents, glass scintillation, field emissions or background radiation [203].

[11] Also a possible illumination of the photocathode with e.g. daylight preceding the measurement can strongly increase the actual dark rate of the PMT, due to residual photo-absorptive excitations in the photocathode. This effect decays over time when the PMT stays in darkness, unless the DCR stabilizes to a certain (only temperature-depend) value, which then is characteristic for the PMT. This effect will also be mentioned several times as "PMT cool-down" in the following chapters (e.g. in section 5.1 and section 5.2 during the discussion of the PMT measurement procedure).

Randomly released dark count electrons act like photon-induced ones, since they produce the same signals at the anode stage and consistent charge spectra as for measurements with low light intensity [246]. In measurements using pulsed light sources, dark counts become distinguishable from photon-induced events by their non-coincident appearance respective to the dedicated external triggers, and so can be suppressed effectively. If only the dark count rate is of interest, dark pulses can also just be counted [12].

- **Rise Time (RT)** and **Fall Time (FT)** of single photo-electron (SPE) events are pulse shape characteristics generated by and depending on the individual PMT. They usually are defined as the time differences, in which the output pulse rises from 10 to 90 % (falls from 90 to 10 %, respectively) of its peak pulse height, thus describing how fast the charges can be accumulated on the PMT's anode or discharge from it.

- The **Transit Time Spread (TTS)** defines the jitter of transit times of photo-electrons, which are their propagation times from photocathode (arrival of a delta-function-like light pulse at the photocathode releasing an electron) to anode (e.g. peak of output pulse). This propagation time can vary, for example due to different release positions on the photocathode or scattering of electrons with residual gas in the PMT, but also depends on the shape of the PMT glass bulb, the design of the focusing electrodes and the applied voltage [201]. The TTS defines the timing resolution of the PMT and thus also affects the position resolution (and reconstruction) of point-like particle events in the detector [201]. It can be specified as either FWHM value or standard deviation σ of the transit time distribution; if the distribution is Gaussian-like, both values are linked via $\mathrm{FWHM} = 2\sqrt{2\ln 2}\cdot\sigma$.

- The **Peak-to-Valley Ratio (P/V)** describes a feature of the PMT's charge spectrum, which is the ratio between the maximum of the SPE peak and the valley between pedestal (non-photon peak produced by noise-only events) and SPE peak. This is also described and illustrated more clearly in subsection 7.3.2. The P/V ratio is kind of an empiric (phenomenological) PMT parameter about the ability of resolving charges from baseline noise events.

- The **Prepulse Ratio (PPR)** describes the ratio of slightly premature pulses compared to other photon-induced pulses, which can occur if the initial photo-electron directly hits the second dynode first or electrons in the charge avalanche skip one stage of the multiplication system [247, 248]. Prepulses can be released also, if the incident photon traverses glass and photocathode without being absorbed and directly strikes the first dynode or collection electrode [201].
  Prepulses usually deposit less charge at the anode than non-prepulses, due to the

[12] In this case, to better separate "physical" dark counts from baseline or electrical noise, usually only events with peak amplitudes above a certain threshold (e.g. 0.25 p.e.) are counted. This will be discussed also in section 5.1.

missing amplification of the (first) stage(s). The PPR represents the contingent of such premature pulses heading "normal" pulses.

- The **Afterpulse Ratio (APR)** describes the occurrence of afterpulses, which are spurious pulses created by charges from secondary processes in the PMT [203]. Afterpulses can be separated into two classes: pulses with only little delay to the initial pulses, which are often also denoted as **Late Pulses**, and pulses with longer delays of up to few μs to the initial pulses, which are the "real" **Afterpulses**. These two classes separate also by their production mechanism: late pulses can originate from UV photons (bremsstrahlung) created by stopping electrons on the dynodes and reaching the photocathode, thus producing a new, yet delayed signal [203]. The probability for the production of these luminous late pulses is the largest at the last dynode, since the absolute number of electrons hitting this dynode is the highest. Also, elastically back-scattered electrons from amplification stages (this time mainly from the first dynode) can become re-accelerated towards the dynode system and produce a late pulse [13] [247, 248]. Depending on the production mechanism, late pulses usually occur between 20 and 100 ns after the initial pulses, depending e.g. on the applied voltage and the transit time of charges through the amplification system. Afterpulses arise, if photo-electrons hit and thereby ionize residual gas atoms on their way to the amplification stages. These ions then slowly drift towards the photocathode due to the applied electric field, where they can release delayed electrons by impact ionization again [249, 250]. Such ionic afterpulses typically occur between a few hundred ns and several μs w.r.t. the true pulses from which they originate [203]. Both mechanisms (for late and afterpulses) increase in probability to happen for high luminosity and so high charge events.
  The afterpulse ratio is defined as the ratio of the integrated charge of all afterpulse events in a certain time window (e.g. $[0.5, 20]$ μs) after an initial (often luminous) pulse, compared to the charge of this "main" pulse. In parallel, also a **Late Pulse Ratio (LPR)** similar to the PPR can be defined.

- The **Operating High Voltage (HV)** is defined as voltage which needs to be applied to the PMT in order to produce a certain gain in the amplification system (in the case of JUNO, a gain of 10^7 is desired). The HV is then distributed by the PMT base to the different stages of the amplification system and the focusing electrodes; information about the bases of the used PMTs can be found in [179].

The so far listed parameters are expected to show sizable variations from tube to tube, since they are individual PMT characteristics and are connected to material properties of the used components (like individual thermal emission coefficients, thickness of deposited photocathode material etc.). These criteria must then be tested for every single PMT.

[13] The amplitude of these late pulses depends on the residual kinetic energy of the back-scattered electrons and thus can be smaller than for the main pulses.

Aside from these, some other characteristics, which are connected to the PMT design and method of production, are expected to show only small variations. For these characteristics there are certain quality criteria defined as well, which should be equally considered before a use in the JUNO detector, but they are not intended to be checked for all PMTs individually [14] (due to the expected small variations). This class of parameters is listed in the following. As these criteria are of only minor interest in the following chapters, they will be only named and shortly described here; continuative information (including plots, measurement descriptions, considerations about their impact on JUNO etc., if available) can be found in the given exemplary references.

- **Charge Response Nonlinearity**: High luminosity events, which generate a large number of photo-electrons in parallel, can cause saturation effects in the amplification of the signals, so that their final pulse height suffers from missing charge with respect to the initial number of generated charges at the photocathode and the applied gain. This saturation effect causes a deviation from the formerly linear relation of pulse height or anode peak current to initial charge, usually starting at events with several hundred of photo-electrons. A high charge response nonlinearity could lead to an underestimation of energies reconstructed from highly energetic events in the JUNO detector. See e.g. [202, 251] for more information.

- The **QE Non-Uniformity** defines the degree of deviation of the actual QE at a certain point on the photocathode to the average QE value integrated over the whole photocathode (or to the QE value at the center of the PMT). Ideally, the QE would be constant over the whole photocathode. See e.g. [202, 231, 243] for more details.

- The **Spectral Response** of the photocathode describes the wavelength regime, in which the PMT photocathode is sensitive to photons for undergoing a photo-electric effect. The regime is usually cut off at wavelengths for which the QE drops below the 1 % level and ideally should peak in the region of the emitted photon wavelengths (of e.g. the used liquid scintillator, see Figure 2.15 again). See e.g. [214, 220, 231] for more details.

- The **(Geo)magnetic Field Sensitivity** sizes up the direct influence of external magnetic fields like e.g. the EMF on PMT parameters like gain and total CE of released photo-electrons. This effect is due to Lorentz force on transiting charges in the PMT. The magnetic field sensitivity usually rises with diameter of tube or travel distance of charges inside the PMT, respectively [203]. The

[14] A large non-uniformity in QE should have a considerable influence on the total PDE of the PMT, since it's only expected to have regions with lower QE on the photocathode and very unlikely to have regions with extraordinary high QE. So if the QE non-uniformity is exceeding the permitted limits, likely one can see also "negative effects" (namely a low PDE) in a PDE measurement. Thus, kind of an "indirect test" for larger QE non-uniformities can be assumed as performed for all PMTs as well.

actual sensitivity also depends on the relative orientation of the field vectors to the PMT axis. For the used 20-inch PMTs in JUNO, even the EMF has large influence on the PMT performance and therefore should be suppressed in both the PMT tests and the final experimental setup, see e.g. [252].

- The residual **Radioactivity or Radio-purity** of PMTs describes the remaining radioactive contaminations in the PMT glass, consisting mostly of ^{238}U, ^{232}Th and ^{40}K. These contaminations can contribute to dark counts, as well as spill into nearby scintillator area, producing unwanted background events in the experiment, see section 2.3 again or [253] for instance for more details.

Instead of individual tests, checking a representative sample of PMTs could already provide enough information to satisfy the needs of a reliable quality assurance for these criteria. Such sample tests are (or will be) performed, partially also in close discussion with the manufacturers (see e.g. [243, 251, 253] for more information), but will not be discussed further here.

As already explained, the energy resolution of the JUNO detector is directly connected to the efficiency of the PMTs, for which reason it is crucial for the success of JUNO that the designated PMTs show a satisfactory performance in all the discussed parameters. Therefore, a list of PMT requirements has been set up by the JUNO management and fixed in contracts for delivery with the PMT manufacturers, see e.g. [12, 201, 243, 254]. Each PMT has to meet certain minimal requirements for the itemized parameters individually, while also the whole PMT batch needs to reach defined values in average for selected parameters as well; this must be tested in dedicated tests for each PMT individually.
The list of requirements is shown in Table 3.1. All noted values assume an applied gain of 10^7 and a temperature of 22° C (which is important in particular for the DCR, see above). Since the listed parameters must be checked for every single PMT, the respective values define acceptance criteria for the PMTs in the to-be-performed tests for a use in JUNO. Assuming these criteria will be fulfilled for all PMTs, JUNO should be able to achieve the aimed energy resolution [15] [201].
In addition to the performance characteristics, also strict visual quality constraints have been defined, regarding defects in the glass of the PMT bulb (bubbles, scratches) or the photocathode (scratches, inclusions) [255, 256], which are inspected in visual checks on all PMTs. These criteria are discussed as well within the JUNO collaboration and fixed in the contracts with the manufacturers, but are not of interest in this thesis and thus aren't listed as requirements in Table 3.1 either. Moreover, all PMTs tested for the listed requirements (as e.g. presented later in chapter 8) have been checked and passed the visual requirements beforehand (see e.g. [257]).

[15] Whether JUNO can meet the aimed energy resolution also depends on whether all other components like liquid scintillator, electronics etc. meet all their requirements.

Table 3.1.: List of performance requirements for PMTs of both types used in JUNO, as specified in [201, 254, 258]. Given limits ('Min.'/'Max.') are valid for each individual PMT, 'typical' values define average values for the whole PMT batch. Parameters investigated with the Container System (described in chapter 4, all PMTs) and/or the Scanning Station (in sample or cross-check test) are indicated via check-marks. APR should have been tested also by the container system, but is now going to be tested only in batch tests due to design restrictions in the mass testing system, see section 5.1.

Parameter	unit	tube type	Min.	typical	Max.	Tested with Cont./SS
PDE @ 420 nm	%	both	24.0	27.0	–	✓/✓
P/V ratio of SPE	–	Hamamatsu	2.5	3.0	–	✓/×
		NNVT	2.5	3.5	–	
DCR @ 0.25 p.e.	kHz	Hamamatsu	–	20	50	✓/✓
		NNVT	–	–	100	
Rise Time	ns	Hamamatsu	–	–	8.5	✓/×
Fall Time	ns	Hamamatsu	–	–	12.0	✓/×
Supply HV (@ $G = 10^7$)	V	Hamamatsu	–	2000	2350	✓/✓
		NNVT	–	2000	2800	
TTS (FWHM)	ns	Hamamatsu	–	2.7	3.5	✓/×
		NNVT	–	12.0	15.0	
PPR	%	Hamamatsu	–	0.8	1.5	✓/×
APR	%	Hamamatsu	–	10	15	(✓)/✓
		NNVT	–	1	2	
QE Non-Uniformity	%	both	–	5	15	×/✓
Non-Linearity < 10 %	p.e.	both	1000	–	–	×/×
Spectral Response	nm	both	–	300–600	–	×/×
Res. Radioactivity of glass (^{238}U)	ppb	Hamamatsu	–	–	400	×/×
		NNVT	–	–	50	
(^{232}Th)		Hamamatsu	–	–	400	
		NNVT	–	–	50	
(^{40}K)		Hamamatsu	–	–	40	
		NNVT	–	–	20	

The system developed in scope of this thesis was able to measure most [16] of these individual PMT parameters (indicated by check-marks in Table 3.1) and thus exactly to perform the necessary tests for a reliable PMT selection for JUNO. Since this system is equipped inside of commercial shipping containers, it will be denoted in the following as **Container System** for simplicity. The container system will be presented in chapter 4 and the following chapters.

Aside from to the container system, a complementary system for examinations of single PMTs were developed, with main focus on the QE homogeneity of the photocathode. This system developed by a group from JINR, Dubna, is able to scan over the whole photocathode and thus to determine local gain and PDE of the PMT with high spatial resolution. This system therefore is called **Scanning Station (SS)**. Such QE non-uniformity measurements are not possible with the container system. Later, also a system optimized for an afterpulse measurement was integrated into the scanning station, see [259, 260].
The scanning station is intended for batch tests of randomly selected PMTs, but acts also as individual system to cross-check measurement results from the container system like overall PDE or DCR [17]. This is especially important, if PMT results from the container system are close to the acceptance criteria listed in Table 3.1 (the actual procedure of the PMT testing will be described later in subsection 4.2.2).
More details about the scanning station can be found in [243, 261] for instance. Since the SS is not part of this thesis, it will not be presented in detail in this work.

[16] All parameters with expected variation in characteristics from tube to tube can be tested with the container system, except the afterpulse ratio, which was not possible to be tested in a sufficient way by the mentioned system. This was mainly due to design restrictions for the optimal light intensity of the used light sources as well as due to limitations of the used electronics modules in the testing setup, which didn't allow ideal conditions for a reliable APR measurement. This will be discussed also in section 5.1.

[17] Due to the expected drop in total PDE in case of large deviations in QE over the PMT's photocathode, the container system can indicate possibly deficient PMTs to be tested for QE non-uniformity by the scanning station, as considered before.

Chapter 4

The Container Based Mass Testing System for Photomultiplier Tubes

This chapter describes the realization of a setup for the individual testing of all 20'000 20-inch PMTs for JUNO, as concluded from the discussion about the PMT requirements in section 3.3. The setup uses in total four commercial shipping containers as main measurement frame and thus is referred as **Container System**, like already noted in the last section. It also constitutes the main work of this thesis.
PMT testing facilities already have been developed in the past for previous experiments, as e.g. IMB [262], Borexino [263, 264], Chooz [265], Auger [266], LHAASO [267] or KM3NeT [268, 269]; however, this will be the first testing facility for 20-inch PMTs, which further has to deal with a significantly higher number of PMTs than in most of the cited setups.

The PMT testing facility for JUNO setup shall be presented in detail, starting with a motivation for the choice of shipping containers as main tool for the PMT testing (in section 4.1). Next, some preconditions for the development of this testing system will be summarized, specifications for the design of the measurement system will be defined, and the final implementation of the PMT mass testing processes for JUNO using the developed container systems will be described (see section 4.2). This section is placed before the actual description of the setup, because the design actually relies to some extent on the suitability for a daily use by frequently changing users (which will be discussed in this section as well). In the subsequent sections, the design of the PMT mass testing will be explained, focusing on the interior structure and mechanical design (see section 4.3), the installed operating and data taking electronics (see section 4.4) and the internal light system the containers are equipped with (covering the light sources, mechanical parts and studies about of the light field, see section 4.5). At the end, the design adjustments applied on the two of the four container systems for the potential operation using the final JUNO electronics in the testing systems will be discussed (see section 4.6). More continuative descriptions about the measurement program and the implemented data acquisition software as well as about the basic performance of the realized systems will be given in the subsequent chapters.

4.1. Motivation and Overview

As pointed out in chapter 2, to ensure that the JUNO detector will be instrumented only with well performing PMTs in order to reach the aimed energy resolution of $3\,\%/\sqrt{E\,[\mathrm{MeV}]}$ at the end, it's important to check all these PMTs to fulfill certain quality criteria. This is in particular important for the 20-inch PMT system [1], since it contributes to more than 95 % of the optical coverage of the central detector volume (see section 3.2 again).

The necessity for a testing and characterization procedure of such a huge number of large PMTs makes it inevitable to set up a system, which is capable to perform a large number of tests in a reliable, comparable and reproducible way. The requirements for such a system are twofold: "operational" and "scientific / instrumental".
Operational constraints are set by the higher-level project management and the necessary measurement conditions. Since the PMT testing should not affect the overall project schedule (start of data taking with JUNO in 2022), the system should be able to complete all test runs in a reasonable time – meaning that a suitable number of PMTs has to be tested in parallel to fit the estimated total number of test runs into the schedule. In a back-of-the-envelope calculation, estimating around 50 working weeks per year including five working days each and considering that every PMT should be tested twice (bare and potted), it would need at least 80 testing channels to check 20'000 PMTs in a total time of two years, assuming a 24-hours testing cycle each PMT has to pass for a full characterization. Further, such a system must be able to perform a variety of different measurements inspecting all the different PMT characteristics described in section 3.3. In best case, these measurements should be done in a fully automated way in order to reduce the work load for people running the system, avoid mistakes or accidental changes of settings or conditions between different runs and therefore ensure comparable results for all 20'000 PMTs.
Instrumental constraints are, that for every batch of PMTs to be tested in parallel (as calculated in the example above), the intended setup has to provide enough measurement places in completely dark surroundings. The places should be optically and spatially separated to avoid crosstalk from the neighboring measurement places, caused e.g. by possible flashing events from bad PMTs (or the PMT bases) or scattered photons from light sources not belonging to the corresponding testing channel. Furthermore, the whole setup has to be free of geomagnetic field influences, which could spoil the measurements and dramatically decrease the PMT performance dependent on the orientation of the PMT with respect to the EMF vectors, see [243, 270] for instance. These measurement conditions together with the environmental conditions

[1] The 3-inch PMT system should also pass through a testing procedure beforehand, but since these PMTs only collect few photons (mainly from higher energetic events) and have an intrinsically good timing performance due to their small size [221, 222], a dedicated characterization of these PMTs is not as crucial for the success of JUNO as it's the case for the large PMTs. More details about the testing of the 3-inch PMT system can be found in [222, 223].

inside the system should be stable not only during a single run, but ideally over the whole period of testing PMTs. A stable and consistent environment is crucial to get comparable, reproducible results. Also, comprehensible and fair specifications for the manufacturers are obligatory, which also necessitates a dedicated calibration of the channels.

These constraints culminate in the use of commercial shipping containers as frame for a dedicated PMT mass testing facility. The choice for these commercial shipping containers provides a lot of advantages which directly fit to the considerations above:

- The interior of such a shipping container offers enough space to host numerous PMTs for testing and characterizing. By equipping the interior with a box system and thus subdivide the room in multiple small sections, the PMTs can be placed in isolated positions from each other within the container. The existing space usage can be optimized for keeping as many PMTs as possible in one 'run', making it a real multi-channel system.

- As long as the container is closed, the interior is already a dark room as no light from outside should be able to come in. Conditions can be further improved by painting the inner walls and all substructures black to minimize reflections and stray light from the light sources and thoroughly take care for light-tightness, in particular around weak spots like the door and the indispensable cable feed-through to the outside.

- The chosen (reefer) containers already have an intrinsic heat insulation. In additional, the ones selected for the PMT testing facility include a ThermoKing HVAC (heating, ventilation and air conditioning) unit. This installation can control the temperature inside the container in the range from $-20°C$ to $+45°C$ and thus guarantee for a stable measurement environment. Since the container system will be placed also in an air-conditioned storage hall, the outside temperature and air humidity is assumed to be kept relatively stable as well, especially over the seasons. Hence, a stable measurement environment can therefore be taken as guaranteed [2].

- Commercial shipping containers are natural Faraday cages, which shield the interior from electromagnetic interferences and background. This is helpful for noise reduction in the measurement channels. In addition, to assure the PMT performances won't be compromised by the influence of stable magnetic fields, i.e. the EMF, the residual magnetic field inside the containers has to be suppressed to a level of less than $10\,\mu$T, see e.g. [12, 243, 271]; perfectly suitable would be a level of around 10 % of the EMF or below. This can be reached by revetting the container walls with a magnetic shielding, generating an almost field-free volume inside the container (see also section 6.1 for details).

[2] The environmental conditions inside the containers will also be monitored in the final setup by a dedicated temperature monitoring system, see subsection 4.4.2.

- The system is scalable. By using not only one but several containers, the number of channels can be multiplied without changing the design or requiring additional R&D work. Further, having multiple identical systems offers flexibility in use, for example for running short or daily tests, long term tests or tests with bare and potted PMTs in parallel, with none or only minor adjustments of the system.

- And finally a very pragmatic reason: A setup in a shipping container is versatile, which allows to develop and construct the system in Germany and then ship everything to the experimental site, where the PMTs are stored (in principle independent from the location, except for some basic conditions enough space for operation, sufficient power supply etc.).

Considering all these items, a dedicated, multi-channel PMT characterization system installed into commercial shipping containers as experimental frame was a successful approach towards a mass testing of ten thousands of 20-inch PMTs for the JUNO experiment. In total, four containers (shown in Figure 4.1 at their final destination in Zhongshan, China, labeled as container 'A' to 'D') were equipped with mechanical structures and an elaborated light system, providing **136 independent channels** in total (2×36 plus 2×32 channels). Two containers were fully equipped with commercial electronics for operation and readout of all "loaded" PMTs in parallel, controlled by a custom-made software based on LabVIEW (see section 5.2 for more information), while two containers were slightly modified in design for the use of the final JUNO electronics for PMT operation and readout (see section 4.6 for details) [3]. Mechanical structure, electronics and light system of these container systems are described in the following sections in all details.
All together, the system has the ability to run an extensive testing program for all 20'000 uncharacterized PMTs and therefore complete all PMT tests in a manageable time of a few years. It is worth to note here, that even the two fully equipped container systems provide enough channels (in total 72) to complete the PMT testing within the aimed schedule of JUNO [4].

4.2. Aims and Specifications

Main purpose of the container system is to provide a smart solution for the individual PMT tests, dealing with the sheer number of 20-inch PMTs in JUNO. Every PMT

[3] These containers are intended to test (potted) PMTs in the final JUNO configuration, which included the use of the underwater electronics (although the operation will be in air instead of water), see [179, 225, 238] for instance.

[4] In comparison to the simple calculation at the beginning of this section, the full testing period was extended to more that 3 years until 2021 (expected) with in average 5.5 working days per week. The prolongation of the testing phase was caused (enabled) by delays in the overall schedule of JUNO. On the other hand, this also allows the system to include reference PMTs to the regular runs, as well as to perform retests of PMTs with performances close to the acceptance criteria from Table 3.1, without adding tension to the total schedule of the PMT testing (see also subsection 4.2.2).

Figure 4.1.: Pictures of the container system at the storage hall in Zhongshan, P.R. China. *Top panel:* view on all four containers, A to D numbered from right to left. *Bottom panel:* containers B and A (fully equipped with commercial electronics), which are used for the regular PMT testing phase; control terminal of container B is visible in the middle.

should be tested at least once in the container system, which is after delivery as bare PMT. They can be tested also a second time in the container system after the potting of the PMTs [5], which will be done at least for a representative fraction of them.
The characterization of such a huge number of PMTs is only possible with fixed routines, double-checks in all processes and a good documentation. The testing procedure also requires a well organized work flow at the storage and testing site in order to neither mix up tested and untested PMTs, nor become a bottleneck in the overall schedule of JUNO. Moreover, operation and handling of the whole system should be easy enough to avoid mistakes and to be quickly learnable for new operators [6]. Similar to an industrial project, such routines and processes should imply high levels of automation and repetition, wherever feasible and reasonable [7]. Last, the accuracy of the system has to guarantee reliable results for individual PMT evaluations.
Hence, beside the definition of quality criteria for single PMTs, also conditions for both the operation of the system and the full testing process need to be defined and worked out. These conditions for the basic operation and specifications for accuracy of the container system will be discussed before presenting the setup of the container system in detail in the following sections, as these also have had impact on the final design of the container system. A discussion on decisions from individual PMT testing results (about what defines a PMT as qualified and what as unqualified in particular) is not included here, but will be given later in subsection 8.1.2 based on an exemplary data analysis and the criteria listed in Table 3.1.

4.2.1. Design Goals and Specifications

To guarantee reliable results from the PMT characterization measurements, design goals for the accuracy of the container system for respective parameters have been appointed. These specifications are listed in Table 4.1.
The listed parameters represent the most important PMT characteristics and therefore their measurability is of special interest. Moreover, the listed accuracy design goals are both well motivated and reasonable:

- An accuracy of 1 % absolute uncertainty for the PDE for example is sufficient regarding a discrimination of proper and improper PMTs. 1 % of absolute uncertainty corresponds to around 3-4 % of relative uncertainty [8]. In case of results

[5] "Potting" means the base sealing on the PMT neck as preparation for the underwater use in the JUNO experiment, see section 3.2 again or e.g. [179, 238, 272].

[6] Container operators will also called "shifter" in the following since operation and data taking cannot be controlled by a single person for more than two years. Thus, a shift system with alternating operators (shifters) was introduced.

[7] Despite these basic considerations, a full automation is of course impossible within this project, but a high manpower and manual work is still necessary. Nevertheless, the system provides basic conditions for an experienced operation within a daily program.

[8] Assuming an average PDE of $\sim 27\,\%$, but depends also on the wavelength, present noise level and systematic uncertainties of the system.

Table 4.1.: Design goals for the accuracy in measurements of several key PMT parameters in the container system, based on [273, 274]. Definitions for the actual parameters based on the PMT data can be found in chapter 7.

Parameter	Design / Accuracy Goal ($1\,\sigma$)
PDE	$\lesssim 1\,\%$ absolute
DCR	$\lesssim 1\,\mathrm{kHz}$
RT/FT/TTS	$\lesssim 1\,\mathrm{ns}$
S/N	≥ 10

close to the edge of the defined acceptance criteria, PMTs can be double-checked or investigated further in the scanning station. On the other hand, a more accurate determination of the PDE in the container is hardly feasible: the accuracy here is limited by systematics in the light field and statistical limitations since the applied light intensity will be very weak (see also subsection 4.5.4 and section 5.1). In addition, the PDE measurement can be performed only relative to a well-known reference but not absolute (see also section 5.1 for details), so that further external uncertainties could be imported by the reference PDE values.

- Opposed to the PDE, the design specification for the DCR measurement describes the acceptable level of remaining noise on the channels and thus the desired cleanness of the setup. Investigations of the actual noise level in the containers will be presented later in section 6.3.

- The timing specification considers the possibility of resolving and determining parameters on even short time scales with the container system, like RT, FT and in particular TTS. The realization of these accuracy goals is mainly connected to the interplay of performance of the data taking electronics, light sources and respective trigger provision.

- The aimed signal-to-noise ratio (S/N) defines the acceptable baseline noise level in the overall system and the electronics. While the residual noise is discussed in section 6.3, a formal definition of the S/N ratio will be given in subsection 7.3.2.

The listed requirements have been considered in the development of the container system, as done e.g. by the choice of the light sources (see section 4.5). The final accuracies of the system for the individual parameters like PDE, DCR and timing parameters will be discussed later in subsection 8.2.6.

4.2.2. Daily Routine in PMT Testing

Around the running system, a stable workday routine fitting to the continuous operation of the container system has been established. As already noted, since the needs for a use in a daily routine were considered during setup of the PMT mass testing

system and also have had an influence on the development of the full setup, the routine operation shall be discussed here even before the actual setup.

The following overview describes the testing procedure for bare PMTs within a 24-hours routine, which has been established on-site since the start of the regular testing phase in 2017. This routine is repetitive and double-checked by several shifters at each step in order to avoid mistakes. Concerning the constraints for the operation, the system was equipped with a highly automated data acquisition software (DAQ) controlling all relevant electronics and independently performing all measurements. It is uncomplicated in handling and easy to learn even for non-exercised shifters. The use of an automated DAQ minimizes the risk of accidental changes in measurement settings by the shifters and leads to a reduction of the individual work load. The total runtime was tailored to fit into the 24-hours routine, including reloading of the container; all necessary interactions between shifters and container operating software are fitting within a standard workday of roughly eight hours. The DAQ will be presented later in detail in section 5.2.
The list below focuses on the operation of the system and describes only parenthetically the physical measurement program; a detailed description of all PMT characterization measurements performed with the container system is given in section 5.1. Some of the mentioned steps are further illustrated in Figure 4.2.

(i) The container is loaded with PMTs (up to 31 untested and 5 reference PMTs [9]) usually in the afternoon after the preceding run has been finished. PMTs are prepared outside of the container and then carried into the container using a mini-lifter, see illustration in Figure 4.2a.

(ii) The new container run starts at the end of the workday with some initial tests. If connection problems between PMTs and electronics are detected, the operators can improve the situation or even replace a PMT or PMT base, before continuing the main part of the run. The PMTs then are resting in darkness over night, so that their dark count rate can stabilize after the unavoidable illumination of the photocathode with daylight during the loading phase.

(iii) The first regular measurement of the container system is the determination of the optimal high voltage for a gain of 10^7 in all channels, which is executed usually in the early morning of the next workday. Data from this measurement needs to be analyzed by the shifters for a respective adaption of the high voltage. After the voltage has been adapted, all other measurements are performed automatically by the DAQ.

[9] The reference PMTs are a selection of few PMTs with good performance, which will be characterized together with the untested PMTs in every container run, one with a fixed position and up to four with changing positions inside the container. These PMTs are used to monitor the stability and performance of the system over the full period of operation, see also section 8.2.

(iv) In parallel, PMTs for a new container run can be prepared. These PMTs have been visually checked for damages beforehand, see illustration in Figure 4.2c. Information about the position of the PMTs in the new run must be prepared and later provided to the DAQ control.

(v) As soon as the measurement procedure is completed, the data can be uploaded to the server and preliminary analyzed, which is usually finished in the early afternoon. Afterwards, the containers can be unloaded and reloaded with new PMTs again, which have been prepared before (see step (iv)).

In order to support the shifters in their daily work, several tools for the PMT mass testing were purchased: to increase safety during handling the PMTs, an electrical mini-lifter for PMT transportation is part of every container system. The PMTs prepared for loading can be fixed onto its transport platform and carried into the container. With the lifter, the PMT can be raised or lowered to the respective height of its predetermined measurement spot. For better sight during the loading, the container inside is equipped with a commercial red light LED sleeve [10], which can be switched on during loading and unloading.

Based on the results of the data analysis in step (v), the tested PMTs can be classified and labeled according to their performance. If all criteria listed in Table 3.1 are fulfilled, the PMT is accepted for the use in JUNO and can be transfered to get potted; if at least one parameter did clearly fail the acceptance criteria, the PMT will be rejected. However, many PMTs cannot be classified that clearly, due to indications or hints for problems in the data taking run, or due to results close to the edges of the acceptance criteria. In such cases, additional criteria have been defined how to proceed with these PMTs in order to increase the overall reliability of the final PMT classification determined in the container tests [275]:

- If single PMT parameters cannot be determined for whatever reason (e.g. bad data quality, analysis methods don't converge, insufficient S/N ratio, wrong voltage applied etc.), the PMT will be retested again in the container system.
- If all PMT parameters can be determined correctly, but any of the results for charge resolution, P/V, operating voltage applied to reach gain of 10^7, PPR, RT or FT cannot satisfy the requirements, the PMT will be tested a second time in the container system to confirm these values. If failed twice or the average of both test results cannot meet the requirements, the PMT will be declined.
- If the gain turns out to not match the aimed value of 1×10^7 (or a small window of $\pm 0.1 \times 10^7$ around it) in the final measurements (due to e.g. a bad/wrong analysis result in step (iii)), the PMT has to be rested as well, because a reliable examination cannot be guaranteed.

[10] Red light was chosen because of its only weak effect to the photocathode due to the almost vanishing QE for wavelengths higher than 600 nm [172, 219, 231]. The LED sleeve is powered externally and so only as long as the container door is open.

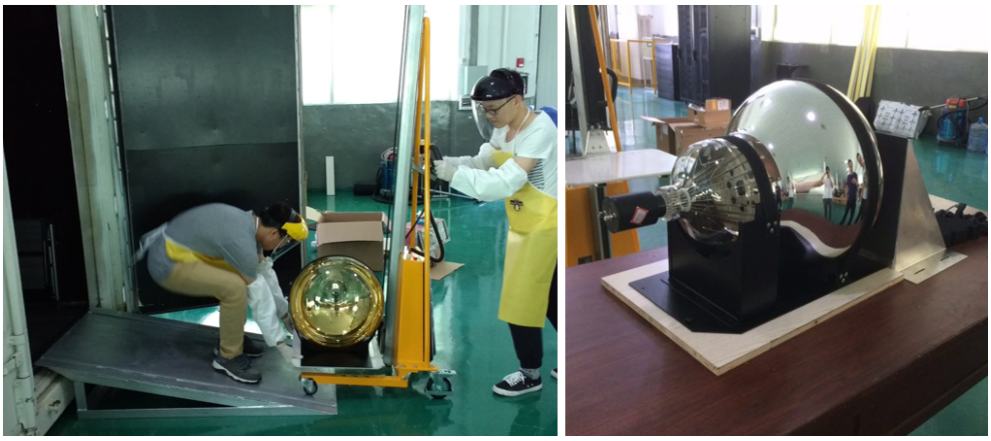

(a) loading/unloading of the container (see step (i))

(b) operation of the container system (see step (ii) and (iii))

(c) preparation for a new container run (see step (iv))

Figure 4.2.: Impressions from the container system operation at the PMT storage hall in Zhongshan. PMTs for a new run are prepared outside of the container and then loaded into the container using a mini-lifter, see panel **(a)**. Access to the container is granted by a ramp, which needs to be removed again to close the container door. In panel **(b)**, the working desk for container control and monitoring is shown. Red LED lights are used for shifters' support during reloading. In panel **(c)**, the staging area for the containers with PMT storage boxes and closeup from the visual inspection of a PMT bulb are shown.

- If the PMT shows a PDE in a range of ±1 % around the acceptance limit of 24 % in the container tests, it will be transfered to the scanning station for a cross-check test [11]. The final value to compare with the PMT acceptance criteria then will be the average of the results from both systems. If a PMT shows a PDE of less than 23 % in the container test, it will be rejected directly.
- Since the DCR is more sensitive to external effects like incident illumination and temperature (see section 3.3 again), a PMT will be rejected only, if it exceeds the acceptance criteria twice in the container system by 50 kHz or more. If the PMT shows a rate of less than 50 kHz above the acceptance criteria (but still have failed it twice in the container tests), the PMT will be transfered to the scanning station as well for a final confirmation.

These criteria are accommodated also in the description of classification criteria discussed in subsection 8.1.2 for the exemplary analysis of a small PMT sample.

4.3. Overall and Mechanical Setup

This section describes overall container system setup as a whole with major focus on the mechanical parts. The following description regards only the setup of **containers A** and **B** – containers C and D have few mechanical modifications applied and are described separately in section 4.6. The mechanical parts of the PMT container system were mainly developed and assembled together by colleagues from University of Hamburg lead by Dr. Björn Wonsak, who was also responsible as level 3 manager inside the JUNO collaboration for the planning of whole container system project.

The containers used for the PMT testing system are commercial "high cube" shipping containers of $20' \times 8' \times 9'6''$ size (L×W×H). All containers have been equipped with a multilayer magnetic shielding and painted black on the inside. The shielding is realized by revetting the container walls with several layers of alternating silicon soft iron [12] and aluminum, with a total thickness of 4 mm. The combined silicon iron-aluminum shielding can reduce the residual magnetic field inside the container to a level of ~ 10 % of the geomagnetic field strength, which is suitable for running the 20-inch PMTs inside (see section 6.1 for more details).
Each container is further equipped with a ThermoKing Magnum HVAC Climate Control Unit [277], permanently mounted in the back wall of the container, see Figure 4.3. It manages the exchange of the inside air via ventilation holes in the upper and lower back wall and conditions it to a set temperature. The climate unit can be controlled via

[11] This considers the systematical uncertainty / accuracy in the PDE measurement of the container system, see also subsection 8.2.6 for a detailed discussion.

[12] Silicon iron is basically iron admixed by a few percents of silicon. Compared to mu-metal, it has a five to ten times lower relative permeability [276], but still sufficient ferromagnetic properties for the needs of the container system and is much less sensitive against mechanical stress, which was important for the shipment of the system.

an integrated Siemens LOGO! Control system or remotely. There is no light-leak from the ventilation openings to the container inside (see more about the light-tightness in section 6.2), whereas these holes are weak spots for a magnetic shielding.

Figure 4.3.: Container's outside and inside. *Left panel:* ThermoKing HVAC Climate Control Unit on the backside of the container. *Right panel:* empty container equipped with bare magnetic shielding and before blackening of the walls. Ventilation openings of climate unit are visible on the back wall (marked by red boxes).

4.3.1. Mechanical Structures inside the Containers

The mechanical setup of the container system consists of a shelf system, holding in total 36 separate **drawer boxes** (in nine columns and four rows), each of them with a size of 53.6 × 56.3 cm and depth of 136.0 cm and thus enough space to keep one 20-inch PMT, see Figure 4.4. The shelf system is an *item*® scaffolding and screwed to the ground and the container walls. The drawer boxes and all other mechanical parts inside of the container are made out of aluminum with tolerances of less than 1 mm only; further, most of them are completely painted black.
The full mechanical structure fits to the container in an optimized way: on one hand the box size is sufficient to keep a PMT, the mountings for the light system (see section 4.5 for details) and to include safety gaps to all sides and mechanical parts within the box (in order to avoid accidental damages to the PMT glass by touching or hitting anything during the loading). On the other hand, there is enough space in the container for cable routing and the support structures of the shelf system, while still allowing a safe and comfortable access to all boxes. This is important for a secure loading and unloading of the container system. Third, the number of boxes has been maximized considering the two preceding points, ending with the denoted number of 36 boxes per container, see Figure 4.5.
The shelf system with the boxes is placed next to the left inner side wall of the container, therefore leaving an alley with a width of around 80 cm on the right side for transporting the PMTs and accessing the boxes, which can be seen in Figure 4.5b and Figure 4.6. Hence, the left container door on the front side can be kept closed

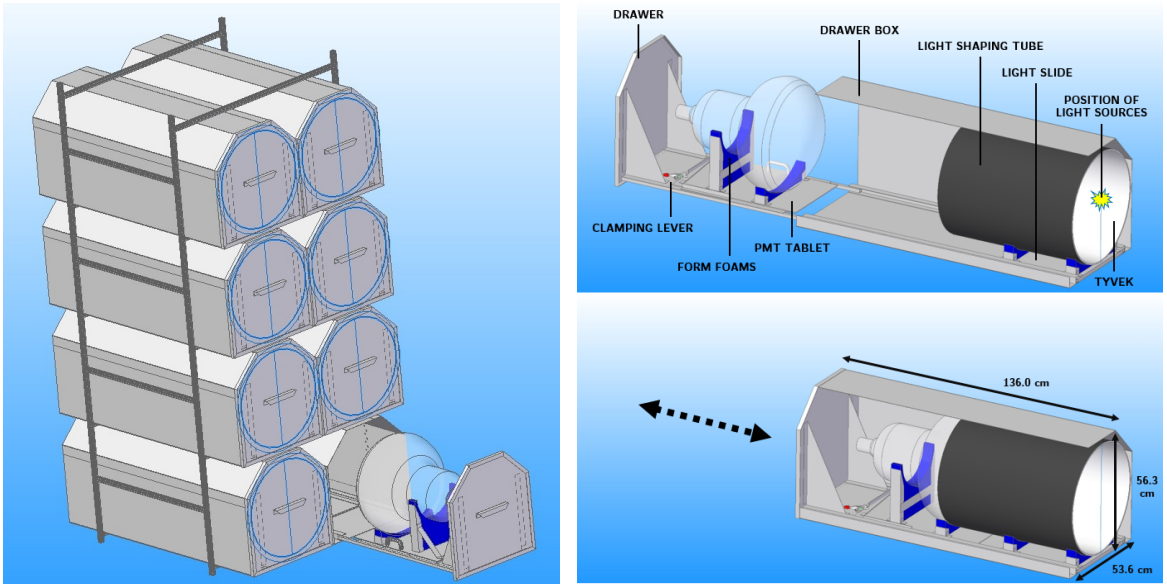

Figure 4.4.: Sketch drawings about the drawer boxes, open and closed. *Left panel:* shelf system element with eight drawer boxes. *Right panel:* structure of drawer box including all elements presented in subsection 4.3.2. Cables are routed out of the boxes through small holes on the inclined sides (for illustrative reasons one side of the drawer box is not depicted). Image credit: Dr. Björn Wonsak, Univ. Hamburg.

all the time, while the right door grants access to the boxes. The doors are framed with thick, black rubber joints to ensure a good light-tightness when closed (see also section 6.2 for more details and measurements about the light-tightness). All cables inside the container are routed in the gaps between the boxes and then guided to a small cable feed-through next to the backside wall of the container (see subsection 4.4.3 for more details about the cabling). Since the cable feed-through is another weak spot concerning the light-tightness of the container, it was explicitly taken care to close this opening using multiple layers of black pond foil on both sides of the wall. In addition, all cables are fed through a swan-neck piece on the outside to ensure that no light can leak into the container's inside, see Figure 4.7. Also negative effects on the magnetic shielding from weak spots like the feed-through and the doors have been considered and compensated by individual improvements for the nearby drawer boxes (see section 6.1 for more details).

4.3.2. Design of the Drawer Boxes (Container Channels)

As visible in Figure 4.4, each drawer box is of half cubic and half octagonal shape. The upper part of the box is of octagonal shape. The inclined top sides of the drawer boxes allow a better cable management between the boxes. Two small holes, one on every inclined side, serve as cable feed-through for the various cables routed into every box, but are protected by rubber gaskets to cover the opening as good as possible.

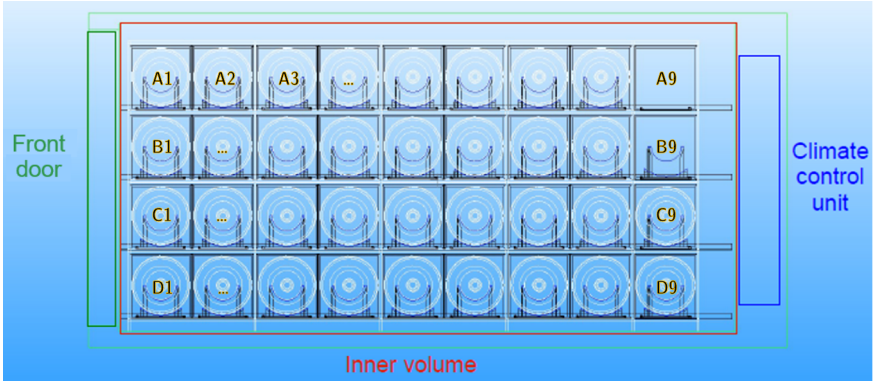

(a) side view on the container, with channel numbers of respective drawer boxes indicated

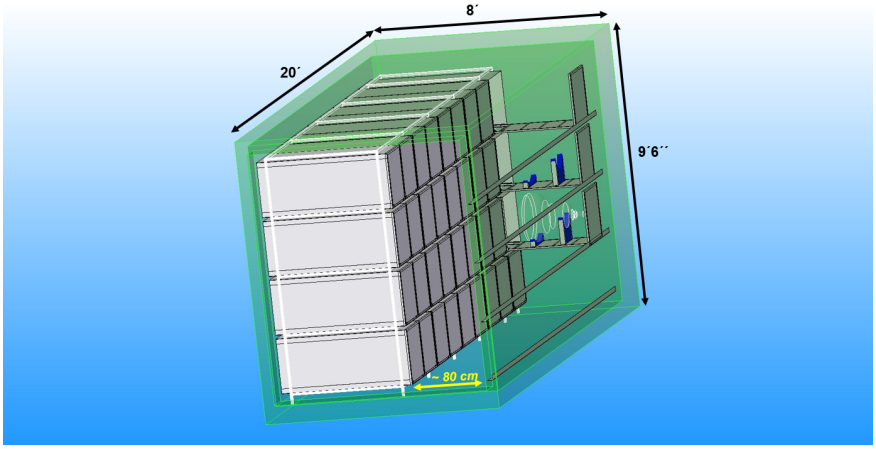

(b) complete shelf system including support brackets on the opposite wall, where drawers can be rested during loading

(c) final drawer box with drawer and PMT tablet inside

Figure 4.5.: Container system sketches with 36 channels and real drawer box. In the drawings in panels **(a)** and **(b)**, all boxes are of rectangular shape for simplicity, real shape of the boxes is half cubic half octagonal, like shown in the picture in panel **(c)**. Alley between shelf system and right wall has a width of $\sim 80\,\mathrm{cm}$ and can be accessed through the front door. Channels are numbered row-wise by `A1..D9` (see panel **(a)**) or `x01..x36` (with `x` indicating the container number). Image credits: Dr. Björn Wonsak, Univ. Hamburg.

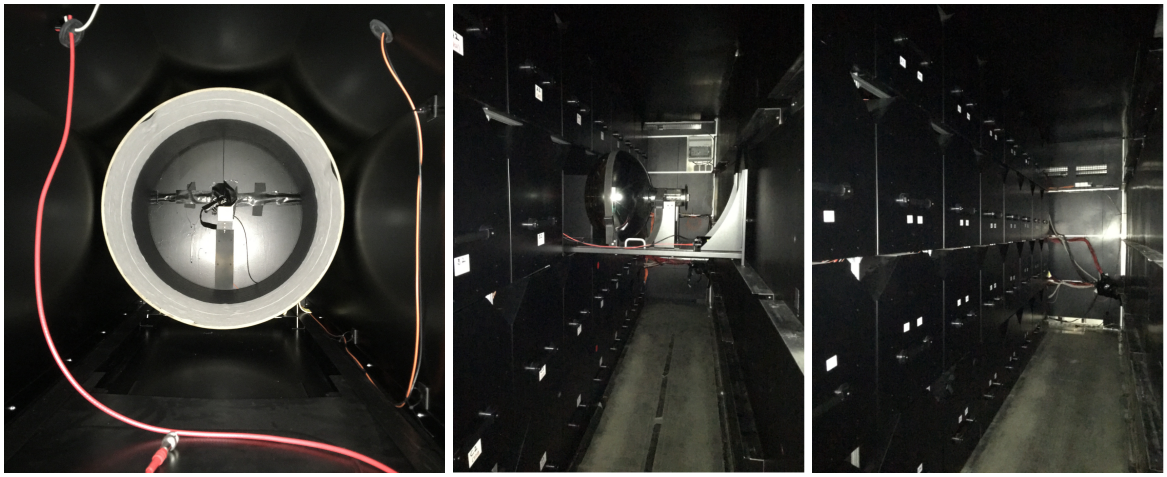

Figure 4.6.: Pictures of container's interior. *From left to right:* view into a drawer box with light shaping tube and light system (see subsection 4.5.3 for more information), a PMT loaded onto a drawer resting on the support brackets in container B, and the container's interior with all drawers closed in container A.

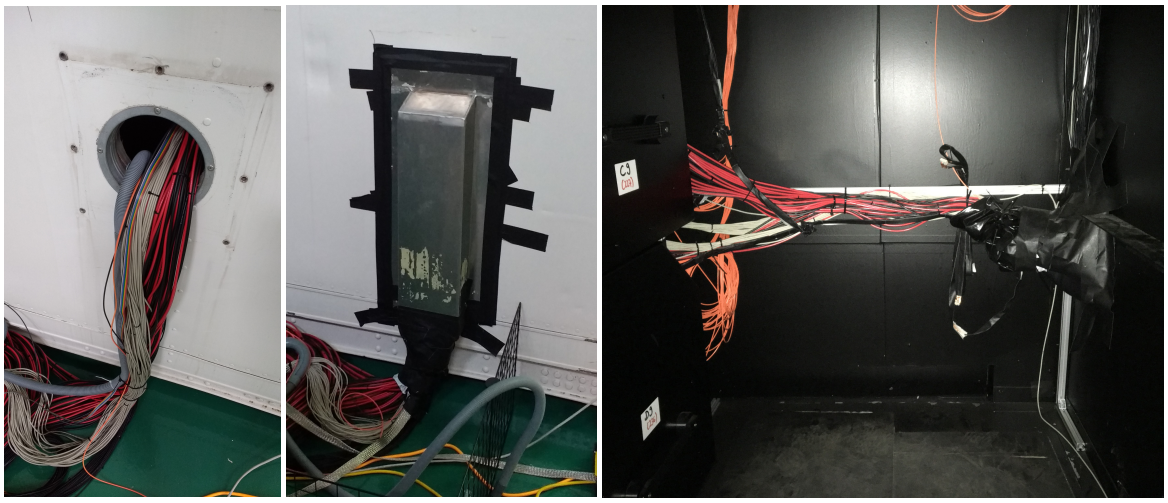

Figure 4.7.: Container cable feed-through, open and closed. The openings of the metal swan neck (centered panel) on the outside and the cable feed-through on the inside are covered with black pond foil and closed with black duct tape, which makes the opening completely light-tight. The inner part of the swan neck is additionally packed with soft foam.

(a) light shaping tube **(b)** PMT tablet

Figure 4.8.: Pictures of light shaping tube (panel **(a)**) and PMT tablet (panel **(b)**). The holder for the light system mounts is also visible in panel **(a)**. The PMT tablet is equipped with form foams, see , in this picture for an MCP-PMT. The PMT neck will be placed on the large form foam when loaded onto the tablet, while anti-static belts (in black) fasten the PMT in position. A similar setup fixes also the light shaping tube. Image credits: Dr. Björn Wonsak, Univ. Hamburg.

The lower half of the drawer box (with the cubic shape) keeps two flexible parts on a rail system.
The first part is the **light slide**, which carries the light system of each drawer box. The light slide is pushed to the backside of each box, like illustrated in Figure 4.4, and fixed at a certain position using small stainless steel pins going through holes in light slide and rail. It is equipped with form foams (cellular plastic foam made of polyethylene), carrying a 6 mm strong cartridge tube with a diameter of 502 mm and length of 600 mm, fastened by two anti-static belts, as depicted in Figure 4.8a. This **light shaping tube** is reaching from the level of the light sources at the backside of the drawer box up to the PMT's equator, only leaving a roughly 2 cm wide gap as safety space [13] between the glass bulb of the PMT and cartridge tube when the drawer is closed, see Figure 4.5 again. The light shaping tube is responsible for providing a well defined light field on the PMT surface. It is completely painted black, except for a 30 cm wide range on the inside from the tube's front end next to the PMT's surface, which is covered by Tyvek®[14] (this is also visible in Figure 4.7). Position and size of the Tyvek-covered part of the tube have been optimized to increase the homogeneity of the light field using simulations and measurements [281, 282] (see subsection 4.5.4 for more details).
At the rear end of the light slide, a small support structure with a height of 25 cm is riveted to the slide (see also Figure 4.8a again), on which the light sources are

[13] This is mainly to avoid scratches or other damages to the PMT glass.

[14] Tyvek is a highly diffuse reflecting material [278–280], which consists of small synthetic fibers glued together and pressed to paper-like sheets. Tyvek is a good choice also from pragmatic reasons, because it's light, cheap and easy to handle.

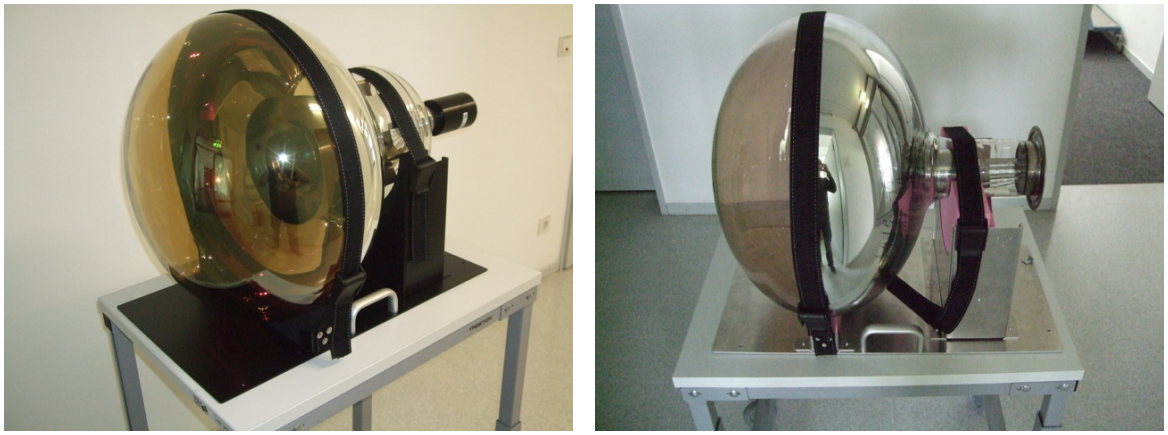

(a) Hamamatsu PMT loaded onto final tablet

(b) NNVT PMT loaded onto a tablet prototype

Figure 4.9.: PMTs of different types loaded onto the PMT tablets (in panel **(b)**, only a prototype is shown). Image credits: Dr. Björn Wonsak, Univ. Hamburg.

mounted. With this, the light sources are placed at the very back position of the drawer box as well as on the central axis of the tube and so in front of the PMT's photocathode center (more details about the light system and light sources can be found in section 4.5).
The second part inserted to the rail system is the **drawer**. If completely closed, it shuts the box light-tight by embracing the outer curb of the box with its edges; only a small pitch of a few cm on the backside between box and container wall is left open for the cabling. The drawer consists of a cover and a plate, where a removable **PMT tablet** can be fixed by a clamping lever. The tablet is carrying the PMT and is equipped with another form foams, fitting to the PMT's shape around its equator and neck, as well as two anti-static belts to fasten the PMT to position, see Figure 4.8b and Figure 4.9. To accommodate both PMT types, the form foam holding the PMT's neck can be interchanged and suitable forms for both PMT types are available. If tied to the drawer, the PMT tablet is stabilizing itself by the weight of the PMT, see also Figure 4.10. Main advantage of the detachability of the PMT tablets from the drawers is, that PMTs can be prepared and tied onto the tablets outside of the container. In addition, the tablets can be fixed with a pin to the platform of the mini-lifter, which also increases the safety during the transportation of the PMT.

The depth of the box together with the size of the drawer is optimized to fit additional quality and safety constraints. On one hand, the drawer can get pulled out far enough to ensure a save and comfortable loading of the PMT tablet onto the drawer (including some safety space to the walls which should be kept all the time), but not far enough to completely release the drawer from the rail system easily and thus make the construction instable (and dangerous) when installing a new PMT into the box. To further increase the stability of the pulled-out drawer, brackets were installed to

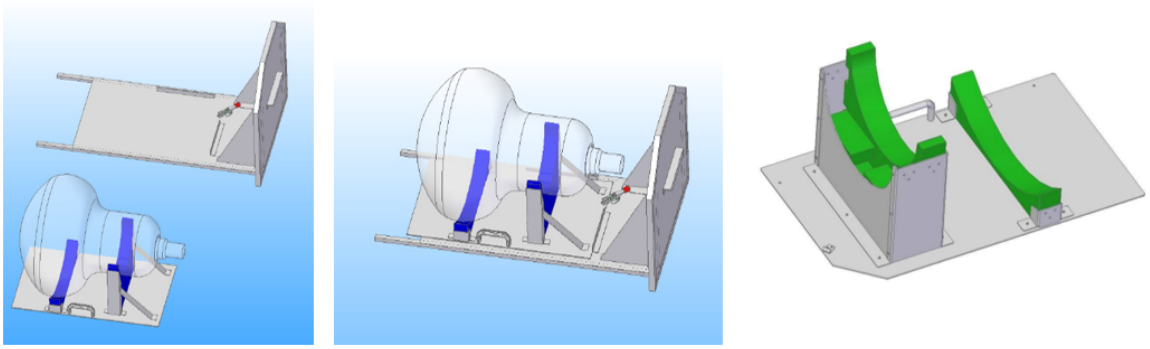

Figure 4.10.: Sketch of a loaded PMT tablet, released and attached to a drawer. The tablet is fixed to the drawer by a clamping lever (located in the right upper corner of the drawer plate, see left panel) and then stabilizes itself by its own weight. Right panel shows a detailed sketch of the PMT tablet with the form foam pieces in green (here for a Hamamatsu type PMT). Image credits: Dr. Björn Wonsak, Univ. Hamburg.

the opposite container wall, where the drawers can be rested when pulled out during loading, as illustrated in Figure 4.6. On the other hand, the distance from PMT surface (the top of the glass bulb) to the light sources within the boxes is chosen as large as possible in order to avoid an only central illumination of the photocathode [15].

4.4. Electronics Setup

Two of the container systems are completely equipped with electronics for data taking and readout of 36 channels per container. Organization, setup and (in part also) development of electronic devices was responsibility of the University of Tübingen group.
In the following, all devices used in the container systems are described, separated by commercial and custom-made. Since the common control of related or compatible commercial electronics devices seemed to be easier to realize and to work more stable, it was decided to use – wherever possible – commercial electronics from only few different companies. As *CAEN S.p.A.*, an Italian company specialized on scientific data acquisition solutions, offered most of the essential devices necessary for the testing facility, they were chosen as deliverer for a majority of the commercial electronics [16].
Figure 4.11 shows a scheme of all electronics devices, which are described in this section. All commercial electronics are active devices (except for the DC power for

[15]Distance from PMT to light sources slightly depends on the PMT type due to the different shapes of the glass bulbs of Hamamatsu and NNVT PMTs, see section 3.1 again. In both cases, the distance from PMT to the light sources is around 50 cm. A support tool for the preparation of the PMTs outside of the container (shown in Figure 4.2a), defining the exact position on the tablet, further ensures a reproducible distance from PMT to the light sources in the drawer box to guarantee the comparability of the light field at the position of the PMT's photocathode.

[16]This also offered the possibility to get the a compatible electronics system "all of a piece".

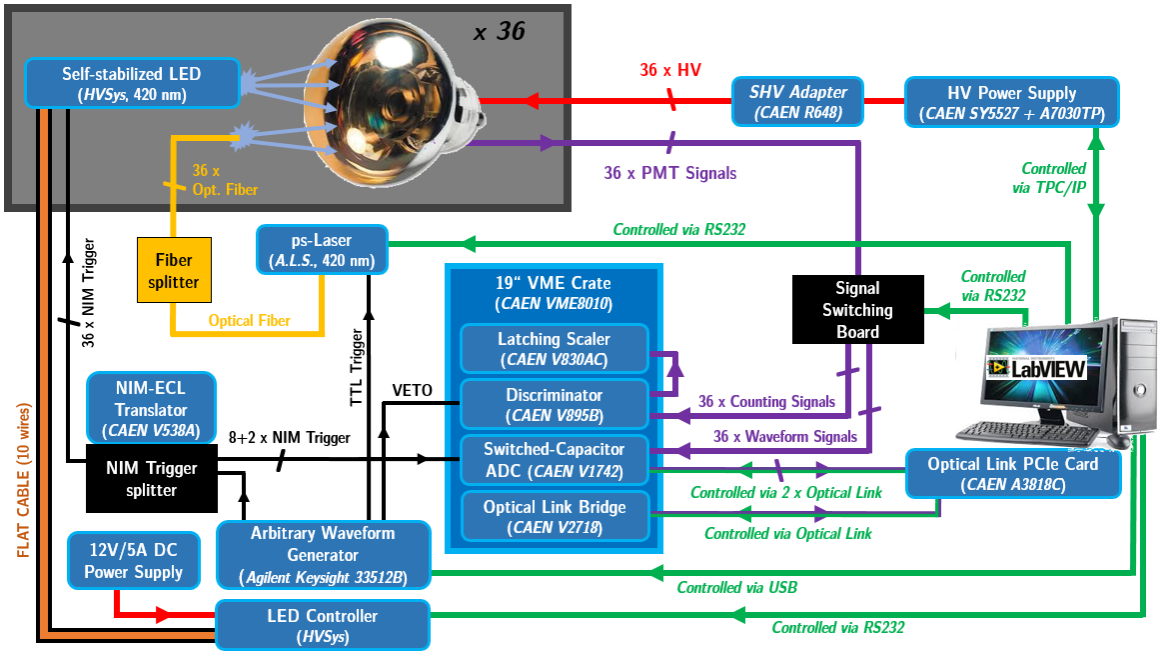

Figure 4.11.: Electronics scheme of the fully equipped container system. Blue boxes mark commercial electronics, the black boxes mark custom-made devices. The green wires show control or communication connections, the black ones show logic signal connections, the purple ones show signal streams. Power connections are illustrated by red wires. LED controller and LEDs are connected via a flat cable tree, reaching to every box. The NIM-ECL Translator is added only to one of the fully equipped systems and there replaces a small trigger splitter. The '8+2 NIM Trigger' signals for the ADC consist of two logic triggers for data acquisition initiation and eight additional trigger waveform inputs to be recorded by the ADCs. With the 'VETO' signal, data acquisition with the discriminator can be suspended (see also subsection 5.2.2). The temperature monitoring system is not displayed here, as this is logically separated from the PMT characterization electronics. Details about the 'fiber splitter' can be found in subsection 4.5.2.

the LED controller, the SHV adapter and the VME crate). A customized but standard commercially available computer remotely controls all active devices and supervises the data taking. It was taken care in the customization process of the computer to choose a high-performance CPU (*AMD Ryzen 5* and *Intel i7-7700* [17]) together with sufficient memory (16 GB) and a large solid-state disk (1000 GB) for quick processing and saving of raw data of all 36 channels in parallel and with high reliability and stability in performance during the regular data taking runs.
The system is complemented by two custom-made devices: a signal switching board, which distributes the outgoing PMT signals to the read-out electronics appropriate for the actual measurements, and a trigger splitter device, which distributes the trigger signals to the various devices. The read-out electronics and also main parts of the

[17] Computers of containers A and B feature a slightly different hardware, but with comparable performance.

light system are located outside of the container boxes, only the used LEDs are placed inside the containers in front of the PMTs. The light system (LEDs, ps-Laser and LED controller and fiber splitter unit) will be described further in section 4.5.
The description of the commercial electronics only refers to the two fully equipped container systems A and B. Electronics equipment for the containers C and D was reduced severely, see section 4.6 for more details.

4.4.1. Commercial Electronics

The HV for each PMT channel is provided by a **CAEN A7030TP High Voltage Board** [283], housed in a **CAEN SY5527 Multi-Channel Power Supply System** [284]. The board can supply 36 channels with up to +3 kV and 1 mA (1.5 W max.). To fit the SHV cable plugs of the cables coming from the boxes inside the container, an **R648 Multipin-to-SHV Adapter** module from CAEN [285] is necessary. The power supply unit is controlled via a TPC/IP connection. The HV board is further connected to a small interlock switch installed at the container door, which closes when the door opens via relaxing a small lever and thus shutting off the high voltage immediately. This protects the PMTs from becoming illuminated with daylight while being under high voltage. It also protects the shifters during the reloading of the container from accidentally applied HV on the cables.

The readout electronics are operated in a **CAEN VME8010 19-inch VME Crate** [286]. The crate provides the power for running all readout modules.
For recording the waveforms, two **CAEN V1742 32+2 Ch. Switched-Capacitor Digitizers** [287] housed in a VME module and based on a DRS4 (Domino Ring Sampler) chip [288] are used as analog-to-digital converters (ADCs). They provide 32 readout channels per module as well as a good timing and voltage resolution (12 bit with 1 V_{pp} dynamic range), combined with a fast sampling rate (up to 5 GS/s). During the data taking, the switched-capacitor ADCs continuously sample the analog input signals on the DRS4 chip into a circular memory buffer with 1024 capacitive cells. If a trigger signal arrives, the whole buffer is frozen and subsequently digitized into another digital memory buffer for processing and readout. This digitization process introduces a dead-time of 110 μs after each registered trigger. The digital memory buffer of the device allows to store up to 128 subsequent events per channel. Moreover, readout activity on the digital memory does not affect write operations of subsequent events, because the digital buffer works as FIFO (Fan-In-Fan-Out) [287, 289]. If further the trigger signal is recorded together with the channel input, this digitizer can reach a timing precision of up to 50 ps [287]. Sampling frequency and length of the circular memory buffer (which defines the data frame size of one event, see also subsection 5.2.2) can be adjusted via software.
For pulse counting measurements, in total three **CAEN V895B Leading Edge Discriminator** boards [290], providing 16 channels each with programmable thresholds and output widths, together with two **CAEN V830AC 32-bit Latching Scaler** modules [291], providing 32 channels each, are used. The discriminator channels cre-

ate an ECL signal output for every pulse above the set threshold, which then can be counted by the scaler module. Thresholds of the discriminator channels can be individually programmed in a range from $-1\,\mathrm{mV}$ to $-255\,\mathrm{mV}$ through a 8-bit DAC, while the output pulse width is adjustable in a range from 5 to 40 ns [290]. Both modules have a high input frequency acceptance of 140 and 250 MHz, respectively. Pulse detection further can be vetoed completely via a specific input, enabling the counting only when the discriminator gate is open. The two modules are connected with a 2×8 wired flat cable provided by CAEN (type **CAEN A954**) as well.
Discriminators and scalers are controlled and read out via VME bus, with connection managed by a **CAEN V2718 CONET2 VME-to-PCI Optical Link Bridge** [292], installed to the VME crate as well. The bridge is connected with an optical fiber (type **CAEN AY2705**) to the data taking computer housing a **CAEN A3818C PCIe Controller Card** [293], which manages the direct data transfer between computer and readout electronics via CONET2 protocol. Also both ADCs are directly connected with an optical link to the A3818 card [18].

The triggers for all electronics are generated by an **Agilent Keysight 33512B Arbitrary Waveform Generator** [294]. Depending on the measurement step, this device provides the required NIM (for LEDs and ADCs) or TTL triggers (laser system) for the actual initialization of the data taking, with minimal jitter of $\lesssim 50\,\mathrm{ps}$. It can further provide logic veto signals for the discriminators. The waveform generator is controlled remotely via USB. The trigger signals are distributed in the following by a custom-made trigger splitter device from JINR (see subsection 4.4.2). The NIM pulses for the trigger recording (in order to save the trigger time information) are also provided by the pulse generator and are distributed to the respective ADC channels by either another (smaller) custom-made trigger splitter or a fan-out device for NIM pulses, which is realized by a **CAEN V538A NIM-ECL Translator** [295] in one of the systems, running passively in the VME crate as well.

For the characterization of the PMT performance, two independent light systems are installed to the container. The first system consists of **36 self-stabilized LEDs** by the Russian JINR-associated company *HVSys* [296], with which every channel is instrumented [19]. These LEDs can guarantee a stable and reproducible light intensity, set by a common **LED controller** for all LEDs connected via USB to the computer. Since a standard USB connection cannot provide enough current to power all 36 LEDs in parallel, a standard **12 V/5 A (60 W) DC Power Supply** is used to energize the LEDs apart from the controller.
The second system consists of an **A.L.S. PiLas 420X Picosecond Laser System**

[18] In principle, control and readout of the ADCs is also possible via the VME bus, but a direct link from each ADC to the computer was preferred due to the expected high data transfer rates.

[19] Originally, the self-stabilized LEDs from *HVSys* came with a wavelength of 470 nm, but have been adapted to 420 nm accordingly to the needs of the container system. LEDs and LED controller were made available by colleagues from JINR.

[297], generating very short and well-timed laser pulses; it is installed as secondary light source into the containers. This system can be controlled remotely via USB as well. The laser light is guided by a fiber into the container and then split up and distributed via a system of multiple fibers to all boxes. A detailed description about the full light system as well as more information about the light sources is presented in section 4.5.

4.4.2. Custom-made devices

The NIM trigger signals produced by the waveform generator need to be distributed to the corresponding light sources and coincidentally to the data taking electronics. For this, two **40 channel Trigger Splitter Systems** were provided by colleagues from JINR, shown in Figure 4.12. The input signal is multiplied by this device and simultaneously sent out on all available channels. The output of this splitter has a delay of 100-200 ns with respect to the input, negligible jitter and is optimized in amplitude and width for the LEDs, but keeping the NIM standard. Additionally, for providing and distributing the NIM trigger pulses to be recorded by the ADCs, there is another 10 channel trigger splitter (similar to the 40 channel splitter, just smaller) used in one of the container systems.

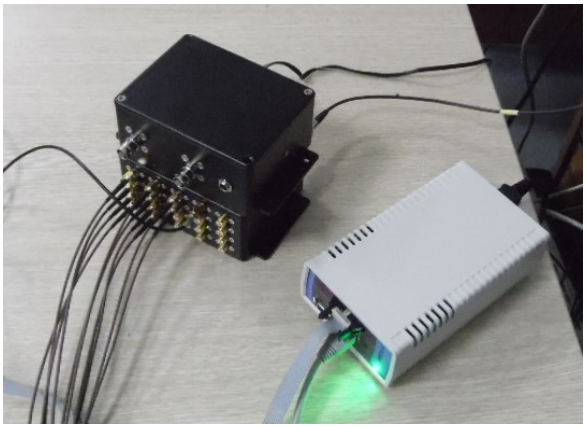

Figure 4.12.: Picture of a 40 (2×20) channels trigger splitter and LED controller device by *HVSys*. Image credit: Nikolay Anphimov, JINR Dubna.

The largest custom-made device is the **Signal Switching Board (SSB)**, which is an in-house-production of the University of Tübingen group and illustrated in Figure 4.13 and Figure 4.14. The SSB acts as a simple switch for the signals coming from the PMTs to route them to either the ADC inputs or the discriminator inputs; a parallel read-out of the PMT signals with both devices is not possible due to a impedance mismatch, which would distort the pulse forms. The SSB features 40 parallel channels, remotely controlled by the computer via USB and a common micro-controller (an ATmega328 chip on an Orangepip Kona328 development board [298]). This micro-controller provides simple boolean-like signals toggling one ARS1612 HF-relay per

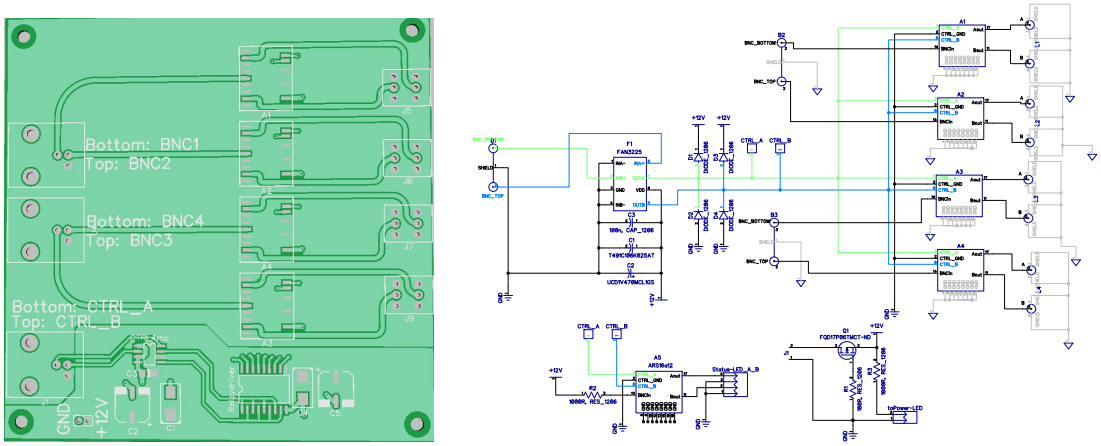

Figure 4.13.: Electric scheme of the signal switching board prototype with four channels. Final board provides 40 channels by just multiplying the prototype scheme in the right panel, see Figure A.1 in the appendix. ARS1612 HF-relays are switching the signals from the input plugs (BNC type) to one of two different output plugs (LEMO-00 type). Image credit and design: Dr. Michael Gschwender and Dr. Matthias Rudolph, Univ. Tübingen.

channel to change position between two outputs. So, the signal fed into the SSB on one side can be output alternately on two different plugs, connected to the respective read-out electronics for further processing. Besides the switching of the relay positions, the SSB is completely passive and thus has no influence on the signals either (this has been checked also in accompanying measurements, see subsection A.2 in the appendix).

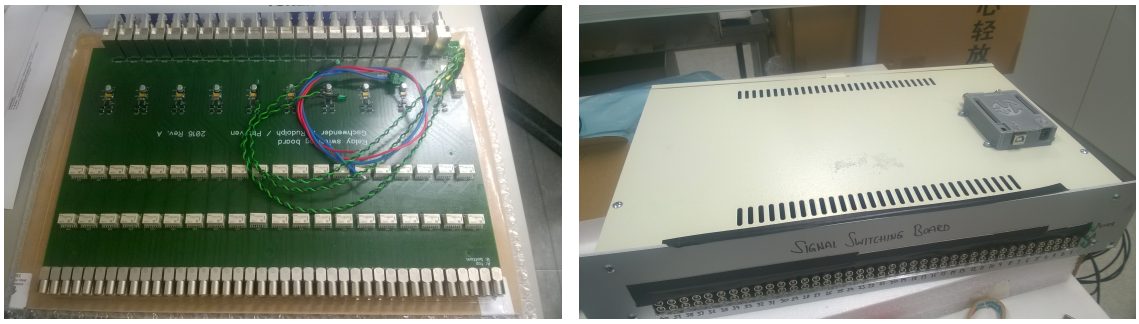

Figure 4.14.: Final 40 channels signal switching board. Input connectors are BNC type, output connectors are LEMO-00 type (two per channel). The small blocks visible in the left panel are the ARS1612 HF-relays responsible for the toggling the signal line. The switching process is triggered by an Arduino board housed in the grey box (attached to the top of the SSB, see right panel) and controlled by the computer via USB.

The **Temperature Monitoring System** is another in-house-production, but developed and set up by the University of Hamburg group in the framework of an own thesis [299]. The system consists of 40 individual temperature sensors (resistance tem-

perature detectors, type PT1000) placed inside the container, with 36 in the drawer boxes and four in the container alley. These sensors are connected to another microcontroller(an ATmega2560 on an Arduino MEGA 2560 development board [300]) and read out sequentially by the computer with a standalone LabVIEW software, also developed and described in [299]. With this device, both the temperatures at the individual measurement spots, as well as an averaged temperature of the container interior will be read our in distinct intervals at least 60 s with an accuracy of 0.25° C. The temperature data of each sensor is logged and saved together with a time stamp. The monitoring system is separated from the temperature control of the containers, which is also controlled by a standalone LabVIEW software, developed and described in [299], but not connected to the monitoring or the full data acquisition software.

4.4.3. Cabling and Trigger Management

The PMTs are connected to the electronics by two main cables, one high voltage and one signal cable. For this purpose, RG11 high voltage coaxial cables with a length of 20.0 m and SHV plugs on both ends are routed from the main power supply through the cable feed-through into every drawer box, acting as power cables for the PMT operation. Another set of coaxial cables of type RG58 with BNC plugs on both ends and same length as the power cables are routed from the readout electronics into every drawer box, acting as signal cables for the PMT output. On the electronics side, the signal cables are connected to the SSB. In every box, both cables are connected separately to the PMT base, see Figure 4.15.

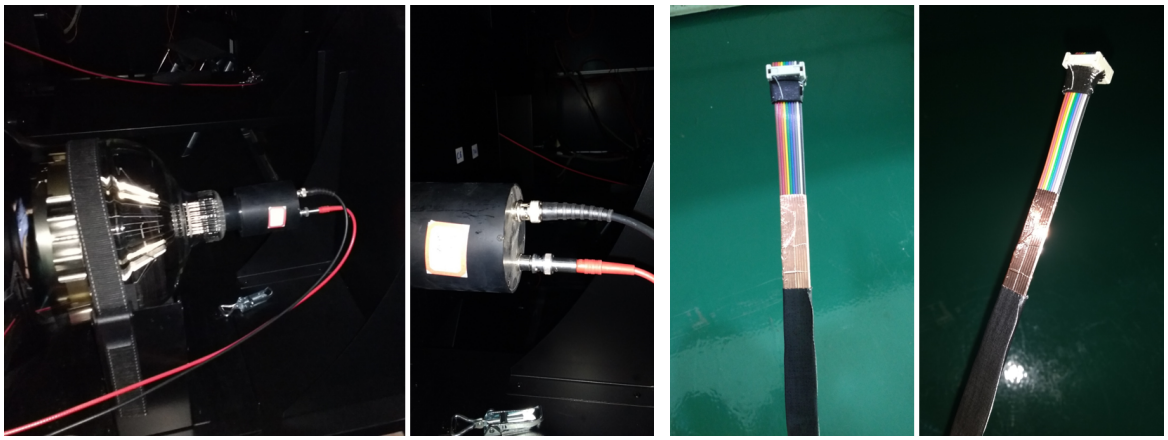

(a) data and power cable for every PMT **(b)** flat cable for LED control

Figure 4.15.: Pictures of cables inside the container boxes. The black (data) and red (power / HV) cables for the PMT operation (see panel **(a)**) are separately connected to the PMT base and both routed from the electronics into every box. The flat cable for the LED controlling (see panel **(b)**) is routed tree-like behind the shelf-system and connected to every LED on one side and a (common) connection to the LED controller on the other side. The flat cable is further wrapped with copper and black duct tape.

Table 4.2.: ADC trigger groups and assignment to the container channels ('x' indicates the container number, with x = 1,2). For each container system, two ADCs are in use. Files are saved using the ADC serial numbers for clear identification, see also subsection 5.3.3 for additional information.

ADC	Trigger Group	Container channels in TG
1	TG1	x01, x02, x03, x04, x05
	TG2	x06, x07, x08, x09
	TG3	x10, x11, x12, x13, x14
	TG4	x15, x16, x17, x18
2	TG1	x19, x20, x21, x22, x23
	TG2	x24, x25, x26, x27
	TG3	x28, x29, x30, x31, x32
	TG4	x33, x34, x35, x36

Two more cables reach from the outside into every drawer box: one low-frequency UNITRONIC® LiYY data cable [301] with 20.0 m length and a temperature sensor at the end belonging to the temperature monitoring system, and one individual trigger cable of type RG174 and a length of 15.0 m for the LEDs, connected to the corresponding trigger splitter device with standard SMA plugs and soldered directly to the LEDs on the other side.
Furthermore, a standard ten-wired AWG26 flat cable for the LED control is routed tree-like behind the shelf system connecting all LEDs with the common LED controller, see also Figure A.5 in the appendix. The complete flat cable tree is wrapped in one layer of copper tape, with keeping the conductive connection at all branches, and one layer of black duct tape, see Figure 4.15. The copper is further connected to the common ground outside of the container and is intended to shield the PMTs in the container from electric noise) caused by the LED controller and then potentially introduced into the container over the flat cables). The outer black layer is for covering the reflecting surfaces in the drawer boxes.

The cabling between the different electronics devices is following the scheme in Figure 4.11: for the communication between computer and electronics devices, multiple USB and Ethernet cables are used; further, several coaxial signal cables (mostly RG188 and RG316 cables with different lengths and both LEMO-00 or both BNC plugs at the ends) are used to distribute the trigger signals to the electronics and to guide the PMT signals coming along the data cables from the SSB to either the corresponding ADC channels (36 cables of type RG316 with 0.5 m length and LEMO-00 to MCX connectors) or discriminator channels (36 cables of type RG316 with 0.5 m length and LEMO-00 to LEMO-00 connectors). A more detailed cabling scheme can also be found in subsection A.3 in the appendix.

In addition to the distribution of the trigger signals to the electronics (in order to trigger the data acquisition or light emission), the trigger pulses are also fed into several ADC inputs, as already indicated in Figure 4.11. The trigger signals will be recorded by four different channels per ADC, one for each internal ADC trigger group (containing eight hardware channels each), thus the same triggers are recorded eight times in total by the two ADCs. The assignment of the individual container channels to the trigger groups and therefore to the saved trigger data files is as listed in Table 4.2. The recording of the trigger data is necessary to reduce the internal jitter in the data acquisition of the ADCs, which will be also described and discussed in section 6.4.

4.5. Light Sources and Light System

The light system of each container consists of two parts, the **LED system** and the **Laser system**. Both systems are used during the measurement run, being activated in separate steps according to different measurements: the LEDs are the main light sources for most of the individual measurement steps in a full data taking run and used whenever a stable and calibrated light intensity is required; the laser system however is used, when a better timing resolution is required.

4.5.1. LED System

Each drawer box is equipped with an LED device produced by the company *HVSys* [296]. These LED devices feature an integrated feed-back loop with a PIN photodiode and a QDC unit continuously measuring the light intensity, see Figure 4.16a. Based on this continuous measurement, the power of the LED driver unit is adjusted regularly [20] in order to stabilize the light output over time with a remaining relative amplitude variation of less than 2 %, see e.g. [252, 271, 296]. Using an an external trigger source, the LED output is pulsed with a FWHM of only around 5 ns [296]; in the container system, the light output is further synchronized with the data taking system by the common triggers. Figure 4.16b shows one of the self-stabilized LEDs like used in the container system and mounted into every drawer box. The top of the boxed LED device is outfitted with a screw thread, which is needed for the assembly in the drawer box setup.
The wavelength of the LEDs in the container systems is around 420 nm, roughly matching the output wavelength of the used scintillator in JUNO, see subsection 2.5.2 again; Figure 4.17 shows the emission spectrum of one bare LED used for the *HVSys* LED devices, taken with a standard lab spectrometer (type LD Didactic 467251 [302]). The lack of a second emission peak or other substructures in the emission spectrum qualifies the LED for the use as light source in the containers [21].

[20] Number of cycles for light output monitoring can be defined in the software settings (see subsection 5.2.3), and is set to 100 by default.

[21] The self-stabilized LEDs are used also in the scanning station, see e.g. [243, 271].

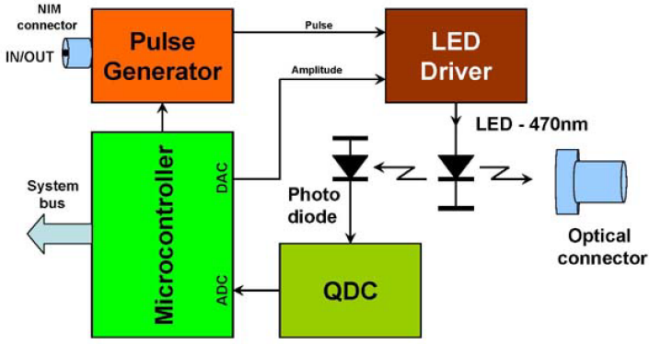

(a) working scheme of the self-stabilized LED

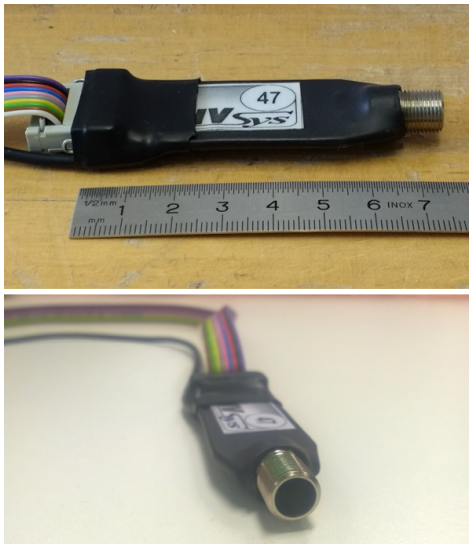

(b) pictures of a self-stabilized LED

Figure 4.16.: Self-stabilized LED by *HVSys*. In panel **(a)**, the working scheme of the LED is shown. Via QDC and micro-controller, the LED driver is monitored and adjusted continuously. For the container systems, LEDs with a wavelength of 420 nm were used. In panel **(b)**, pictures of the boxed LED device are shown. The LED control is established by the flat cable using a specific hardware address. The external trigger NIM trigger connection is directly soldered to the device. Light output is through the top opening (with the screw thread around). Image credit panel **(a)**: [296].

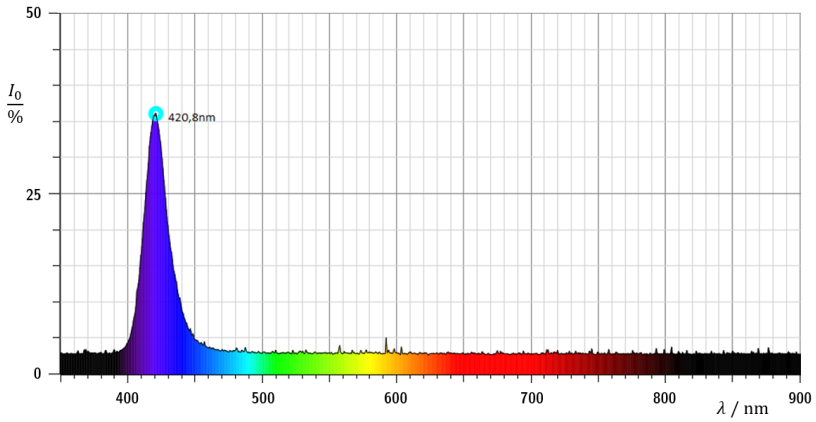

Figure 4.17.: Measurement of output wavelength of randomly chosen bare LED, using a simple lab spectrometer [302], showing $\lambda_p = 420.8\,\text{nm}$ as peak wavelength. Peak amplitude depends on incident angle of light source to spectrometer window and can be ignored here. Such bare LEDs (same sample) were integrated by *HVSys* in the self-stabilized LEDs used for the container systems.

All LEDs mounted in the container are connected via one ribbon cable tree to a shared controller device using a common ten-wired AWG26 flat cable, also shown in

Figure 4.15 in the section about the cabling. The cable tree splits in four branches of nine LEDs each (also illustrated in Figure A.5 in the appendix). The LEDs can be addressed by an individual hardware address to adjust the light output of each LED individually, generating an allocatable (and reproducible) light intensity for all measurement steps and runs. The output intensity can be adjusted by setting a so-called *LED setpoint* in a range of 1 (vanishing intensity) to 4000 (maximum intensity, in a.u.), with a roughly proportional of output intensity to setpoint in between. With the chosen setpoints the LEDs are providing an individual dynamic range factor of ∼20 in the measurements. The LED settings are controlled and adapted by the data taking software appropriate for the respective measurement (see subsection 5.2.3).

4.5.2. Laser System

The laser system is used for the measurements requiring a high timing performance. The used picosecond laser, a PiLas 420X system from Advanced Laser Systems (A.L.S.) company, can provide light pulses with a wavelength of $\lambda = 420\,\text{nm}$ and a width of only 80 ps (FWHM, pulse profile depends on output power and pulse frequency [297]). Also the dynamic range in light output is larger than for the LEDs. Figure 4.18 shows the emission spectrum of the laser, recorded with the same lab spectrometer as used for the LED in Figure 4.17.

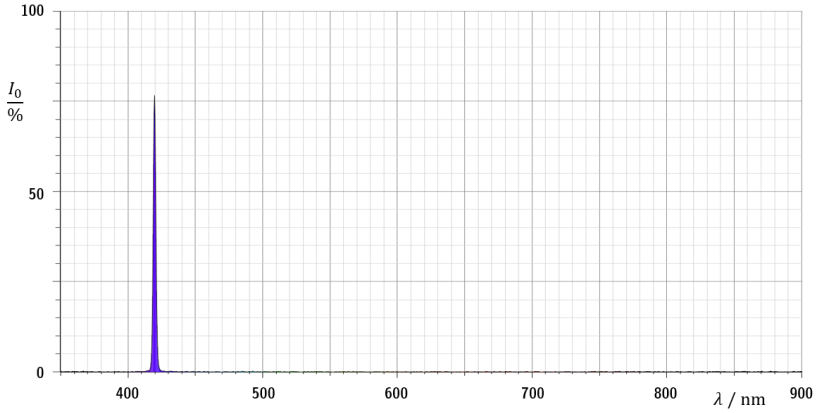

Figure 4.18.: Measurement of output spectrum of the PiLas 420X laser system, using a simple lab spectrometer (same as for the LED measurement in Figure 4.17). The measurement shows a sharp peak around $\lambda = 420\,\text{nm}$; its width is consistent with the resolution of the spectrometer.

The laser system consists of a controlling unit, which can be operated remotely via USB, and a separate laser head, providing the short laser pulses. Output power and shape of the emitted light pulses depend on the set *tuning value* of the laser system (in ‰). The laser tuning empirically defines the intensity of the laser pulse, with tuning values between 900–1000 ‰ provide the lowest light intensity, while tuning values close to 0 ‰ provide the highest intensity. The tuning is connected to both pulse width and peak amplitude, so that a higher (lower) tuning value does not automatically give a

lower (higher) light intensity or photon number in the released laser pulse; see also [297] for more information.

For using the laser as light source in the container systems, the emitted laser pulses are guided by a multi-mode fiber (with core diameter of 200 μm and a numerical aperture (NA) of 0.50) into the container; right at the beginning, they are attenuated by an upstream neutral density (ND) filter. The attenuation factor of these filters is defined by their optical depth $OD = \log_{10}(1/T)$ with T the transmission coefficient at the respective wavelength. Using a filter with $OD = 1.0$, the laser light intensity is already reduced to a level of only few photons per pulse. The light is then distributed to a bunch of multi-mode fibers, which are guiding the light into all boxes. The splitting of the laser light into multiple fibers happens in a work piece called "**Laser Splitter**" or "**Fiber Splitter**" for simplicity; it is depicted (without fibers) in Figure 4.19 as sketch and images. Since a commercial device for a proper distribution of the laser light to multiple fibers was either not available or unreasonably expensive, a custom-made in-house-production has been worked out. Idea and design are based on the fiber splitting system described in [303].
The custom-made laser splitter consists of two separated parts, one made out of aluminum and one of brass. The first (aluminum) part is keeping the "major fiber", a short fiber with a large core (1500 μm), a wide acceptance and emittance angle (0.39 NA). One end of this fiber features an FC/PC connector which is coupled to the fiber guiding the laser pulses into the container. The other end is flat cleaved and glued into the aluminum work piece, which features a long hole inside matching to the fiber dimensions, see also Figure 4.19. The dimension of this piece was chosen to support the major fiber's stability. The flat cleaved end is reaching to a 20 mm deep and wide cavity, equipped with a thread where the brass work piece can be screwed into. The brass piece keeps up to 40 thinner fibers (200 μm core and 0.50 NA, with a length of 10 m each) in another cavity. The ends housed in the brass part are flat cleaved and their fiber tubing was partially removed, so that they can be collected very close together. The bare fibers then are guided through a hole in the work piece, with their ends fixed in position by gluing all fibers into the brass piece with optical epoxy. When now both parts of the work piece are screwed together, both fiber endings directly face each other in a close distance. To better match the refraction index, the gap is filled with an index matching gel. On the other end, the thin fibers are patched into stainless steel ferrules of 1.25 mm diameter and are routed into the container boxes [22]. The installed laser splitter system of one of the container systems is shown in Figure 4.20.
Purpose of this splitter is to collect as much light as possible from the laser and distribute it onto the 36 individual fibers, ending in the drawer boxes of the container. All fibers should be able to collect light from the major fiber without extreme dif-

[22] In order to include spare fibers for possible broken or blind wires, in total 40 exiting fibers are installed into every laser splitter. In the containers, the 36 best performing ones of them are finally routed into the drawer boxes.

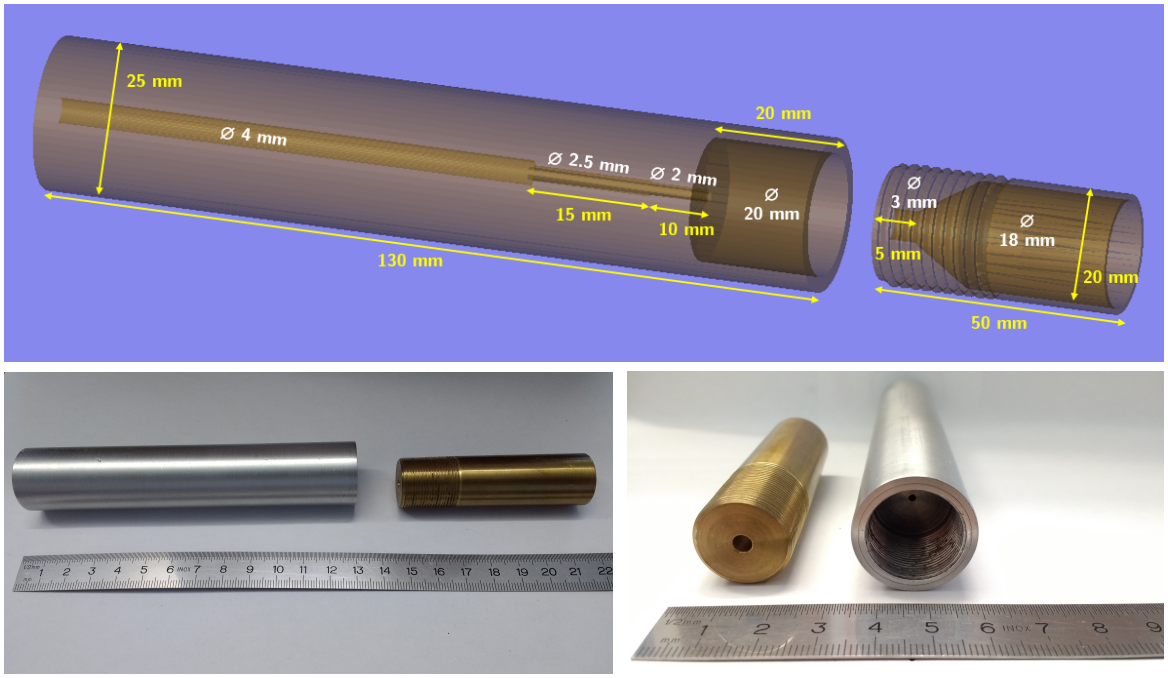

Figure 4.19.: Sketch and pictures of the fiber splitter work piece. The long piece is made of aluminum and is holding the major fiber, which is connected to the laser. The hole in the work piece is matching the thickness of the fiber. The short piece is made of brass and is holding up to 40 fibers, which then are routed to the drawer boxes. These fibers have bare, polished ends, that are aligned and collected closed together. Both pieces can be screwed together so that the fiber ends directly face each other, while the gap in between is filled with an index matching gel for a smoother light transition. For gaining additional stability, fibers are glued into the work piece and everything is tightly packed.

ferences in the relative brightness. While the absolute (average) light intensity going through every fiber is dispensable and can vary statistically between the pulses[23] (and container channels), since the fiber splitter was not optimized for a homogeneous light distribution to all individual fibers. With the applied tuning and attenuation, an average light intensity of < 0.5 p.e. per laser pulse is aimed (see subsection 8.2.4 for final results). Since the NA of the used fibers is relatively large, a broad but however central illumination of the PMT's photocathode can be assumed [24], which is suitable for the purposes of the container system. Unlike more important than the individual light intensity is to keep the good timing resolution of the laser pulses for the measurements, although the laser pulse width may increase a little by traversing the splitter device. A final jitter of the whole laser system (including the data taking elec-

[23]In the limit case of only a few photons per laser pulse in total, there can be also channels with no light at all from a certain pulse coupling into the respective fiber.

[24]Since the used fibers are multi-mode fibers, the emitted light profile is a superposition of all light modes present in the fibers. The assumption of a mostly central illumination of the photocathode is therefore reasonable.

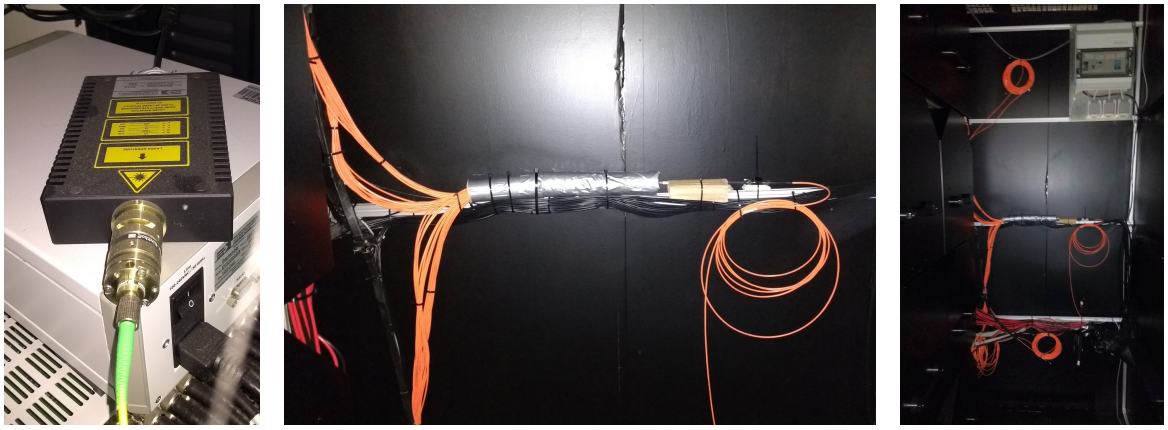

Figure 4.20.: Laser head and fiber splitter (here from container B). The light pulses produced by the laser head are guided through the connection fiber and is then coupled into the major fiber of the laser splitter. In between, an additional ND filter for light attenuation is placed. Due to unavoidable losses in the fiber coupling, the light intensity is further weakened, ending with roughly a few photons per pulse.

tronics) of $\leq 1\,\text{ns}$ was design goal for the full container system, as it was mentioned already in Table 4.1. The actual jitter of the container systems was investigated by using reference PMTs in the container system during operation; results of these will be discussed in subsection 8.2.3 and subsection 8.4.2.

4.5.3. Support Structures for Light Sources

LEDs and fiber endings are mounted together into each drawer box and are placed on the support structure riveted to the light slide (see Figure 4.8 again). The light system is completed by several small add-ons for mounting, attenuation and diffusion, presented in the following.

The LEDs are mounted with their screw threaded top to a small PVC holder fixing them in position, see Figure 4.21. The PVC holder itself is screwed on the support structure for the light system, so that the LED is aligned to the central PMT axis and symmetry axis of the light shaping tube.
The PVC holder further keeps all parts responsible for light attenuation and diffusion: on top of the LED, a small collimator piece made of aluminum (pictured in Figure 4.22) is screwed on the LED thread. This piece passes light only through a small hole with 1.2 mm diameter. The collimator can further keep an ND filter of half an inch diameter [304, 305] fixed by two retaining rings. Depending on the individual brightness of the LEDs [25], neutral density filters with optical depths between 2.0 to 3.0 were applied. With the combined light attenuation of collimator and ND filter,

[25]The light intensity of the individual LEDs can vary inherent to the design. Differences in light intensity are addressed by a dedicated calibration of each container channel, see section 6.6.

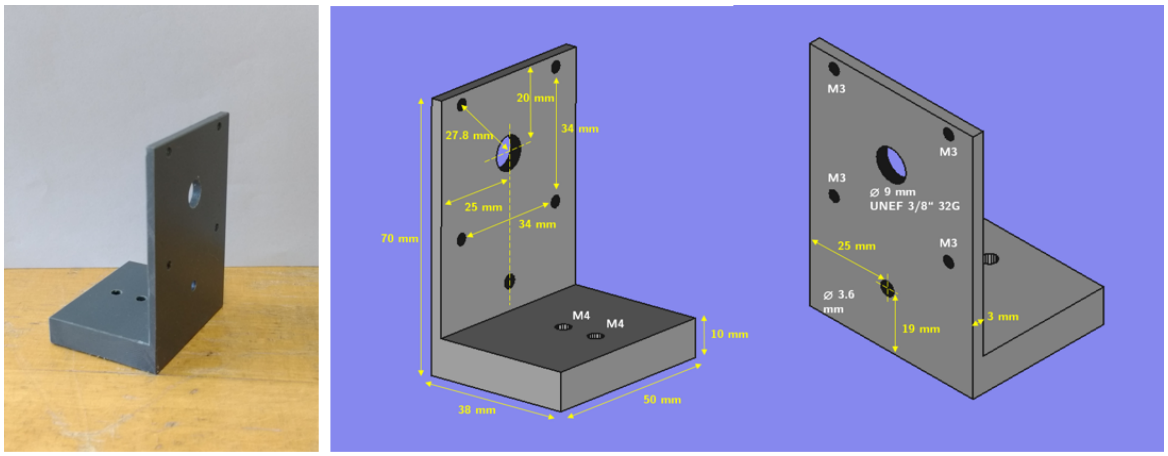

Figure 4.21.: PVC holder for the light system in the drawer boxes. The holder is screwed on the support structure riveted to the light slide. The big hole in the middle keeps the LED, which is screwed to the holder and fixed by the collimator from the other side. The four small holes around are for the fixation of the PTFE diffuser attachment. The middle sized hole below the big hole is a guiding hole for the fiber from the laser system ending in the drawer box.

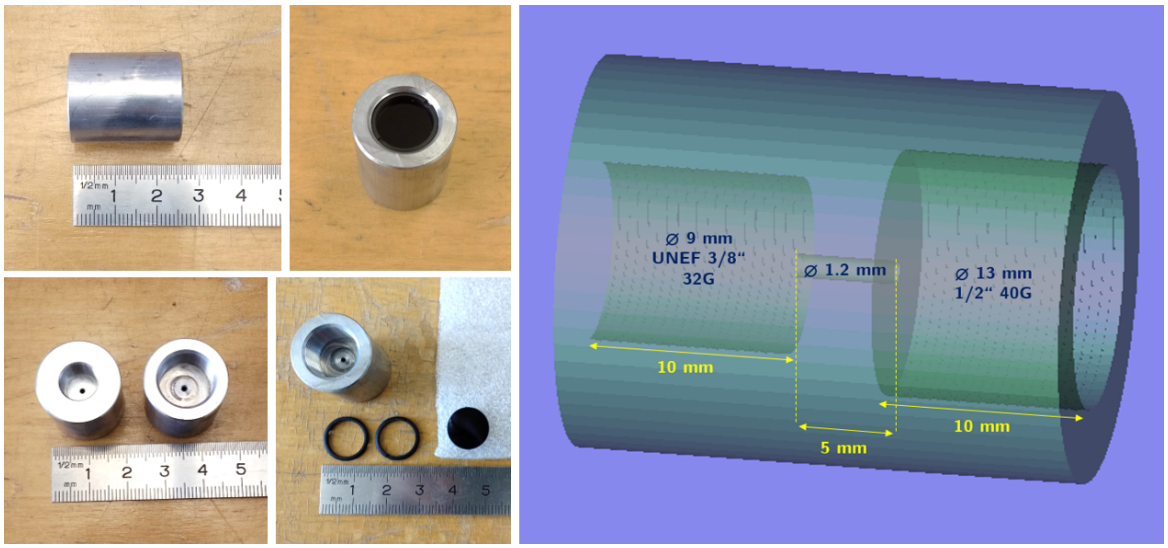

Figure 4.22.: Collimators used in the container system for LED light attenuation. They are screwed on the LED tops and can be further equipped with neutral density filters (retaining rings are used for the fixation of the filters in the collimator). Right panel shows a sketch of the inner structure of the collimator.

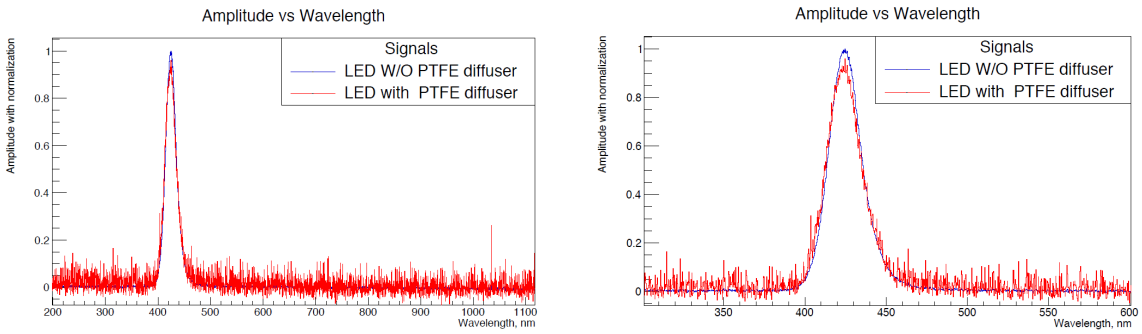

Figure 4.23.: PTFE diffuser measurements. The emission spectrum of the LEDs is not influenced by the PTFE diffuser (due to attenuation, spectra are normalized to 1 at peak wavelength). Right panel is a zoom into the wavelength's region of interest. Image credit: Nikolay Anphimov, JINR, see [306].

the LED system is tailored to a final light output intensity of single photons per pulse (see also subsection 8.2.4 for corresponding measurement results using real PMT data from the containers). Convoluted with an average QE value of the JUNO PMTs, the dynamic range of the light intensity in the measurements using the LEDs varies from ∼0.05 up to ∼2 photo-electrons per trigger pulse (accessible light intensity depends on the individual LED). In front of collimator and filter, a 2 mm thick PTFE layer is mounted and fixed by four additional screws to the PVC holder. Since the opening angle of the light beam after the collimator would be too small (only $\leq 5°$) to illuminate the whole photocathode of the PMT [26], a diffuser is needed to spread the light beam as isotropically as possible to all angles of the half space. The PTFE diffuser provides an almost Lambertian light emission profile and is therefore a good choice for this purpose [281]. It also doesn't distort the spectrum of the emitted light, as shown in Figure 4.23. Together with the light shaping tube, an almost homogeneous illumination of the whole PMT photocathode is achieved with only minor degradation on the very edges of the PMT surface [281, 282] (see also subsection 4.5.4 for more information). Thus, all parts of the PMT photocathode contribute to the measurement results.
Additionally, the PVC holder features another hole below LED and diffuser sheet, which is a guiding hole for the fibers of the laser system. Further, a ferrule clamp is screwed to the support structure right in front of the holder, necessary for the fixation of the fibers from the laser system. After routing them from the backside through the hole in the PVC holder, as illustrated in Figure 4.24, the fibers are fastened and aligned by the clamp in a way that the laser light is emitted towards the center of the PMT, but without passing the PTFE diffuser.

[26] A homogeneous illumination of the photocathode is important, since the PDE measurement in the containers can be done only relative to a well-known reference, see also section 5.1 for more information. An only partial illumination of the PMTs like e.g. reduced to an area around their center could hide regions with lower QE (local non-uniformities in the photocathode), especially close to the PMT's equator. Not considering this could lead to a bias to better, but unjustified results.

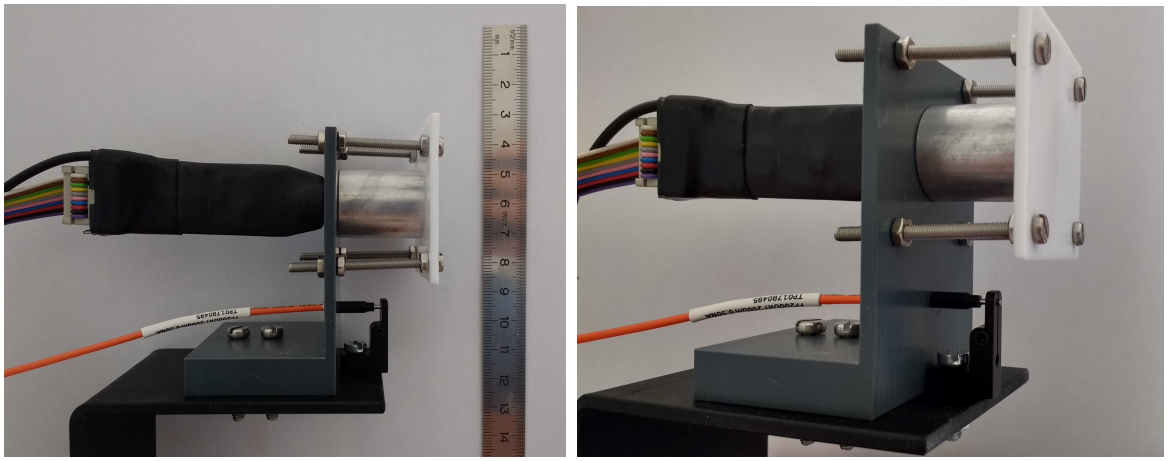

Figure 4.24.: Full light system mounted on a drawer's support structure as done in the drawer boxes (see also Figure 4.6 again). The PVC holder keeps LED, collimator and diffuser. LED and collimator further stabilize each other in position, and PTFE diffuser is affiliated to collimator without any gap in between. Outgoing light intensity is reduced to a single photon level per trigger pulse, with an almost Lambertian irradiation profile. The fiber from the laser system is guided through a hole in the PVC holder and then fixed by a ferrule clamp (fiber end is not covered by diffuser).

4.5.4. Light Field Simulations and Measurements

This subsection summarizes the studies of [281] and [282], which both did elaborated surveys about the light field inside the drawer boxes and the illumination of the PMT's photocathode in order to determine the optimal design and materials for components of the light system. Main goal of these analyses was to optimize the setup towards an illumination of the whole PMT photocathode being as isotropic as possible. All technical details about the simulations as well as about the particular studies, assumptions and results of all individual analyses can be found in given citations.

For a fair and position-independent estimation of the total PDE (integrated over the whole photocathode and respecting all inhomogeneities), every area element A of the photocathode should receive the same amount of photons with the same distribution of incident angles of the incoming photons with respect to the surface of the PMT's glass bulb. This is indeed an idealistic, at least a challenging quest, if using only a single light source [27]. The best configuration for a single, point-like light source therefore would be to realize a Lambertian emitter, which characterizes a perfect diffuse emission with the radiant intensity following the cosine of the radiation angle [307]:

$$I(\theta) \propto A \cos\theta \tag{4.1}$$

[27] In the scanning station, where seven LEDs are mounted on a rotatable arch so that the full photocathode can be checked spatially resolved [243, 271], the PDE can be estimated much better, yet this is not applicable for a mass testing setup.

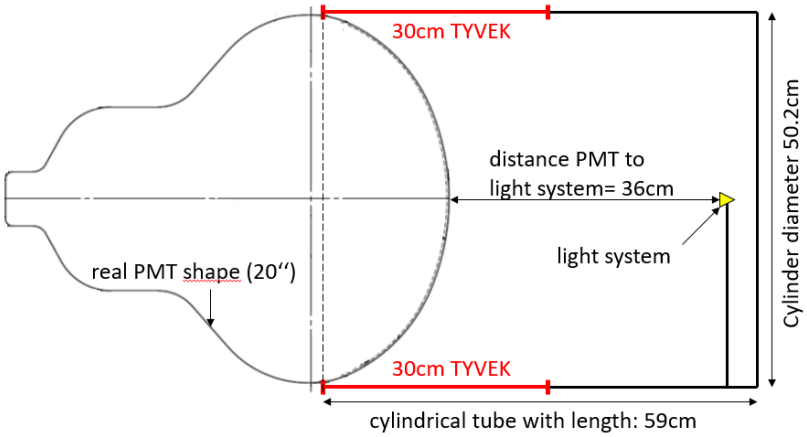

Figure 4.25.: Final configuration of the light system as realized in the container setup, with a 2 mm thick PTFE diffuser directly in front of the light source, a 2 cm wide gap between PMT and light shaping tube and a 30 cm wide range of the tube covered with Tyvek. Image credit: [281].

with $\theta \in [-\pi, \pi]$ the emission angle and A an area element. Hence for the container systems, light system and surroundings need to be optimized to converge to this ideal, Lambertian configuration.
The light field in the drawer boxes has been investigated in two independent MC studies to find the best configuration of all components in the light system to provide the best possible homogeneity in illuminating the PMT photocathode and thus to guarantee a fair PDE estimation [281, 282]. Further, the benefit of additional lenses or diffuser sheets added to the light system has been investigated as well.
In [281], trajectories of up to two million photons from a diffuse light source were simulated, with different emission profiles: isotropic, Lambertian and Gaussian. In these simulations, different regions of Tyvek coverage on the inside of the light shaping tube and their influence on the light field were tested, including realistic reflective properties of Tyvek (see also [279, 308]) and assuming full absorption in regions without a Tyvek coverage. Also, a 20 mm wide gap between PMT and end of the tube was taken into account. All photons reaching the surface of the PMT are treated in a realistic way, including respective probabilities for reflection, absorption and transmission depending of the incident angle of the incoming photons w.r.t. the PMT surface. Also, correct refractive index as well as optical properties of a bialkali photocathode (vaporized on the inside of the glass bulb) were implemented.
A similar approach was chosen in [282], using realistic optical properties for Tyvek coverage and photocathode as well. Here, a point-like light source with isotropic emission profile was used. The results were optimized by adapting the settings and optical properties to the point of smallest relative deviation between maximal and minimal illumination (number of detected photons, normalized by area) on the photocathode, which was aimed to be less that 10 %. As opposed to the first survey, also possible influences on the light field by a tilted light source has been investigated.

Both surveys independently confirmed a Tyvek coverage of a 300 mm wide range of the light shaping tube's inside close to the PMT as optimal configuration. This final configuration like shown in Figure 4.25 was then realized in the light system of every single drawer box in the container system. Tyvek further excelled other reflective materials in the simulation with its optical properties due to its highly diffuse and only weak specular light reflection profile [281]. On the other hand, adding additional elements like a Fresnel lens or an extra diffusive sheet along the transversal section of the light shaping tube was found to have negligible (or only little) effect on the homogeneity of the photocathode's illumination. It was also figured out, that even small tilts by a few degrees of the light source as a whole would deform the light field significantly.

In additional, real irradiation profiles from different diffuser materials were measured in the lab. It was found, that PTFE shows an almost perfect Lambertian irradiation profile, independent from the thickness of the tested sheets and not affected by any incident (non-perpendicular) angle of the light source placed behind the diffuser plate [281]. In Figure 4.26, the main results from this survey are shown [28].
These results have lead to the final choice of a 2.0 mm thick PTFE sheet selected as diffuser in the light system of the containers. The PFTE diffuser will be placed directly in front of LED and collimator, as depicted in Figure 4.24. The thickness of the sheet was chosen due to practical reasons, since an adequate thickness increases the stability and facilitated the installation.
The emission profile from the PTFE diffuser was also included into the light field simulation again, generating a realistic scenario of the final configuration of the system in order to get verifiable simulation results. These results from the two MC simulations are shown in Figure 4.27, illustrating the expected light distribution on the PMTs projected on the equatorial plane; this therefore constitutes the best configuration within the limits of the setup.
The results of the simulations have also been checked and finally confirmed by lateral profile measurements in a real drawer box (including diffuser and light shaping tube), using a partially covered 20-inch PMT from Hamamatsu; results from this lateral profile measurement can be found in [281].

4.6. Design Changes for Container Systems C and D

After the acceptance tests of all bare PMTs in the containers A and B and the potting of the individual PMTs, there is a need to test at least a larger fraction of the potted PMTs for another functionality check. These tests are also necessary to review whether the before measured values for the PMT parameters can be reproduced after the potting or a change (or worse, a degradation) in performance sustained from the potting can be observed.

[28] Measurements were performed with diffuser sheets of four different thicknesses between 0.25 and 2.0 mm, irradiated with one of the LEDs used in the containers; see [281] for details.

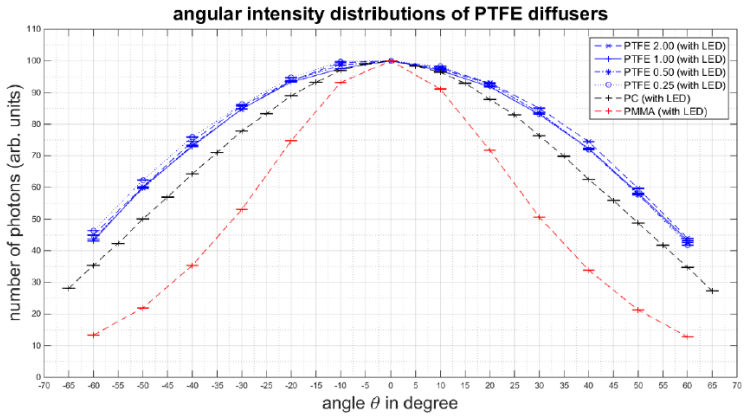

(a) with intensity normalized to 0°

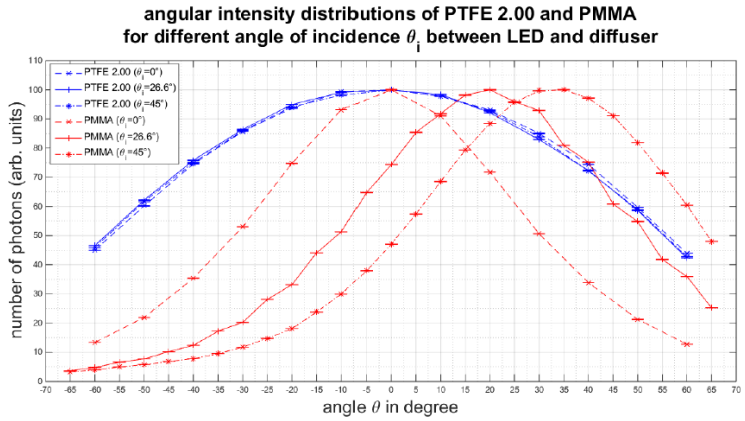

(b) with incident angle of light source

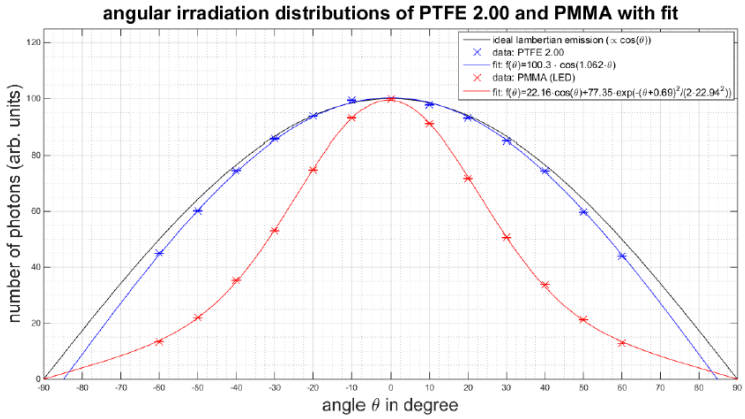

(c) compared to ideal Lambertian emitter (black)

Figure 4.26.: Plots of the angular intensity distributions of different diffuser materials (mainly PTFE and PMMA). All plots are normalized to the intensity at 0° and with statistical errors. PTFE (in blue) shows a stable emission profile, independent from thickness, see **(a)**, and from incident angle of illuminating light source (behind diffuser sheet), see **(b)**. Also, the emission profile of PTFE is very close to an ideal Lambertian profile, see **(c)**. Image credit: [281].

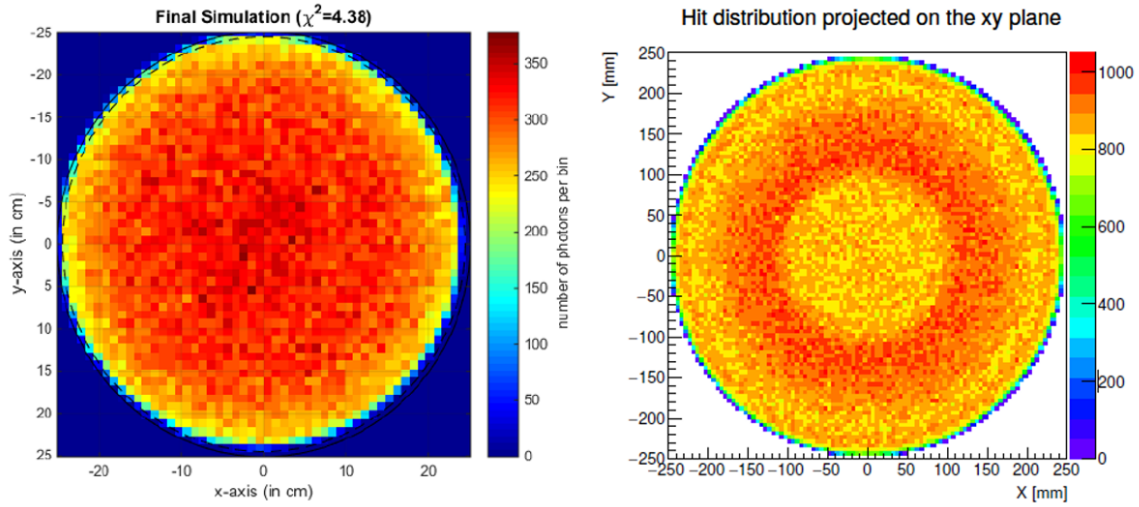

(a) photon hit distribution on photocathode

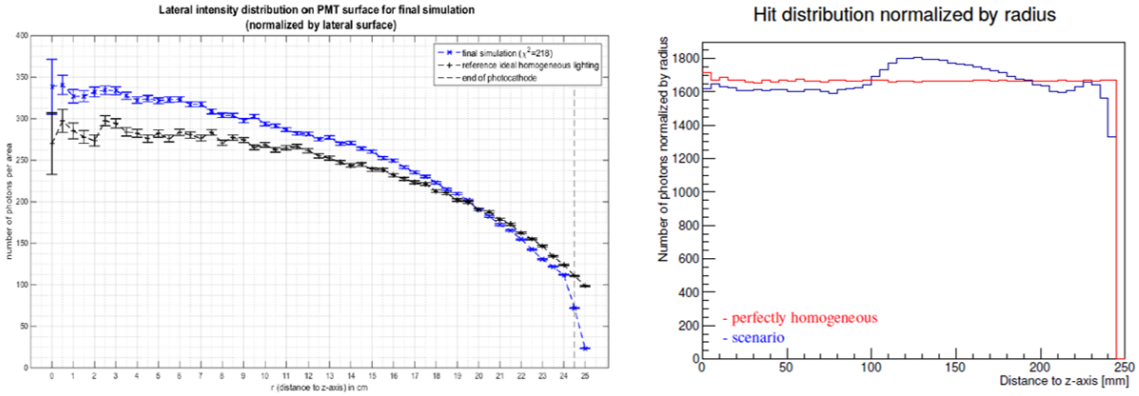

(b) lateral intensity profile on PMT surface

Figure 4.27.: Final results of both independent MC simulations (*left*: [281]; *right*: [282]; in both panels). Small differences in the photon hit distribution originate from different assumptions for the light sources and different binning in the result plane. Both surveys independently confirm a highly homogeneous illumination of the PMT surface with the final design. Image credits: [281, 282].

Basically, a potted PMT can be operated in container A and B as well. However, from the potted base only a single cable is left inside of a stainless steel bellow, since in the final PMT base design the signal will be stacked on the supplied HV. Thus, for operating potted PMTs within these containers, a HV-signal decoupler is needed to separate the high voltage from the actual PMT signals. Such a signal decoupler must provide the standard SHV and BNC connectors of the container system, to establish a connection to the commercial electronics; then a PMT operation with the standard commercial electronics is possible in container A and B as well. Such a potted PMT is shown in Figure 4.28, loaded to a drawer box of container A.

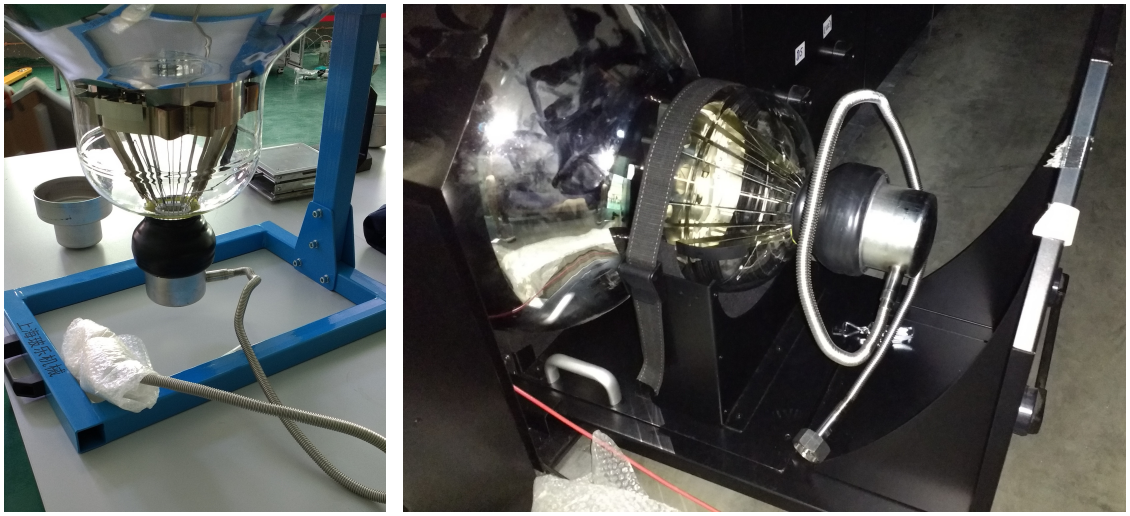

Figure 4.28.: Hamamatsu PMT after potting, with final JUNO base sealed to its back. The stainless steel bellow houses the cable connection to the underwater box. The potted PMTs fit into the drawer boxes without problems, leaving also enough space for a HV-signal decoupler, which can be placed e.g. on the drawer behind the PMT.

The containers C and D were originally foreseen to test PMTs using the final JUNO electronics [309]. They come with minor changes in design to accommodate the situation for the potted PMTs and to enable tests using the final JUNO electronics (see section 3.2 again). The final JUNO electronics design keeps most of the operating and readout electronics (such as HV supply, digitizer unit and trigger management) in the underwater (UW) box, as shown and discussed in section 3.2 (see also [236, 237] again for more information about the UW boxes). These boxes are connected to three PMTs each via the bellow connectors and process the acquired PMT data close to the tubes. Since the UW boxes are too large to be placed within a drawer box and the shared use of one UW box by three PMTs makes the connection and arrangement more difficult, the UW boxes need to be placed outside of the drawer boxes in the container, but still close to the tubes due to the limited length of the bellows. To match these constraints, it was necessary to remove one of the columns in the shelf system to provide enough space for placing the UW boxes. This leads to the already mentioned reduction of container channels from 36 to 32 in these two containers [29]. A sketch and a picture of the inside of container C and D can be seen in Figure 4.29. The use of the final JUNO electronics also requires an adequate data acquisition software similar to the one used for the containers A and B (see chapter 5 for details) and covering a suitable measurement program to examine the performance of the PMTs. The development of such a data acquisition software for container D was defined as responsibility of the respective JUNO electronics and software subgroups and is therefore not presented in this thesis.

[29] All other mechanical parts, as well as the climate control unit and the magnetic shielding are completely identical to the containers A and B.

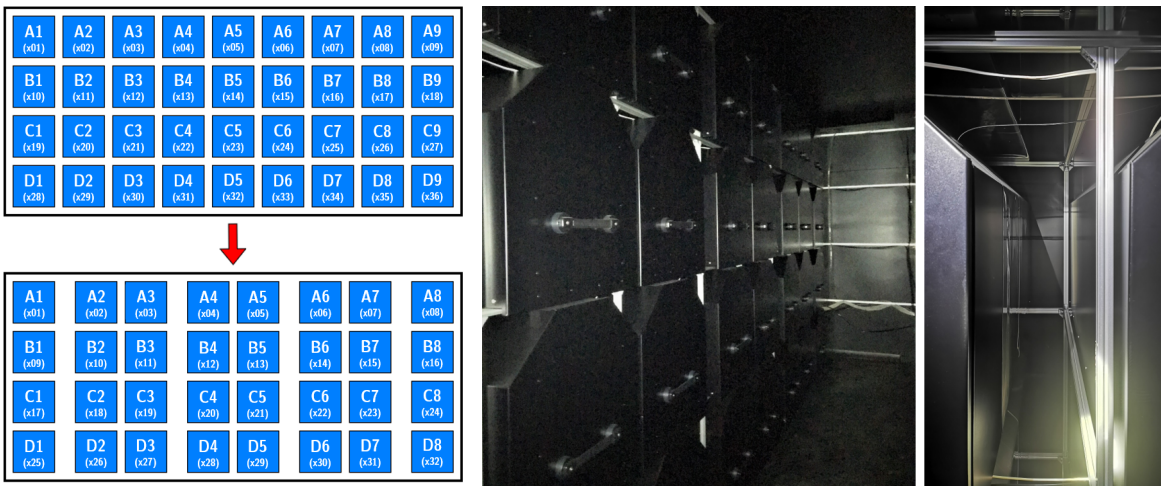

(a) sketch of the design changes from containers A/B to C/D

(b) shelf system in container D, with gaps between columns for UW boxes

Figure 4.29.: Sketch and pictures of containers C and D. In panel **(a)**, the changes from the first to the last two containers (channel number reduced from 36 to 32) are illustrated. In panel **(b)**, the shelf system of one of these containers is shown with focus on the spaces in between of some of the box columns, where the UW boxes can be placed at practical positions (one box will support three channels).

As a consequence from the intended use of the final JUNO electronics in the containers C and D, there are much less commercial electronics installed to or used at these container systems. This covers in particular the readout electronics (all CAEN modules as described in subsection 4.4.1) and the SSB. Nevertheless, both containers feature a fully functioning light system, consisting of 32 self-stabilized LEDs by *HVSys* per container (one installed to each box) including LED controller and external power supply, the standard signal generator as well as necessary trigger splitter devices. A laser system is only installed in container D; since the timing performance of the NNVT PMTs, which add up to 75 % of the total PMT number, does not require a timing performance better then provided by the LED system (see [173, 231, 296] for details), it was decided to equip only one of these containers with a high timing precision laser system in order to reduce costs. Both containers are further equipped with the usual temperature monitoring system described in subsection 4.4.2. Figure 4.30 shows a scheme of the reduced electronics setup of containers C and D, similar to Figure 4.11 in the electronics section.

Due to delays in the development of the final JUNO electronics (and so the schedule), it was decided to test only a smaller fraction of the full PMT sample together with the UW boxes. For this reason, only container D will be equipped with the final JUNO electronics and used to test potted PMTs in the final configuration. To the date this thesis has been finished, container D was not in use, since no UW boxes ready to use have been available so far. However, enough HV-signal decouplers have been provided

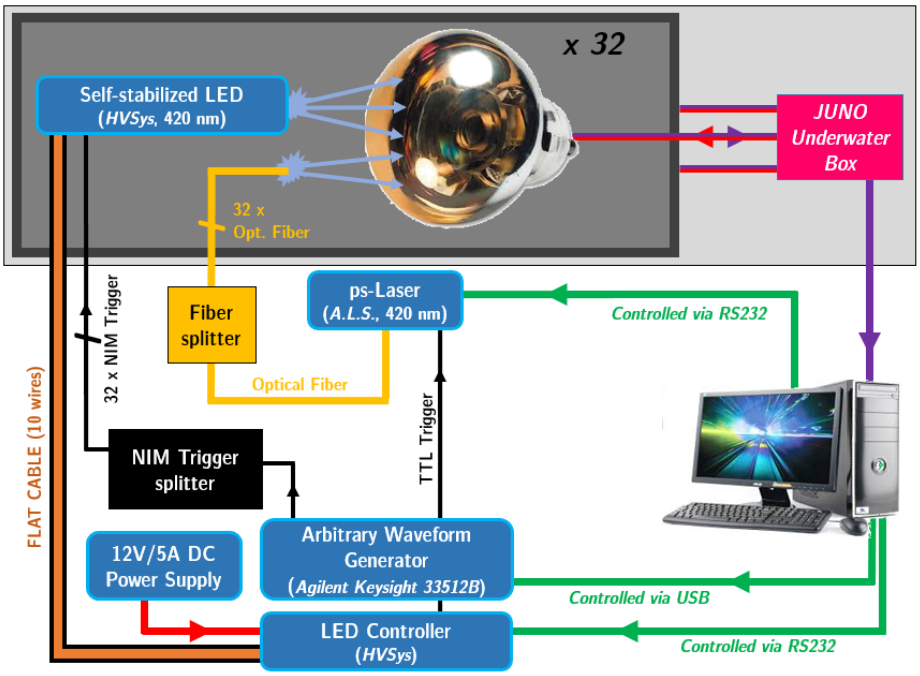

Figure 4.30.: Reduced electronics scheme of containers C and D, similar to Figure 4.11. Blue boxes mark commercial electronics, the black boxes mark custom-made devices. The pink box represents the JUNO underwater box, which is placed close to the PMTs inside of the containers and keeps the operating and readout electronics for three individual PMTs (see section 3.2 and [236, 237] for more details). The green wires show control or communication connections, the black ones show logic signal connections, the purple ones show signal streams. Power connections are illustrated by red wires. LED controller and LEDs are connected via a flat cable tree, reaching to every box (same as in containers A and B). A laser system is only installed into container D. The temperature monitoring system is still not displayed, as it's logically separated from the PMT characterization electronics.

by the JUNO electronics group to regularly test potted PMTs also in containers A and B together with the bare PMT tests [30].
On the contrary, container C was slightly modified to feature a long-term PMT monitoring system. For the realization of this setup, the container was equipped with another complete set of commercial readout electronics (similar but not completely equal the setup of container A and B) in a joint effort of JINR and IHEP. Furthermore, a set of less attenuated LEDs were installed to the drawer boxes, with a significantly higher light intensity and pulsing with a low frequency – with these LEDs, also strains for the PMTs comparable to those from highly energetic muon events in the JUNO detector can be simulated. 32 PMTs will then be selected to stay in container C for a long period of time (several months up to one year) to be frequently tested and thus monitored for their stability and performance under permanently applied HV

[30]The potting of PMT has started in September 2019.

and light pulses. By the continuous illumination, also an accelerated aging of the PMTs can be simulated and investigated within the long-term testing setup. Since this long-term monitoring setup was not developed within the scope of this thesis (but under responsibility of colleagues from JINR), it will not presented here; additional information can be found e.g. in [310–312].

Chapter 5

Measurement Scheme and Data Acquisition Software

The container system presented in the last chapter offers a plethora of possibilities for individual tests of a large number of PMTs. To accomplish a full PMT characterization, several measurement steps using different read-out electronics are necessary and have to be arranged to both guarantee comparable results and a container operation fitting into the daily work scheme.
For a full PMT characterization, the PMTs will be illuminated frequently by different pulsed, weak light sources in a controlled way. The resulting photo-electron (PE) pulses need to be recorded by the read-out electronics adequate to the type of measurement. Pulsing and recording has to rely on a distinct trigger management. With the collected raw data, a decent evaluation of the PMT performance has to be facilitated up to the point of deciding to accept or decline a certain PMT for JUNO (this will be presented later for an exemplary data sample in section 8.1). This characterization process must be done in a stable setting to allocate data of comparable quality and to generate reproducible results over a large number of container runs. The equality of the daily processes does not only enable a reliable classification of untested PMTs, it also makes it easy to perform multiple, directly comparable test runs of a PMT batch without changing the daily routine. It further allows to use a small amount of "reference PMTs" being part of every single run as monitoring devices of the systems in order to verify the stability of the measurement conditions and container performance over the entire period of operation (see also section 8.2).

Following these considerations, a distinct measurement scheme has been established to determine all parameters of interest. This will be presented in section 5.1. The operation of the container system and thus the stepwise execution of the defined measurement program is completely overtaken and coordinated by an in-house-developed, LabVIEW-based data acquisition software (DAQ), including the control of all electronics devices, the data processing and saving. This DAQ software will be introduced in section 5.2, including a description of the full measurement sequence, which is executed by the DAQ in every run, and all its specific software and hardware settings.

The chapter concludes with details about structure and content of the acquired raw data, which is shown in section 5.3, to provide necessary information for the actual evaluation of the PMT data presented later in chapter 7.

5.1. Measurement Program and Constraints

The measurement program should cover all parameters, which have been listed in section 3.3: photo-detection efficiency (PDE), dark count rate (DCR), peak-to-valley ratio (P/V), rise time (RT), fall time (FT), transit time spread (TTS), as well as pre- and afterpulse ratio (PPR/APR) [1]. All these parameters should be determined at a gain of 10^7. Not all the listed PMT parameters can be determined in a combined measurement, since e.g. different light intensities are required or different read-out electronics are needed. The full characterization of the PMTs rather has to be done in different, subsequent steps. Thus, a reasonable series of individual measurement steps has to be defined.
As a first step, a list of individual measurements has been defined and will be presented in the following. All listed data acquisition steps must be considered in a standard data taking run; individual settings applied for the various measurements can be found in subsection 5.2.2 (hardware) and subsection 5.2.3 (software).

- The correct high voltage applied at the PMT's voltage divider base for a gain of 10^7 has to be determined before other measurements can be executed. The corresponding voltage can be found by a scan over a voltage range: in seven equidistant sub-steps, waveform measurements will be performed with voltages $V_i \in [V_0, V_0 \pm \Delta, V_0 \pm 2\Delta, V_0 \pm 3\Delta]$ around a seed voltage V_0, which is the supply voltage of the PMT provided by the manufacturers (see also subsection 5.2.3 for the default setting of the step size Δ). For the measurements of the gain at the applied voltages, the LEDs will be used as light sources, ensuring a stable and comparable light intensity over all the individual measurement steps. All seven measurements will be performed with low light intensity. The gains can then be determined from the charge spectra of all recorded photo-electron events; the voltage for the desired gain of 10^7 can be finally extracted from a fit of the relation of determined gains to applied high voltages, see subsection 7.3.2 for details.

- DCR measurements can be performed at multiple times in the measurement run, e.g. for monitoring the cool-down of the PMTs (so that the de-excitation of the photocathode can be investigated) or at the beginning and end of the full measurement sequence for comparison. The DCR is the only parameter determined with all light sources switched off. For the final DCR classification

[1] Additional information like pulse shape parameters (amplitude, FWHM of single photo-electron pulses), late pulse ratio (LPR) or the signal-to-noise level (S/N) can be determined in parallel without introducing additional measurements, see also chapter 7.

of the PMT, at least one measurement has to be done after adjusting the HV to match a gain of 10^7, and with a sufficiently long resting time in darkness before, so that the PMT could stabilize its dark current, see e.g. [203] for more information; therefore, a DCR measurement performed at the very end of the measurement sequence will be the best for that purpose.
To better separate "physical" dark counts from baseline or electronics noise, usually only events with peak amplitudes above a certain threshold (ideally 0.25 p.e., as defined in Table 3.1) are counted (see also subsection 5.2.2 for the default setting in the container measurements).

- The determination of the PDE and thus the measurement of a clean photo-electron spectrum is the most important task of the container system, considering the PDE as the most important PMT parameter. For this measurement, a sufficient light intensity is recommended for a better significance and lower relative statistical uncertainty in the determination of the average photo-electron count per trigger pulse μ (see also subsection 7.3.2 for a definition of μ and subsection 6.6.2 for the relation between μ and PDE); a light intensity of around 1.5 p.e. per trigger pulse would be the best choice here [313].
  The LED system is extraordinary applicable for such a purpose as it's a stable and self-monitored light system, with an individually settable and reproducible light intensity [271, 296]. Since not all LEDs can reach the same light intensity due to construction-related differences, a common, high setpoint for all LEDs will be used instead.

- Most PMT parameters can be directly extracted from the waveforms of single photo-electron pulses (see subsection 7.2.3 for details) or from the associated charge spectrum of these PMT pulses (see [203] or subsection 7.3.2 for details). For these measurements, the intensity of the light source has to be weak enough to release (almost) only single photo-electrons per trigger event at the photocathode. To ensure such a clean spectrum and waveform sample, a light intensity of $\mu \ll 1$ p.e. is needed, so a value of $\mu \sim 0.1$ p.e. can be assumed as suitable for this kind of measurement (this is equally valid for the gain measurement described above).
  The LEDs are again the logical choice for this measurement, and LED setpoints have been set accordingly. Since the light intensity should further be similar in all container channels (to provide comparable conditions to all PMTs), "calibrated" LED setpoints should be used here [2].

- For the TTS determination, a measurement with the laser system is recommended due to its better timing performance compared to the LEDs. In doing so, also the acquisition of the individual trigger times by recording the trigger pulses with the ADCs is crucial to enable a measurement with high accuracy in

[2] "Calibrated" means here, that all LEDs are set to individual setpoints to produce roughly the same light intensity, see subsection 6.6.1 for details.

timing. High timing performance can then be gained by comparing the recorded hit times of both trigger and PMT pulses (see subsection 7.4.2 for details). Since the analysis of only single photo-electron (SPE) events is preferable for a reliable and good TTS determination, the light intensity of the laser will be weak as well (in the same order as the LEDs in the low light intensity measurement).

Besides the steps including the acquisition of PMT raw data, important conditions and constraints for the measurement process as a whole have to be considered as well, precisely:

- Every run should start with a series of simple tests to verify the cable and base connections in the beginning. If an error is showing up, the shifter should have the possibility to orderly abort the measurement and improve the situation, instead of waiting a full day until the run has finished or interrupting the DAQ while running, which usually leads to software or related driver issues. With this, the number of malfunctioning and so "lost" channels in a run can be minimized. In addition, such tests can also detect major problems with e.g. the HV module or individual data channels.

- The measurement software should take care for the creation of necessary directories on the operating computer and a unique file naming for a failure-free and clearly assigned saving of all raw data files.

- The organization of the measurement sequence has to be optimized in time: on one side, the whole run has to fit into a 24 hours workday (see also subsection 4.2.2 again), including a preliminary data analysis and reloading of the container. On the other side, the cool-down time for the PMTs should be as long as possible, at least 12 hours. The cool-down is necessary for the PMTs to reduce their internal noise and dark current after illumination of the photocathode with daylight [203], which is inevitable during the loading into the container.

- In order to provide a high modularity level in the software (which will be described in detail in section 5.2), some redundancy steps must be added to catch up possible conflicts from the sequential operation.

- At the end of the run, the HV should be switched off automatically to avoid an accidental opening of the container with HV still ramped up [3]. Also, all software connections to read-out electronics need to be terminated properly, in order to avoid possible crashes of hard- and/or software in the next run.

[3] Thanks to an interlock system in the container door, the PMTs will be save even if the door is opened under HV on. In this case, the interlock would kill the HV immediately, preventing the PMT from becoming illuminated with daylight while under HV. The proper ramp down however is to prevent possible damages from PMT bases and HV board from these "kill" actions.

Following these considerations and constraints, the final measurement sequence was built up and integrated into the final data acquisition software for the container system. The actual structure of this software, including all individual and technical steps and applied settings for the measurement will be presented in section 5.2.

The container system though has some limitations, which have to be mentioned before:
First, a reliable afterpulse measurement with the container system was not realizable. Since the laser system, which was foreseen to be used also for the APR measurement, is tailored for a very low light intensity (see item about TTS), the maximum available intensity ($\ll 10$ p.e.) is still way to low for a completely reliable APR measurement [4]. Besides this, due to the limited acquisition time windows of the ADCs (max. 1024 ns, see also subsection 5.2.2 for more details), afterpulses in the container system can only be counted, similar to the way the DCR is measured [5]; this will be done in defined 20 μs windows after a main pulse with maximum light intensity from the laser system. However, for a reliable afterpulse measurement, the total charge of all afterpulses should be set into relation to the initial pulse, see section 3.3 again. With these restrictions, the container system can only provide indications for a too large afterpulse rate, but unfortunately is not able to give resilient results of APR values for the PMTs; it is therefore skipped also in the data analyses in chapter 7 and chapter 8. In exchange, a dedicated system suitable for afterpulse measurements was integrated into the scanning station using less attenuated light sources, see e.g. [259, 260].
Second, since the total light intensity at the PMT surface inside of each drawer cannot be calibrated exactly, the PDE can be measured with the container system only relative to a well-known reference. This is due to the missing ability of determining the absolute number of released photons per trigger pulse from the light sources. Instead, only the number of released photo-electrons per trigger pulse μ can be determined using a PMT, which is a convolution of light intensity (or photon number) and PDE of the to-be-tested PMT at the present photon wavelength. For a full and reasonable calibration of the light field within a drawer box, a perfect photo-detector with the same shape as the glass bulb would have had to be placed at every point, where the PMT photocathode is located later – like using a 20-inch PMT with 100 % QE. As this is of course not possible, the PDE of the tested PMTs has to be derived from μ using an individual calibration factor, unique for each light source (or drawer box) in the container and based on measurements using several 20-inch PMTs with well-known PDE [6]. These calibration factors link the μ values from a set light intensity (respec-

[4] Ideally, the light intensity in the APR measurement should be approx. 100 p.e. [258, 260].

[5] There are FADCs like e.g. the V1751 or V1730 from CAEN [314, 315] providing a much larger acquisition window, which would have been the perfect choice for the APR measurement. But due to the limited budget for the electronics and considering the number of channels per board, resolution and available sampling rate of the ADC modules, the best trade-off was the decision for the use of V1742 digitizer boards.

[6] Values were provided by the manufacturers and confirmed by the scanning station.

tive LED setpoint), which can be determined in the measurements, to the actual PDE of the used PMT, so that a "relative" measurement of the PDE is possible [7]. The determination of the calibration factors is described later in subsection 6.6.2.
A similar situation arose for the settings of the low LED setpoints, added by the fact, that a fixed photo-electron count per pulse cannot be specified by a calibration, since it always depends on the individual PMT detection efficiency (see also subsection 6.6.1).

5.2. Data Taking Software O.P.S.

The full measurement program is implemented in the data acquisition software **O.P.S.** ("Onsite PMT Testing Software"), which is based completely on LabVIEW (short for "Laboratory Virtual Instrument Engineering Workbench", a visual programming language from National Instruments (NI), see e.g. [316–318] for more information). The DAQ software was partially (pre-)developed within several theses, see [281, 319, 320], and then further enhanced for the purposes of the container system. Since LabVIEW interfaces are already available for most of the commercial electronics devices used in the container system [8], the choice of LabVIEW as basis for the DAQ software was reasonable. For the developed software, LabVIEW 2017 was used and is running on the computers of both container systems.

5.2.1. Basic Conception

In the implementation of this software, the needs of the daily operation by mostly non-expert shifters were respected. Initial design goals for this DAQ have been

- a full automation of the whole measurement process with least remaining interactions with the shifter necessary,
- a DAQ execution which is as easy as possible to control and supervise,
- nevertheless, full control of all hardware devices (which is especially important for maintenance and debugging) and the ability to easily access all measurement settings if necessary, ideally without the need of modifying the source code,
- a well-structured saving routine and naming of all raw data files with minimal remaining risk of accidentally overwriting (and thus loosing) data
- and a high modularity in the measurement sequence.

[7] For estimating the absolute PDE of the tested PMT, also the wavelength dependence of the reference PDE as well as the present noise level should be taken into account. Also the scanning station is able to determine only the relative PDE of a PMT, but is in contrast to the container system frequently calibrated using a small 1 ⅛-inch PMT type R1355 from Hamamatsu with well-known QE [243].

[8] Interfaces (and accompanying libraries, if necessary) are provided ready to start by the manufacturers. This is the case i.e. for the CAEN modules and the pulse generator.

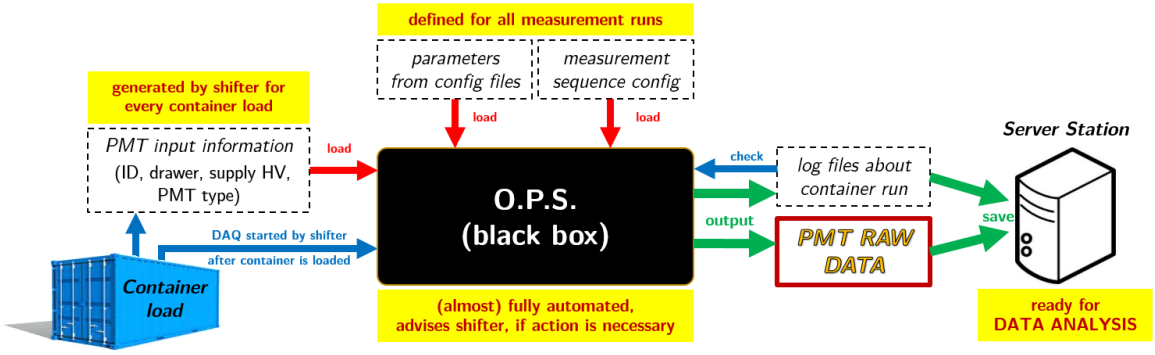

Figure 5.1.: Work flow of the data taking software O.P.S. Information about container load is the main input and has to be prepared before starting the run. The DAQ then works as 'black box' and fetches all settings from respective "config files" (see also subsection 5.2.3). The measurement steps to be executed can be switched on and off via a corresponding "sequence config" file. Raw data and log files about the current run are saved locally and have to be transferred to a server station for data analysis later on.

Ideally, the shifter shouldn't need to operate any electronics devices directly, but rather just have to press a "`START`" button. A simple user interface can provide information about the run execution, while the DAQ controls all electronics and light sources remotely. To start a new run, there should be only few information about the container load needed as input. All of these design goals have been considered and are realized in the final version of O.P.S.

By using the O.P.S. data acquisition software, the container system was enabled to determine most [9] of the parameters indicated in Table 3.1. A sketch of the DAQ workflow is depicted in Figure 5.1. For non-expert shifters, the DAQ is coming as a "black box" with no need to deeply understand the functionality, but easy to use and operate in the daily tests and able to quickly adapt the measurement settings (by modifying the corresponding "config files", see subsection 5.2.3), if somehow necessary. If an intervention is actually necessary at some point, the software provides detailed information and tasks to the shifters. Due to the high modularity level the software was outfitted with in the implementation, it's further possible to run only segments of the full measurement program or to skip single steps of the sequence without any interference in execution. This is particularly useful e.g. for additional tests (if necessary or focus shall be laid on a certain parameter in particular), debugging, in order to redo single measurement steps or to skip already finished steps after errors have been lead to an abort of the sequence before.
Besides the raw PMT data, the DAQ also creates log summary files for every PMT and run with additional information about the DAQ run (like time stamps of individual measurements etc.).

[9] Except for the APR measurement, see section 5.1 again.

5.2.2. Hardware Settings for Data Acquisition

All measurement data is recorded by either the ADCs or the discriminator and scaler modules. Since the basic data acquisition settings for these modules are the same in all of the individual measurement steps, they shall be discussed before the actual DAQ software will be explained finally. Also a short overview on the mode of operation of the individual modules will be given here to better understand the structure of the DAQ, which electronics module is adequate for which measurement and the selection of the respective hardware settings.

Data from counting measurements is acquired by the discriminator (CAEN V895B) and scaler (CAEN V830AC) modules. In such a measurement, the discriminator receives the PMT signals on a certain channel and checks all inputs for being above a set threshold. The acceptance of input signals can be vetoed by another external signal, which is used e.g. in the APR measurement in the containers; if no veto signal is present, all inputs will be processed and checked w.r.t. the threshold. Input signals exceeding the set threshold lead the discriminators to output a defined ECL signal, which is fed directly into the scaler. If the scaler detects such ECL signals, it incrementally increases the counter of the corresponding channel (defined register on the scaler board). That way, the scaler counts all events over a defined measurement time [321, 322].
The settings for the threshold of the discriminator channels as well as the width of the out-coming ECL pulses can be set global for all channels in the DAQ. Default settings for all counting (DCR) measurement are a threshold of **3 mV** [10] and the maximum possible ECL output width of **40 ns**, which limits the measurable rate to 25 MHz due to the signal induced dead-time [11]. The default time between two readouts of the scaler registers (defining also the step size in time inside of the raw data) is **1 s** (which also is the minimal possible step size). Total acquisition times are set individually in every counting measurement and vary between 60 s and 900 s, depending on the actual measurement step, see subsection 5.2.3. Before the start of every counting measurement, all counters are reset to 0 by the DAQ.

All data containing waveforms is taken by the switched-capacitor ADC (CAEN V1742) modules. In these measurements, the output voltages of the PMT base are recorded over a short, well defined period of time after a dedicated trigger hooked in. Each ADC records 18 PMT channels in parallel, added by four channels which capture the

[10] Assuming a gain of 10^7, single photo-electron pulses come with amplitudes between 6 and 7 mV, see e.g. the analysis results later in subsection 8.1.3. A threshold of 3 mV thus corresponds to around $0.3 - 0.5$ p.e., which is higher than the originally aimed 0.25 p.e. (as discussed in section 3.3 and section 5.1), but the best value to respect both a low threshold and a low noise level in the data (measurements during the commissioning have shown a good noise level applying this threshold, see section 6.3). The threshold can further be set only in steps of 1 mV, with 1 mV as lowest applicable value [321].

[11] Also depends on operational mode of the discriminator, see [321, 322] again.

input NIM trigger signal to be recorded as well, see subsection 4.4.3 for more details. If a trigger signal arises, the ADC freezes its ring buffer, which was continuously filled before with the chosen sampling frequency, and starts reading out the capacitor cells [323]. Then it writes the measured voltages consecutively into a file. The total number of the saved values per trigger defines the size of a single event, which is also referred as **measurement frame** (or just "frame") in the following. The dedicated trigger time of the ADC though can be shifted to a later time with respect to the incoming trigger signal; this can be used to compensate for different cable lengths and thus delays in the system. Since this "post-trigger" has to be fitted to the real system and its cabling situation, it is individually adjusted to the container systems and hard-coded into the DAQ.
The sampling frequency defines, how fast the analog signals are sampled into the DRS4 buffer of the digitizer unit. Only four options are selectable here: 0.75, 1, 2.5 and 5 GS/s. Also for the frame size (or record length), only four options are available: 1024, 520, 256 or 136 bins [287]. Sampling frequency and record length together define the frame's size and resolution (of its raw data points) in time. By default, all measurements are taken with a sampling frequency of **1 GS/s** using a **520 bin** frame, so that a time window of 520 ns is recorded by the ADC after each trigger.
Further, before saving the data to file, a software data correction for the DRS4 chip in the ADCs is applied. This correction considers the physical properties and small differences from the construction process of the actual built-in capacitor cells, which are unavoidable and unique for every chip, and slightly corrects the individual bins in timing, amplitude offsets and noise level [323]. Without these correction, a useful data taking wouldn't be possible, because the preprocessed raw data cannot be interpreted correctly. This also leads to slightly "different" (variable) precisions, even though the ADCs themselves are tagged with a 12-bit resolution. The DRS4 correction is enabled in the DAQ by default. For more information, refer the manual of the CAEN V1742 boards directly, see [323].

All of the here mentioned hardware settings (except from the ADC post-trigger) can be adjusted in the DAQ via corresponding "config files", see the following subsection for details.

5.2.3. O.P.S. Measurement Sequence

Main purpose of O.P.S. is to control HV, readout electronics, light sources and the pulse generator for trigger provision. The software is completely based on LabVIEW and puts all single measurement steps and support actions (like ramp HV up/down, switch SSB to next position, adjust light intensities etc.) together to a big sequence, which then is operated subsequently in a total time of roughly 16 to 18 hours (depending on the actual settings).
The individual measurement steps are separated from each other within the DAQ structure and added modular, so that single steps can be (de)activated by simple `True`/`False` switches. The software is tailored in a way, that the remaining sequence

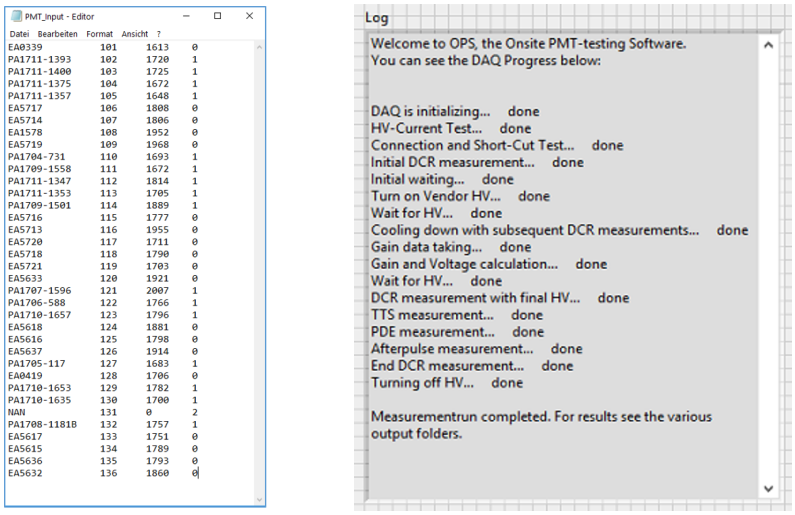

(a) DAQ input file example

(b) GUI (log output window) for DAQ user (shifter)

Figure 5.2.: I/O of the data taking software O.P.S. The PMT input file (panel **(a)**) provides all necessary input information about the container load to the DAQ and has to be prepared before starting the run. It consists of only PMT ID, channel number, supply HV and PMT type (`'0'` = dynode, `'1'` = MCP). Panel **(b)** shows the log output GUI for providing information about the operation (current measurement step) to the shifters.

with several steps deactivated is still able to run without any disturbances; only few safety-related steps at the beginning and end of the DAQ execution are mandatory and cannot be skipped [12].
The user I/O was reduced to a minimum, and only a specific input file has to be provided by the shifters as input for the DAQ preceding to every run, see also Figure 5.1 again. This input file delivers few, but indispensable information about the current container load: individual PMT IDs, corresponding channel numbers where the PMTs have been loaded into (`x01..x36`, with `x` the container number, see also Figure 4.5a and Figure 4.29), supply voltages (acting as seed voltage for the gain measurement) and an index for the types of the loaded PMTs in the respective boxes (`0` for Hamamatsu, `1` for NNVT, `2` for empty boxes). The input file is important mainly for the setting of the HV and a reasonable, correct file naming [13]. However, it is the central and most important input parameter collection of the DAQ. An example for such an input file is shown in Figure 5.2a. As graphical user interface, a simple log screen with few information about the current and already finished steps is provided to the shifter, see Figure 5.2b. Additional information, like errors or requests to the shifter to become active, are provided in pop-up windows just in time.

[12] Deactivating these steps is only possible inside the code level for debugging purposes.

[13] The naming of data files is managed automatically by the DAQ, mainly based on PMT ID and measurement channel. The correspondent information has to be provided as input information to the DAQ. See more details about the file naming in section 5.3.

Most of the individual measurement settings are kept in a bunch of "**config files**". These files are read in by the DAQ within the measurement steps, see also Figure 5.1 again, defining communication properties to the hardware, applying the respective settings to the electronics devices (as it was described already in subsection 5.2.2) and specify measurement parameters for the actual data taking steps. Only very few variables are hard-coded into the O.P.S. source code like register and hardware addresses of the used VME modules, which belong to the very system and must stay untouched, or few, specific measurement settings which have to stay at zero access by the shifters for the same reason. For each run of the DAQ, the software further allocates an increasing run number, added to all file names to guarantee uniqueness of all measurement raw data files [14]. The run number is also managed in a config file. Also the modularity of the whole measurement sequence is braced in a respective config file, where every modular step can simply be switched on and off, see also subsection B.1 in the appendix.
Finally, the final measurement sequence with all individual steps is shown in Figure 5.3. Additional plots of the DAQ scheme, with highlighted modular and data taking steps, can be found in subsection B.1 in the appendix as well.

For a better understanding, all individual steps displayed in Figure 5.3 will be explained in detail in the following. The $*$ marks indicate that these steps are mandatory for the execution of the measurement sequence and therefore cannot be switched off. The values in the respective steps represent the applied measurement software settings (default settings in config files or hard-coded).

(i) $*$ **Initialize DAQ:** Check communication to hardware, increase run number for new run and create directories for data on the computer.

(ii) $*$ **SSB command:** Switch outputs to `B` (discriminator $\oplus$ scaler).

(iii) **Current Test:** Check (cable) connection of HV to base by applying a small voltage (300 V, hard-coded) and read out the monitored current. If current exceeds a small threshold (set to 10 μA, hard-coded), connection to the base (resistor circuit) is assumed to be established.

(iv) $*$ **Connection and Short-Cut Test:** HV is ramped up to individual supply voltages of the PMTs, taken from the PMT input file (see Figure 5.2a again). If the voltage is stable at the set level after a waiting time of 120 s, a short-cut

[14] The run number displays the number of DAQ executions of each container and is increased by 1 always when the DAQ is started (started from 0 with the very first DAQ execution). Apart from its uniqueness and thus its benefit to avoid identical file names (if e.g. a PMT is tested twice in the same container channel within different runs), the run number has no further meaning or influence to the data. In the data storage, all files are further sorted by their container run ("mass") number. While the mass number is rising incremental with the container runs, the DAQ run number might not due to e.g. performed test/maintenance runs between two "normal" container runs, or if the DAQ had to be aborted and restarted during a single run. The mass number is further assigned manually, while the run number is assigned automatically by the DAQ.

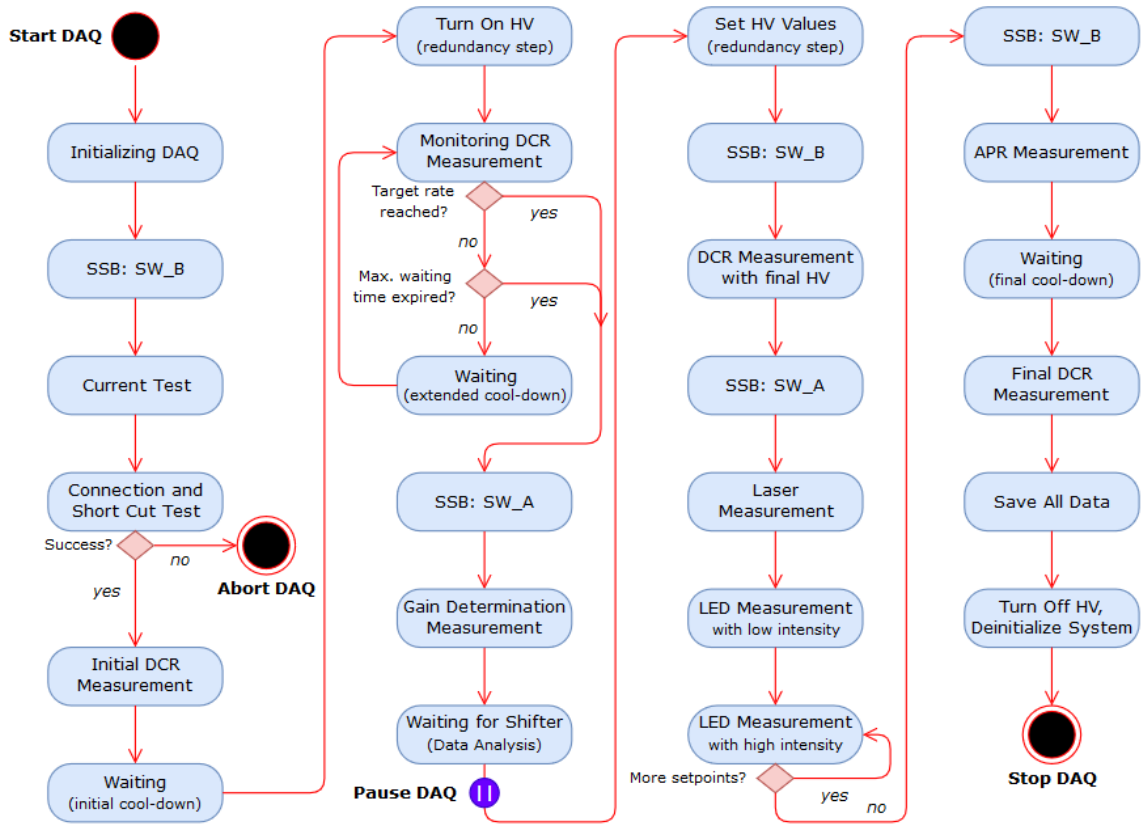

Figure 5.3.: Complete measurement sequence of the DAQ software O.P.S., used in both container systems equipped with commercial electronics. Abort command is optional and can be confirmed (if e.g. some channels have failed the initial tests due to a bad base connection) or skipped by the shifter. The "Pause" command is the only mandatory interaction between shifter and DAQ in every run; it needs confirmation from the shifter for continuing the run, after the data from the gain measurement has been analyzed and HV has been adapted accordingly. All other steps will be executed automatically.

can be excluded most likely [15]. Afterwards, a quick measurement (10 s, hard-coded) with the discriminators is performed. If the measured rate exceeds a set threshold of 5 kHz (hard-coded), a proper connection of base to PMT can be assumed as guaranteed [16]. Data from this measurement is not saved. The HV will be left switched on for the rest of the run.

If one of the tests in (iii) or (iv) fails, a warning is showing up for the shifter, indicating the failing channel and test. If at least one channel is failing, the

[15] Otherwise the HV would have been ramped down automatically for the respective channel.

[16] A measured rate of less than 5 kHz would be un-physically low to originate from PMT dark counts (i.e. for PMTs which haven't had time to stabilize their DCR after the loading), while the threshold of 5 kHz is defined high enough to get passed by noise only. Thus, measured rates higher than the defined threshold have to contribute PMT dark counts, so that a proper connection can be fairly assumed, whereas lower rates hint for a bad connection.

DAQ proposes to the shifter to abort the DAQ (for e.g. an additional check of the channels found malfunctioning or disabling the affected channels [17]). If the shifter decides to abort the run, the HV is ramped down and DAQ is terminated afterwards. If shifter decides to continue, the DAQ proceeds with the next step.

(v) **Initial DCR Measurement:** This is the first DCR measurement of the (still un-cooled) PMTs. Data is taken for 300 s (default value).

(vi) **Initial Waiting Time:** First cool-down period of the system, no further actions happen for 60 mins (default value).

(vii) **Turn On HV:** This is a redundancy step, in case that the initial connection and short-cut test has been deactivated (which is only possible in the source code for debugging purposes, but hidden for the shifters). All channels will be ramped up to individual supply voltages.

(viii) **DCR Monitoring and Cool-Down:** For the next hours, the system waits and performs DCR measurements every 30 mins (by default). Data is taken for 60 s (default value) in each measurement and saved separately. If all 36 PMTs individually are showing a dark rate of equal or less than a target rate (30 kHz by default) in one of the monitoring measurement, the cool-down will be stopped and the DAQ will proceed with the next step. If the target rate hasn't been reached by just one PMT, the system waits for another turn. This will be repeated unless a maximum waiting time (12 hours by default [18]) is expired. Then, after finishing the next monitoring DCR measurement, the DAQ continues with the next step independently of the DCR results.

(ix) **SSB command:** Switch outputs to `A` (digitizers).

(x) **Gain Measurement:** For the determination of the best voltage for a gain of 10^7, a series of seven measurements is executed, as explained in section 5.1 already. The default setting for the voltage step size is $\Delta = 50\,\mathrm{V}$, so that a window of 300 V is covered by measurements with voltages $V_i \in \{V_0,\ V_0 \pm 50\,\mathrm{V},\ V_0 \pm 100\,\mathrm{V},\ V_0 \pm 150\,\mathrm{V}\}$ applied to the PMT. For these measurements, first only the baseline is recorded in 10'000 frames (with lights off) [19], averaged and then

[17] This can be done e.g. via the PMT input file by removing the information of the respective channel (i.e. setting the HV value to zero and adding a '2' as PMT type).

[18] Observations from the PMT testing indicate, that not all PMTs can reach their minimum DCR after a waiting time of 12 hours; nonetheless, all PMTs show at least a considerably reduced rate (this is shown exemplarily for a few PMTs in subsection B.2 in the appendix). Thus, 12 hours seems to be a fair compromise w.r.t. the restrictions from the daily routine. Over the weekends, the cool-down time can be extended to 36 hours by modifying the respective config file.

[19] It was originally planned to perform the gain data analysis to get the adjusted HV values for a gain of 10^7 as part of the DAQ as well, inside this measurement step. The baseline correction measurement performed here was intended to improve the results of this analysis. But since the gain data analysis was outsourced from the DAQ at the end (see step (xi)), this is now only a leftover from this earlier included, respectively projected step.

subtracted from the following PMT waveform measurement, where (by default) 20'000 frames are acquired with 100 Hz using the LEDs at low intensity and at individual setpoints roughly matching a intensity of 0.1 p.e. per pulse [20]. This is done for all seven sub-steps of the gain measurements. Only the waveform measurements (with lights switched on) are saved into respective directories. LEDs are switched off at the end. Details about the analysis of the raw data from the gain measurement and the determination of the best HV for a gain of 10^7 will be discussed later in subsection 7.3.2.

(xi) **Waiting for Shifter (PAUSE):** After all measurements in the gain step have been finished, the DAQ pauses itself and opens a dialog window with instructions for the shifter. The data from the gain measurement then needs to be uploaded and analyzed on the server, generating a set of new HV values for the DAQ. This step was first intended to be done automatically by the DAQ as well, but was then outsourced to the server system due to performance and accuracy reasons. After the shifter has changed the HV settings [21] of all channels accordingly, the DAQ execution can be continued again.

(xii) **Set new HV Values:** Another redundancy step for the HV setting, like explained before in (vii). Since the output of the gain data analysis on the server produces an updated version of the PMT input file with the new HV values included, this step can also be used to update the HV settings accordingly.

(xiii) **SSB command:** Switch outputs to `B` (discriminator $\oplus$ scaler).

(xiv) **DCR Measurement with new HV:** The first measurement after adjusting the HV is another DCR measurement. Data is taken for 300 s (default value).

(xv) **SSB command:** Switch outputs to `A` (digitizers).

(xvi) **Laser Measurement:** Laser is switched on at low intensity (950 ‰ tuning [22] by default, with a frequency of 100 Hz). 50'000 frames (default value) will be acquired in this step. Further, the NIM pulses, which trigger the laser system and the ADCs simultaneously, are recorded by four individual channels per ADC and saved as well (see also subsection 4.4.3 and section 5.3 for more information). The laser is switched off at the end.

(xvii) **Low Intensity LED Measurement:** For this step, all LEDs are set to their individual setpoints again to roughly match a light intensity of 0.1 p.e. per pulse, like done in step (x). By default, 25'000 frames at 100 Hz are recorded.

[20] The individual setpoints were determined in a calibration phase using a bunch of already characterized PMTs with known PDE, as shortly mentioned before. See subsection 6.6.1 for details.

[21] This is done e.g. by using a separate script to avoid mistakes in operation by the shifter.

[22] See subsection 4.5.2 for a description about the laser output and tuning again.

(xviii) **Additional LED Measurements:** If enabled, the system performs multiple more measurements with the same ADC settings like in the LED measurement before. This time, the LED setpoint is common for all LEDs. The number of measurements is defined by the number of setpoints provided to the system by the corresponding config file (step is skipped automatically, if no values are committed). Each measurement is saved to its own directory to not mix up data files. By default, at least one LED measurement using a setpoint of 3000 ("high light intensity") is performed in every run, suitable for the determination of the PDE. At the end, the LEDs are switched off.

(xix) **SSB command:** Switch outputs to `B` (discriminator $\oplus$ scaler).

(xx) **APR Measurement:** For this measurement, the laser is switched on again and set to its maximum light output intensity (0 ‰ tuning), while being triggered with a frequency of 10 kHz (by default). The discriminator is vetoed most of the time by a logic '`HIGH`' output of the pulse generator (see subsection 5.2.2 and [321] for more details again) leaving open only a short gate following each trigger pulse, so that only events in a time window of $[0.5, 20]$ μs after the initial laser pulse are counted. Data is saved the same way like the DCR data. By default, the measurement time is 300 s. The laser is switched off again at the end again.

(xxi) **Final Waiting:** Before the last DCR measurement is started, the system is resting for another 30 mins (default value) for the DCR to stabilize again after the measurements with the light sources.

(xxii) **Final DCR Measurement:** This is the last measurement of the DAQ run. Since this is also the DCR measurement with the PMTs staying the longest in darkness, it is taken for the final classification of the PMTs [23]. Therefore, also the measurement time is extended to 900 s (default value) to increase statistics.

(xxiii) $*$ **De-initialize system:** The last step is saving of the remaining data to the files, ramping down the HV of all channels and closing all open connections to the electronics devices. Then the DAQ stops and the container is ready for unloading, while the raw data can be analyzed.

The O.P.S. is only responsible for the PMT raw data acquisition. Other functions like the temperature monitoring system, the remote container control system or the data

[23] At the time of this measurement, the PMT stays in darkness for at least 16 hours. The exact time slightly depends on how long the gain data analysis has lasted (see step (xi)). Anyway, small variations in the "total cool-down time" until to this measurement doesn't play a large role, since the PMT has either stabilized its dark rate to that time (so the DCR becomes independent from staying any longer in darkness, or the PMT still has an increased rate – in this case, the PMT has maxed out the available time (limited by the daily schedule, see subsection 4.2.2 again) and in worst case, its DCR thus might be overestimated in the measurement, making the acceptance criteria "more strict" for this PMT. So a chance to falsely accept a bad PMT is not given here.

transfer to the servers are not purpose of this software, but separate tasks. So is the temperature monitoring and the container control system realized in own LabVIEW-based programs, see [299], and are duty of the shifter to be executed and supervised as well. Moreover, also the data analysis is separated completely from the data taking; a detailed description of the data analysis methodology can be found in chapter 7.

5.3. Raw Data Structure and Format

The raw data acquired and saved by the DAQ can be distinguished into different classes. These classes are data from counting measurements, data from waveform measurements and data from the trigger periphery. All data from measurements connected to rates (DCR, APR) is recorded as counting data; all data from measurements, where the actual pulse form is needed for the analysis (gain/HV, photo-electron spectrum, RT, FT, TTS etc.) is recorded as waveform data. The trigger data is used for an improved timing of the waveform data (see also section 6.4 and subsection 7.4.2) and thus recorded the same way.
Raw data from the counting and waveform measurements is taken and processed for every channel individually and saved into particular files for each PMT. Data containing trigger information is taken for each ADC trigger group combined, belonging to four to five ADC channels each (see also Table 4.2 again).

5.3.1. Counting Measurement Data

All data taken with the discriminator and scaler boards has the same data format and structure and is saved in ASCII-coded `.txt`-files. For each active channel and each measurement, one single file is created. The file names contain the main information about the performed PMT test, such as PMT serial number and type ('`Ham`', '`MCP`'), container channel number, individual DAQ run number in which the data was acquired and specific type of measurement the data was taken at, so that a clear identification of data content is possible by the respective file name.

The counting raw data contains time steps and the actual counter status (count number) of the corresponding scaler channel preceded by the average count rate (added as information in the first line). The data structure is a list of `[time, counter]` tuples, with total measurement time and total number of counts over threshold up to this step as list entries. The actual count rate over time can be calculated then from the list entries as described in section 7.1, where also some plots of counting raw data are depicted, see e.g. Figure 7.1.

5.3.2. Waveform Measurement Data

Waveform data can be recorded in two different data formats: *ASCII-coded* and *big-endian binary coded* format. Data was saved in ASCII format (`.txt`-files) mainly in

Table 5.1.: Summary of important facts about the waveform raw data file formats.

Data Format	total #bins/frame	corrections?	disk space/frame
ASCII [.txt]	521	–	∼5700 bytes
Binary [.dat]	522	1/10'000	2088 bytes

the first phase of the container operation, since it is easily readable by any editor and therefore was useful in the beginning for maintenance and debugging of the system and the development of analysis scripts for the data. Later [24], the data format was changed to binary (.dat-files, with 4-byte float representation). With data taking in binary format, the performance of the DAQ is increased a lot with respect to data taking in ASCII, since converting the digital information into ASCII is computationally more expensive. Furthermore, data saved in binary format is more compact and needs less disk space. As an additional feature, each binary value will be multiplied in the DAQ by a factor of 10'000 before saved to the file. With this trick, decimal values could be saved more efficiently in the 4-byte float-representation [25].
Apart from the way of saving the data, also the content keeps minor differences between the two data formats. The data structure of all files is a simple list of voltage values of all frames sticked together in one column, independent of the data type. The data frames (containing 520 bins if using the default settings, see subsection 5.2.2 again) are separated by delimiter values: one in case of ASCII format leading to **521 values** per frame in total, and two [26] in case of binary format, leading to **522 values** per frame in total. The different frame length has to be considered in the data analysis to proper separate the individual frames from each other.
Due to the DRS4 raw data correction (see subsection 5.2.2 and [323] again) and some other unavoidable effects of the delimiter setting, not only the last, but more the last 20 bins of each frame will be skipped in the data analysis later to avoid spoiling the results by data artifacts or patterns from these effects.
All important information about the ASCII and binary raw data format is finally summarized in the Table 5.1. Exemplary plots of waveform raw data are shown later in section 7.2, where also the treatment of the waveform data is explained in detail.

The waveform raw data file names contain the main information about the performed PMT test, such as PMT serial number and type ('Ham', 'MCP'), container channel number and individual DAQ run number in which the data was acquired, similar to the

[24]Data format was changed to binary from beginning of data taking with the second container system.

[25]This factor was implemented into the DAQ in an early development stage to increase efficiency and to test precision of the binary data saving routine. It stayed as remnant feature in the DAQ at the end.

[26]While in ASCII format, the delimiter value is placed at the and of the frame, in binary format delimiter values are placed in front and at the end of each frame.

naming of the counting raw data; the corresponding measurement is indicated here by the parent directory, which is created and named by the DAQ automatically, so that again a clear identification of data content is possible by the respective file name and path. Independent from the data format, it turned out that creating four files for each channel and measurement, each containing a quarter of the acquired frames, further increases the performance and stability of the data acquisition a lot.

5.3.3. Trigger Data

In addition to the PMT waveform data, each ADC also records the incoming NIM trigger signal (which triggers the ADCs at first) on four different channels (one for each internal trigger group of the ADC, see subsection 4.4.3 again) in order to improve the timing information of the system. Although the inner structure of the recorded trigger data is identical to the waveform measurement data, it is described separately, since it is not directly assignable to a single container channel or PMT; the assignment of the individual channels to the trigger groups was already noted in Table 4.2.
The trigger data files are named with the corresponding trigger group and ADC serial number, completed by the type of measurement for a clear identification and relation to the individual container channels. Exemplary trigger waveforms are displayed e.g. in Figure 7.19.

Decent timing information can be gained from comparing the signal "hit times" in the waveform raw data files with the pulse hit times in the trigger files. By this comparison, internal effects of the ADC can be reduced significantly; otherwise the jitter of a single ADC channel (usually $> 10\,\text{ns}$) would easily cover the PMT timing resolution, as especially the Hamamatsu PMTs are expected to have much smaller TTS values, see e.g. [214]. Using the trigger information, the remaining jitter of the ADC can be borne down to roughly a few hundred ps. Despite that the trigger pulse data acquired for all ADC measurements, the TTS measurement is the only measurement the trigger files really become important in the analysis.
Details about the trigger data analysis can be found in section 7.4. A more detailed measurement of the remaining jitter is described and discussed in section 6.4.

Chapter 6

Commissioning and Calibration of the Container System

Commissioning and calibration of the container system are essential steps to better understand the capability and performance of the setup and to ensure the readiness of the system for the use as a mass testing system for 20-inch PMTs. Therefore, some performance conditions need to be checked and ascertained, covering e.g. the reduction (or ideally: absence) of external magnetic fields as well as a sufficient darkness inside the containers and an acceptable noise level in the readout channels. Equally important is the calibration of the light sources, i.e. of the self-stabilized LED, as well as the determination of systematic effects influencing the measurement, such as crosstalk or hardware-related systematic uncertainties.

To ensure these conditions, some groundworks and tests with the realized container systems have been done and will be portrayed in this chapter, starting with the effectiveness of the magnetic shielding (see section 6.1), followed by surveys about light-tightness (see section 6.2), the internal noise levels of the system (see section 6.3), residual systematics in the electronics concerning the timing of the waveform data acquisition (see section 6.4) and a possible crosstalk between container channels (see section 6.5). The chapter will be concluded by a description of the calibration of the LEDs, which are the main light sources in the containers (see section 6.6).
The here presented measurements have been performed during the commissionings of the containers in June 2017 and March 2018, as well as during maintenance phases in November 2018 and July 2019. They further cover only the containers A and B, since containers C and D haven't been available at the time where most of the here presented measurements were performed; further, only containers A and B have been used for the PMT mass testing to the date of this thesis.

6.1. Magnetic Shielding and Residual Magnetic Field

The magnetic shielding enables the container system in the first place to predicate about the PMT performance in a reliable way, since PMTs of a size like the JUNO

PMTs can exhibit a degradation in performance if operated in magnetic fields, such as e.g. the EMF. Tests with the scanning station have proven, that even weak magnetic fields in the order of 10 μT can change the electron trajectories inside the large PMTs and start to affect the uniformity of the collection efficiency and thus PDE and local gain over the photocathode, which worsens the overall performance of the PMT during operation [1]. At around 20 μT, the PMTs already fail the requirements for homogeneity from Table 3.1 [243, 270, 271]. To make sure that the influence of any external magnetic field on the PMT performance will be negligible, the residual field inside the containers must be suppressed to the level of $\sim$ 10 % of the EMF or below.

An effective suppression of external static magnetic fields can be reached by a passive magnetic shielding of the entire container's inside. For this purpose, the container walls are revetted with a 4 mm thick multiple layers shielding of alternating silicon soft iron and aluminum, as described in section 4.3. Silicon iron, which basically is iron admixed by a few percents of silicon, was chosen instead of mu-metal, although it has a five to ten times lower relative permeability, but shows an excellent shielding against high frequency fields [276] and is much less sensitive for mechanical stress, which was important for the shipment of the system. The multilayer shielding can reduce the residual magnetic field inside the container to a level of $\sim$ 10 % of the geomagnetic field strength, which is suitable for running the 20-inch PMTs inside.
Preparatory measurements done inside the bare containers, before adding a magnetic shielding, have shown an average value of 32.0 $\pm$ 7.6 μT for the magnetic field [2], with an EMF value of around 48 μT in Hamburg [324], where these measurements have been performed. Measurements performed after the installation of the magnetic shielding and before the shipping of the containers have shown a reduction of the residual field to below 5 μT, see Figure 6.1 and [299]. Unavoidable weaker spots as next to the doors, the ventilation holes of the climate control unit or the cable feed-through have been reinforced by adding an additional layer of FINEMET, a soft foil made out of a amorphous, nano-crystalline Fe-Si-Nb-B-Cu compound [325] and marketed by Hitachi Metals Ltd. [326], around the drawer boxes close to these weaker spots, leading to residual magnetic fields of around 2 μT or below in these boxes.
After the shipment to China, the shielding effect has been measured again. Figure 6.2 shows the results of on-site measurements using a commercial Gauss-meter roughly at

[1] Depending on the orientation of the PMT axis to the magnetic field vectors, photo-electrons can be redirected by Lorentz force to either miss the amplification system or be accelerated additionally towards it. This could lead to a position-dependent decrease or increase of collection efficiency, local gain and transit time (in all stages), increasing the non-uniformity of the PMT performance significantly w.r.t. the absence of a magnetic field. The magnetic influence is the greatest in the electron-optical input system, where electron trajectories are the longest. Tubes with linear focusing dynodes (like the R12860 PMTs from Hamamatsu) are most sensitive to a magnetic influence when the field is parallel to the dynodes [203].

[2] Value displays mean and standard deviation from multiple measurements performed in all four containers and at different positions inside the containers.

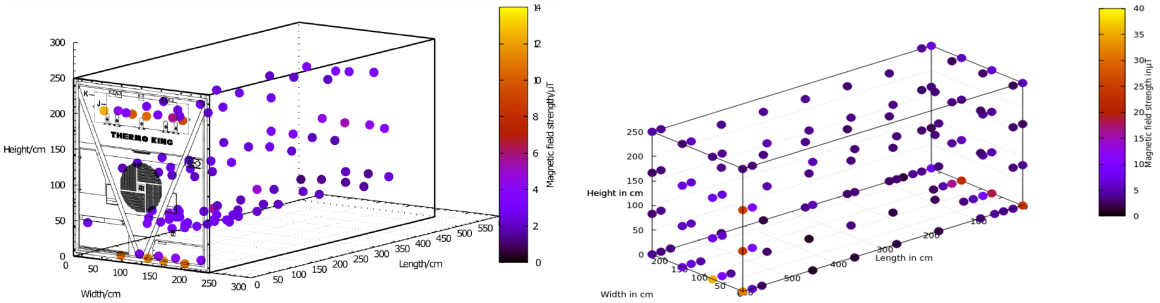

Figure 6.1.: Measurement of the residual magnetic field inside the containers A and B (from left to right), performed in Hamburg. Drawer boxes next to weak spots have been additionally shielded with FINEMET. Small deviations between the systems are due to the production and installation of the shielding material, as well as from effects connected to mechanical stress during the transport of the system in Germany. Image credit: [299] and Dr. Björn Wonsak, Univ. Hamburg.

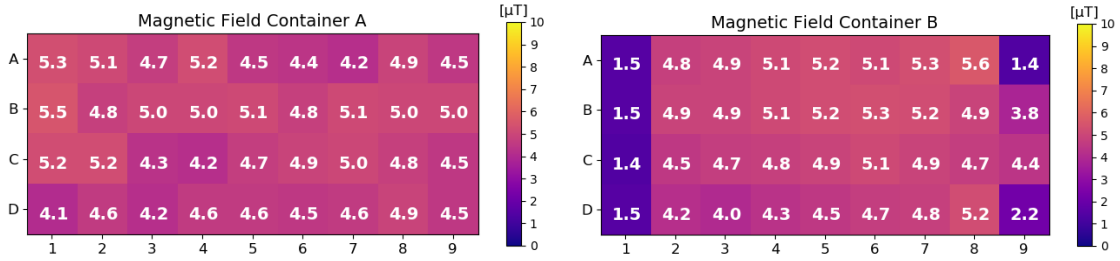

(a) residual magnetic field in the channels of container A

(b) residual magnetic field in the channels of container B

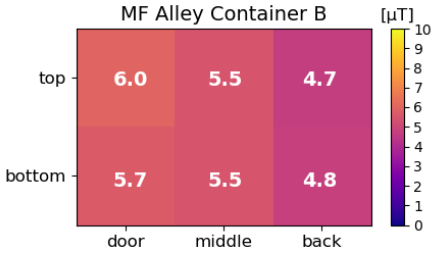

(c) residual magnetic field in the alley of container B

Figure 6.2.: Measurement of the residual magnetic field inside the containers, performed on-site in Zhongshan after the shipment in the center of the drawer boxes and for container B also in the alley (see panel **(c)**). Boxes A1, A9, B1, B9, C1, D1 and D9 of container B are additionally shielded with another layer of FINEMET wrapped around the boxes.

the positions of the PMT's center when loaded into a drawer box. The accuracy of the Gauss-meter was $\pm 0.3\,\mu$T. A small degradation in the magnetic field suppression was observed w.r.t. to measurement done in Hamburg, caused most likely by an intrinsic magnetization the container itself suffered from hits or shocks during the transportation with a commercial container ship. This leads to residual magnetic fields slightly above the 10 % level of the EMF in a few drawer boxes [3]. For container B, a few more measurements were done at different positions in the alley: close to the door, in the middle and on the backside wall of the container, at each position once close to the roof and once close to the ground, as double-check for the residual magnetic field without the additional FINEMET shielding of some boxes. Results of this additional measurement are shown in Figure 6.2c.
From Figure 6.2a and Figure 6.2b, the average values of the residual magnetic fields inside the drawer boxes have been derived to

$$4.8 \pm 0.3\,(\text{stat.}) \pm 0.3\,(\text{sys.})\,\mu\text{T}$$

for container A, and

$$4.4 \pm 1.3\,(\text{stat.}) \pm 0.3\,(\text{sys.})\,\mu\text{T}$$

for container B. Since all measured values are significantly below $10\,\mu$T and the aimed value of 10 % of the EMF for the residual magnetic field strengths inside the containers still has been reached in average, the magnetic shielding can be confirmed as sufficient for the purpose of testing the 20-inch PMTs for JUNO.

6.2. Light-Tightness

Due to their high sensitivity for even diminutive amounts of light, PMTs have to be operated in darkness. A sufficient light-tightness of the system when doors are closed is crucial not only for the sake of reliable measurements with the light sources, but also to save the PMTs from a possible damage by over-illumination when the HV is switched on. Although the container doors are fitted with thick rubber joints and the cable feed-through is tightly sealed, see subsection 4.3.1 again, these openings are natural weak spots and need to be checked for remaining light-leaks (e.g. for possible door slits or tiny holes in the sealing).

In order to test this, several waveform measurements were performed using randomly chosen PMTs with HV switched on, but all light sources switched off. From the data of this measurement, the average number of photo-electrons per trigger μ was calculated for every channel (see subsection 7.3.2 for more details about the analysis methods). A stable residual light field as expected from a potential light-leak would lead to an increased non-vanishing photon number, even in a measurement using a short distinct

[3] The EMF at the PMT testing site in Zhongshan, P.R. China (located at 22.757° N 113.362° E) is around $45.6\,\mu$T [324].

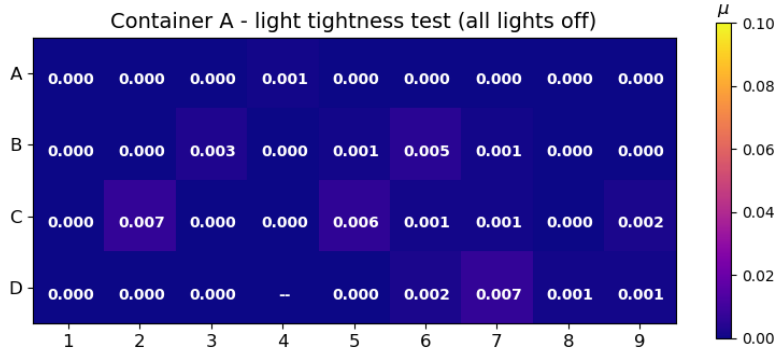

Figure 6.3.: Light-tightness measurement in container A (fully loaded with PMTs) with HV switched on, but all light sources switched off. Ch. 131 (box D4) suffers from a broken HV channel and was therefore ignored here. Mean value of average event number per trigger is $\langle \mu_{dark} \rangle = 0.001 \pm 0.002$, thus a light-leak in this container can be excluded.

acquisition windows. This effect should further concentrate around the boxes close to the light-leak, so should be occur most likely next to the doors (boxes A1/B1/C1/D1) or to the cable feed-through (boxes C9/D9). The results of this survey for container A are shown in Figure 6.3. The determined values didn't show any indication for a residual light field in the container, which excludes the existence of a non-negligible light-leak. The small, yet non-zero values found in the measurements for some channels can be explained with the contribution of dark count from the PMTs [4].
In a second, qualitative measurement, a PMT was placed at different locations inside container A, in closed drawer boxes, half-opened drawer boxes as well as sitting on the alley, looking in direction of the door and of the cable feed-through. Several dark count measurements were performed and DCR values from the selected PMT could have been reproduced within only small statistical variations, which can be explained by the abstinence of an extended cool-down time between the measurements. In additional, some of the measurements have been repeated at the same locations, but with a black foil and secondary a black curtain wrapped around the PMT bulb for shadowing the PMT against possible stray light in the container, showing the same results. Moreover, the measurements didn't show any preference or indication for an increased rate closer to a certain spot or location.
As a conclusion from both measurements, container A can be assumed to be fully light-tight.

Similar measurements for container B didn't take place due to lack of time during the commissioning of this system. But since container B features a better rubber gasket around the door (thicker and sitting tighter on the edges, which makes it harder to even close the door) and a thicker pond foil was used for covering the cable feed-

[4] Assuming a DCR of 50 kHz and a pulse integration window of 75 ns as it is used later in the regular data analysis, see subsection 7.3.1, the expected average photon number per trigger would be $\mu \sim 0.004$, which matches very well to the observed numbers.

through, the situation was assumed to not have worsened compared to container A. Further, a check for light-tightness using PMTs is of course limited by the present DCR of the used PMTs, which constitutes a non-reducible background for this measurement. A residual light in the containers field would therefore be measurable only as offset to the true DCR of these PMT. This has been checked using a large number of low DCR PMTs; the results of this survey are presented later in subsection 8.4.1.

6.3. ADC Baseline and Electrical Noise

The noise level defines the cleanliness of the measurement environment on the electronics site and thus affects the significance of results from the acquired data. Therefore, the situation of electrical noise in the readout electronics has been carefully observed during the commissioning of the containers A and B and is under continuous control over the operation of the container systems. So is e.g. the flat LED cable shielding, shown before in Figure 4.15, added only in order to reduce electrical noise on the channels. It was further explicitly taken care to connect all electronic components linked to the data acquisition to the same common ground and without creating any loops. This ground was offered by the local organization team as "clean" ground with reduced noise level. All other electronics with no direct connection to the data streams have been connected to a different ground connection (via the usual neutral conductor of the power network), carefully separated from the "clean" ground.
To estimate the noise situation at the containers, three checks have been performed: a simple noise (baseline) recording with the ADC boards, the analysis of acquired noise waveform data and counting of electronic noise events with the discriminators and scaler boards (counting of signals over threshold).
In benchmarking the situation here, the focus will be laid on the environment of the whole system, meaning that the overall situation can be rated as acceptable although individual channels can suffer from a higher noise level, which usually indicates issues with the corresponding electronics channels. Such issues can show up occasionally due to wear-and-tear effects or single incidents [5] and demand a continuous maintenance and check for a proper functioning of the systems. The now presented measurements (performed during a maintenance period in summer 2019) have been identified a few noisy channels, which then were repaired by changing the affected hardware channels, but are practical to exemplarily show both "clean" and "noisy" channels side by side to sharpen the definition of both and to substantiate the importance of a continuous control and maintenance of the system.

During the commissioning of the containers, the baseline noise level was checked using the ADCs by recording noise only waveform data (baseline noise from the signal outputs of the PMTs, but with HV switched off this time to exclude any contributions

[5] Broken or bad PMTs or PMT bases can destroy single electronics channels, if over-voltages are applied accidentally on the signal inputs of the boards, which indeed happened a couple of times during the operation of the system.

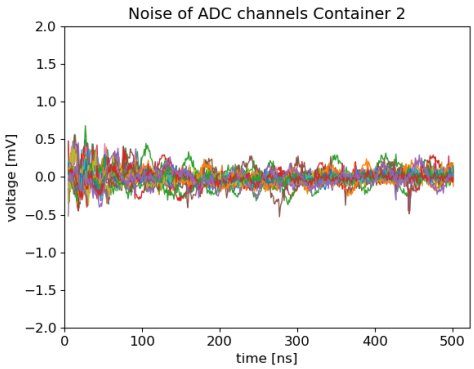

(a) avg. baselines at container A

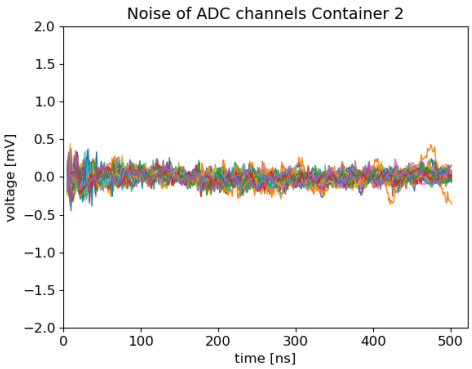

(b) avg. baselines at container B

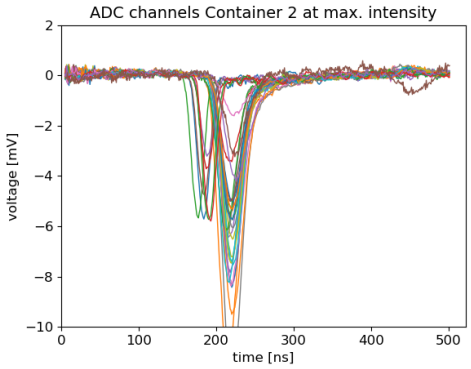

(c) avg. waveforms at container B with max. LED light intensity

Figure 6.4.: Averaged ADC baselines of both containers (panels **(a)** and **(b)**), with all 36 channels per container plotted together. 10'000 events have been acquired here and are averaged in every bin. All plots are drawn including baseline offset and linear slope correction (fitted and subtracted, see subsection 7.2.1 for details). Panel **(c)** shows average of 25'000 events using PMTs at maximum LED light intensity, which directly illustrates the good signal-to-noise ratio in this measurement.

from the PMTs, such as dark counts). Therefore, 10'000 frames have been acquired with just baseline. The measurement settings have been the same like for the usual data taking with the light sources. Figure 6.4 shows the recorded baselines of all channels from container A and B. In all plots, the baseline offset and slope was corrected to fit around the 0 mV value [6]. The averaged noise level of all channels is clearly inside a ± 0.5 mV window around zero, which is suitable for the needs of the container system. It shall be mentioned here that a higher noise level in single frames is unproblematic as long as the average noise level is acceptable, since random or

[6] Although the ADCs already provide an internal baseline calibration and specific correction tables for the individual cells of the DRS4 registers [323], as also described in subsection 5.2.2 before, the baseline of some ADC channels still can show an offset and/or a linear slope. Since this is a stable feature of these channels, it can be corrected in the data analysis, see also subsection 7.2.1.

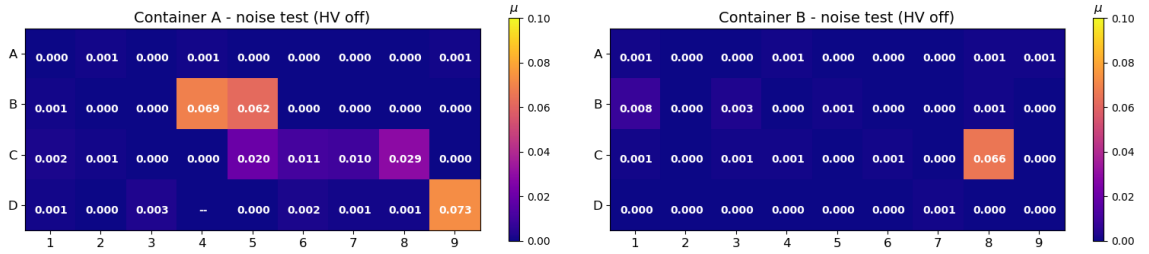

(a) noise measurement at container A **(b)** noise measurement at container B

Figure 6.5.: Noise measurements at the containers, with average "event number" μ per trigger. The measurement is similar to the light-tightness measurement in section 6.2, but with HV switched off this time to exclude all effects connected to the PMTs. Ch. 113, 114, and 136 (B4, B5, D9 at container A) and 226 (C8 at container B) have been found noisy in the tests and were exchanged afterwards. Ch. 131 (box D4 at container A) suffers from a broken HV channel and was therefore ignored here. Further, possible contributions from electronic crosstalk (see section 6.5) have not been removed and are contributing to ch. 123 to 126 (boxes C5 to C8 in container A, see also Figure 6.13b).

statistical fluctuations in the noise level diminish with larger statistics. In additional, static noise contributions, which are independent from the statistics, can be identified and subtracted in the data analysis, as it is described later in subsection 7.2.1, further reducing the average noise level (this step has been skipped in Figure 6.4 for a better estimation of the present noise level).

In the next step, the noise contribution has been quantified better by analyzing the raw waveform data and calculating the average "event number" per trigger pulse μ, similar as for the measurement of the light-tightness in section 6.2, though this time none of detected "events" was photon-induced, since the HV was switched off all the time. The results of both containers from this measurement are depicted in Figure 6.5. Most channels show a vanishing noise event contribution, except for a few channels (in total three with heavy and four with medium noise level in container A, and one with heavy noise level in container B), which then have been replaced by spare channels on the electronics boards, as noted in the beginning. The determined average event number is purely connected to noise-only events, which can be seen in the charge spectra from these measurements depicted in Figure 6.6, consisting of only the pedestal. While the "clean" channels show a quite narrow pedestal, see Figure 6.6a as example, it is clearly broadened in the noisy channels, see Figure 6.6b. Since integrated charges above a threshold of 0.25 p.e. (compared to the case where a gain of 10^7 is applied) are contributing as PE events to the calculation of the average event number μ (see also subsection 7.3.2 for more details), a broad pedestal influences this value.

Last measurement to better estimate the noise contribution was a counting measurement using the discriminator and scaler boards. During the data taking, the set threshold in this measurement was the same like in all regular testing runs (3 mV,

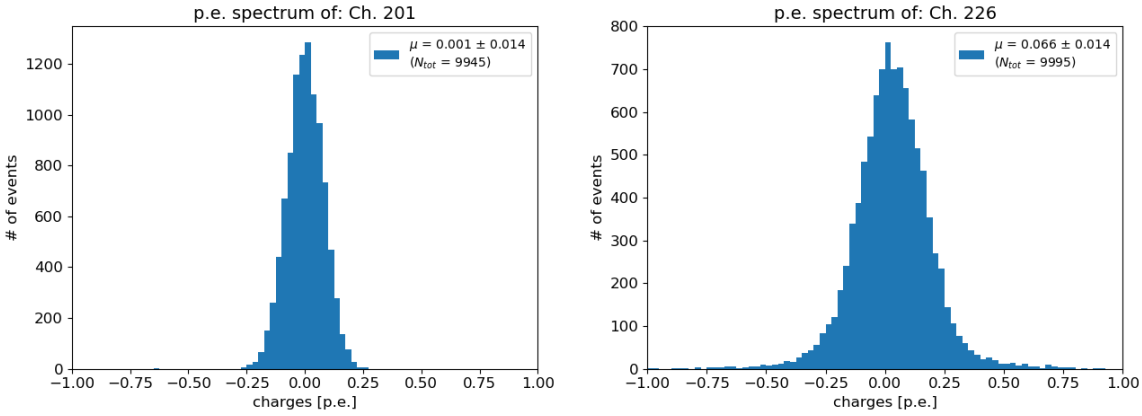

(a) noise measurement of ch. 201 **(b)** noise measurement of ch. 226

Figure 6.6.: Charge spectra from noise measurements with HV off for two exemplary channels of container B. Panel **(a)** shows an example for a good noise level, panel **(b)** for an insufficient noise level. Events with a calculated charge above the threshold of 0.25 p.e. usually are contributing to the average event number μ. Although no voltage is applied, the scale (x-axis) is assuming a gain of 10^7 in the charge calculation to get comparable results to the situation of a PMT under HV.

see subsection 5.2.2 again). Test data was taken in several runs of minimum 60 s each, with HV switched off again. Also, an artificial signal with amplitude over the counting threshold and fixed rate of 50 kHz was inserted in different channels, in order to monitor the functionality of the counting devices. Figure 6.7 shows the results of this survey. Only a few channels have exceeded a level of 1 kHz, while most channels doesn't recognize any noise events at all. A noise contribution of less than 1 kHz can be neglected, since both statistical fluctuations as well as temperature-dependent fluctuations of the DCR doesn't allow to reliably determine the DCR on a level of less than 1 kHz [7] (this will be discussed further in subsection 8.2.6). The noisy container channels have been repaired afterwards by changing the hardware channels on the discriminator boards to less noisy spare channels [8].

As conclusion, the overall noise level in the container systems can be stated as very low. The situation is controlled frequently and improved where and whenever nec-

[7] From the PMT data analysis to be presented in section 7.1, DCR results can be determined with given 1 σ errors of less than 1 kHz (depending on the individual PMT), this might underestimate the influence of present environmental effects. On the other hand, from experience with the PMT mass testing, a determination of the DCR with only $\mathcal{O}$(kHz) precision was found to be both reasonable and sufficient for the PMT mass characterization.

[8] Even noise rates in the discriminator channels slightly above the set specifications of 1 kHz max. are no show-stopper for the system. PMTs, which would fail the test due to this small excess, would have been very close to the limit for an acceptable DCR, see Table 3.1 again. In this case, a more careful look or a retest for confirmation would be useful either way. However, making the measurement environment as noise-free as possible is always both desired and sought.

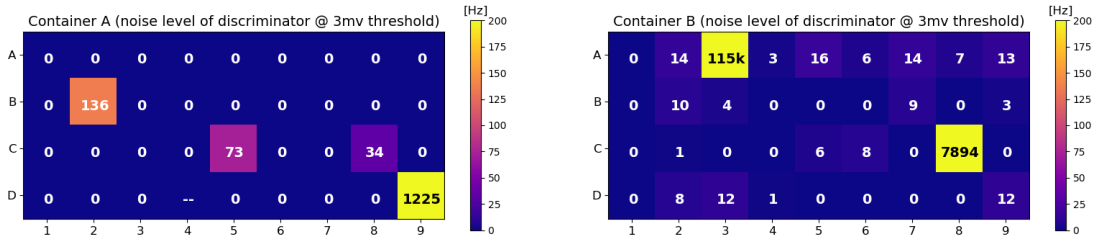

(a) noise measurement at container A **(b)** noise measurement at container B

Figure 6.7.: Noise rates in Hz measured with the discriminator and scaler system, with no HV applied. Channels 136 (D9 of container A), 203 and 226 (A3 and C8 of container B), which have shown an (highly) increased noise rate in this tests, have been exchanged with spare channels on the discriminator board afterwards. Reference channels, counting artificial pulses with a rate of 50 kHz (for monitoring purposes in the measurement, see text), have been excluded from the average calculation.

essary. In the data analysis later, an individual S/N value will be determined for every run and PMT (see subsection 7.3.2 for more details), which can help to monitor whether the situation becomes worse for individual channels; if the S/N ratio drops below a value of 10 in a measurement run for a certain channel, a retest of the respective PMT is further recommended (see also subsection 8.1.2), ensuring that the noise level is kept on a acceptable level for all tested PMTs and in all measurements.

6.4. ADC Jitter

To enable a TTS measurement with high precision at the container systems, it was taken care to provide a suitable performance in the used devices to determine even the small TTS values typical for e.g. the Hamamatsu PMTs [216]. This was implemented by the use of the picosecond laser system as light source in the measurement, as well as by enabling the ADCs to acquire PMT pulses with the highest possible precision. The latter requires an accurate recording of the waveforms itself and a sufficient timing in the trigger processing and recording. To make sure that the results of the analyzed data will be reliable and to further exclude a large systematic influence from the electronics onto the measurement, the accuracy of the waveform recording process should be confirmed.
The manufacturer (CAEN) specifies the timing resolution of the used V1742 ADC modules when using the fast trigger setting (including the recording of the trigger information together with the acquired signal, as it was integrated into the container systems) to around $50 - 200$ ps, depending on software settings like e.g. the sampling frequency etc. [323]. Without the trigger recording, the internal jitter of the ADCs is specified as ~ 17 ns in the ADC manual [323], which would be much larger than e.g. the typical TTS of the Hamamatsu PMTs [216]. Aside from the ADCs, all other components handling the data stream or organizing the data acquisition can also in-

fluence the timing of the signals: so is the signal generator, which initially produces the trigger signals both recorded and used by the ADCs, specified to have a small jitter of around 50 ps [294]; the trigger splitter, for which e.g. a CAEN V538 NIM-ECL fan-out was used (see subsection 4.4.1 again), is expected to have a small jitter of $\mathcal{O}(100\,\text{ps})$ as well, although it is not exactly specified, see [327]. Further, the achieved timing precision at the end also relies on a precise data analysis, for which it's not trivial to reach a sub-ns accuracy from raw data acquired with usually 1 GS/s only [9], as noted in subsection 5.2.2 already.

To estimate the combined influence of all these components in the system together, the timing accuracy has been checked using both ADC modules of one of the container systems for a test survey as well as the standard data analysis methods for the TTS analysis, as it will be presented later in section 7.4. In the preformed test survey, artificial pulses with 50 mV amplitude and pulse edges of 10 ns (for both rising and falling edge) and standard NIM trigger pulses like used in the PMT characterization runs were produced using the pulse generator, in order to provide maximum possible accuracy and reproducibility for the test pulses. Both the test and trigger pulses have been guided the standard way into the ADCs [10] and were recorded with the usual setting from the DAQ (see section 5.2 again). With this setup, the full internal jitter of the electronics system can be investigated. In Figure 6.8, both the used artificial pulses and the trigger pulses as recorded by the ADCs in the tests are displayed.
The recorded test and trigger pulses are analyzed the exactly same way as it will be done later for the trigger and PMT pulses in the TTS analysis. In doing so, the high timing precision can be achieved in the first place by comparing the individual hit times of the test (or PMT) pulses to the recorded trigger pulses; hence, the largest part of the internal ADC jitter can be removed form the data. To illustrate the effect of the trigger recording on the internal timing resolution of the ADCs, the hit time distribution of the test pulses from the survey is shown in Figure 6.9 exemplarily for a single ADC channel with and without the trigger correction (the analysis methods will be explained more in detail in subsection 7.4.2).
From the analyzed artificial pulses, the full jitter, representing the combined influence of jitters from ADCs, trigger splitter and signal generator as well as from the fit accuracy in the data analysis, was found to be 415 ± 106 ps in average over all channels. In assessing these results, the jitter was observed to be almost constant within a single ADC trigger group, while different trigger groups have shown a larger discrepancy, varying from around 260 ps in the best channel up to around 590 ps for the total jitter of the system in the worst channel. Exemplary hit time distributions are shown in Figure 6.10 for two different channels.

[9] The accuracy of the data analysis is mainly limited by how well the "hit times" of the respective (PMT and NIM trigger) pulses can be estimated from the data.

[10] The artificial test pulses are guided through a long cable to have comparable conditions for signal delay and attenuation, as it's the case in the container system. The trigger signals are fed into the trigger splitters and distributed to the devices as usually done in the PMT test runs.

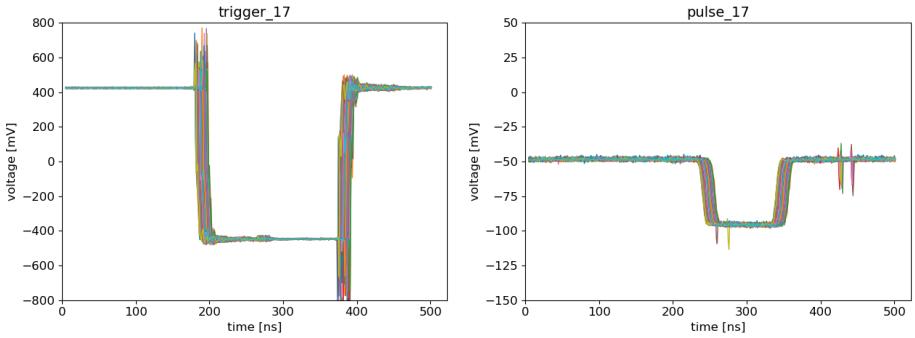

(a) plot of 100 trigger pulses

(b) plot of 100 artificial test pulses

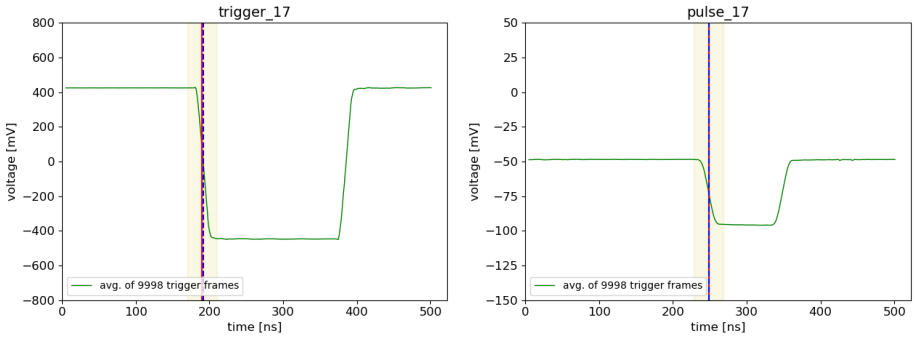

(c) plot of average trigger pulse

(d) plot of average test pulse waveform

Figure 6.8.: Artificial test and trigger pulses used for the jitter measurement. Arbitrary channels are selected for the plots. Tests were done at container B (using ADCs with serial no. 127 and serial no. 161). The red and blue dashed lines in the average plots define the average hit times, yellowish region defines the fit range for the determination of the individual hit times (see subsection 7.4.1 for details about the analysis).

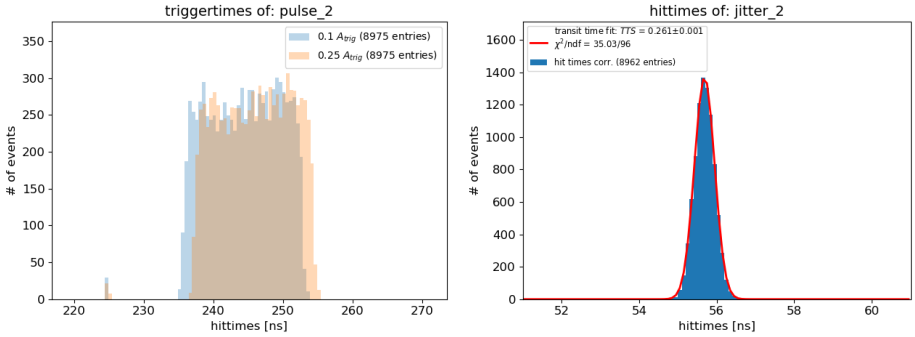

(a) pulse hit time without correction for trigger input

(b) pulse hit time with correction for trigger input

Figure 6.9.: Pulse hit time distributions recorded with the ADC. In both panels, a simple rectangular pulse was recorded on a single channel. In panel **(a)**, the hit times are shown like recorded by the ADC and hit times at 10 % or 25 % level of its rising edge were stacked in the histogram. In panel **(b)**, the pulses hit times have been corrected w.r.t. the incoming trigger signals and so the actual trigger time. See also subsection 7.4.2 for more information about the corresponding data analysis.

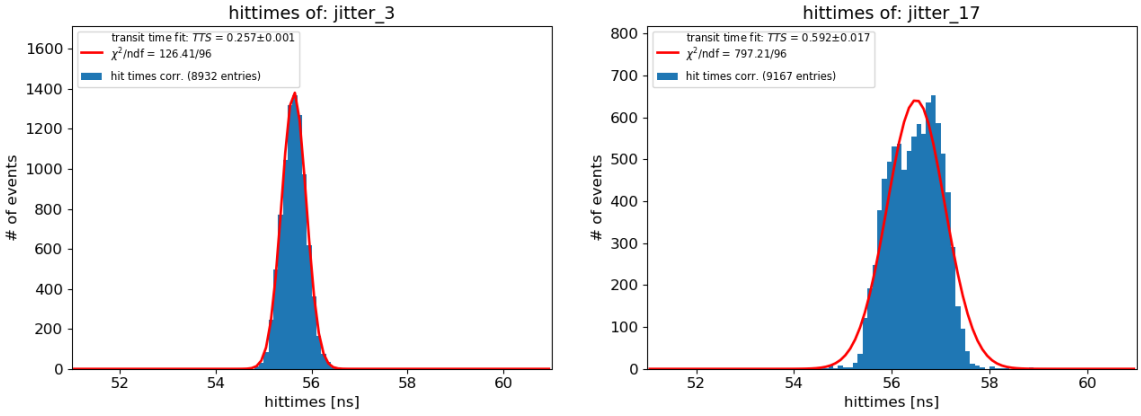

(a) example for a very small internal jitter

(b) example for a relatively large internal jitter

Figure 6.10.: Exemplary measurement results from the ADC jitter measurement. Analysis method is the same as for the TTS measurement described in subsection 7.4.2. Hit times are defined here at 25 % amplitude of leading edge for both test and trigger pulse, distribution is fitted with a Gaussian function (jitter value is σ of distribution).

As main conclusion from these measurements can be derived, that the remaining jitter is much smaller that the aimed uncertainty in timing defined in Table 4.1. Although there are small differences between some channels (or ADC trigger groups, respectively) and further the found value for the jitter is higher than expected from the individual jitters of the electronics devices alone ($\sim 230\,\text{ps}$ combined, if assuming the values noted above), it is still much less than a typical TTS value of even a fast Hamamatsu PMTs. Thus, the internal jitter of the electronics system is not expected to have any bigger influence on the TTS measurements.
A similar, exemplary survey of the jitter introduced by the laser system (and i.e. the fiber splitter) was not possible due to the lack of a light detection device with a suitable high timing precision ($\mathcal{O}(100\,\text{ps})$) for such a survey. However, the jitter of the fiber splitter can be roughly estimated from the analyzed data of a larger PMT sample, which has been done and is presented later in subsection 8.4.2.

6.5. Channel Crosstalk

Another crucial point for the reliability of the PMT data taken in a specific measurement is to avoid or at least minimize a possible crosstalk between different hardware (container) channels or electronics channels. By minimizing the influence of crosstalk in the data taking, one can make sure that the data samples from a certain channel and taken in a specific measurement only represent information about the performance of the PMT tested in the corresponding channel.
There can be two main sources for crosstalk in the container system: optical and electrical. Optical crosstalk describes photons from stray light of another light source not

belonging to the corresponding container channel. Since the single drawer boxes are not completely light-tight due to a small gap between the backside of the drawer system and the wall (which is necessary for the LED cabling, see also subsection 4.4.3), photons from the light sources could be back-scattered in the drawer boxes, reflected at the wall and enter a neighboring box, where they could release a photo-electron in the "wrong" PMT. Such events are very unlikely to happen due to several design precaution in the setup [11], but nevertheless should be checked for. Electrical crosstalk describes noise events in electronic channels – e.g. on the ADC boards – caused by (large amplitude) events in neighboring input channels on the same electronics board. Such events could arise time-coincident with a real event on the neighboring electronics channel, producing a "fake" signal in the affected channel (i.e. if there was no real photon-induced event in this channels at the same time). Since the electronics channels on the ADCs and discriminators as well as on the SSB are both well-shielded against and separated from each other, such events again should be very unlikely in case of "standard" (few p.e.) PMT pulses (and completely negligible for the measurement with the discriminators since they are used only for the DCR measurement [12]).

To better quantify possible optical crosstalk effects in the system, some exemplary tests were performed on both containers for randomly selected channels:
First, as a control measurement, a full container load was tested for their average detected photon numbers μ in the respective channels using the LEDs at maximum possible light intensity [13]. The calculated values for μ from these measurements are shown in Figure 6.11, but are only acting as reference values, since they strongly depend on the PDE of the used PMTs.
In a second step, the light sources of several channels (six per container, at different positions) were switched off and their μ value was measured again [14]. For container A, channels **101**, **109**, **113**, **125**, **127** and **130** were chosen and tested for a possible crosstalk: while the LEDs of the to-be-tested channels were switched off (not in parallel, but one by another), all other 35 LEDs stayed switched on during the individual

[11] The probability for photons leaving the drawer box and entering a neighboring box is very low, because (1) all light sources are pointing inside the drawers and off the wall, so only back-scattered photons can advance in direction of the wall, (2) except the PMT surface, the complete interior of the drawer boxes as well as the container walls are painted black, so that (multiple) scattering of photons is unlikely, and (3) the gap between the end of the drawer box frame and the wall is only around 2 cm wide, while the distance between two drawer boxes is another few cm – thus scattering into a neighboring box is possible only under few certain angles.

[12] As consequence from the the noise level measurements, even if occasional crosstalk events would appear in this measurement, their rate can be fairly assumed as way too low to significantly contribute to the measured dark rates of the PMTs.

[13] For these measurements, LED setpoints of 3000 (4000) at container A (B) were chosen.

[14] While the μ value usually describes the average number of released photo-electrons per trigger pulse, it is used here as average number of "detected events" per trigger pulse (with a threshold corresponding to 0.25 p.e. at a gain of 10^7, exactly as in section 6.3), although the observed events may not necessarily caused by a released photo-electron in the PMTs.

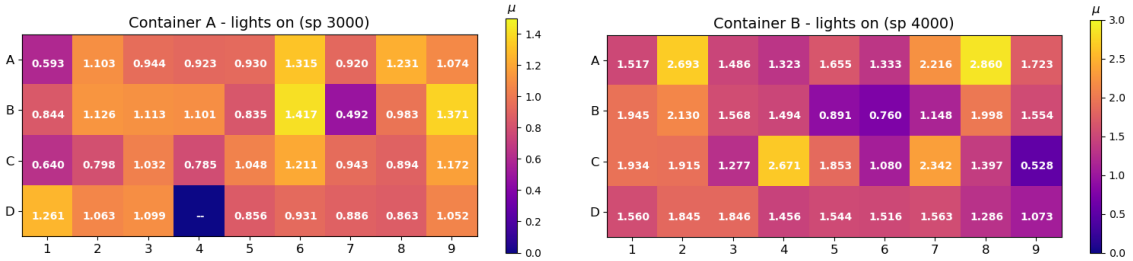

(a) control measurement at container A **(b)** control measurement at container B

Figure 6.11.: Measurement of full containers A and B at maximum LED light intensity (setpoint 3000 at container A, setpoint 4000 at container B). Individual average p.e. numbers per trigger μ (noted in the boxes) depend on the actual PDE of the PMTs loaded into the containers, so don't directly describe the actual light intensity in the boxes and are noted only as reference for the subsequent measurements. Channel 131 (D4 of container A) was deactivated due to a malfunctioning HV channel.

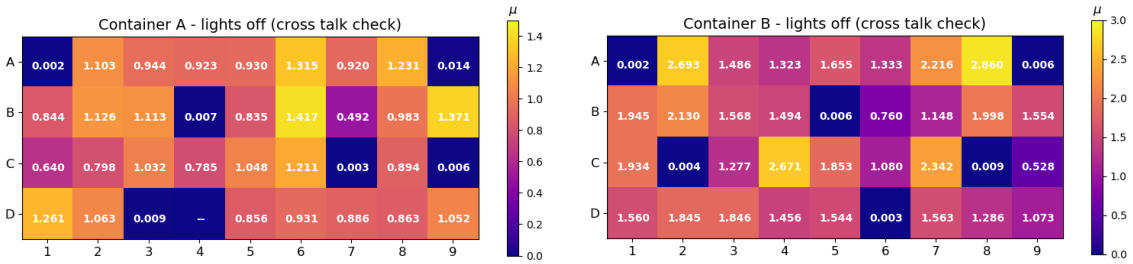

(a) crosstalk measurement at six channels of container A **(b)** crosstalk measurement at six channels of container B

Figure 6.12.: Crosstalk check measurements at containers A (in channels A1, A9, B4, C7, C9, D3) and B (in channels A1, A9, B5, C2, C8, D6). Only one channel was tested in parallel while all other LEDs stayed switched on; the result of the six individual measurements, however are collected together in one plot per container. μ values in other boxes are taken from control measurement before (see Figure 6.11) as references.

measurements. For container B, channels **201**, **209**, **214**, **220**, **226** and **233** have been tested the same way. The results from these measurements are collected together in Figure 6.12. Possible randomly coincident dark counts can be neglected here, as the effect was determined to be very small in section 6.2 already. Thus, an increased "event" can originate only from stray light coming from neighboring boxes (optical crosstalk), electrical crosstalk in the ADC channels or naturally from additional, yet unavoidable noise fluctuations in the channels. As all investigated channels with lights switched off show a very low event number μ (as visible in Figure 6.12), optical crosstalk can be therefore confirmed as completely negligible in the container systems.

In contrast to the optical crosstalk, electronic crosstalk cannot be quantified easily in a dedicated measurement, but is known from the data analysis as problematic

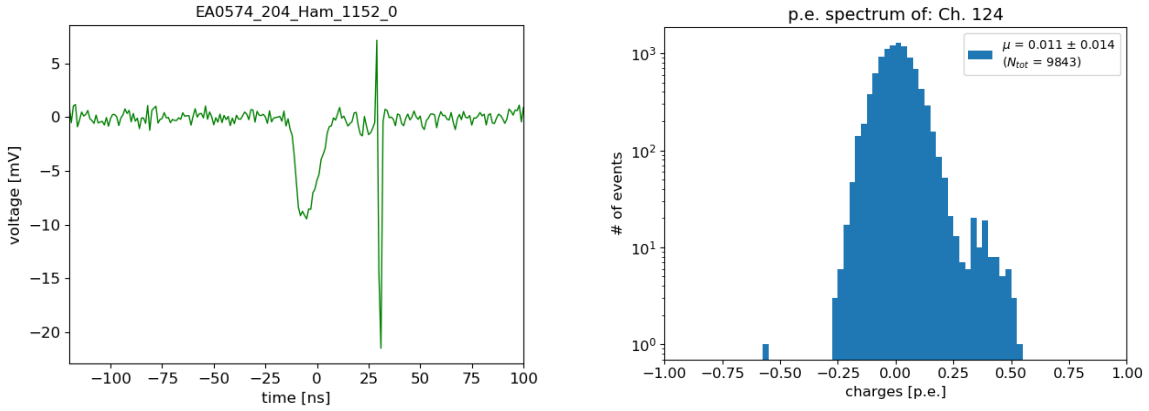

(a) narrow spike in a raw data frame acquired by an ADC

(b) influence of these spikes on the charge spectrum (logarithmic plot)

Figure 6.13.: Examples for electrical crosstalk between ADC channels in the container system. Panel **(a)** shows a characteristic, narrow spike in a raw data frame acquired by an ADC. These spikes are caused by electronic crosstalk from neighboring ADC channels, if pulses partially exceeding the dynamic range limit values of the ADC in these channels. In panel **(b)**, the influence of such events on the charge spectrum is shown (for this plot, data of ch. 124 (box C6 of container A) from the noise measurement shown in Figure 6.5 is presented). Since crosstalk events would spoil the results of the PMT tests, frames containing such spikes must be identified and excluded from the data analysis.

feature in some channels. In Figure 6.13a, a data frame recorded by an ADC and containing a characteristic, narrow spike is shown; these spikes depict electronic crosstalk events in the waveform data. As visible in Figure 6.13b, such crosstalk events can also influence the charge spectrum of a PMT (or measurement) by causing a visible shoulder on the right side of the pedestal. In that case, particularly the P/V ratio measurement would be spoiled by these events, leading to worse results.
The emergence of such spikes happens only occasionally and is most likely correlated to the exceedance of the dynamic range limits in a neighboring channel, which happens mostly in the channels which are responsible for the trigger pulse recording [15]. They therefore could hint for a suboptimal configuration of the dynamic range window these ADC channels [16]. Although the situation was improved after the first occurrence, the electronic crosstalk couldn't excluded completely for some channels. However, since these spikes occur randomly and independent from the frame content

[15] Very high amplitude events also have been observed occasionally in ADC channels assigned to container channels; these can be produced e.g. by voltage spikes from the PMT bases or heavy noise events. However, the exact reason for such events is unknown.

[16] The recorded NIM trigger pulses have an amplitude of 800-900 mV, while the dynamic range of the ADC channels is limited to 1 V_{pp}. The dynamic range window therefore need to be well adjusted for the channels recording the trigger waveforms. Nonetheless, overshoots around the edges of the trigger waveforms still can exceed the dynamic range limits of the respective ADC channel.

in the affected channels (and thus whether they contain a PMT pulse or just noise), these frames can be discarded from the data analysis without introducing a bias to the pulse statistics; only the overall frame statistics would be slightly reduced [17]. As these spikes are very narrow (usually they show a width of only 2 ns, while their amplitude is between -10 mV and -20 mV), it is easy to identify frames containing such crosstalk spikes and exclude them from the data analysis (more details about this can be found in subsection 7.2.2).

6.6. LED Calibration

One of the most essential tasks of the container system is the measurement of the individual PDE of the PMTs. The PDE measurement is of high importance for the examination and final quality classification of the PMTs, since the PDE of the PMTs directly impacts the energy resolution of JUNO, see section 2.4 again. The self-stabilized LED are predestined for such an measurement as they provide a stable and reliable light intensity over time (see subsection 4.5.1). Therefore the PDE is determined as part of the LED measurement. Since the absolute QE of the to-be-tested PMT is unknown, as well as the actual number of released photons from the LED and the number of absorbed or scattered photons in the full light system, only the average photo-electron number per trigger pulse μ can be determined using a PMT in the drawer boxes and can give a measure about the PDE. Hence, a drawer-related calibration to determine the correlation between μ and PDE value becomes necessary. In order to keep statistic uncertainties in the determination of μ at a low level, the number of trigger events in the LED measurements was set to 25'000 events per measurement run (which was found to be sufficiently high for the purposes of the container system) and the applied light intensity was chosen to be close to the ideal light intensity of around 1.5 p.e. per trigger pulse as supposed in [313].
In parallel, the use of calibrated LED setpoints at low light intensity, featuring a measurement to around 0.1 p.e. per trigger pulse in average would be ideal for e.g. the measurement of the pulse shape characteristics. The strong attenuation of the LEDs described in subsection 4.5.3 was chosen to optimize the light intensity for the calibrated setpoints in the low light intensity to exactly this value.
As a consequence, two separate LED measurement are performed in every container run (see also subsection 5.2.3 again): a low light intensity measurement with calibrated LED setpoints to provide a light intensity of $\mu \sim 0.1$ p.e. in all channels, and a high light intensity measurement optimized for the PDE determination. Since not all LEDs can reach a light intensity of $\mu \sim 1.5$ p.e. due to design inherent limitations and the used light attenuation parts (which are necessary for the low light intensity measurement), the LED setpoints were set to a common value which was chosen to be as high as possible while still a stable operation of the LEDs could be ensured.

[17] The discarded frames have to be considered also in the TTS analysis to preserve the mapping of waveform and trigger frames, see section 7.4 for details.

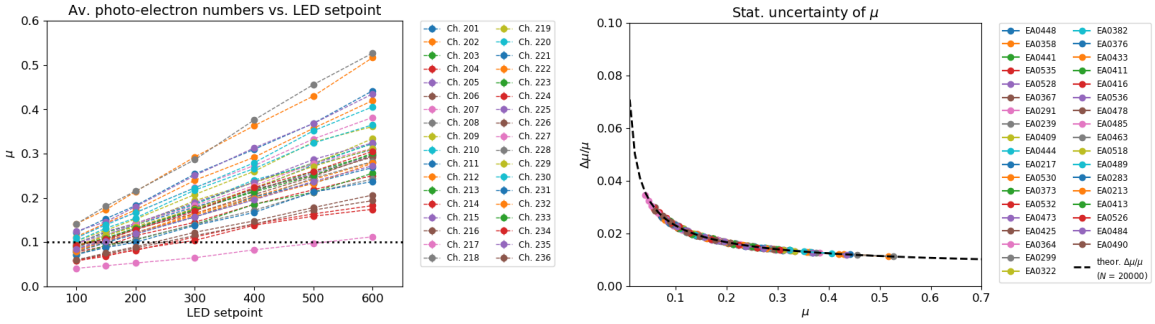

(a) light intensities at container B for different LED setpoints

(b) stat. uncertainty of μ for different LED setpoints

Figure 6.14.: Low light intensity LED calibration at container B. In panel **(a)**, the average photo-electron number per pulse μ has been determined at different LED setpoints for all channels. "Calibrated" setpoint for a light intensity of $\mu \sim 0.1$ p.e. can be derived by an extrapolation of the determined values from the different measurements. In panel **(b)**, the statistical uncertainties for the different μ values based on [313] are plotted.

6.6.1. Low Light Intensity: Calibrated LED Setpoints

The individual LED setpoints for the low light intensity measurement were determined using a full container load of PMTs with known PDE in the range of 25 to 30 % [18]. Then, the optimal setpoint for these PMTs to get a light intensity of 0.1 p.e. in every drawer box was determined by extrapolating from results of several measurements at different low setpoints.
In Figure 6.14, the results from measurements at LED setpoints **100**, **200**, **300**, **400**, **500** and **600** are shown; as example, the calibration of container B is shown here. The determined values of μ depend at the same time on the actual light intensity of the LEDs, but also on the QE of the used PMTs (see section 7.3 for details about the analysis methods). Since every PMT is unique and so is its PDE, the chosen setpoint usually does not exactly represent a 0.1 p.e. light intensity for any other PMT, but are distributed in a range between ~ 0.05 and ~ 0.2 p.e., so that the aimed light intensity for this measurement is reached only in average. To get a distinct light intensity for every PMT is not relevant anyway, because as long as the excessive part of all recorded signals are SPE pulses and statistics are sufficient, the light intensity is suitable for the pulse shape measurement in any case, whatever its absolute value finally is [19].

The used LED setpoints for both containers are listed in Table 6.1. In case of container A, the estimated setpoints from the calibration are directly used for the measurements,

[18] For the calibration of container A, the PDE values provided by the manufacturers are used, while for the calibration of container B, the PDE values of the used PMTs have been determined using container A.

[19] For this reason, also the exact PDE values of the calibration PMTs in this measurement is of minor importance.

Table 6.1.: Calibrated LED setpoints for a low light intensity at containers A and B. The setpoints have been extrapolated from measurements at different setpoints, in order to provide a light intensity of $\mu \sim 0.1$ p.e.; in container B, the estimated setpoint have been additionally rounded to better respect the PDE of the PMTs used for the calibration. Setpoints below a value of 50 are further not recommended to apply in order to avoid problems for the LEDs with the stabilization due to too less light.

(a) calibrated LED setpoints for a low light intensity at container A

#A	1	2	3	4	5	6	7	8	9
A	497	328	303	407	325	286	272	252	276
B	358	320	267	309	359	182	652	354	156
C	505	421	407	503	269	204	367	321	244
D	302	297	355	238	525	482	435	464	366

(b) calibrated LED setpoints for a low light intensity at container B

#B	1	2	3	4	5	6	7	8	9
A	90	50	110	120	100	130	70	60	100
B	80	60	100	150	210	100	240	100	150
C	110	90	180	70	120	230	50	100	450
D	140	100	80	160	140	120	100	140	220

while for container B, the setpoints have been rounded up or down to better respect the actual PDE of the PMT used for the calibration (in case of a PMT with higher PDE, the setpoint has been rounded up to better match to the case of a PMT with average PDE, and vice versa). As it can be seen later in subsection 8.2.4, the light intensity is well adjusted around $\mu \sim 0.1$ p.e. for all channels and the majority of tested PMTs.

6.6.2. High Light Intensity: PDE Calibration

For the PDE determination, the amount of light measurable by a PMT with a certain QE in the drawer boxes has to be known as good as possible. As explained above, the LEDs of all container channels are driven at a common setpoint in this measurement. An LED setpoint of **3000** has been chosen here, which is high enough for most of the LEDs to provide the desired light intensity of $\mu \sim 1 - 1.5$ p.e. per trigger event, but not at the maximum capacity of the LEDs, which should ensure a more stable light provision and further avoid aging effects at the LEDs (such as a degradation of their capacity) from operating the devices at their limit over a long time. The chosen, common setpoint is further the same for both container A and B.
Since the absolute number of photons cannot be determined independently with the container systems, as explained in section 5.1, the light intensity can be measured only relative to a detector (e.g. another 20-inch PMT) with a well-known PDE. Further, the

Table 6.2.: List of PMTs used for the drawer box calibration of container B (to determine the relation between μ and PDE for every container channel) with PDEs as provided from the manufacturer (Hamamatsu).

PMT	PDE [%]	PMT	PDE [%]	PMT	PDE [%]	PMT	PDE [%]
EA0213	28.33	EA0367	31.70	EA0433	27.38	EA0489	28.62
EA0217	27.42	EA0373	27.14	EA0441	30.30	EA0490	27.51
EA0239	31.81	EA0376	28.06	EA0444	26.82	EA0518	26.88
EA0283	25.37	EA0382	28.95	EA0448	29.18	EA0526	28.05
EA0291	28.28	EA0409	29.23	EA0463	30.07	EA0528	28.50
EA0299	26.75	EA0411	28.90	EA0473	28.07	EA0530	26.84
EA0322	29.94	EA0413	29.30	EA0478	27.54	EA0532	28.76
EA0358	28.96	EA0416	29.43	EA0484	28.26	EA0535	27.91
EA0364	29.87	EA0425	29.68	EA0485	26.42	EA0536	28.01

design inherent discrepancies in light output intensity between the individual LEDs are rather large, which necessitates a dedicated calibration of each drawer box in order to precisely determine the correlation between the number of detected photons per pulse μ and the actual detection efficiency of the PMTs in each container channel.
The finally determined PDE value then represents the photo-detection efficiency of the tested PMT at a wavelength of 420 nm (output wavelength of the LED, see subsection 4.5.1 again) based on the PDE values of the PMTs used for the calibration of the drawer boxes.

As example, the calibration of container B is presented here in detail [20]. In the process, a bunch of **36 PMTs** with known PDE have been selected for the calibration of the drawer boxes. A list of the used PMTs including the assigned PDE is shown in Table 6.2. The here used PDE values are the ones provided by the manufacturers for these PMTs, which also have been cross-checked by the scanning station. These 36 PMTs have been tested in 15 different channels each and the corresponding μ values have been determined in all runs.
The calculated μ values then were be plotted vs. the PDE values of the PMTs and fitted with a linear function. This is done individually for each container channel to account for the different LED lights output. The slope thereby defines the correlation between μ and PDE values and is named calibration factor cf_i in the following. Figure 6.15 depicts this exemplarily for one container channel (205 or box A5 in container B); plots for all other channels of container B from this analysis can been found in

[20]The calibration of container A was performed analogue, however the one of container B is better documented since daily routines onsite have been much better established already at the time of the commissioning of container B, as well as data taking routines were running more smoothly since the DAQ has been upgraded and several bugs fixed in the meantime between the commissionings of both containers.

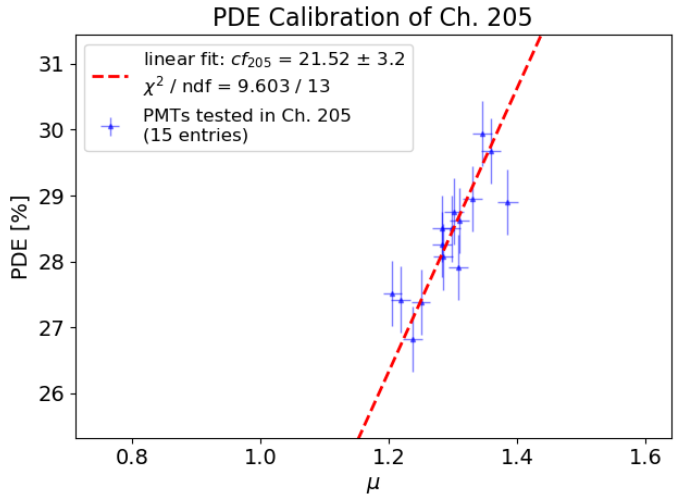

Figure 6.15.: Plot with results from the PDE calibration measurements of ch. 205 (box A5 in container B). 15 PMTs have been measured in this channel and the results have been fitted with a linear slope (intersection has been contained in this fit to [-0.5,0.5] %). From this plot, the drawer box related calibration factor would have been determined to $cf_{205} = 21.52$.

Figure C.1 in the appendix. An overview about the calibration factors of all channels of the containers A and B is given in Table 6.3; the here presented calibration factors are taken from [254] and describe the official factors as used in the PMT data analysis onsite and for the results presented in chapter 8 [21].

For the final transformation from the photon count number μ to the actual PDE of the PMT, another linear correction aside from the calibration factors cf_i of each container channel is needed, in order to account for e.g. the small differences of the PMT form and thus for the actual shape of the photocathode between Hamamatsu and NNVT PMTs, as well as for residual inhomogeneities of the light field. This second correction is therefore individual for each PMT type and has been derived from a comparison of the PDE results determined in the container systems and in the scanning station. In this comparison, the scanning station has been defined as absolute reference, since the PDE determination is much more sophisticated and precise due to the use of multiple light sources which provide a much more homogeneous illumination of the photocathode, the ability to account for the differences between the shapes of the PMT bulbs

[21] The plots in Figure 6.15 and Figure C.1 illustrate the data analysis results based on the methods presented in chapter 7 and are shown only here to depict the method of the PDE calibration. They were not used as the "official" calibration factors of container B as listed in Table 6.3; however, they reproduce the results from the "official" calibration to the sub-percent level in average. Further, the official calibration factors (for both containers) have been cross-checked and confirmed independently after the respective calibration phases as well, and thus are reasonable and suitable for the use in the various data analyses.

Table 6.3.: μ-to-PDE calibration factors cf_i of containers A and B. Channel 131 (box D4 in container A) suffers from a broken HV channel and is therefore ignored here. The here shown cf_i factors are taken from [254] and are the official calibration factors as used in the analysis of the PMT data (onsite and in this work).

(a) μ-to-PDE calibration factors cf_i of container A

#A	1	2	3	4	5	6	7	8	9
A	40.30	29.39	30.71	34.94	33.53	27.37	32.74	26.04	28.01
B	36.44	29.65	27.39	30.23	37.42	23.56	50.93	33.56	20.84
C	42.45	36.54	27.71	40.96	27.94	22.98	34.38	36.58	23.66
D	27.45	28.69	28.17	–	37.16	29.56	35.42	39.74	31.65

(b) μ-to-PDE calibration factors cf_i of container B

#B	1	2	3	4	5	6	7	8	9
A	21.67	13.37	23.56	25.86	21.52	26.26	18.39	13.56	20.57
B	18.94	14.79	22.75	24.64	37.47	19.19	35.18	22.17	26.64
C	18.32	18.74	28.93	15.44	24.49	34.52	15.38	22.88	60.22
D	23.68	19.48	16.56	21.10	23.50	22.46	21.40	24.33	30.42

and not least due to the spatial resolution of the photocathode scans [22]. The introduced correction functions therefore constitute a conversion between container and scanning station results, with the scanning station defined as "true reference". From these inter-system cross-checks, the final relation between average photon number μ and absolute PDE of both PMT types could be determined to

$$PDE_{\mathrm{Ham}}\,[\%] = 0.9718 \cdot (\mu \times cf_i) + 1.1696\ , \tag{6.1}$$

$$PDE_{\mathrm{NNVT}}\,[\%] = 1.0121 \cdot (\mu \times cf_i) - 0.8040\ . \tag{6.2}$$

This conversion has been derived from the comparison of hundreds of tested PMTs of both types [254] (see also Figure 6.16) and is used in the PDE determination of both the onsite PMT data analysis and the analysis results presented later in chapter 8. The plot further illustrates that the results of both the container system and the scanning station show a good agreement between the systems in case of the PDE determination. More details about this can be found also in [254, 328].

To monitor the stability of the light field over the full time of operation and thus the reliability of the determined results for μ and the PDE, a small sample of reference

[22] The scanning station test system subdivides the photocathode surface into 7x24 small areas, which are individually calibrated to a small 1 1/8-inch PMT type R1355 from Hamamatsu with well-known QE [243, 254]. By weighting the subdivided parts, the detection efficiency of the entire PMT can be determined with high precision, also considering possible deviations in the local QE over the photocathode.

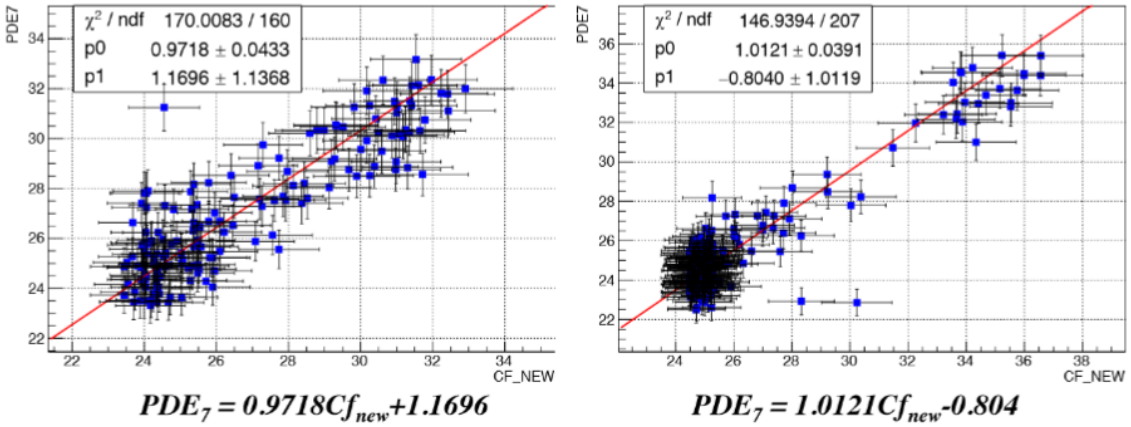

Figure 6.16.: Plots for the calculation of the correction functions (correlations) between container systems and scanning station, calculated for both PMT types individually. CF_{new} describes here the drawer-dependent calibration factor of the containers, while PDE_7 describes the measured PDE value of the scanning station from a full photocathode scan. Image credit: [254].

PMTs will be added to each container run and tested together with the untested PMTs. From the results of these reference PMTs, the stability of the container systems and so the validity of the calibration can be monitored over time; this is also shown and discussed later in section 8.2.

Chapter 7

PMT Data Analysis Methodology

After presenting the setup for the PMT mass testing in chapter 4 and the full measurement program in chapter 5, this chapter will now introduce the methods used for the analysis of PMT mass testing data. The to be discussed algorithms have been used already for the data analysis of the test measurements presented in chapter 6 and are further the basis for the full analysis work of an exemplary PMT sample presented in chapter 8.

All parameters of interest and gaugeable by the container system are examined by specific measurements as described in section 5.1. As a basis for the analysis of the PMT raw data, accurate definitions of all relevant PMT parameters based on this data as well as methods how to extract them from the specific measurement outputs are needed.
The methodology and definitions of these PMT parameters will be explained according to the individual raw data types: First, the analysis methods for the counter data is presented (see section 7.1). The waveform data analysis is separated into the analysis of the raw waveforms (see section 7.2), including the preprocessing of the data (to subtract unwanted ADC features and noise) and the definition of dedicated data cuts for the PMT pulse selection, and the analysis of the charge spectrum (see section 7.3), which have been created as a consecutive analysis step from the waveform data. Last, the methods and corresponding definitions for the analysis of the trigger data will be presented (see section 7.4).
At the end of this chapter, the introduced data analysis methods will be used exemplarily on the acquired raw data of two reference PMTs (one of each type) tested with the containers (see section 7.5).

7.1. Counter Data Analysis

The determination of a signal rate out of the raw data is the main goal of the counter data analysis. the corresponding dark count measurements are performed after several different steps in the measurement sequence with different resting times in darkness (see subsection 5.2.3 again), but only the very last measurement (with the maximum

resting time in darkness) is taken for the final determination of the DCR of the PMT. The counting raw data produced in all these measurements contains the actual counter values of the corresponding channels over time in fixed time intervals (see also subsection 5.3.1 for a reminder about the data structure).

Assuming that the signals are produced with a stable rate over the full measurement time, the signal rate can be estimated by just dividing the final counter value N_{tot} by the total time of data acquisition t_{tot},

$$\mathbf{DCR} = \frac{N_{tot}}{t_{tot}} \ . \tag{7.1}$$

For a PMT with a stable DCR and an ideal measurement system, this is already a fair estimation, because only minor statistical fluctuations around this average value are expected, which further should cancel out over the total measurement time [1].
A more sophisticated method to determine the DCR from the raw data is to use the differences between two counter values,

$$N_i = \frac{\text{counts}\,[i] - \text{counts}\,[i-1]}{\Delta t} \tag{7.2}$$

with a read-out interval of $\Delta t = 1\,\text{s}$ (see subsection 5.2.3 again), and then performing a fit to the data assuming a stable rate,

$$\mathbf{DCR} = fit(N_i\,;\, f(t) = c) \ . \tag{7.3}$$

If choosing a weighted least-square fit (see e.g. [329]), it's possible to include the Poisson errors $\sqrt{N_i}$ of the individual data points as a weight factor w for the fit, which is also better for a fair uncertainty estimation of the final rate result:

$$\mathbf{DCR} = fit(N_i\,;\, f(t) = c\,;\, w) \quad \text{using} \quad w^{-1} = \sqrt{N_i} \ . \tag{7.4}$$

The results of these different methods applied on an exemplary data set of a stable PMT are illustrated in Figure 7.1. In case of a stable rate over the full measurement time (like in the example plots) and using an ideal measurement system, all methods should lead to the same results.
Unfortunately, the raw data doesn't look always that clean: neither all PMTs are stable in their dark rate (even over the short DCR measurement times) [2], nor the

[1] Based on experience from numerous DCR measurements using the container system, this is indeed valid for the majority of measurements, i.e. for PMTs with an already stabilized dark rate.

[2] This can be caused by the PMT itself (e.g. small sparks in the micro-channel plate or the anode), noise in the read-out electronics or by an insufficient connection between PMT and base. Since for the acceptance tests the base is just plugged by hand onto the neck of the bare PMTs, a satisfactory connection between base and PMT at all pins cannot be fully guaranteed, which makes this issue one of the main reasons for an instable DCR or an additional source of (electric) noise in the data.

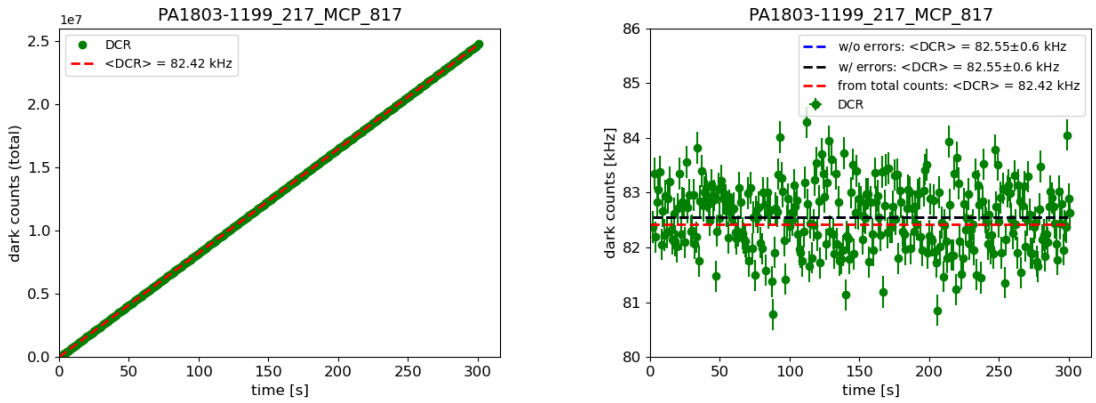

(a) data content as in raw data **(b)** differential plot of same raw data

Figure 7.1.: Example for stable DCR raw data, with different methods to estimate for the exact rate. Red lines display the average count rate (total counts divided by total time, see Equation 7.1) and thus the expectation for a completely stable DCR measurement. Blue and black line (only in panel **(b)**) show a flat fit of all data points without using error bars (Equation 7.3) and including Poisson error bars (Equation 7.4).

electronics are faultless or insensible for internal (heavy) noise events or mistakes in read-out of the counter register. Although the reasons for these issues are not fully clear, they can bias the DCR results or lead to very large uncertainties in the final results. Specifically isolated "noisy" data points (with a very high rate w.r.t. the data points before and after) appear to occur randomly and occasionally [3]. Thus, in order to get more reliable results, such non-physical or unwanted features must be sorted out in the data analysis.

There are three different classes of issues found in the data, which have to be treated together: 'instable rates', 'noise excesses' and 'counter undulations'. Examples for these classes are depicted in Figure 7.2.
An instable rate, as shown in Figure 7.2a usually only leads to larger uncertainties, while the results of the three presented methods match quite well among themselves. Such cases are difficult to identify and improve; this is also discussed further at the end of this section. For noise excesses and counter undulations, the situation is more complicated: as shown in Figure 7.2b, a simple average or an unweighted fit neglecting the error bars of the data points would include some very large values (produced e.g. by heavy noise), leading to a higher rate than reasonable from the data. Including the Poisson errors however would assign only a small weight to the "noisy" values in the fit, which so wouldn't influence the fit too much (compared to weighting all values

[3] If a discriminator channel appeared to suffer from noise issues in multiple runs, the channel would be replaced (see also discussion in section 6.3). This was done already a few times for both containers and is part of the continual maintenance work on the systems. But due to the limited number of spare channels on the discriminators, usually only very noisy channels can be replaced.

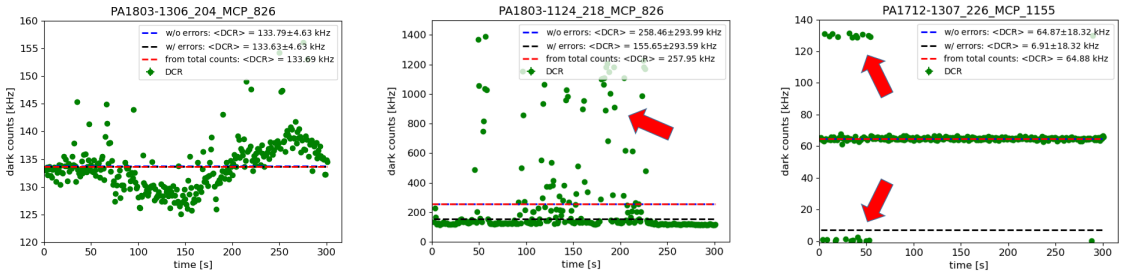

(a) example for an instable DCR

(b) example for noise excesses in the data

(c) example for undulations in the counting data

Figure 7.2.: Examples for different features found in the DCR raw data, which could affect the final result if not treated correctly. Red lines display the average count rate (total counts divided by total time, see Equation 7.1) and thus the expectation for a completely stable DCR measurement. Blue lines show a flat fit of all data without using error bars (see Equation 7.3). Black lines show a flat fit of all data points including Poisson error bars for the individual data points (see Equation 7.4).

the same). Thus, including the error bars would make the fit more robust against these large noise events. This depends of course on number and content of the noisy data points. The case in Figure 7.2c leads to the opposite result: here, a mismatch in timing (or a randomly occurring lack in performance) causes one bin to keep too many and the following bin to few events, leading to short "undulations" in the counting data. While unweighted data points or a simple average would cancel out this issue naturally, weighted data points using the Poisson errors would assign the points with only few counts an unreasonably high weight compared to the other data points and would therefore pull the whole fit towards lower values. Thus, including the errors in this case would make the fit very sensitive for these counter undulations in this case. In additional, outliers can have a disproportional large influence on the uncertainty estimation of the final result in all three cases. A common analysis though should be able to handle all these classes of data issues.
The discussed issues can be accommodated by a preselection of the raw data sample: In a first step, the data points will be presorted by calculating the mean μ_{raw} and standard deviation σ_{raw} of the full sample and dropping all data points n_i with $n_i \notin (\mu_{\text{raw}} \pm 3 \cdot \sigma_{\text{raw}})$. This selection is tolerable, because for a good PMT one would expect all data points normally distributed around a stable mean value [4]. In this case, only 0.3 % of all data points would be lost, but most likely most of the un-physical, extreme values can be sorted out [5]. This is shown for two examples in Figure 7.3.

[4] This should be specifically valid for short measurement times (so isothermal conditions can be assumed) and after long times of resting in darkness, so that the PMT could stabilize its dark rate.

[5] In principle, this method could also be iterated until the number of remaining data points does not change anymore (removal of outliers in statistical analyses). In practice, the situation does not improve with more iterations for the very most data samples, since the window for accepted statistical dispersion is chosen quite conservative by using the $3\,\sigma$ range as cut for only very extreme outliers.

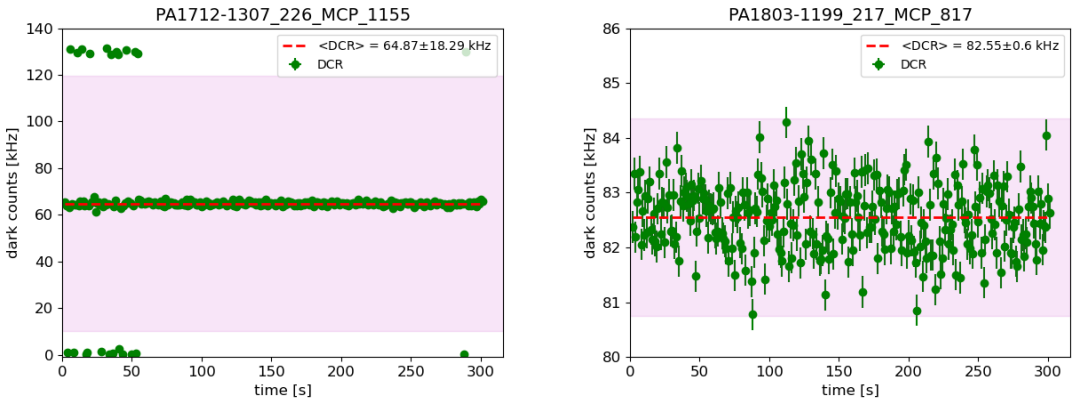

(a) example with few counter undulations (same as in Figure 7.2c)

(b) example with a stable DCR (same as in Figure 7.1b)

Figure 7.3.: Examples for treatment of raw data to sort out extreme values from the data sample. The reddish bands include a $3\,\sigma$ window around the mean of all points. In panel **(a)**, all extreme values can be sorted out from the data sample by this cut. In panel **(b)**, a good (stable) data set is shown, which is not affected from the exclusion of values.

With this method, not necessary all of the mentioned outliers are covered. In order to not "overweight" remaining noise excesses and counter undulations, a penalty term is introduced to the weighted fit of Equation 7.4 as a second step. For this penalty term, mean μ_{ps} and standard deviation σ_{ps} of the presorted data sample are calculated. The final fit of this preselected sample will be performed then using modified weights w_p:

$$\mathbf{DCR} = fit(N_i\,;\, f(t) = c\,;\, w_p) \quad \text{with} \quad w_p^{-1} = \max\left(\sqrt{N_i}, \sqrt{N_i} \cdot \frac{|N_i - \mu_{\mathrm{ps}}|}{\sigma_{\mathrm{ps}}}\right) \,, \tag{7.5}$$

which assigns larger error bars and therefore smaller weights in the fit to all data points which are outside of the $1\,\sigma_{\mathrm{ps}}$ band around the "updated" mean μ_{ps}. With this penalty term for deviant data points one can achieve for the fit to match with the bulk of the raw data points and suppress influence by the shown non-PMT-related features. The penalty algorithm admittedly works successfully only if all extreme values have been removed in the first step before. The final fits of the data sets shown in Figure 7.1 and Figure 7.2 are finally depicted again in Figure 7.4, together with the their final DCR results as determined in the analysis. This method of course has its limitations. The introduction of such a penalty term to the fit is only possible under the assumption of a stable dark count rate over the measurement, which is well motivated and also valid for most of the PMTs. Nevertheless, PMTs showing a very unstable rate [6], as e.g. shown in Figure 7.2a, are treated the same way like PMTs with a stable rate, which could lead to non-significant results for these PMTs;

[6] Whether the rate is spoiled by noise or the PMT itself is instable in its performance is indistinguishable in the container measurements.

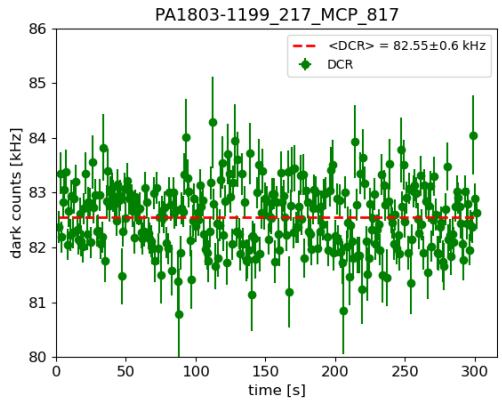

(a) PMT data example with a stable dark rate (same as in Figure 7.1b)

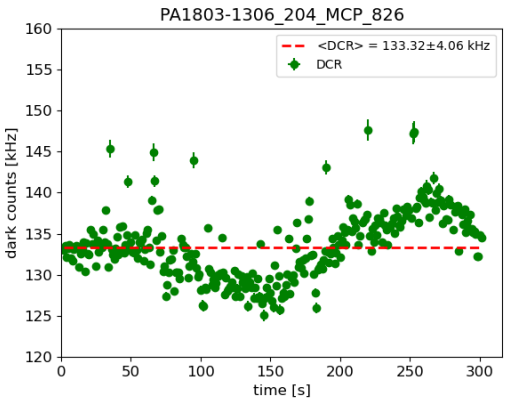

(b) PMT data example with an instable dark rate (same as in Figure 7.2a)

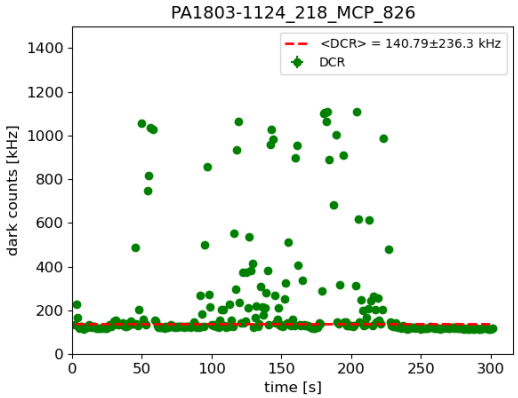

(c) PMT data example with massive noise excesses (same as in Figure 7.2b)

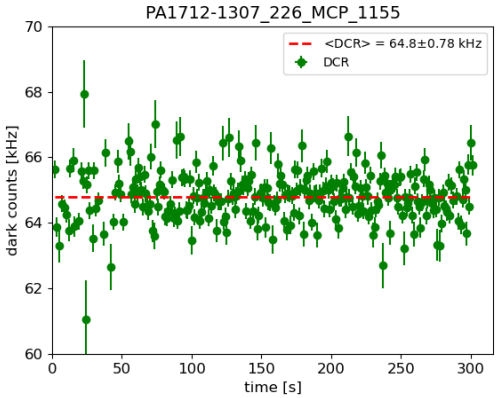

(d) PMTs data example with counter undulations (same as in Figure 7.2c)

Figure 7.4.: Exemplary PMTs as shown before in Figure 7.1 and Figure 7.2, but this time after the full analysis process and including the final fits of the treated data samples (red dashed lines). Final rates and uncertainties are mentioned in the plot legends.

admittedly, in such cases, the definition of a "significant" result is hardly possible at all. However, the final uncertainty values of such instable PMTs would be certainly enlarged. A very large DCR uncertainty can be used as indicator for a double-check of this PMT in another container run or by the scanning station (see also discussion in subsection 8.1.2). Anyway, for the vast majority of the PMTs, this method is completely suitable to determine the DCR.

7.2. Waveform Data Analysis

In the waveform data analysis, the individual PMT pulse identification as well as the pulse form analysis (fitting) are the main tasks. All parameters connected to

the waveforms (and also to the resultant charge distribution) can be extracted from raw data acquired in measurements using the LEDs as light source at very low weak light intensity (see subsection 5.2.3 again). From the results of the individual pulse form analysis, final values for PMT pulse parameters like RT, FT, average amplitude etc. can be determined at the end using the full statistics.
In order to get clear and reliable results, the raw data needs to be treated for unwanted features and noise in the first place (see subsection 7.2.1), and selected according to certain, defined selected cuts (see subsection 7.2.2). In doing so, the ADC raw data is split into frames of a fixed framesize 'fs', depending on the data type (see subsection 5.3.2 again for details). To describe bin ranges inside of waveform data frames, the notation "$[x : y]$" (including both the starting and ending bin) will be used in the following; so is e.g. $[0 : fs - 1]$ displaying the whole frame.

7.2.1. Baseline Correction and Noise Subtraction

The acquired PMT waveforms can be spoiled or influenced by patterns not originating from the PMTs or not linked to their performance and characteristics. These effects are caused e.g. by properties of the ADCs or manifests as noise induced to the system from outside or from the electronics itself. In order to estimate quantities like pulse form, charge and timing information correctly and thus get reliable results for the individual PMT parameters from the data analysis, the acquired waveform raw data needs a correction for these ADC features as well as a subtraction of residual noise patterns.

Although the ADCs provide an internal data correction, their baseline can suffer from offsets or slopes. These are stable features, but not covered by the DRS4 correction (see subsection 5.2.2 again), because they also depend on the impedance the channel is terminated with when connected to the signal source (in this case, $50\,\Omega$ from the PMT base). External noise was reduced by cable shielding and decent grounding, as described in subsection 4.4.3 and section 6.3. The remaining noise consists of arbitrary noise, which is unavoidable to some extent and does not contribute in average over larger statistics, and noise patterns from the electronics itself caused for example by the internal trigger response, which appears to be static. Therefore, this kind of noise can be subtracted from the raw data (this was already tested and described in [330]). An example for untreated raw data frames can be seen in Figure 7.5.
Baseline correction and noise subtraction are executed successively. In a first step, the average frame (including the PMT pulses) is calculated from the full data set by averaging every single bin in $[5 : fs - 20]$ of all frames separately, like depicted in Figure 7.5b. Due to some the artificial features from the ADCs in the raw data, the first five and last twenty bins of each frame are dropped always and so are missing in the plots. With this initial average frame, the average pulse position (possible due to the use of a pulsed light source in the measurements) as well as both baseline offset and slope can be determined. The average pulse position is thereby defined as the

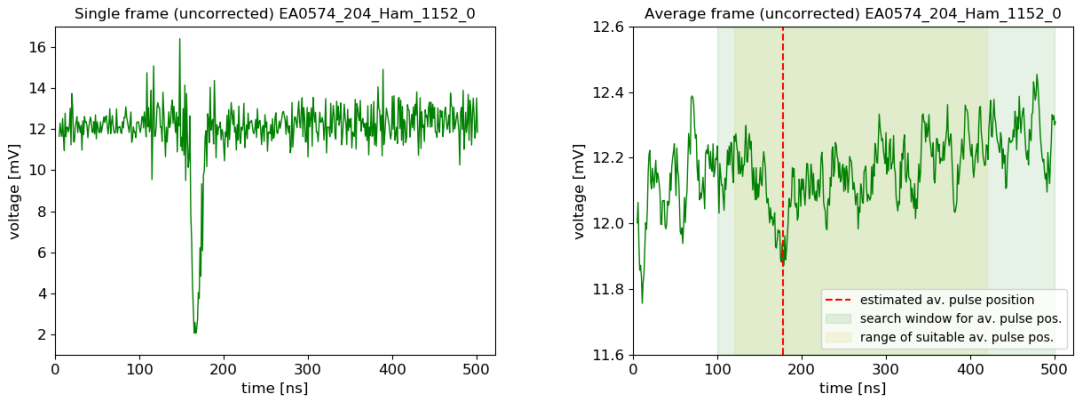

(a) single frame from waveform raw data (uncorrected)

(b) average of 25'000 frames from waveform raw data (uncorrected)

Figure 7.5.: Uncorrected waveform raw data sample, like acquired with the ADCs. Data shown here is from a Hamamatsu PMT (EA0574, used as reference PMT in container B) in a low-intensity LED measurement. Average pulse position in panel **(b)** is indicated by the red dashed line and defined as position of the minimal value within the greenish band; the average pulse amplitude is "compressed" due to many frames without any pulse contributing to the average as well.

bin with the smallest voltage measured in the range $[100 : fs - 20]$ [7]. The system (with all delays from cables, software post-trigger settings etc.) further was tailored to have the average pulse positions roughly in the middle of the frame. However, in order to reduce possible issues with the analysis later on, the average pulse position was checked for being in $[120 : 420]$, otherwise the data would be discarded from the analysis. Both ranges are also visualized in Figure 7.5b.
The baseline of the average frame is now fitted with a linear function over the range $[100 : fs-20]$ to determine both slope and baseline offset. The region $[x_0-50 : x_0+50]$ with the average pulse position x_0 though is excluded from the fit as well, in order to avoid a bias from the PMT pulses to the result of the baseline fit. The linear fit can be subtracted afterwards from all frames to get a flat (yet still noisy) baseline around a value y_{base} of 0 mV, see Figure 7.6.

After the offset and slope of the baseline is corrected, the remaining static noise has to be subtracted. For this, frames containing a PMT pulse need to be sorted out in the first place, which is achieved by omitting all frames containing bins with values less than $y_{\text{base}} - 2.5\,\text{mV}$. The remaining, preselected frames can be assumed as noise-only frames [8] and will be averaged bin-by-bin in the range $[5 : fs - 20]$ as well. In such

[7] The first 100 bins of every frame are excluded here, because for some channels these bins are heavily affected by a static noise pattern produced by the internal response on the external ADC trigger, which could spoil the determination of the average pulse position, see e.g. Figure 7.5b.

[8] This is valid except for very low gains. See also SPE pulse selection cuts in subsection 7.2.2.

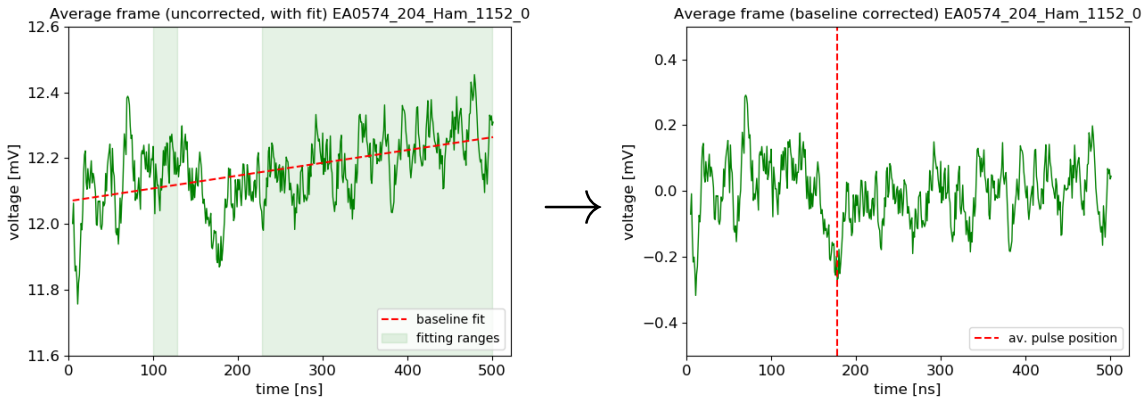

(a) before correction, including baseline fit and fitting range

(b) after baseline correction (offset and slope subtracted for all frames)

Figure 7.6.: Average waveform data of 25'000 frames as already shown in Figure 7.5b, before and after correction for baseline offset and slope. Greenish colored regions in panel **(a)** show the data ranges used for the baseline fit (dashed line shown in red). The first 100 ns of the frame are excluded from fit, because in some channels these bins can be affected by heavy internal noise from the ADC.

an averaged noise frame, as depicted in Figure 7.7, the arbitrary noise cancels out, while the static noise remains. This static noise contribution can now be subtracted bin-by-bin from all frames of the full sample (including the frames containing PMT pulses).
The fully corrected sample thus finally consists of baseline-corrected frames with contributions of only arbitrary noise, which becomes negligible for larger statistics. Plots from such a fully corrected sample are shown in Figure 7.8. The effect of the noise reduction is further visualized in subsection D.1 in the appendix using a Fourier transformation.

7.2.2. Single Photo-Electron Pulse Selection and Fit

The actual waveform data analysis is starting after the baseline correction and noise subtraction of the raw data, described in the subsection before.
In a first step, only frames containing PMT pulses shall be selected, and their individual pulse positions needs to be determined. This selection can be achieved by some dedicated cuts applied on the PMT pulse data:

- The individual PMT pulse position x_0 has to fulfill $x_0 \in [x_{\text{avg}} - 30 : x_{\text{avg}} + 30]$, with x_{avg} the average pulse position, determined in subsection 7.2.1 before. The position of the PMT pulse candidate is therefore defined as the bin with the lowest value in this region.

- The amplitude (lowest data point) of this pulse candidate has to be below a threshold of **-3 mV** in order to exclude noise (see also Figure 7.8a as example).

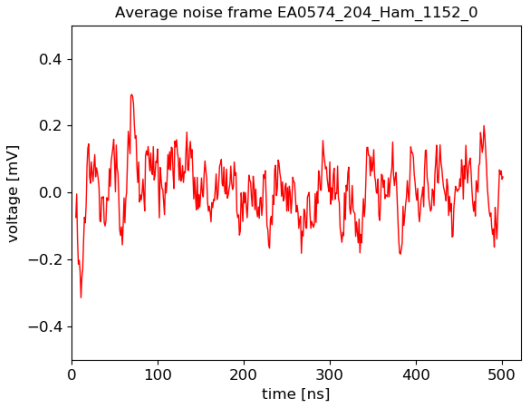

Figure 7.7.: Average of preselected frames (of same data set as in Figure 7.6), which are not containing any values below a threshold of $y_{\text{base}} - 2.5\,\text{mV}$ in $[100 : fs - 20]$ (noise-only frames). Thereby, all frames containing PMT pulses have been sorted out, so that only the static noise contribution remains. This contribution can be subtracted from the data sample.

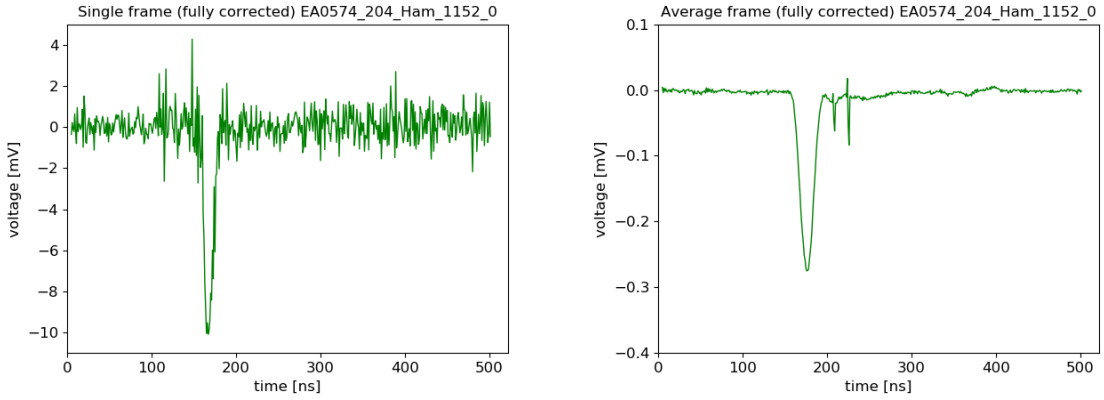

(a) single frame from waveform raw data, with full correction applied

(b) average of 25'000 frames from waveform raw data, with full correction applied

Figure 7.8.: Fully corrected waveform raw data with applied baseline correction and noise subtraction. Original data sample is again the same as in Figure 7.5. While plot in panel **(a)** doesn't show big differences compared to the uncorrected raw data shown in Figure 7.5a, the noise reduction is clearly visible in panel **(b)** when compared to Figure 7.5b. Narrow spikes in the average plot are caused by internal crosstalk from the trigger recording, see also discussion in section 6.5. Since these spikes occur randomly and with a large amplitude (usually below noise threshold of $y_{\text{base}} - 2.5\,\text{mV}$), they cannot be removed in the noise subtraction, but can be easily distinguished and separated from PMT pulses in the later analysis (see subsection 7.2.2 for details). Remaining structures on the baseline in panel **(b)** are likely connected to the PMT pulses (otherwise they would have been covered in the noise subtraction as well), but doesn't play a role as long as they are small.

- The FWHM of the so far detected pulse candidates must also exceed a threshold of **3 ns**, which is checked in a first step by comparing the distance in time of data points at the FWHM level.

- For investigating the pulse form parameters, the use of only single photo-electron (SPE) events is recommended to get clearer and more reliable results. Thus, another threshold is introduced, ignoring all events with an amplitude of less than **-10 mV** in these analyses [9].

Only frames passing the first three (all four) criteria will be used for the following (SPE pulse) analyses; i.e. the FWHM threshold helps to identify non-physical spikes caused by channel crosstalk within the ADC (see section 6.5 again for details). Frames containing such spikes will be excluded completely from the data sample and won't be used for the charge integration described in subsection 7.3.1, either [10].
The selected PMT pulses then are fitted using a Levenberg-Marquardt algorithm [331, 332], for which two different approaches have been tested: first, a log-normal function, which has been used as well in [333, 334] for PMT pulse form modeling:

$$f_p(x) = A \cdot \exp\left(-\frac{1}{2}\left(\frac{\ln((x - x_{\text{off}})/\tau)}{\sigma}\right)^2\right) \ . \tag{7.6}$$

A defines here the pulse amplitude, while τ and σ define width and shape of the pulse (with $\tau, \sigma > 0$); x_{off} further considers the position of the pulse inside of the frame [11]. Second, a double-Gaussian function was used, motivated by [213]:

$$f_p(x) = A \cdot \left(\exp\left(-\frac{(x - x_0)^2}{2\sigma_{\text{rise}}^2}\right) \cdot \Theta(x_0 - x) + \exp\left(-\frac{(x - x_0)^2}{2\sigma_{\text{fall}}^2}\right) \cdot \Theta(x - x_0)\right) + c \ , \tag{7.7}$$

with A the pulse amplitude, x_0 the pulse position, σ_{rise} and σ_{fall} the half pulse widths of the rising and falling edges, c considering a possible remaining baseline offset and $\Theta(x)$ the heaviside function, ensuring a continuously differentiable transition between the two parts of the function. This sum of two halves of a Gaussian function accommodate for the different shapes of rising and falling edge of the pulse. Figure 7.9 shows fitted

[9] The pulse form parameters are defined based on the shape of single photo-electron pulses and are moreover expected to be different for 2+ p.e. pulses. For this reason, they are determined using data from the LED measurement with a low light intensity of only around 0.1 p.e. per trigger event in average (see also section 5.1 again). By using this threshold, the contribution of double (and more) photo-electron events should be further reduced although the probability for such events is already low with the used weak light intensity setting.

[10] Since the appearance of these crosstalk related spikes is not correlated to the occurrence of PMT pulses in the frame, no bias is introduces by removing these affected frames from the full data sample. If the FWHM threshold was failed, but the pulse amplitude is not below -5 mV, the event is rather a (large) noise event than a spike caused by crosstalk. In this case, the event is kept for the charge integration, but not completely discarded from the analysis.

[11] This is necessary for mathematical reasons, as the log-normal function is not defined for $x < x_{\text{off}}$.

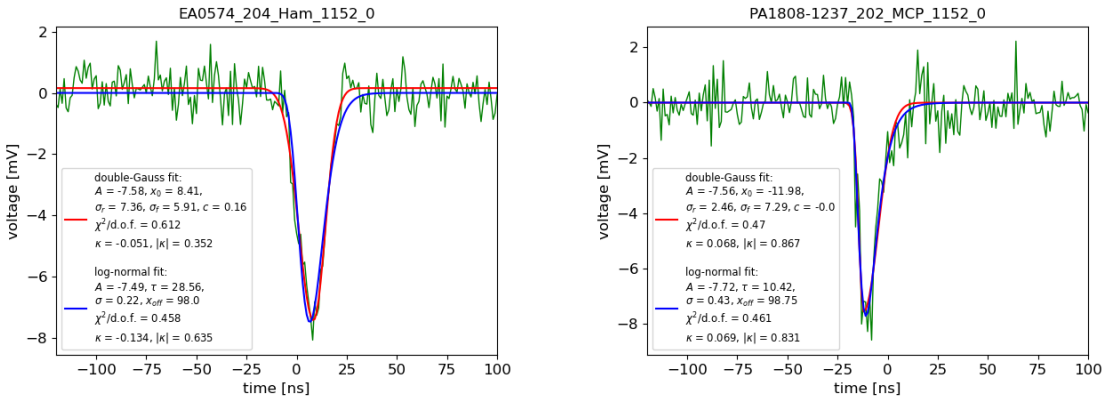

(a) pulse from a Hamamatsu PMT **(b)** pulse from an NNVT PMT

Figure 7.9.: Single photo-electron pulses from both PMT types, fitted successfully with both a log-normal (blue curve) and a double-exponential function (red curve).

PMT pulses for Hamamatsu and NNVT PMTs using both the log-normal and double-Gaussian function.
To estimate the fit quality and how well it describes the actual data, a new parameter was introduced. Although the χ^2-value of the fit is usually a good choice for such an estimation, it was refrained from using it here, because neither the influence of the residual baseline noise on the actual χ^2-value could be estimated in a satisfying way, nor individual uncertainties for the data points could be determined, nor was it possible to define a distinct criteria for a suitable goodness of fit based on the χ^2-value enabling a selection of reliable and non-reliable fit results. Hence, two new parameters κ and $|\kappa|$ were defined instead, with

$$\kappa = \frac{1}{19} \sum_{i=x_0-9}^{x_0+9} (V_i - f_p(x_i)) \ , \tag{7.8}$$

$$|\kappa| = \frac{1}{19} \sum_{i=x_0-9}^{x_0+9} |V_i - f_p(x_i)| \ , \tag{7.9}$$

and are already indicated in Figure 7.9 as well. These parameters represent kind of an average deviation of the fit $f_p(x_i)$ from the actual data points V_i in a small window (chosen to ± 9 data points) around the peak position x_0 of the pulse. The choice for the κ parameters simplifies the evaluation of the goodness of the fits. So is the range, where the fit is evaluated, concentrated around the peak position and thus less affected by the baseline noise. Also the definition of a quality criteria (as a maximum allowable deviation in average) is clearer and easier to relate to the data, as explained below. Finally, following limits have been defined to accept a fit as successful:

- $\boldsymbol{\kappa \leq 0.5}$ and $\boldsymbol{|\kappa| \leq 1.0}$,
- the fitted amplitude must match with the lowest data point by $\pm 2\,\mathrm{mV}$,

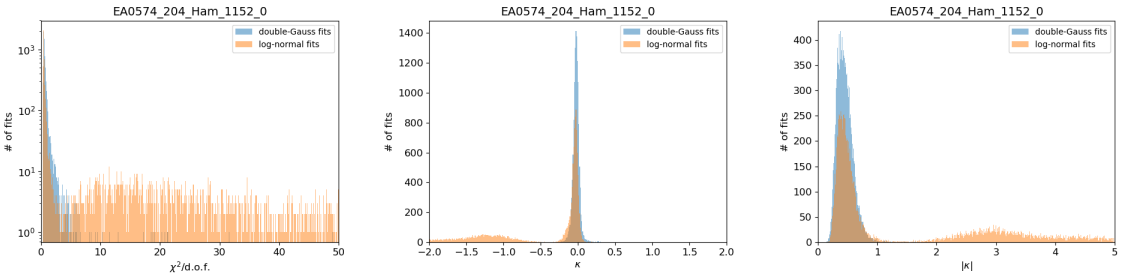

(a) χ^2-distribution from analysis of a Hamamatsu PMT

(b) κ-distribution from analysis of a Hamamatsu PMT

(c) $|\kappa|$-distribution from analysis of a Hamamatsu PMT

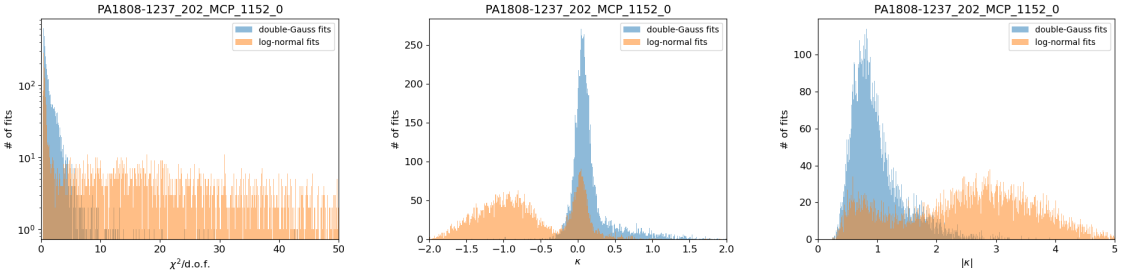

(d) χ^2-distribution from analysis of an NNVT PMT

(e) κ-distribution from analysis of an NNVT PMT

(f) $|\kappa|$-distribution from analysis of an NNVT PMT

Figure 7.10.: Distributions of χ^2, κ and $|\kappa|$ to estimate goodness of pulse fits in the analysis of a raw data sample (panels **(a)** to **(c)** show results for a Hamamatsu PMT, panel **(d)** to **(f)** for a NNVT PMT). All distributions individually show that the double-Gaussian function describes the pulse shape more accurate than the log-normal function.

- and the fitted pulse position x_{fit} must match with the aforementioned pulse position x_0 by $x_{fit} \in [x_0 - 5 : x_0 + 5]$.

All fitted PMT pulses which fail one of these limits will be excluded from the analysis of the pulse shape parameters [12].
Although both fit functions from Equation 7.6 and Equation 7.7 performing good in the presented example in Figure 7.9 and actually describe the data rather well (red. χ^2-values below 1, small κ and $|\kappa|$ values), using the double-Gaussian fit function turned out to be more stable and better converging, while for the log-normal function in particular more asymmetric pulse forms lead the fit to converge badly sometimes (or even to not converge at all). This is also illustrated in Figure 7.10 showing the distribution of both the reduced χ^2-values as well as of the κ and $|\kappa|$ values from the

[12]The definition of the goodness limits for the fits is a compromise between a "purification" of the data (including only fits matching well to the data, thus increasing the quality of the data sample) and a loss in statistics (by excluding pulses failing the defined criteria). The same situation arises for the SPE pulse selection thresholds. During development and optimization of the analysis algorithms, the listed limits and selection cuts have been found to be optimal for the needs of this analysis.

analysis of a low light intensity measurement of both a dynode and an MCP-PMT. The plotted distributions clearly show, that the double-Gaussian function reaches a higher goodness of fit more often than the log-normal function. Therefore, the double-Gaussian function was selected for the mass data analysis. Looking on the fit distribution of i.e. the dynode PMTs, also the choice of the limits for κ and $|\kappa|$ defining an acceptable goodness of fit becomes well motivated (see Figure 7.10b and Figure 7.10c).

7.2.3. Definition of Waveform-Based PMT Parameters

From the fits of the individual PMT pulses using Equation 7.7, dedicated points in time on the rising and falling edges can now be calculated via

$$x_{r,f} = x_0 \mp \sigma_{r,f} \cdot \sqrt{-2\ln(c_i)} \tag{7.10}$$

with $\sigma_{r,f}$ the width of the corresponding edge (rising or falling) and c_i a constant factor for the calculation of rise time (RT), fall time (FT), hit time (HT) and FWHM of the PMT pulse [13]:

$$\mathbf{RT} = (x_r(0.9\,A) - x_r(0.1\,A)) = \sigma_r \left(\sqrt{2\ln(10)} - \sqrt{2\ln(10/9)}\right) , \tag{7.11}$$

$$\mathbf{FT} = (x_f(0.1\,A) - x_f(0.9\,A)) = \sigma_f \left(\sqrt{2\ln(10)} - \sqrt{2\ln(10/9)}\right) , \tag{7.12}$$

$$\mathbf{FWHM} = x_f(0.5\,A) - x_r(0.5\,A) = (\sigma_f + \sigma_r) \cdot \sqrt{2\ln(2)} , \tag{7.13}$$

$$\mathbf{HT} = x_r(0.1\,A) = x_0 - \sigma_r\sqrt{2\ln(10)} . \tag{7.14}$$

The pulse amplitude is directly defined as the amplitude of the fitted pulse:

$$\mathbf{Amplitude} = f_p(x = x_0) - c = A . \tag{7.15}$$

In Figure 7.11, this is illustrated exemplarily for PMT pulses of both PMT types. Results for the pulse parameters still have to pass the defined thresholds for amplitude ($A < -3\,\mathrm{mV}$) and width (FWHM $> 3\,\mathrm{ns}$) after the fit. If the fit was not successful, this event would be skipped in the pulse parameter analysis.
Final values for these parameters describing the actual PMT pulse characteristics can be derived from the statistical distribution of all individually determined pulse shape parameter results via a Gaussian fit of the distribution (using the mean as final value and the width as estimated uncertainty). This is also shown in subsection D.3 in the appendix as part of the exemplary PMT data analysis presented in section 7.5.

[13] The rise time (fall time) is defined as the time the PMT pulse rises from 10 % to 90 % of its full amplitude level (falls from 90 % to 10 % of its full amplitude), as described already in section 3.3.

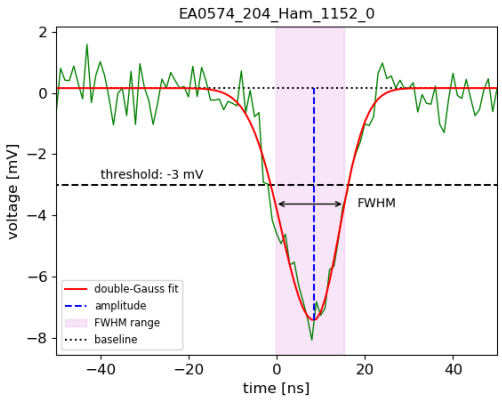

(a) FWHM range of a Hamamatsu PMT pulse

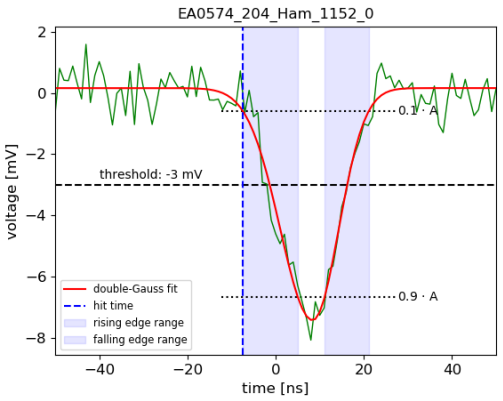

(b) rising and falling edge ranges of a Hamamatsu PMT pulse

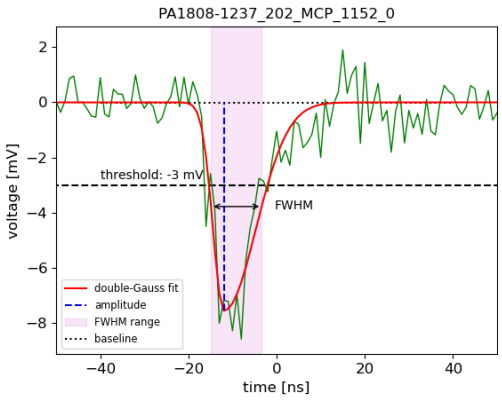

(c) FWHM range of an NNVT PMT pulse

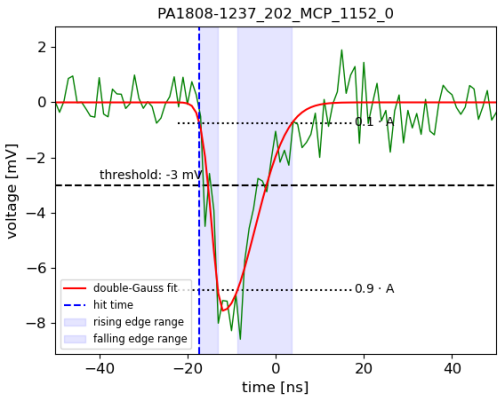

(d) rising and falling edge ranges of an NNVT PMT pulse

Figure 7.11.: PMT pulses from a Hamamatsu PMT (serial number EA0574, panels **(a)** and **(b)**) and from an NNVT PMT (serial number PA1808-1237, panels **(c)** and **(d)**), fitted with a double-Gaussian function. From fit function, several PMT parameters can be derived like indicated in the plots: **(a)** FWHM (covered reddish region), **(b)** rise and fall time (covered by blueish regions), as well as pulse hit time (blue dashed line). Pulse shape analysis will only be performed if amplitude is below a set threshold of -3 mV (indicated by the black dashed line) and pulse width above a threshold of 3 ns.

The search for prepulses and late pulses is also done using the raw data from the LED measurement at low light intensity, though without applying the SPE selection cut for the main pulses. Characteristics for these kind of pulses are not investigated, only the ratio of their occurrence accompanying main PMT pulses is determined. However, for the search of possible prepulses or late pulses in the frame windows, mainly the same criteria are applied as for the identification of the corresponding main pulses:

- Pre- and late pulses will be counted only in dedicated windows Δt_{pp} and Δt_{lp}, with $\Delta t_{\mathrm{pp}} = [x_0 - 90 : x_0 - 10]$ for the prepulses and $\Delta t_{\mathrm{lp}} = [x_0 + 20 : x_0 + 70]$

for the late pulses, before and after a main pulse located as position x_0.

- The same thresholds for width ($> 3\,\mathrm{ns}$) and amplitude ($< -3\,\mathrm{mV}$) as for the main pulses are valid in order to efficiently exclude noise or crosstalk events.
- Detected pre- or late pulse are sole in a window $[x_{pp} - 10 : x_{pp} + 10]$ around their pulse position x_{pp}. Further, these pulses must have their FWHM points (half amplitude levels of rising and falling edge) inside on the indicated window.

With the latter condition, it can be avoided, that neither noisy pre- or late pulses are counted as multiple pulses, nor that "wiggles" on the edges of main pulses with large rise or fall times already are counted as pre- or late pulses [14].
The number of counted pulses yields to a fraction of events, in which pre- or late pulses come up together with a main PMT pulse. To not add randomly coincident dark count events from within the defined counting windows to this rate, their contribution (see section 7.1 again) further needs to be subtracted from the number of detected pulses to get reliable results for both the "prepulse ratio" (PPR) and "late pulse ratio" (LPR):

$$\mathbf{PPR} = \frac{N_{\mathrm{pp}}}{N_{\mathrm{pulses}}} - DCR \times \Delta t_{\mathrm{pp}} \ , \tag{7.16}$$

$$\mathbf{LPR} = \frac{N_{\mathrm{lp}}}{N_{\mathrm{pulses}}} - DCR \times \Delta t_{\mathrm{lp}} \ , \tag{7.17}$$

with N_{pp} and N_{lp} the number of detected pre- or late pulses and N_{pulses} the number of main pulses in the data sample. In Figure 7.12 and Figure 7.13, example frames with a pre-, respectively late pulses, are shown.
It is important to note, that standalone pre- or late pulses without a main pulse won't be searched for, although there are processes which were able to produce such pulses [15]; but without the coincidence to a main PMT pulse, these events are indistinguishable from randomly coincident dark counts within the set windows and the used statistics.

7.2.4. Pulse Parameters from Average SPE Waveforms

Instead of calculating the PMT pulse shape parameters for every PMT pulse individually and extracting final results for RT, FT, FWHM and amplitude from the distribution of all individual results, they can be also determined from the average shape of all SPE pulses, as described also in [330].

[14] This is necessary only to avoid miscounting the number these pulses.

[15] Standalone prepulses can be produced, if the release photo-electron misses the first dynode and starting the amplification from the second stage or if the charge avalanche is missing the last dynode and instead directly hits the anode. Here, only one pulse with smaller amplitude (due to the missing amplification stage) and premature hit time will be produced [247]. Standalone late pulses can be produced by elastic backscattering of photo-electrons from the first dynode stage, without releasing secondary electrons in the first hit, but just after becoming re-accelerated towards the dynode system again [248]. Both conceived processes would have only low probabilities to happen.

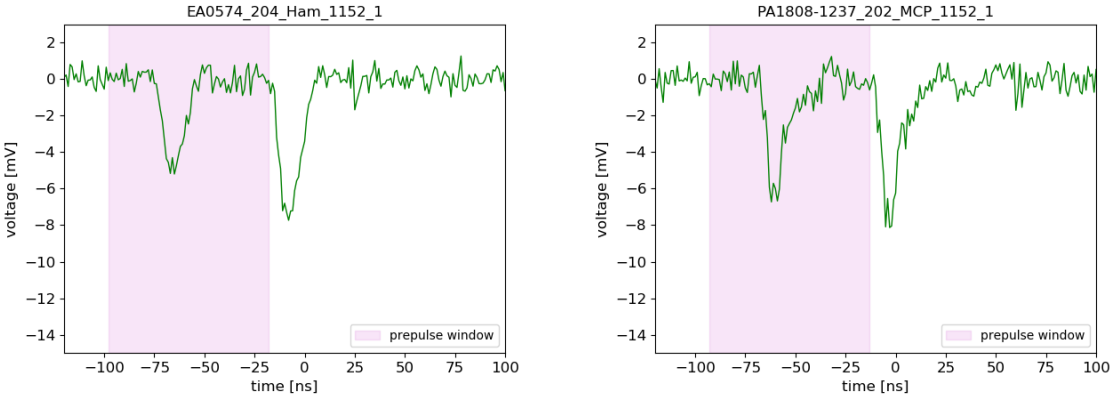

(a) Hamamatsu PMT data containing a prepulse

(b) NNVT PMT data containing a prepulse

Figure 7.12.: Frames containing prepulses. Such pulses need to pass the same thresholds as the main pulses and need to have a "clean" environment, in order to not count noise wiggles on pulse edges accidentally as prepulses. Window of interest (reddish colorized) is $[x_0 - 90 : x_0 - 10]$ with x_0 the position of the main pulse.

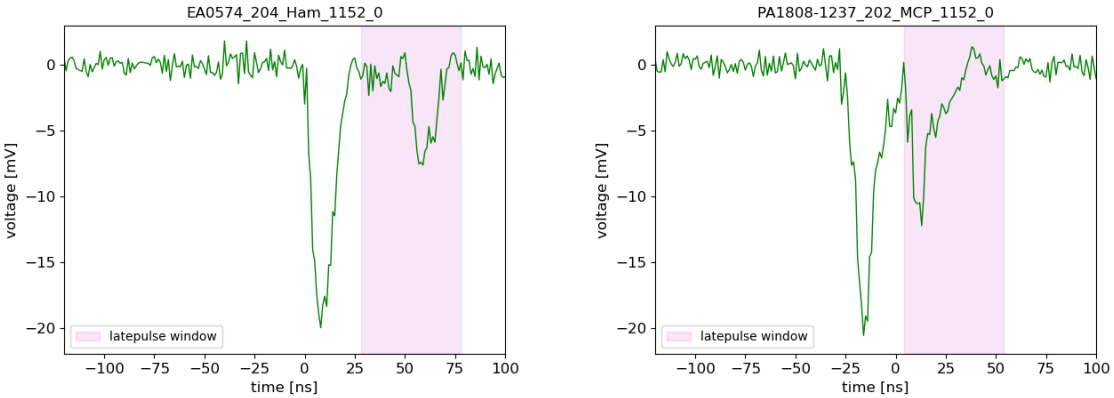

(a) Hamamatsu PMT data containing a late pulse

(b) NNVT PMT data containing a late pulse

Figure 7.13.: Frames containing late pulses. Such pulses need to pass the same thresholds as the main pulses and need to have a "clean" environment, in order to not count noise wiggles on pulse edges accidentally as late pulses. Window of interest (reddish colorized) is $[x_0 + 20 : x_0 + 70]$ with x_0 the position of the main pulse.

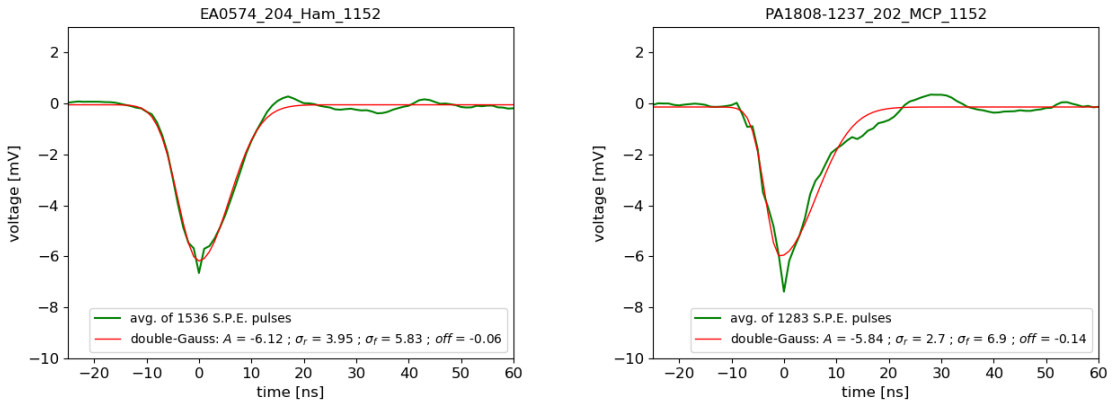

(a) average SPE pulse from a Hamamatsu PMT

(b) average SPE pulse from an NNVT PMT

Figure 7.14.: Averaged single photo-electron pulses from both PMT types, fitted successfully with a double-exponential function (red curve). The selection of SPE pulses contributing to this average pulse was done based on the cuts described in subsection 7.2.2.

Therefore, all selected SPE pulses (using the selection criteria listed in subsection 7.2.2) are averaged similar to the creation of the average raw data waveform shown in Figure 7.5b. To consider the ADC jitter included in the data, the pulses are aligned on their peak position (data point of minimal value). By using the selection cuts beforehand, a "compression" of the pulse amplitude, as visible in Figure 7.8b, thus can be avoided, and also most of the crosstalk related spikes can be removed from the averaged sample. The so produced average SPE pulse can then be fitted again using Equation 7.7; this is shown exemplarily in Figure 7.14. The respective pulse parameters (RT, FT, FWHM, amplitude) can then be extracted from the fit again, as described in subsection 7.2.3 and using the same parameters definitions.
The calculated results for these parameters usually match quite well with the results determined from the individual pulse fits, or are mostly consistent within the found uncertainties. Small remaining variations can be explained by the difficulties in aligning the pulses in the presence of the overlying jitter and with the different rise / fall times and amplitudes of the individual pulses. This causes the average pulse to be smeared out a little, as well as can boost the influence of specific patterns (such as the baseline ringing after the pulse or the very sharp tip of the pulses, which is an artificial pattern originating from the finite sampling frequency and the fixed position on which all SPE pulses are aligned) on the fit.
The results of the analysis of the average SPE pulses will be added for comparison to the results of the exemplary PMT data analysis presented in section 7.5, as well as in the analysis of the large PMT sample presented in chapter 8. The average SPE pulse is also a good tool to cross-check the SPE selection cuts by calculating the charge of the displayed average frame, which should be close to 1 p.e. for an accurate selection. This is indeed the case in the depicted examples, as shown in Table 7.1.

Table 7.1.: Charges of the exemplary average SPE pulses shown in Figure 7.14. Method for charge calculation is explained below in subsection 7.3.1. In both cases, the charges calculated using the averaged data points and the fit match very well, and all charges are close to the expected value of 1 p.e., which confirms a proper selection of the SPE pulses based on the discussed selection cuts.

PMT	based on...	calculated charge [p.e.] [16]
Hamamatsu (EA0574)	data points	0.992
	fit	0.991
NNVT (PA1808-1237)	data points	1.023
	fit	1.013

7.3. Charge Spectrum Analysis

All remaining PMT parameters based on the data from the LED measurement but not yet discussed, such as P/V ratio, S/N ratio, charge resolution, gain or the average number of photo-electrons per trigger event μ, are related to the combined spectrum of integrated charges from all acquired frames. Therefore, raw data from the LED measurement at very low light intensity (the same raw data as used in the waveform analysis before), and from the measurement at higher light intensity is used.

7.3.1. Charge Integration

The charge spectrum is generated via charge integration of all individual frames from the PMT waveform raw data, independent of their actual content (and so whether they contain PMT pulses or just noise [17]). Only frames affected by electronic crosstalk events within the ADCs and thus containing spikes will be sorted out (see section 6.5 again for details).

If a frame contains a PMT pulse, the charge is calculated via the trapezoidal rule from the data points over a 75 ns window around the position x_0 of the PMT pulse:

$$Q\,[\text{p.e.}] = \frac{1}{R \cdot g \cdot e} \cdot \sum_{i=x_0-20}^{x_0+55} \frac{y_i + y_{i+1}}{2} \cdot \Delta t \ , \tag{7.18}$$

with $R = 50\,\Omega$ the resistance of the PMT base at the signal output (and also impedance of the signal cable), e the elementary charge, g a conversion factor of

[16] 1 p.e. equals here 1.602 pC, assuming a gain of 1×10^7. See also subsection 7.3.1 for details.

[17] Also randomly coincident dark counts can add to the charge spectrum as irreducible background contribution, if they are released perfectly aligned to the incoming trigger. But due to the very short integration time window, the contribution from thermally released and randomly coincident electrons would be only around 3 ‰ for a PMT with 50 kHz DCR and thus can be neglected.

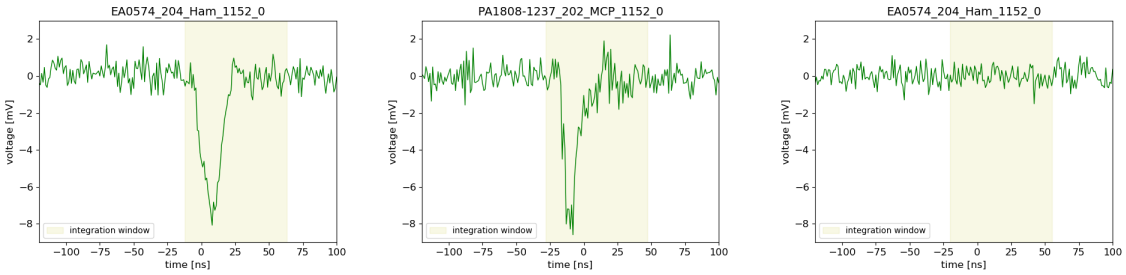

(a) integration of a Hamamatsu PMT pulse

(b) integration of an NNVT PMT pulse

(c) integration of noise-only frame

Figure 7.15.: Integration windows for charge integration (indicated by yellowish regions). For actual PMT pulses (like in **(a)** for a Hamamatsu and in **(b)** for an NNVT PMT pulse), the integration window is covering $[x_0 - 20 : x_0 + 55]$ around the actual pulse position x_0. For frames containing just noise (like depicted in **(c)**), the integration window is always covering the range $[x_{\text{avg}} - 20, x_{\text{avg}} + 55]$ around the average pulse position x_{avg} (which is set to 0 in these plots).

10^7 considering the gain of the PMT [18], y_i the value of the data points in mV and $\Delta t = 1\,\text{ns}$ the distance in time between two data points (using the default setting of 1 GS/s in the ADCs, see subsection 5.2.2). If the integrated charge is divided by $g \cdot e$, the final charge is provided directly in units of photo-electrons (p.e.) [19], which is a more natural choice with view on the charge spectrum.
If the frame contains just noise, a region around the average pulse position x_{avg} is integrated instead, with an integration window of the same size as in Equation 7.18:

$$Q\,[\text{p.e.}] = \frac{1}{R \cdot g \cdot e} \cdot \sum_{i=x_{\text{avg}}-20}^{x_{\text{avg}}+55} \frac{y_i + y_{i+1}}{2} \cdot \Delta t \ . \tag{7.19}$$

The integration of such frames would give a charge of 0 p.e. for a perfectly flat baseline; for a baseline containing random noise of low amplitude, values will be distributed in a narrow band around 0 p.e., making up the *pedestal* of the charge spectrum.
Examples for integration windows of actual data frames are shown in Figure 7.15.

For the analysis of the charge spectrum, only charges within a range of $(-3, 10)$ p.e. are kept, because values outside of this range would suggest issues or incidents not related to the PMT performance: larger negative results would hint for a faulty baseline

[18] The gain was specifically set to 10^7 for all waveform measurements as result of the gain/HV-measurement, see section 5.1 and subsection 5.2.3 again.

[19] In transforming the charge in units of p.e., a correct determination and corresponding adjustment of the applied HV is intrinsically assumed. Furthermore, using the fixed conversion factor of 10^7, the position of the single PE peak in the spectrum with respect to the 1 p.e. mark on the x-axis will indicate whether the applied gain is actually lower, higher or indeed well adjusted to the level of 10^7 in the respective measurement, see also subsection 7.3.2.

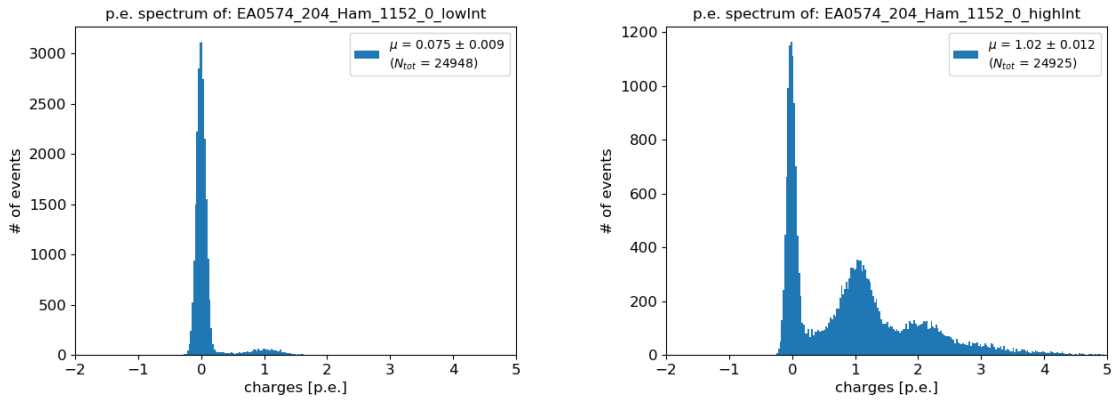

(a) charge spectrum at low light intensity **(b)** charge spectrum at high light intensity

Figure 7.16.: Charge spectra of a Hamamatsu PMT containing approx. 25'000 events. Panel **(a)** shows the spectrum of a low light intensity LED measurement, with average photo-electron number per trigger $\mu \sim 0.08$. Panel **(b)** shows the spectrum of a high light intensity LED measurement, with $\mu \sim 1.02$. The bin width in the histogram is set to 0.025 p.e./bin (which equals to 0.040 pC) by default (same for all charge histograms in the following).

correction or a heavy noise (overshoot) event, causing a positive pulse, largely positive charges would directly hint for heavy noise issues, since multi p.e. events are very unlikely in view of the only weak light intensities used in the container measurements (light intensity is adjusted to the SPE range, see subsection 5.2.3 again). These could be caused e.g. by flashes from PMT or base or even by external events like muon-induced events in the photocathode or the amplification system of the PMT. In any case, such events would not originate from the PMT's standard behavior or be linked to the PMT performance, so they can be excluded from the analysis for good reasons in order to not bias the results.
From the full list of integrated charges, finally the charge spectrum is built by sorting all calculated charges into a histogram. In Figure 7.16, exemplary charge spectra from a low and high light intensity LED measurement of a Hamamatsu PMT are shown.

7.3.2. Spectrum Analysis and Parameter Definition

Charge spectra are created from all individual LED measurements, though not all parameters will be extracted from all created spectra. So is the data acquired in the gain determination measurement used only to determine the applied gain from the charge spectrum; the data from the low light intensity LED measurement is used to determine applied gain in the final measurements [20], S/N ratio, charge resolution and

[20]This is done as a cross-check of the aforementioned gain determination measurement and the corresponding adjustment of the HV to apply a gain of 10^7 in the waveform measurements, see section 5.1 again and also subsection 8.1.2.

P/V ratio of the PMT, while the high intensity LED measurement is used to determine the average photo-electron number per trigger event μ and thereby the PDE (see section 5.1 again).

For the determination of most of the parameters extractable from the charge spectrum (except for μ), different features of the spectrum need to be fitted: the pedestal peak and the SPE peak of the spectrum will be fitted using separate Gaussian functions,

$$G_i(x) = A_i \cdot \exp\left(-\frac{(x-q_i)^2}{2\sigma_i^2}\right) \quad \text{with} \quad i = \text{ped}, \text{sig} \ , \tag{7.20}$$

while the valley between pedestal and SPE peak is approximated with a parabola function,

$$V(x) = ax^2 + bx + c \ . \tag{7.21}$$

For all fits, a Levenberg-Marquardt algorithm is used again. Since the high voltage has been adapted to provide a gain of 10^7 at the beginning of the measurement sequence (as first measurement step after the cool-down of the PMTs, see subsection 5.2.3 again), the position of the signal peak q_{sig} should be close around 1 p.e., while the position of the pedestal peak q_{ped} should be close around 0 p.e., i.e. after the baseline and noise correction. An example for the use of the chosen fit functions on real PMT charge spectra is depicted in Figure 7.17.

The use of separate Gaussian function for fitting pedestal and SPE peak rather than using a global fit function for the full spectrum [21] is a justifiable approximation, since the used light intensity is very weak (around 0.1 p.e. in average in the respective measurements from which the corresponding charge spectrum will be fitted), so that no other features as pedestal and SPE peak are expected to be part of the spectrum (meaning that the contribution of multi p.e. events is small). Since only position or width of these sub-peaks are of interest in the given parameter definitions (see below), using individual fit functions is reasonable, as no additional information or accuracy would be expected from using a global fit function for the full spectrum instead of individual fits. Further, both peaks are clearly separated due to the applied gain and present noise level [22], which legitimates the use of two separate fit functions in this case.
The fit of the valley is another approximation, since determining the exact position of the valley is difficult due to contributions from pedestal, photon peak [23] and back-

[21] A more accurate description of the full PMT response function (and so the charge spectrum) is given e.g. in [335–337].

[22] Due to the extensive noise reduction described in subsection 7.2.1, the width of the pedestal peak should be small, while the shape of the charge peak is influenced by noise contributions only in a negligible amount.

[23] The actual P/V value slightly depends on the average photon number μ and is therefore not a completely robust parameter.

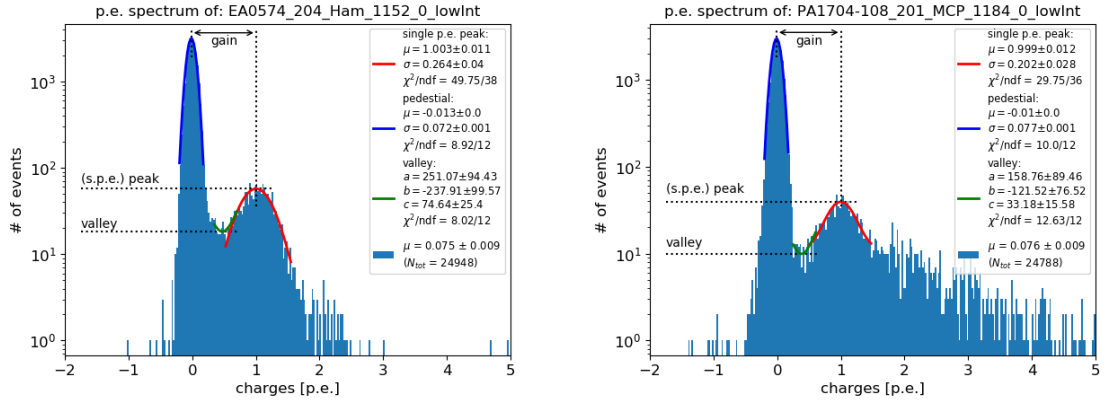

(a) charge spectrum from a Hamamatsu PMT

(b) charge spectrum from an NNVT PMT

Figure 7.17.: Fitted charge spectrum of PMTs at low light intensity (here with $\mu \sim 0.08$, in logarithmic scale). Fitted features are indicated by different colors: pedestal fit in blue (Gaussian function), SPE peak fit in red (Gaussian function) and valley fit in green (parabola function). Fit results are marked in the legend of the plot.

ground processes as e.g. described in [335] (for which reason using the intersection of both pedestal and photon peak fits wouldn't be accurate). In addition, the valley is spread over only a small amount of bins with usually low content, making it difficult to even define the exact charge representing the valley [24]; thus again justifies the use of an approximative fit function.

The fitting range of the pedestal is fixed to $[-0.2, 0.2]$ p.e., as the position of the pedestal q_{ped} is centered to ~ 0 p.e. The fitting region of the SPE peak however is defined dynamically depending on the position of the peak and thus the actual gain [25]. The fitting range covers at least 40 bins around the peak position q_{sig}, which is identified by searching for a local maximum in bin values at charges higher than 0.3 p.e. The fitting range is defined as $[L, R]$ with $L = \max(0.25\,\text{p.e.}, 0.5 \times q_{\text{sig}})$ and $R = \min(L + \max(1.0\,\text{p.e.}, q_{\text{sig}}), 5.0\,\text{p.e.})$, and hence can reach from 0.25 p.e. on the left up to 5 p.e. on the right edge. With this dynamical approach, the SPE peak will be lying always in the fitting range and considers also its larger width expected in case of larger gains.
The fitting range of the valley is defined dynamically as well. In a first step, the rough position q_{val} of the valley is determined by searching for a local minimum between

[24] The content of single bins can be affected by statistical fluctuations between neighboring bins, since the binning is always finite.

[25] This is necessary i.e. for the analysis of data from the gain determination measurement, where gains $< 1 \times 10^7$ and $> 1 \times 10^7$ are highly expected in the different sub-steps of the measurement. For the analysis of the LED measurement data (to determine the PMT parameters listed at the beginning of this section), the gain is expected to be adjusted closely around 1×10^7.

pedestal and SPE peak using a moving average over five concatenated bins:

$$q_{\text{val}} = \min\left(\frac{1}{5}\sum_{k=i-2}^{i+2} Bin(q_k) \mid \; i \in (q_{\text{ped}} + 0.05\,\text{p.e.}, q_{\text{sig}} - 0.05\,\text{p.e.})\right) \;, \tag{7.22}$$

with $Bin(q_i)$ indicating the bin content of bin at position i with central charge value q_i. The fitting range is then defined as $[q_{\text{val}} - 0.125\,\text{p.e.}, q_{\text{val}} + 0.25\,\text{p.e.}]$, accommodating the asymmetrical shape of the spectrum around the valley. As the valley itself is made from only a few bins containing only few events, the fit might not converge correctly [26]; in such cases, the valley value y_{val} will be assumed as the mean of bin contents around q_{val}:

$$y_{\text{val,alt.}} = \frac{1}{5}\sum_{k=i-2}^{i+2} Bin(q_k) \mid q_i = q_{\text{val}} \;. \tag{7.23}$$

By using the individual fits, the associated PMT parameters (gain g, S/N ratio, charge resolution and P/V ratio) can be calculated from the charge spectrum via:

$$\boldsymbol{g} = (q_{\text{sig}} - q_{\text{ped}}) \cdot 10^7 \;, \tag{7.24}$$

$$\mathbf{S/N} = \frac{q_{\text{sig}} - q_{\text{ped}}}{\sigma_{\text{ped}}} \;, \tag{7.25}$$

$$\mathbf{Resolution} = \frac{\sigma_{\text{sig}}}{q_{\text{sig}} - q_{\text{ped}}} \;, \tag{7.26}$$

$$\mathbf{P/V} = \frac{y_{\text{sig}}}{y_{\text{val}}} = \frac{G_{\text{sig}}(q_{\text{sig}})}{V(q_{\text{val}})} = \begin{cases} A_1/(c - b^2/4a) \\ A_1/y_{\text{val,alt.}} \end{cases} \;, \tag{7.27}$$

see also e.g. [213, 254, 338].
The definition of the gain is important in particular in the analysis of the gain/HV measurement. In this measurement step, seven individual measurement at different voltages are performed (see section 5.1 again) and the gains are calculated from charge spectra of the respective acquired data sets using Equation 7.24. In case the mean of the SPE peak is below the 1 p.e. position, the applied gain is lower than 10^7 in the performed measurement, while a mean positions above the 1 p.e. position corresponds to a larger gain [27]. To estimate the high voltage for generating a gain of 10^7, the individual gain results are fitted using a power-function [213, 214]:

$$g(V) = \alpha \cdot V^{\beta} \;. \tag{7.28}$$

The final voltage can be extrapolated then from the fit, which is shown e.g. in Figure D.10 and Figure D.11 in the appendix as part of the exemplary PMT data analysis presented in section 7.5.

[26] This is checked by comparing the fit results with the expectation from q_{val}.

[27] This is due to the fixed conversion factor of 10^7 used in Equation 7.18 and Equation 7.19.

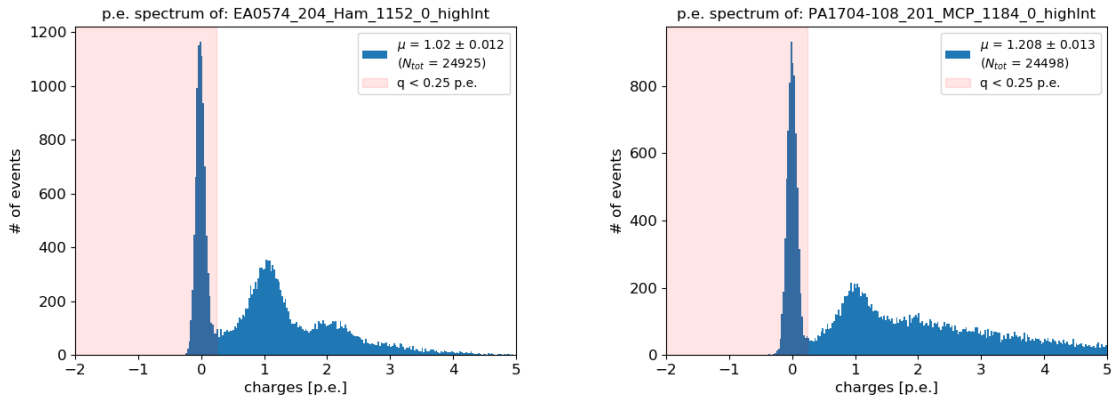

(a) charge spectrum from a Hamamatsu PMT

(b) charge spectrum from an NNVT PMT

Figure 7.18.: Charge spectra of PMTs containing approx. 25'000 events from a high light intensity LED measurement. Colorized area marks all charges with $q_i < 0.25\,\text{p.e.}$; the threshold to separate pedestal from non-pedestal values for the calculation of μ is further close to the position of the valley. In panel **(a)** showing a Hamamatsu PMT charge spectrum, pedestal, single PE and also double PE peak are visible. In panel **(b)** showing an NNVT PMT charge spectrum, pedestal and single PE peak are visible, added by a broad tail up to higher charges, which is typical for NNVT PMTs.

As last missing parameter, the average number of photo-electrons per trigger event μ is calculated using the charges from the waveform data of the high light intensity LED measurement. The μ value is essential for the calculation of the PDE (see subsection 6.6.2 for the relation between PDE and μ again) and can be derived from the charge spectrum as well using Poisson statistics [313] via

$$\boldsymbol{\mu} = -\ln\left(\frac{N_{ped}}{N_{tot}}\right) \ , \tag{7.29}$$

with the total number of calculated charges N_{tot} (and so the number of entries in histogram), and N_{ped} the number of all events with a charge of less than 0.25 p.e. (analogously to the DCR definition in Table 3.1),

$$N_{tot} = \sum_i N_{q_i} \qquad \text{and} \qquad N_{ped} = \sum_{q_i < 0.25\,\text{p.e.}} N_{q_i} \ . \tag{7.30}$$

This is illustrated in Figure 7.18 on real PMT charge spectra again.

7.4. Trigger Raw Data Analysis

Only goal of the trigger pulse data analysis is the determination of the trigger arrival times (hit times). Together with the pulse hit times defined in Equation 7.14, these are needed to determine the TTS results for the PMT with high timing accuracy; without the trigger hit time information, the internal ADC jitter would superimpose the TTS of the PMT, making a correct determination impossible (see also section 6.4 again for details about the jitter).
By comparing the trigger hit times with the pulse hit times, the ADC jitter can be removed from the data, thus enabling the desired high timing accuracy in the TTS measurement. This was demonstrated already in section 6.4 (together with the estimation of the residual ADC jitter after the trigger correction [28]). In Figure 7.19a, an example for such a trigger waveform as recorded by the ADCs is shown.

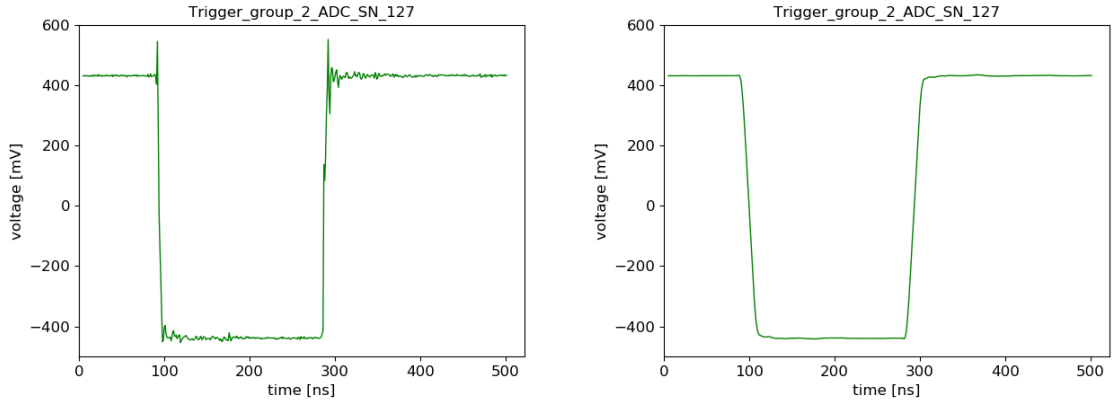

(a) single trigger frame from trigger raw data

(b) average of 25'000 trigger frames from trigger raw data

Figure 7.19.: Trigger raw data (standard NIM pulses), like acquired with the ADCs; in this example, data was recorded using ADC serial no. 127 at trigger group 2 (see also Table 4.2 again).

7.4.1. Trigger Time Determination

To enable a precise determination of the trigger arrival times t_{trig} from the recorded trigger raw data, the leading edges of the individual trigger waveforms need to be fitted. This can be achieved using a four-step algorithm:
First, the average trigger signal is calculated from the data in the already known range $[5 : fs - 20]$ (see subsection 7.2.1 again); this is shown also in Figure 7.19b. Since the trigger amplitude is huge compared to the baseline noise or effects from the baseline slope, it was abstained from a dedicated raw data correction like it was done for the

[28] The here presented methods have been used in the analysis of the jitter measurement already.

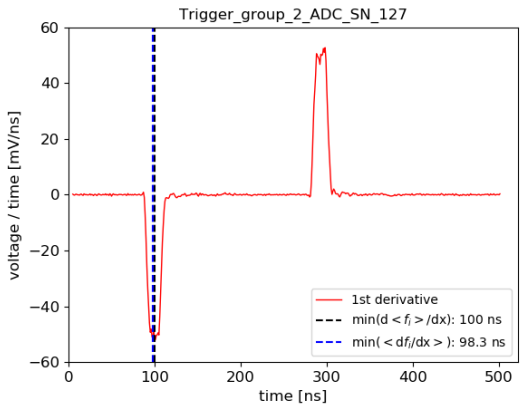

Figure 7.20.: First derivate of the averaged trigger frame shown in Figure 7.19b. Minimum (roughly) indicates the position of the leading edge of the trigger pulses, also marked with a black dashed line. As comparison, average of minima of the first derivate of all individual frames is marked as blue dashed line.

waveform data [29]. To estimate the position of the leading edge in this average frame, its derivative was calculated via

$$\left(\frac{\partial f}{\partial x}\right)_i \cong \frac{1}{2}\left(f(x_{i+1}) - f(x_{i-1})\right) \tag{7.31}$$

so that the minimum $\overline{x}_{\text{edge}}$ of this representation roughly defines the position of the leading edge (maximum decline of the trigger edge, see also Figure 7.20).
In a second step, the positions of the individual trigger edges for all individual frames are calculated using the same method. The edge position of the averaged frame $\overline{x}_{\text{edge}}$ is used here as constraint for the position of the edges $x_{\text{edge},i}$ in the individual frames: if the determined position cannot fulfill the condition $x_{\text{edge},i} \in [\overline{x}_{\text{edge}} - 30 : \overline{x}_{\text{edge}} + 30]$, the frame will be discarded from the analysis [30].
In the next step, the amplitudes of the individual trigger pulses are calculated, which are defined as the absolute difference between the baseline mean μ_{base} and the mean of the pulse plateau μ_{pulse},

$$A_{\text{trig}} = \left|\mu_{\text{base}} - \mu_{\text{pulse}}\right| \ . \tag{7.32}$$

For estimating these means, several bins covering the baseline and several bins covering the pulse plateau will be selected, depending on the individual positions of the leading

[29] The baseline correction is important for a correct charge integration of the frame content. Since noise level and baseline slope are in the low mV to sub-mV regime while the amplitude of the trigger pulses is around 800 mV, these effects can be neglected here. The slope is further incorporated a little by the choice of two windows for the baseline calculation, before and after the pulse.

[30] This helps to exclude false results from the derivatives, which can be caused i.e. by overshoots on the kinks of trigger pulse, especially around the trailing edge.

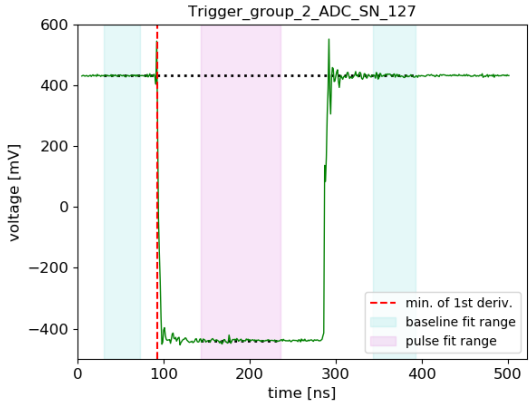

Figure 7.21.: Single trigger frame with colored areas, showing the windows for mean baseline calculation (greenish) and mean pulse level calculation (reddish). Black dotted lines indicate the mean values of both data point samples, defining the pulse amplitude by $|\mu_{\text{base}} - \mu_{\text{pulse}}|$. Position of the leading edge reference point x_{edge} is marked in red (minimum of first derivative of this particular frame).

edge. By default, bins in $[x_{\text{edge},i} - 70 : x_{\text{edge},i} - 20]$ and $[x_{\text{edge},i} + 250 : x_{\text{edge},i} + 300]$ are chosen for the baseline, and bins in $[x_{\text{edge},i} + 50 : x_{\text{edge},i} + 150]$ for the pulse, as illustrated in Figure 7.21 for a single trigger frame. If the leading edge of an individual trigger pulse were found too close to the frame borders, the windows for baseline and pulse level calculation would be adapted, keeping at least 50 bins in both (combined) baseline and pulse windows for averaging [31].
As final step, the leading edges can be fitted for the determination of the individual trigger times. In doing so, all data points in the range $[x_{\text{edge},i} - 20 : x_{\text{edge},i} + 20]$ of the frame are selected, if their values y_i also satisfy the condition $y_i \in (\mu_{\text{base}} - 0.05 \cdot A_{\text{trig}}, \mu_{\text{base}} - 0.95 \cdot A_{\text{trig}})$. These data points are now fitted with a linear function [32] $y_{fit} = a_{fit} \cdot x + b_{fit}$, using the least square method. The trigger hit time is finally defined as the time where the fitted leading edge reaches the 10 % (or 25 %) level of the trigger pulse amplitude,

$$t_{\text{trig}} = x(\mu_{\text{base}} - 0.1 \cdot A_{\text{trig}}) = \frac{\mu_{\text{base}} - 0.1 \cdot A_{\text{trig}} - b_{fit}}{a_{fit}} \ , \tag{7.33}$$

and similar in case of using the 25 % level of the amplitude as criteria. This is also displayed exemplarily in Figure 7.22 for a single trigger pulse. Since usually the number

[31] While setting up the container systems, it was taken care that the trigger pulses are located at a reasonable position within the frames. As additional plausibility check, if the leading edge is found to be outside of [75:400], the frame is discarded from the analysis as well

[32] As a first order approximation, the edges of the trigger pulses can be treated as linear. This approximation becomes less valid close to the kinks of the trigger pulse (beginning and end of the leading edge), for which reason only data points between 5 % and 95 % of the full trigger pulse amplitude are considered in the fit.

of data points passing the requirements to get included to the fit is small, "intermediate data points" are calculated (as means from the values before and after, with both lying in the defined fitting range) and added to the sample for the fit as well, in order to help the fit to converge [33]. As an additional plausibility check, the determined hit times should be inside of $[x_{\text{edge},i} - 20 : x_{\text{edge},i} + 20]$, otherwise the frame will be discarded in order to avoid including bad or unreasonable fit results.
The final distribution of the trigger hit times for a full data set is shown in Figure 7.23, including results of using both the 10 % level and the 25 % level condition. To better estimate the effect of the slightly different methods on the actual TTS results from PMTs, the differences were further investigated based on three exemplary PMTs, which is shown in subsection D.2 in the appendix, affirming e.g. the positive effect of the use of intermediate data points.

It shall be mentioned as a last important note, that it's essential in the trigger raw data analysis to not simply drop frames, which have been excluded from the final TTS analysis, but rather keep them (e.g. by using a default value instead) in order to preserve the correct mapping between trigger frames and corresponding waveform frames in the later analysis. A one-to-one relation between the recorded frames containing PMT and trigger pulses is crucial to get rid of the ADC jitter. This is equally valid also for the corresponding analysis of the PMT pulses as shown before in section 7.2 and has been considered there as well.

7.4.2. Transit Time Spread Definition and Determination

The transit time spread (TTS) is a feature of the propagation of photo-electrons inside of the PMT bulb and manifests in the variation of the pulse hit times. The hit time of an individual PMT pulse has been defined in Equation 7.14 to 10 % of the full amplitude and is also illustrated in Figure 7.11b and Figure 7.11d.
For the TTS measurement, the laser system (also running at a low light intensity) is used as light source, due to its better timing performance. In the data analysis, only frames containing SPE pulses were selected from the full data sample, following the description in subsection 7.2.2. Two distributions of all (successfully determined) hit times from a laser measurement are shown in Figure 7.24.

[33] Such a trick is only justifiable under various, yet well motivated assumptions: (a) the distance between two regular data points is large compared to the expected influence of noise etc. on these data points, (b) all regular data points are expected to be in line, as it's also done in the approximation for the linear fit, so that intermediate data points would just follow that expectation, and (c) the additional points can be used only to strengthen the hypothesis for the fit, which is achieved by giving less weight to the data points close to the kinks (by simple increasing the number of data points in the middle of sample). All these assumptions are reasonable and valid for at least the majority of the to-be-fitted frames, i.e. since the trigger edges indeed are linear in first order approximation. Thus, even if in few cases the fit has been lead to describe the "real" data points worse than without using the intermediate points, the overall results will improve in accuracy if the fit performs better for most of the frames (and if the total statistics are sufficiently high).

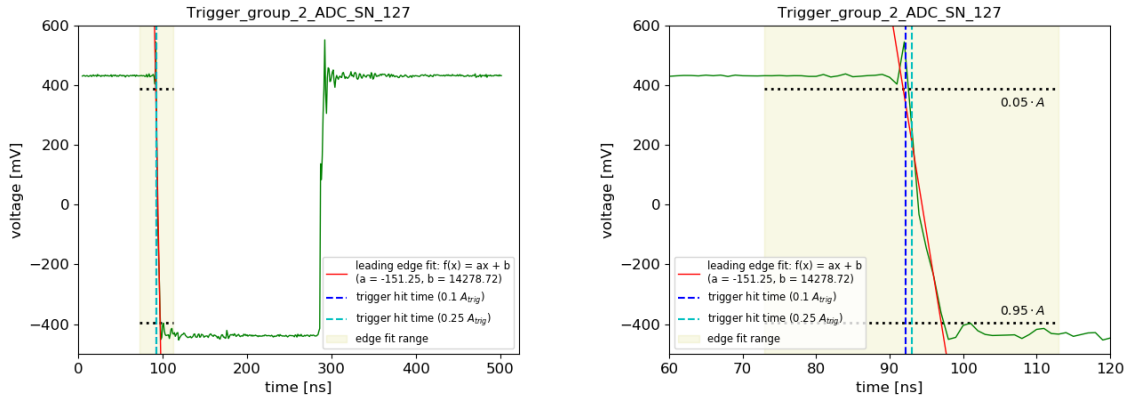

(a) single trigger frame with fitted leading edge

(b) zoom into window around fitting range and leading edge

Figure 7.22.: Trigger raw data frame and zoom into interesting range, with fitting range (yellowish region) and final fit (red line) indicated in the plots. Black dotted lines delimit the data points used for the fitting (only data points in the yellow band and between the two dotted lines, representing 5 % and 95 % of the full trigger pulse amplitude, are selected), thus ensuring that only the edge of the pulse is fitted. Final trigger hit time (position at which the edge has risen to a certain percentage level of the full trigger pulse amplitude) is marked for a 10 % trigger level by the blue line and for a 25 % trigger level by the cyan line.

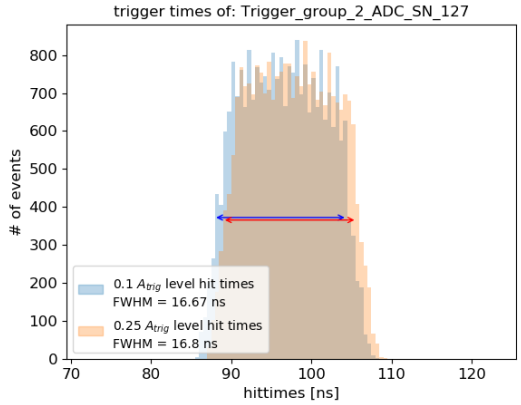

Figure 7.23.: Histogram of all calculated trigger times from one exemplary data sample (in this case only 25'000 triggers from one trigger group, acquired with ADC serial no. 127). Different distributions correspond to the hit time condition, also shown in Figure 7.22 before (light blue for 10 % trigger amplitude level, orange for 25 % trigger amplitude level). The rectangular distributions of hit times illustrate the internal jitter of the ADC trigger group (width $\sim$ 17 ns, which is consistent to the ADC specifications [323]), see also discussion in section 6.4 again. The fact, that results and distributions are identical for both trigger level conditions can be taken as strong evidence that the fitting of the trigger edges performs reasonable here.

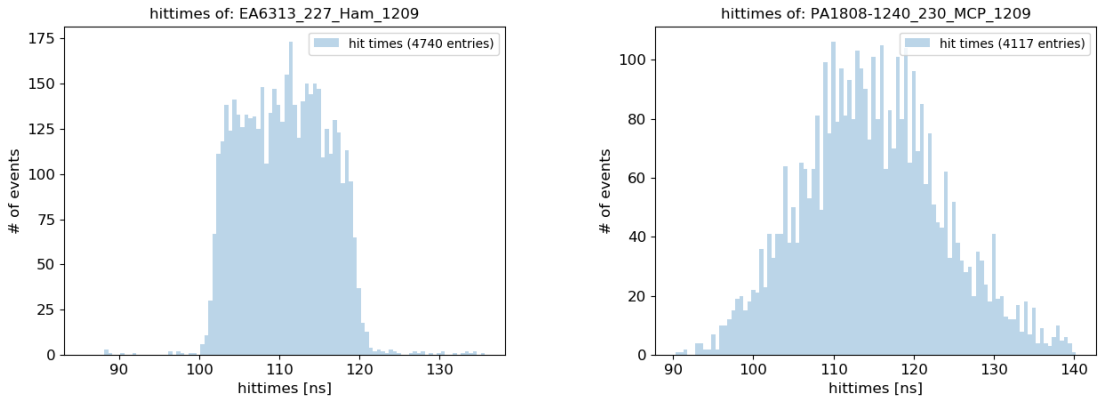

(a) distribution of pulse hit times from a Hamamatsu PMT

(b) distribution of pulse hit times from an NNVT PMT

Figure 7.24.: Histogram of all successfully calculated pulse hit times for a Hamamatsu PMT (panel **(a)**) and an NNVT PMT (panel **(b)**) from one data sample (originally 50'000 trigger events in total). Both distributions individually are dominated by the ADC jitter.

A high timing performance can be now achieved by combining the information of both the pulse and the corresponding trigger hit times (as shown in Figure 7.23) in order to exclude the overlying ADC jitter. In doing so, a frame-by-frame subtraction of the individual (successfully determined) hit times of PMT pulse and trigger is performed. In the process, taking care of the coherence between pulse frame and corresponding trigger frame is essential for a successful removal of the ADC jitter.
The final TTS value of the investigated PMT can be identified finally as the width of the full "transit time" distribution [34] from all valid pulse/trigger pairs,

$$\mathbf{TTS} = \sigma(HT_i - t_{\mathrm{trig},i}) \ . \tag{7.34}$$

Therefore, the distribution is fitted using a Gaussian function again. In order to increase the reliability of the results, a fit is performed only for transit time distributions with at least 1000 entries.

Exemplary results of such a fit are illustrated in Figure 7.25 for both PMT types. It can be seen that the distribution for a Hamamatsu PMT is perfectly Gaussian, while it's not in case of MCP-PMTs: these PMTs often show a substructure in their transit time distribution, with multiple peaks spread over a larger range (compared

[34] This distribution does not display the actual transit times of charges within the PMT, which is not measurable with the container system, but rather shows the difference between incoming trigger signal and PMT pulse signal on the ADC. The width of this distribution further represents the combination of the TTS of the PMT and the residual jitter of the system (which is in case of the ADC negligibly low if correctly considering the trigger times, see section 6.4). Residual systematic effect will be discussed later in subsection 8.2.3

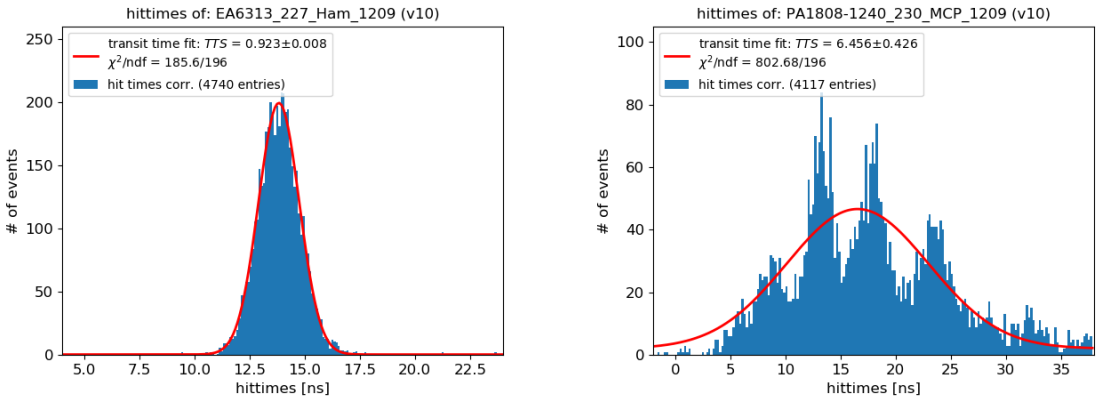

(a) distribution of transit times from a Hamamatsu PMT

(b) distribution of transit times from an NNVT PMT

Figure 7.25.: "Transit time" distributions of a Hamamatsu PMT (see panel **(a)**) and an NNVT PMT (see panel **(b)**). Both distributions are fitted using a Gaussian function, which matches well for the Hamamatsu PMT, but not for the NNVT PMT. The substructure in the transit time distribution of the MCP-PMT originates from its internal design, which has been optimized for maximum collection efficiency, see also [233]. In the illustrated plots, only the transit time distributions using the 10 % level trigger times is shown. If using the 25 % level trigger times, the determined TTS values are even a little smaller, which can be seen exemplarily also in subsection D.2 in the appendix.

to the Hamamatsu PMTs). This substructure originates from the internal design of the MCP-PMT, which is optimized for maximum collection efficiency [35]. The non-Gaussian profile makes it difficult to even define a value for the transit time spread of MCP-PMTs, since neither a reasonable FWHM value can be defined, nor a reliable standard deviation can be calculated without determining the edges of the distribution [36]. As a compromise, this distribution is also fitted with a Gaussian function in order to cover the full distribution with a function and to be able to define a "width", although the distribution is not Gaussian-like in most cases. Since the fit is sensitive to the exact edges of the distribution and could even converge over one of the sub-peaks (which would lead to an underestimation of the actual TTS), the results for multiple measurements of the same PMT may show larger variations and usually have larger error bars than in the case of the Hamamatsu PMTs.

[35] The sub-peaks in the transit time distribution are connected to the way how the photo-electrons are collected within the PMT and directed into the micro-channels: most likely, they originate from re-collected electrons, which have been hit the spacing between the channels in the first place, see e.g. [233]; such features have been reported also in [231].

[36] The calculation of the standard deviation of the full transit time sample (including all valid hit/trigger time pairs) would include also outliers and thus unduly increase (or overestimate) the TTS value.

7.5. Full Analysis of two (exemplary) Reference PMTs

The outcome of this raw data analysis methods shall now be presented exemplarily for one PMT of each type. Therefore, two reference PMTs from the container systems have been selected: PMT **EA1437** from Hamamatsu and PMT **PA1704-108** from NNVT [37]. Both are used in container B; data for this exemplary analysis was taken from **mass 84**. In this run, PMT EA1437 was located in channel **234** (drawer box D7, see also Figure 4.5a), and PMT PA1704-108 was located in channel **201** (box A1).
The results from the full analysis of the chosen PMTs are listed together in Table 7.2. Accompanying to the results, there are several plots produced in the various analysis steps, which can be found in subsection D.3 in the appendix. According to the results, both PMTs would have passed the container acceptance tests (see Table 3.1 again).

The introduced algorithms will be used also for all analyses presented in chapter 8. It shall be mentioned here, that the analysis methods which have been described in this chapter are used only for this thesis and with the main purpose to prove the capability of the PMT mass testing system based on the analysis of a subsample of PMTs presented in the next chapter.
Since a (quick) data analysis is mandatory also during and shortly after the actual container run [39], analysis scripts for the onsite operation were set up, too (see e.g. [254, 275, 328] for some details), and are in use as part of the daily routine. The results of these "competitive" analyses for the chosen PMTs were added to Table 7.2 as "reference analysis", to simply compare the outcome of both. Although the used definitions of parameters presented in this chapter are the same as in the onsite analysis scripts, the used methods might be different as both works are independent. This may lead to slightly different results. However, as it can be seen in Table 7.2, most of the determined results are fully consistent within their uncertainties. Since the exact algorithms of the "reference analysis" scripts are unknown and of only minor interest here, remaining differences in particular PMT results will not be discussed further.

[37] The full list of reference PMTs is shown later in section 8.2.

[38] In the "reference analysis", the S/N ratio is defined as the inverse of the definition in Equation 7.25, see also [254]. For better comparison, the results have been inverted in this table to match to the here used definition.

[39] This is necessary for the analysis of the gain measurement during the container run, see subsection 5.2.3, and for the onsite organization to be able to directly distinguish between good, bad and edgy PMTs after the tests, see subsection 4.2.2 again.

Table 7.2.: Results of full characterization of reference PMTs **EA1437** (subtable **(a)**) and **PA1704-108** (subtable **(b)**), measured with container B as part of **mass 84**. Column "Ref. Analysis" shows the output of the independent onsite data analysis, "Evaluation" classifies the PMT performance in the analysis of this work with respect to the requirements shown in Table 3.1. Given uncertainties for RT, FT, amplitude and FWHM describe $1\,\sigma$ width of parameter distributions, see Figure D.14. Values in brackets show the results determined using the fit of the average SPE pulse (see subsection 7.2.4 again) for comparison.

(a) results of PMT EA1437, measured at channel 234

Parameter	This work	Ref. Analysis	Evaluation
Applied voltage	1612 V	1619 V	**OK**
Gain @ applied voltage	1.026×10^7	1.025×10^7	**OK**
PDE	26.83 %	26.95 %	**OK**
DCR	18.8 ± 0.6 kHz	18.8 kHz	**OK**
RT of (av.) SPE pulse	6.9 ± 1.0 ns (7.3 ns)	7.7 ns	**OK**
FT of (av.) SPE pulse	10.7 ± 1.6 ns (10.6 ns)	11.6 ns	**OK**
FWHM of (av.) SPE pulse	12.2 ± 0.8 ns (12.5 ns)	11.4 ns	**OK**
Amp. of (av.) SPE pulse	5.97 ± 1.53 mV (5.58 mV)	6.26 mV	**OK**
TTS (σ)	1.3 ± 0.1 ns	3.0 ns	**OK**
Peak-to-valley ratio	4.04	3.16	**OK**
Resolution	0.267 ± 0.042	0.266	**OK**
Signal-to-noise ratio [38]	14.29 ± 0.20	13.89	**OK**
Prepulse ratio	0.16 ± 0.14 %	0.29 %	**OK**

(b) results of PMT PA1704-108, measured at channel 201

Parameter	This work	Ref. Analysis	Evaluation
Applied voltage	1758 V	1762 V	**OK**
Gain @ applied voltage	1.007×10^7	1.029×10^7	**OK**
PDE	25.69 %	26.33 %	**OK**
DCR	23.6 ± 0.9 kHz	23.6 kHz	**OK**
RT of (av.) SPE pulse	3.7 ± 0.5 ns (4.5 ns)	4.1 ns	**OK**
FT of (av.) SPE pulse	10.8 ± 1.5 ns (11.0 ns)	16.0 ns	**OK**
FWHM of (av.) SPE pulse	9.7 ± 1.0 ns (10.8 ns)	7.4 ns	**OK**
Amp. of (av.) SPE pulse	6.57 ± 1.59 mV (5.76 mV)	7.92 mV	**OK**
TTS (σ)	5.4 ± 0.3 ns	5.6 ns	**OK**
Peak-to-valley ratio	3.80	6.44	**OK**
Resolution	0.285 ± 0.067	0.287	**OK**
Signal-to-noise ratio	13.16 ± 0.17	13.89	**OK**
Prepulse ratio	2.52 ± 0.40 %	0.67 %	**OK**

Chapter 8

PMT Sample Data Analysis

This chapter finally presents the data analysis result of a larger subsample of the JUNO PMTs. Up to date [1], more than 17'000 20-inch PMTs have been delivered from the manufacturers to the PMT testing site in Zhongshan, China, and more than 950 container loads have been run in total by two container systems.
From this huge data sample, a subsample has been selected to be analyzed and presented here. The purpose of this analysis is both to show the performance of the data analysis methods presented in chapter 7, but also to prove the capability of the container systems to test a large number of PMTs in a reliable and comparable way and thus to work as a "mass testing facility" for JUNO PMTs.

In section 8.1, the results from the analysis of this PMT subsample are presented, featuring a description of the chosen sample, a definition for the PMT classification and final results from the full analysis chain. Further, the results will be compared to official results from the PMT mass testing presented at international conferences.
In a second step, the stability and accuracy of the running system is investigated by surveying the measured performance of the reference PMTs. These reference PMTs are a major tool to monitor the performance of the testing system over the full time of operation. This is done in section 8.2 for also a larger data sample and for both containers, with focus on the stability over time, the comparability between different channels, the stability of the light sources over the measurement process and also the stability of the single PMTs within multiple measurements. From the latter, also conclusions about the accuracy of the containers system for different parameters can be extracted.
Aside from the stability of a single container system, also the reproducibility of the results between the two system can be checked. This is presented in section 8.3 on the results of another PMT subsample tested in both containers as cross-check between the systems.
In a last step, systematic uncertainties of the two container systems, which have been indicated in the prior analyses in this chapter, will be additionally checked and better quantified; this is shown in section 8.4.

[1] Status of March 2020.

8.1. Full PMT Characterization from Data Sample

In order to prove that the container systems are able to test a large number of PMTs, a comprehensive data sample has been analyzed using the presented methods from chapter 7. The results of this analysis shall be presented in this section. The selected subsample covers more than 1400 PMTs (including more than 600 Hamamatsu PMTs) and thus around 7 % of the full PMT sample and around 12 % of the full Hamamatsu PMT sample.
The analysis of this sample can be used as strong example for the capability of the container systems and to exemplarily illustrate how the average PMT performance (of this respective subsample) looks like. Besides the individual PMT results, also the distributions of the individual parameters are of interest for JUNO, as they can work as input for distinct and precise detector simulations as well as for improving the JUNO detector calibration later.

8.1.1. Data Sample Selection

The following subsample of **60 masses** has been chosen for a full data analysis:

Container A:

- mass 270 – mass 280 (11 masses, taken in September 2018)
- mass 300 – mass 315 (16 masses, taken in October / November 2018)

Container B:

- mass 84 (taken in November 2018)
- mass 86 – mass 100 (15 masses, taken in November / December 2018)
- mass 115 – mass 125 (11 masses, taken in January 2019)
- mass 215 – mass 220 (6 masses, taken in June / July 2019)

The total number of analyzed Hamamatsu PMTs in the subsample is **626**, the total number of analyzed NNVT PMTs is **817** (both without counting the reference PMTs). If a PMT was tested twice or more in the containers within the selected masses, only the latest result has been taken into the statistics (the total number of analyzed PMTs is noted below in Table 8.1). However, the actual numbers of valid results for individual parameters can vary, due to bad data quality of some PMT data sets or if a certain parameter could not be determined [2]. The results from this sample are presented later in subsection 8.1.3.

It should be noted here, that although this to-be-analyzed subsample is large, the

[2]This can happen e.g. due to failing fits in the analysis steps, missing data or insufficient statistics from a certain measurement, but can also depend on the functionality (or performance) of the individual PMTs and/or the used PMT base.

distributions of individual parameters from this data sample do not necessarily represent the performance of the full PMT sample: every PMT performs unique, so an easy extrapolation from the to-be-shown results to the performance of all 20'000 PMT deployed in JUNO might not be suitable. Main reason for the missing possibility for a fair extrapolation is the lack of arbitrariness in choosing the subsample from the available full data set. This concerns both the selected masses as well as each single of the masses. The selected masses have been chosen without care for a representative choice and thus are not covering PMTs from many different delivery batches [3] or are recorded at different, equally distributed times over the full operation time, et cetera. Further, a single container mass does not consist of a representative sample either, as they aren't compounded by randomly chosen PMTs from the full set of 20'000, but mostly by PMTs from even the same delivery batch. These batches are usually (or ideally) tested "just in time" after their arrival and so also these PMTs are naturally tested together. The development in PDE of the NNVT PMTs acts here as good example for the not-representativeness of the PMT selection within a single mass [4]. Consequentially, the selected subsample of PMTs cannot be assumed representative and the parameter distributions and averages of the tested subsample may deviate from the ones of the full data set.
Anyhow, without loss of generality, the results of the selected PMT subsample are valid and describe the performance of the selected and analyzed PMTs in a proper way.

Moreover, general conclusions from the here presented results about the typical performance of a certain PMT type in particular, i.e. the NNVT PMTs, can not be deduced from and are not intended to be made in this thesis; the main focus in all following discussions will be laid solely on the assessment of the performance of the container systems [5].

8.1.2. PMT Classification Criteria

To better distinguish and benchmark the results, the analyzed and characterized PMTs will be sorted into one of four categories: ***passed***, ***passed (incomplete)***, ***double-check*** and ***failed***. The statistics for the PMT classification of the analyzed data subsample is shown Table 8.1.
For the classification of PMTs in this thesis a quite conservative approach was chosen,

[3] New PMTs usually have been delivered in batches of 330-360 PMT, which can be assumed to be produced subsequently (also PMT IDs are mostly in ascending order).

[4] In the beginning, MCP-PMTs came with a PDE slightly lower than compared to the dynode PMTs, which then changed with the introduction of the HighQE MCP-PMTs by NNVT in summer 2018 (see subsection 3.1.2 as a reminder). This has lead to a significant increase in the average PDE values of the NNVT delivery batches. In the process, early container masses show a significantly lower PDE for MCP-PMTs than late masses consisting of (almost) only HighQE MCP-PMTs.

[5] For this reasons, a '`PRELIMINARY`' note will be added to all PMT sample analysis plots in subsection 8.1.3 and subsection E.1 in the appendix.

Table 8.1.: Full PMT analysis statistics from chosen data subsample (without reference PMTs). Numbers in columns 'Hamamatsu' and 'NNVT' ('Cont. A' and 'Cont. B') add up to total PMT number. Numbers of classified PMTs are cleared from double-counts (in such cases, only the latest PMT results are taken into account). Numbers in brackets represent statistics without considering the TTS requirements. The low amount of passed (and high amount of failed) PMTs especially in container A is connected to a bad performance in TTS determination, see also subsection 8.1.3 for details.

	All	Hamamatsu	NNVT	Cont. A	Cont. B
Tested	1682	686	996	809	873
(w/o doubles)	1443	626	817	735	708
PASSED	229 (915)	158 (496)	71 (419)	20 (539)	209 (376)
Passed (incomplete)	103 (103)	61 (61)	42 (42)	0 (0)	103 (103)
DOUBLE-CHECK	607 (327)	121 (39)	486 (288)	274 (143)	333 (184)
FAILED	504 (98)	286 (30)	218 (68)	441 (53)	63 (45)

meaning that already small doubts on the reliability of data or the determined results from the analyses would lead to either recommend a double-check of the respective PMT or excluding these particular results from the statistics [6].
A PMT will be labeled as '*passed*', if its results are complete (nothing remained undetermined) and the PMT has fulfilled each of the listed acceptance criteria from Table 3.1. If at least one criteria couldn't be benchmarked for whatever reason (no valid/reliable output from analysis) but all other parameters are fine, it will be labeled as '*passed (incomplete)*'.
Labeling a PMT with '*double-check*' can have different reasons. First, for PDE, DCR and TTS, the acceptance criteria have been added by defined regions close to their edges, where a cross-check in another, additional test by container system or scanning station was recommended [7], see Table 8.2. Hence, a PMT will be labeled with '*double-check*', if its results for certain parameters are in such a defined region. For the PDE, this region is ±1 % (absolute value) around the minimal PDE acceptance criteria of 24 %, which considers the systematic uncertainty of the container systems in a PDE measurement (this will also be discussed in detail in subsection 8.2.6). For the DCR, this region is +50 kHz above the acceptance criteria, considering exterior effects like individual illumination with daylight during loading, outside temperature in the storage hall or electric noise from an insufficient base connection, which all can influence the results. Further, results below 5 kHz are assumed as unphysical for a 20-inch PMTs, so such results would also lead to a retest. For the TTS, different re-

[6] Classifications and thus requirements on data quality do not completely match with PMT classification in the on-site daily tests, where a less conservative counting is done. The here presented restrictions on data quality etc. are therefore more strict.

[7] Procedure of classification and values for these regions have been defined in elaborated discussions during the PMT testing phase within the JUNO PMT instrumentation group.

Table 8.2.: Parameter-related classification criteria, defining whether a PMT can be accepted or should be rejected (see also Table 3.1 again) or should better double-checked due to large uncertainties of (probably) unphysical results in either another container run or by the scanning station. (*) Since a fair TTS estimation might not be guaranteed for all channels due to systematic effects (see subsection 8.4.2 for details), this criteria can also be omitted. (**) Very large PPR results should also get double-checked to exclude a possible bias from (noise) artifacts in the data in this case.

Parameter	PMT type	**PASSED**	**DOUBLE-CHECK**	**FAILED**
PDE	both	$\geq 25\,\%$	$23\,\% \leq \text{PDE} < 25\,\%$	$< 23\,\%$
DCR	Hamamatsu	$\leq 50\,\text{kHz}$	$50\,\text{kHz} < \text{DCR} \leq 100\,\text{kHz}$	$> 100\,\text{kHz}$
	NNVT	$\leq 100\,\text{kHz}$	$100\,\text{kHz} < \text{DCR} \leq 150\,\text{kHz}$	$> 150\,\text{kHz}$
	both	–	$< 5\,\text{kHz}$	–
TTS*	Hamamatsu	$\leq 1.5\,\text{ns}$	$1.5\,\text{ns} < \text{TTS} \leq 2.0\,\text{ns}$	$> 2.0\,\text{ns}$
	NNVT	$\leq 6.5\,\text{ns}$	$6.5\,\text{ns} < \text{TTS} \leq 8.0\,\text{ns}$	$> 8.0\,\text{ns}$
HV	both	–	$> 300\,\text{V}$	–
Δ HV	both	–	$> 100\,\text{V}$	–
Δ DCR	both	–	$> 10\,\text{kHz}$	–
Δ FT / Δ RT	both	–	$\Delta > 10\,\text{ns}$ or $\Delta < 0.1\,\text{ns}$	–
PPR**	both	–	$> 10\,\%$	–

gions have been defined for Hamamatsu PMTs (+0.5 ns) and NNVT PMTs (+1.5 ns), considering the fact that the TTS analysis for MCP-PMTs is less reliable (due to the non-Gaussian transit time profile of some PMTs, see Figure 7.25b again). This transition region between acceptable and unacceptable performance was introduced to cover possible systematic influences between different container channels caused by e.g. the fiber splitters. As it can be seen later in subsection 8.1.3 and subsection 8.2.3, such systematic influences in fact play a role for the TTS measurement. In additional, PMTs will be labeled with '*double-check*', if they fail one of the soft criteria listed in Table 8.3 or if individual parameters show a large uncertainty value, suggesting an unphysical behavior or a bad or unsuitable fit. Although these soft criteria haven't been listed in Table 3.1, they are good indicators for proper conditions in all measurement steps and thus are used here as additional acceptance criteria as well; to cover the unphysical results, a few individual, parameter-related cross-check criteria have been defined and are added to Table 8.2, following the mentioned conservative approach in classifying the PMTs.
If a PMT is not able to meet the requirements in at least one of the determined parameters, and this PMT cannot be labeled as '*double-check*' following the criteria from Table 8.2 and Table 8.3, it will be labeled as '*failed*'.

As an alternative for the classification of PMTs based on their results, the PMTs can be also assessed preliminary without respecting the acceptance criteria for the

Table 8.3.: Soft criteria for PMT data quality checks. If a PMT cannot meet these criteria in the analysis, it was recommended to retest the PMT in the container system again. **GCC** defines "Gain Cross-Check", which means the value of the actually applied gain of a PMT determined from the LED measurement (should have been adjusted to 1×10^7 therefore still has to be in a narrow region around this value). **S/N** and **Resolution** are defined in Equation 7.25 and Equation 7.26.

Parameter	Acceptance value
GCC	$\in [0.95, 1.10] \cdot 10^7$
S/N	> 10
Resolution	< 0.40

TTS; this is already indicated in Table 8.1 by the numbers in the brackets. This exception is motivated by the observation, that in particular container A seems to suffer from a larger systematic effect in the TTS measurement; this will be discussed also in details in subsection 8.1.3. As a conclusion from this, the TTS criteria can be skipped in the classification, since a fair estimation of the true TTS performance occasionally cannot be estimated solely by the raw data analysis.

While most PMTs show a bad or edgy result in only one parameter, few PMTs fail in several parameters, like illustrated in Figure 8.1. A large contribution to the bad or edgy results is originating from the TTS measurement; therefore, as discussed above, the TTS data can be preliminary excluded from the PMT classification. Further, determining a TTS result fails completely in many cases, as illustrated in Figure 8.2. This is caused by e.g. the threshold on the transit time statistics to become fitted or if the Gaussian fit couldn't converge to a clearly non-Gaussian transit time distribution for some NNVT PMTs (see discussion in subsection 7.4.2 again).

8.1.3. Data Analysis Results

The data of all PMTs from the selected subsample have been analyzed using the introduced methods. The analysis results lead to a certain classification of every single PMT as explained above. An overview on the result statistics was already given in Table 8.1, displaying also the total PMT statistics of the analyzed sample, apportioned by container and PMT type.
Individual data analysis statistics for each PMT parameter can be found in Table 8.4, again apportioned by PMT type, and also indicating the number of PMTs which have passed all individual criteria ("OK"), and which are labeled with '*double-check*' due to results being close to the edges of the acceptance criteria ("edgy") or due to like unphysical results ("err."); the latter are both following the criteria of Table 8.2. Since there might be some analysis steps in which no valid result of a certain parameter could be determined for a single PMT, the individual numbers of results for the different PMT parameters can vary.

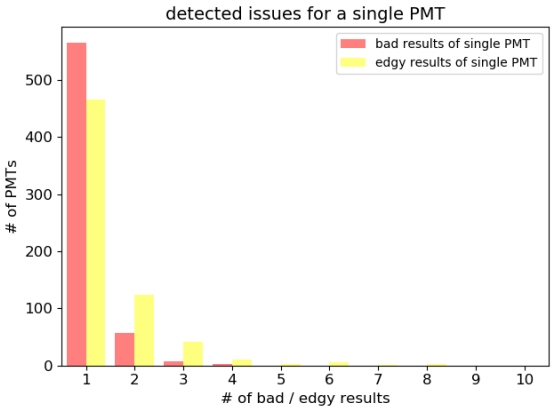

(a) cases of failed criteria and edgy parameters per PMT

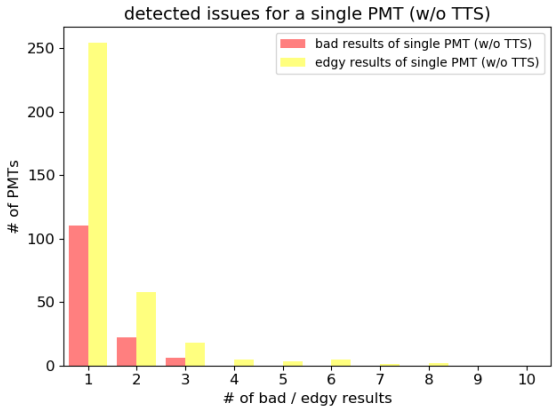

(b) cases of failed criteria and edgy parameters per PMT, w/o TTS

Figure 8.1.: Distribution of numbers of bad and edgy results of individual parameters per PMT, including (panel **(a)**) and excluding (panel **(b)**) the TTS results in the statistics. Most PMTs show bad performance for only one parameter. Maximal number of parameters leading to a '*failed*' classification for one PMT in the selected data sample is four, maximal number or edgy results leading to a '*double-check*' classification for one PMT is eight.

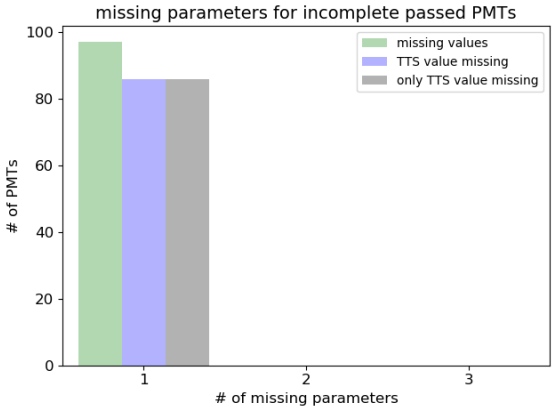

(a) statistics of missing parameters per analyzed PMT of PMTs with '*passed (incomplete)*' classification

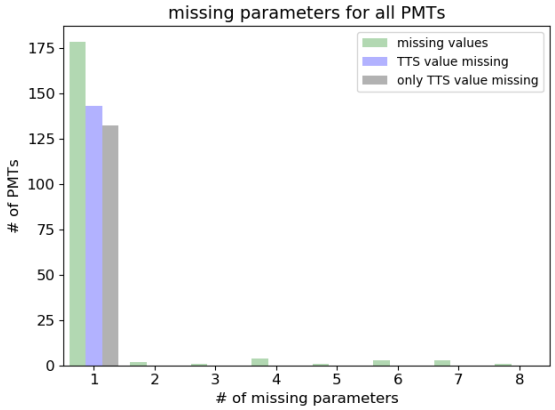

(b) statistics of missing parameters per analyzed PMT of all PMTs

Figure 8.2.: Distribution of numbers of missing results of individual parameters per PMT. In the analyzed sample, not more than one parameter is missing for PMTs with a '*passed (incomplete)*' classification, and in almost all cases, the TTS result is the missing parameter (see panel **(a)**). If looking on the full sample (all classifications), maximum number of missing parameters per PMT is eight (see panel **(b)**). Parameters from the av. SPE pulse fit analysis are not included in the here presented statistic.

Table 8.4.: Detailed PMT analysis statistics from analyzed PMT subsample. Number of valid values must not necessarily match with number of tested PMTs in Table 8.1, because not all tested PMTs provide valid results in all parameters. Indicated 'err.' values show results with e.g. unphysically large or small errors, as described in Table 8.2. Values in upper section of the table represent parameters with dedicated acceptance criteria as defined in Table 3.1. Values in second section define soft acceptance criteria as defined in Table 8.3 (failing here leads to a retest). Values in third section do not have any defined acceptance criteria, so indicated 'err.' cases don't lead to a retest here. Values in last section are determined from average SPE pulses (see subsection 7.2.4 for details). If no acceptance criteria is defined for a certain parameter (or PMT type), number of valid and 'OK' results are identical.

Parameter	Total			Hamamatsu			NNVT		
	valid	OK	edgy/err.	valid	OK	edgy/err.	valid	OK	edgy/err.
PDE	1439	1267	127 / –	626	602	19 / –	813	665	108 / –
DCR	1439	1302	65 / 48	624	604	10 / 9	815	698	55 / 39
HV	1437	1430	– / 4	626	621	– / 2	811	809	– / 2
P/V ratio	1438	1375	– / –	626	616	– / –	812	759	– / –
RT	1433	1432	– / 1	626	626	– / 0	807	806	– / 1
FT	1433	1343	– / 90	626	626	– / 0	807	717	– / 90
TTS	1316	321	451 / –	580	188	99 / –	736	133	352 / –
PPR	1423	1390	– / 6	610	583	– / 0	813	807	– / 6
GCC	1443	1373	70 / –	626	617	9 / –	817	756	61 / –
S/N	1443	1426	17 / –	626	622	4 / –	817	804	13 / –
Resolution	1443	1404	39 / –	626	622	4 / –	817	782	35 / –
Amplitude	1434	1434	– / –	626	626	– / –	808	808	– / –
FWHM	1412	1407	– / 5	604	604	– / –	808	803	– / 5
LPR	1437	1426	– / 11	625	624	– / 1	812	802	– / 10
av. SPE RT	1427	1427	– / –	612	612	– / –	815	815	– / –
av. SPE FT	1427	1427	– / –	612	612	– / –	815	815	– / –
av. SPE Amp.	1427	1427	– / –	612	612	– / –	815	815	– / –
av. SPE FWHM	1427	1427	– / –	612	612	– / –	815	815	– / –

Table 8.5.: Average results of selected data sample for individual parameters, separated by container and PMT type. Only valid values fulfilling the acceptance criteria (where existing) are considered here. Given uncertainties are $1\,\sigma$ (std. deviation) of all considered values.

Parameter	unit	PMT type	All	Container A	Container B
S/N ratio	–	Hamamatsu	13.62 ± 0.58	13.55 ± 0.64	13.69 ± 0.50
		NNVT	14.03 ± 0.74	14.12 ± 0.74	13.91 ± 0.71
Resolution	–	Hamamatsu	0.274 ± 0.017	0.273 ± 0.016	0.275 ± 0.017
		NNVT	0.326 ± 0.037	0.328 ± 0.032	0.324 ± 0.043
DCR	kHz	Hamamatsu	13.9 ± 5.0	13.4 ± 5.2	14.4 ± 4.7
		NNVT	47.4 ± 21.4	48.6 ± 22.2	46.0 ± 20.2
HV	V	Hamamatsu	1866 ± 96	1869 ± 106	1863 ± 86
		NNVT	1762 ± 55	1762 ± 49	1762 ± 61
Gain (GCC)	$\times 10^7$	Hamamatsu	0.996 ± 0.016	0.996 ± 0.014	0.995 ± 0.018
		NNVT	1.032 ± 0.032	1.037 ± 0.029	1.026 ± 0.034
PDE	%	Hamamatsu	27.80 ± 1.52	28.12 ± 1.67	27.49 ± 1.28
		NNVT	28.92 ± 2.24	29.12 ± 2.43	28.69 ± 1.98
P/V ratio	–	Hamamatsu	3.66 ± 0.52	3.85 ± 0.48	3.48 ± 0.49
		NNVT	3.88 ± 1.83	3.84 ± 0.78	3.93 ± 2.58
TTS (σ)	ns	Hamamatsu	1.3 ± 0.1	1.3 ± 0.1	1.3 ± 0.1
		NNVT	5.6 ± 1.1	5.9 ± 0.6	5.6 ± 1.1
RT	ns	Hamamatsu	6.7 ± 0.4	6.7 ± 0.4	6.8 ± 0.5
		NNVT	3.6 ± 0.2	3.6 ± 0.2	3.6 ± 0.2
av. SPE RT	ns	Hamamatsu	7.2 ± 0.3	7.2 ± 0.3	7.2 ± 0.4
		NNVT	4.4 ± 2.4	4.3 ± 0.3	4.6 ± 3.4
FT	ns	Hamamatsu	10.2 ± 0.5	10.2 ± 0.4	10.1 ± 0.6
		NNVT	12.7 ± 1.9	12.7 ± 2.0	12.7 ± 1.7
av. SPE FT	ns	Hamamatsu	9.9 ± 0.4	9.9 ± 0.3	9.9 ± 0.5
		NNVT	12.8 ± 3.0	12.8 ± 2.3	12.8 ± 3.6
Amplitude	mV	Hamamatsu	6.24 ± 0.18	6.21 ± 0.18	6.26 ± 0.20
		NNVT	6.10 ± 0.54	6.14 ± 0.56	6.05 ± 0.51
Av. SPE amplitude	mV	Hamamatsu	5.82 ± 0.13	5.80 ± 0.12	5.84 ± 0.14
		NNVT	5.45 ± 0.40	5.51 ± 0.36	5.38 ± 0.44
FWHM	ns	Hamamatsu	11.8 ± 0.3	11.8 ± 0.3	11.8 ± 0.3
		NNVT	10.7 ± 1.3	10.7 ± 1.4	10.7 ± 1.3
Av. SPE FWHM	ns	Hamamatsu	12.0 ± 0.3	11.8 ± 0.3	11.8 ± 0.3
		NNVT	12.0 ± 3.3	11.9 ± 1.5	12.2 ± 4.6
PPR	%	Hamamatsu	0.37 ± 0.25	0.43 ± 0.30	0.30 ± 0.18
		NNVT	2.47 ± 0.85	2.61 ± 0.68	2.32 ± 0.99
LPR	%	Hamamatsu	0.81 ± 0.59	0.83 ± 0.78	0.79 ± 0.30
		NNVT	4.63 ± 2.71	4.49 ± 1.54	4.78 ± 3.58

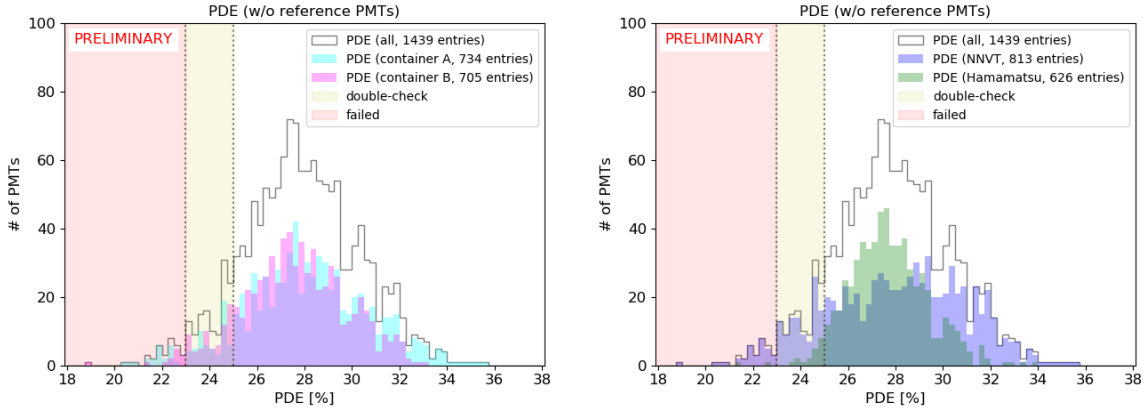

(a) PDE results (total and separated by container)

(b) PDE results (total and separated by PMT type)

Figure 8.3.: Analysis results for PDE from selected data sample (reference PMTs excluded). In total, 1439 valid results are contributing to the statistics. Results are depicted separated by container (panel **(a)**) and as individual distributions for Hamamatsu and NNVT (panel **(b)**). Values between 23 and 25 % lead to a retest of these PMTs, values below 23 % to a rejection.

The average results for the individual parameters are collected together in Table 8.5, again separated for both PMT types and containers. For the given numbers, only the results passing the individual requirements for the different parameters (or valid data if no criteria are defined) have been taken into account; given uncertainties are the standard deviations of the so consisting sample. The results for each parameters of the regular analysis from the chosen data sample have also been collected in plots. The result plots for PDE (Figure 8.3), DCR (Figure 8.4), P/V ratio (Figure 8.5), GCC (Figure 8.6) and TTS (Figure 8.7) will be shown here, plots for all other parameters can be found in subsection E.1 in the appendix. It shall be noted again, that the presented results do not allow general conclusions about neither the average performance of a certain PMT type nor the average performance of the full PMT sample for JUNO. Nevertheless, the determined results for the individual PMTs are reasonable, proving that the container system is able to characterize a large number of PMTs in an adequate way.

Several observations can be made from the average results in Table 8.5 and the plotted distributions shown here and in the appendix:
First, both containers show consistent average results for all parameters within $1\,\sigma$ of the considered values. The plotted distributions of the individual PMT results from the analyzed sample also substantiate this observation, but with a few important exceptions: First, the distribution of DCR results shows a slightly shifted edge for PMTs with a low rate, see Figure 8.4e. This could hint for a small systematic difference between the two system, with container B tending towards increased rates. This effect

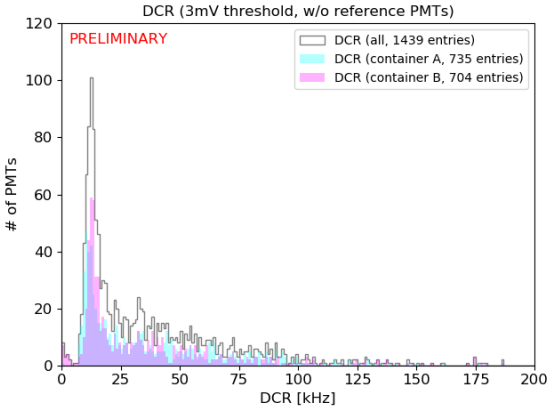

(a) DCR results (total and separated by container)

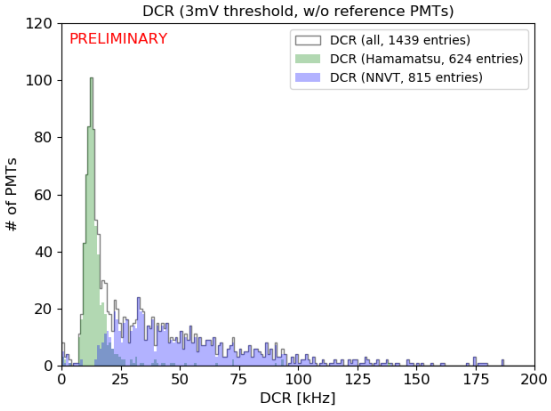

(b) DCR results (total and separated by PMT type)

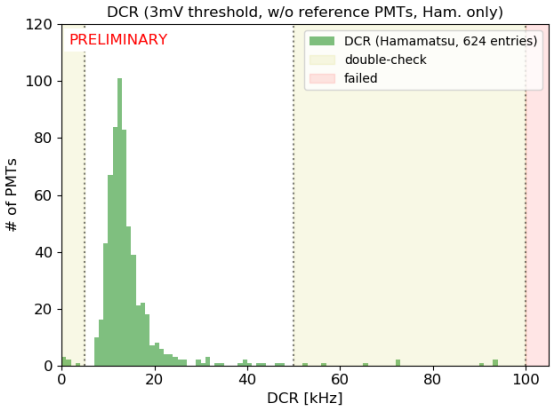

(c) DCR results of Hamamatsu PMTs

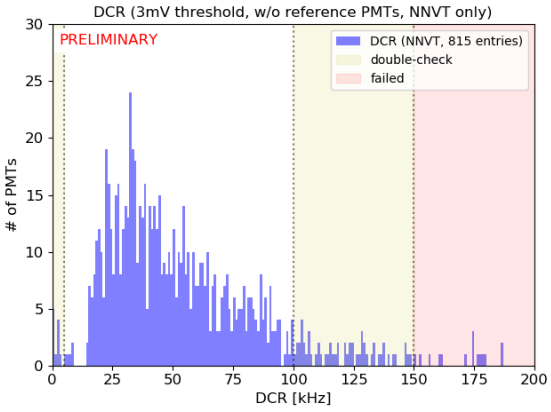

(d) DCR results of NNVT PMTs

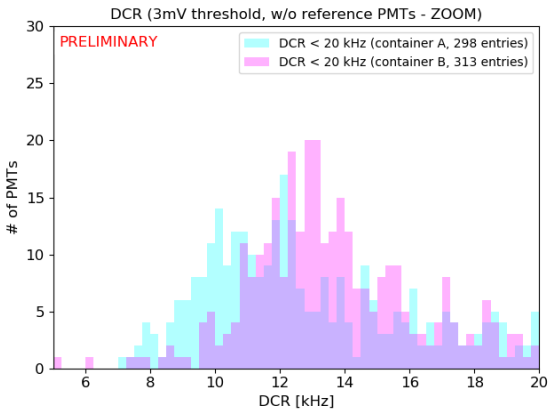

(e) DCR results below 20 kHz (separated by container)

Figure 8.4.: Analysis results for DCR from selected data sample (reference PMTs excluded). In total, 1439 valid results are contributing to the statistics. Results are depicted separated by container (panel **(a)**) and as individual distributions for Hamamatsu and NNVT (panel **(b)**). In panels **(c)** and **(d)**, results of respective PMT types are drawn with criteria for double-checks (>50 kHz for Hamamatsu and >100 kHz for NNVT) and rejection (>100 kHz for Hamamatsu and >150 kHz for NNVT). Panel **(e)** shows a zoom of panel **(b)** into the region below 20 kHz. The results hint for a small systematic difference between container A and B.

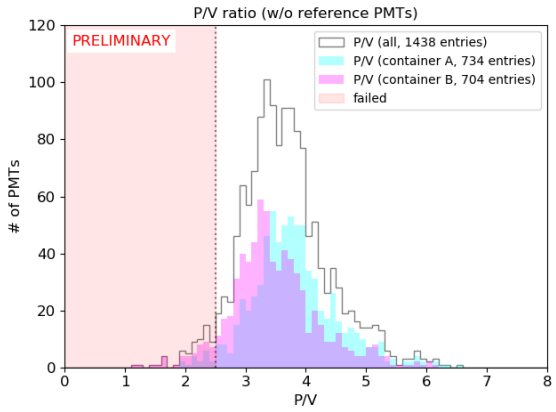

(a) P/V ratio results (total and separated by container)

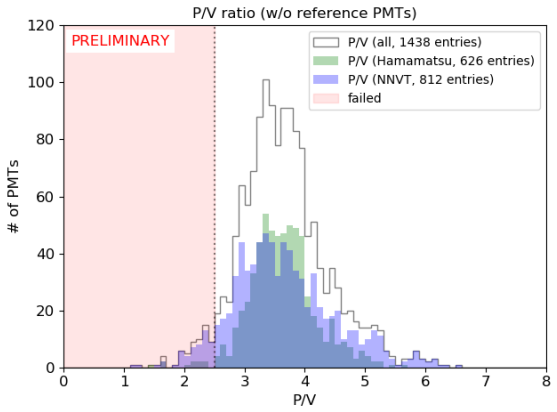

(b) P/V ratio results (total and separated by PMT type)

Figure 8.5.: Analysis results for P/V ratio from selected data sample (reference PMTs excluded). In total, 1438 valid results are contributing to the statistics. Individual distributions are displaying container system (panel **(a)**) or PMT type (panel **(b)**). Values below 2.5 lead to a rejection of these PMTs.

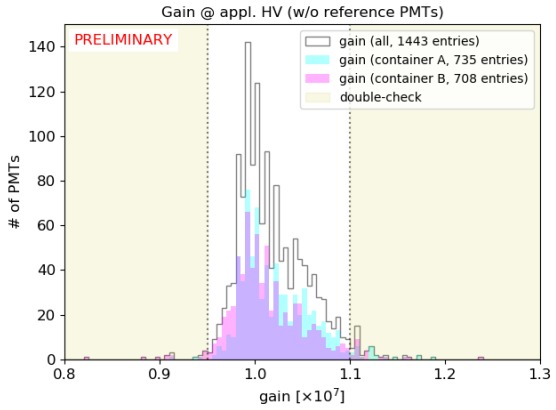

(a) GCC results (total and separated by container)

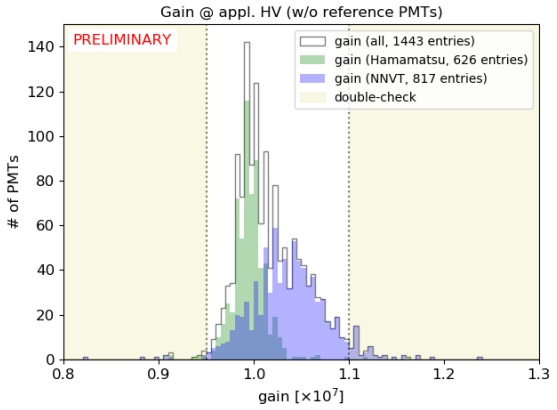

(b) GCC results (total and separated by PMT type)

Figure 8.6.: Analysis results for gain cross-check (GCC) during the LED measurement from selected data sample (reference PMTs excluded). In total, 1443 valid results are contributing to the statistics. Individual distributions are displaying container system (panel **(a)**) or PMT type (panel **(b)**). Values below 0.95×10^7 or above 1.1×10^7 lead to a retest of the PMT.

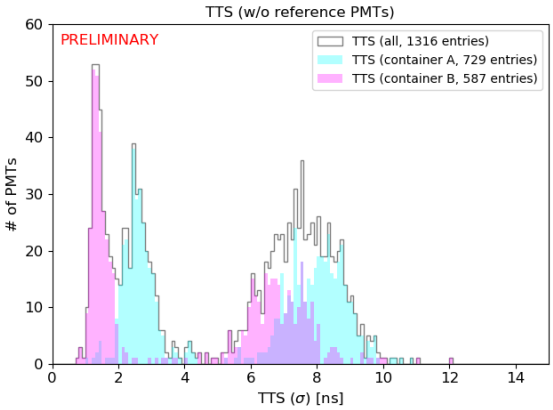

(a) TTS results (total and separated by container)

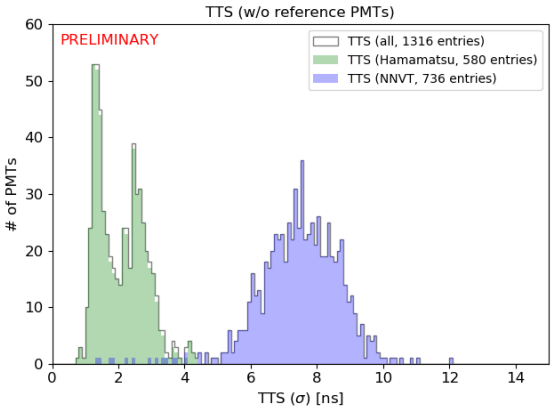

(b) TTS results (total and separated by PMT type)

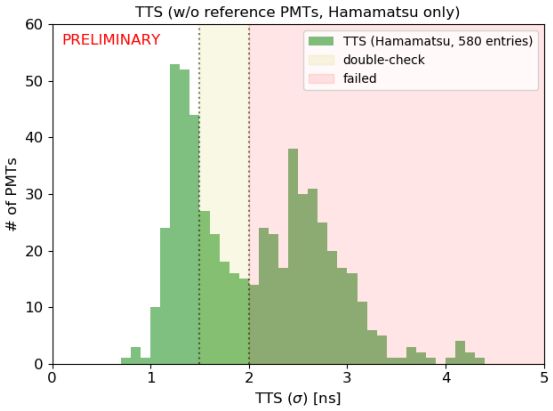

(c) TTS results of Hamamatsu PMTs

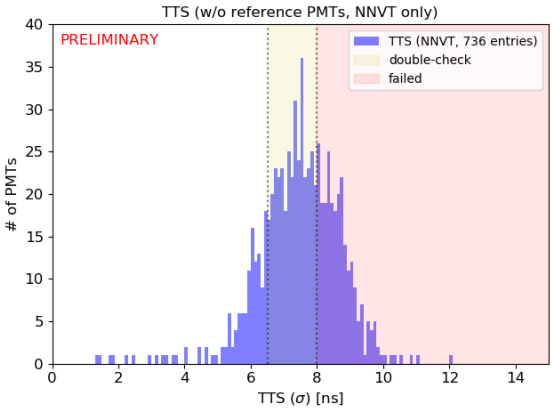

(d) TTS results of NNVT PMTs

Figure 8.7.: Analysis results for TTS (σ) from selected data sample (reference PMTs excluded). In total, 1316 valid results are contributing to the statistics. Individual distributions are displaying container system (panel **(a)**) or PMT type (panel **(b)**). In panels **(c)** and **(d)**, results of respective PMT types are drawn with criteria for double-check (σ>1.5 ns for Hamamatsu and σ>6.5 ns for NNVT) and rejection (σ>2.0 ns for Hamamatsu and σ>8.0 ns for NNVT). Looking specifically on panel **(a)**, it is clearly visible that a systematic effect between the two container systems exist, leading to larger results in container A, independent of the PMT type. Therefore, the TTS criteria can also be skipped preliminary in the PMT classification.

will be investigated also in detail in subsection 8.4.1. Second, the distribution of the P/V results is visibly shifted to lower values for results collected in container B, see Figure 8.5a (this shift is also visible in the average P/V results of container A and B in Table 8.5). This effect could be directly connected to the higher dark rates measured in container B – an additional noise source producing signal above the DCR threshold could spoil into the valley, thus reducing the P/V result while increasing the DCR. Such an additional noise source would also be invisible in the S/N ratio as it described only the baseline noise below the DCR threshold; in fact the S/N ratio shows stable and consistent results independent from PMT type or container, which is at least a good proof for a stable baseline noise level. The consistency of results between the two containers and possible systematic effects between them, i.e. for DCR and P/V ratio, are further investigated in section 8.3.
Last and most clear exception is the TTS distribution. Although the average results of the PMTs passing the acceptance criteria for TTS matches perfectly between container A and B, the distribution of values shows a clear shift for container A towards larger TTS values, see Figure 8.7a. In the light of the full sample of valid results, it appears that the average TTS result of container A consists of only very few good values. Looking on the performance of the specific PMT types in Figure 8.7b, even two separated peaks for each type can be identified and are connected to the system where these PMTs have been tested in. Based on these plots, a large systematic uncertainty for the TTS measurement in container A must be fairly assumed. Since this systematic effect has huge influence on the classification of PMTs (i.e. in assessing their TTS performance, see e.g. Figure 8.1b), the TTS acceptance criteria can be skipped preliminary; this has already been remarked in Table 8.1. A similar, however smaller systematic uncertainty in container B cannot be fully excluded; but since PMTs tested in container B have been measured for a TTS of even below 1 ns as well, see Figure 8.7a and Figure 8.7c (which impartially is a very good performance for such a large PMT), the situation of container B can be stated as clearly better. The observed systematic effects on the TTS between the containers will also be investigated and discussed further in subsection 8.4.2.

A second observation is the different distribution in the gain cross-check (GCC) values in Figure 8.6. While the distribution of both container systems is highly consistent here, the distribution for Hamamatsu PMTs is shaper and more centered around the expected value of 1×10^7, while the MCP-PMT results are broader and slightly above 1×10^7 in average. Since the HV should be adjusted for all PMTs to generate a gain of 1×10^7, this is not a performance issue of the PMTs but more an indication that the power law used for the gain-to-HV fit in the analysis (see Equation 7.28 again) might need some corrections for the MCP-PMTs. While the power law describes the behavior of the dynode PMTs very well, it only approximates the region around a gain of 1×10^7 for MCP-PMTs; this is also visible in the example in Figure D.11. An inadequate fitting function can lead to a not perfectly adjusted HV setting for the MCP-PMTs. A better approximation could be e.g. an exponential approach for the gain like $g \approx \exp(G(V) \cdot \alpha)$, with α a design inherent parameter (length-to-diameter

ratio of the micro-channels) and $G(V)$ a gain factor describing the secondary emission characteristics of the MCP [202, 339, 340]. However, it was decided to use only the power law function from Equation 7.28, since the gain factor of the NNVT MCPs could not finally determined yet and to enable a fair comparison with the official results in subsection 8.1.4 (in that case also only the power law function was used to calculate the operating voltage of the MCP-PMTs). A detailed survey of MCP-PMTs gain measurements and results indeed would be interesting and helpful to better determine the actual gain-to-voltage dependence and define an accurate operating voltage, but would go beyond the scope of this thesis.

Last interesting observation which shall be discussed here is the distribution of results for RT, FT, amplitude and FWHM from the individual pulse fittings compared to the fitting of an average SPE pulse. The fitting of the averaged SPE pulses leads to slightly higher rise times and smaller amplitudes (see Figure E.4 and Figure E.6); effects on the distribution of FWHM values and FT seem to be negligible. This observation can be explained by the different pulse shapes causing a smearing effect on the average pulse form due to the way the average pulse form has been calculated (see subsection 7.2.4 for details again). A fit of a distribution of individual rise / fall times (see e.g. Figure D.14 in the appendix) or pulse amplitudes can still fit around the maximum of the distribution by giving values on the edges (away from the maximum) less weight, while for an averaged pulse form, all considered values are weighted the same, thus leading to a broader and slightly smaller pulse form.

8.1.4. Comparison with Official Results

At NEUTRINO 2018 and TAUP 2019, a few "official" results from the PMT mass testing have been shown for several PMT parameters [275, 328] and are listed in Table 8.6. For better comparison, also the corresponding analysis results from this work are added. The data of the analyzed subsample in this thesis was taken completely in the time between these two conferences, so they are not included in the NEUTRINO 2018 results, but are fully included in the TAUP 2019 results.
Overall, both the here presented and official results are in good agreement. Although the statistics are different, the average result values match very well for HV, resolution, P/V, and in case of the Hamamatsu PMTs also for the pulse shape parameters (RT, FT, amplitude). Further, trends in the average values from NEUTRINO 2018 to TAUP 2019 are also consistent with the average values of this work, e.g. for PDE, DCR and P/V: the values presented at NEUTRINO 2018 show, that Hamamatsu PMTs tested in earlier masses than the here selected sample tend to larger PDE, higher P/V and higher DCR values, while for NNVT PMTs, the PDE was lower in the past [8]. Hence, small deviations between the official results to the here presented subsample can be explained as direct selective (statistical) effect from the different

[8] Delivery of the HighQE MCP-PMT started in summer 2018, so the here analyzed subsample consists of mostly HighQE MCPs, while in the full statistics "LowQE" MCP-PMTs are contributing.

Table 8.6.: Preliminary PMT testing results as presented at NEUTRINO 2018 and TAUP 2019 conferences [275, 328], separated by PMT type.

Parameter	unit	NEUTRINO 2018		TAUP 2019		this work	
		Ham.	NNVT	Ham.	NNVT	Ham.	NNVT
tested PMTs	–	~ 1900	~ 2300	~ 5000	~ 7500	~ 600	~ 800
PDE	%	28.5	27.5	28.1	28.3	27.8	28.9
DCR	kHz	19.1	42.5	15.3	48.3	13.9	47.4
HV	V	1859	1790	1863	1766	1866	1762
RT	ns	6.7	4.5	6.9	4.8	6.7	3.6
FT	ns	10.2	15.9	10.2	16.5	10.2	12.7
Amplitude	mV	6.5	7.7	6.4	7.5	6.2	6.1
Resolution	–	0.277	0.330	0.279	0.324	0.274	0.326
P/V	–	4.0	4.6	3.8	4.1	3.7	3.9

samples. Larger discrepancies between the official results and those of this work can be found only for the pulse shape parameters of NNVT PMTs (RT, FT, amplitude), but can be explained by the use of different methods for determining these parameters (e.g. with / without fit of pulse shape etc.).

8.2. Reference PMT Data Analysis

A small number of so-called reference PMTs are tested in every container run together with the untested PMTs. Up to five reference PMTs per container are used, with one reference PMT staying at the same box in most of the runs [9], while the others are shuffled around the other channels. The selected reference PMTs are proven to be of good performance, have a known PDE and further are investigated particularly by the scanning station to cross-check the PDE value provided by the manufacturers. The ten PMTs listed in Table 8.7 have been chosen as reference PMTs in the containers A and B.
The reference PMTs can be used to monitor the performance of the containers by comparing the individual parameter results over the time, meaning the numerous tested masses, or in different channels (boxes). They also deliver valuable information about the overall systematic uncertainties of the container system as a whole, for e.g. TTS or PDE determination, about systematic effects between different container channels (for example, if some channels systematically provide results which are significantly

[9] Box A1 (which corresponds to channel 101 or 201 in the containers) has been chosen here, because these drawer boxes are the most difficult ones to access, as box A1 is very close to the door and the magnetic shielding of the door frame. One reference PMT per container mostly stays in the respective box, except for few runs in which it is the turn of one of the other reference PMTs to get measured in this box in the next run.

Table 8.7.: List of reference PMTs in the containers A and B. PMT in first line (written in italic) is mostly at fixed position (occupying channel 101 or 201, respectively), while other PMTs are at circulating positions to cover all other container channels by time.

Container A	Container B
EA0339	*EA0586*
EA0419	EA0574
EA1578	EA1437
PA1704-731	PA1704-108
PA1705-117	PA1705-12

better or worse than in other channels) and about the overall reliability of the containers in the measurements over a long time. Further, the reference PMTs can be used as indicators for possible hardware-related issues, such as noisy or broken electronics channels, wear-and-tear effects in the cables or plugs (which may occur after a long period of daily use), or even degradations of the light sources or the reference PMTs itself [10]. For the reference PMT survey in this thesis, data for investigating the following parameter has been analyzed: **PDE**, **DCR**, **HV** for a 10^7 gain, SPE pulse characteristics as **RT**, **FT**, **amplitude** and **FWHM**, **S/N ratio** and **resolution**, as well as **P/V ratio**, **gain** (GCC values) and **TTS**.

8.2.1. Statistics of Reference PMT Data Analysis

From the collected reference PMT data, a sufficiently large (and so representative) sample of 200 masses from each container has been chosen, analyzed and investigated in detail, in order to show and prove the stability of the system and the reproducibility of PMT results over an operating time period of almost a year, and also to estimate the systems' accuracies in determining PDE, operating voltage and timing parameters. From container A, **masses 200 − 400** have been chosen, taken between June 2018 and March 2019, for container B, **masses 50 − 250** were selected, taken from September 2018 to August 2019. Unfortunately, due to some software bugs and also a misconfiguration of the light sources and post-trigger settings for the trigger recording, TTS data for container A is missing for longer periods. So, valid TTS data at container A could just be acquired for masses 255 to 315 within the selected subsample.

To illustrate how the channels of the containers are monitored by the reference PMTs, the statistics of valid results per channels are plotted in histograms, individually for every parameter. These plots thus show also the basic functioning of the individual channels. As an exemplary selection, the statistics of valid results per channels from

[10] Since most of the reference PMTs are in daily use, and further are illuminated by daylight during loading/unloading of the containers in the same time, it's not unlikely for the PMTs to suffer from accelerated aging effects (like e.g. a decreasing PDE or instable HV values for a 10^7 gain over time); nonetheless, these effects do not need to occur in either way.

the reference PMT analysis can be seen in Figure 8.8 and Figure 8.9 for PDE, HV and TTS. More plots covering all other parameters can be found in Figure E.9 and Figure E.10 in the appendix.

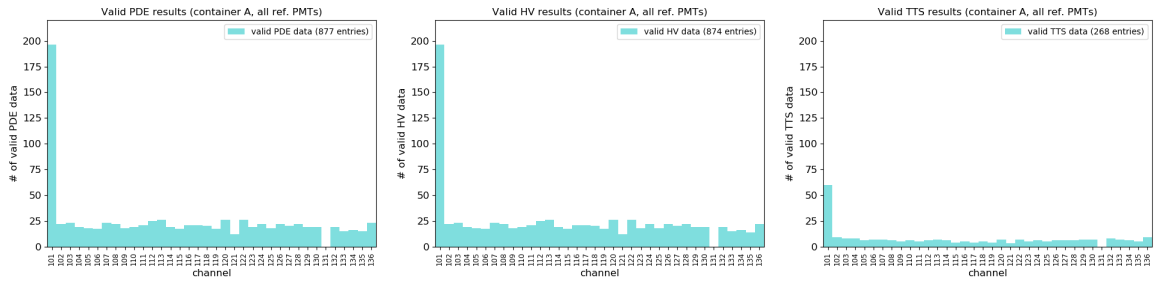

(a) PDE results of reference PMTs in container A

(b) HV results of reference PMTs in container A

(c) TTS results of reference PMTs in container A

Figure 8.8.: Statistics of valid results of analyzed reference PMTs in container A for PDE (panel **(a)**), applied HV (panel **(b)**) and TTS (panel **(c)**).

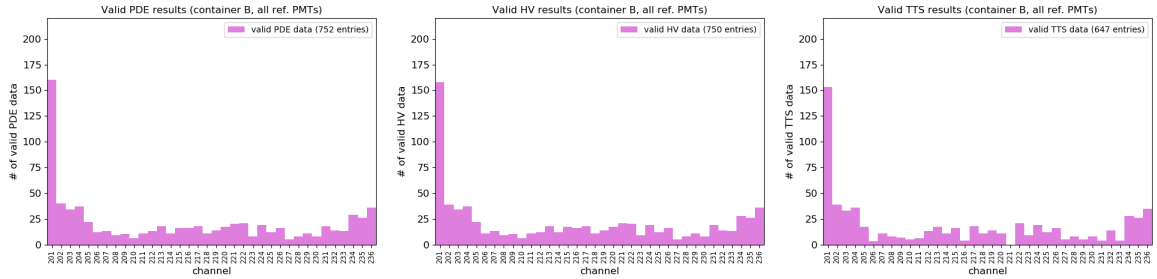

(a) PDE results of reference PMTs in container B

(b) HV results of reference PMTs in container B

(c) TTS results of reference PMTs in container B

Figure 8.9.: Statistics of valid results of analyzed reference PMTs in container B for PDE (panel **(a)**), applied HV (panel **(b)**) and TTS (panel **(c)**).

Aside from some statistical fluctuations between single channels, all channels of container A deliver roughly the same number of valid results for the chosen parameters, which proves that all channels perform equally. There are only two exceptions for container A: channel 101, which (usually) keeps the reference PMT with fixed position, leading to a large over-representation of this channel (all other channels are covered by the four other reference PMTs in a cyclic order). And second, channel 131, which has a broken HV power supply channel on the A7030TP board from almost the beginning, so no results are obtained from this channel at all.
For container B, the situation is slightly different. On one hand, during almost its full operational time, this container suffers from several broken channels (for different reasons and at different time periods). This has lead to both a lower number of PMTs in the daily tests at this container, as well as a more "unstable" pattern in the statistics plots for the reference PMTs. In additional, from comparison of the chosen plots,

it can also be seen that e.g. channel 221 didn't show any valid TTS results, which is here a hint for issues with the light provision in the measurement, meaning that most likely too few light can be delivered by the optical fiber for this channel. Such cases could also contribute to the higher fraction of PMTs with a '*passed (incomplete)*' classification in container B (see Table 8.1 again).

8.2.2. Stability Over Time: Reproducibility of Results

The main purpose of the reference PMTs is to monitor the system for stability over the full period of operation. To investigate this, the results of each parameter from the analyzed reference PMT data can be plotted over the time (or mass number respectively). As exemplary selection, the results for PDE, HV, S/N ratio, DCR, P/V ratio and gain cross-check (GCC) value of all reference PMTs individually are shown in Figure 8.10. Three of them are key parameters to estimate the stability over the time: the PDE as most important PMT parameter to measure, the applied HV as check whether the PMT is stable operated and the S/N ratio to estimate the cleanliness of the system in terms of noise level. More plots covering all the other parameters can be found in the appendix in Figure E.11.

It can be seen in the plots, that all reference PMTs in principle perform very stable for most parameters within the calculated uncertainties (error bars). So is e.g. the HV and S/N ratio very stable at a suitable level, see Figure 8.10c to Figure 8.10f, proving that noise is fully under control in both container systems; from these plots already, the design goal of the container systems for the S/N ratio defined in Table 4.1 can be stated as fulfilled. Only a few parameters show larger deviation in results, but most of them are easily explainable by external effects or the adequateness of the analysis methods:
First, the DCR results of the MCP-PMTs show an unstable behavior, see Figure 8.10g and Figure 8.10h. This suggests that these PMTs are much more sensitive to external effects like outside temperature changes or preceding illumination during the loading. The much more stable performance of the Hamamatsu PMTs however proves that the container system in principle provides a stable measurement environment [11].
As next example, the P/V ratio shows a larger spread in results, see Figure 8.10i and Figure 8.10j for both PMT types. This can be explained with the limitations in the analysis of the PMT charge spectra: since the valley is spread over only a few bin with low content, determining the exact position (and thus value of the valley) is complicated. Increasing the binning would help to find the exact position of the valley, but reinforces statistical effects between neighboring bins due to their typically low content. Enlarging the bin size worsens the accuracy, although statistical effects

[11] This also demands a discussion about whether the cool-down time of 12 hours is enough for the MCP-PMTs to stabilize their dark rate. Some preliminary surveys with much longer cool-down times (for one week or even more over e.g. the Chinese national holidays) have already indicated, that MCP-PMTs might stabilize their dark rate later than the Hamamatsu PMTs.

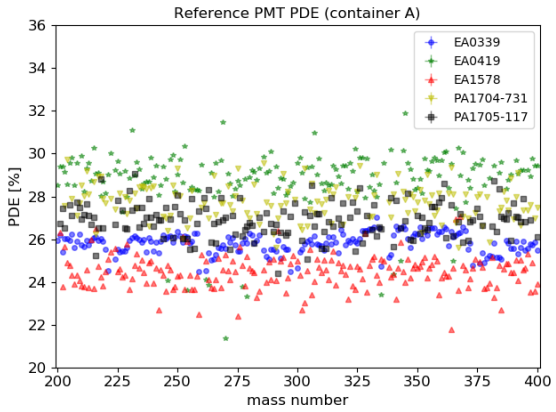

(a) PDE results of reference PMTs in container A

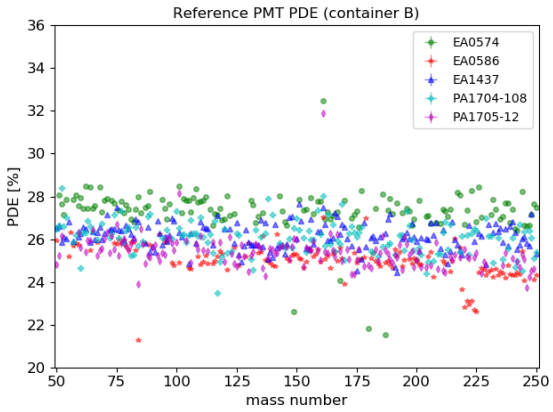

(b) PDE results of reference PMTs in container B

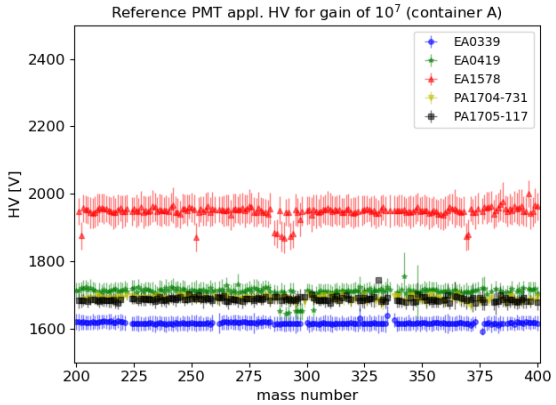

(c) calculated HV results of reference PMTs in container A

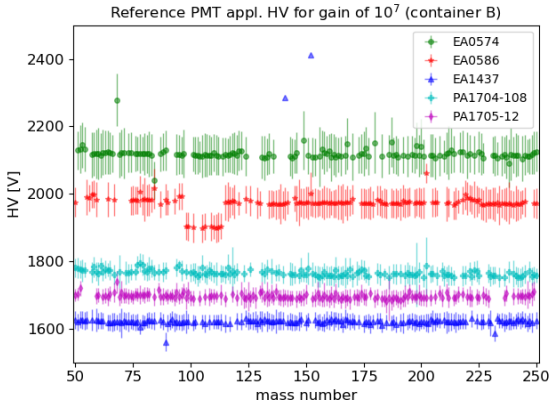

(d) calculated HV results of reference PMTs in container B

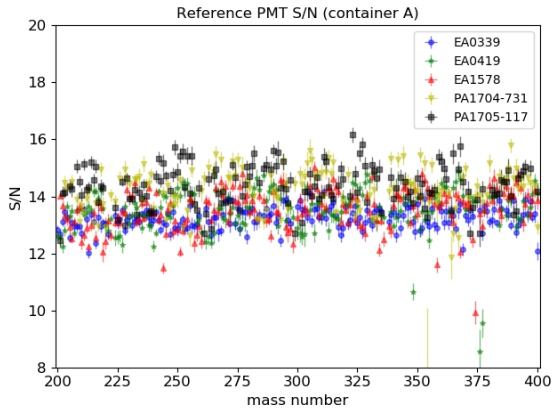

(e) S/N ratio results of reference PMTs in container A

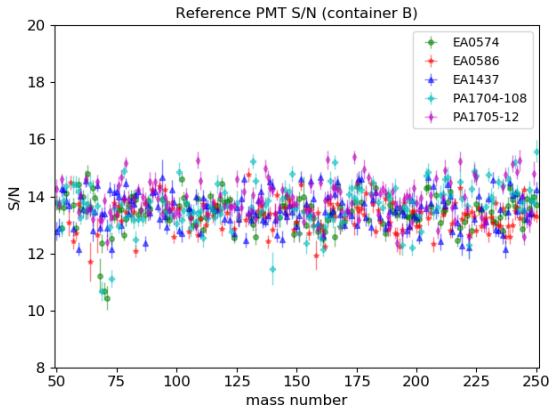

(f) S/N ratio results of reference PMTs in container B

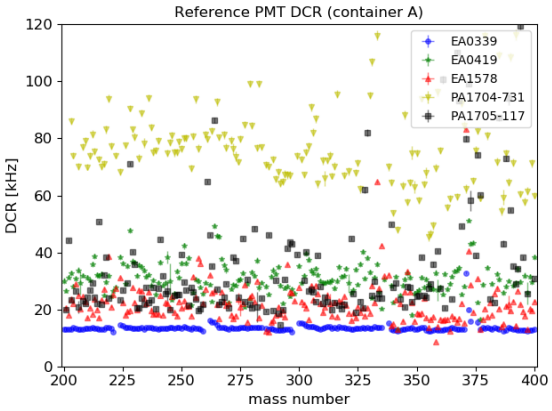

(g) DCR results of reference PMTs in container A

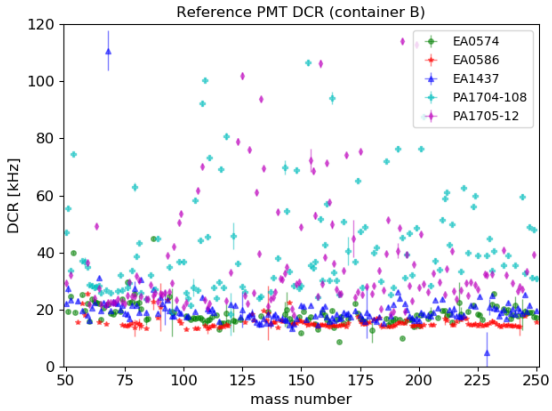

(h) DCR results of reference PMTs in container B

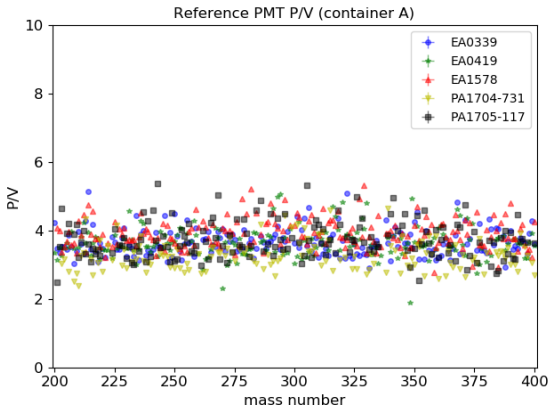

(i) P/V ratio results of reference PMTs in container A

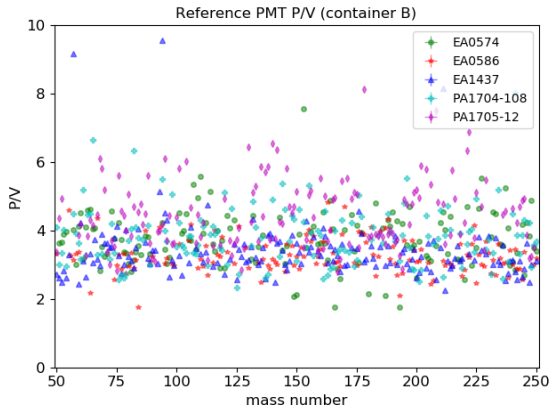

(j) P/V ratio results of reference PMTs in container B

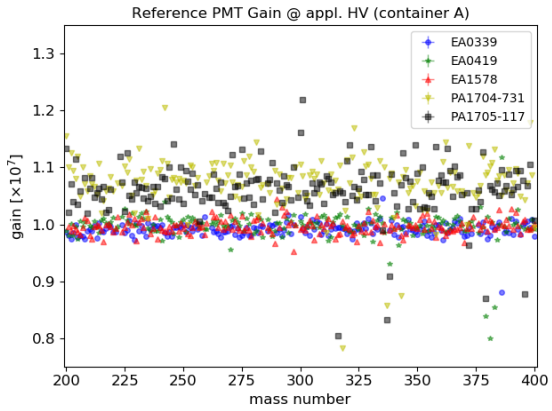

(k) GCC results of reference PMTs in container A

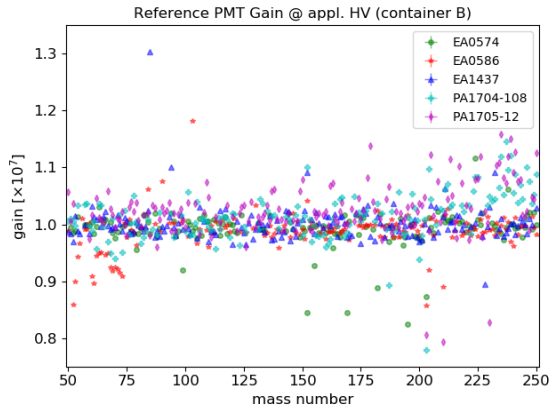

(l) GCC results of reference PMTs in container B

Figure 8.10.: Results of reference PMTs for selected parameters from container A and B, plotted over the mass number. For container A (container B), masses 200–400 (masses 50–250) have been investigated for this analysis.

between single bins become less significant. Best solution would be to noticeable increase the statistics of the whole number of entries in the spectrum (and thus meaning the amount of acquired data in the measurement), but this is limited by the measurement time as the daily schedule is fixed (see subsection 4.2.2 again) and would also increase costs for data storage. So, the actual data acquisition settings are already a compromise between all these aspects.
Another is the course of the cross-checked gain value (GCC) in the reference PMT measurements: while the Hamamatsu PMTs are grouped in a narrow band around a value of 1×10^7 (with few exceptions only, causing by obviously failed gain-to-HV fits), the MCP-PMTs tend to show GCC values between 1 and 1.15×10^7. This effect is very clear at container A, see Figure 8.10k, while at container B the spread is much smaller but rises after the mass 200, again tending to higher GCC values, see Figure 8.10l. This behavior can be partially explained again by the use of the power-law fitting of the gain-to-HV curves, as discussed in subsection 8.1.3 already. The evolution in container B to higher GCC values after around mass 200 could additionally hint for a small aging effect of the tube, since a similar behavior in the determined voltage cannot be observed (see Figure 8.10d). This directly reduces the statistics for these PMTs in the monitoring analysis sample, since a badly adjusted gain also questions the reliability of the results for all other parameters. However, in case that the gain differs only a little from the intended value of 1×10^7, effects on other parameters like PDE or pulse shape can be assumed as not significant.
At last, the TTS results of the reference MCP-PMTs are more unstable than the results of the dynode PMTs, see Figure E.11k and Figure E.11l. This is due to the observed substructures which are typical for these kind of PMTs and make it a lot more complicated to determine the actual TTS of the PMTs (see subsection 7.4.2 again). The stable results of the Hamamatsu PMTs however prove the stability of the systems and the reproducibility of TTS results with the containers (within their systematic uncertainties); this becomes more clear also in subsection 8.2.3.

While most of the parameters show a relative uniformly performance over the full selected reference PMT data sample, there is a slight decrease over time visible in the PDE results for container B, Figure 8.10b. To better investigate this effect, not only the performance of the PDE, but also of applied HV and S/N ratio has been checked for their stability over time for all reference PMTs combined. This is done in plots containing all individual data points from all five reference PMTs normalized by their individual average value from the sample and fitted with a linear slope:

$$f(t) = fit(y = at + b \mid y_{t,r} = p_{t,r} / \langle p \rangle_r \quad \text{for} \quad r \in \text{reference PMTs}) \ , \tag{8.1}$$

with $f(t)$ the fit, t the mass number, $y_{t,r}$ the normalized value of mass t and respective reference PMT r and $\langle p \rangle_r$ the average of values of the respective reference PMT from all selected masses. The produced monitor plots for PDE value, HV stability and S/N level are depicted in Figure 8.11. While both HV plots as well as the PDE of container A and the S/N stability of container B show a very stable behavior (no

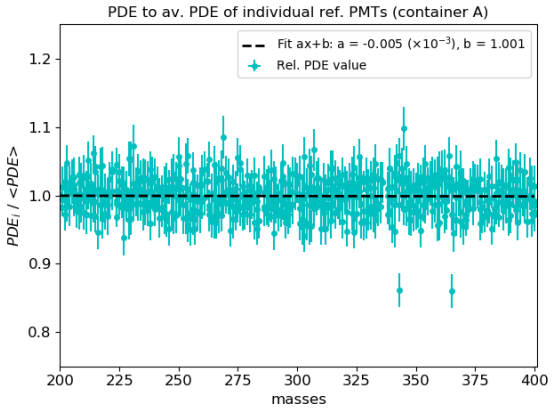

(a) PDE stability of reference PMTs in container A

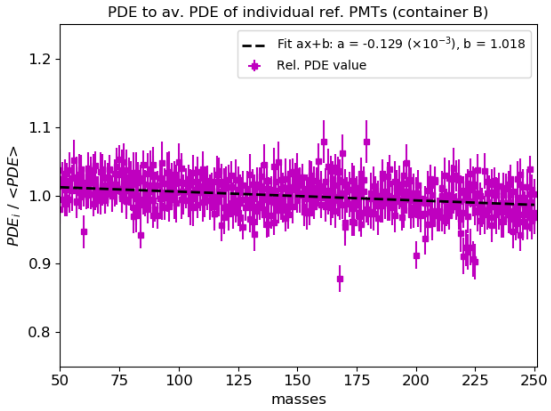

(b) PDE stability of reference PMTs in container B

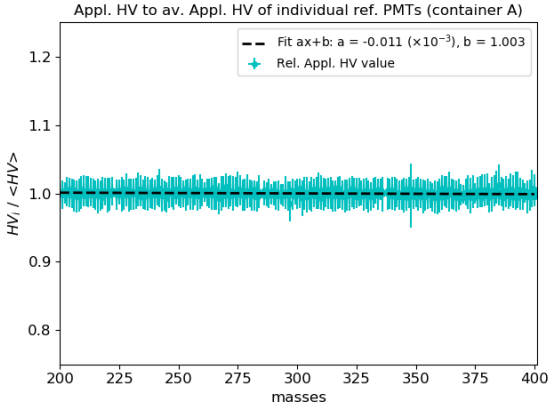

(c) stability of calculated HV of reference PMTs in container A

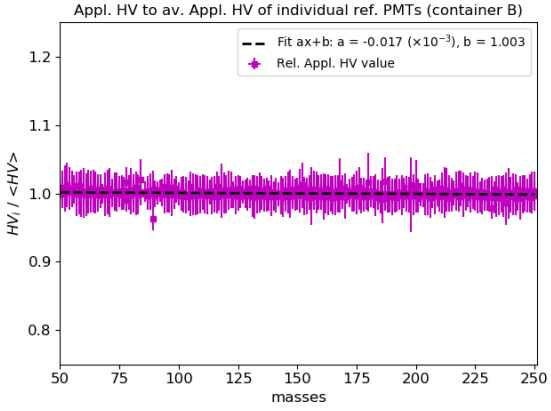

(d) stability of calculated HV of reference PMTs in container B

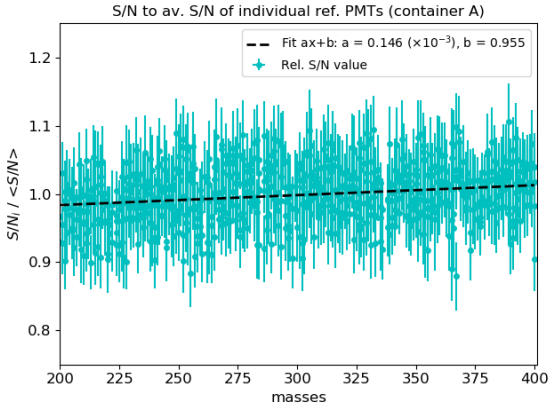

(e) S/N stability of reference PMTs in container A

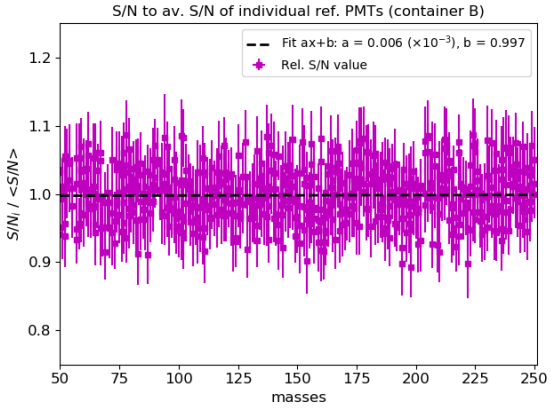

(f) S/N stability of reference PMTs in container B

Figure 8.11.: Stability monitoring plots using all five reference PMTs per container. Values of reference PMT for PDE, HV and S/N ratio from all selected masses are normalized to average value of data sample and respective reference PMT.

significant slopes could be observed), the PDE results in container B visibly decrease over time. Assuming the values from the slope fit and an average PDE value of 26 % for the reference PMTs in container B (see Figure 8.10b), the measured PDE performance worsens at container B by around 1 % absolute value over a time of roughly 300 masses. Further, the S/N ratio in container A increases over time, which could hint for a decaying noise source [12].
The observed behavior could arise from a decrease of QE of the reference tubes caused by aging of the PMTs [13], or from a slow degradation of the LEDs causing an instable light intensity over a long time of extensive usage. The first could be checked by a measurement in the scanning stations, which are frequently calibrated. The latter would imply the necessity of a second (or also frequent) re-calibration [14] of the container system, to make sure the determined PDE values are correct and stable over time. As some more detailed investigations have shown, this effect is likely connected to the LED performance, see subsection 8.2.4 for more details; however, an aging of the PMTs cannot be excluded either. Such an effect as visible in Figure 8.11b substantiate the monitoring power and the clear necessity of keeping the reference PMTs continuously within the container systems. Either way, negative influences on JUNO from a degradation of the light sources is not expected, because this only leads to a possible underestimation of PDE and so would end in a more restrict selection of PMTs for JUNO in terms of a suitable PDE performance.

8.2.3. Channel Stability: Reference PMT in Different Boxes

The stability of results between different channels is equally important than the stability over time, as it can prove the independence of measurements from certain locations in the containers and thus the equivalence of different measurement channels. As exemplary plots, PDE, S/N ratio and TTS results of all reference PMT individually have been chosen, see Figure 8.12. The TTS performance moreover shows here the ability of the fiber splitter to provide light to all channels. As already mentioned in subsection 8.2.1, channel 131 does not contain any values for any parameter, also channel 221 doesn't get any valid TTS values. Channel stability plots covering all the other parameters can be found in the appendix in Figure E.12.

[12] In container A, it was observed during the commissioning that the light shaping tubes constitute an additional (small) noise source, originating from the glue used to fix the Tyvek sheets to the inside of the light shaping tubes. This effect is correlated to the drying on the glue and thus was assumed to decay over time, which could be a possible explanation for the increasing S/N ratio in container A. To avoid a similar effect in container B, the Tyvek was fixed here with staples to the light shaping tubes, which could also explain the lack of a similar effect in this container.

[13] Since most of the reference PMTs are unloaded and loaded again daily, and so are frequently illuminated with daylight, an accelerated aging of these PMTs is (at least) likely.

[14] Also a concluding cross-calibration measurement at the very end of the measurement process could help to confirm the monitored behavior. In this case also a belated correction of the determined PDE values would be possible by extrapolating between both calibration values (assuming a linear degradation in the meantime).

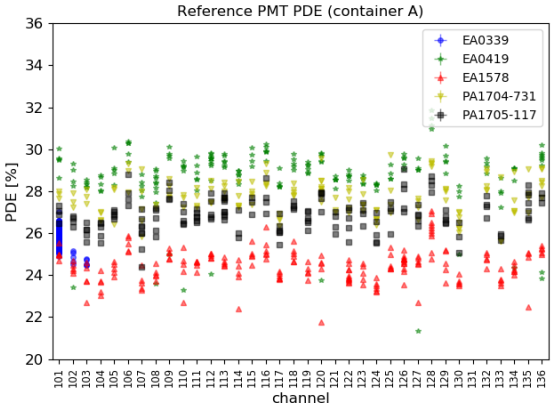

(a) PDE results of reference PMTs in container A

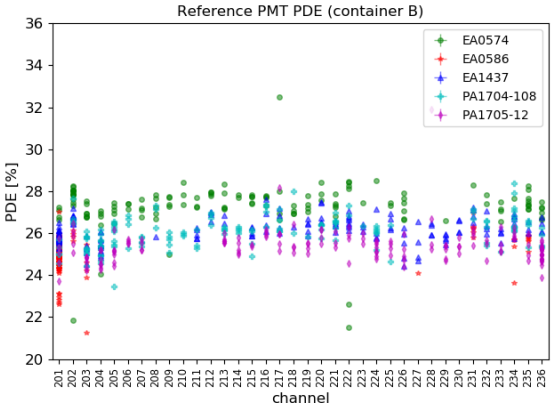

(b) PDE results of reference PMTs in container B

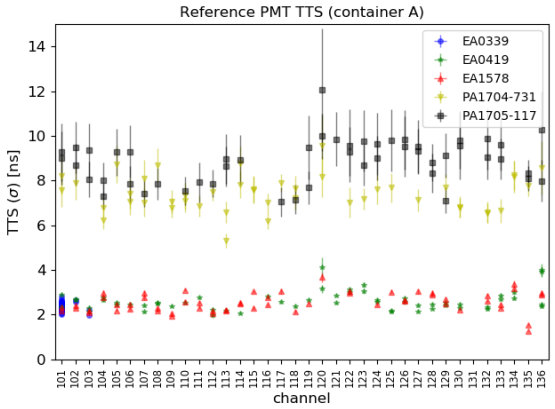

(c) TTS results of reference PMTs in container A

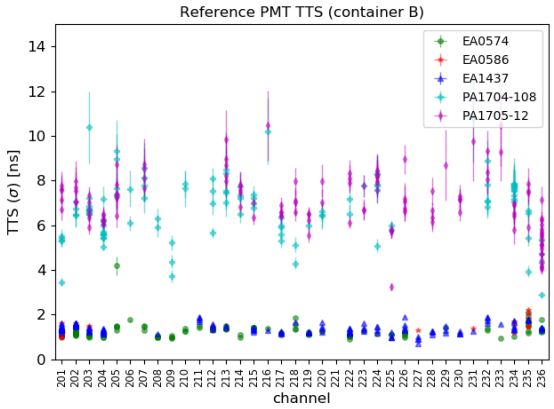

(d) TTS results of reference PMTs in container B

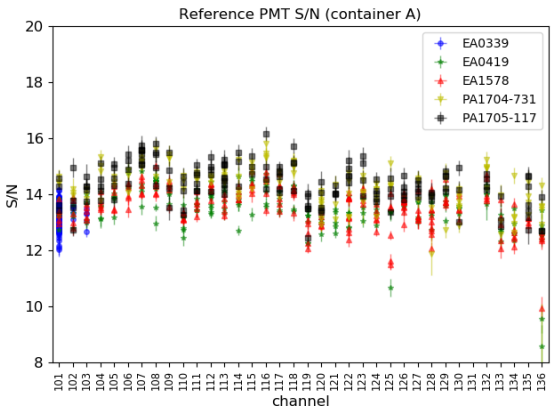

(e) S/N ratio results of reference PMTs in container A

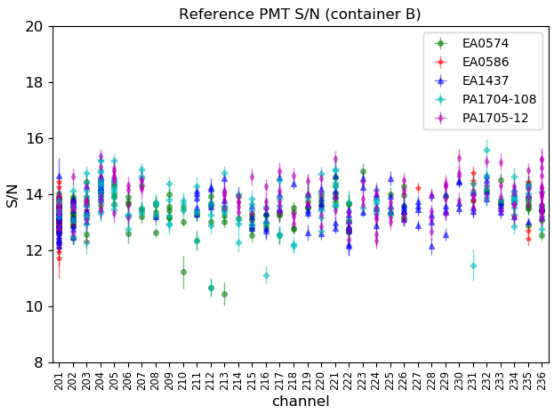

(f) S/N ratio results of reference PMTs in container B

Figure 8.12.: Results of reference PMTs from container A and B for PDE, TTS and S/N ratio, plotted over the channel numbers of container A and B (multiple measurement per channel are possible here).

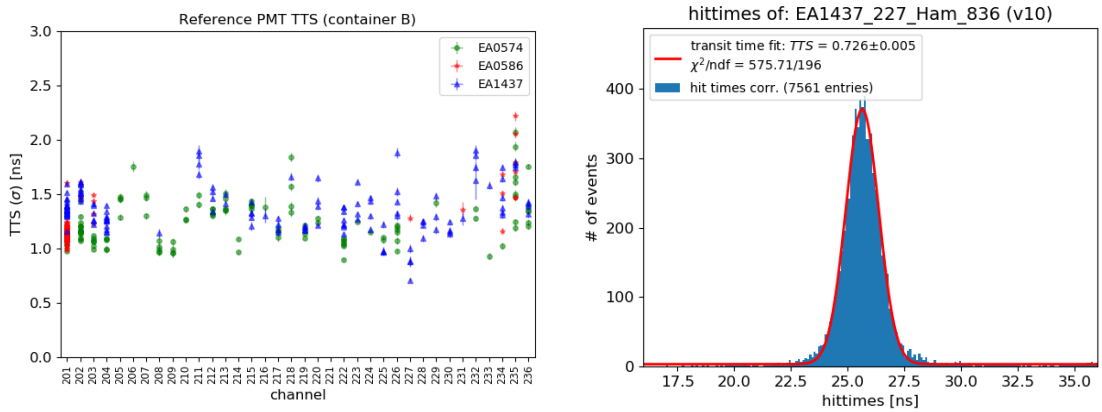

(a) TTS results of Hamamatsu reference PMTs in container B

(b) hit time distribution of PMT EA1437 at ch. 227 in mass 68

Figure 8.13.: TTS results of different Hamamatsu reference PMTs at container B. In panel **(a)**, results are plotted over the channel number. Panel **(b)** shows the measurement with the lowest result from the selected distribution, acquired at channel 227 in mass 68.

Some observations on the performance of the different container channels can be made: So is the S/N ratio stable on a good level ($\pm 3 - 4\,\%$ around the average value) and independent from the channel, which shows that all ADC channels are working properly and comparably in performance.
Concerning the TTS performance, small differences in TTS values between different channels can be observed by focusing especially on the performance of the Hamamatsu PMTs: while at container A all results are shifted to higher values compared to the situation at container B (see Figure 8.7b again), also at container B some channels show systematically higher or lower results than the average values suggest [15]. The systematic differences of container B can be illustrated better by a zoom into the channel-dependent TTS results of the Hamamatsu reference PMTs, see Figure 8.13a: while most values for the selected reference PMTs show TTS values between 1.0 and 1.5 ns, a few channels show higher values even in multiple measurements (e.g. channels 211, 218, 232, 234 and 235) and a few channels show very low results (e.g. channels 207, 208 and 227). As it can be seen exemplarily in Figure 8.13b, even the very low results are reasonable. The observed, channel-dependent effect is below 1 ns, but still are recognizable here. Especially the existence of the lower values indicate that there are residual systematic uncertainties in the laser (or fiber splitter) system pushing the TTS values in several channels to slightly higher values than, most likely, the true TTS values actually are. Since the TTS values of Hamamatsu PMTs typically are in the order of 1–2 ns, even such small effects become significant.
As conclusion, it can be stated that the determination of TTS values cannot be taken

[15] The larger deviation for MCP-PMTs doesn't seem to be connected to the system, since the stability of TTS results for Hamamatsu PMTs is much better here and further a reliable TTS determination for NNVT PMTs is much more difficult.

as fully reliable if sub-ns precision is requested [16] and therefore should be treated with caution, leading to their already discussed possible dismissal from the PMT classification criteria, see subsection 8.1.2 again. On the other hand, Hamamatsu PMTs with TTS results below the acceptance threshold of 1.5 ns can be definitely classified as '*passed*', since due to the systematic uncertainty, the measured TTS value usually is worse than the real one. The aimed accuracy of 1 ns between the individual channels, as noted in Table 4.1, could be accomplished, yet still might be too bad to provide a reliable classification for all Hamamatsu PMT. In every case, repeated measurements of Hamamatsu PMTs in the container system would be the best solution to get more reliable results for the TTS performance, although this is difficult up to impossible to include into the daily and overall PMT testing schedule due to the large number of PMTs to test. The general systematic uncertainty overlying the TTS data particularly in container A will be discussed later in subsection 8.4.2. Also for the PDE, small systematic differences between channels appear to be possible. Due to the missing information about the mass number in this plot and so about the slope in the PDE results (discussed in the last section), the drift in results over time could also influence this impression; by looking on only one reference PMT separately, in fact it could not be steadied, see also Figure E.13 for some exemplary plots. Furthermore, the overall (estimated) accuracy in PDE determination is too low for a more detailed and fair estimation here (more details about the PDE accuracy can in found in subsection 8.2.6).

8.2.4. Stability of the Light Sources

The stability of the light sources is difficult to assess, since every LED is individual and each monitoring PMT has a different quantum efficiency, which make them unequal sensitive to the light intensities of the LEDs. Further, only the LEDs at low light intensity have been calibrated to a roughly comparable light intensity in order to provide around 0.1 p.e. per pulse for most of the PMTs. Since this was no absolute calibration but again based on a distinct reference with a specific QE (see subsection 6.6.1), a spread around this aimed value is natural. At high light intensity, the LEDs are set to a common setpoint, thus providing a design inherent, individual light intensity and requiring a dedicated calibration to connect light intensity to PDE, see subsection 6.6.2 again. A channel-wise comparison therefore makes no sense. The laser system didn't get any calibration, since the light intensity is not individually adjustable for the different channels anyway. Aside from that, potential instabilities of the light sources, i.e. a degradation, can be hardly distinguished from a potential aging effect of the PMTs (a decrease of their QE over time due to the extensive use). Figure 8.14 shows the distributions of the measured μ values from the sample analysis presented in section 8.1. In Figure 8.15, the μ values from the low light intensity LED measurements over the mass number are illustrated; more plots from the other

[16] Unfortunately, no dedicated timing calibration with an accuracy of $\mathcal{O}(100\,\text{ps})$ could have been provided due to missing light detection devices with such a high timing accuracy.

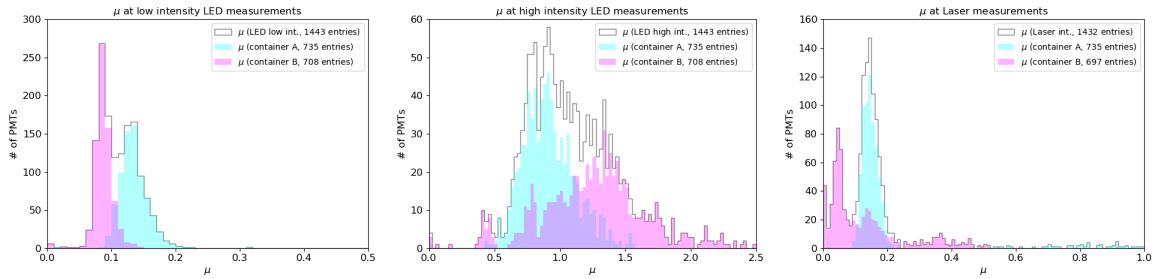

(a) μ from low intensity LED measurements

(b) μ from high intensity LED measurements

(c) μ from laser measurements

Figure 8.14.: μ values from the analysis of the selected PMT sample, separated by measurement. LED setpoints have been "calibrated" for the low light intensity measurement to a value around 0.1 p.e. in average, the distribution of the measured values in panel **(a)** thereby represents the different quantum efficiencies of the PMTs. A similar calibration is not applied for the high LED light intensity measurement in panel **(b)**. The laser intensity is not adjustable for the individual channels and thus cannot be calibrated; however, the light intensity in panel **(c)** is at least comparable for most of the fibers.

measurements, as well as a channel comparison of the low intensity measurement can be found in subsection E.2 in the appendix. As visible in the figures, the low light intensity level is sufficiently adjusted and stable for the needs of the PMT mass testing.

However, a slope towards lower PDE values in the measurements of the reference PMTs of container B has been discovered already in Figure 8.11b. To better understand this effect, the development of the light intensity was investigated for all reference PMTs combined and every PMT individually. In doing so, the determined μ value from the low light intensity measurement was plotted for each PMT normalized to its average value over the selected masses and fitted with a linear slope. To remove outliers, only data points within $\pm 25\,\%$ around this average value have been accounted for the fit. Since a direct comparison to the μ values of the high light intensity measurement is not possible (due to the different light intensities of the single LEDs), the PDE development will be used here instead [17]. The results are shown in Figure 8.16.
The first clear conclusion from this comparison is, that the values determined in container A are very stable (showing negligible slopes) over the selected masses, confirming the observation from Figure 8.11a. Second conclusion is, that the detected slopes in container B are different for the individual PMTs; the slope of the combined plots containing data points of all reference PMTs is mainly driven by PMT EA0586. Last conclusion is, that the determined slopes are consistent for both low light intensity (see Figure 8.16d) and high light intensity (PDE, see Figure 8.16f), which indicates a contribution of PMT aging effects over time. Regardless, a degradation of the LED

[17] PDE and μ values are linearly connected via Equation 6.1 considering the design inherent differences of the LEDs. Thus, a first order comparison becomes possible, although both are not directly proportional.

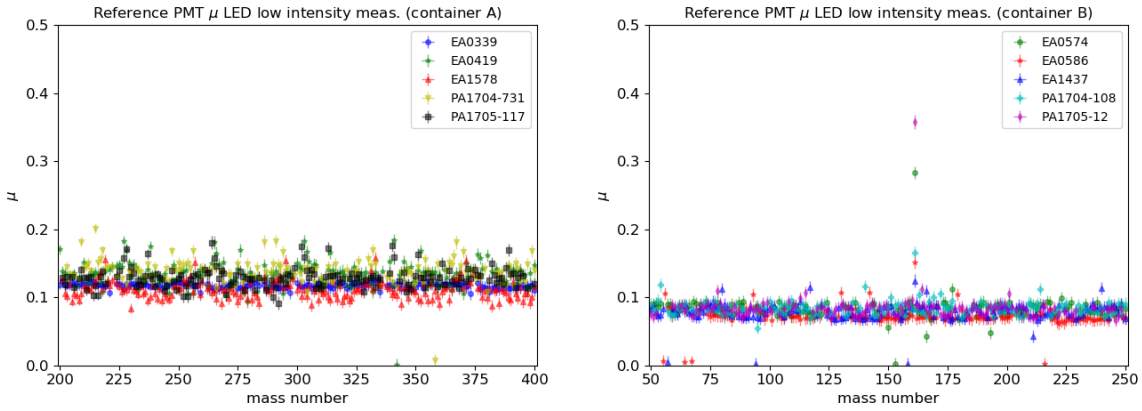

(a) low intensity μ values of reference PMTs in container A

(b) low intensityμ values of reference PMTs in container B

Figure 8.15.: μ values of the reference PMTs from the low light intensity LED measurement, plotted over the mass number. Light intensities have been adjusted for all LED to a level of $\mu \sim 0.1$.

performance over time is still likely and cannot be excluded [18]. A direct measurement of a potential LED degradation by a second calibration phase of the containers would be helpful to better differentiate contributions from the light sources and from the PMTs. Also, a cross-check measurement of the PDE of all reference PMTs in either the each other container system or the scanning station could help to measure a possible aging of the PMTs' QE.

8.2.5. PMT Stability: Same PMT Multiple Times in Single Box

Two of the reference PMTs (one per container) are loaded in the same box for most of the measurement runs, with few exceptions only. Therefore, these PMTs can be used to check their performance in a large number of measurements under identical conditions (without channel-dependent systematic uncertainties regarding the light field / sources etc.), and thus their individual stability over time. These reference PMTs are EA0339 and EA0586 (see also Table 8.7). They are mostly occupying the channels 101 and 201 (boxes A1 of both containers) and have been tested in around 180 runs (PMT EA0339), or 120 runs (PMT EA0586) respectively, which makes them

[18]It was reported already during production and delivery of the self-stabilized LED, that the LED batch of container B performs worse than the one of container A. Further, in the high light intensity measurements, the LED are driven close to their maximum performance level, and it was observed already during the commissioning that at max. setpoint of 4000 a couple of LED already struggled to provide a stable light intensity (therefore, a setpoint of 3000 was selected for the high light intensity measurement). From both, it seems likely that an extensive use of the LEDs over a longer time could lead to a degradation of the LED performance even for lower setpoints. In addition, explaining the observed slope by a pure aging effect of the PMTs seems unlikely since a similar behavior would have been expected for container A, which is even around nine months ahead in operation.

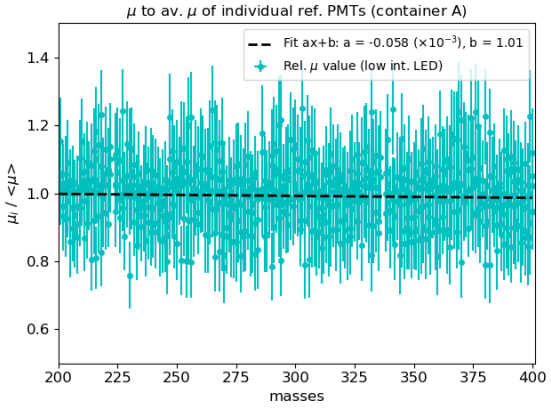

(a) normalized μ values of reference PMTs in container A

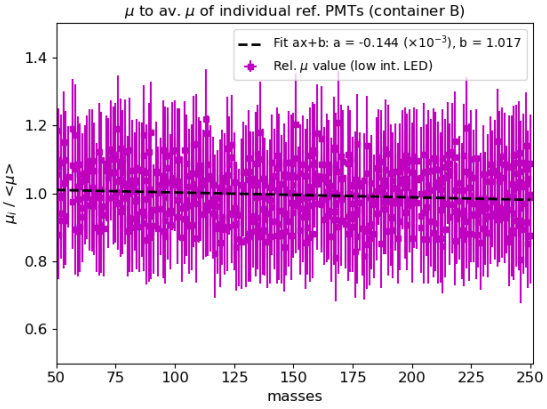

(b) normalized μ values of reference PMTs in container B

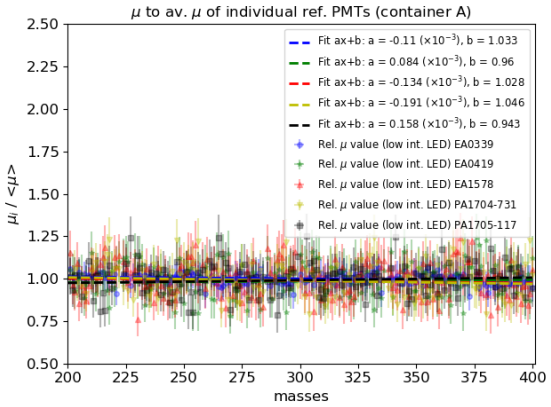

(c) normalized μ values of reference PMTs in container A (separated by PMT)

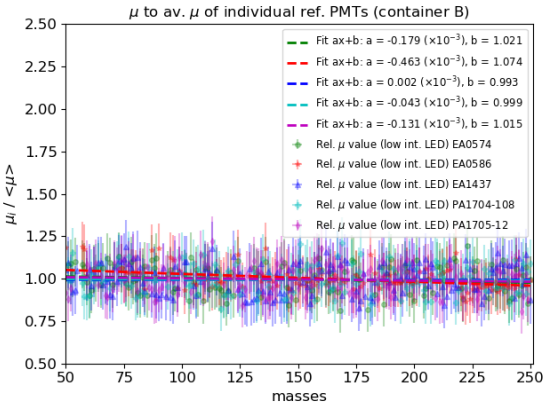

(d) normalized μ values of reference PMTs in container B (separated by PMT)

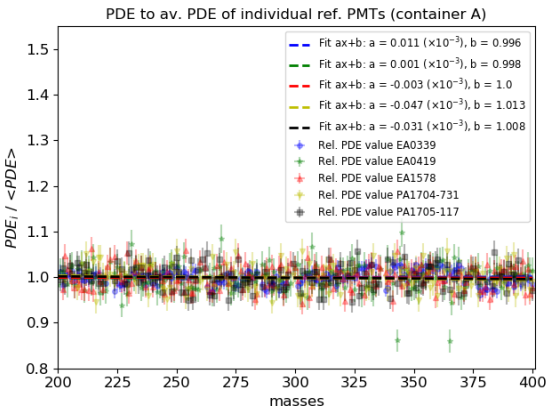

(e) PDE stability of reference PMTs in container A (separated by PMT)

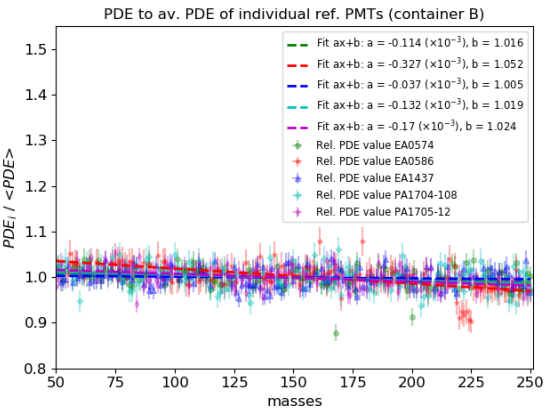

(f) PDE stability of reference PMTs in container B (separated by PMT)

Figure 8.16.: Stability monitoring plots of all five reference PMTs per container (combined and single) for μ values (low light intensity measurement) and PDE values (high light intensity measurement). Values are again normalized to average value of data sample and respective reference PMT and fitted with a linear slope.

the best (or most intensively) tested PMTs of the whole sample of JUNO PMTs.
To exemplarily illustrate the results of these PMTs, a few parameters (this time PDE, applied HV, TTS and DCR) are selected and presented here, see Figure 8.17 for PMT EA0339 and Figure 8.18 for PMT EA0586; also, as addition to the observations from subsection 8.2.4, the μ values will be plotted from both the low and high light intensity LED measurements over the mass number (this is possible here due to the focus on a single channel only). Results for the other parameters are shown in Figure E.18 and Figure E.19 in the appendix. The determined distributions of these PMTs basically confirm the considerations about the uncertainty of the system discussed in subsection 8.2.2 and subsection 8.2.3 and prove a stable performance of the tested PMTs for all tested parameters, including good pulse shape results (widths of distributions are much below 1 ns for RT, FT and FWHM, and much below 1 mV for the amplitude), a very stable HV to provide a gain of 1×10^7 and even stable results for the DCR with a width of less than 1 kHz. This was already visible in the reference PMT plots over the masses, see Figure 8.10g and Figure 8.10h, where the DCR values of the fixed reference PMTs are much more stable than for the other PMTs, which is due to their very long stay in darkness (without unloading and reloading in the meantime), so that their rate is already perfectly stabilized in most of the measurements. Also the TTS is stable and shows a distinct sub-ns width of its distribution of result.

8.2.6. Estimation of Measurement Accuracies

A similar procedure as used in the preceding subsection to illustrate the PMT stability can be used now to estimate the measurement accuracies of the container systems. This time, the results of all reference PMTs are collected independent from the channel in which they have been tested. The distribution of the reference PMT results for a certain parameter gives a measure on the result reproducibility of the container systems as a whole and thus on its measurement accuracy. In that way, the accuracies of the container systems for **PDE**, **DCR**, calculated **HV**, **P/V ratio**, **charge resolution**, **RT** and **TTS** shall be determined (the two latter are exemplary for the timing precision of the measurements).
It is important to note here, that although the reference PMTs can be assumed as good representatives for a standard JUNO PMT with acceptable performance, the individual results still can be affected by external effects (such as temperature and illumination during the loading in case of the DCR) or have been found to show an unstable behavior due to statistical effects in the data analysis (for e.g. P/V ratio or TTS). The to-be-determined precision in the measurements therefore pictures not only the capability of the container system, but also characteristics of the testing procedure and the implemented data analysis methods.
Up to 200 results for each reference PMT are contributing to this accuracy estimation, with again varying numbers of valid results for the individual parameters. The results are put separately into histograms and are fitted using a Gaussian function. The mean of this function defines the best estimated value for the investigated parameter of the respective reference PMT, the width of the distribution however defines the accuracy

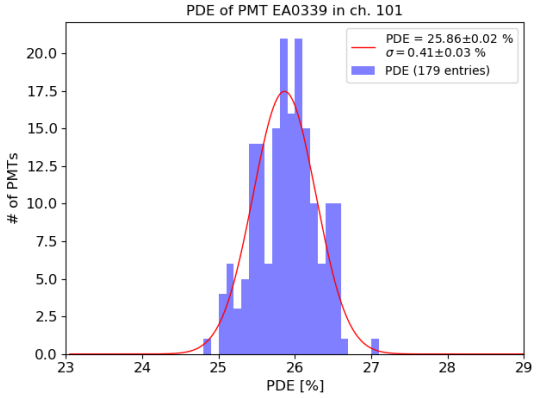

(a) PDE results of EA0339 in ch. 101

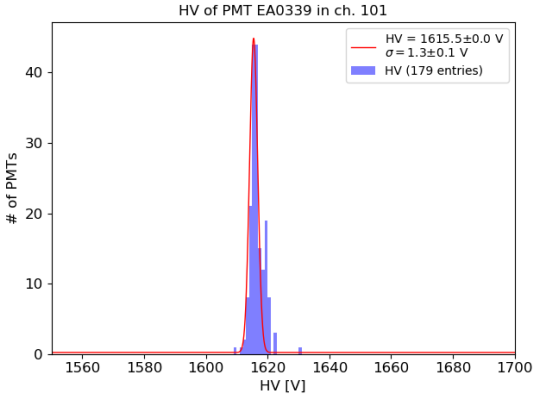

(b) HV results of EA0339 in ch. 101

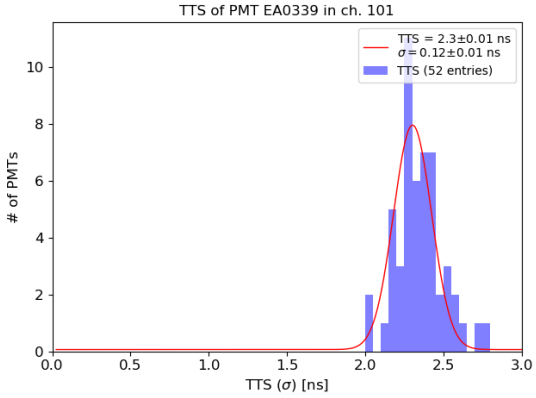

(c) TTS results of EA0339 in ch. 101

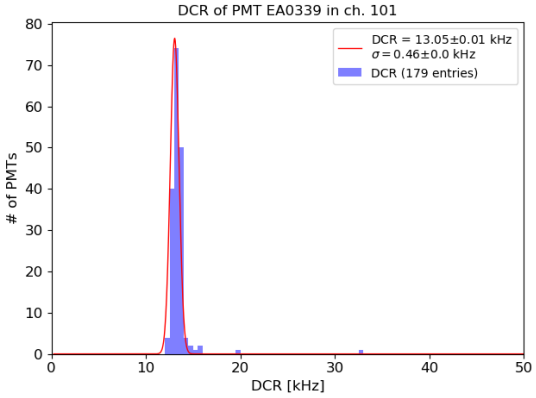

(d) DCR results of EA0339 in ch. 101

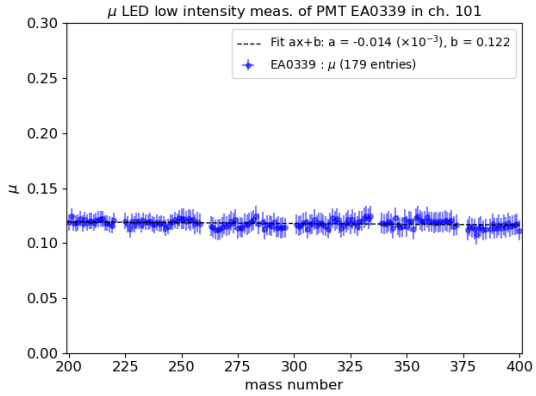

(e) μ values of EA0339 in ch. 101 from LED at low intensity

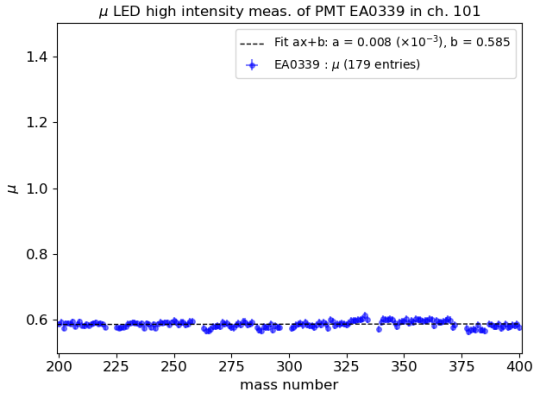

(f) μ values of EA0339 in ch. 101 from LED at high intensity

Figure 8.17.: Histograms of results for PDE, applied HV, TTS and DCR from reference PMT EA0339, taken at container A in ch. 101 over 179 runs (reduced statistics for TTS due to issues with the laser/trigger system, as reported). Distributions of results are fitted with a Gaussian function, proving stability of PMT performance over a large number of measurements, and confirming a high accuracy of the container system in determining these results. In panels **(e)** and **(f)**, the absolute μ values from the LED measurements at low and high light intensity are plotted over the mass number; their slope is fitted with a linear function to check for a possible decrease in the measured light intensity.

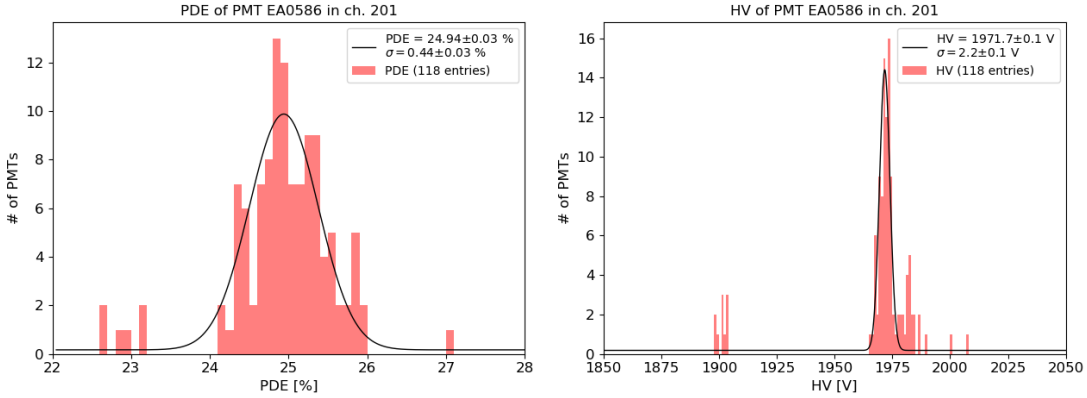

(a) PDE results of EA0586 in ch. 201

(b) HV results of EA0586 in ch. 201

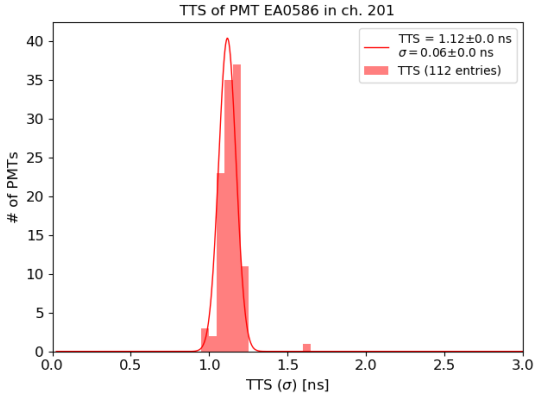

(c) TTS results of EA0586 in ch. 201

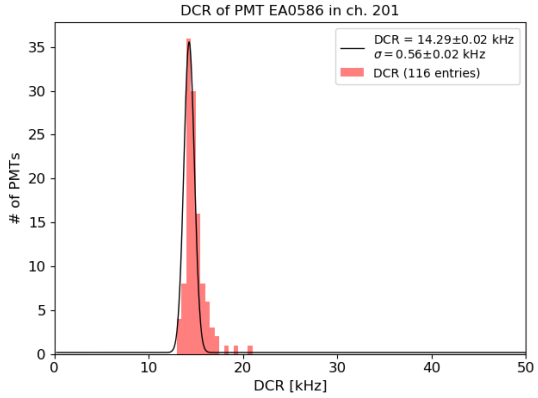

(d) DCR results of EA0586 in ch. 201

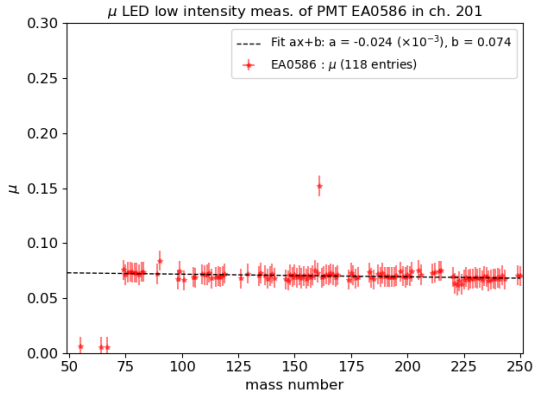

(e) μ values of EA0586 in ch. 201 from LED at low intensity

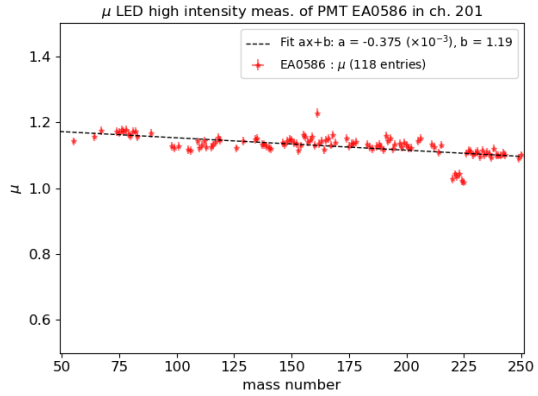

(f) μ values of EA0586 in ch. 201 from LED at high intensity

Figure 8.18.: Histograms of results for PDE, applied HV, TTS and DCR from reference PMT EA0586, taken at container B in ch. 201 over 118 runs. Distributions of results are fitted with a Gaussian function, proving stability of PMT performance over a large number of measurements, and confirming a high accuracy of the container system in determining these results. In panels **(e)** and **(f)**, the absolute μ values from the LED measurements at low and high light intensity are plotted over the mass number; their slope is fitted with a linear function to check for a possible decrease in the measured light intensity.

Table 8.8.: Fit results of data sample from reference PMT **EA1437**, tested multiple times in container B. Individual result distributions are shown in Figure 8.19. Mean results define best fit value for the analyzed sample and thus the best value for the PMT parameters; the corresponding errors define the pure statistical uncertainties and might be rounded down to zero due to the large statistics. 'System's accuracy' describes the width of the fitted sample and thus gives a measure for the precision of the testing process for this parameter of this particular PMT.

Parameter	Valid results	Mean Result of EA1437	System's Accuracy
PDE	166	$26.12 \pm 0.02\,\%$	$0.59\,\%$
DCR	155	$18.44 \pm 0.09\,\mathrm{kHz}$	$2.51\,\mathrm{kHz}$
Appl.	168	$1620.8 \pm 0.0\,\mathrm{V}$	$3.2\,\mathrm{V}$
P/V ratio	166	3.17 ± 0.03	0.42
Resolution	166	0.2640 ± 0.0006	0.0116
RT	164	$7.00 \pm 0.02\,\mathrm{ns}$	$0.33\,\mathrm{ns}$
av. SPE RT	166	$7.46 \pm 0.02\,\mathrm{ns}$	$0.30\,\mathrm{ns}$
TTS	146	$1.30 \pm 0.00\,\mathrm{ns}$	$0.14\,\mathrm{ns}$

of the container system (more precisely, of the full PMT testing process) as estimated from the data sample. This is illustrated here exemplarily for reference PMT EA1437 of container B, see Figure 8.19; final values from the performed parameter fits are listed in Table 8.8. Plots of all other reference PMTs as well as tables with the determined fit results from the corresponding PMTs can be found in the appendix in subsection E.2 again.

For a final accuracy estimation, the results from all reference PMTs are averaged, independently from the container system the reference PMT is assigned to (a single PMT usually will be tested only once in a randomly selected container), but also separated by the container system in order to screen for possible differences [19]. Although differences between the PMT types are visible in the results as well, they will not be discussed separately here, since they are clearly not inherent to the accuracy of the container system but rather to the design and characteristics of the PMTs itself.
The finally estimated accuracies of the container system are listed in Table 8.9. It can be seen that the accuracies of both containers match very well for all parameters; only for the P/V ratio, the accuracy of container B is clearly worse, which matches to the observations discussed in subsection 8.2.2 (see also Figure 8.10i and Figure 8.10j). The estimated accuracies further are on a very good level for all parameters and moreover hit the design goals from Table 4.1 i.e. for the PDE ($\leq 1\,\%$ accuracy aimed, even without compensating for the aging effects discussed above) and for the timing parameters ($\leq 1\,\mathrm{ns}$ aimed). The determined accuracies seem further to be independent

[19] The result of the TTS fit of PMT PA1705-117 was ignored in the averaging due to its low statistics, see Figure E.25e and Table E.1f.

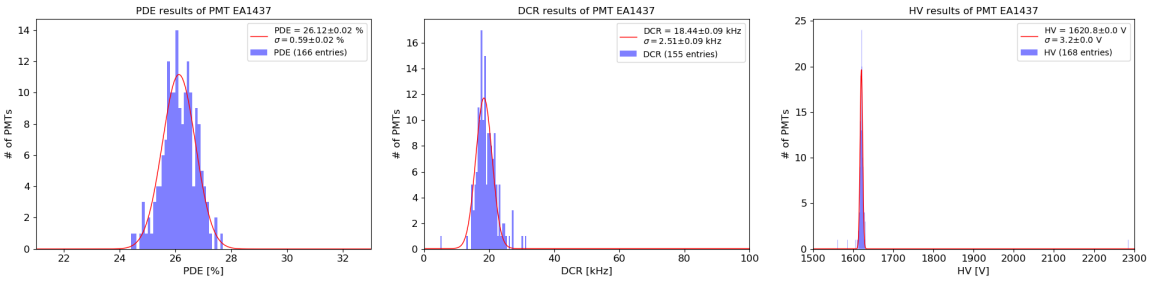

(a) all PDE results of reference PMT EA1437

(b) all DCR results of reference PMT EA1437

(c) all HV results of reference PMT EA1437

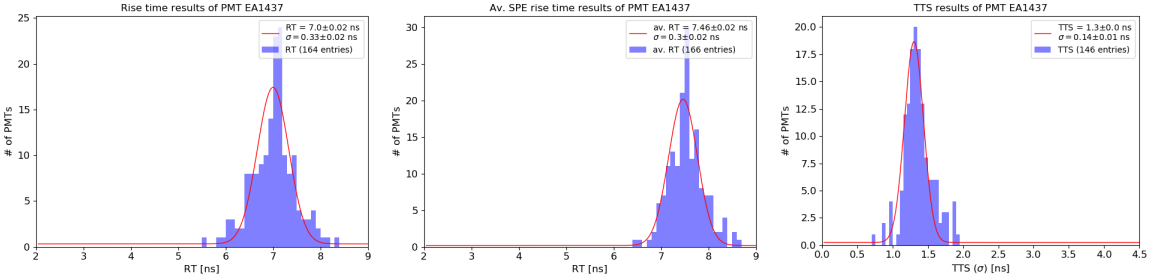

(d) all RT results of reference PMT EA1437

(e) all av. SPE RT results of reference PMT EA1437

(f) all TTS results of reference PMT EA1437

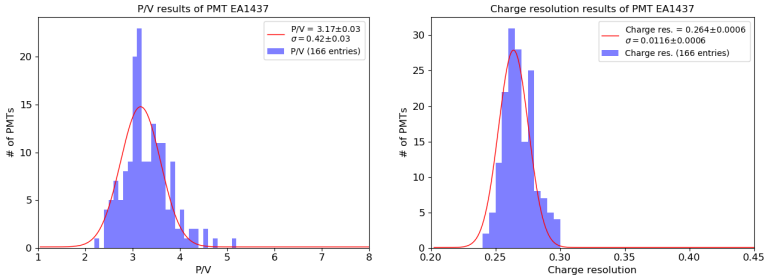

(g) all P/V results of reference PMT EA1437

(h) all resolution results of reference PMT EA1437

Figure 8.19.: Combined PMT testing results of reference PMT **EA1437**, tested more than 160 times in container B. Individual result distributions are fitted using a Gaussian function, with its width indicating the accuracy of the testing process (container accuracy + data analysis + process repeatability). Fit results are listed also in Table 8.8.

Table 8.9.: Final accuracies of the container systems (combined and separated by container). The TTS results of PMT PA1705-117 have been excluded here due to low statistics. Given uncertainties represent the standard deviations of the means from the individual PMT results. Since these values are based on only 10 reference PMTs, they can be partially biased to slightly worse results (due to a bad performance/behavior of a single PMT); this is e.g. the case for the DCR accuracy. The estimated values prove that the precision of the container systems is suitable for the needs of the PMT mass testing.

Parameter	Overall Accuracy	Container A only	Container B only
PDE	$0.62 \pm 0.11\,\%$	$0.66 \pm 0.15\,\%$	$0.57 \pm 0.05\,\%$
DCR	$3.7 \pm 2.6\,\mathrm{kHz}$	$4.3 \pm 3.1\,\mathrm{kHz}$	$3.1 \pm 2.3\,\mathrm{kHz}$
Appl. HV	$4.8 \pm 1.9\,\mathrm{V}$	$4.7 \pm 1.9\,\mathrm{V}$	$4.9 \pm 2.1\,\mathrm{V}$
P/V ratio	0.49 ± 0.21	0.36 ± 0.06	0.61 ± 0.24
Resolution	0.0141 ± 0.004	0.0134 ± 0.0046	0.0148 ± 0.0038
RT	$0.24 \pm 0.08\,\mathrm{ns}$	$0.19 \pm 0.05\,\mathrm{ns}$	$0.29 \pm 0.08\,\mathrm{ns}$
av. SPE RT	$0.23 \pm 0.08\,\mathrm{ns}$	$0.19 \pm 0.05\,\mathrm{ns}$	$0.26 \pm 0.09\,\mathrm{ns}$
TTS	$0.46 \pm 0.41\,\mathrm{ns}$	$0.39 \pm 0.25\,\mathrm{ns}$	$0.51 \pm 0.53\,\mathrm{ns}$

from the analysis method, as the values from the RT and average SPE RT results indicate. Only the accuracy of the DCR determination is lower than aimed ($\leq 1\,\mathrm{kHz}$, see Table 4.1 again), but can be explained by external effects as discussed above. Also PMT-specific differences contribute to the overall accuracies (see fit result tables of the other reference PMTs in subsection E.2), particularly for DCR, determined HV value and TTS, but also for the P/V ratio; the reasons for these have been discussed already several times.
As combined conclusion, the initially defined design goals of the container system can be stated as achieved and the estimated precision in the measurements of the various PMT parameters are suitable for the needs of the PMT mass testing for JUNO.

8.3. Cross-Check between Container Systems A and B

Another way to check the reproducibility of the results from the container tests and the reliability in the PMT characterization is to cross-check the individual results for a sample of PMTs measured in both containers. Therefore, several PMTs have been investigated in both containers (A and B), covering the full measurement program from section 5.1. For this survey, a couple of PMTs tested regularly over the **masses 185 – 188** and **197 – 212** at container A has been selected and tested a second time in container B. From the chosen sample, only the Hamamatsu PMTs are used for this container cross-check, since they have shown more stable results in the prior analyses and appear to have a faster cool-down and to be less affected by external influences. By using only one PMT type for this kind of analysis, also typical differences between the two types (such as differences in the average PMT performance or robustness of

Table 8.10.: Overview on the container cross-check statistics. "Full Sample" counts all characterizations of Hamamatsu PMTs from the chosen sample of both containers combined, not considering the PMT IDs (and so the actual number of cross-checks). Number of "cross-checked PMTs" shows number of PMTs tested in both containers, while PMTs "w/ good gain" represents final sample size for this survey (only PMTs with gain adjusted correctly to $[0.95, 1.1] \cdot 10^7$ are taken into account). Number of valid results for individual parameters can still differ from that value.

	Hamamatsu PMTs	Container A	Container B
Full Sample	702	365	344
Cross-checked PMTs	284	–	–
w/ good gain	256	–	–

the analysis methods) cannot contribute, which enables a better comparison of the container performance. The selected PMTs have been tested for the following parameters: **PDE**, **DCR**, **applied HV**, pulse parameters as **RT**, **FT**, **FWHM** and **amplitude**, **charge resolution** and **P/V ratio**. Since settings for the trigger acquisition (necessary for a good TTS determination) turned out to be insufficient later (as noted also in subsection 8.2.1) and have been improved only after the cross-check tests were finished, the TTS performance couldn't be tested in this cross-check survey. Also the results from the average SPE pulse analysis have been skipped here, since the differences between the analysis methods are not of interest here.

The final sample of PMTs, which have been tested twice with different systems and showing a well adjusted gain, consists of **256 Hamamatsu PMTs**. All valid results of the listed parameters have been taken into account, independent of whether the particular results would have led to a '*passed*' or '*failed*' classification, in order to get a fair and, as far as possible, representative PMT sample [20]. Only results indicating a faulty data analysis (large error bars) or issues within the measurement process (covering unphysical results or PMTs with gain not well adjusted to 10^7) have been excluded from the final container cross-check: while a badly adjusted gain leads to a complete dismissal of the PMT from the selected sample, parameter-related issues (following the criteria in Table 8.2) cause the exclusion of only the results for the respective parameter, leading again to slightly different statistics for the different PMT parameters as it was the case in the sample analysis in subsection 8.1.3. An overview over the PMT statistics can be found in Table 8.10, the classification of these PMTs from the standard analysis (without the TTS criteria) is listed in Table 8.11. Plots for the results from the analyzed sample for each individual parameter can be found in Figure E.28 in the appendix.
The selected PMT results are now compared for each PMT parameter individually. The relative differences Δ_p between the parameters p_A and p_B determined in the

[20] This doesn't derogate the consideration from subsection 8.1.1 about the representativeness of the analyzed subsample.

Table 8.11.: Number of PMTs characterized with both container systems individually and individual statistics of results from the full PMT characterization (without TTS data) per container.

	Hamamatsu PMTs	
	Container A	Container B
Cross-Checked PMTs	284	
PASSED	258	187
Passed (incomplete)	0	4
DOUBLE-CHECK	24	87
FAILED	2	6

containers A and B and calculated via

$$\Delta_p = \frac{p_A - p_B}{0.5 \cdot (p_A + p_B)} \tag{8.2}$$

have been plotted for each PMT parameter p and were fitted using a Gaussian function. If assuming that both containers have the same errors, the relative reproducibility (or repeatability) value R of the individual parameters for a single container system is then defined as

$$R_p = \frac{\sigma(\Delta_p)}{\sqrt{2}} \ , \tag{8.3}$$

with $\sigma(\Delta_p)$ the width of the Gaussian distribution from the differences Δ_p of the analyzed PMT sample for the corresponding parameter p [254]. Results for R from this survey are listed in Table 8.12. Exemplary plots for the distributions for the relative differences of PDE, HV, DCR, RT and P/V ratio are shown in Figure 8.20, plots for all other parameters are depicted in Figure E.29 in the appendix.
The determined results from this survey confirmed most of the aforesaid observations and consideration. So, the reproducibility of results is well assured between the systems: almost all parameters show mean values for Δ_p very close to zero, which means that results from container A could have been confirmed by container B (only exceptions are DCR and P/V, which will be discussed below). Taking the widths of the distributions into account, all mean Δ_p values are well compatible with zero. Further, also all determined values of the relative reproducibility R_p are in the range of a few percents only (again, except for DCR and P/V). The observed deviations between the results determined at the two container systems are further within the aimed accuracies of these parameters: for the PDE, assuming a value of 28–29 % in average as found for the analyzed subsample noted in Table 8.5, a relative reproducibility value R of less than 3 % corresponds to less than 1 % absolute uncertainty in PDE, which was the design goal for the containers (see Table 4.1 again). This also matches to the accuracies of the systems determined in subsection 8.2.6. Slightly broader distributions for e.g. the pulse shape parameters with widths of up to more than 5 % are

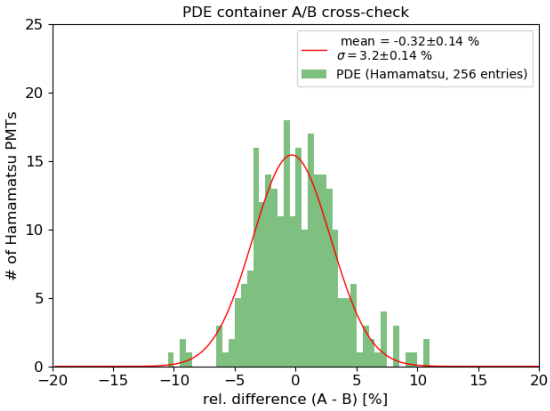

(a) rel. differences of PDE results

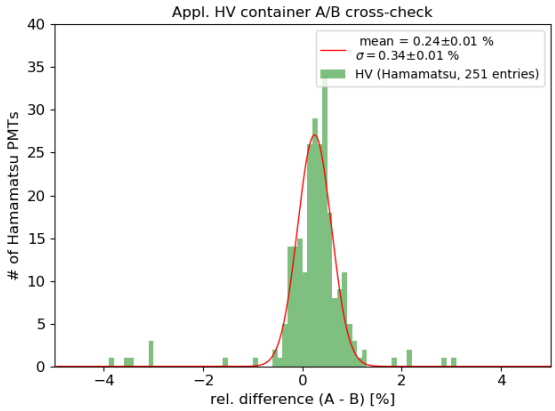

(b) rel. differences of HV results

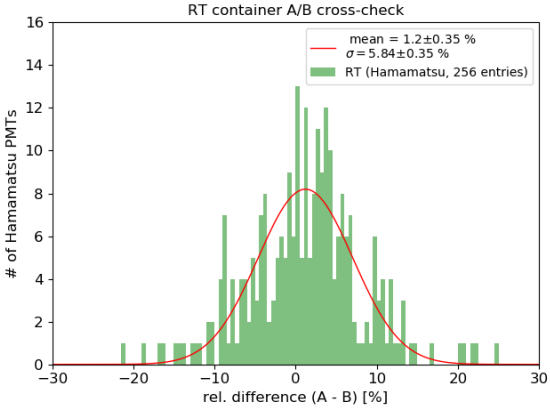

(c) rel. differences of RT results

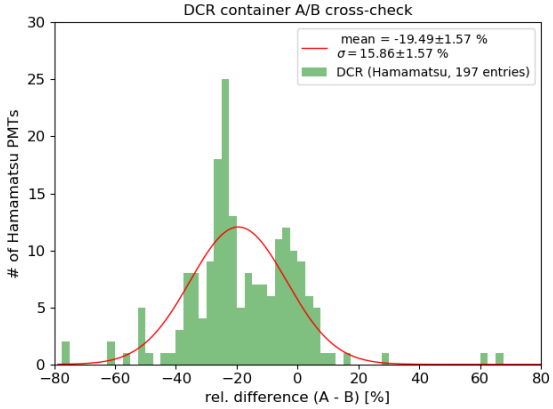

(d) rel. differences of DCR results

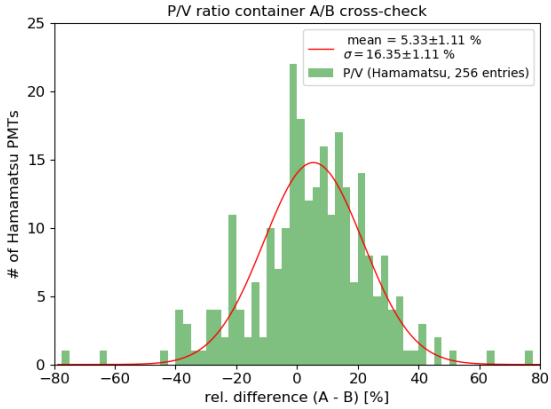

(e) rel. differences of P/V ratio results

Figure 8.20.: Relative differences between results of container A and B from the container cross-check measurements. Distributions are fitted with a Gaussian function. Statistics for individual parameters can vary due to different numbers of valid analysis results.

Table 8.12.: Results of mean relative differences Δ_p and relative reproducibility values R for 256 PMTs tested in both containers (with correctly adjusted gain). Uncertainty values of Δ_p indicate the width of the respective distribution, while uncertainty values for R indicate the uncertainty of the fit result (including Gaussian error propagation from Equation 8.3), see also Figure 8.20 and plots in subsection E.3 in the appendix. Number of valid results for individual parameters can vary, due to discussed criteria for data quality / reliability of analysis results (see subsection 8.1.2 again).

Parameter	Valid results	$\langle \Delta_p \rangle$ [%]	rel. R [%]
PDE	256	-0.32 ± 3.20	2.26 ± 0.10
Appl. HV	252	0.24 ± 0.34	0.24 ± 0.01
DCR	197	-19.49 ± 15.86	11.21 ± 1.11
Resolution	255	0.41 ± 5.33	3.77 ± 0.17
P/V ratio	256	5.33 ± 16.35	11.56 ± 0.79
RT	256	1.20 ± 5.84	4.13 ± 0.25
FT	256	-0.31 ± 6.45	4.56 ± 0.25
Amplitude	256	-0.84 ± 2.48	1.75 ± 0.08
FWHM	179	0.01 ± 3.56	2.52 ± 0.15

reasonable due to their typically small values ($< 10\,\text{ns}$) and moreover confirm e.g. an absolute accuracy of $\ll 1\,\text{ns}$ in average for the timing/pulse shape parameters.
In contrast to these, DCR and P/V ratio show larger discrepancies in their results, as mentioned above. The observed differences, manifesting in a larger deviation of their means from zero and a very broad distribution, however match to the conclusions from the analyzed PMTs subsample in section 8.1, where DCR and P/V ratio results have also shown a slight difference between the distributions of both container systems; such a behavior is also present in the result distributions of the cross-checked sample, see Figure E.28a and Figure E.28h. This again hints at a different noise contribution in the containers, which could influence the results of these parameters. To better estimate this effect, also the absolute differences of the results for these parameters has been plotted, indeed revealing a small offset for DCR and P/V ratio, see Figure 8.21. Although the effect in not large in absolute numbers for both DCR and P/V ratio, it is clearly detectable here. The absolute distributions shows an increase in the measured DCR at container B of around 2.5 kHz in average (this will be investigated further in subsection 8.4.1), while the P/V ratio is reduced by around 0.2. These offsets in results further seem to be independent from the absolute values of both parameters, see Figure 8.21 again. On the other hand, the DCR is the parameter which is the most sensitive to external conditions (such as temperature, preceding illumination during the loading process and conceded cool-down time), while the determined P/V also relies on the analysis and connected difficulties in finding the correct position and value of the valley (see also discussion in subsection 8.2.2 again). These effects can also contribute to the reproducibility values R_p and can further explain the large

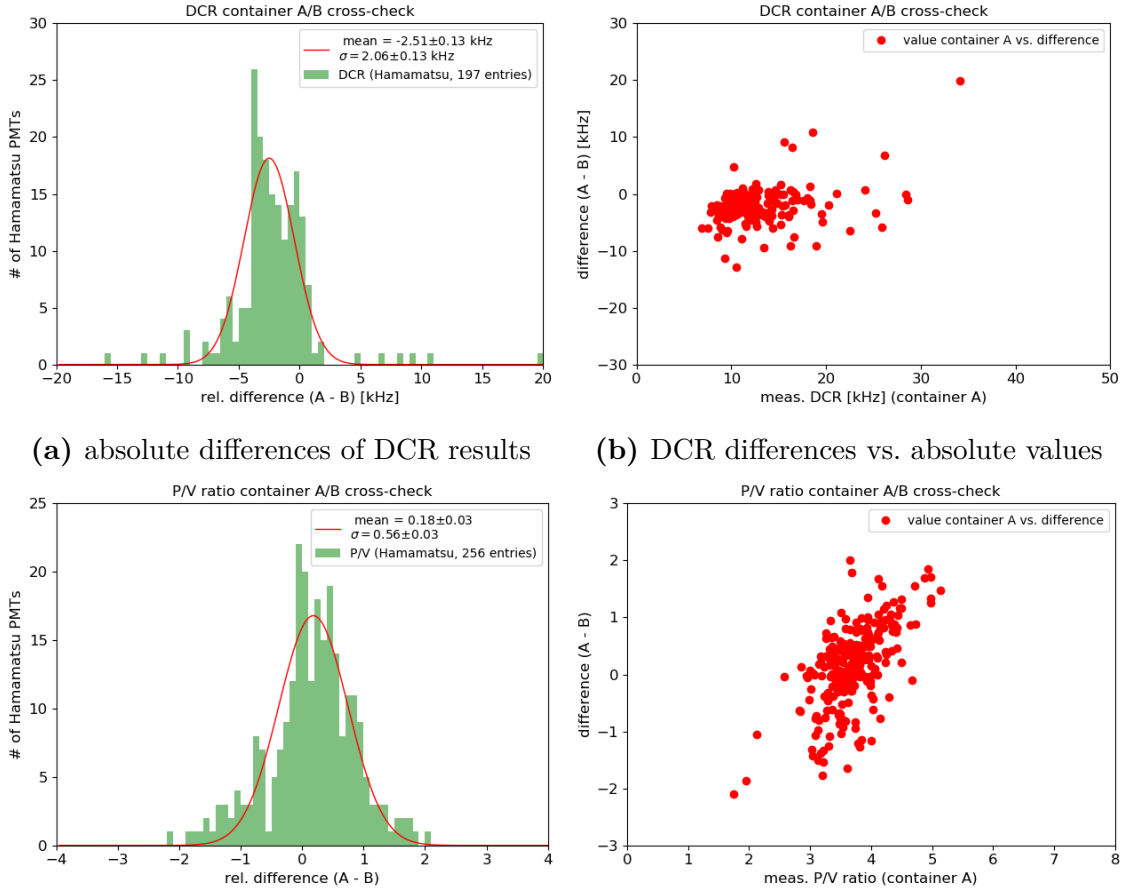

(a) absolute differences of DCR results

(b) DCR differences vs. absolute values

(c) absolute differences of P/V results

(d) P/V differences vs. absolute values

Figure 8.21.: Absolute differences of results for DCR (panels **(a)** and **(b)**) and P/V ratio (panels **(c)** and **(d)**) between the containers A and B, revealing a systematic discrepancy between the two systems. The scatter plots in panels **(b)** and **(d)** further indicate, that this effect is independent from the actual measured value in container A (used here as reference for this comparison).

values here; they are therefore not completely inherent to the system, but are also due to "external" conditions.

8.4. Investigations of Systematic Effects in the Containers

Following the observation from subsection 8.1.3 and section 8.3 about an additional noise contribution in container B and a large systematic effect in the TTS measurement in container A, these two issues shall be investigated in the following, with the aim to confirm the observed systematic effects and moreover to estimate their absolute contribution to the results.

8.4.1. Absolute Noise Levels in the Containers

The existence of an additional noise contribution on container B has been indicated already by the distribution of the analyzed PMT sample, see Figure 8.4e again, and was proven in the cross-check measurements between the two containers, see Figure 8.21a again. Now, this effect shall be confirmed and better quantified by an additional investigation of PMT results. This analysis can further substantiate the conclusion from section 6.2 and section 6.3 about the light-tightness and overall noise level in the containers by deriving upper bounds for additional, so far unknown noise contributions.

For the noise analysis, a large data sample has been selected in order to provide a good statistical base. Therefore, the DCR data of all PMTs from **masses 200 − 400** in container A, and of all PMTs from **masses 50 − 250** in container B has been selected and analyzed, which makes in total more than 10'500 PMTs. Since the noise offset seems to be only in the order of a few kHz, the analyzed sample has been sorted further:

- Only PMTs with a DCR below 20 kHz have been kept; further, DCR results below 5 kHz has been sorted out to sustain physical plausibility of the sample (a DCR below 5 kHz is assumed here as unphysically low, meaning that this results might not be representing the actual DCR of the to be tested PMT,as also considered in the classification criteria in Table 8.2).
- In contrast to the criteria listed in Table 8.2, only results with an individual uncertainty of $\leq$ 1 kHz from the analysis have been kept; by this selection, less reliable results (those which might be affected from the effects discussed in section 7.1) will be omitted.

Using these selection criteria, a sample of **2185** PMT results remains for container A (from which 92.4 % are Hamamatsu PMTs) and a sample of **742** PMT results remains for container B (87.5 % Hamamatsu PMTs). The individual statistics for each

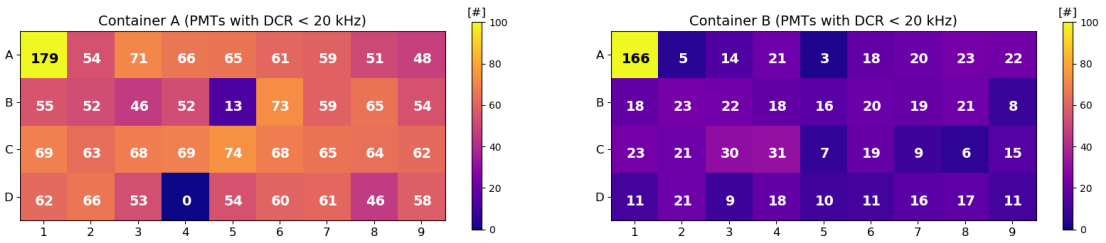

(a) result statistics for DCR $< 20\,\mathrm{kHz}$ per box in container A

(b) result statistics for DCR $< 20\,\mathrm{kHz}$ per box in container B

Figure 8.22.: Individual low DCR statistics for each container channel. Only results with DCR $\in [5, 20]\,\mathrm{kHz}$ and $\Delta\mathrm{DCR} < 1\,\mathrm{kHz}$ are taken into account. Statistics between boxes depend on the actual PMTs which have been tested in these boxes. Ch. 131 (box D4 of container A) is broken, so no PMTs have been tested here. High number of values in boxes A1 are due to the reference PMT data.

container channel are shown in Figure 8.22. The absolute numbers in the channels thereby underly statistical effects from the PMT testing: there are different numbers of (low DCR) PMTs tested in the containers, with the PMTs assigned randomly to the channels in the individual masses. Thus, the significance of the following investigations, i.e. for differences between single channels, is directly connected to the testing statistics (meaning the available PMTs) as well as to the testing "history" of the selected PMT sample [21].

For investigating the overall noise level, first the lowest measured DCR result has been selected for each container channel individually. This is shown in Figure 8.23a and Figure 8.23b. Now the average of all these individual channel results can be calculated, which gives an estimation on the maximum (averaged) noise level present in the containers. Results are listed in Table 8.13.
As first conclusion here, the offset of 2-3 kHz between container A and B could be confirmed. This can be further substantiated by looking on the average values per container from the full sample. If comparing the results averaged individually for each container channel (see Figure 8.23c and Figure 8.23d), the noise offset seems to be channel-independent. By further looking on the statistics per channel for the best 100 results of the selected sample, see Figure E.30 in the appendix, this can be confirmed at least for container B, while for container A also some better and worse performing channels can be identified (admittedly, the absolute DCR values are very low here for all PMTs and channels). The second conclusion, which can be made here, is that the overall residual noise levels within the containers are low. Especially for container A,

[21] A specified survey using a small sample of PMTs with very low DCR tested in all 72 container channels would have been perfect for such an examination. However, since this feature became visible firstly with larger statistics (as shown in Figure 8.4), such a survey was not performed during the commissioning and couldn't realized during the regular operation due to restrictions in the testing schedule (such a test would be very time consuming).

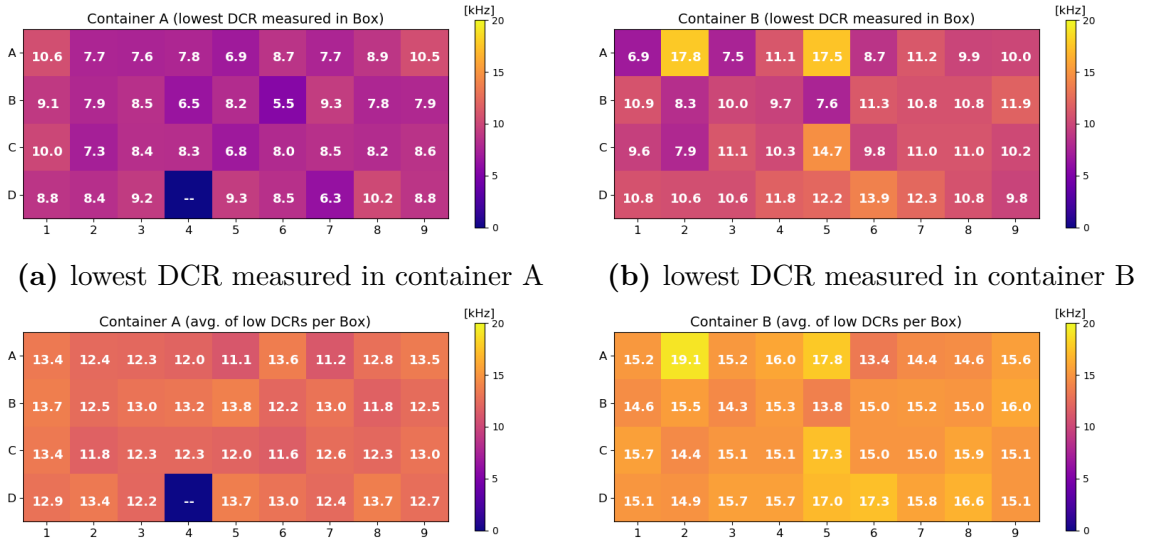

(a) lowest DCR measured in container A

(b) lowest DCR measured in container B

(c) avg. of low DCR results per box in container A

(d) avg. of low DCR results per box in container B

Figure 8.23.: Low DCR sample results per container channel. In panels **(a)** and **(b)**, the lowest DCR values measured in the individual containers channels are displayed (data covers only analyzed subsample). In panels **(c)** and **(d)**, all low DCR results per container channel from the selected subsample are averaged. Differences between the boxes might not be significant, since they underly the actual testing statistics and "history"; hence, exact values directly depend on the available PMTs.

light-leaks and additional, so far unknown noise sources are very unlikely, since the lowest measured DCR values already represent very well-performing PMTs (typical DCR for a cooled Hamamatsu PMT is around 20 kHz [216]); therefore, a light-leak in container A can be fully excluded finally. Even if assuming that the "true value" were in the order of 5 kHz (which would be extraordinary low for a 20-inch PMT), the residual noise level here would have been only a few kHz. However, it has to be stated, that such a case cannot be fully excluded.
The situation for container B is different since here a small noise offset is definitely present. The origin of this noise is not clear – since it produces counts above the set DCR threshold (see subsection 5.2.2 again), a static baseline noise is unlikely. Also a light-leak can be excluded since both containers are equally sealed. More likely, there is an additional electro-magnetic noise introduced to the system, which is more distinct at the location of container B than for container A (could be originate from somewhere at the testing site). Also, weak fluorescence light from the glue of the sticky tapes used in the drawer boxes can be imagined, although such an effect should be visible in container A as well.

Anyway, the observed offset of 2-3 kHz is mostly unproblematic for the DCR measurement of PMTs: from experience, the illumination of the PMTs during the loading, a

Table 8.13.: Average results of the low DCR sample from the containers. The first part of the table shows the average of the lowest results measured in the individual drawer boxes (full sample / only considering boxes with statistics $n > 5$ or $n \geq 10$). The second part of the table shows the average results of the full low DCR subsample (average of individual average values per box / average of full sample per container).

Sample	Avg. Container A [kHz]	Avg. Container B [kHz]
all channels	8.3 ± 1.1	10.8 ± 2.3
only ch. with $n > 5$	8.3 ± 1.1	10.4 ± 1.6
only ch. with $n \geq 10$	8.3 ± 1.1	10.2 ± 1.5
avg. of channel results	12.7 ± 0.7	15.2 ± 0.8
avg. of full sample	12.6 ± 2.9	15.2 ± 2.7

varying cool-down behavior for the individual PMTs as well as the outside temperature in the testing hall usually have a larger influence on the actually measured DCR that this offset. It further would affect only the classification of PMTs very close to the edges of the acceptance criteria. Since this noise contribution also seems to affect the P/V ratio a little (see Figure 8.21c again), also the P/V criteria will become more strict for PMT tested in this container. Thus, at least a negative impact from the examination of the PMT performance for JUNO can be excluded.

8.4.2. Systematic Effects in the TTS Measurement

Although a direct cross-check of TTS results between both containers is missing, the existence of a significant systematic effect between container A and B is unquestionable in the light of the observed distribution of TTS results from the analyzed PMT sample, see Figure 8.7a again. Since the measurement of the ADC jitter performed at container B and presented in section 6.4 could determine the systematic uncertainty of the read-out electronics to a level of clearly below 1 ns, and further no differences in the electronics systems of both containers are present, this systematic effect is likely introduced by the light system, concrete as jitter (pulse broadening) of the fiber splitter. Such a behavior on container A is not completely surprising, because its fiber splitter got broken during a lab test before the commissioning of container A and had to be refitted completely (including a cleaving of the individual fibers). A degradation in quality due to this repair (which is at least likely) could explain a broadening of the light pulses in the fiber system of container A.
Similar to the noise offset above, this general (fiber splitter specific) effect shall be better quantified by an additional investigation of PMT results. In best case, if the additional contribution can be estimated, the determination of the true TTS values from the measured ones becomes possible.

For the TTS analysis, another large data sample has been selected in order to provide a good statistical base for the jitter estimation. In doing so, the TTS data of all

Hamamatsu PMTs from **masses 255 − 315** in container A [22], and of all Hamamatsu PMTs from **masses 30 − 250** in container B has been selected and analyzed, which makes in total more than 2'100 PMTs. A use of MCP-PMT for this analysis doesn't make sense, since the MCP-PMTs typically have a much larger TTS; in additional, the TTS analysis for Hamamatsu PMTs is more robust and thus generally more reliable, see subsection 7.4.2 again.
In order to estimate the actual performance of the containers, the analyzed sample has been sorted further as well:

- Only PMTs with a TTS below 3 ns will be taken into account for the following survey.

- Further, only results with an individual uncertainty of ≤ 1 ns from the analysis have been kept; by this selection, less reliable analysis results can be omitted.

Using these selection criteria, a sample of **624** Hamamatsu PMT results remains for container A and a sample of **1185** Hamamatsu PMT results remains for container B. The individual statistics for each container channel are shown in Figure 8.24. The absolute numbers in the channels underly statistical effects from the PMT testing, similar as in case of the DCR above. Thus again, the significance of the following investigations is directly connected to both the testing statistics (meaning the available PMTs) and the testing "history" of the selected PMT sample [23].

In a first step, the lowest measured TTS values have been selected for each container channel individually, similar as done above for the low DCR values. This is shown in Figure 8.25a and Figure 8.25b. Although the observed differences between single channels are not significant due to their dependence of the actual data, individual systematic effects between single channels cannot be excluded but seem to be clearly in the order of below 1 ns. Only exception here is ch. 135 (box D8 of container A), which performs on the same level as the channels of container B. The result of this channel also affirms the assumption, that the jitter is introduces by the individual conditions of the fibers – an additional jitter introduced by the electronics would equally affect all channels of the same trigger group (see subsection 4.4.3 and subsection 5.3.3 again). This result has been confirmed also by the individually averaged channel results in Figure 8.25c.

[22] Valid data was available only for these masses, see also subsection 8.2.1 again.

[23] A specified survey using a small sample of PMTs with very low TTS tested in all 72 container channels would have been perfect for such an examination. Since this feature was unknown during the commissioning and moreover hidden for a longer time by the reported issues in the laser/trigger system (which caused a large amount of invalid data from the TTS measurements), such a survey couldn't realized during the regular operation due to restrictions in the testing schedule (same as in case of the DCR offset above).

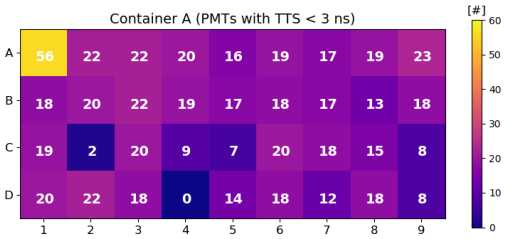

(a) result statistics for TTS < 3 ns per box in container A

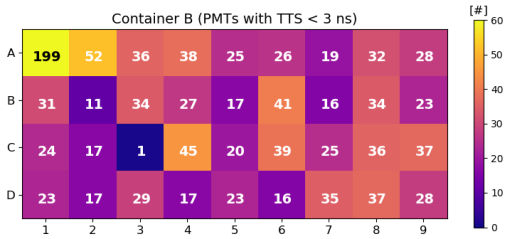

(b) result statistics for TTS < 3 ns per box in container B

Figure 8.24.: Individual low TTS statistics for each container channel. Only results with TTS < 3 ns and ΔTTS < 1 ns are taken into account. Statistics between boxes depend on the actual PMTs which have been tested in these boxes. Ch. 131 (box D4 of container A) is broken, so no PMTs have been tested here; ch. 120 (box C2 in container A) as well as ch. 221 (box C3 in container B) are performing only very weakly (detected light intensity was too low in most runs).

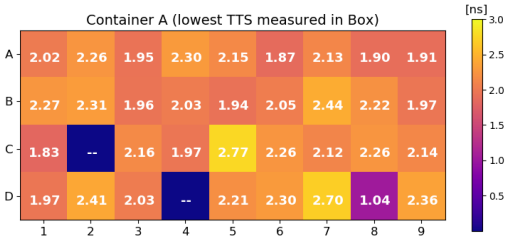

(a) lowest TTS measured in container A

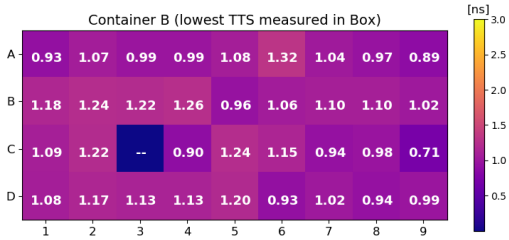

(b) lowest TTS measured in container B

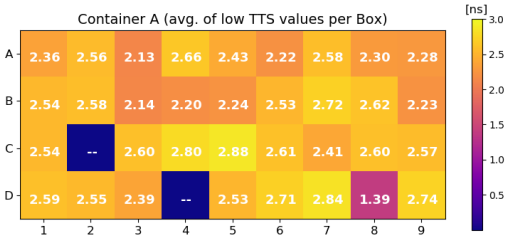

(c) avg. of low TTS results per box in container A

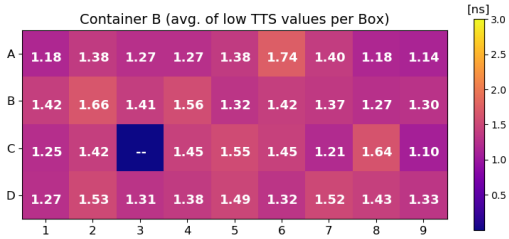

(d) avg. of low TTS results per box in container B

Figure 8.25.: Low TTS sample results per container channel. In panels **(a)** and **(b)**, the lowest TTS values measured in the individual containers channels are displayed (data covers only analyzed subsample; boxes with statistics of $n < 5$ are ignored). In panels **(c)** and **(d)**, all low TTS results per container channel from the selected subsample are averaged. Differences between the boxes might not be significant, since they underly the actual testing statistics and "history"; hence, exact values directly depend on the available PMTs.

The averages of the lowest TTS results from all the individual channels give again a first estimation on the present systematic difference between the containers. The

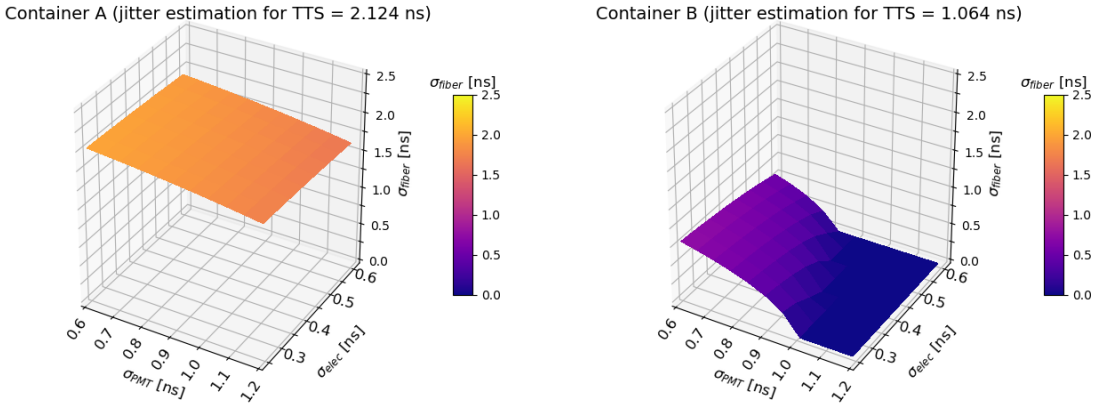

(a) jitter estimation of the fiber splitter of container A

(b) jitter estimation of the fiber splitter of container B

Figure 8.26.: Average jitter estimation introduced by the fiber splitters for both containers. Actual values depend on present jitter from the read-out electronics σ_{elec} and true TTS value, here named as σ_{PMT}. For container A (container B), the average value of the lowest measured TTS per channel was $TTS_{\text{meas,A}} = 2.12\,\text{ns}$ ($TTS_{\text{meas,B}} = 1.06\,\text{ns}$).

results are

$$\langle TTS_{\text{min}} \rangle_A = 2.12 \pm 0.29\,\text{ns}$$

for container A and

$$\langle TTS_{\text{min}} \rangle_B = 1.06 \pm 0.13\,\text{ns}$$

for container B. Since the statistics of channels 120 (container A) ans 221 (container B) are very low, they were excluded from the average calculation here.
The actually measured TTS value depends on the influence from the electronics jitter σ_{elec} (which has been determined to around $0.42^{+0.17}_{-0.16}\,\text{ns}$ for the ADCs, see section 6.4 again) [24], the introduced jitter from the fiber splitter σ_{FS}, and not least on the true TTS of the PMT, which is hidden in the first place:

$$TTS_{\text{meas}} = \sqrt{TTS^2_{\text{true}} + \sigma^2_{\text{elec}} + \sigma^2_{\text{FS}}}\ . \tag{8.4}$$

An estimation for σ_{FS} therefore strongly depends on the assumption for TTS_{true}. Since the here displayed values can be fairly assumed to originate from well-performing PMTs only, and the typical TTS value of Hamamatsu PMTs type R12680 as used in JUNO is around 1.0 ns [216], true values in a range of $[0.7, 1.2]\,\text{ns}$ seem to be reasonable. With these assumptions and using the above listed average values for TTS_{meas} of both containers, the average contribution from the fiber splitter can be estimated as shown in Figure 8.26. Using further Equation 8.4 as well as the means of the lowest TTS values measured in the containers, lower and upper bounds for

[24] This includes also the ability on how well the used analysis methods from section 7.4 can identify the true hit times of both trigger and PMT pulse from raw data with 1 GS/s sampling frequency.

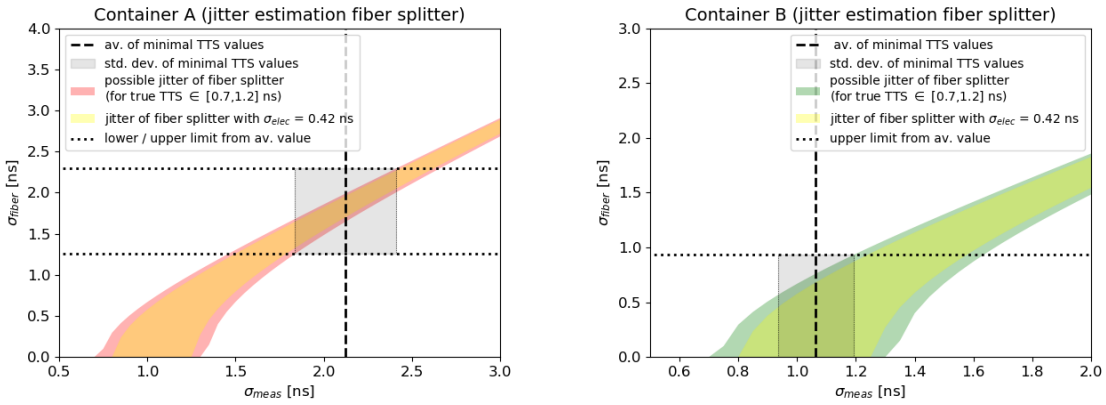

(a) jitter bounds for fiber splitter of container A

(b) jitter bounds for fiber splitter of container B

Figure 8.27.: Estimations for lower and upper bounds of the jitter introduced by the fiber splitter to the TTS measurement in the containers. Using the calculated TTS means from the values in Figure 8.25a and Figure 8.25b, bounds can be contained to $\sigma_{\mathrm{FS,A}} = [1.25, 2.29]\,\mathrm{ns}$ for container A and $\sigma_{\mathrm{FS,B}} = [0, 0.93]\,\mathrm{ns}$ for container B.

σ_{FS} can be estimated. This is illustrated in Figure 8.27 for both containers. Using the discussed assumptions for the true TTS and the measured, residual jitter of the electronics, the jitter from the fiber splitter can be contained to

$$\sigma_{\mathrm{FS,A}} = [1.25, 2.29]\ \mathrm{ns}$$

for container A and to

$$\sigma_{\mathrm{FS,B}} = [0, 0.93]\ \mathrm{ns}$$

for container B. If using only the central values for TTS_{meas} and σ_{elec}, and assuming a true average TTS value of 0.80 ns (which would be reasonable since the chosen TTS results represent the best performing PMTs of the selected data sample), the jitters can be estimated to

$$\sigma_{\mathrm{FS,A,central}} \approx 1.92\,\mathrm{ns}$$

and

$$\sigma_{\mathrm{FS,B,central}} \approx 0.57\,\mathrm{ns}$$

respectively. A more precise determination of the jitter contribution from the fiber splitters is only possible with either a detailed knowledge of the true TTS of the used PMTs [25] or a measurement device (e.g. another PMT of a different type) with a very high timing precision in the order of $\mathcal{O}(100\,\mathrm{ps})$.

[25] At least one PMT with a precisely determined TTS value would be necessary for a detailed survey of the individual jitters of the container channels. For a precise measurement of the fiber splitter's contribution, the TTS value of this PMT should be known with at least the same accuracy as the residual jitter of the electronics has been determined.

At last, with the determined estimations for the participating jitters, the effect on the testing statistics by using modified classification criteria based on these estimations can be considered. For this comparison, the acceptance criteria for both PMT types will be raised, respecting the systematic contribution from the fiber splitters via

$$\sigma^2_{\text{sys}} = \sigma^2_{\text{elec}} + \sigma^2_{\text{FS,central}} \ , \tag{8.5}$$

with $\sigma_{\text{elec}} = 0.42\,\text{ns}$ and $\sigma_{\text{FS,central}}$ as noted above. The criteria for a '*double-check*' classification can be raised accordingly, this time respecting the maximum possible contributions from both jitters,

$$\sigma^2_{\text{sys,edge}} = \sigma^2_{\text{elec,max.}} + \sigma^2_{\text{FS,up}} \tag{8.6}$$

with $\sigma_{\text{elec,max.}} = 0.59\,\text{ns}$ and $\sigma_{\text{FS,up}}$ the upper bounds of the estimated values for σ_{FS}. Although the main systematic effect from both fiber splitters seems to be channel-independent, there likely are some additional (yet smaller) systematic effects between the individual channels, see Figure 8.13 again. Therefore, for defining the upper limit of the '*double-check*' region, the upper bound values $\sigma_{\text{FS,up}}$ will be additionally increased by $+0.5\,\text{ns}$ to cover also the channel-dependent systematic effects [26].
Before finally defining new classification criteria, two additional points need to be considered as well: since the transit time distribution of the MCP-PMTs doesn't follow a Gaussian distribution, also a Gaussian error propagation is not allowed in this case [27]. As a direct consequence, a systematic effect of even a few ns as present in container A does not become negligible even in case of higher TTS values of the MCP-PMTs; they moreover add up to the measured TTS. This is also visible in the distribution of TTS results from the analyzed PMT sample in Figure 8.7a, where not only the results for Hamamatsu PMTs but also the ones from the MCP-PMTs are shifted towards higher values for container A. Therefore, the determined systematic effects will be added quadratically for the Hamamatsu PMTs, but linear for the MCP-PMTs. The second point is the significantly better performance of ch. 135 in container A; since it's comparable with the performance of the channels from container B, this channel will be treated the same way and thus different to all other channels from container A in order to not overestimate the systematic uncertainty for this particular channel.
The finally modified criteria for the TTS classification are listed in Table 8.14. The effect from these modified classification criteria on the statistics of the analyzed PMT sample described in section 8.1 is shown in Table 8.15, while the direct effect on the

[26] In order to not extent this region too much, the maximum '*double-check*' range will be limited to 1.5 ns (this limitation only affects the '*double-check*' range of NNVT PMTs in container A).

[27] If assuming the contribution of the systematic effect from the jitter as Gaussian, a convolution of such a Gaussian distribution with a transit time distribution as shown in Figure 7.25b would mainly broaden the sub-peaks of the spectrum. Since the fit of this distribution is however sensitive to the edges of the whole distribution, this can directly affect the width of the fitted Gaussian function, although the systematic jitter was much smaller than the actual transit time distribution.

Table 8.14.: Modified parameter-related criteria for TTS results, defining whether a PMT can be accepted or should be rejected (see also Table 3.1 again) or should better be double-checked in another container run.
(*) Since ch. 135 is performing equally as the channels from container B, PMTs tested in this channel will be classified according to the criteria of container B as well.
(*) '*Double-check*' range for NNVT PMTs has been defined equally to the one of container B (and thus cut to values $\leq 10\,\text{ns}$).

Parameter	PMT type	**PASSED**	**DOUBLE-CHECK**	**FAILED**
TTS (Container A)*	Hamamatsu	$\leq 2.5\,\text{ns}$	$2.5\,\text{ns} < \text{TTS} \leq 3.2\,\text{ns}$	$> 3.2\,\text{ns}$
	NNVT**	$\leq 8.5\,\text{ns}$	$8.5\,\text{ns} < \text{TTS} \leq 10.0\,\text{ns}$	$> 10.0\,\text{ns}$
TTS (Container B)	Hamamatsu	$\leq 1.7\,\text{ns}$	$1.7\,\text{ns} < \text{TTS} \leq 2.2\,\text{ns}$	$> 2.2\,\text{ns}$
	NNVT	$\leq 7.2\,\text{ns}$	$7.2\,\text{ns} < \text{TTS} \leq 8.7\,\text{ns}$	$> 8.7\,\text{ns}$

assessment of the TTS performance of these PMTs is further shown in Table 8.16. If compared to the more strict criteria from Table 8.2, which do not consider the large systematic uncertainties of the fiber splitters, the ratio of accepted PMTs is significantly increased.

Table 8.15.: Full PMT analysis statistics from analyzed PMT sample (as presented in section 8.1) using different criteria to assess the measured TTS performance. Values from subtables **(a)** and **(c)** are the same as in Table 8.1, while values in subtable **(b)** show statistics if using the modified TTS criteria from Table 8.14.

(a) classification statistics, using the criteria from Table 8.2

	All	Hamamatsu	NNVT	Cont. A	Cont. B
PASSED	229	158	71	20	209
Passed (incomplete)	103	61	42	0	103
DOUBLE-CHECK	607	121	486	274	333
FAILED	504	286	218	441	63

(b) classification statistics, using the criteria from Table 8.14 for the TTS performance

	All	Hamamatsu	NNVT	Cont. A	Cont. B
PASSED	600	307	293	310	290
Passed (incomplete)	103	61	42	0	103
DOUBLE-CHECK	609	204	405	347	262
FAILED	131	54	77	78	53

(c) classification statistics, without any acceptance criteria for TTS results

	All	Hamamatsu	NNVT	Cont. A	Cont. B
PASSED	915	496	419	539	376
Passed (incomplete)	103	61	42	0	103
DOUBLE-CHECK	327	39	288	143	184
FAILED	98	30	68	53	45

Table 8.16.: Classification statistics of only the TTS results, based on the criteria listed in Table 8.2 (upper part) and based on criteria listed in Table 8.14 (lower part). Total pass rate increased from 24.4 % to 64.8 % (from 32.4 % to 61.9 % for Hamamatsu PMTs and from 18.1 % to 67.1 % for NNVT PMTs).

	All	Hamamatsu	NNVT	Cont. A	Cont. B
Valid results	1316	580	736	729	587
PASSED	321	188	133	23	298
DOUBLE-CHECK	451	99	352	196	255
FAILED	544	293	251	510	34
PASSED	853	359	494	419	434
DOUBLE-CHECK	417	192	225	277	140
FAILED	46	29	17	33	13

Conclusion and Outlook

The Jiangmen Underground Neutrino Observatory (JUNO) experiment aims to determine the neutrino mass ordering from the oscillation spectrum of neutrinos from two nuclear power plants with a significance of $3-4\,\sigma$ in six years. To reach this goal, JUNO requires an unprecedented energy resolution of at least $3\,\%/\sqrt{E\,[\mathrm{MeV}]}$, which therefore is the key design goal of this experiment. This can be realized only with high requirements on the detector design, as i.e. a dense instrumentation of the detector volume leading to the tremendous number of 20'000 20-inch PMTs and 25'000 3-inch PMTs to be deployed in the experiment. Particularly the large PMTs are moreover demanded to show an excellent performance in terms of e.g. photo-detection efficiency, dark count rate, timing and charge resolution. Therefore, a dedicated performance test of all 20-inch PMTs is crucial for the success of JUNO, where each PMT has to individually fulfill a set of quality criteria to be accepted for a use in the detector.

In the work at hand, the development, installation and operation of a PMT mass testing system for the 20-inch PMTs of the JUNO experiment based on commercial shipping containers has been presented. The commercial shipping containers are acting as large dark rooms and main frame for the PMT tests. They have been equipped with a shelf system featuring 36 drawer boxes per container, which constitute independent measurement stations for a single PMT in each of them. The containers are further equipped with a HVAC climate control unit, enabling a stable measurement environment with comparable conditions inside, and outfitted with an additional magnetic shielding to suppress the residual magnetic field inside to a level of only around 10 % of the local EMF.
As part of this thesis, vital contributions to these container systems have been made: Two specified light sources have been installed to the drawer boxes, a self-stabilized LED system as well as a picosecond laser system. The light intensities of these light sources have been selected and tailored to match the requirements for a precise determination of various PMT characteristics in different measurement steps. The full light system of the individual channels are moreover optimized to provide a homogeneous illumination of the whole PMT photocathode in the measurements; this has been confirmed also by simulations in accompanying works [281, 299]. Two of the containers were further equipped with (mostly) commercial data taking and readout electronics for the operation and characterization of the PMTs. The control of the electronics as well as the light sources is supervised by a fully automated data acquisition software based on LabVIEW, which has been developed in parallel to the

container systems in the scope of this thesis and an accompanying work [319] as well. This software ensures a reliable and controlled data taking with fixed measurement settings and covers a distinct and sophisticated measurement sequence performing a series of individual measurements on the PMTs for an almost full characterization of all PMT performance parameters; only the originally planned measurement of the afterpulse ratio could not be realized in a reliable way within the container systems, due to conflicting design restrictions for other measurements.
Besides the mechanical and electronic contributions, the readiness and basic performance of each container has been checked in a dedicated commissioning and calibration phase also presented in this thesis. In the process, a sufficient suppression of external magnetic fields inside of the containers down to a level of around $5\,\mu$T could be confirmed. Also, a good light-tightness of the containers even close to the naturally weak spots, as well as a low noise level in the electronics with only negligible contributions to the results was ensured. Further, a measurable influence by crosstalk between the channels of one container was excluded as well.

As second, large part of this thesis, the performance of the container system in the daily operation was verified based on acquired PMT raw data.
At first, a subsample of more than 1400 PMTs has been selected and analyzed in this work in order to prove the capability of the containers to work as a mass testing system for JUNO. The used analysis methods and data-related PMT parameter definitions have been well introduced and explained in detail.
Second, a special focus was laid on the results of the reference PMTs, which are tested together with the untested PMTs in every container run. These reference PMTs are intended to monitor the stability of the system over the entire period of operation and thus are perfect instruments to study the performance of the PMT mass testing system as a whole. In the presented analysis, a stable behavior over time and between the container channels could be observed. The S/N ratio was determined to a stable value clearly above 10 in both systems and for all reference PMTs. Also the light sources (i.e. the measured intensities of the self-stabilized LEDs) are showing a very stable behavior over time, although there are indications for an aging of either the reference PMT or the optical system in container B. For the timing resolution, channel-dependent systematic differences of clearly less than 1 ns are indicated by the results, but are acceptable for the needs of the container system. Only for DCR and P/V ratio, slightly more unstable results have been found; these however can be explained also by e.g. the influence of external effects (such as temperature or illumination prior to the test) in case of the DCR or limitations in the analysis methods in case of the P/V ratio.
Finally, also the overall accuracies in determining the PMT results could be derived from the multiple measurements of the reference PMTs. They are found to be $\sigma \approx 0.6\,\%$ for the absolute uncertainty for the PDE, $< 0.5\,$ns uncertainty for the timing parameters (TTS and PMT pulse shape parameters), $\sigma \approx 3\,$kHz for the DCR, $\sigma \approx 5\,$V in the gain determination measurement for the to-be-applied HV to produce a gain of 10^7, as well as $\sigma \approx 0.5$ for the determination of the P/V ratio and $\sigma \approx 0.015$

for the charge resolution. These values have been confirmed also in a direct comparison of PMT results between the container systems, which further have shown a very good agreement between the two systems. With the noted results, the preassigned goals for the accuracy of the container systems could be proven as achieved.
However, two major systematic effects have been observed in the data analyses: the first is an increased rate of DCR results at container B, most likely caused by an additional yet unknown noise contribution. This offset could be estimated to around $2 - 3\,\mathrm{kHz}$ and seems to be channel-independent. But since the influence of external effects on the DCR is at least in the same order for most of the PMTs, this offset does not constitute a large problem. The second is a large systematic effect in the TTS measurement at container A, which is most likely introduced by the fiber splitter of this container and caused by a deficient repair after a lab incident thus leading to a suboptimal light transfer. The estimated influence (jitter) of the fiber splitter of both systems could be estimated to around $0.6\,\mathrm{ns}$ ($< 0.9\,\mathrm{ns}$) for container B and around $1.9\,\mathrm{ns}$ ($< 2.3\,\mathrm{ns}$) for container A. Based on these results, unfortunately only container B could achieve the design goal of less than 1 ns timing resolution, while container A features a increased timing resolution of around 2 ns.

The two fully equipped PMT container systems have been running for almost three years now in Zhongshan, P.R. China, at the PMT storage site of JUNO with a capacity of 72 tested PMTs per day. Over this time, more than 17'000 PMTs have been examined with the container systems [341, 342] and classified based on their measurement results and dedicated criteria for acceptance, rejection or a retest for a result confirmation. That way, more than 1000 PMTs could be identified as unqualified for a use in JUNO. This is definitely a huge success, emphasizing the importance of the PMT testing for JUNO. It also proves, that the developed and here presented container system can vitally contribute to reach the 3 % goal for the energy resolution in JUNO.

The collected data of ten thousands of 20-inch PMTs constitutes a "treasure", which can be used for JUNO as valuable inputs for both precise detector simulations and a correct interpretation of detector data later on, but could also help to achieve a much deeper knowledge of the performance of the used 20-inch PMTs. Many other topics are worth to be investigated, but would have gone far beyond the scope of this thesis and so are not included into this work: to name only a few, continuative analyses about the long-time stability of the used reference PMTs, possible differences in performance of the tested PMTs before and after the potting or the already discussed features of in particular the MCP-PMTs (such as the observed sub-structures in the TTS plots or the tail of higher charges in the charge spectra, which are not well understood up to date) can be mentioned here. They can also play a role in the final energy reconstruction in the JUNO detector or could even contribute to a better general understanding of the PMT response.
Also the container systems itself can be used as tool for additional surveys. As already noted shortly in section 4.6, container C has been modified by colleagues from JINR to a dedicated long term stability testing system, where PMTs can be tested

for their stability in operation over a full year, but also for possible aging effects by using additional light sources in the channels, which can mimic the constant stress applied to the PMTs by high luminosity muon events in the central JUNO detector. Also a performance test of the potted PMTs using of the final JUNO electronics, as planned to do in container D, will become an interesting topic, especially for JUNO. Furthermore, since few preliminary studies have already indicated that some PMTs are highly sensitive to even small changes in temperature, the containers could be used to test a larger sample of PMTs at different (varying) temperatures using the integrated climate control units, with the possibility to simulate also effects from an accelerated aging.
Summarized, the developed container systems constitute an efficient tool to a deeper understanding of PMTs and can deliver valuable information for JUNO, even long time after their original purpose of providing functionality and acceptance tests for the JUNO instrumentation will have been completed.

If JUNO can reach its aimed specifications, it will become one of the world leading low energy neutrino experiments in the next decade, with the ability to contribute to a broad spectrum of topics in neutrino physics. Preparatory tools for the precise test of detector components (like the container system) will become important also in the planning and realization of other, future experiments to enable even better resolutions and more precise experimental setups and thus to effectively push the frontiers in particle physics forwards more and more on the way to the next pioneering discovery.

Appendix

A. Additional Information about the Container Electronics

A.1. Complete Signal Switching Board PCB

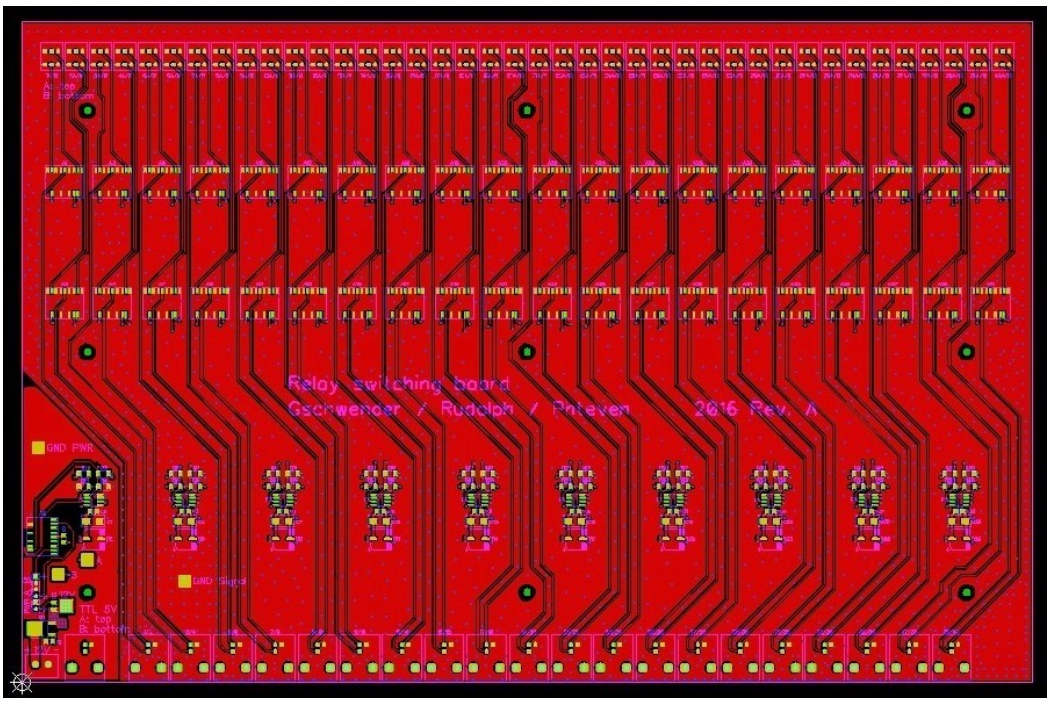

Figure A.1.: This image shows the complete PCB of the SSB, which is basically identical to the one shown in Figure 4.13, but multiplexed to 40 channels. Image credit: Dr. Michael Gschwender and Dr. Matthias Rudolph, Univ. Tübingen.

A.2. Test Measurements using the SSB

A simple test measurement with the SSB have been performed to check for a possible, non-negligible influence on the signal shape of pulses guided through the SSB, which could have a negative effect on the PMT pulse shapes during a use of the SSB in the container system. To investigate this, artificial pulses with an amplitude of 100 mV

and width of 100 ns provided by the pulse generator have been measured using a CAEN V1742 ADC (pulse generator and ADC are of the same type as used in the container system [287, 294]). 5000 pulses have been recorded directly by the ADC as well as after guiding the signals through both SSB outputs. The average pulse forms (including the average arrival time) of all three measurements are shown in Figure A.2.

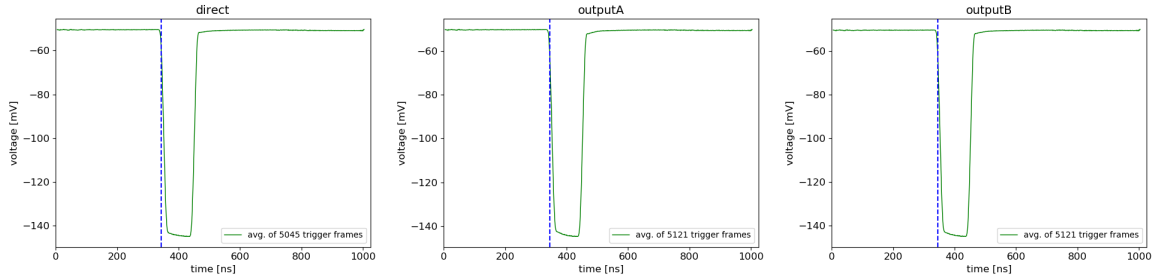

(a) direct connection **(b)** output A of SSB **(c)** output B of SSB

Figure A.2.: Average of 5000 artificial pulses, acquired using the ADC during the SSB test. Pulses are recorded directly or with the SSB connected in between.

From the individual measurements, three subtraction plots have been calculated, with differences *direct to output A*, *direct to output B* and *output A to output B*; the differences are displayed combined in Figure A.3. As visible in the plot, the observed differences are very small. The slightly larger deviations around the pulse edges can be explained with the influence of the ADC jitter on the determination of the average pulse hit time and thus the difficulties to align the pulses in a proper way. Further, the pulse generator seems to struggle with providing reproducible pulses of such a narrow width, leading to a reduced peak amplitude and a slightly oblique pulse plateau, see Figure A.2 again.

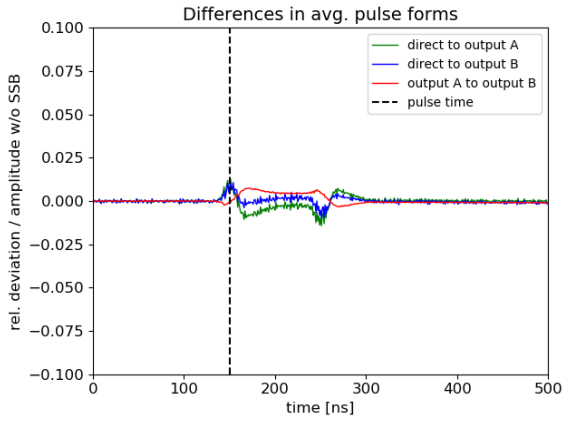

Figure A.3.: Differences of average pulse forms in the SSB test relative to the pulse amplitude of the measurement with the direct connection. Relative differences are in the range of 1 % or less and can be (partially) explained by measurement features. Thus, an influence of the SSB on the pulse shapes or amplitudes can be assumed as negligible.

However even with these difficulties, the observed relative differences in between the measurements are at the level of 1 % or even below. Thus, no significant influence of the SSB on the pulse shape could be confirmed, at least within the measurement conditions / systematics.

A.3. Detailed Container Cabling Scheme

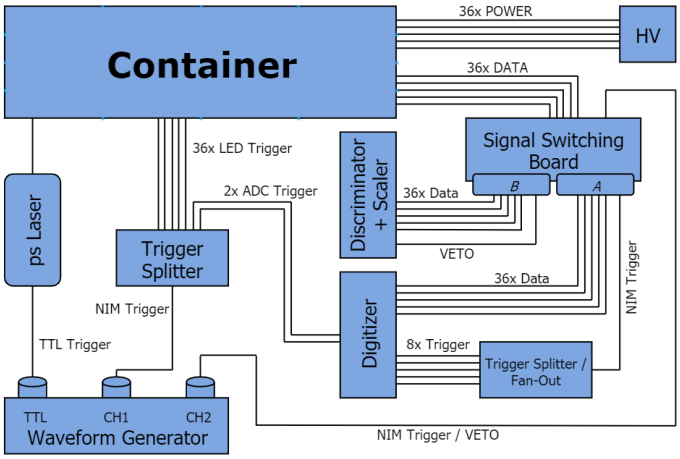

Figure A.4.: Cable scheme of all trigger and signal cables. Triggers for LEDs and ADCs are provided by the waveform generator and distributed by the trigger splitter devices from JINR. The SSB is switching the PMT signals between output `A` (to ADCs) and output `B` (to discriminators). SSB ch. 40 is used as switch for the recorded trigger signals (distributed to ADC channels by a NIM fan-out) and the discriminator VETO signal (only necessary for the APR measurement), both provided by the waveform generator.

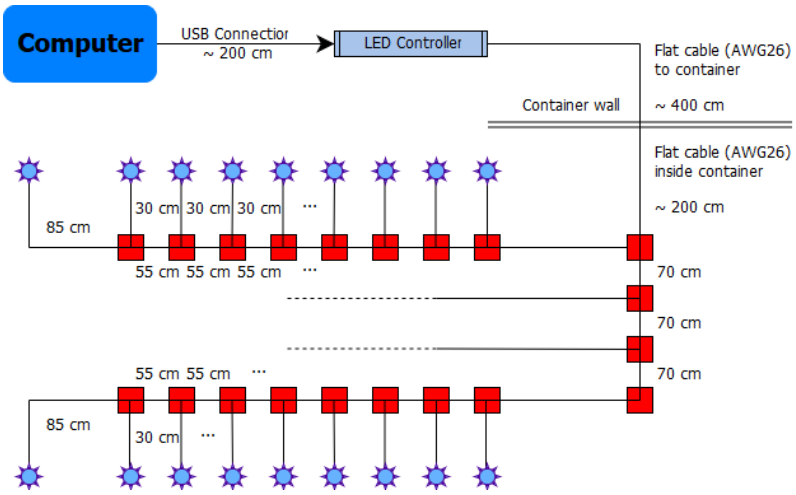

Figure A.5.: Sketch of the flat cable tree inside the container. The flat cable establishes the connection from the LED controller to every LED, placed in the backside of each drawer box. The red boxes are plugs, where flat cable pieces are connected together.

B. Additional Information about the DAQ

B.1. Details about the O.P.S. Scheme

The here shown DAQ scheme is the same as shown in Figure 5.3, but supplemented by some I/O information. Figure B.1 shows the complete modularity of the system with 12 steps individually (de)activatable (highlighted in green). The modular steps can be switched on and off in the "measurement sequence config file" (see Figure B.2) by changing the indicators (`0` / `1`) on the corresponding position.

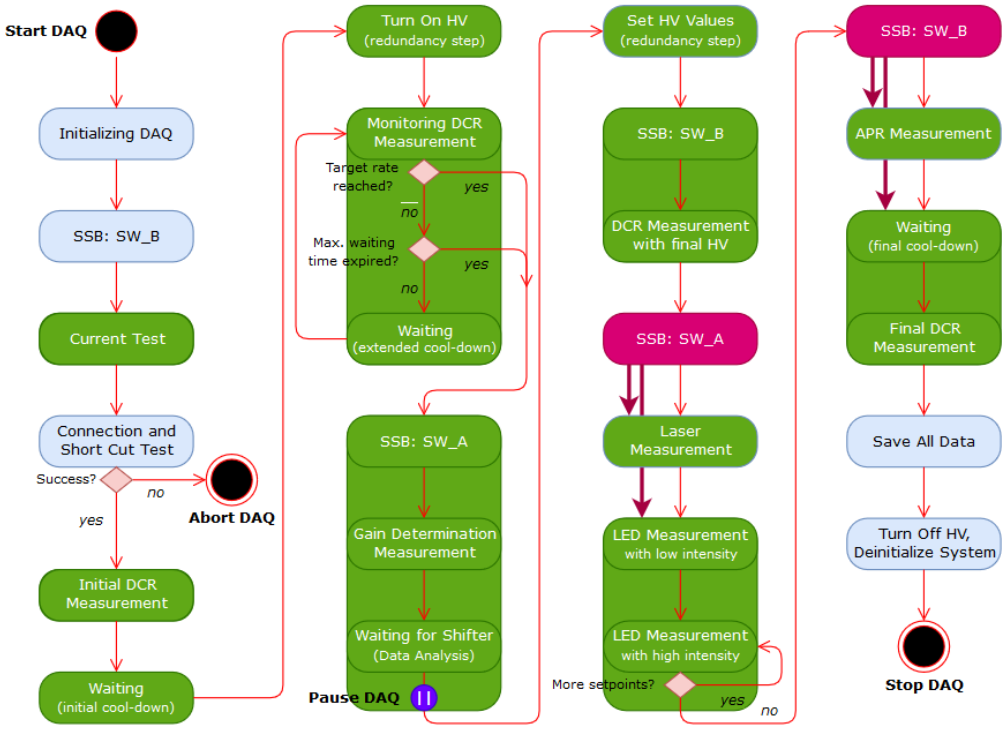

Figure B.1.: Modularity scheme of the DAQ. Blue steps are mandatory, green panels can be (de)activated individually. SSB commands in pink are sent if either of the following two steps is activated (otherwise they are skipped as well).

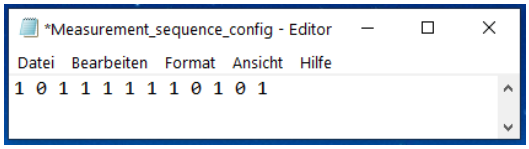

Figure B.2.: Measurement sequence config file of container's DAQ software. In this specific example, all steps are activated except for the initial DCR, the laser measurement and the APR measurement, see also Figure B.1.

For a better overview, the modular steps will be listed again in the following. Each

step is assigned to one `0/1` indicator in the measurement sequence config file (items are listed in correct order):

- `0/1` Initial current test
- `0/1` Initial DCR measurement
- `0/1` Initial waiting time (without DCR monitoring)
- `0/1` HV on redundancy step
- `0/1` PMT cool-down with DCR monitoring
- `0/1` Gain/HV measurement
- `0/1` Set new HV redundancy step
- `0/1` DCR measurement with new gain
- `0/1` Laser measurement
- `0/1` LED measurement
- `0/1` APR measurement
- `0/1` Final DCR measurement, preceded by a short waiting time

Figure B.3 shows the PMT data taking steps of the software (including nine measurement steps with actual data acquisition, highlighted in red).

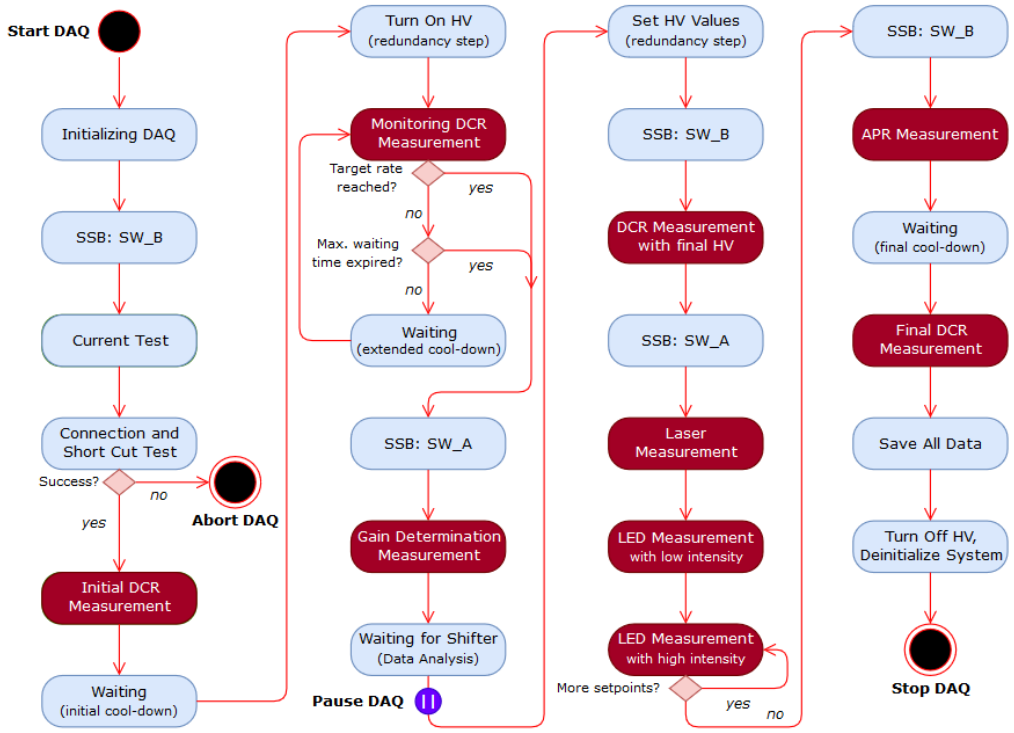

Figure B.3.: Data taking processes of the DAQ. Red boxes indicate steps in which PMT data is acquired and saved to file.

B.2. Assessing the Effect of a 12 Hours Cool-Down Time

To estimate, how well the dark count rates of the PMTs have been stabilized after the nominal cool-down time of $12 - 13$ hours in the containers, the DCR behavior of 20 PMTs from each of the masses **83** and **84** of container B will be checked here. Mass 83 has been selected, because the DCR monitoring was intensified in this run by performing a DCR measurement every 15 minutes instead of the usual 30 minutes (see subsection 5.2.3 again) and by extending the DCR monitoring time to a total of 15 hours; this was done for testing reasons only. Mass 84 has been selected, because this run was performed over a weekend and the cool-down time has been extended therefore to even 36 hours in total at the end.
In Figure B.4 the absolute DCR values from all measurements performed in the container runs are shown, while in Figure B.5, only the values during the monitored cool-down are shown, which have been further normalized to the DCR value measured at the nominal end of the monitored cool-down phase after 12 hours (including the initial waiting time before, the PMTs are staying for 13 hours in darkness at that time, see subsection 5.2.3 once more).

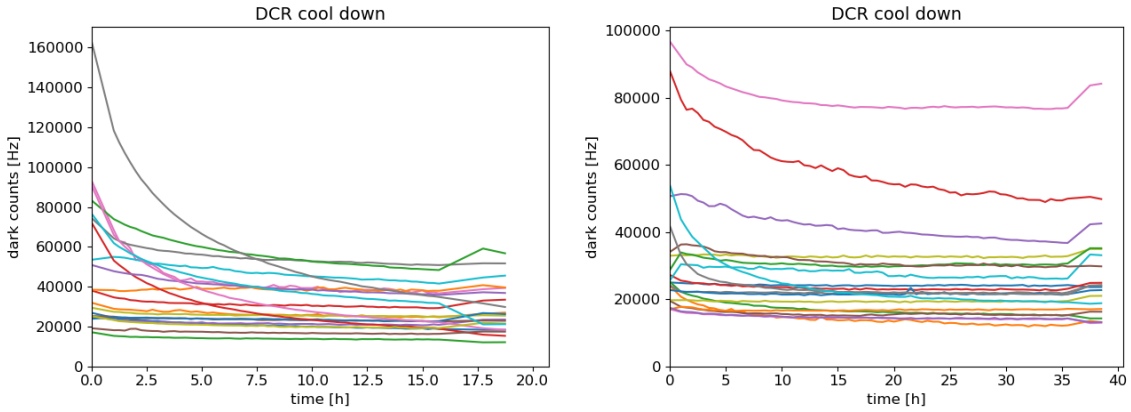

(a) DCR of 20 PMT in mass 83 of container B

(b) DCR of PMTs in mass 84 of container B

Figure B.4.: Monitored DCR cool-down of PMTs from masses 83 and 84 (error bars of individual measurements not displayed here). Not all PMTs can stabilize their dark rate after reaching the end of the defined cool-down phase, however all PMTs show a considerably reduced rate. Therefore, the defined cool-down time of 13 hours within the containers can be stated as suitable for the needs of the PMT testing.

It can be seen, that the vast majority of the here tested PMTs has been at least significantly reduced their DCR up to the end of the nominal cool-down time, although some PMTs still shown a non-stabilized (decreasing) DCR; few of them still show a decreasing trend even after more than 35 hours of staying in darkness. Since the characterization of a single PMT must be completed within 24 hours (including the reloading of the containers), 12 hours seems to be a reasonable compromise, which

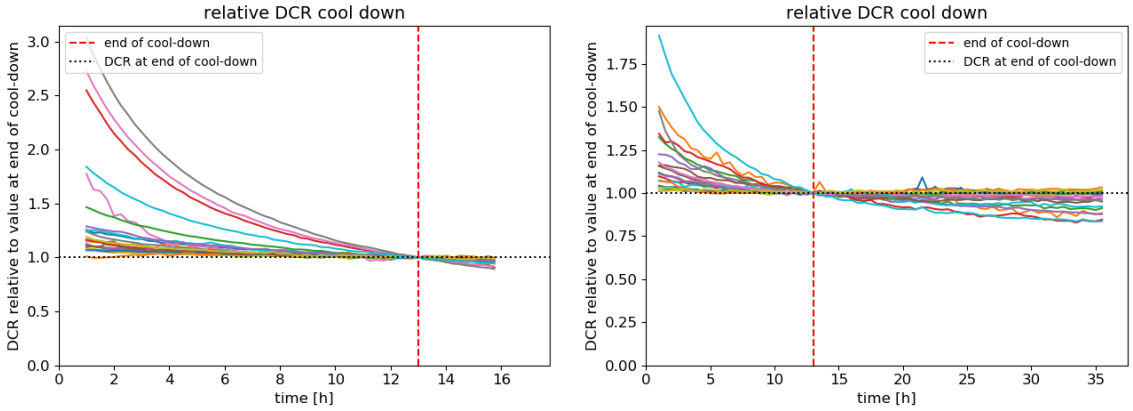

(a) DCR of PMTs during cool-down in mass 83 of container B

(b) DCR of PMTs during cool-down in mass 84 of container B

Figure B.5.: DCR stabilization behavior of PMTs from masses 83 and 84. Data is identical to Figure B.4, but this time normalized to the individual DCR values of the PMTs at the time of the nominal end of the cool-down phase (13 hours in total) .

is also suitable for the needs of the PMT mass testing system. Moreover, a longer waiting time in a regular container run would not be justifiable considering the PMT testing schedule as well as the overall JUNO schedule.

C. PDE Calibration Plots of Container B

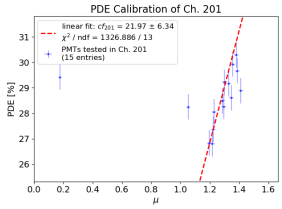

(a) ch. 201

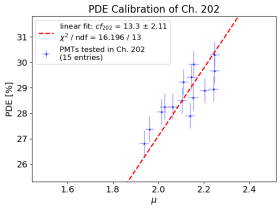

(b) ch. 202

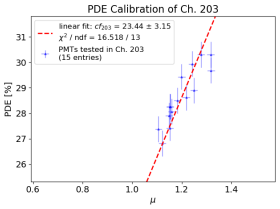

(c) ch. 203

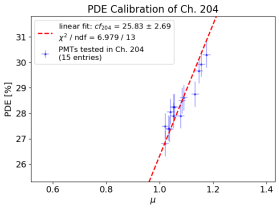

(d) ch. 204

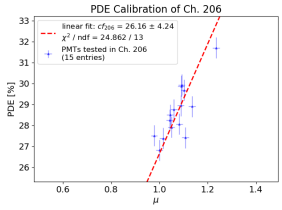

(e) ch. 206

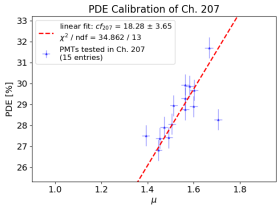

(f) ch. 207

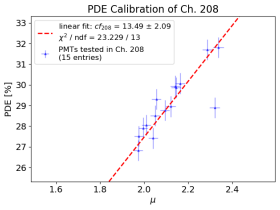

(g) ch. 208

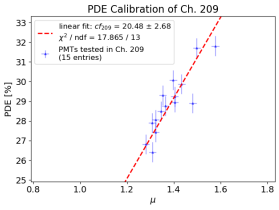

(h) ch. 209

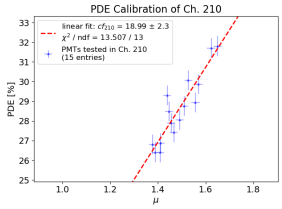

(i) ch. 210

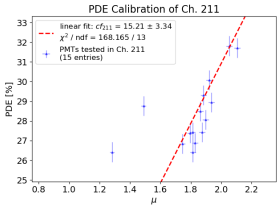

(j) ch. 211

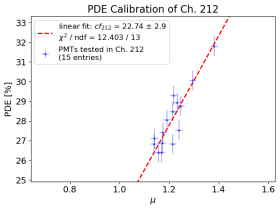

(k) ch. 212

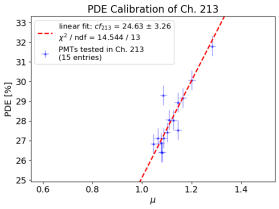

(l) ch. 213

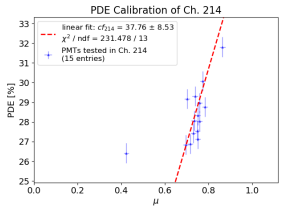

(m) ch. 214

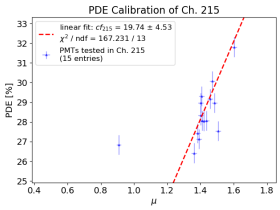

(n) ch. 215

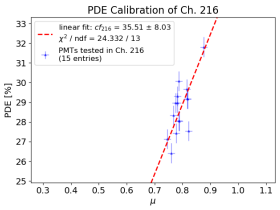

(o) ch. 216

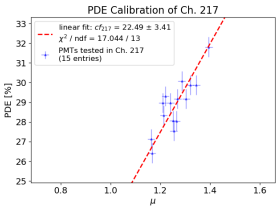

(p) ch. 217

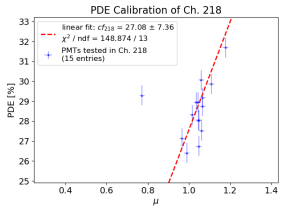

(q) ch. 218

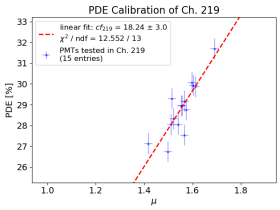

(r) ch. 219

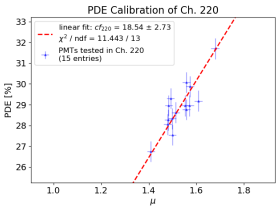

(s) ch. 220

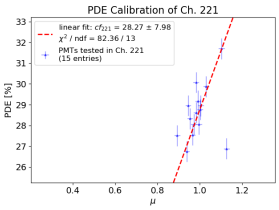

(t) ch. 221

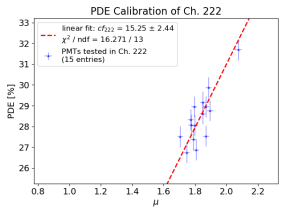

(u) ch. 222

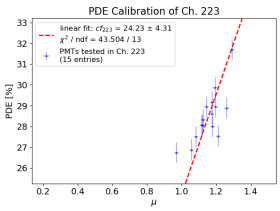

(v) ch. 223

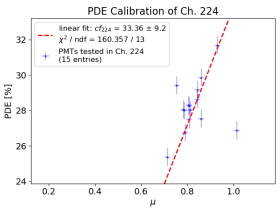

(w) ch. 224

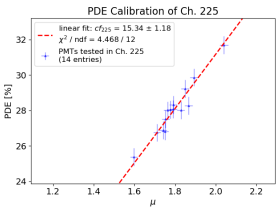

(x) ch. 225

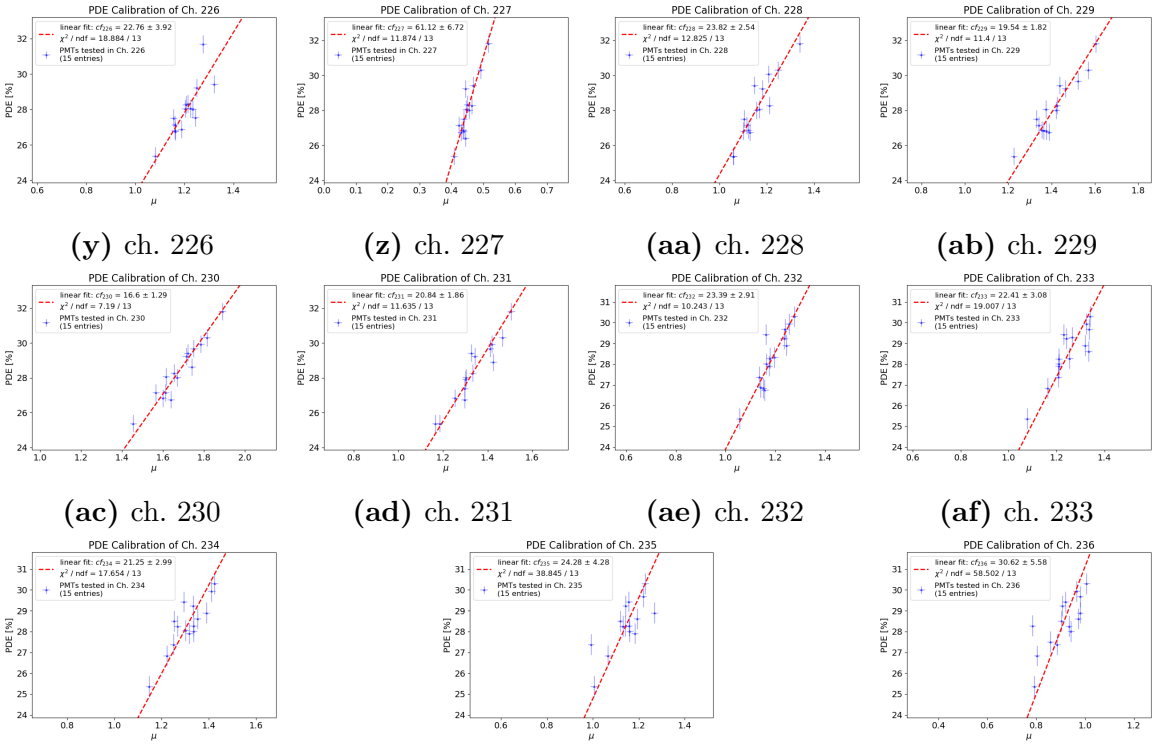

(y) ch. 226 **(z)** ch. 227 **(aa)** ch. 228 **(ab)** ch. 229

(ac) ch. 230 **(ad)** ch. 231 **(ae)** ch. 232 **(af)** ch. 233

(ag) ch. 234 **(ah)** ch. 235 **(ai)** ch. 236

Figure C.1.: Plots with results from the PDE calibration measurements of all channels in container B (except ch. 205, which has been shown already in Figure 6.15). 15 PMTs have been measured in each channel and the results have been fitted with a linear function (intersection has been contained in this fit to [-0.5,0.5] %). The slope of this fit function represents the drawer-dependent calibration factors cf_i of the respective channel i.

D. Additional Information about the Data Analysis Methodology

D.1. Fourier Transforms for Visualization of Noise Reduction in the Raw Data Analysis

Here, the effect of the noise reduction has been visualized by Fast Fourier Transformations (FFTs) of the displayed single frames before (see Figure 7.5a) and after (see Figure 7.5b) the noise subtraction, as well as of the displayed average frames before (see Figure 7.8a) and after (see Figure 7.8a) the noise subtraction.
Figure D.1 shows the FFTs of the single frames before and after the noise subtraction. The plots show, that both frames are dominated by random noise of various frequencies; also the difference of both FFTs shows no clear pattern (see Figure D.1c), but illustrate on the other hand, that contributions of lower frequencies to the random noise are difficult to remove, since they overlap with the PMT pulse.

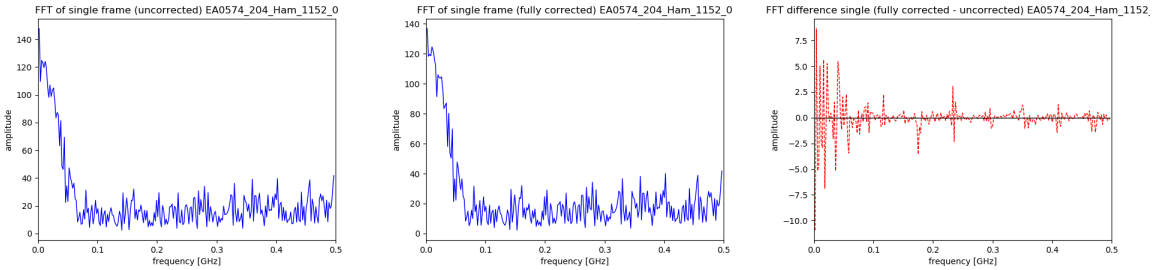

(a) FFT of single frame (uncorrected)

(b) FFT of single frame (corrected)

(c) difference of FFTs after to before the correction

Figure D.1.: Frequency plots after FFT of a single frame (containing a PMT pulse), before (panel **(a)**) and after (panel **(b)**) the noise reduction following the methods presented in subsection 7.2.1. In panel **(c)**, the difference of both plots (fully corrected to uncorrected) is shown.

On the other hand, the situation is more clear for the average frame, as shown in Figure D.2. The plots show again the FFT before and after the noise subtraction. As one would expect from a random noise distribution, its contribution vanished in average leaving only the static noise consisting of mainly a few distinct frequencies; these have been hidden by the random noise in Figure D.1 before. In this case, the difference of both FFTs before and after the correction can clearly prove the removal of these frequencies (see Figure D.2c). The achieved reduction is as intended by the noise subtraction presented in subsection 7.2.1.
Since obviously no frequencies above a values of roughly 100 MHz are contributing to the PMT pulse anymore, which becomes visible especially in Figure D.2b, the possibility of using a low-pass filter for higher frequencies seems to be a good tool to further improve the noise level in the individual frames. The effect of such a

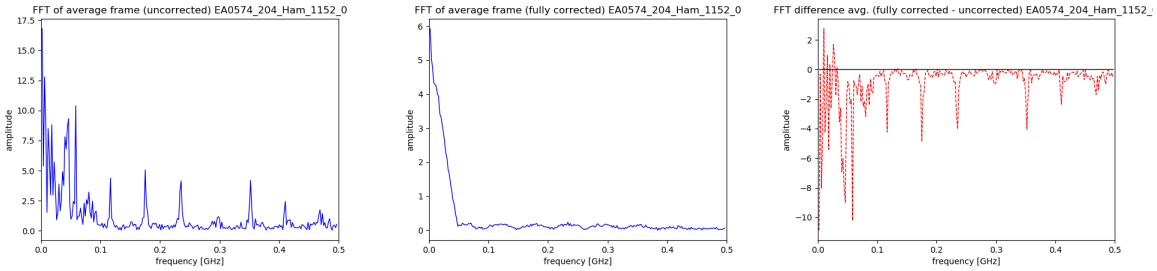

(a) FFT of average frame (uncorrected)

(b) FFT of average frame (corrected)

(c) difference of FFTs after to before the correction

Figure D.2.: Frequency plots after FFT of an average frame (of 25'000 events), before (panel **(a)**) and after (panel **(b)**) the noise reduction has been applied on the individual frames, following the methods presented in subsection 7.2.1. In panel **(c)** the difference of both plots (fully corrected to uncorrected) is shown., indicating the successful removal of few, distinct frequencies related to the static noise.

low-pass filter has been investigated also in [330, 343] before: while in [330] a visible improvement of the random noise level and also no negative influence on the integrated pulse charge has been observed, in [343] however no positive effects on parameters as the S/N ratio or the P/V ratio could be confirmed from such a frequency filter. Further, effects on the actual PMT pulse shape (and thus influences on the results of parameters as RT, FT, amplitude etc.) couldn't be fully excluded in neither of them. Since such a data-related low-pass filter would have been also computationally expensive to process for a large amount of data, it was decided to not use such a low-pass filter in this analysis and rather perform a fit on the PMT pulse forms (as described in section 7.2) to deal with the remaining random noise in the single frames.

D.2. Effect of Different Fitting Methods for the Leading Trigger Edges on the TTS Results

The effect from using different methods to estimate the trigger hit time on the determined TTS values will be estimated here based on few exemplary PMTs. As presented in section 7.4, the trigger hit time can be calculated using different definitions: at 10 % of the leading edge, at 25 % of the leading edge, as well as with and without using "intermediate data points" for the fit of the leading edge. Although the differences between the methods are assumed to be small, they can cause a significant improvement (or worsening) of the determined TTS values particularly in case of the Hamamatsu PMTs, since these can reach a timing resolution of even less than 1 ns.
Since both the pulse generator and the used ADC are providing a very good timing resolutions in the order of $50 - 200$ ps (as stated in their manuals [294, 323]), the contribution of residual jitters from the trigger provision to the determined TTS value should be negligible in case of a perfect data analysis – a non-perfect analysis method therefore cannot underestimate the true TTS of the PMT, while on the other side,

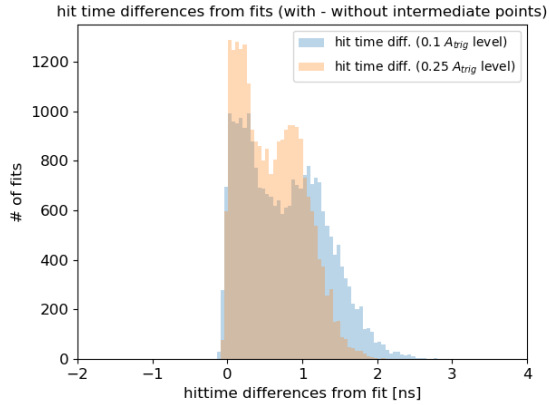

Figure D.3.: Histogram showing the differences between the methods of determining the trigger hit times from the fit of the leading edge for 50'000 triggers. For every trigger waveform, the hit times have been determined with and without using "intermediate data points" in the fit; only the differences from both methods (at both the 10 % and 25 % amplitude level) are collected in this histogram.

an insufficient estimation of the trigger hit time could increase the determined TTS value at the end. This is valid i.e. since the determination of the pulse hit times is not changed between the different, here presented cases. Hence, a possible to-be-observed effect will be directly (and only!) connected to the ability of how well the trigger time can be estimated by the used data analysis method.

Figure D.3 shows the difference in the estimated trigger hit times if using the method with and without the use of "intermediate data points" (IDPs) in fitting the leading trigger edge. The plot shows that the difference in results between both methods is less than 1 ns for most trigger events and, in most cases, smaller if comparing the 25 % amplitude levels w.r.t. comparing the 10 % levels. Furthermore, the plot shows that in very most cases the trigger time is determined closer to the start of the leading edge if using the method without the intermediate data points (for this reason, almost all differences are positive in this plot).
To illustrate the effect on the final TTS values determined in the analysis, data of the three Hamamatsu reference PMTs of container B (**EA0574**, **EA0586** and **EA1437**) have been selected from two masses (**mass 154** and **mass 163**) and analyzed with both methods and with using both hit time criteria (10 % and 25 % amplitude level). The results are listed in Table D.1 and further depicted in Figure D.4. The absolute TTS values also depend of the systematic effects between the container channels and therefore are not of interest here; only the differences from the analysis methods using the same data will be assessed. The results show that in all cases, the hit time defined at 25 % the trigger pulse level shows lower results than in case of the 10 % pulse level condition, and further the method using the IDPs provides significantly lower TTS values in most cases and for both hit time conditions. Moreover, the differences be-

Table D.1.: Data analysis results for the TTS of three reference PMTs of container B, tested in masses 154 and 163. The results of the different analysis methods have been listed separately. While the results from the method using the intermediate data points (IDPs) on the leading trigger edge show very consistent results between the different hit time definitions, the discrepancy is larger if not using the IDPs, and significantly in between the two methods (with and without the IDPs). Absolute values further depend on different systematic uncertainties between the container channels (see also subsection 8.2.3 and subsection 8.4.2) and are therefore not of interest here.

PMT	Ch.	Mass	determined TTS [ns]			
			10 % w/o IDP	25 % w/o IDP	10 % w/ IDP	25 % w/ IDP
EA0586	201	154 (B)	1.26 ± 0.02	1.19 ± 0.02	1.16 ± 0.02	1.14 ± 0.02
EA0574	210	154 (B)	1.39 ± 0.03	1.33 ± 0.03	1.27 ± 0.02	1.25 ± 0.02
EA1437	227	154 (B)	1.42 ± 0.03	1.18 ± 0.02	0.92 ± 0.01	0.84 ± 0.01
EA0586	201	163 (B)	1.29 ± 0.02	1.22 ± 0.02	1.17 ± 0.02	1.15 ± 0.02
EA0574	209	163 (B)	1.44 ± 0.02	1.23 ± 0.02	1.03 ± 0.02	0.95 ± 0.02
EA1437	228	163 (B)	1.57 ± 0.02	1.41 ± 0.01	1.27 ± 0.01	1.22 ± 0.01

tween the different hit time conditions are larger if not adding the IDPs, and are only small (< 0.1 ns in this example) if using this trick. Since the chosen analysis methods can only worsen the determined result but not bias it to better (lower) values than the actually true TTS of the PMT (as discussed above), the method including the additional points and using the 25 % trigger pulse level as hit time definition can be stated as the best performing of all tested methods. This is also as expected from the discussion in subsection 7.4.1: this method concentrates more on the trend around the center of the leading edge and further better straightens out the effects of noise (and therefore is able to provide more precise results for the true position of the leading trigger edge), while the method without the IDPs is more sensitive to noise on the leading trigger edge and the 10 % trigger level condition can be easier influenced by noise at the kinks of the trigger edges or overshoot effects from the trigger pulse generation.
In the final data analysis as shown in chapter 8, the given TTS values usually represent the means of the TTS values using the 10 and 25 % level condition, with always using the IDP method.

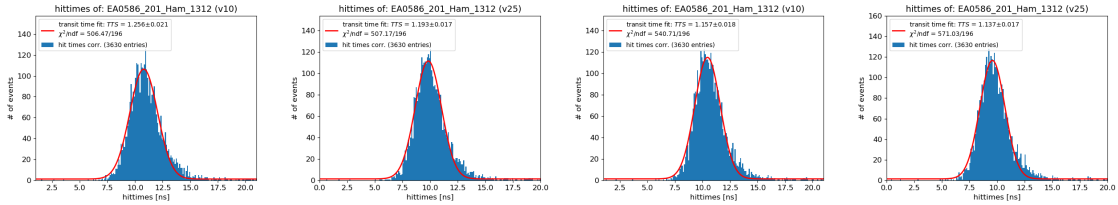

(a) EA0586, 10 % w/o IDP **(b)** EA0586, 25 % w/o IDP **(c)** EA0586, 10 % w/ IDP **(d)** EA0586, 25 % w/ IDP

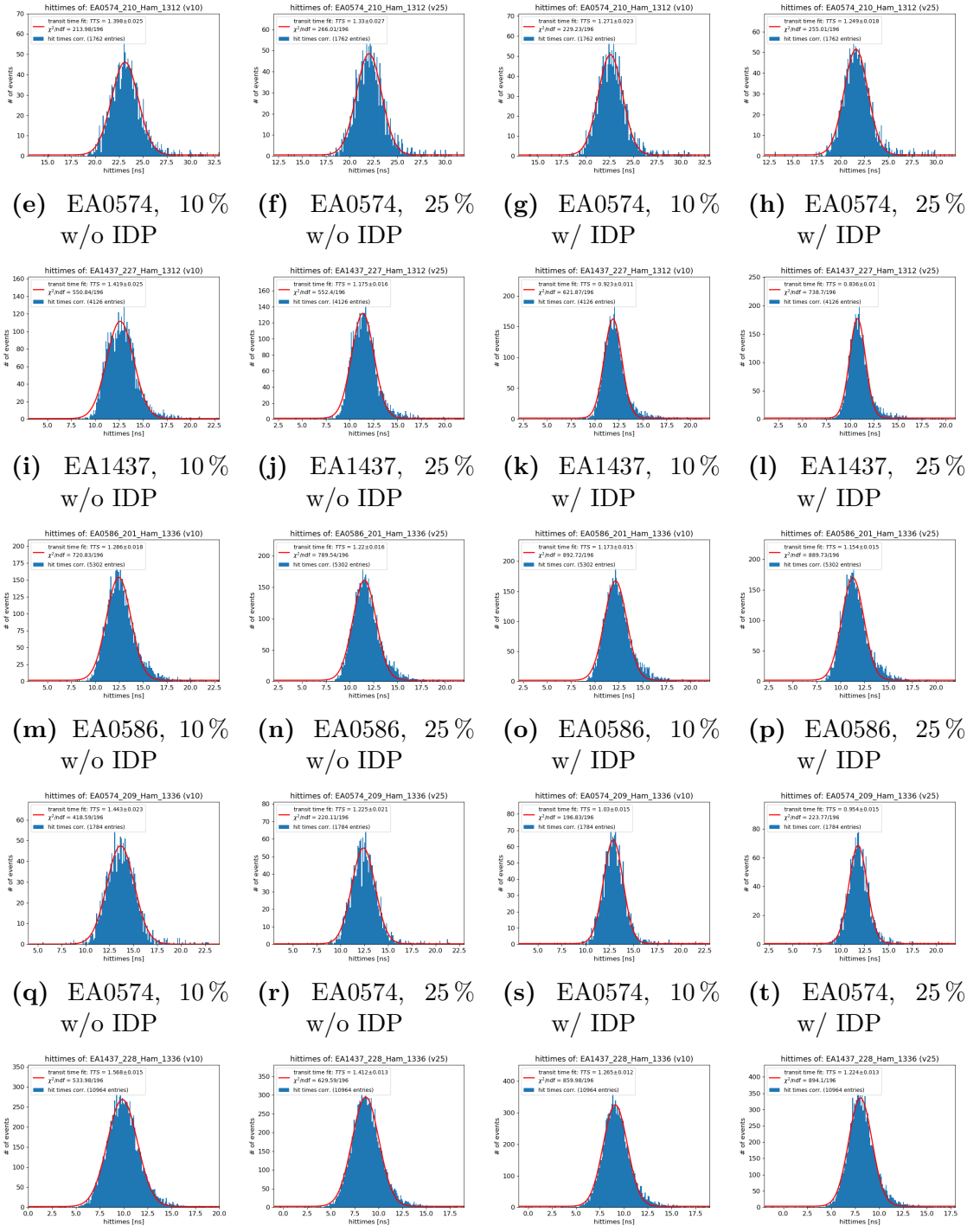

(e) EA0574, 10 % w/o IDP **(f)** EA0574, 25 % w/o IDP **(g)** EA0574, 10 % w/ IDP **(h)** EA0574, 25 % w/ IDP

(i) EA1437, 10 % w/o IDP **(j)** EA1437, 25 % w/o IDP **(k)** EA1437, 10 % w/ IDP **(l)** EA1437, 25 % w/ IDP

(m) EA0586, 10 % w/o IDP **(n)** EA0586, 25 % w/o IDP **(o)** EA0586, 10 % w/ IDP **(p)** EA0586, 25 % w/ IDP

(q) EA0574, 10 % w/o IDP **(r)** EA0574, 25 % w/o IDP **(s)** EA0574, 10 % w/ IDP **(t)** EA0574, 25 % w/ IDP

(u) EA1437, 10 % w/o IDP **(v)** EA1437, 25 % w/o IDP **(w)** EA1437, 10 % w/ IDP **(x)** EA1437, 25 % w/ IDP

Figure D.4.: TTS data plots of reference PMTs using different methods and hit time definitions for the trigger time determination. Although the different methods lead to only small changes in the widths of the spectra (and so the determined TTS values of the PMTs), the effect can however become significant due to the overall low TTS values of the Hamamatsu PMTs. Plots in panels **(a)** to **(l)** represent data from mass 154, plots in panels **(m)** to **(x)** represent data from mass 163.

D.3. Detailed Results from the Reference PMT Data Analysis

Here, all result plots belonging to the data analysis (full characterization) of the two reference PMTs **EA1437** and **PA1704-108**, as discussed in section 7.5, are shown. All details about the analysis algorithms can be found in chapter 7. Results from the analysis of these PMTs are listed in Table 7.2.

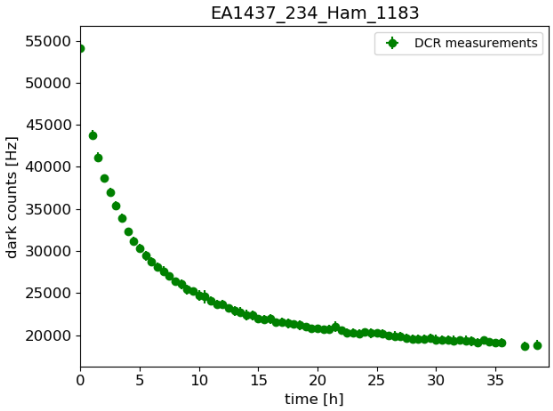

(a) DCR cool-down over a total time of 36 hours (EA1437)

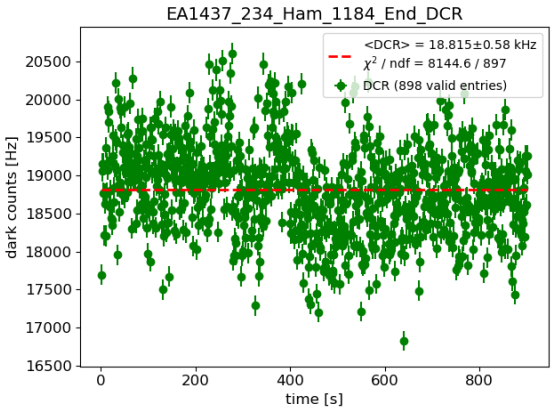

(b) raw data from final DCR measurement (EA1437)

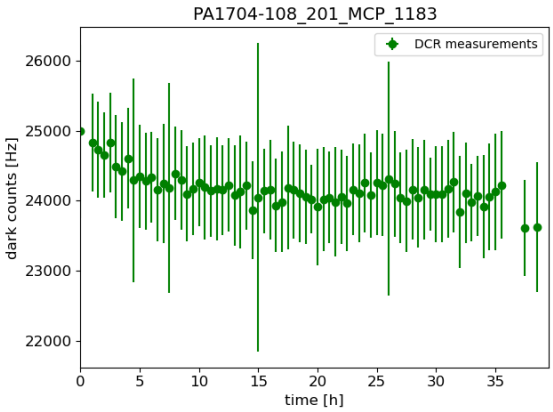

(c) DCR cool-down over a total time of 36 hours (PA1704-108)

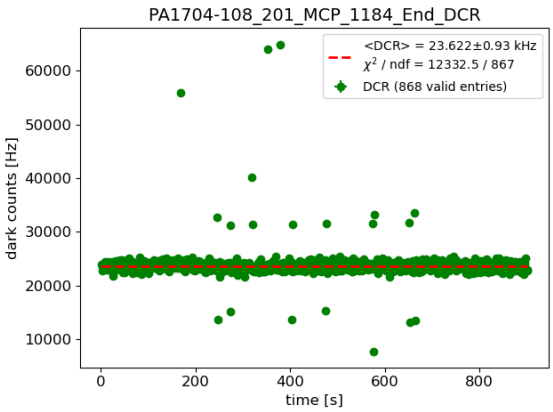

(d) raw data from final DCR measurement (PA1704-108)

Figure D.5.: Data plots of PMTs **EA1437** (panels **(a)** and **(b)**) and **PA1704-108** (panels **(c)** and **(d)**) from DCR measurements of mass 84. In the left panels, the results from multiple DCR measurements during the container run are depicted, showing the stabilization of the DCR over the time of staying in darkness (DCR "cool-down"). Since this run was taken over the weekend, the total cool-down time was extended to 36 hours (from 12 hours usually). In the right panels, DCR raw data from final step at the very end of the measurement sequence is shown (last data point in the left panels). Distributions are fitted with a flat function (red line).

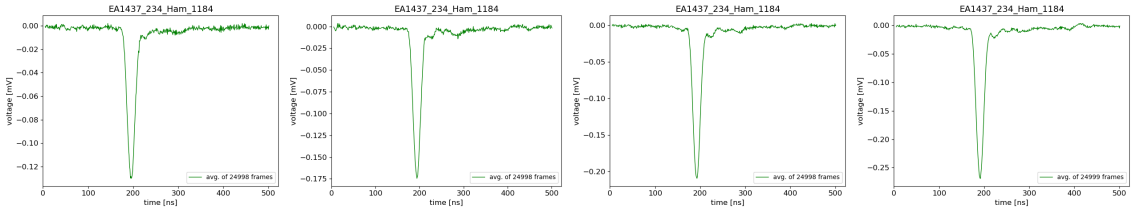

(a) avg. waveform at $V_0 - 150\,\mathrm{V}$ **(b)** avg. waveform at $V_0 - 100\,\mathrm{V}$ **(c)** avg. waveform at $V_0 - 50\,\mathrm{V}$ **(d)** avg. waveform at V_0

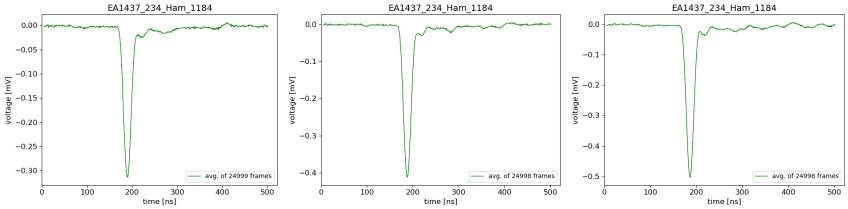

(e) avg. waveform at $V_0 + 50\,\mathrm{V}$ **(f)** avg. waveform at $V_0 + 100\,\mathrm{V}$ **(g)** avg. waveform at $V_0 + 150\,\mathrm{V}$

Figure D.6.: Average waveforms (with full baseline correction and noise reduction) of PMT **EA1437** from gain determination measurement of mass 84. 25'000 frames have been recorded in each step at different voltages (with a light intensity of $\mu \sim 0.1\,\mathrm{p.e.}$). Voltage $V_0 = 1630\,\mathrm{V}$ is the supply voltage proposed by the manufacturer (Hamamatsu).

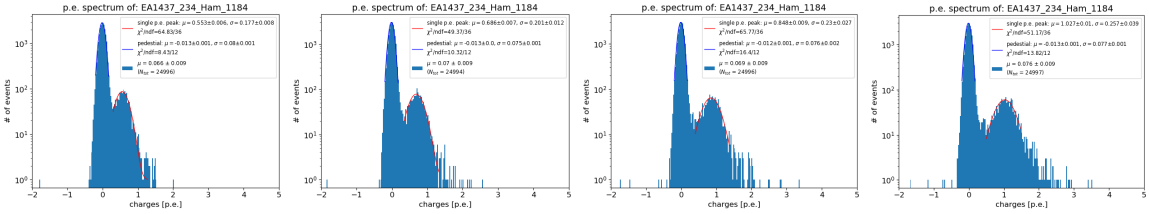

(a) charge spectrum at $V_0 - 150\,\mathrm{V}$ **(b)** charge spectrum at $V_0 - 100\,\mathrm{V}$ **(c)** charge spectrum at $V_0 - 50\,\mathrm{V}$ **(d)** charge spectrum at V_0

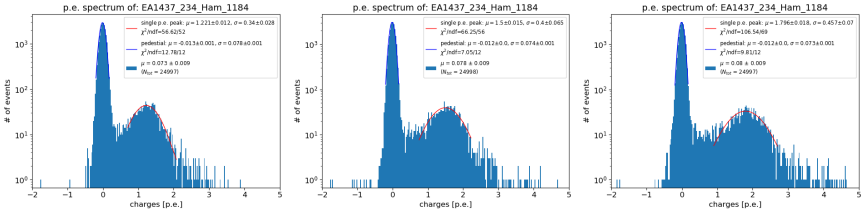

(e) charge spectrum at $V_0 + 50\,\mathrm{V}$ **(f)** charge spectrum at $V_0 + 100\,\mathrm{V}$ **(g)** charge spectrum at $V_0 + 100\,\mathrm{V}$

Figure D.7.: Charge spectra of PMT **EA1437** of all steps in the gain determination measurement of mass 84 with different voltages applied (with $\mu \sim 0.1\,\mathrm{p.e.}$, see plots). X-axis displays charge in units of p.e. for an applied gain of 10^7 ($1\,\mathrm{p.e.} \equiv 1.602\,\mathrm{pC}$, binning $0.040\,\mathrm{pC/bin}$). Fit of pedestal (in blue) and SPE peak (in red) are used for determination of the actual gain of the PMT from the spectrum. Voltage $V_0 = 1630\,\mathrm{V}$ is the supply voltage proposed by the manufacturer (Hamamatsu).

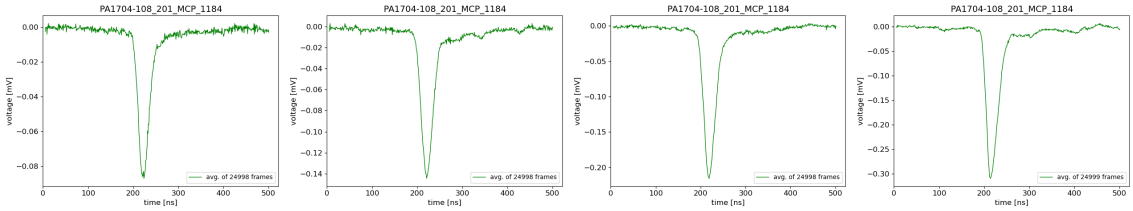

(a) avg. waveform at $V_0 - 150\,\mathrm{V}$ **(b)** avg. waveform at $V_0 - 100\,\mathrm{V}$ **(c)** avg. waveform at $V_0 - 50\,\mathrm{V}$ **(d)** avg. waveform at V_0

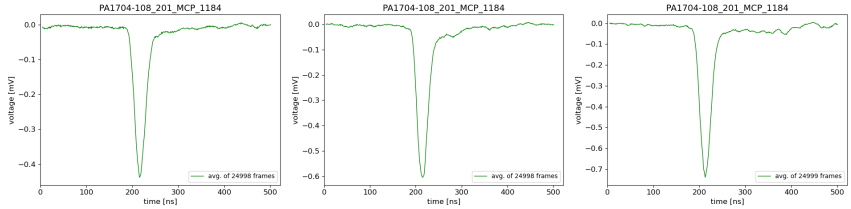

(e) avg. waveform at $V_0 + 50\,\mathrm{V}$ **(f)** avg. waveform at $V_0 + 100\,\mathrm{V}$ **(g)** avg. waveform at $V_0 + 150\,\mathrm{V}$

Figure D.8.: Average waveforms (with full baseline correction and noise reduction) of PMT **PA1704-108** from gain determination measurement of mass 84. 25'000 frames have been recorded in each step at different voltages (with a light intensity of $\mu \sim 0.1\,\mathrm{p.e.}$). Voltage $V_0 = 1770\,\mathrm{V}$ is the supply voltage proposed by the manufacturer (NNVT).

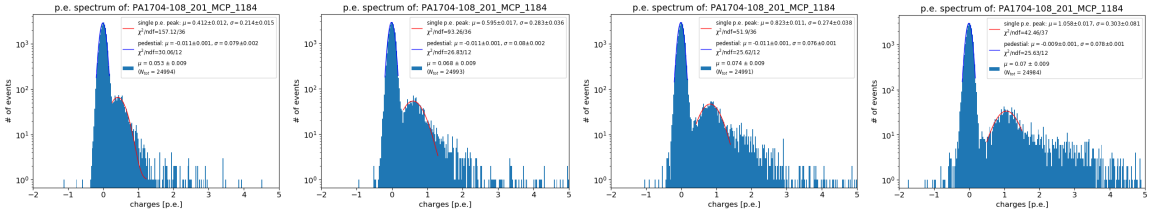

(a) charge spectrum at $V_0 - 150\,\mathrm{V}$ **(b)** charge spectrum at $V_0 - 100\,\mathrm{V}$ **(c)** charge spectrum at $V_0 - 50\,\mathrm{V}$ **(d)** charge spectrum at V_0

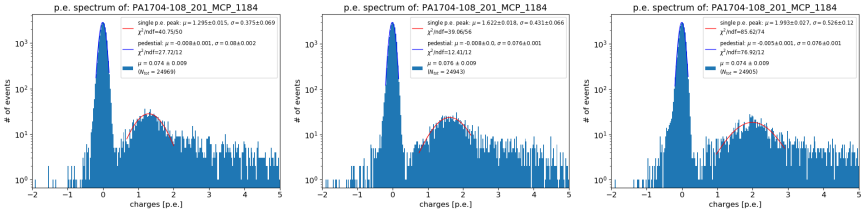

(e) charge spectrum at $V_0 + 50\,\mathrm{V}$ **(f)** charge spectrum at $V_0 + 100\,\mathrm{V}$ **(g)** charge spectrum at $V_0 + 100\,\mathrm{V}$

Figure D.9.: Charge spectra of PMT **PA1704-108** of all steps in the gain determination measurement of mass 84 with different voltages applied (with $\mu \sim 0.1\,\mathrm{p.e.}$, see plots). X-axis displays charge in units of p.e. for an applied gain of 10^7 ($1\,\mathrm{p.e.} \equiv 1.602\,\mathrm{pC}$, binning $0.040\,\mathrm{pC/bin}$). Fit of pedestal (in blue) and SPE peak (in red) are used for determination of the actual gain of the PMT from the spectrum. Voltage $V_0 = 1770\,\mathrm{V}$ is the supply voltage proposed by the manufacturer (NNVT). At higher gains, the tail of the charge spectrum becomes more distinct.

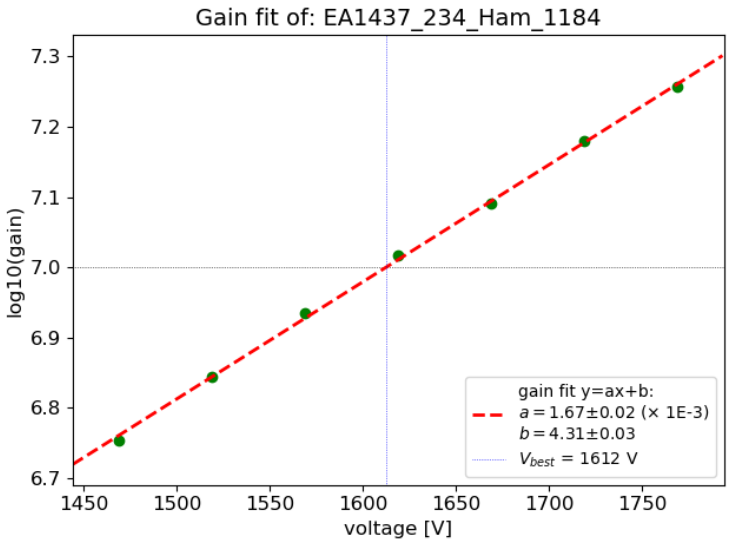

Figure D.10.: Result of gain/HV-measurement of PMT **EA1437** from mass 84. Data points display the individual gains extracted from the plots in Figure D.7. Y-axis is logarithmic, so displayed linear fit (red line) is actually a power function. Final voltage V_{best} for a gain of 10^7 is indicated by the black/blue dotted cross and displayed in the legend.

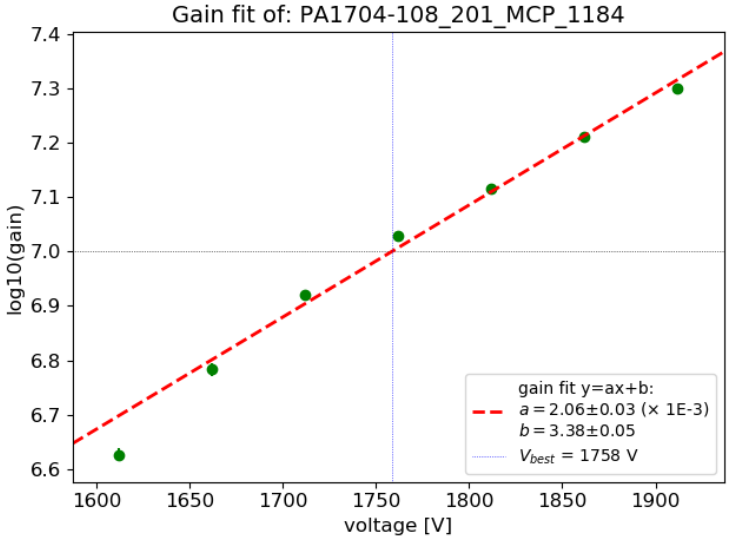

Figure D.11.: Result of gain/HV-measurement of PMT **PA1704-108** from mass 84. Data points display the individual gains extracted from the plots in Figure D.9. Y-axis is logarithmic, so displayed linear fit (red line) is actually a power function. From displayed results, dependence of gain to voltage seems to be slightly hyperbolic, which is caused by the tail in the charge spectrum that becomes more distinct at higher gains (at expenses of the shape of the SPE peak, see also Figure D.9). Final voltage V_{best} for a gain of 10^7 is indicated by the black/blue dotted cross and displayed in the legend.

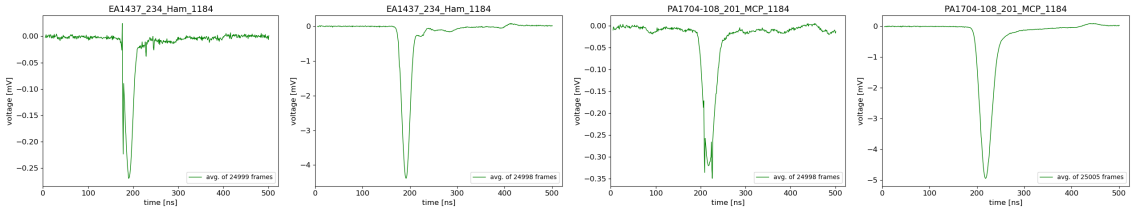

(a) avg. waveform at low light intensity (EA1437)

(b) avg. waveform at high light intensity (EA1437)

(c) avg. waveform at low light intensity (PA1704-108)

(d) avg. waveform at high light intensity (PA1704-108)

Figure D.12.: Average waveforms (with full baseline correction and noise reduction) of PMTs **EA1437** (panels **(a)** and **(b)**) and **PA1704-108** (panels **(c)** and **(d)**), from LED measurement of mass 84, using a low (panels **(a)** and **(c)**) and a high (panels **(b)** and **(d)**) light intensity. 25'000 frames have been recorded in each measurement.

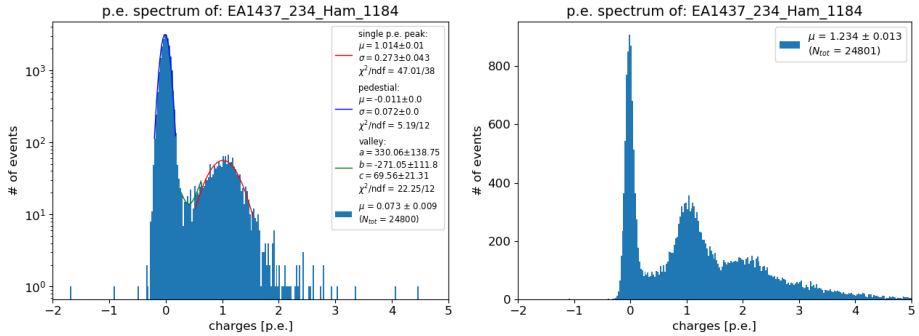

(a) charge spectrum at low light intensity (EA1437)

(b) charge spectrum at high light intensity (EA1437)

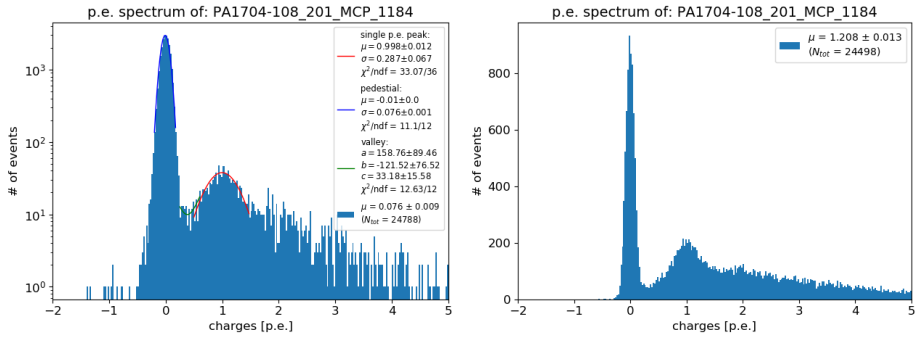

(c) charge spectrum at low light intensity (PA1704-108)

(d) charge spectrum at high light intensity (PA1704-108)

Figure D.13.: Charge spectra of PMTs **EA1437** (panels **(a)** and **(b)**) and **PA1704-108** (panels **(c)** and **(d)**) from LED measurement of mass 84. X-axis displays charge in units of p.e. for an applied gain of 10^7 (1 p.e. $\equiv$ 1.602 pC, binning 0.040 pC/bin). Fits of pedestal (in blue), SPE peak (in red) and valley (in green) in panels **(a)** and **(c)** are used for calculation of several PMT parameters; spectra in panels **(b)** and **(d)** are used only for PDE calculation.

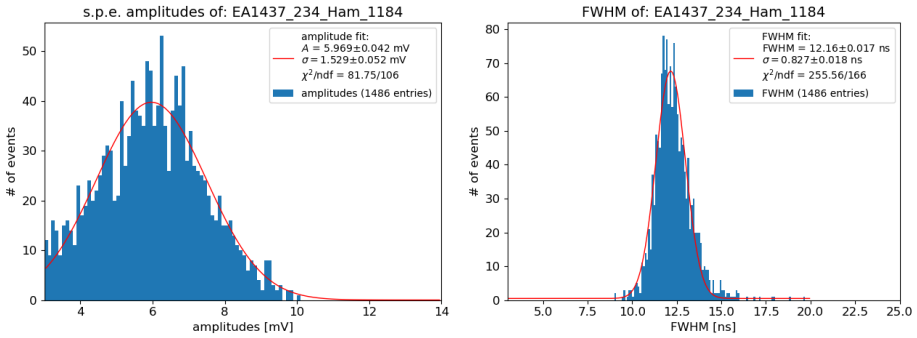

(a) amplitudes of EA1437

(b) FWHMs of EA1437

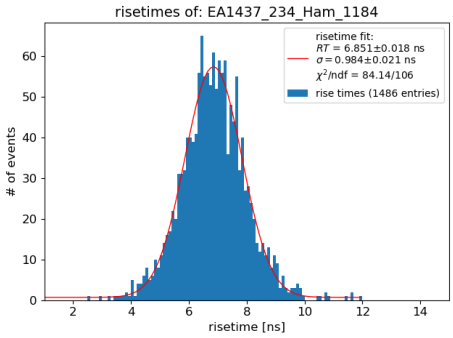

(c) RTs of EA1437

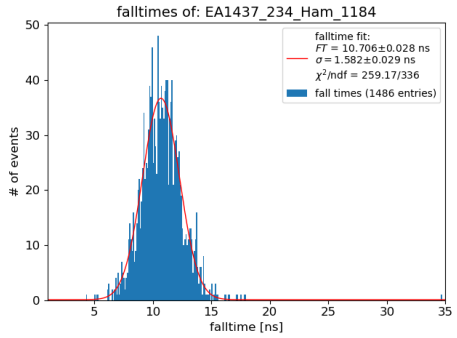

(d) FTs of EA1437

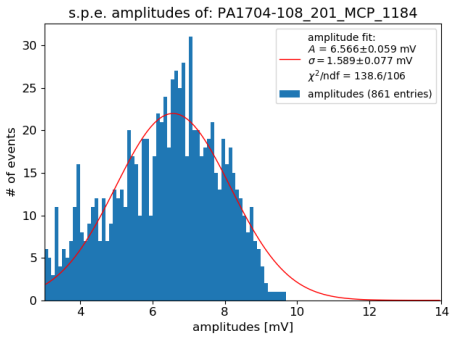

(e) amplitudes of PA1704-108

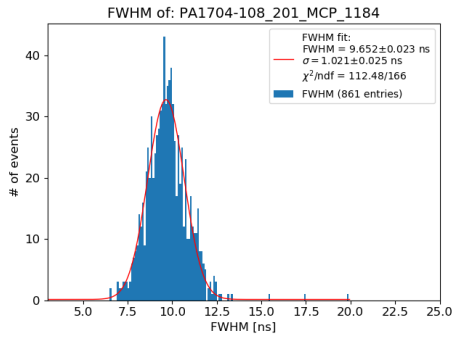

(f) FWHMs of PA1704-108

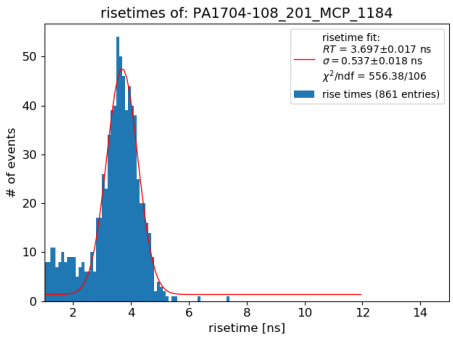

(g) RTs of PA1704-108

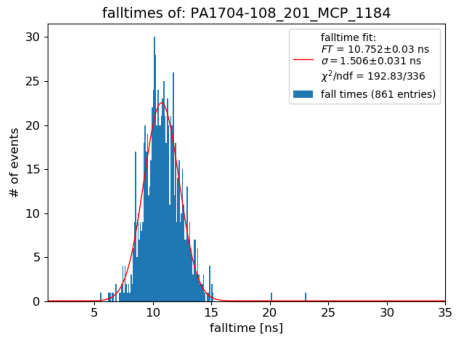

(h) FTs of PA1704-108

Figure D.14.: Parameters of PMTs **EA1437** (panels **(a)** to **(d)**) and **PA1704-108** (panels **(e)** to **(h)**), extracted from SPE pulse shapes from the LED measurement of mass 84. Distributions are binned with 0.1 mV/bin or 0.1 ns/bin respectively, and fitted with Gaussian functions.

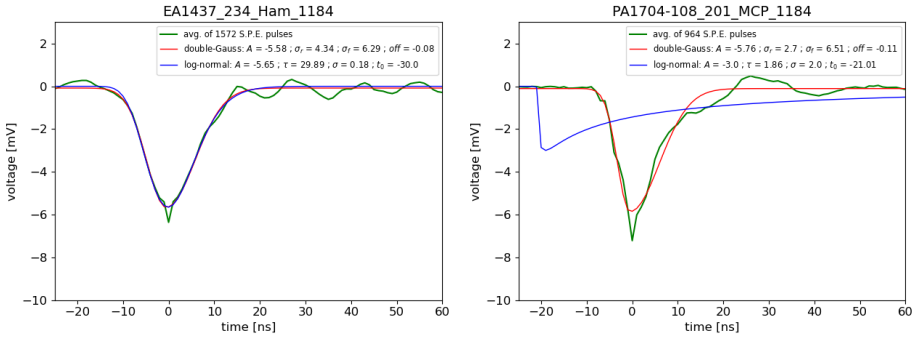

(a) fitted average SPE waveform of EA1437

(b) fitted average SPE waveform of PA1704-108

Figure D.15.: Fit of average SPE waveforms of PMTs **EA1437** (panel **(a)**) and **PA1704-108** (panel **(b)**) from LED measurement of mass 84 at low light intensity. 25'000 frames have been recorded selected for frames containing SPE pulses (1572 in panel **(a)**, 964 in panel **(b)**); these frames have been averaged and fitted using Equation 7.6 and Equation 7.7. In panel **(b)**, the log-normal fit completely fails for this average pulse form.

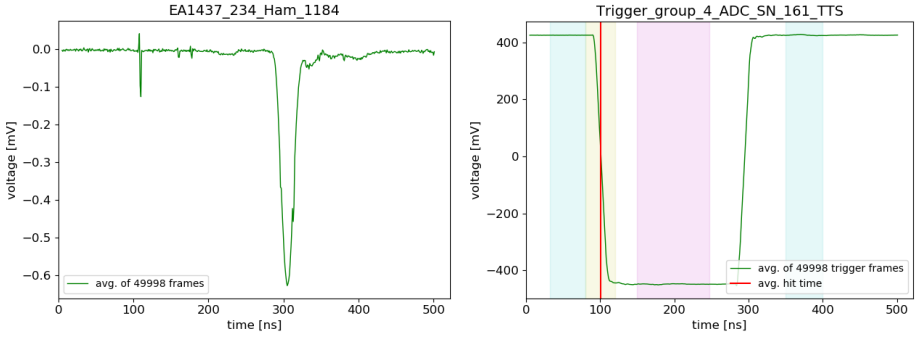

(a) average waveform of laser measurement (EA1437)

(b) corresponding average trigger pulse

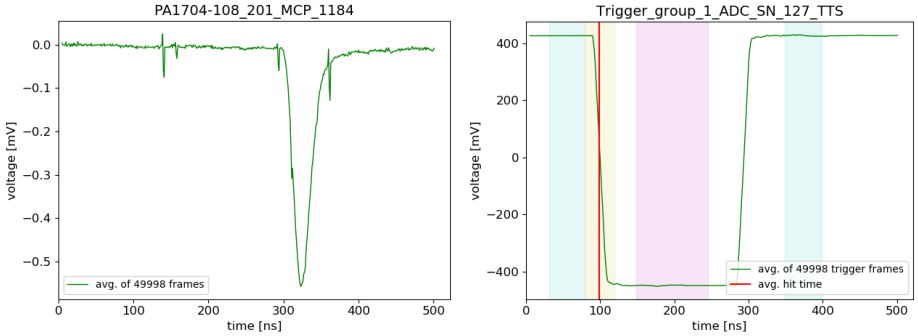

(c) average waveform of laser measurement (PA1704-108)

(d) corresponding average trigger pulse

Figure D.16.: Average waveforms (with full baseline correction and noise reduction) of PMTs **EA1437** (panel **(a)**) and **PA1704-108** (panel **(c)**) from laser measurement of mass 84, and corresponding average trigger pulse forms (panels **(b)** and **(d)**) from the same ADC trigger group. 50'000 frames have been recorded for each PMT. The fitting ranges for the trigger pulses are colorized, see subsection 7.4.1 for details.

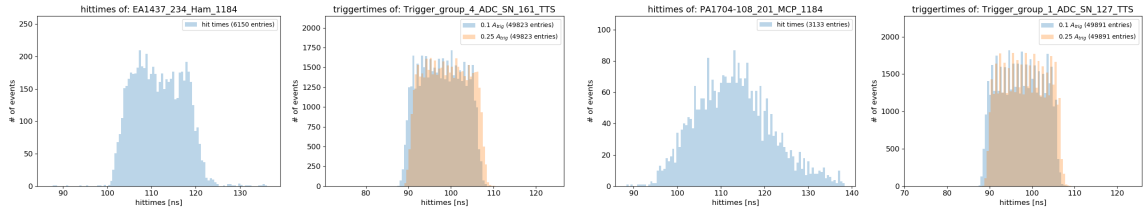

(a) pulse hit time distribution (EA1437)

(b) corresponding trigger hit time distribution

(c) pulse hit time distribution (PA1704-108)

(d) corresponding trigger hit time distribution

Figure D.17.: Hit time distributions of laser measurement (pulses of PMTs **EA1437** and **PA1704-108** in panels **(a)** and **(c)** and corresponding trigger pulses in panels **(b)** and **(d)**) of mass 84. Small spikes are artifacts from the binning in the plots (0.5 ns/bin). For the trigger hit times, the two slightly shifted distributions are displaying different hit time definitions ($0.1 \cdot A_{\text{trig}}$ or at $0.25 \cdot A_{\text{trig}}$), see subsection 7.4.1 for details.

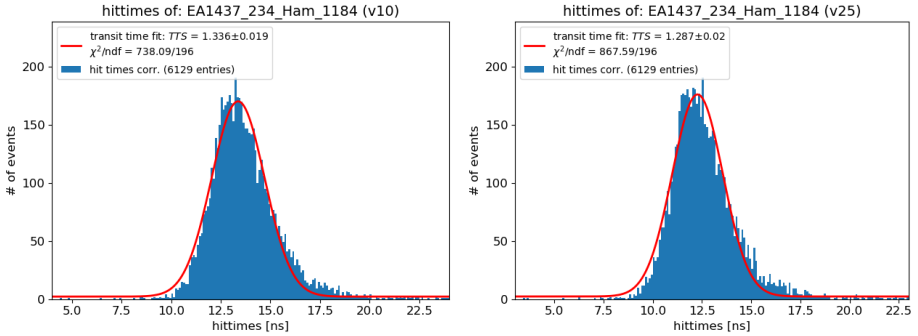

(a) TTS of EA1437 (using $0.1 \cdot A_{\text{trig}}$ as reference)

(b) TTS of EA1437 (using $0.25 \cdot A_{\text{trig}}$ as reference)

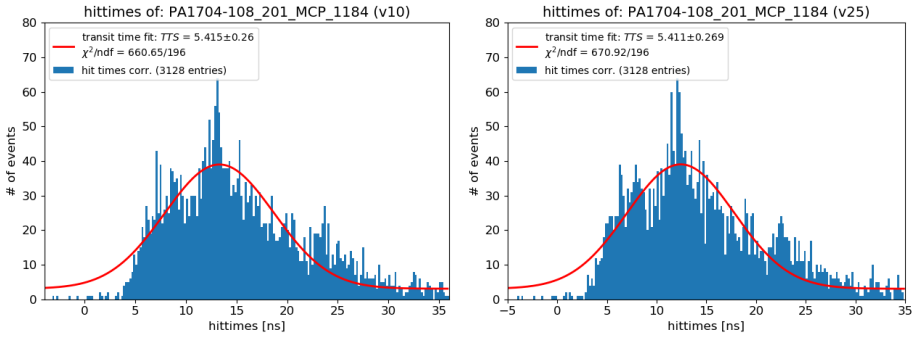

(c) TTS of PA1704-108 (using $0.1 \cdot A_{\text{trig}}$ as reference)

(d) TTS of PA1704-108 (using $0.25 \cdot A_{\text{trig}}$ as reference)

Figure D.18.: Net hit time distribution (cleared from ADC jitter) of PMTs **EA1437** (panels **(a)** and **(b)**) and **PA1704-108** (panels **(c)** and **(d)**) from mass 84, using the data from Figure D.17 and the two different trigger time definitions ($0.1 \cdot A_{\text{trig}}$ in panels **(a)** and **(c)** and $0.25 \cdot A_{\text{trig}}$ in panels **(b)** and **(d)**). TTS can be extracted by a Gaussian fit of the distribution (final TTS value is defined here as mean of both). Some MCP-PMTs show a substructure in their transit time profiles, which raises the question whether a single Gaussian function is suitable to estimate the TTS of an MCP-PMT (see also discussion in subsection 7.4.2).

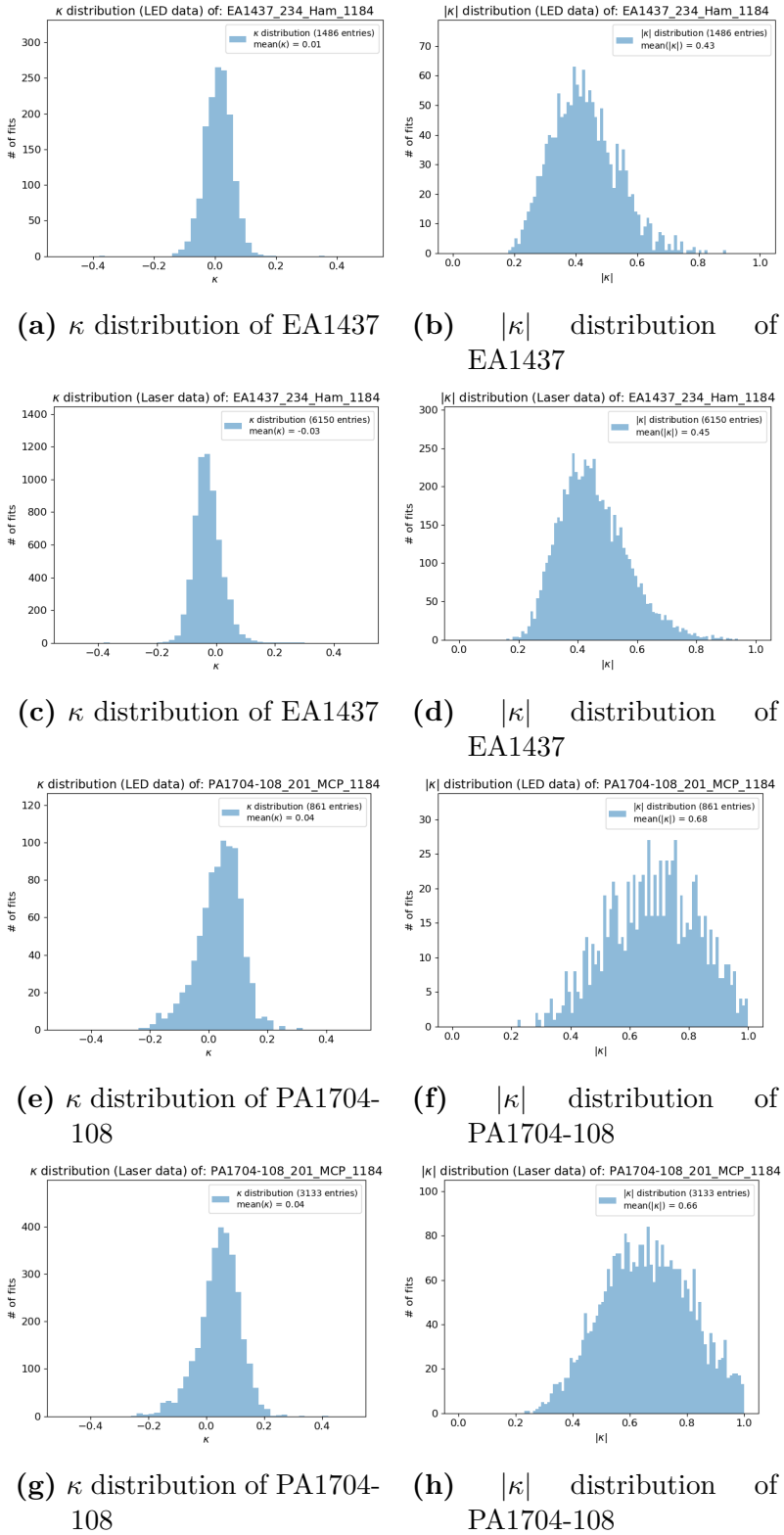

(a) κ distribution of EA1437 **(b)** $|\kappa|$ distribution of EA1437

(c) κ distribution of EA1437 **(d)** $|\kappa|$ distribution of EA1437

(e) κ distribution of PA1704-108 **(f)** $|\kappa|$ distribution of PA1704-108

(g) κ distribution of PA1704-108 **(h)** $|\kappa|$ distribution of PA1704-108

Figure D.19.: Distributions of goodness of fit parameters κ, $|\kappa|$ for PMTs **EA1437** (panels **(a)** to **(d)**) and **PA1704-108** (panels **(e)** and **(h)**) from analysis of the LED measurement at low light intensity (panels **(a)**, **(b)**, **(e)**, **(f)**) and of the laser measurement (panels **(c)**, **(d)**, **(g)**, **(h)**) in mass 84. Values are calculated for each SPE pulse fit following Equation 7.8 and Equation 7.9.

E. Additional PMT Analysis Plots

E.1. Additional Sample Analysis Plots

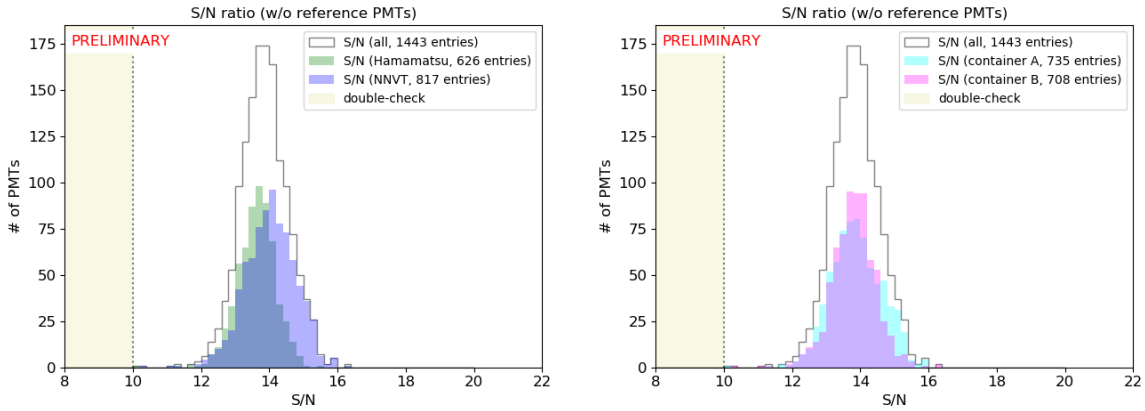

(a) S/N results (total and separated by PMT type)

(b) S/N results (total and separated by container)

Figure E.1.: Analysis results for S/N ratio from selected data sample (reference PMTs excluded). In total, 1443 valid results are contributing to the statistics, values below 10 would lead to a retest of these PMTs. Individual distributions are displaying PMT type (panel **(a)**) or container system (panel **(b)**).

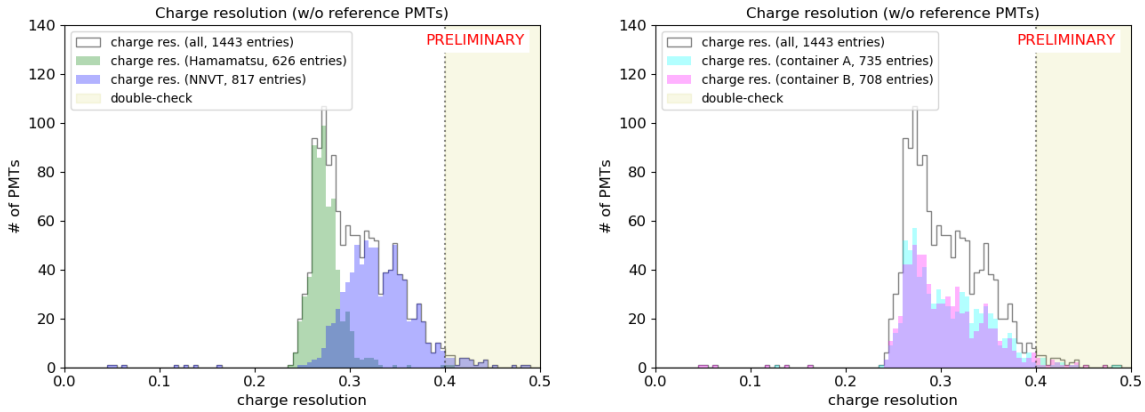

(a) charge resolution results (total and separated by PMT type)

(b) charge resolution results (total and separated by container)

Figure E.2.: Analysis results for charge resolution from selected data sample (reference PMTs excluded). In total, 1443 valid results are contributing to the statistics, values above 0.40 lead to a retest of these PMTs. Individual distributions are displaying PMT type (panel **(a)**) or container system (panel **(b)**).

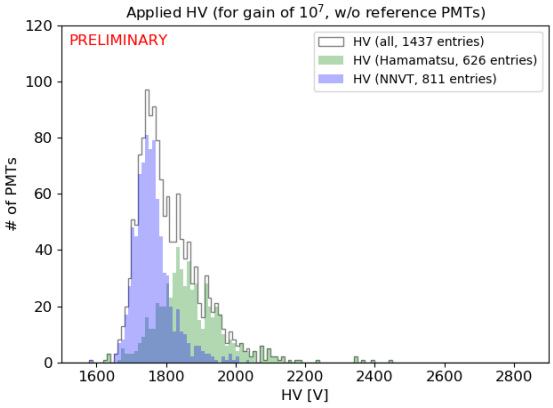

(a) HV results (total and separated by PMT type)

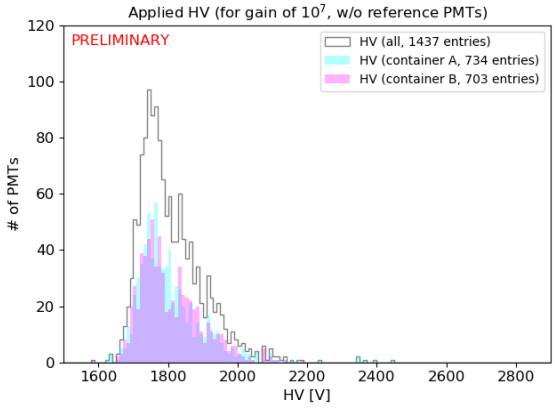

(b) HV results (total and separated by container)

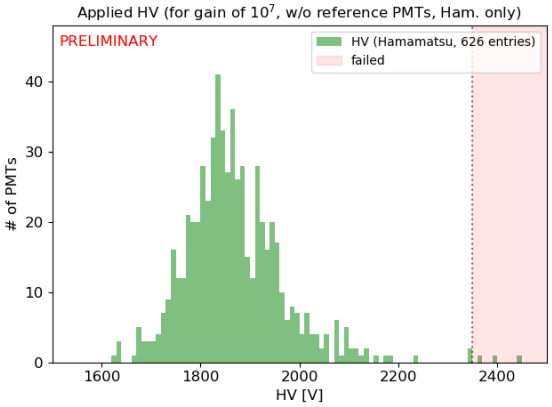

(c) HV results of Hamamatsu PMTs

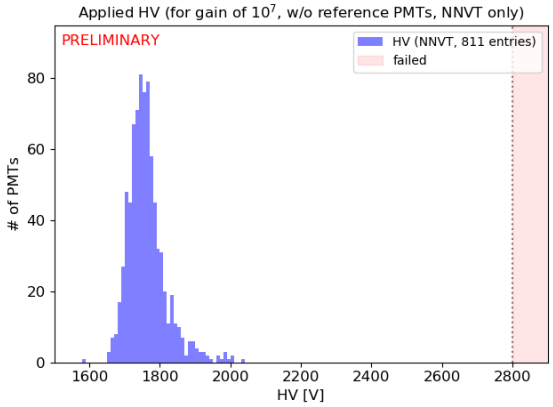

(d) HV results of NNVT PMTs

Figure E.3.: Analysis results for determined HV providing a gain of 10^7 from selected data sample (reference PMTs excluded). In total, 1437 valid results are contributing to the statistics. Individual distributions are displaying PMT type (panel **(a)**) or container system (panel **(b)**). In panels **(c)** and **(d)**, results of respective PMT types are drawn with criteria for rejection ($> 2350\,\mathrm{V}$ for Hamamatsu and $> 2800\,\mathrm{V}$ for NNVT).

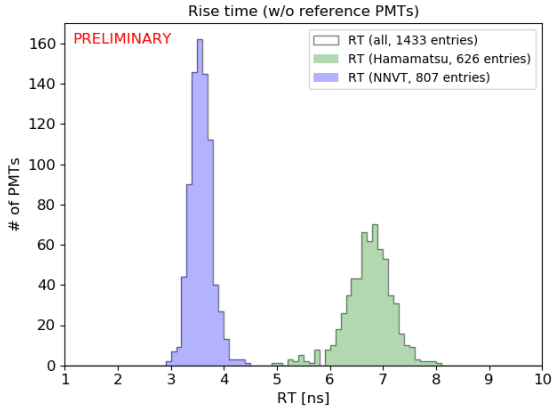

(a) RT results (total and separated by PMT type)

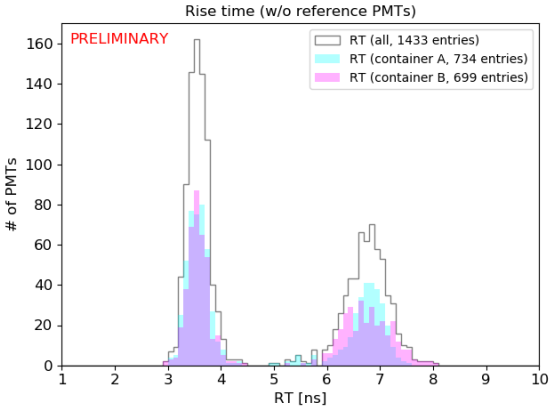

(b) RT results (total and separated by container)

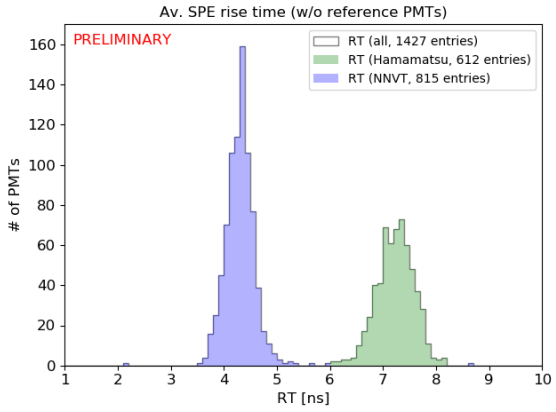

(c) av. SPE RT results (total and separated by PMT type)

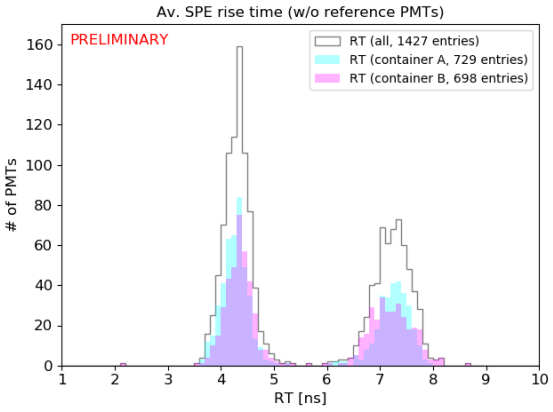

(d) av. SPE RT results (total and separated by container)

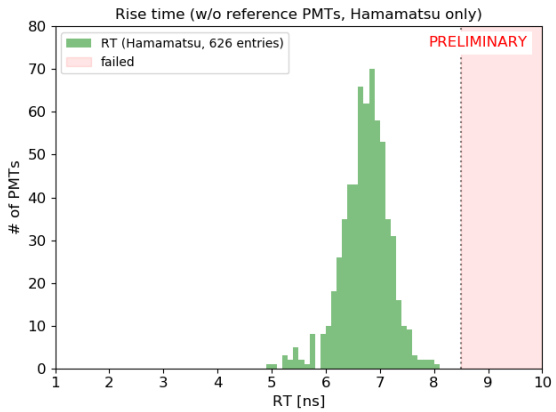

(e) RT results of Hamamatsu PMTs

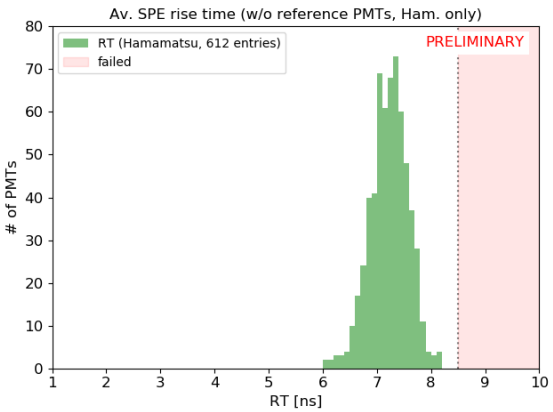

(f) av. SPE RT results of Hamamatsu PMTs

Figure E.4.: Analysis results for rise times from selected data sample (reference PMTs excluded). Values are extracted from individual pulses and via fit from an averaged SPE pulse. In total, 1433 (1427) valid results are contributing to the statistics. Individual distributions are displaying PMT type (panels **(a)** and **(c)**) or container system (panels **(b)** and **(d)**). In panels **(e)** and **(f)**, criterion for rejection are illustrated (> 8.5 ns, only for Hamamatsu PMTs).

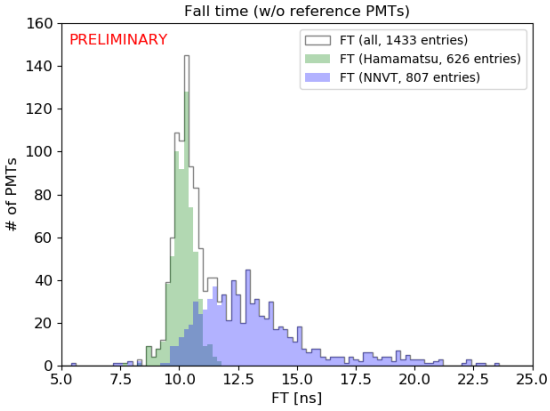

(a) FT results (total and separated by PMT type)

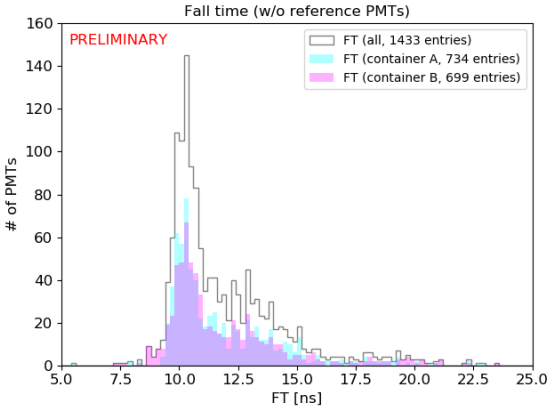

(b) FT results (total and separated by container)

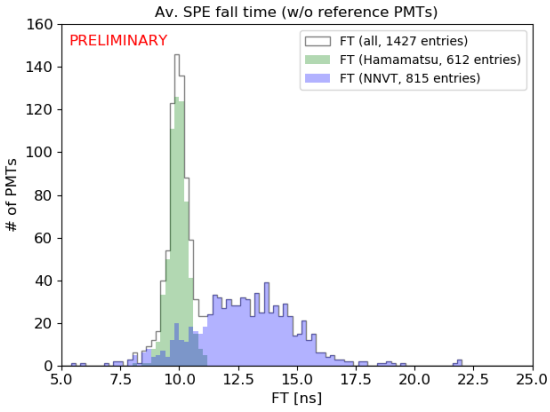

(c) av. SPE FT results (total and separated by PMT type)

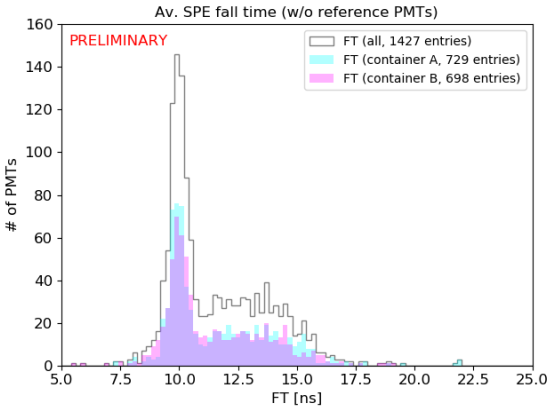

(d) av. SPE FT results (total and separated by container)

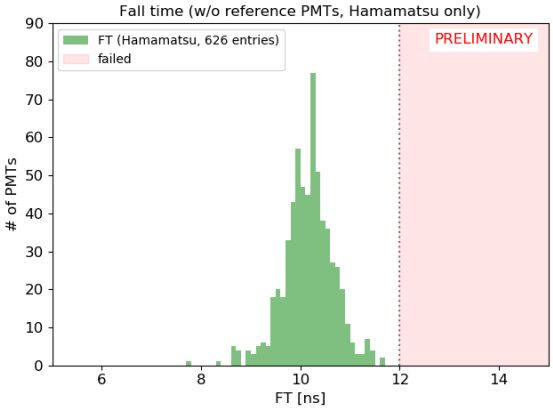

(e) FT results of Hamamatsu PMTs

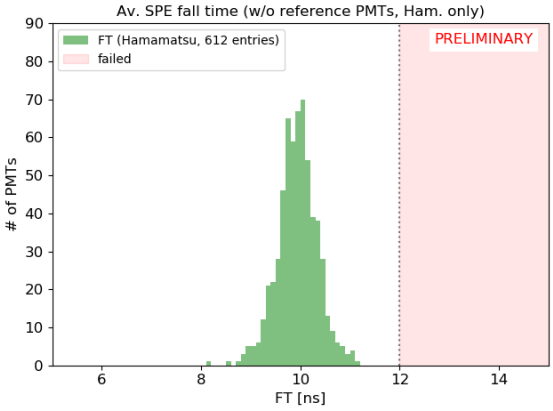

(f) av. SPE FT results of Hamamatsu PMTs

Figure E.5.: Analysis results for fall times from selected data sample (reference PMTs excluded). Values are extracted from individual pulses and via fit from an averaged SPE pulse. In total, 1433 (1427) valid results are contributing to the statistics. Individual distributions are displaying PMT type (panels **(a)** and **(c)**) or container system (panels **(b)** and **(d)**). In panels **(e)** and **(f)**, criterion for rejection are illustrated (> 12.0 ns, only for Hamamatsu PMTs).

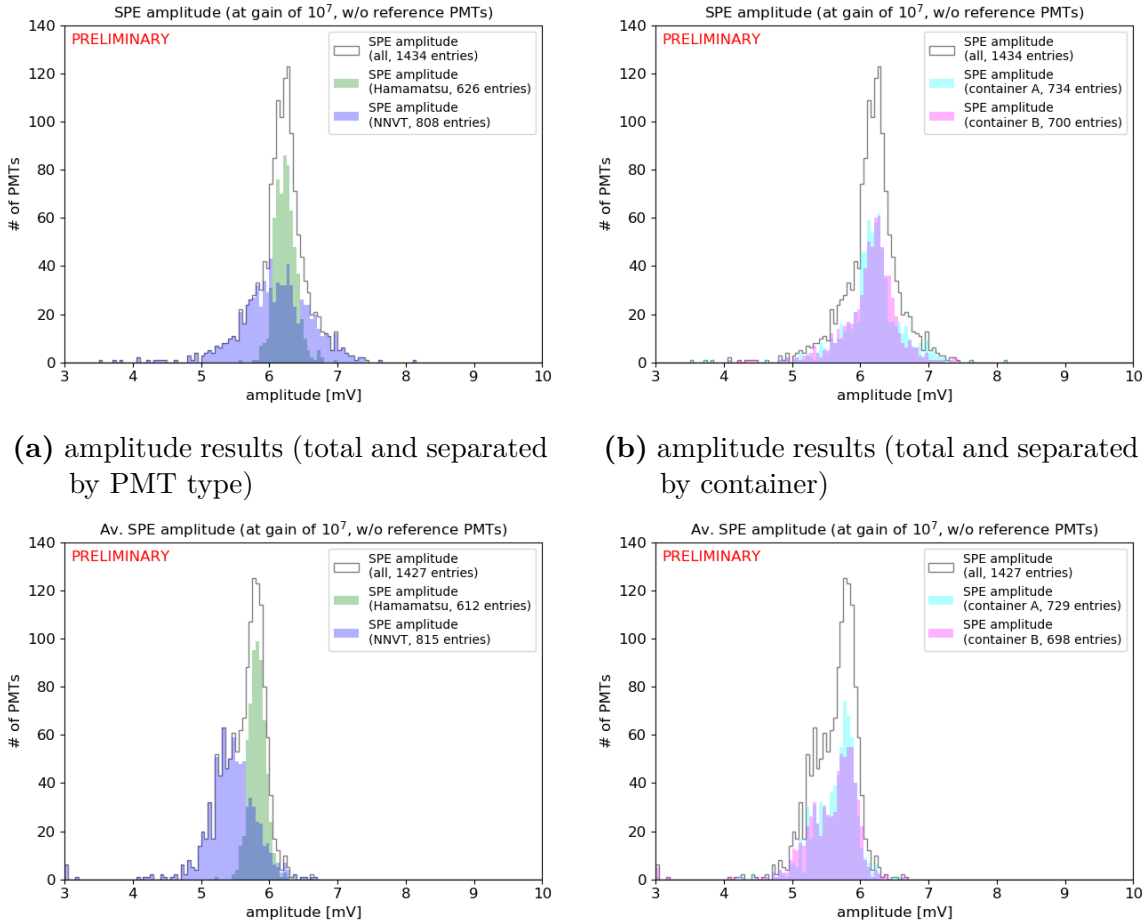

(a) amplitude results (total and separated by PMT type)

(b) amplitude results (total and separated by container)

(c) av. SPE amplitude results (total and separated by PMT type)

(d) av. SPE amplitude results (total and separated by container)

Figure E.6.: Analysis results for single PE amplitudes from selected data sample (reference PMTs excluded). Values are extracted from individual pulses and via fit from an averaged SPE pulse. In total, 1434 (1427) valid results are contributing to the statistics. Individual distributions are displaying PMT type (panels **(a)** and **(c)**) or container system (panels **(b)** and **(d)**).

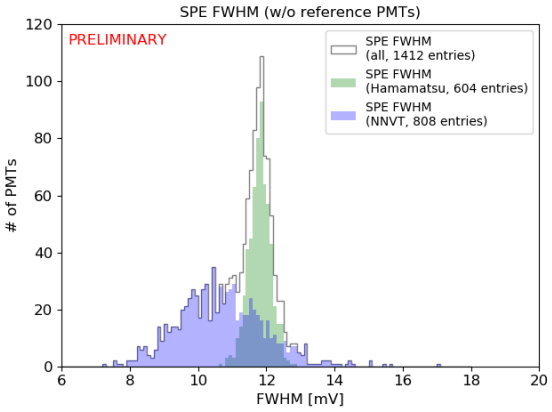

(a) FWHM results (total and separated by PMT type)

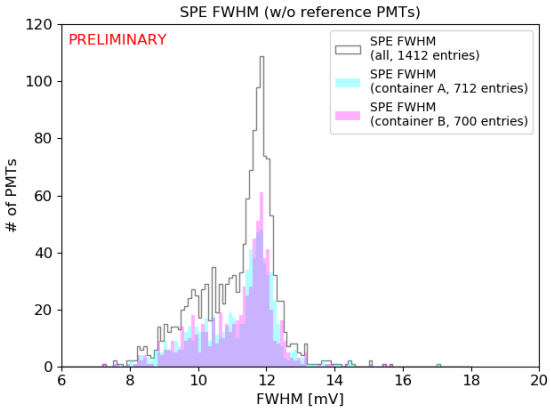

(b) FWHM results (total and separated by container)

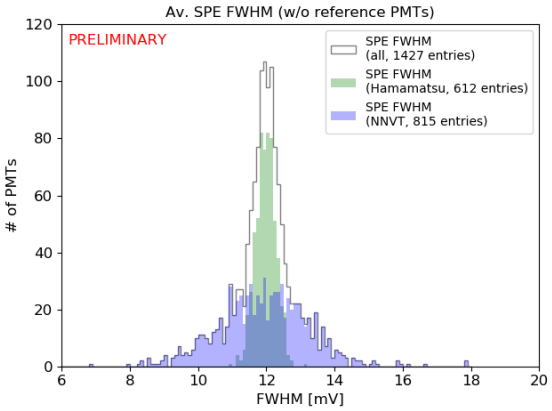

(c) av. SPE FWHM results (total and separated by PMT type)

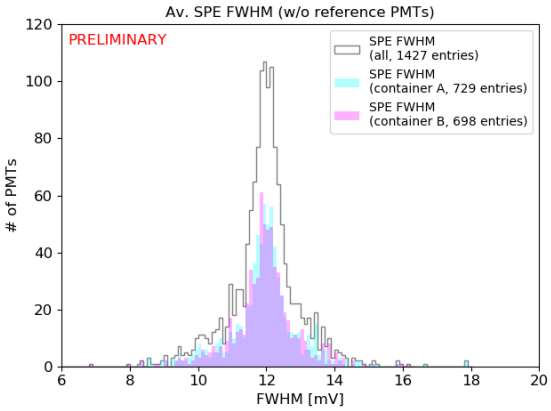

(d) av. SPE FWHM results (total and separated by container)

Figure E.7.: Analysis results for single PE FWHM from selected data sample (reference PMTs excluded). Values are extracted from individual pulses and via fit from an averaged SPE pulse. In total, 1412 (1427) valid results are contributing to the statistics. Individual distributions are displaying PMT type (panels **(a)** and **(c)**) or container system (panels **(b)** and **(d)**).

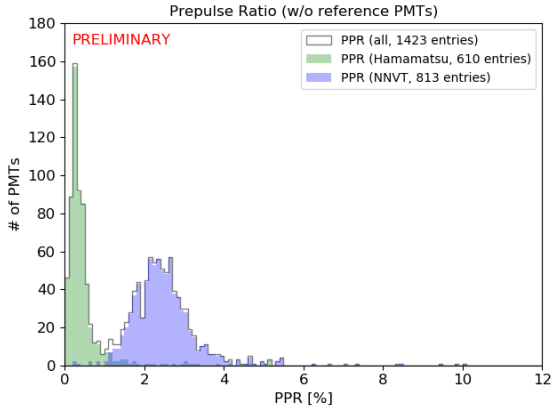

(a) PPR results (total and separated by PMT type)

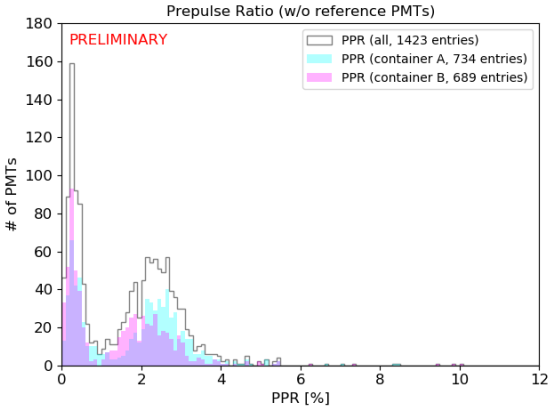

(b) PPR results (total and separated by container)

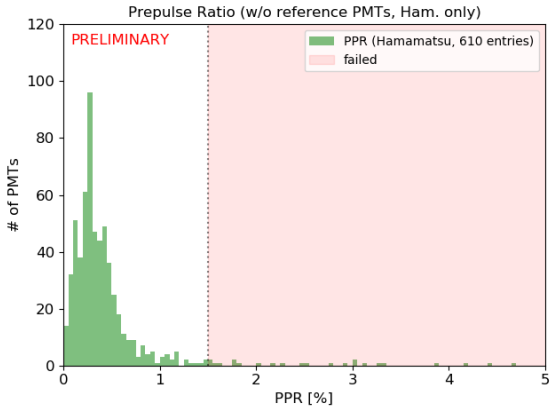

(c) PPR results of Hamamatsu PMTs

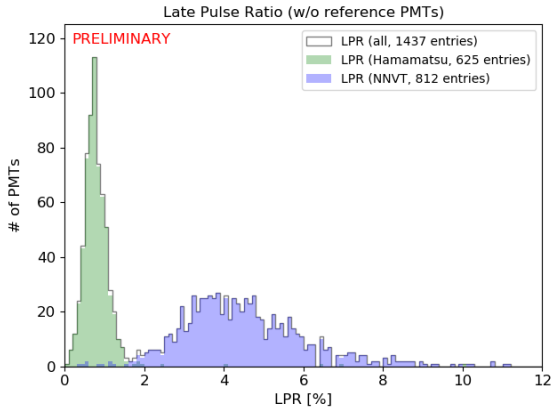

(d) LPR results (total and separated by PMT type)

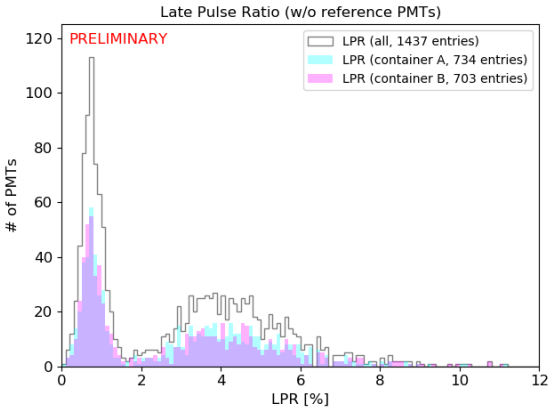

(e) LPR results (total and separated by container)

Figure E.8.: Analysis results for pre- and late pulse ratios from selected data sample (reference PMTs excluded). In total, 1423 valid results for the PPR and 1437 valid results for the LPR are contributing to the statistics. Individual distributions are displaying PMT type (panels **(a)** and **(d)**) or container system (panels **(b)** and **(e)**). In panel **(c)**, PPR criterion for rejection is illustrated (>1.5 %, only for Hamamatsu PMTs).

E.2. Additional Reference PMT Analysis Plots

E.2.1. Statistics of Valid Results per Channel

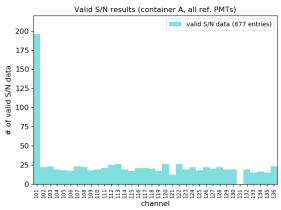

(a) valid S/N ratio results in container A

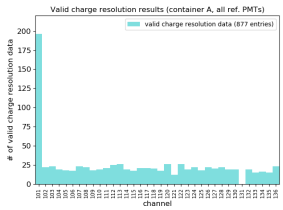

(b) valid charge res. results in container A

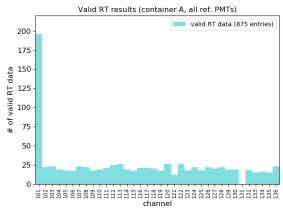

(c) valid RT results in container A

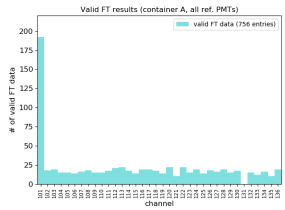

(d) valid FT results in container A

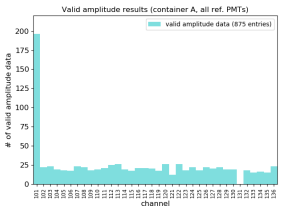

(e) valid amplitude results in container A

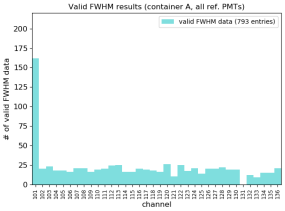

(f) valid FWHM results in container A

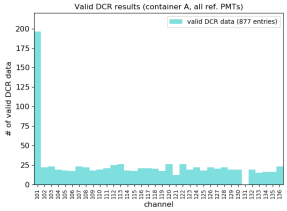

(g) valid DCR results in container A

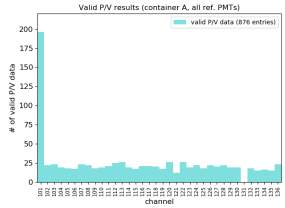

(h) valid P/V ratio results in container A

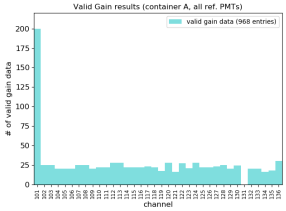

(i) valid gain results in container A

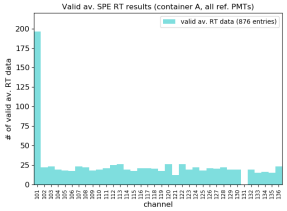

(j) valid av. SPE RT results in container A

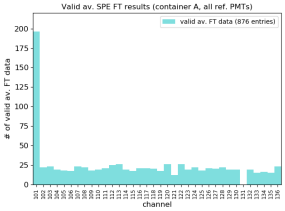

(k) valid av. SPE FT results in container A

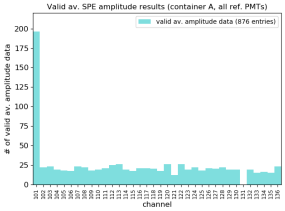

(l) valid av. SPE amplitude results in container A

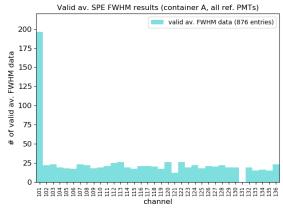

(m) valid av. SPE FWHM results in container A

Figure E.9.: Additional statistics of valid results of reference PMTs in container A for various parameters.

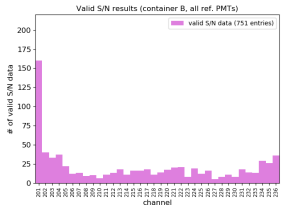

(a) valid S/N ratio results in container B

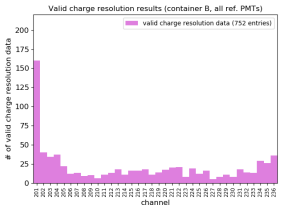

(b) valid charge res. results in container B

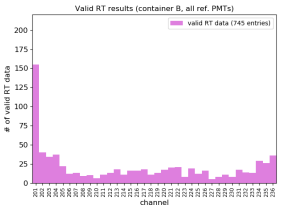

(c) valid RT results in container B

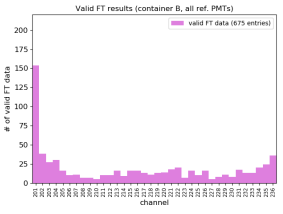

(d) valid FT results in container B

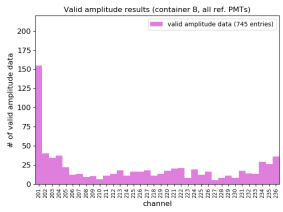

(e) valid amplitude results in container B

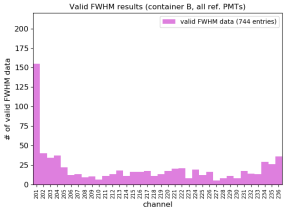

(f) valid FWHM results in container B

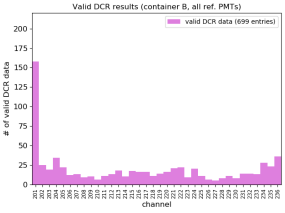

(g) valid DCR results in container B

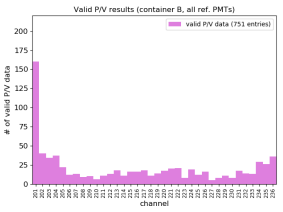

(h) valid P/V ratio results in container B

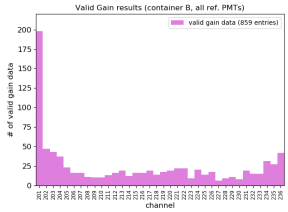

(i) valid gain results in container B

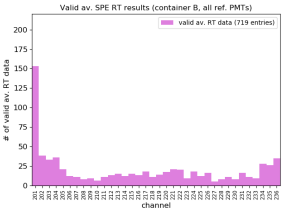

(j) valid av. SPE RT results in container B

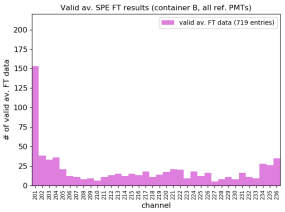

(k) valid av. SPE FT results in container B

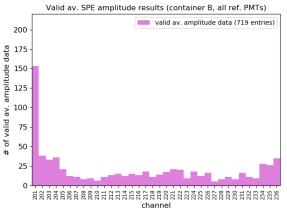

(l) valid av. SPE amplitude results in container B

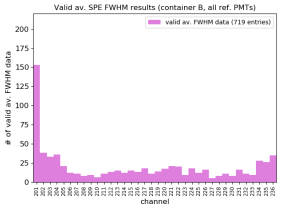

(m) valid av. SPE FWHM results in container B

Figure E.10.: Additional statistics of valid results of reference PMTs in container B for various parameters.

E.2.2. Stability over Time (Mass Number)

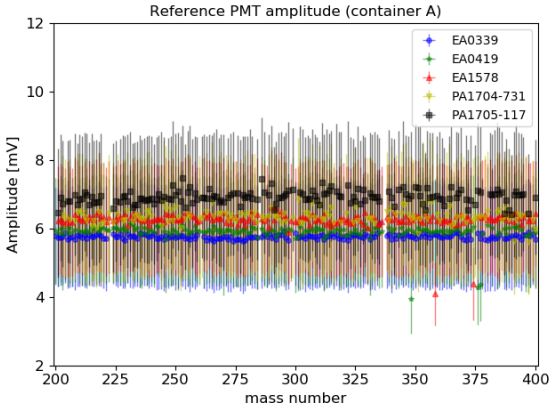

(a) amplitude results of reference PMTs in container A

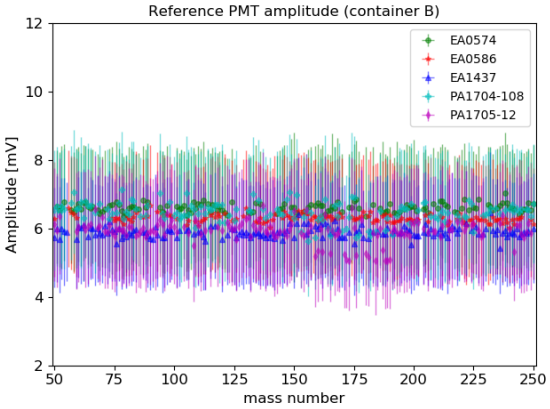

(b) amplitude results of reference PMTs in container B

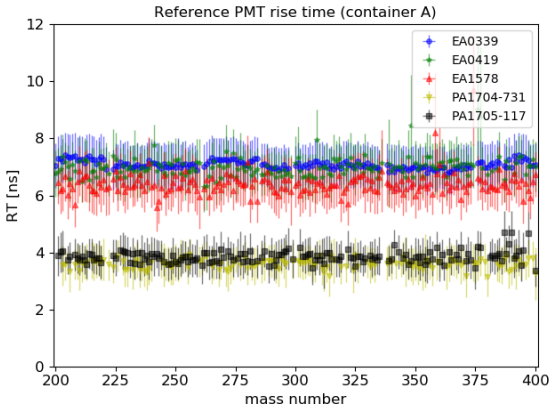

(c) RT results of reference PMTs in container A

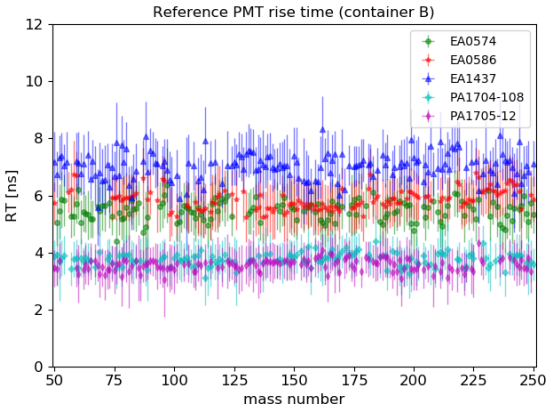

(d) RT results of reference PMTs in container B

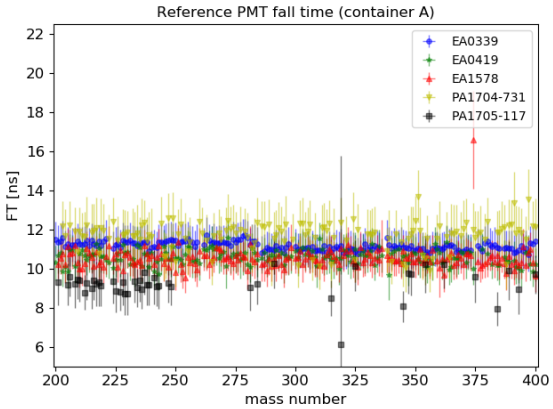

(e) FT results of reference PMTs in container A

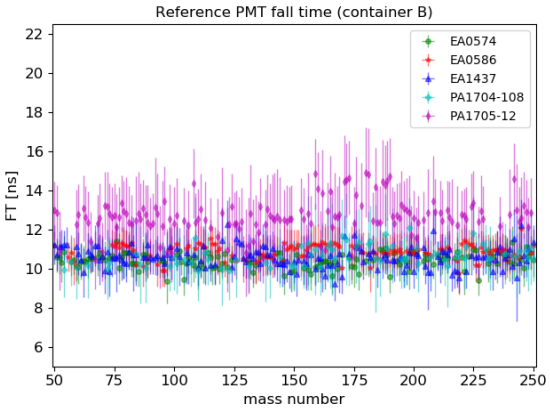

(f) FT results of reference PMTs in container B

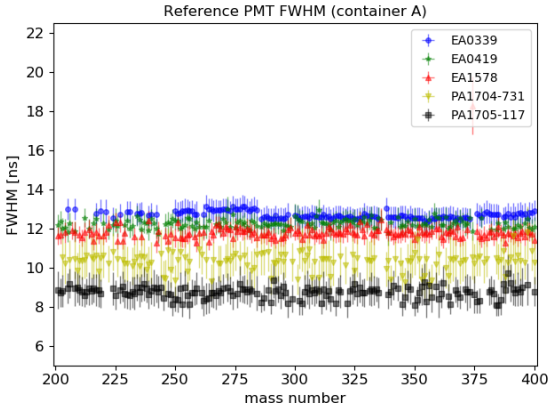

(g) FWHM results of reference PMTs in container A

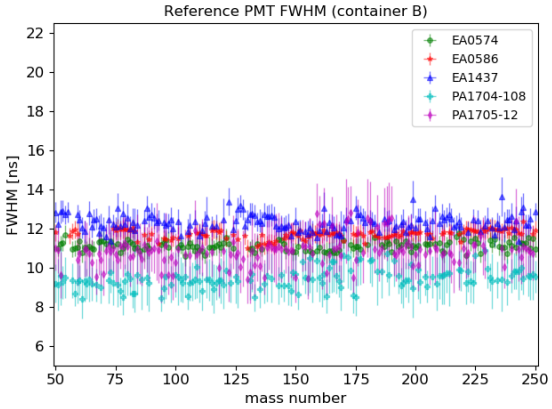

(h) FWHM results of reference PMTs in container B

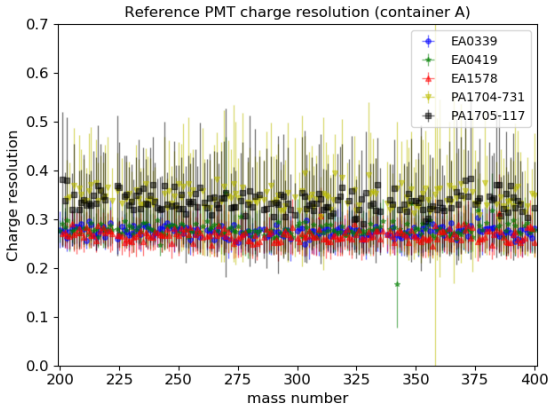

(i) charge resolution results of reference PMTs in container A

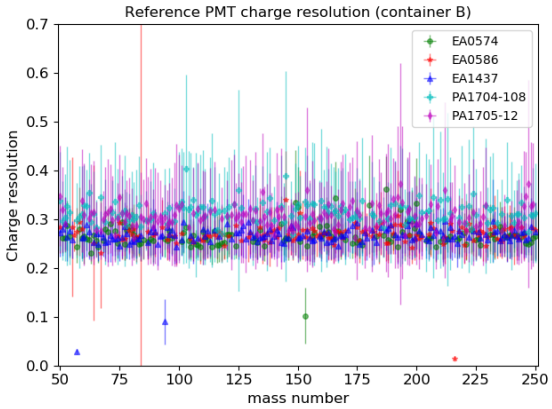

(j) charge resolution results of reference PMTs in container B

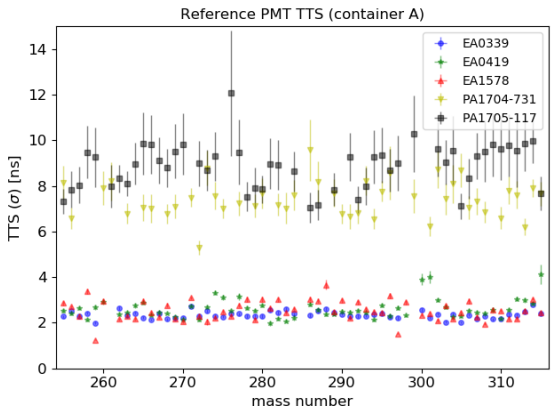

(k) TTS results of reference PMTs in container A

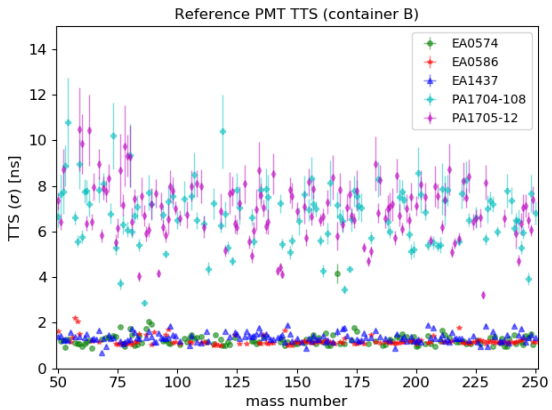

(l) TTS results of reference PMTs in container B

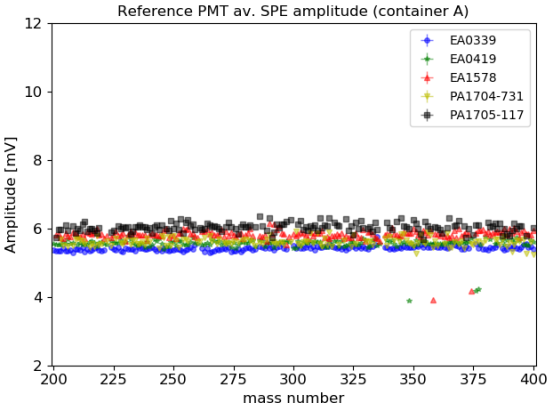

(m) av. SPE amplitude results of reference PMTs in container A

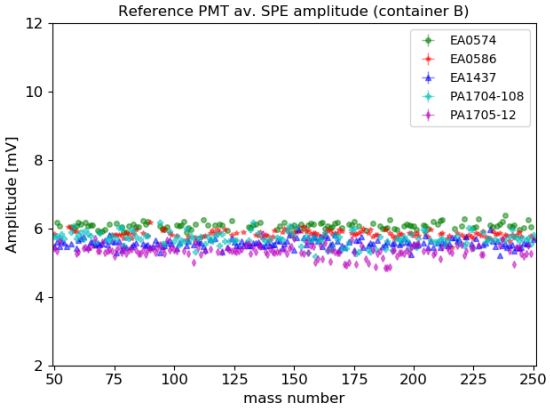

(n) av. SPE amplitude results of reference PMTs in container B

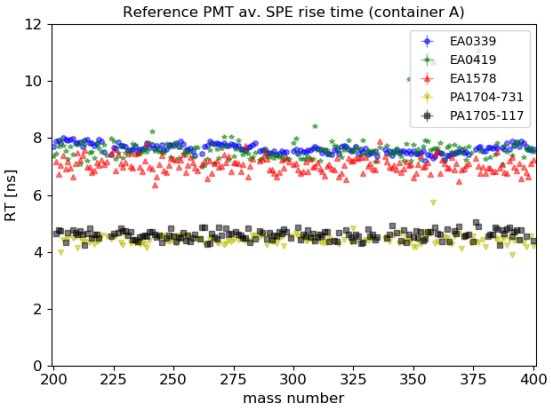

(o) av. SPE RT results of reference PMTs in container A

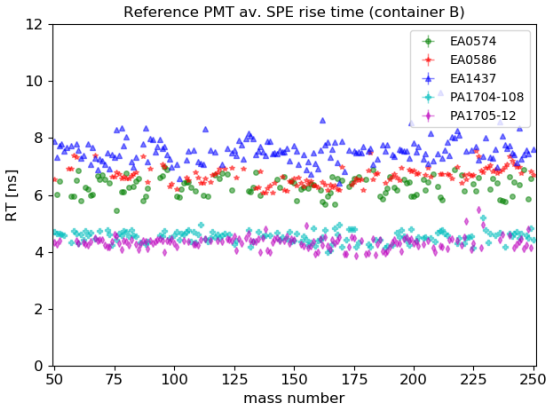

(p) av. SPE RT results of reference PMTs in container B

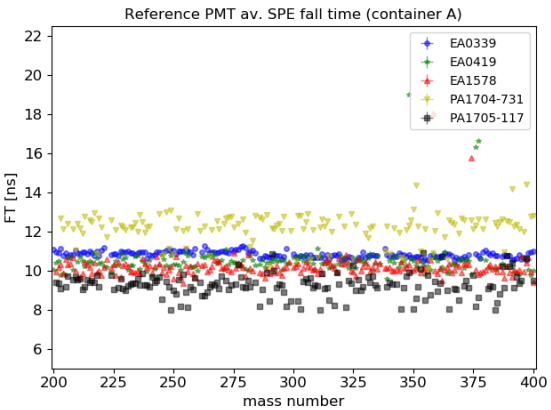

(q) av. SPE FT results of reference PMTs in container A

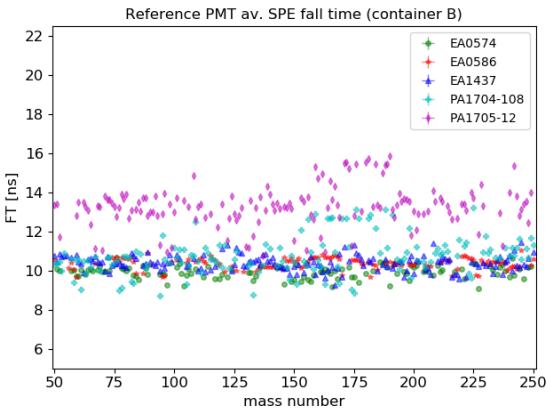

(r) av. SPE FT results of reference PMTs in container B

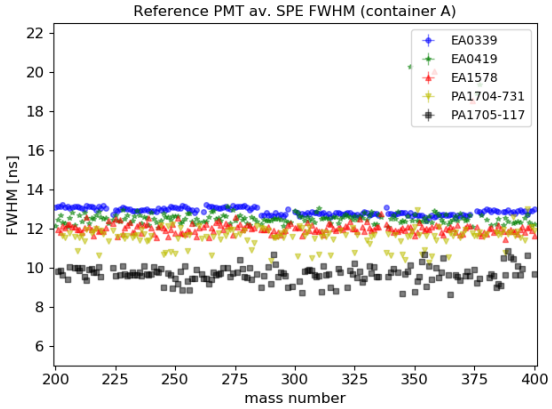

(s) av. SPE FWHM results of reference PMTs in container A

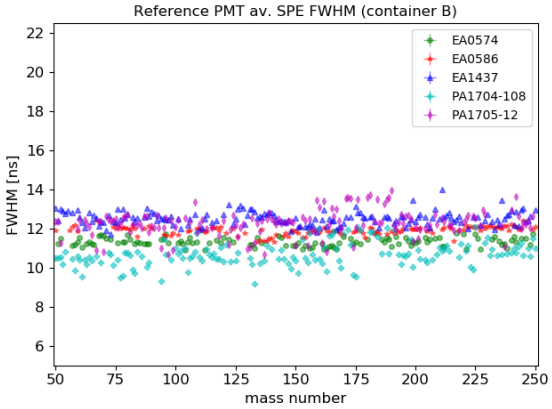

(t) av. SPE FWHM results of reference PMTs in container B

Figure E.11.: Additional plots of reference PMT results from containers A and B for various parameters, plotted over the mass number. The FT results of PMT PA1705-117 in panel **(e)** for almost all masses higher than 250 in container A are missing due to bad fit results, which is connected to the performance of either the analysis methods or the PMT itself (or a combination of both), and so no issue of the container system. For the TTS results of container A in panel **(k)**, valid data was available only for masses 255 – 315.

E.2.3. Stability over Channel (Box Number)

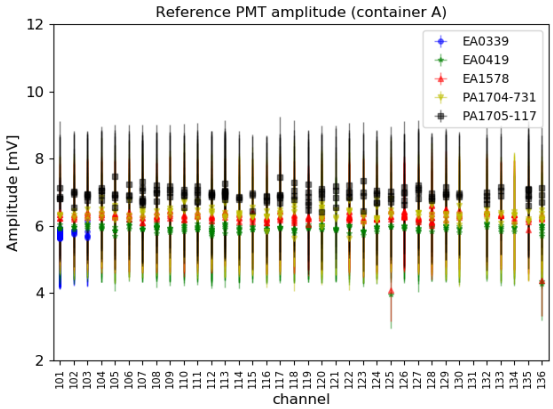

(a) amplitude results of reference PMTs in container A

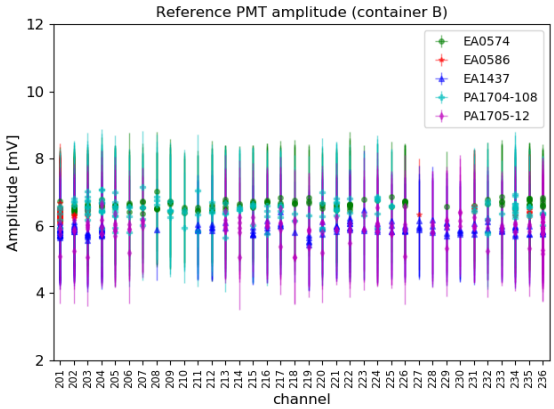

(b) amplitude results of reference PMTs in container B

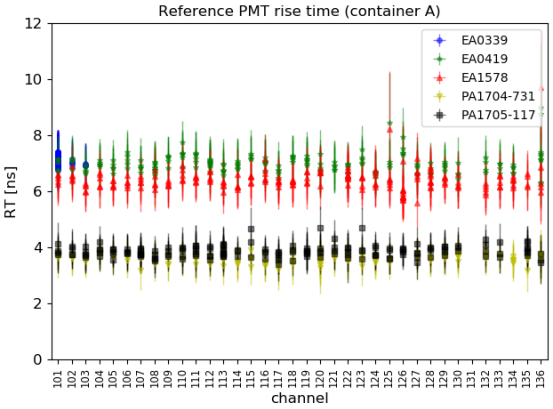

(c) RT results of reference PMTs in container A

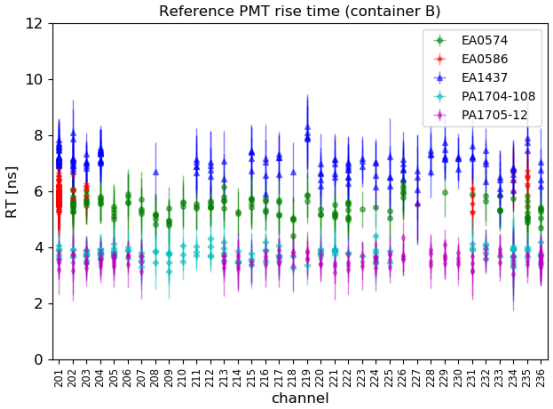

(d) RT results of reference PMTs in container B

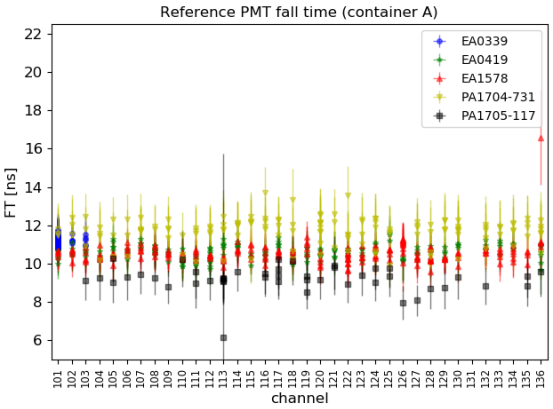

(e) FT results of reference PMTs in container A

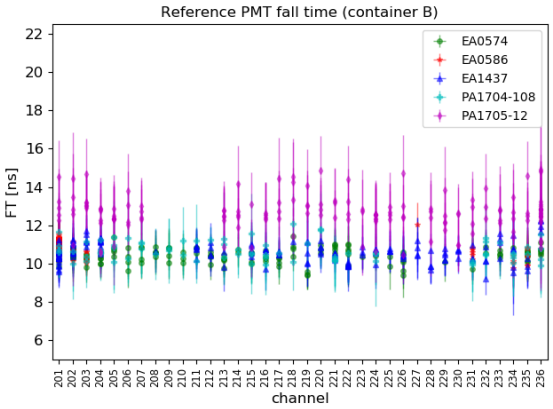

(f) FT results of reference PMTs in container B

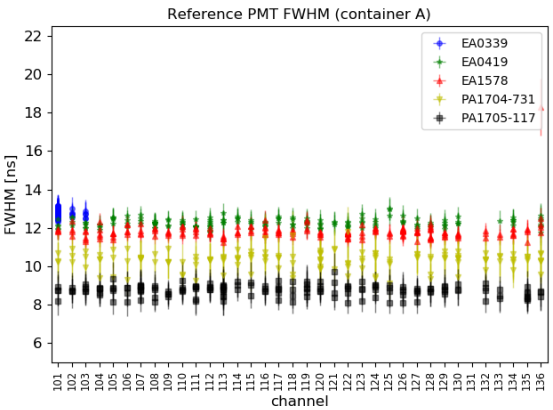

(g) FWHM results of reference PMTs in container A

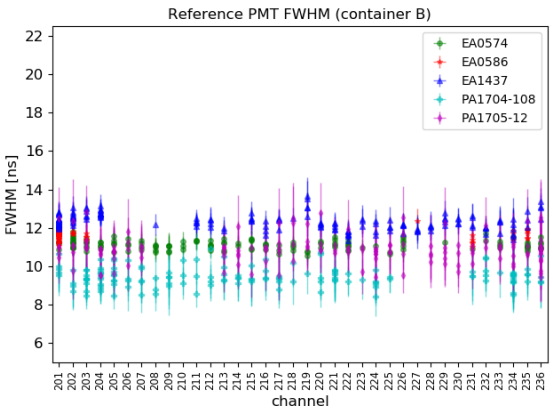

(h) FWHM results of reference PMTs in container B

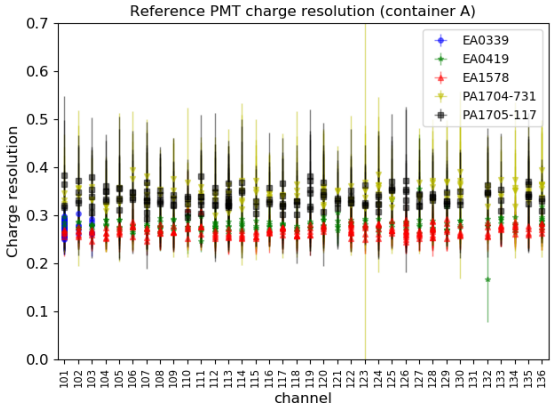

(i) charge resolution results of reference PMTs in container A

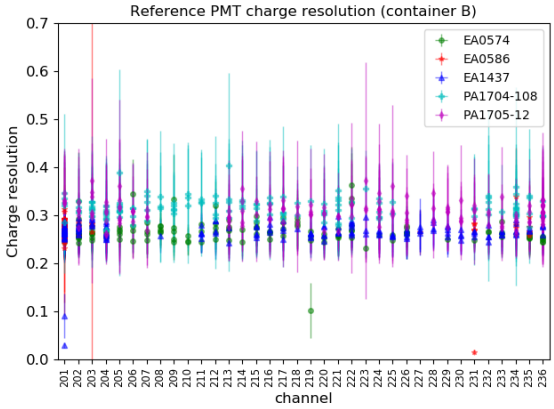

(j) charge resolution results of reference PMTs in container B

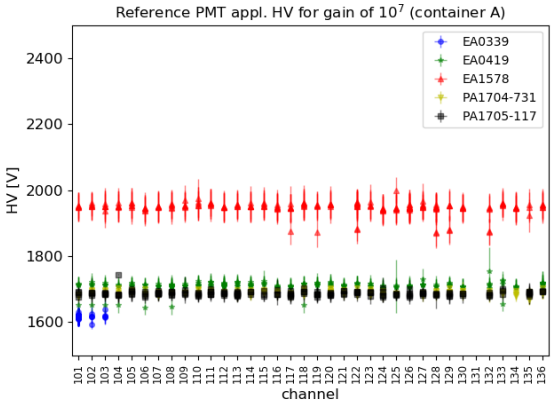

(k) HV results of reference PMTs in container A

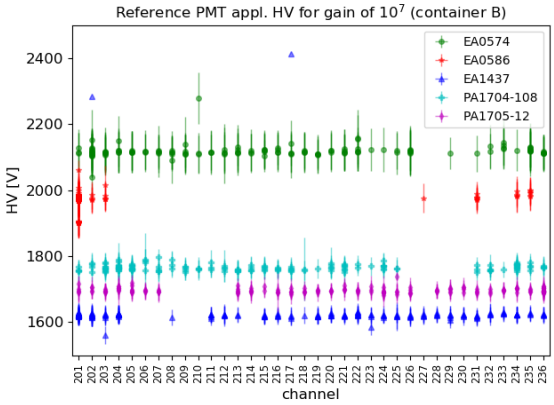

(l) HV results of reference PMTs in container B

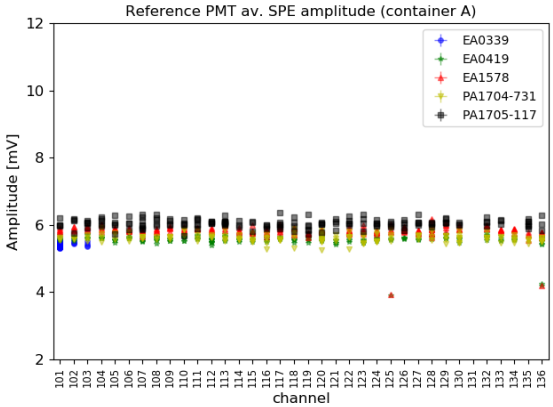

(m) av. SPE amplitude results of reference PMTs in container A

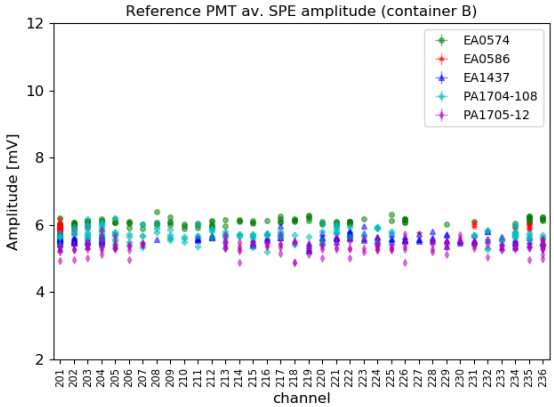

(n) av. SPE amplitude results of reference PMTs in container B

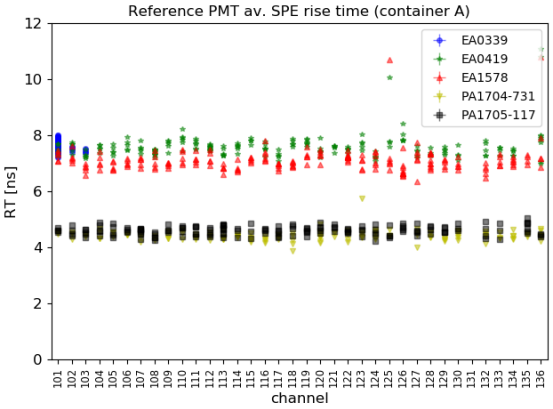

(o) av. SPE RT results of reference PMTs in container A

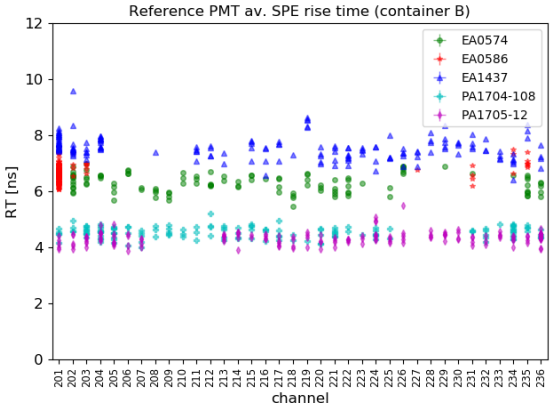

(p) av. SPE RT results of reference PMTs in container B

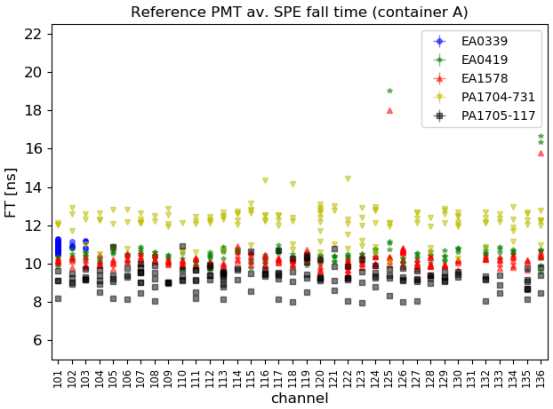

(q) av. SPE FT results of reference PMTs in container A

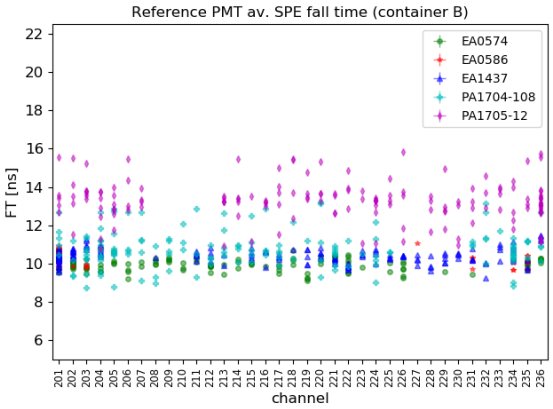

(r) av. SPE FT results of reference PMTs in container B

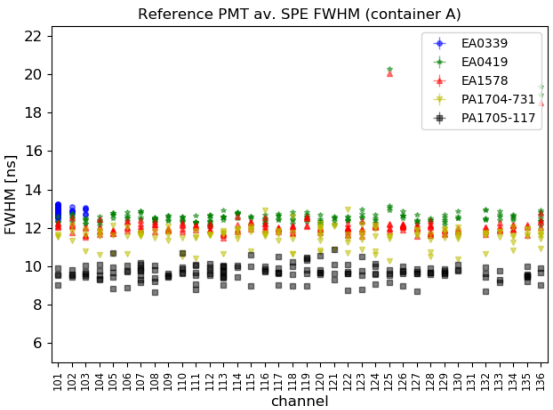

(s) av. SPE FWHM results of reference PMTs in container A

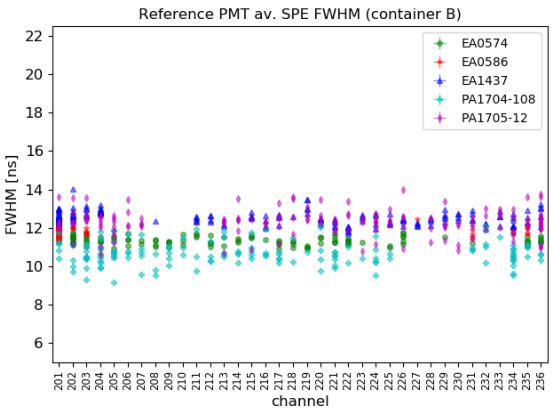

(t) av. SPE FWHM results of reference PMTs in container B

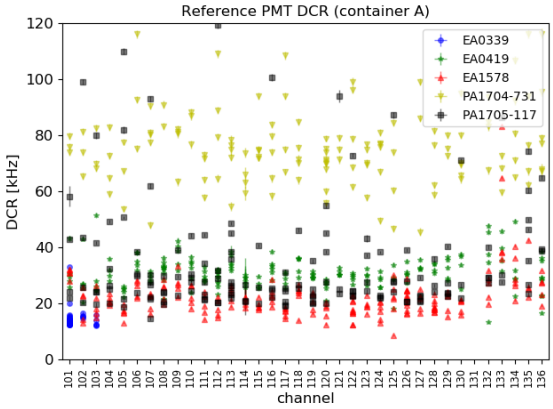

(u) DCR results of reference PMTs in container A

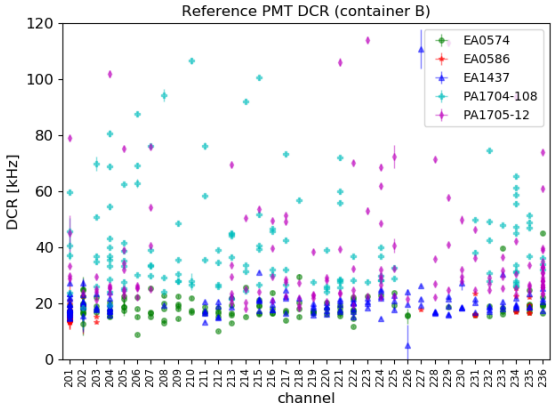

(v) DCR results of reference PMTs in container B

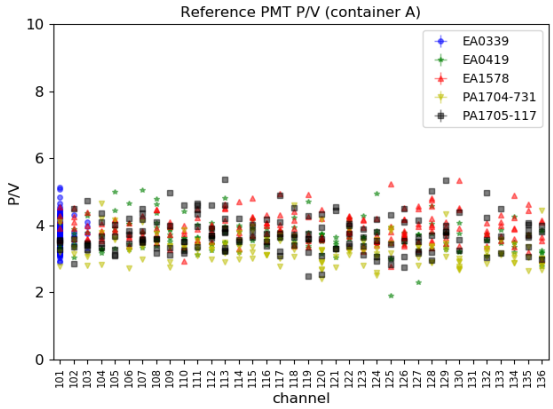

(w) P/V ratio results of reference PMTs in container A

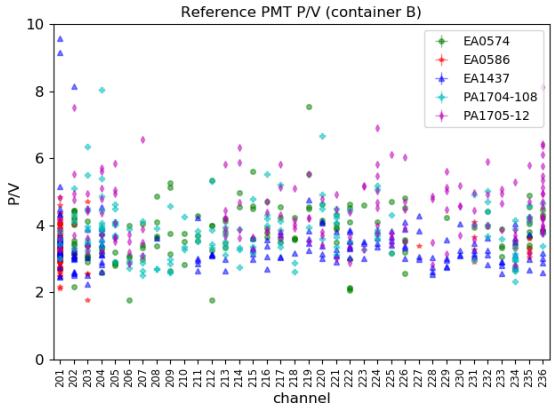

(x) P/V ratio results of reference PMTs in container B

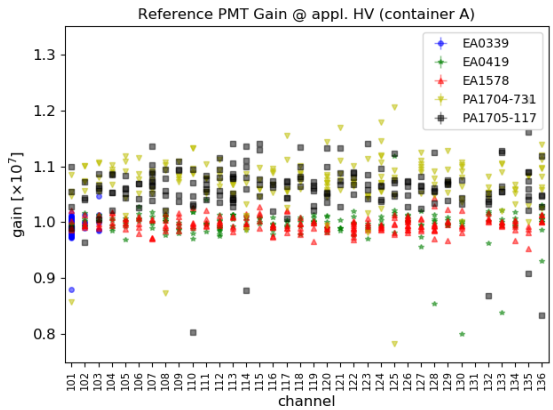

(y) GCC results of reference PMTs in container A

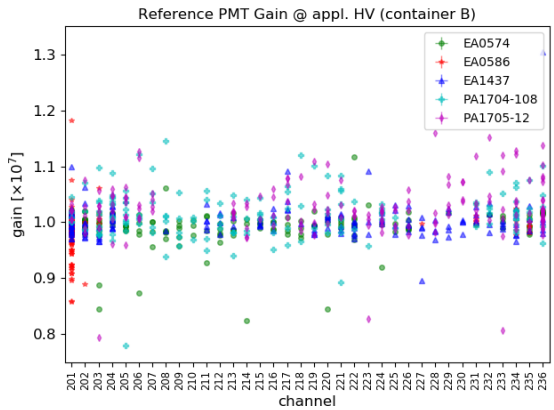

(z) GCC results of reference PMTs in container B

Figure E.12.: Additional plots of results of reference PMTs from containers A and B for various parameters, plotted over the channel number (multiple measurement per channel are possible here).

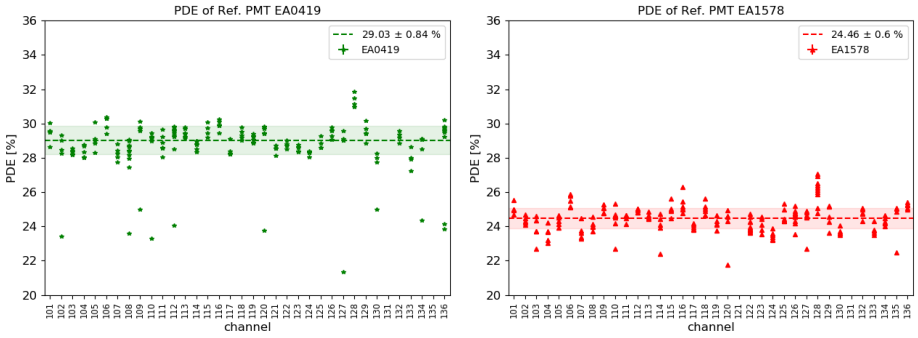

(a) PDE results of EA0419

(b) PDE results of EA1578

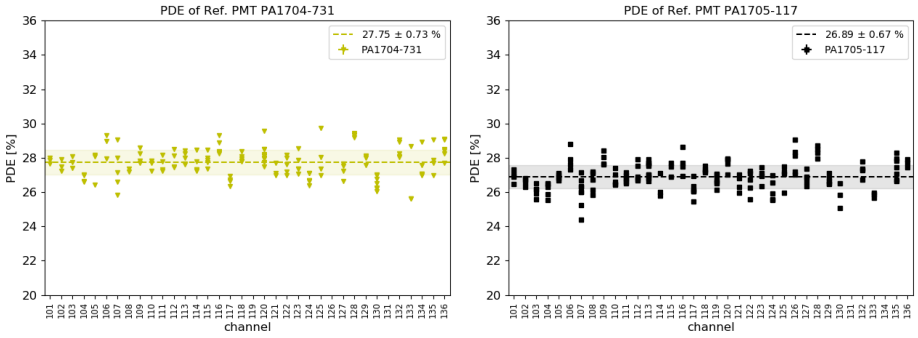

(c) PDE results of PA1704-731

(d) PDE results of PA1705-117

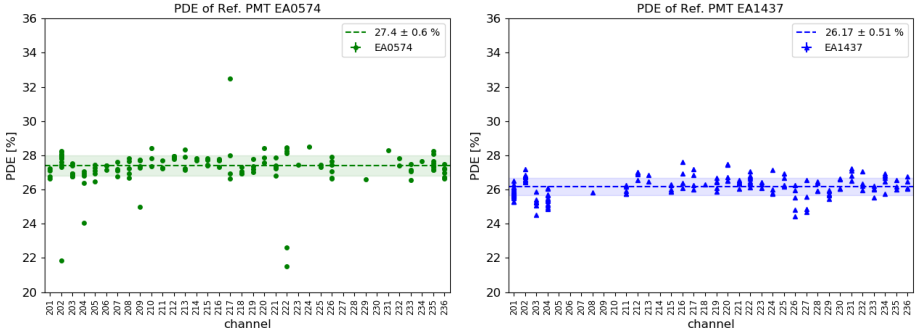

(e) PDE results of EA0574

(f) PDE results of EA1437

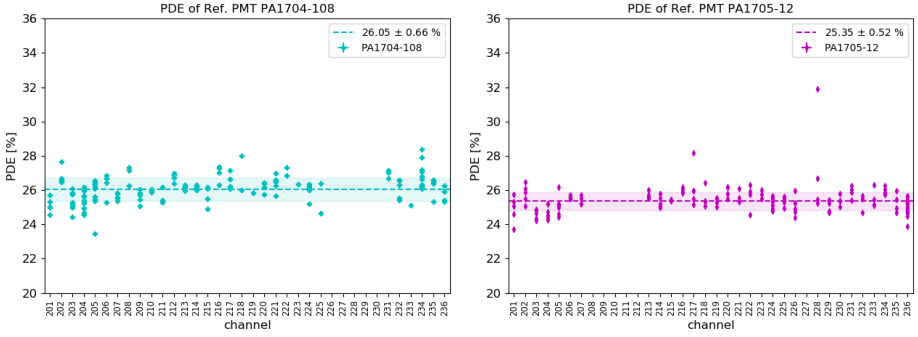

(g) PDE results of PA1704-108

(h) PDE results of PA1705-12

Figure E.13.: PDE results of individual reference PMTs from container A and B, plotted over the channel number (multiple measurement per channel are possible here). Only reference PMTs circulating through the channels over the various runs are shown; reference PMTs with fixed location inside the container are spared here.

E.2.4. Stability of Light Sources

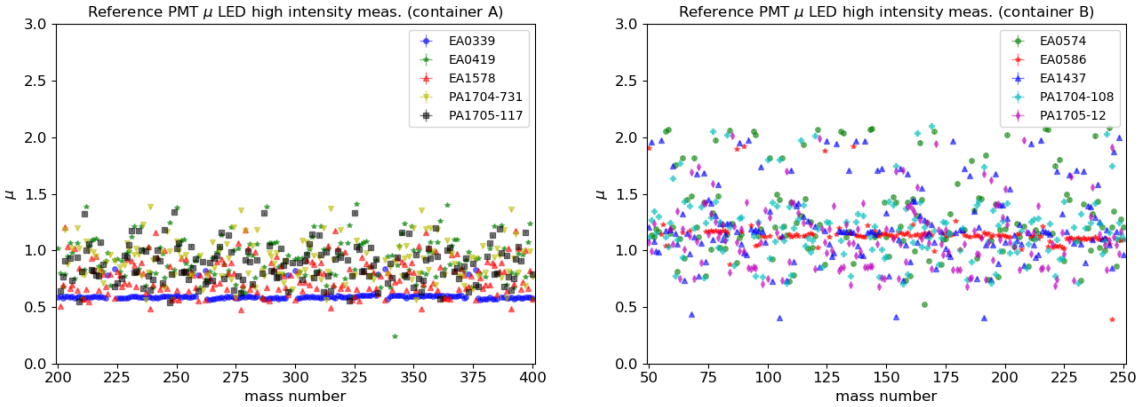

(a) μ values from container A **(b)** μ values from container B

Figure E.14.: μ values of the reference PMTs from the high light intensity LED measurement. PMTs EA0339 (in container A) and EA0586 (container B) have been tested mostly in the same drawer boxes, while other PMTs are circulated through the other channels over the container runs.

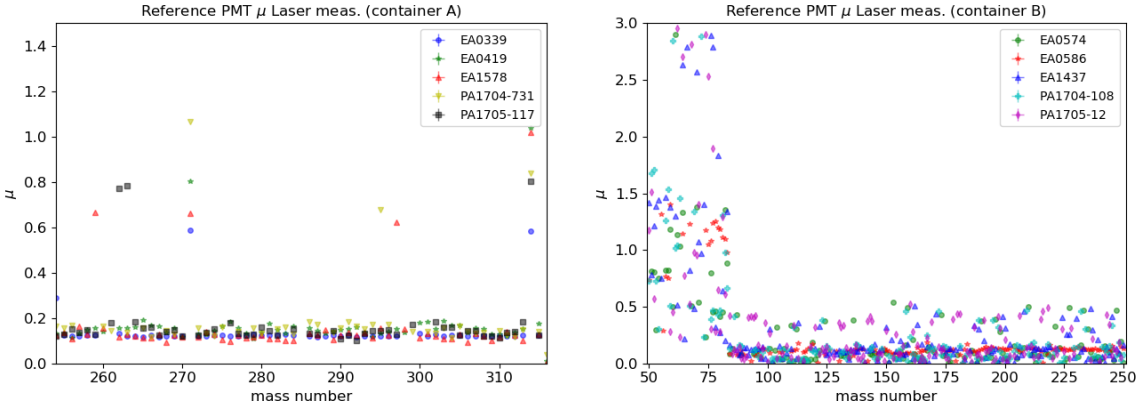

(a) μ values from container A **(b)** μ values from container B

Figure E.15.: μ values of the reference PMTs from the laser measurement. In container A, valid results are available only for masses 255 – 315. At container B, laser light intensity was adjusted after mass 82, causing the different behavior before and after.

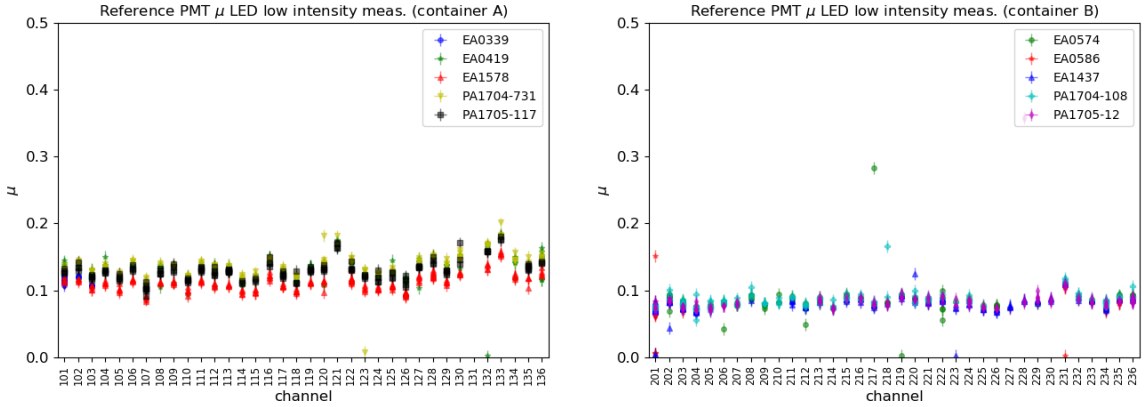

(a) μ values from container A **(b)** μ values from container B

Figure E.16.: μ values of the reference PMTs from the low light intensity LED measurement, plotted over the channels. Light intensity has been calibrated to a level of $\mu \sim 0.1$ p.e. in all channels.

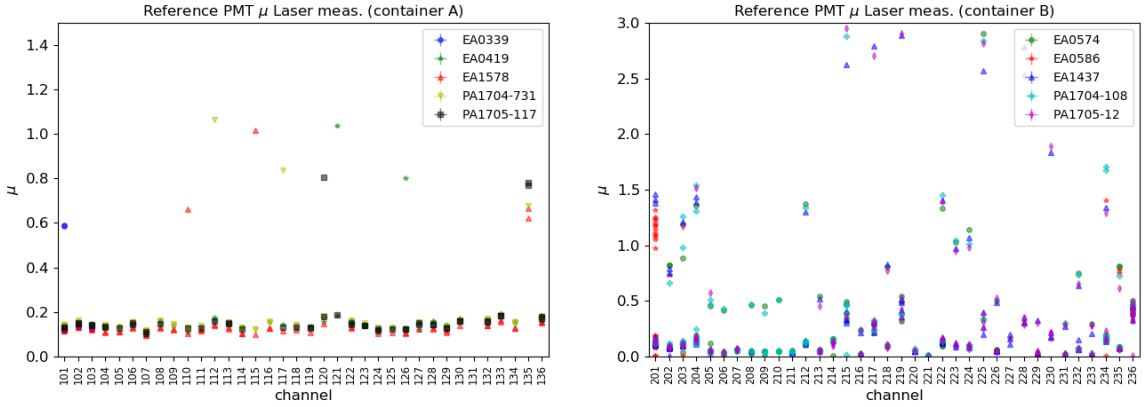

(a) μ values from container A **(b)** μ values from container B

Figure E.17.: μ values of the reference PMTs from the laser measurement, plotted over the channels. A channel-wise calibration of the light intensity is not possible for the laser measurement due to the design of the fiber splitter; the absolute light intensity in the individual channels is further not relevant, nonetheless should be on roughly the same level in an ideal case. In container A, plot contains only results from masses 255 – 315, see also Figure E.15a.

E.2.5. PMT Stability (Reference PMTs at Fixed Positions)

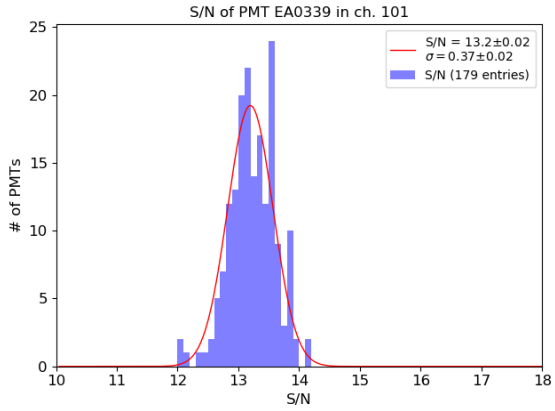

(a) S/N ratio results of EA0339 in ch. 101

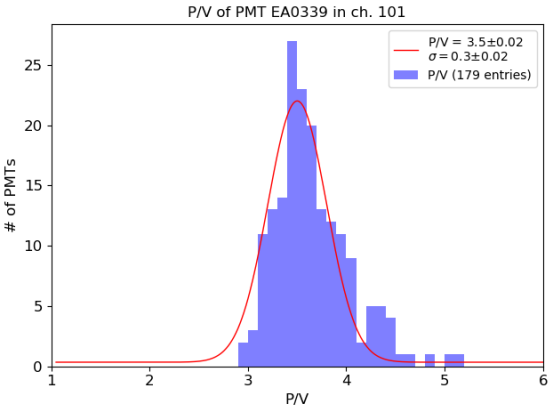

(b) P/V ratio results of EA0339 in ch. 101

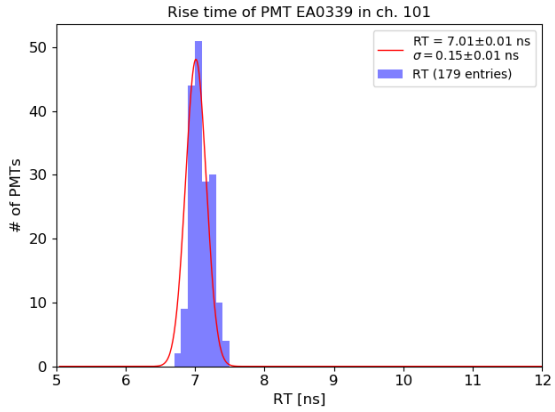

(c) RT results of EA0339 in ch. 101

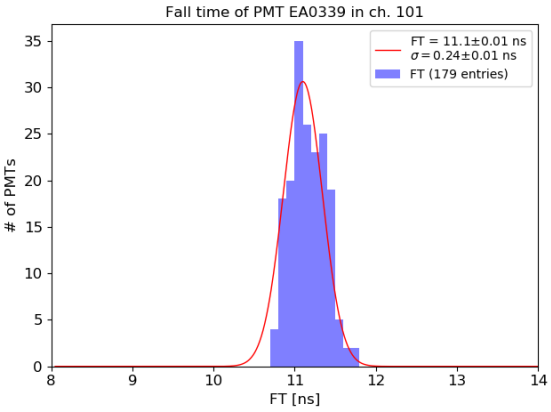

(d) FT results of EA0339 in ch. 101

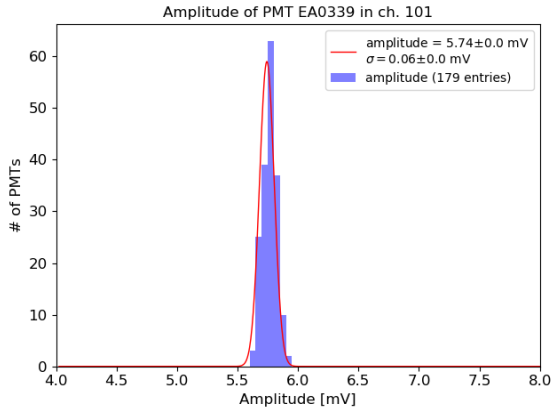

(e) amplitude results of EA0339 in ch. 101

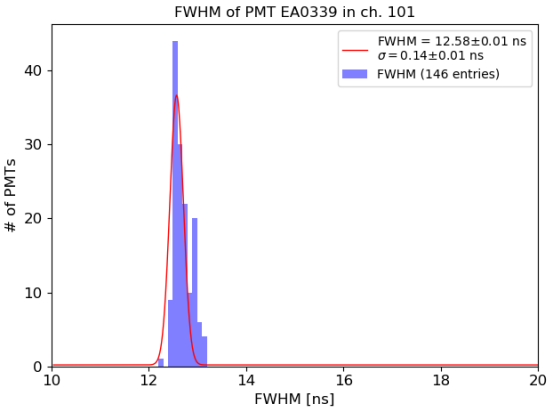

(f) FWHM results of EA0339 in ch. 101

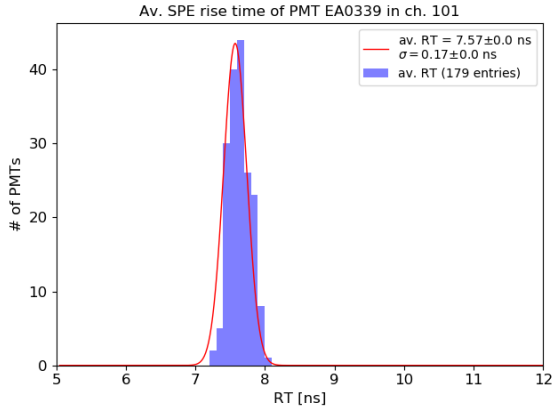

(g) av. SPE RT results of EA0339 in ch. 101

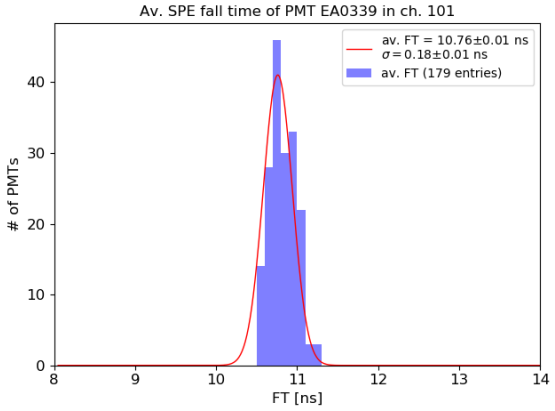

(h) av. SPE FT results of EA0339 in ch. 101

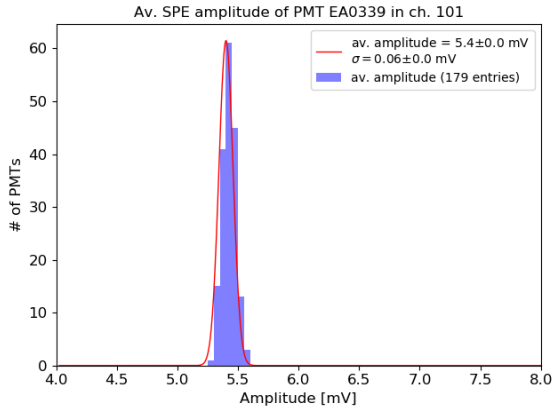

(i) av. SPE amplitude of EA0339 in ch. 101

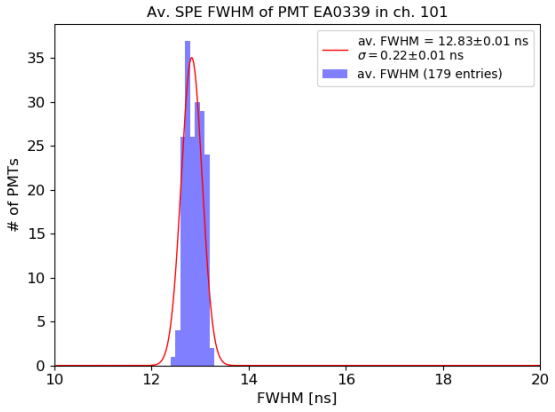

(j) av. SPE FWHM of EA0339 in ch. 101

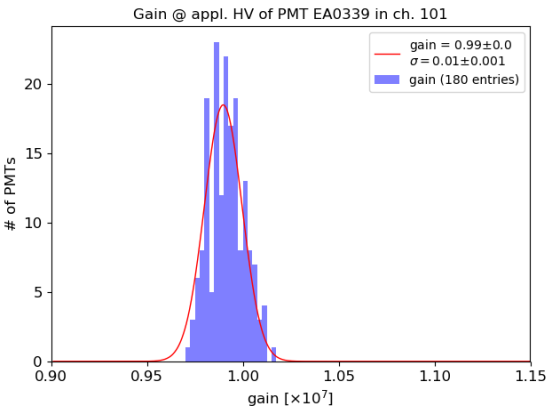

(k) gain results of EA0339 in ch. 101

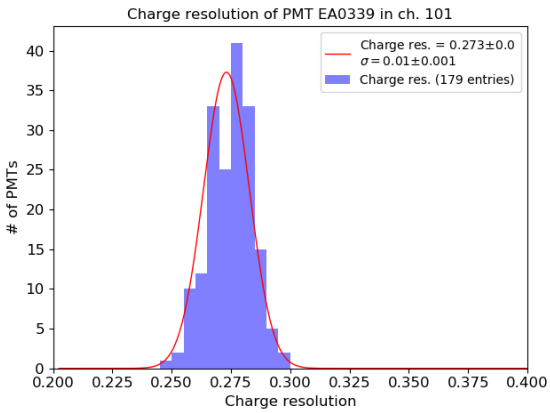

(l) charge resolution results of EA0339 in ch. 101

Figure E.18.: Additional histograms of results from reference PMT EA0339, taken at container A in ch. 101 over 179 valid runs (reduced statistics for FWHM are due to failing fits in the analysis). Distributions of results are fitted with a Gaussian function, proving again the stability of PMT performance over a large number of measurements, and confirming a high accuracy of the container system in determining these results.

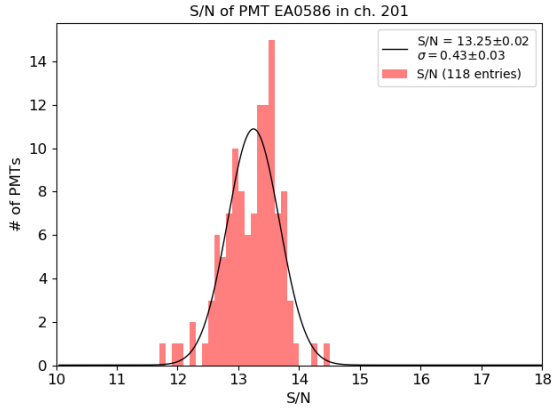

(a) S/N ratio results of EA0586 in ch. 201

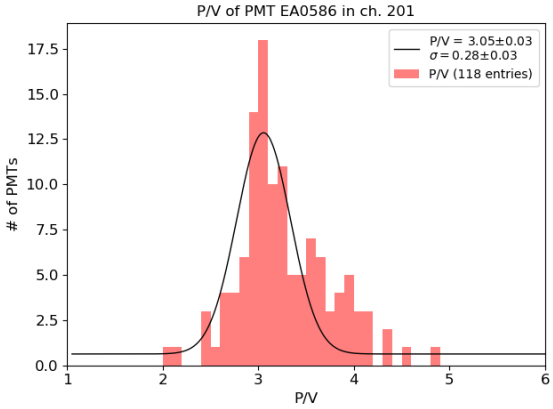

(b) P/V ratio results of EA0586 in ch. 201

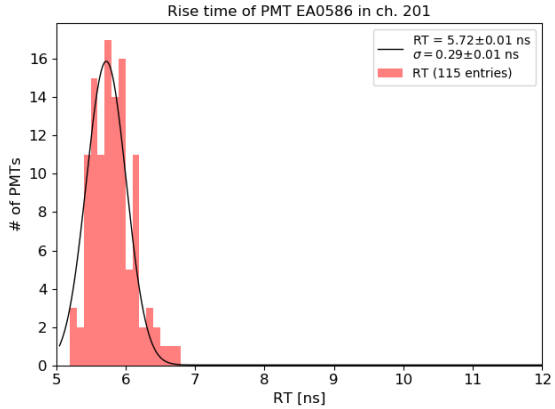

(c) RT results of EA0586 in ch. 201

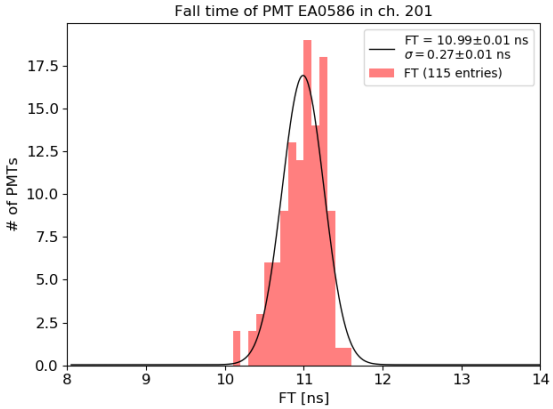

(d) FT results of EA0586 in ch. 201

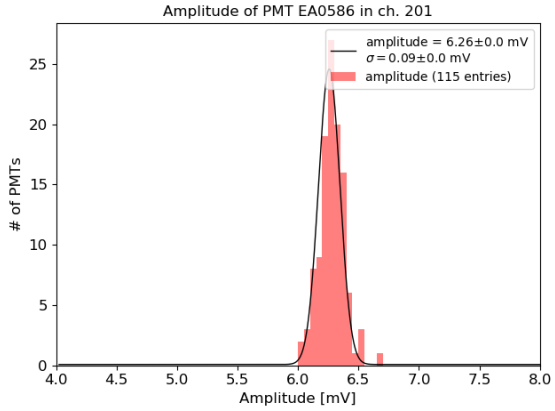

(e) amplitude results of EA0586 in ch. 201

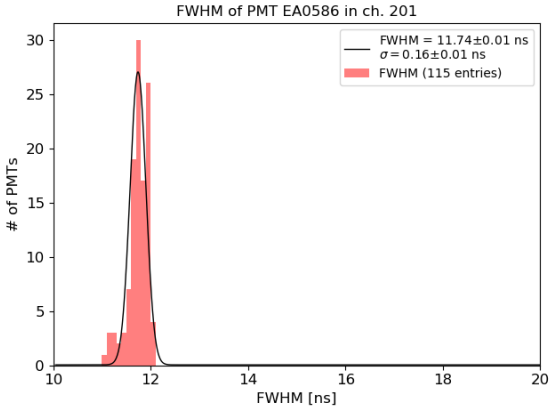

(f) FWHM results of EA0586 in ch. 201

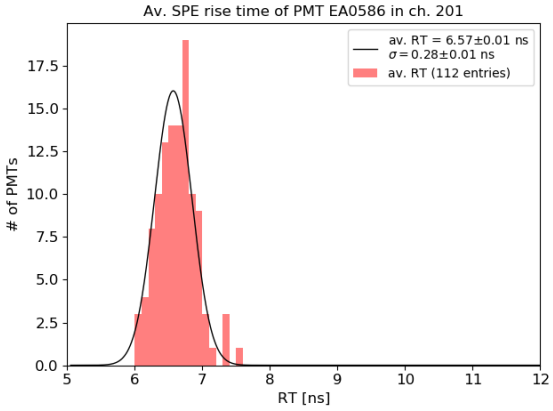

(g) av. SPE RT results of EA0586 in ch. 201

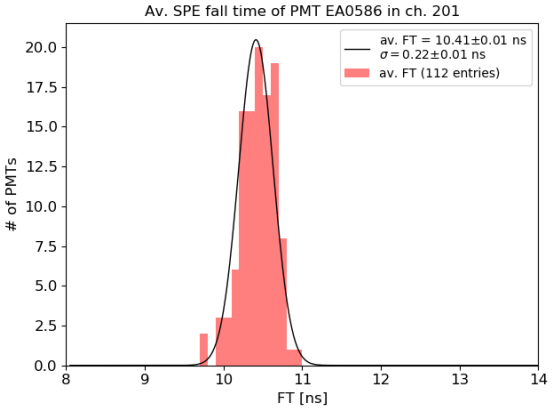

(h) av. SPE FT results of EA0586 in ch. 201

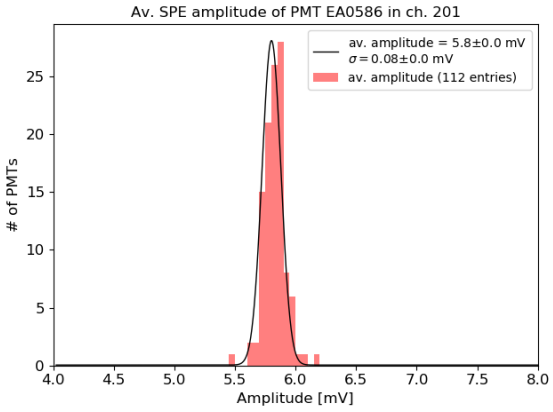

(i) av. SPE amplitude of EA0586 in ch. 201

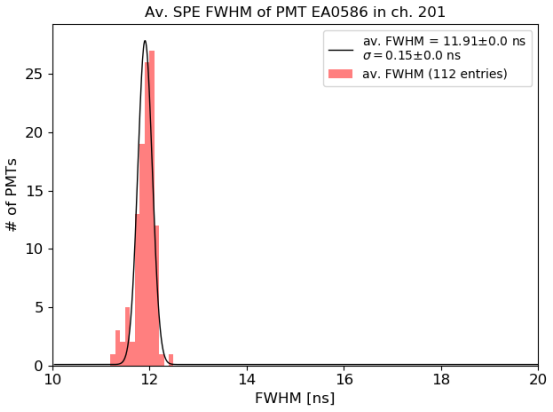

(j) av. SPE FWHM of EA0586 in ch. 201

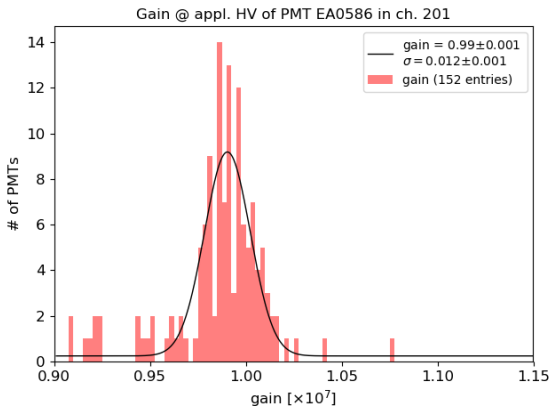

(k) gain results of EA0586 in ch. 201

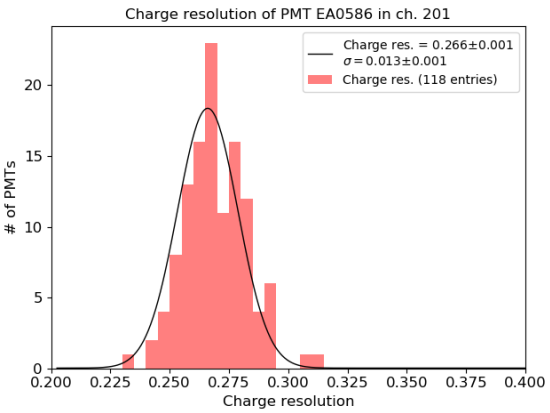

(l) charge resolution results of EA0586 in ch. 201

Figure E.19.: Additional histograms of results from reference PMT EA0586, taken at container B in ch. 201 over 118 valid runs (slightly reduced statistics for pulse shape parameters are due to failing fits in the analysis). Distributions of results are fitted with a Gaussian function, proving again the stability of PMT performance over a large number of measurements, and confirming a high accuracy of the container system in determining these results.

E.2.6. Measurement Accuracies

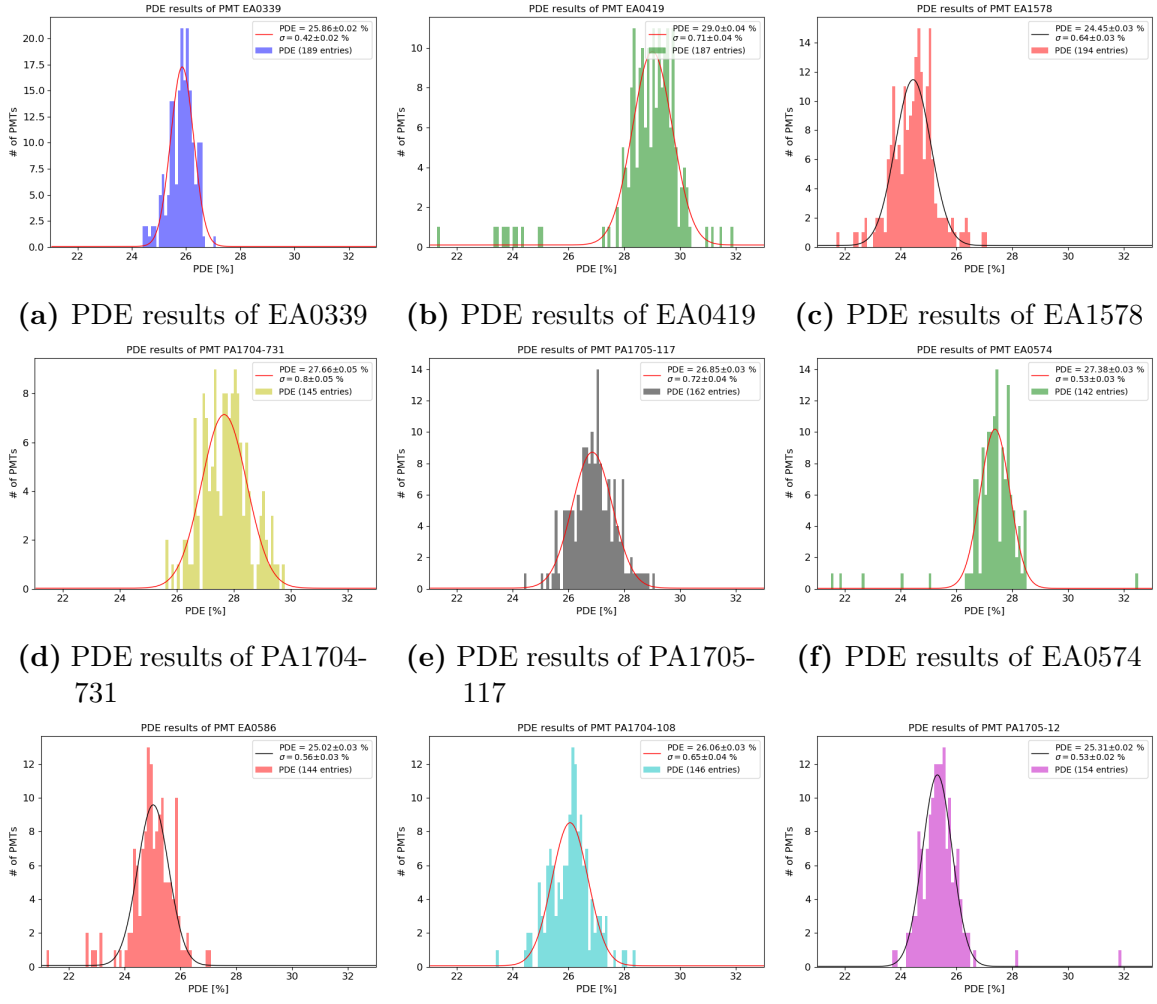

(a) PDE results of EA0339 **(b)** PDE results of EA0419 **(c)** PDE results of EA1578

(d) PDE results of PA1704-731 **(e)** PDE results of PA1705-117 **(f)** PDE results of EA0574

(g) PDE results of EA0586 **(h)** PDE results of PA1704-108 **(i)** PDE results of PA1705-12

Figure E.20.: PDE results of all reference PMTs from the analyzed data sample (masses $200-400$ at container A, see panels **(a)** to **(e)**, masses $50-250$ at container B, see panels **(f)** to **(i)**). Distributions were fitted with Gaussian functions to estimate the system's accuracy, see Table E.1a.

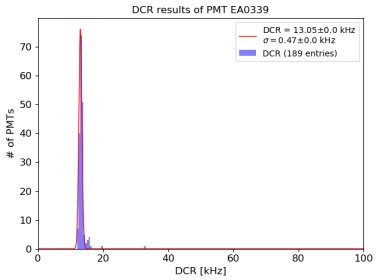

(a) DCR results of EA0339

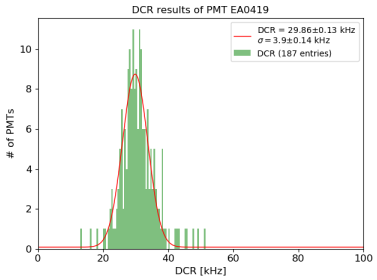

(b) DCR results of EA0419

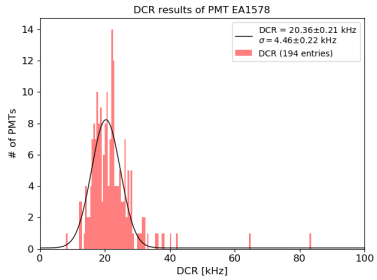

(c) DCR results of EA1578

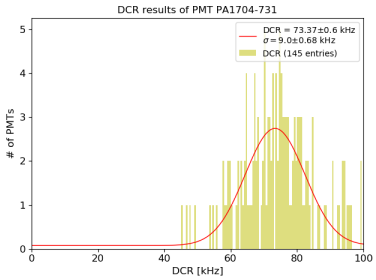

(d) DCR results of PA1704-731

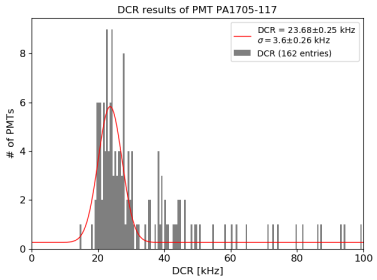

(e) DCR results of PA1705-117

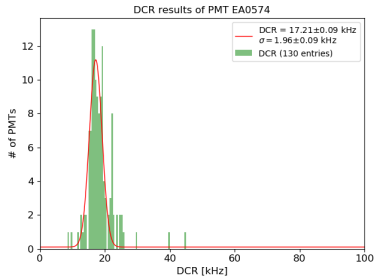

(f) DCR results of EA0574

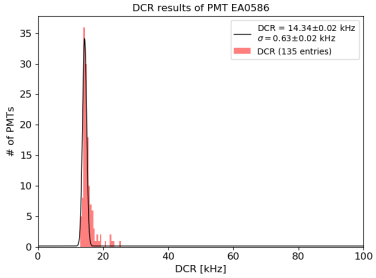

(g) DCR results of EA0586

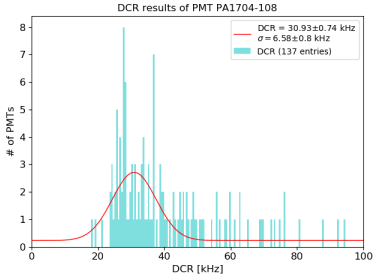

(h) DCR results of PA1704-108

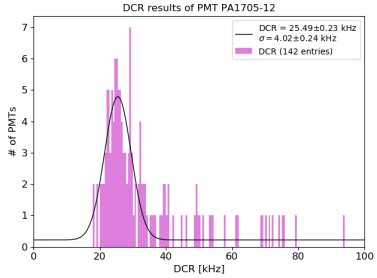

(i) DCR results of PA1705-12

Figure E.21.: DCR results of all reference PMTs from the analyzed data sample (masses $200-400$ at container A, see panels **(a)** to **(e)**, masses $50-250$ at container B, see panels **(f)** to **(i)**). Distributions were fitted with Gaussian functions to estimate the system's accuracy, see Table E.1b.

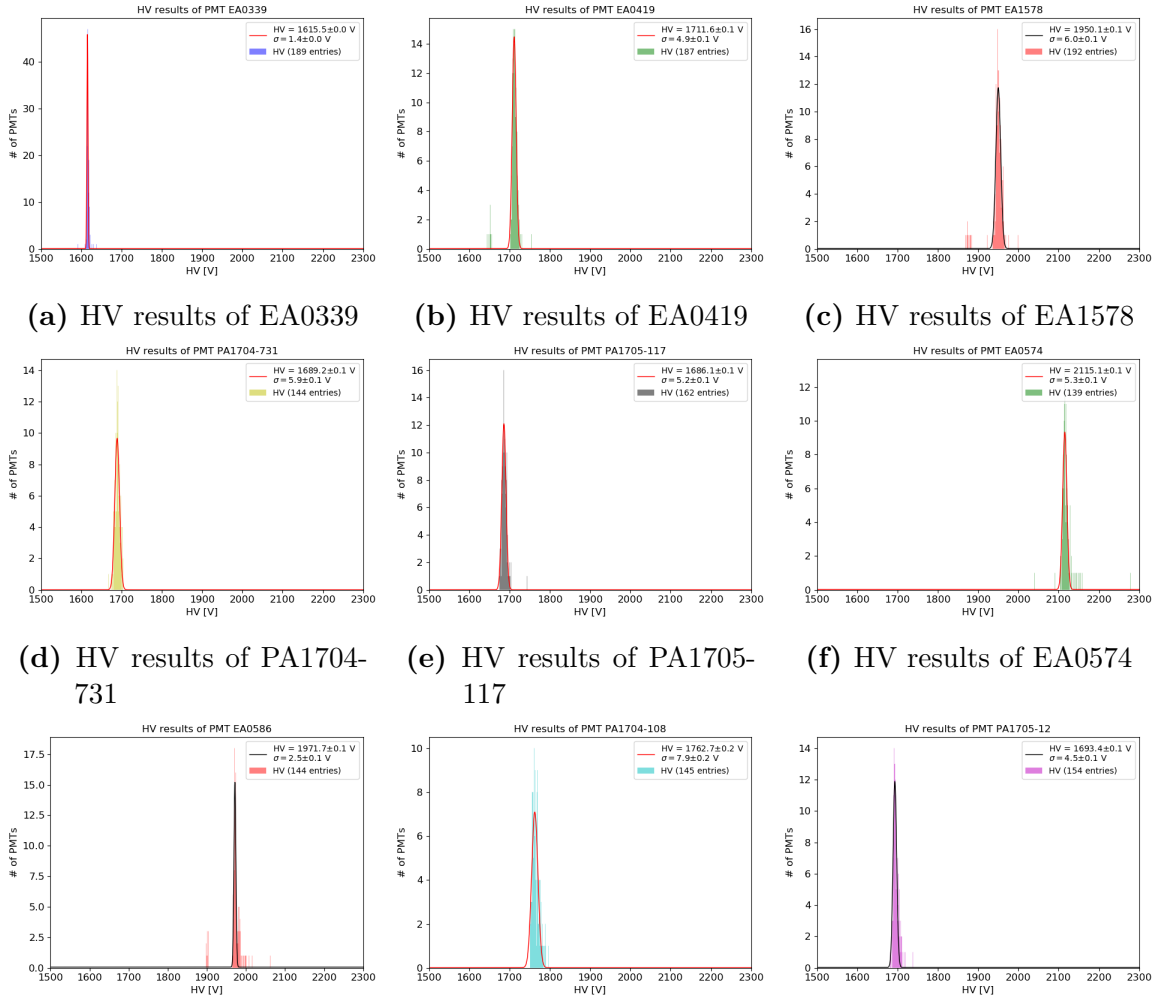

(a) HV results of EA0339 **(b)** HV results of EA0419 **(c)** HV results of EA1578

(d) HV results of PA1704-731 **(e)** HV results of PA1705-117 **(f)** HV results of EA0574

(g) HV results of EA0586 **(h)** HV results of PA1704-108 **(i)** HV results of PA1705-12

Figure E.22.: HV results of all reference PMTs from the analyzed data sample (masses $200-400$ at container A, see panels **(a)** to **(e)**, masses $50-250$ at container B, see panels **(f)** to **(i)**). Distributions were fitted with Gaussian functions to estimate the system's accuracy, see Table E.1c.

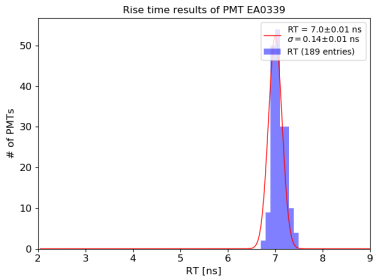

(a) RT results of EA0339

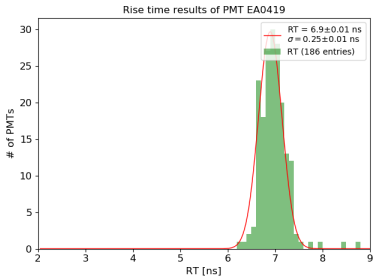

(b) RT results of EA0419

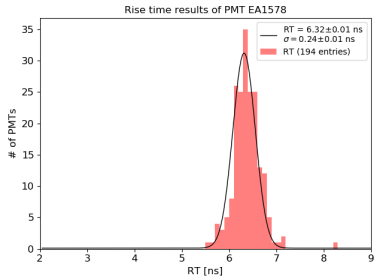

(c) RT results of EA1578

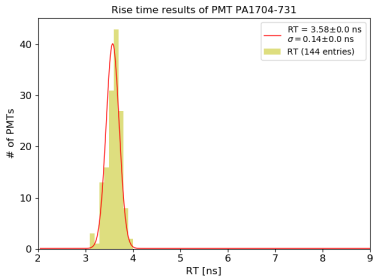

(d) RT results of PA1704-731

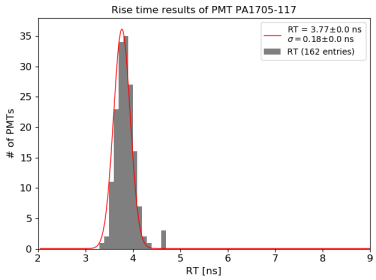

(e) RT results of PA1705-117

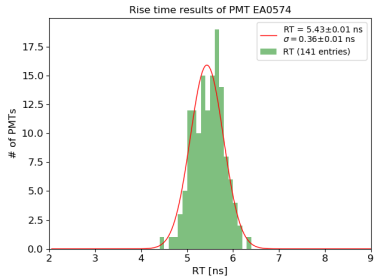

(f) RT results of EA0574

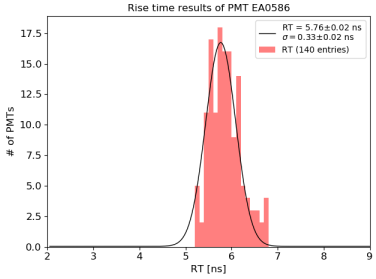

(g) RT results of EA0586

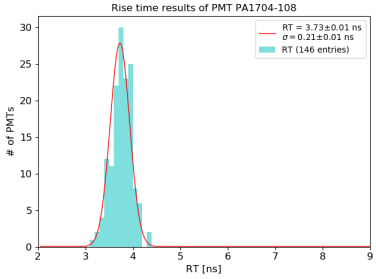

(h) RT results of PA1704-108

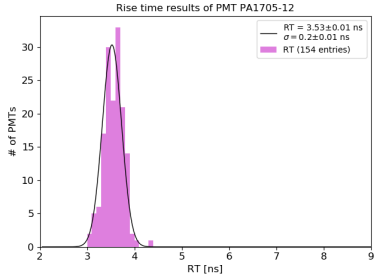

(i) RT results of PA1705-12

Figure E.23.: RT results of all reference PMTs from the analyzed data sample (masses $200 - 400$ at container A, see panels **(a)** to **(e)**, masses $50 - 250$ at container B, see panels **(f)** to **(i)**). Distributions were fitted with Gaussian functions to estimate the system's accuracy, see Table E.1d.

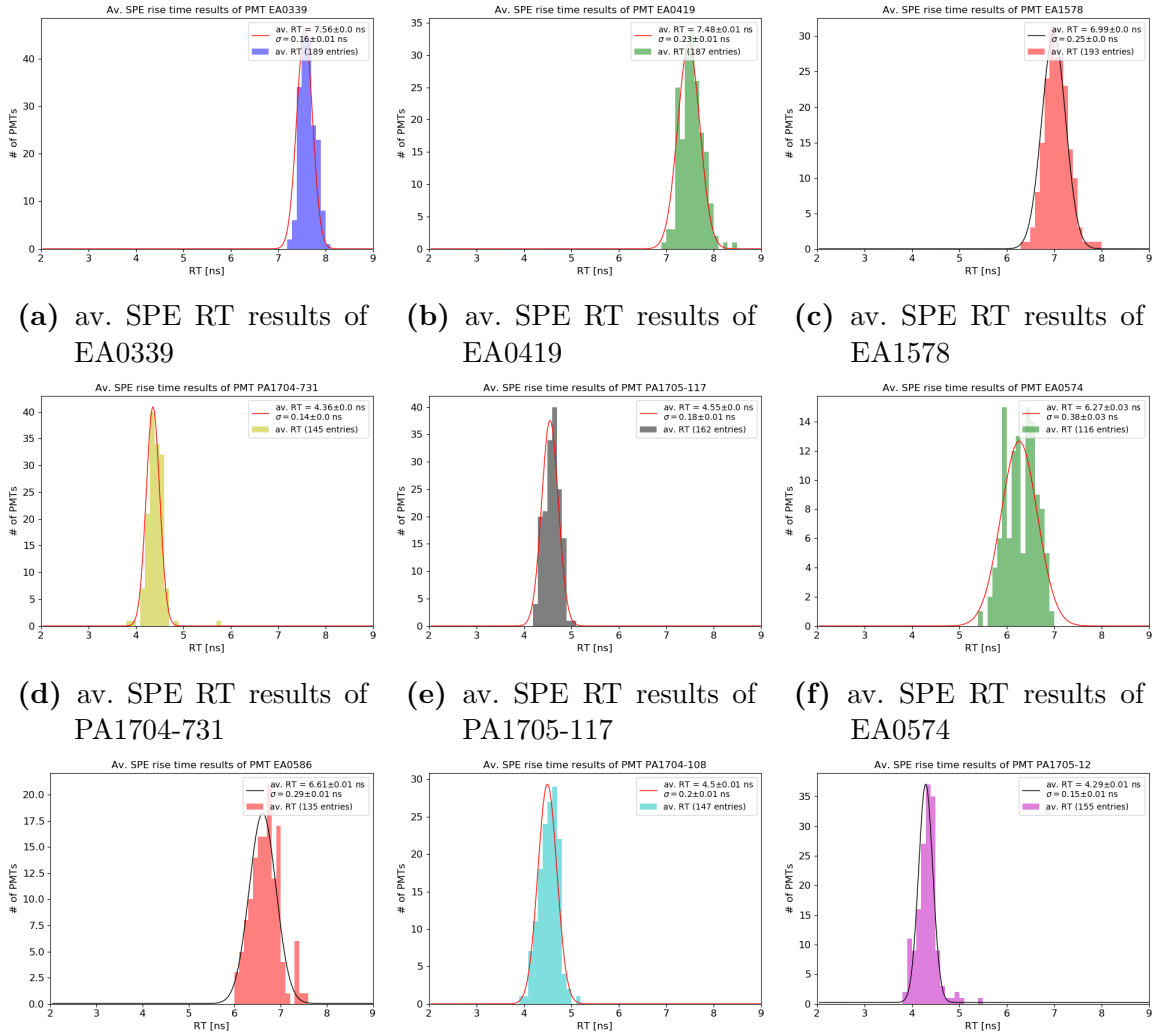

(a) av. SPE RT results of EA0339

(b) av. SPE RT results of EA0419

(c) av. SPE RT results of EA1578

(d) av. SPE RT results of PA1704-731

(e) av. SPE RT results of PA1705-117

(f) av. SPE RT results of EA0574

(g) av. SPE RT results of EA0586

(h) av. SPE RT results of PA1704-108

(i) av. SPE RT results of PA1705-12

Figure E.24.: Av. SPE RT results of all reference PMTs from the analyzed data sample (masses $200 - 400$ at container A, see panels **(a)** to **(e)**, masses $50 - 250$ at container B, see panels **(f)** to **(i)**). Distributions were fitted with Gaussian functions to estimate the system's accuracy, see Table E.1e.

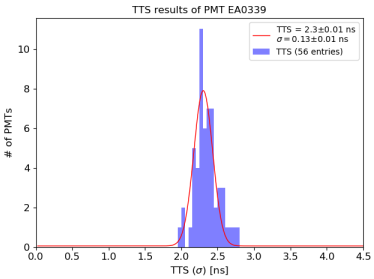

(a) TTS results of EA0339

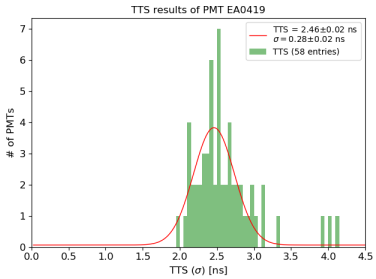

(b) TTS results of EA0419

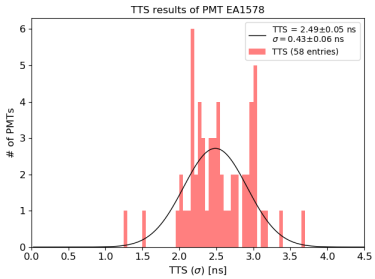

(c) TTS results of EA1578

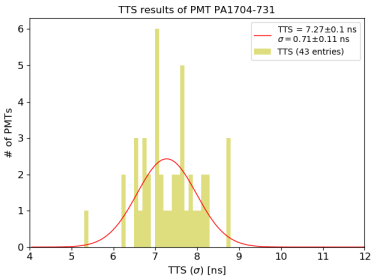

(d) TTS results of PA1704-731

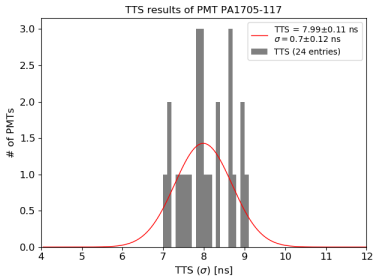

(e) TTS results of PA1705-117

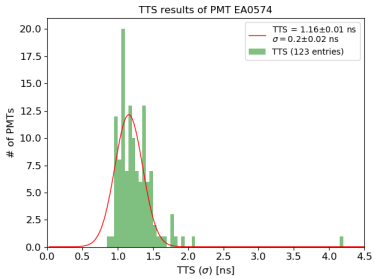

(f) TTS results of EA0574

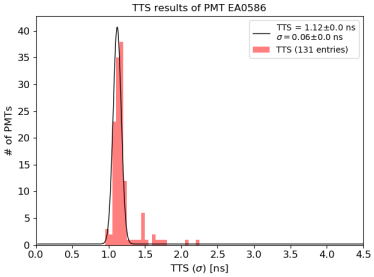

(g) TTS results of EA0586

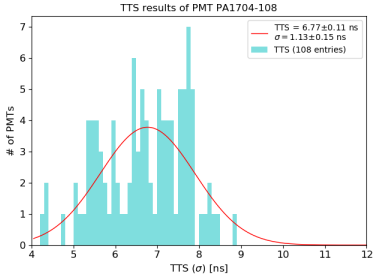

(h) TTS results of PA1704-108

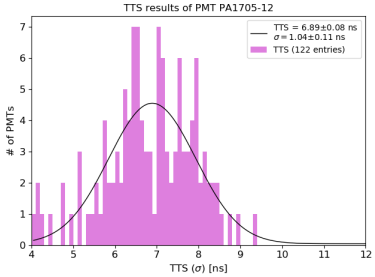

(i) TTS results of PA1705-12

Figure E.25.: TTS results of all reference PMTs from the analyzed data sample (masses $255-315$ at container A, see panels **(a)** to **(e)**, masses $50-250$ at container B, see panels **(f)** to **(i)**). Distributions were fitted with Gaussian functions to estimate the system's accuracy, see Table E.1f. Due to its low statistics, the result of PMT PA1705-117 (see panel **(e)**) have not been taken into account for the final accuracy estimation of this container.

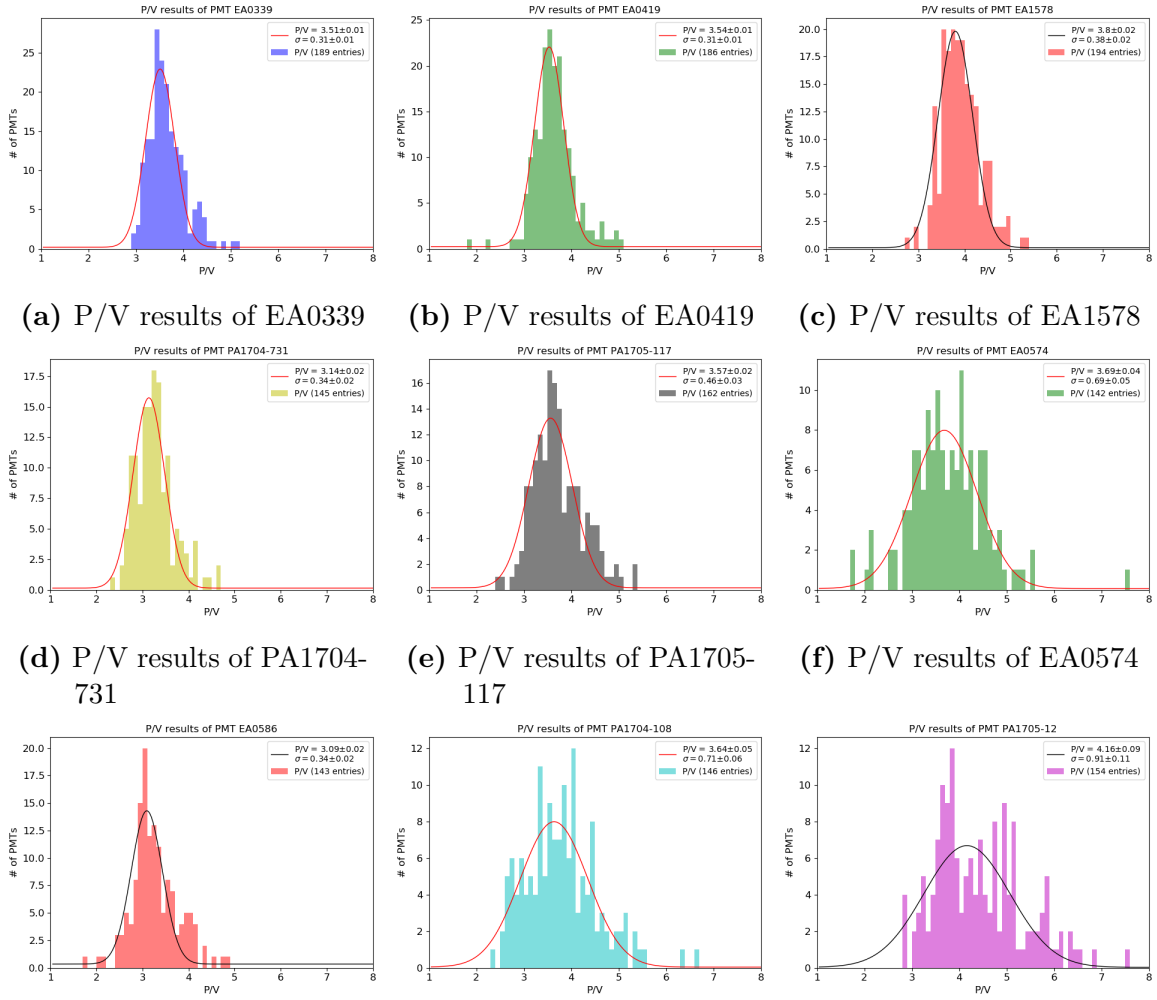

(a) P/V results of EA0339 **(b)** P/V results of EA0419 **(c)** P/V results of EA1578

(d) P/V results of PA1704-731 **(e)** P/V results of PA1705-117 **(f)** P/V results of EA0574

(g) P/V results of EA0586 **(h)** P/V results of PA1704-108 **(i)** P/V results of PA1705-12

Figure E.26.: P/V ratio results of all reference PMTs from the analyzed data sample (masses $200 - 400$ at container A, see panels **(a)** to **(e)**, masses $50 - 250$ at container B, see panels **(f)** to **(i)**). Distributions were fitted with Gaussian functions to estimate the system's accuracy, see Table E.1g.

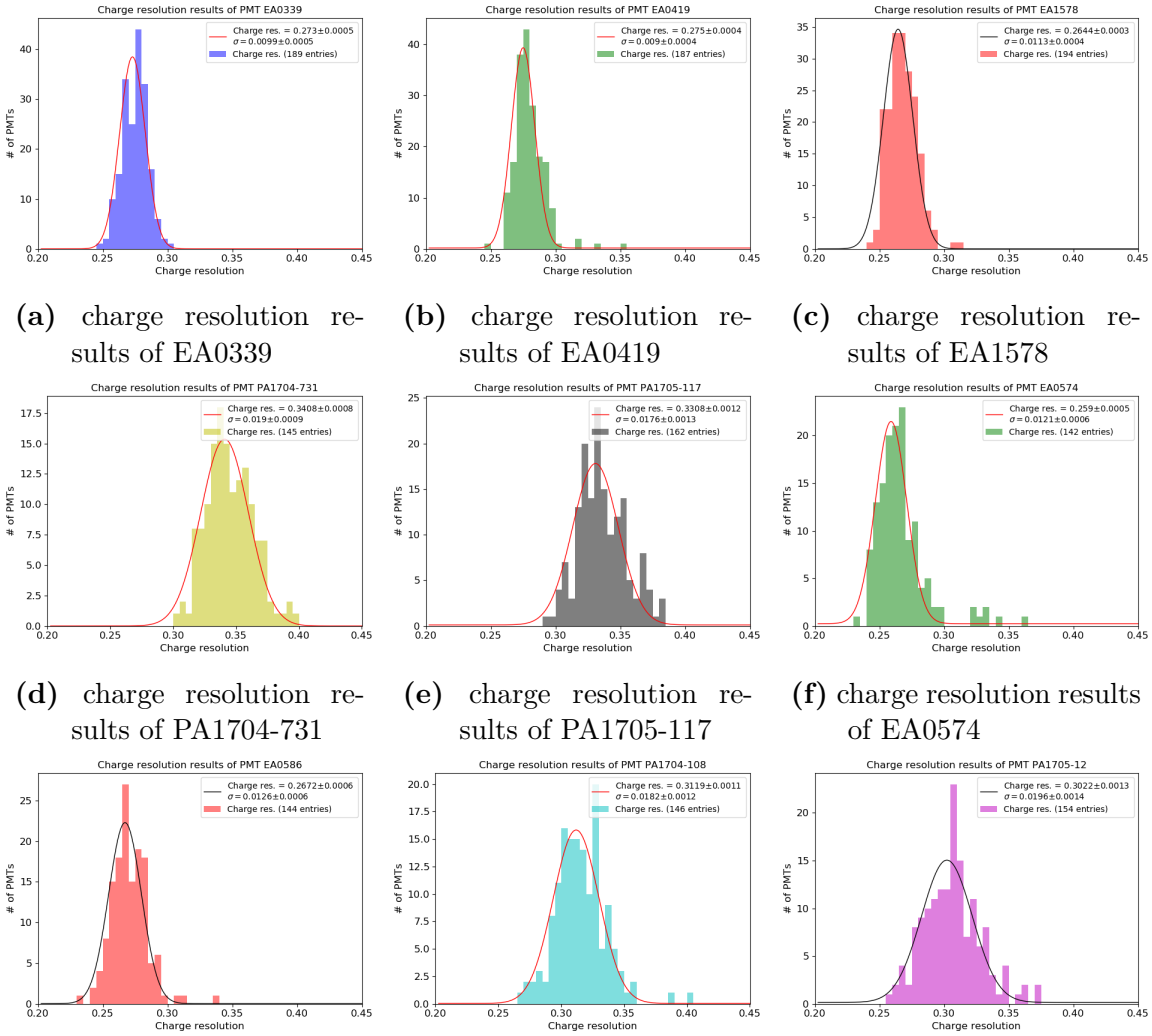

(a) charge resolution results of EA0339

(b) charge resolution results of EA0419

(c) charge resolution results of EA1578

(d) charge resolution results of PA1704-731

(e) charge resolution results of PA1705-117

(f) charge resolution results of EA0574

(g) charge resolution results of EA0586

(h) charge resolution results of PA1704-108

(i) charge resolution results of PA1705-12

Figure E.27.: Charge resolution results of all reference PMTs from the analyzed data sample (masses $200 - 400$ at container A, see panels **(a)** to **(e)**, masses $50 - 250$ at container B, see panels **(f)** to **(i)**). Distributions were fitted with Gaussian functions to estimate the system's accuracy, see Table E.1h.

Table E.1.: Fit results of the parameter distributions for all reference PMTs. Widths of the individual distributions are taken as measure for the system's accuracy. For the mean results, the rounded statistical uncertainties are given (might be also rounded to 0 in some cases due to large statistics).

(a) fit results of PDE distributions, see Figure E.20

PDE of...	Container	Valid results	Mean Result	System's Accuracy
EA0339	A	189	$25.86 \pm 0.02\,\%$	$0.42\,\%$
EA0419	A	187	$29.00 \pm 0.04\,\%$	$0.71\,\%$
EA1578	A	194	$24.45 \pm 0.03\,\%$	$0.64\,\%$
PA1704-731	A	145	$27.66 \pm 0.05\,\%$	$0.80\,\%$
PA1705-117	A	162	$26.85 \pm 0.03\,\%$	$0.72\,\%$
EA0574	B	142	$27.38 \pm 0.03\,\%$	$0.53\,\%$
EA0586	B	144	$25.02 \pm 0.03\,\%$	$0.56\,\%$
PA1704-108	B	146	$26.06 \pm 0.03\,\%$	$0.65\,\%$
PA1705-12	B	154	$25.31 \pm 0.02\,\%$	$0.53\,\%$

(b) fit results of DCR distributions, see Figure E.21

DCR of...	Container	Valid results	Mean Result	System's Accuracy
EA0339	A	189	$13.05 \pm 0.00\,\mathrm{kHz}$	$0.47\,\mathrm{kHz}$
EA0419	A	187	$29.86 \pm 0.13\,\mathrm{kHz}$	$3.90\,\mathrm{kHz}$
EA1578	A	194	$20.36 \pm 0.21\,\mathrm{kHz}$	$4.46\,\mathrm{kHz}$
PA1704-731	A	145	$73.37 \pm 0.60\,\mathrm{kHz}$	$9.00\,\mathrm{kHz}$
PA1705-117	A	162	$23.68 \pm 0.25\,\mathrm{kHz}$	$3.60\,\mathrm{kHz}$
EA0574	B	130	$17.21 \pm 0.09\,\mathrm{kHz}$	$1.96\,\mathrm{kHz}$
EA0586	B	135	$14.34 \pm 0.02\,\mathrm{kHz}$	$0.63\,\mathrm{kHz}$
PA1704-108	B	137	$30.93 \pm 0.74\,\mathrm{kHz}$	$6.58\,\mathrm{kHz}$
PA1705-12	B	142	$25.49 \pm 0.24\,\mathrm{kHz}$	$4.02\,\mathrm{kHz}$

(c) fit results of HV distributions, see Figure E.22

HV of...	Container	Valid results	Mean Result	System's Accuracy
EA0339	A	189	$1615.5 \pm 0.0\,\mathrm{V}$	$1.4\,\mathrm{V}$
EA0419	A	187	$1711.6 \pm 0.1\,\mathrm{V}$	$4.9\,\mathrm{V}$
EA1578	A	192	$1950.1 \pm 0.1\,\mathrm{V}$	$6.0\,\mathrm{V}$
PA1704-731	A	144	$1689.2 \pm 0.1\,\mathrm{V}$	$5.9\,\mathrm{V}$
PA1705-117	A	162	$1686.1 \pm 0.1\,\mathrm{V}$	$5.2\,\mathrm{V}$
EA0574	B	139	$2115.1 \pm 0.1\,\mathrm{V}$	$5.3\,\mathrm{V}$
EA0586	B	144	$1971.7 \pm 0.1\,\mathrm{V}$	$2.5\,\mathrm{V}$
PA1704-108	B	145	$1762.7 \pm 0.2\,\mathrm{V}$	$7.9\,\mathrm{V}$
PA1705-12	B	154	$1693.4 \pm 0.1\,\mathrm{V}$	$4.5\,\mathrm{V}$

(d) fit results of RT distributions, see Figure E.23

RT of...	Container	Valid results	Mean Result	System's Accuracy
EA0339	A	189	7.00 ± 0.01 ns	0.14 ns
EA0419	A	186	6.90 ± 0.01 ns	0.25 ns
EA1578	A	194	6.32 ± 0.01 ns	0.24 ns
PA1704-731	A	144	3.58 ± 0.00 ns	0.14 ns
PA1705-117	A	162	3.77 ± 0.00 ns	0.18 ns
EA0574	B	141	5.43 ± 0.01 ns	0.36 ns
EA0586	B	140	5.76 ± 0.02 ns	0.33 ns
PA1704-108	B	146	3.73 ± 0.01 ns	0.21 ns
PA1705-12	B	154	3.53 ± 0.01 ns	0.20 ns

(e) fit results of av. SPE RT distributions, see Figure E.24

Av. SPE RT of...	Container	Valid results	Mean Result	System's Accuracy
EA0339	A	189	7.56 ± 0.00 ns	0.16 ns
EA0419	A	187	7.48 ± 0.01 ns	0.23 ns
EA1578	A	193	6.99 ± 0.00 ns	0.25 ns
PA1704-731	A	145	4.36 ± 0.00 ns	0.14 ns
PA1705-117	A	162	4.55 ± 0.00 ns	0.18 ns
EA0574	B	116	6.27 ± 0.03 ns	0.38 ns
EA0586	B	135	6.61 ± 0.01 ns	0.29 ns
PA1704-108	B	147	4.50 ± 0.01 ns	0.20 ns
PA1705-12	B	155	4.29 ± 0.01 ns	0.15 ns

(f) fit results of TTS distributions, see Figure E.25

TTS of...	Container	Valid results	Mean Result	System's Accuracy
EA0339	A	56	2.30 ± 0.01 ns	0.13 ns
EA0419	A	58	2.46 ± 0.02 ns	0.28 ns
EA1578	A	58	2.49 ± 0.15 ns	0.43 ns
PA1704-731	A	43	7.27 ± 0.10 ns	0.71 ns
PA1705-117	A	24	7.99 ± 0.11 ns	0.70 ns
EA0574	B	123	1.16 ± 0.01 ns	0.20 ns
EA0586	B	131	1.12 ± 0.00 ns	0.06 ns
PA1704-108	B	108	6.77 ± 0.11 ns	1.13 ns
PA1705-12	B	122	6.89 ± 0.11 ns	1.04 ns

(g) fit results of P/V ratio distributions, see Figure E.26

P/V ratio of...	Container	Valid results	Mean Result	System's Accuracy
EA0339	A	189	3.51 ± 0.01	0.31
EA0419	A	186	3.54 ± 0.01	0.31
EA1578	A	194	3.80 ± 0.02	0.38
PA1704-731	A	145	3.14 ± 0.02	0.34
PA1705-117	A	162	3.57 ± 0.02	0.46
EA0574	B	142	3.69 ± 0.04	0.69
EA0586	B	143	3.09 ± 0.02	0.34
PA1704-108	B	146	3.64 ± 0.05	0.71
PA1705-12	B	154	4.16 ± 0.09	0.91

(h) fit results of charge resolution distributions, see Figure E.27

Resolution of...	Container	Valid results	Mean Result	System's Accuracy
EA0339	A	189	0.2730 ± 0.0005	0.0099
EA0419	A	187	0.2750 ± 0.0004	0.0090
EA1578	A	194	0.2644 ± 0.0003	0.0113
PA1704-731	A	145	0.3408 ± 0.0008	0.0190
PA1705-117	A	162	0.3308 ± 0.0012	0.0176
EA0574	B	142	0.2590 ± 0.0005	0.0121
EA0586	B	144	0.2672 ± 0.0006	0.0126
PA1704-108	B	146	0.3119 ± 0.0011	0.0182
PA1705-12	B	154	0.3022 ± 0.0013	0.0196

E.3. Additional Plots from Container Cross-Check Measurements

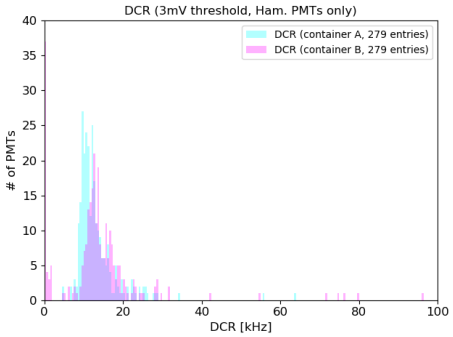

(a) DCR results of both containers

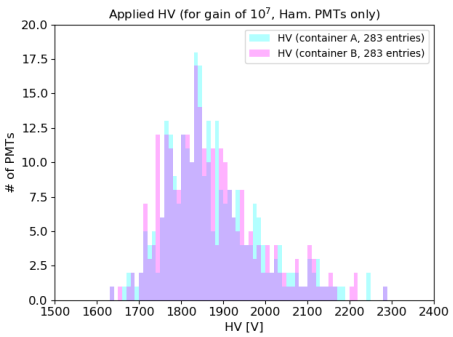

(b) HV results of both containers

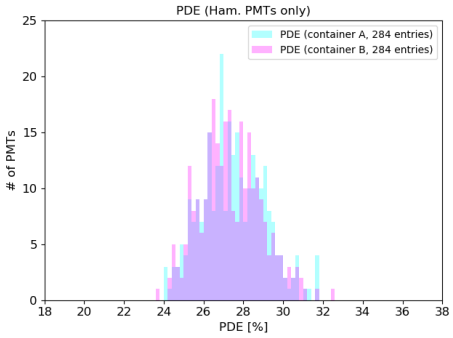

(c) PDE results of both containers

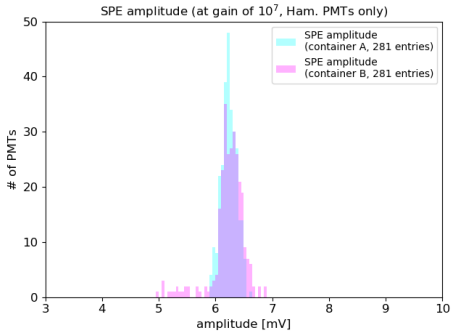

(d) amplitude results of both containers

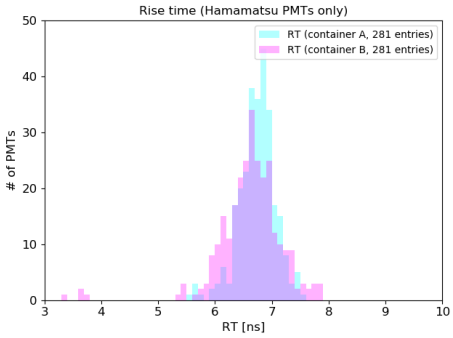

(e) RT results of both containers

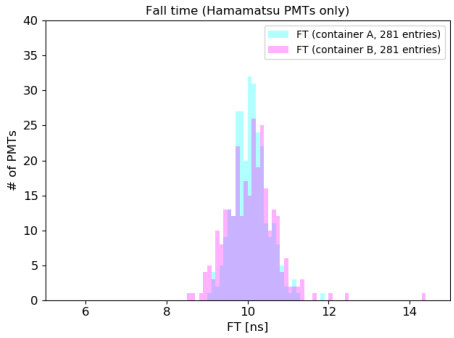

(f) FT results of both containers

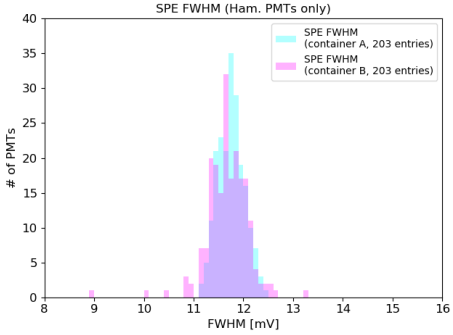

(g) FWHM results of both containers

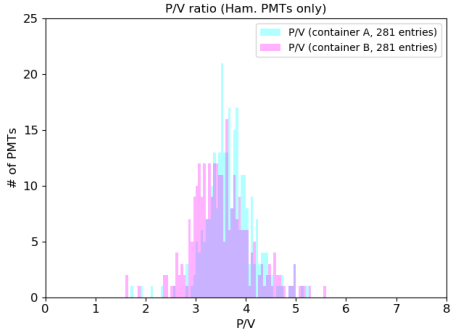

(h) P/V results of both containers

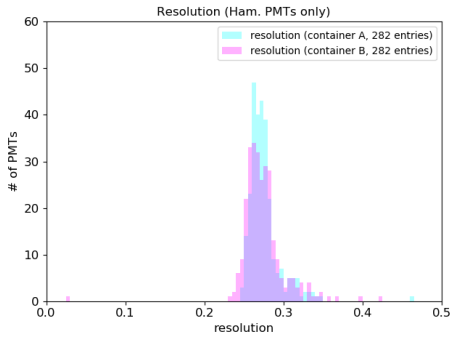

(i) charge resolution results of both containers

Figure E.28.: Valid parameter result distributions of 284 PMTs from container cross-check.

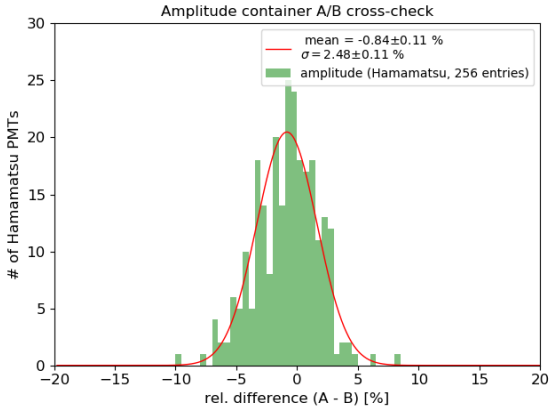

(a) rel. difference of amplitude results

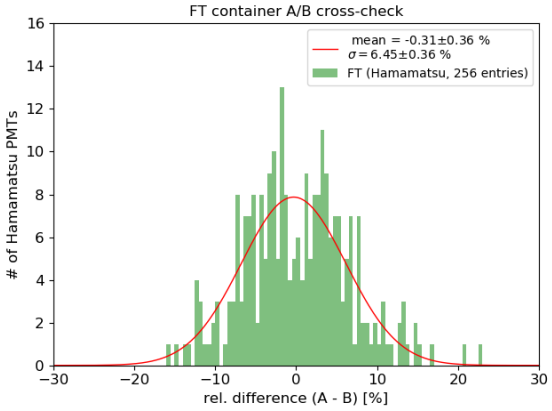

(b) rel. difference of FT results

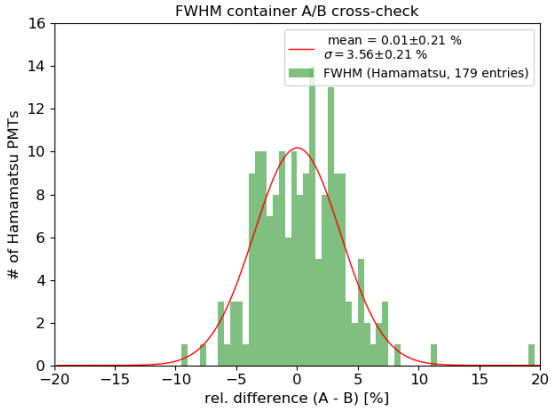

(c) rel. difference of FWHM results

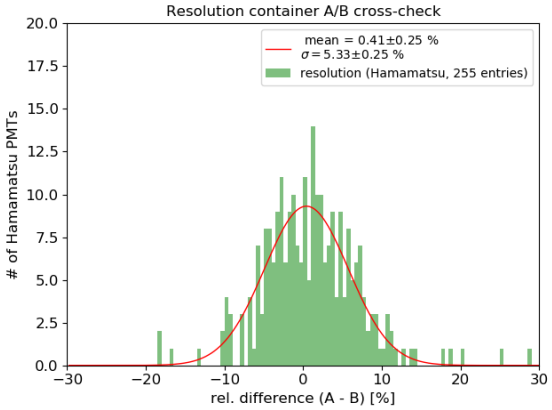

(d) rel. difference of charge resolution results

Figure E.29.: Additional plots of relative differences between results of containers A and B from the container cross-check survey.

E.4. Additional Plots from Investigations about Systematic Uncertainties

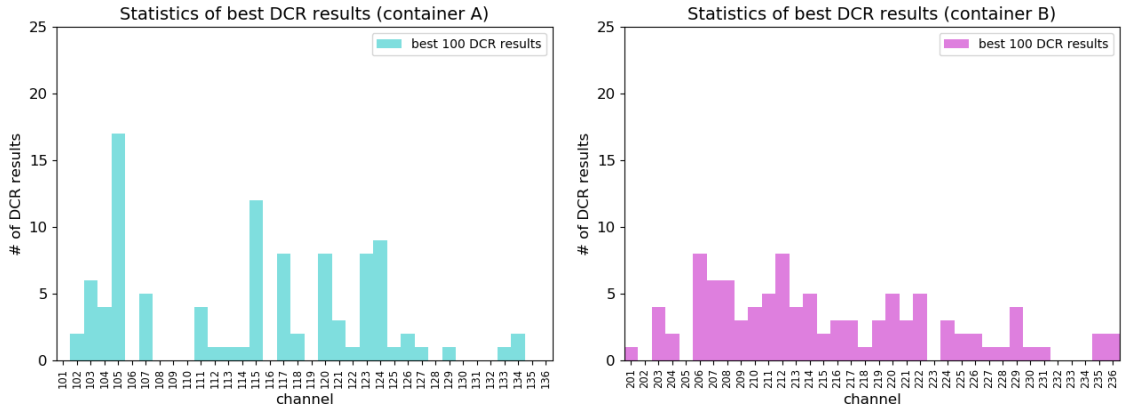

(a) best DCR results in container A per channel

(b) best DCR results in container B per channel

Figure E.30.: Statistics of best 100 DCR results in containers A (panel **(a)**) and B (panel **(b)**) plotted over the channels. DCR results in these plots cover values from 5.5 kHz to 8.7 kHz for container A and from 6.9 kHz to 12.1 kHz for container B.

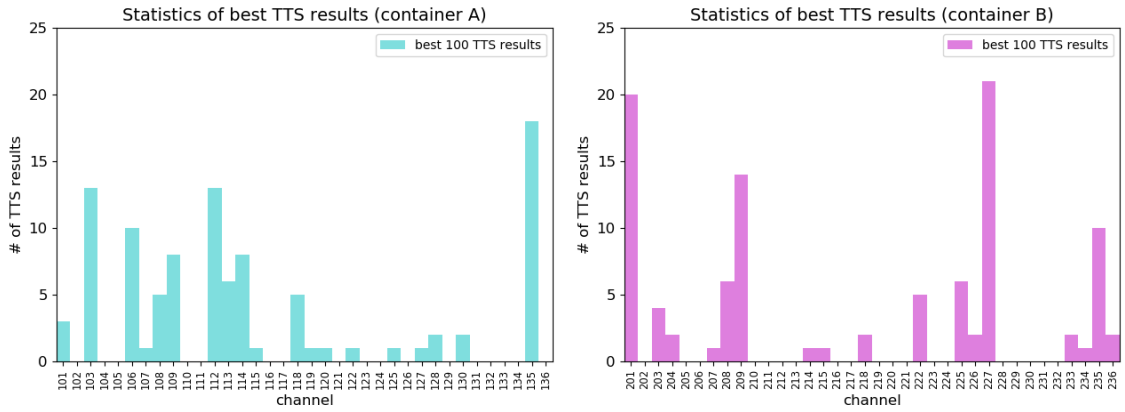

(a) best TTS results in container A per channel

(b) best TTS results in container B per channel

Figure E.31.: Statistics of best 100 TTS results in containers A (panel **(a)**) and B (panel **(b)**) plotted over the channels. TTS results in these plots cover values from 1.04 ns to 2.15 ns for container A and from 0.71 ns to 1.07 ns for container B.

List of Figures

List of Tables

List of Acronyms

$0\nu\beta\beta$	–	Neutrinoless Double Beta Decay
ABC	–	ASIC (Application-Specific Integrated Circuit) Battery Card
ACU	–	Automatic Calibration Unit
ADC	–	Analog to Digital Converter
ADU	–	Analog to Digital (converter) Unit
A.L.S.	–	Advanced Laser Systems GmbH
AMD	–	Advanced Micro Devices, Inc.
APR	–	Afterpulse Rate / Ratio
ASCII	–	American Standard Code for Information Interchange
AWG (n)	–	American Wire Gauge (wire cross section and resistance)
BaBar	–	B and B-bar experiment
BEC	–	Back-End Card
bfp	–	best fit point
bis-MSB	–	p-bis-(o-Methylstyryl)-Benzene
BNC	–	Bayonet Neill-Concelmann (standard coaxial cable connector)
Borexino	–	Boron solar neutrino Experiment
CAEN S.p.A.	–	Italian company for HV and data acquisition solutions
CAT-5e	–	Category 5 twisted pair cable (Ethernet)
CC	–	Charged Current (weak interaction)
CD	–	Central Detector (of JUNO)
CE	–	Collection Efficiency
cf_i	–	calibration factor of container channel (drawer box) i
CKM	–	Cabbibo Kobayashi Maskawa matrix / formalism
C.L.	–	Confidence Level
CLK	–	Clock unit
CMB	–	Cosmic Microwave Background
CNO	–	Carbon-Nitrogen-Oxygen (solar burning cycle)
CONET2	–	Chainable Optical NETwork (proprietary protocol by CAEN)
CP	–	Combined Charge Conjugation and Parity Symmetry
CPT	–	Combined Charge Conjugation, Parity and Time Reversal Symmetry
CPU	–	Central Processing Unit (of computer)
CUORE	–	Cryogenic Underground Observatory for Rare Events experiment
DAC	–	Digital to Analog Converter
DAQ	–	Automated Data Acquisition (software)
DC	–	Double Chooz experiment
DC power	–	Direct Current power (opposite of AC)
DCR	–	Dark Count Rate
DE	–	Detection Efficiency (see also: PDE)

DFG – Deutsche Forschungsgesellschaft e.V.
DMDL – Deutsche Magnet Dart Liga
DRS4 – Domino Ring Sampler 4th Gen. (developed by PSI, Switzerland)
DSNB – Diffuse Supernova Neutrino Background
DUNE – Deep Underground Neutrino Experiment
DYB – Daya Bay experiment / NPP (see also: NPP)
ECHo – Electron Capture on ^{163}Ho experiment
ECL – Emitter Coupled Logic
EMF – Earth's Magnetic Field
ES – Elastic Scattering
EXO – Enriched Xenon Observatory experiment
FADC – Flash ADC (see also: ADC)
FC/PC – Ferrule (or Fiber) Connector / Physical Contact
FFT – Fast Fourier Transformation
FIFO – Fan-In-Fan-Out
FINEMET – Nano-crystalline soft magnetic material (trade name by Hitachi Metals Ltd.)
FS – Fiber Splitter
fs – frame size
FT – Fall Time (see also: RT)
FWHM – Full Width Half Maximum
GALLEX – Gallium Experiment
GCC – Gain Cross-Check (value)
GCU – Global Control Unit
GERDA – Germanium Detector Array experiment
GNO – Gallium Neutrino Observatory experiment
GS – Gigasamples (unit, equals 10^9 samples)
GUI – Graphical User Interface
GUT – Grand Unified Theory
HDPE – High Density Polyethylene
HF (relay) – High Frequency relay
HT – Hit Time
HV – High Voltage
HVAC – Heating, Ventilation and Air Conditioning
HVU – High Voltage Unit (see also: HV)
HyperK – Hyper-Kamiokande experiment
HZ – Huizhou NPP (see also: NPP)
HZC – Hainan Zhanchuang Company
IBD – Inverse Beta Decay
IceCube – IceCube neutrino observatory experiment
IceCube-PINGU – see: IceCube, PINGU
IDP – Intermediate Data Point (method)
IHEP – Institute for High Energy Physics, Beijing, P.R. China
ILL – Institute Laue-Langevin, Grenoble, France
IMB – Irvine-Michigan-Brookhaven experiment
INO – India-based Neutrino Observatory experiment
IO – Inverted (mass) Ordering (see also: NMO, NO)

iPMT – intelligent PMT (see also: PMT)
I/O – Input/Output
JINR – Joint Institute for Nuclear Research, Dubna, Russia
JUNO – Jiangmen Underground Neutrino Observatory experiment
JUNO-TAO – see: JUNO, TAO
K2K – KEK (High Energy Accelerator Research Organization) to Kamioka experiment
KamLAND – Kamioka Liquid Scintillator Antineutrino Detector experiment
KamLAND-Zen – KamLAND upgrade for $0\nu\beta\beta$ search (see also: KamLAND)
KATRIN – Karlsruhe Tritium Neutrino experiment
KM3NeT – Cubic kilometer (km^3) Neutrino Telescope experiment
LAB – Linear Alkylbenzene
LabVIEW – Laboratory Virtual Instrument Engineering Workbench
LBNE – Long-Baseline Neutrino Experiment (see also: DUNE)
LED – Light Emission / Emitting Diode
LEGEND – Large Enriched Germanium Experiment for Neutrinoless Double beta decay
LEMO – Swiss connector company (connector standard)
LHAASO – Large High Altitude Air Shower Observatory experiment
LHCb – Large Hadron Collider b-experiment
LPMT – Large PMT (system); see also: PMT
LPR – Late Pulse Rate / Ratio (see also: PPR)
LSc / LS – Liquid Scintillator
LV – Low Voltage
L × W × H – Length × Width × Height
MC – Monte Carlo (simulation)
MCP – Micro-Channel Plate
MCP-PMT – see: MCP, PMT
MCX – Micro Coaxial (connector)
MH – see: NMH
MiniBooNE – Mini Booster Neutrino Experiment
MINOS – Main Injector Neutrino Oscillation Search experiment
MO – see: NMO
MSW – Mikheyev-Smirnov-Wolfenstein (effect)
m.w.e. – meter water equivalent
NA – Numerical Aperture
NC – Neutral Current (weak interaction)
ND – Neutral Density (filter)
ndf – number of degrees of freedom (in fit)
NEUTRINO – Biannual international conference on neutrino physics and astrophysics
nEXO – next EXO experiment (see also: EXO)
NI – National Instruments Corp.
NIM – Nuclear Instrumentation (Module) standard
NMH – Neutrino Mass Hierarchy
NMO – Neutrino Mass Ordering
NNVT – Northern Night Vision Technology Ltd.
NO – Normal (mass) Ordering (see also: NMO, IO)
NOνA – NuMI Off-Axis ν_e Appearance experiment

NPP – Nuclear Power Plant
OD – Optical Depth
OPERA – Oscillation Project with Emulsion tRacking Apparatus experiment
O.P.S. – Onsite PMT testing Software
OSIRIS – Online Scintillator Internal Radioactivity Investigation System
PB – Power Board
PC – Photocathode
PCB – Printed Circuit Board
PCI(e) – Peripheral Component Interconnect (express)
PDE – Photon Detection (or Photo-Detection) Efficiency
PE / p.e. – Photo-Electron (also used as unit)
PIN (diode) – Positive Intrinsic Negative diode
PINGU – Precision IceCube Next Generation Upgrade experiment
PMMA – Poly Methyl Methacrylate
PMNS – Pontecorvo-Maki-Nakagawa-Sakata (neutrino mixing matrix)
PMT – Photomultiplier Tube
PMT ID – PMT Identification / serial number (see also: PMT)
PoE – Power over Ethernet
PPO – 2,5-Diphenyloxazole
PPR – Prepulse Rate / Ratio (see also: LPR)
P.R. China – People's Republic of China
PT1000 – highly sensitive Platinum Temperature sensor ($R = 1000\,\Omega$)
PTFE – Polytetrafluoroethylene, commonly known as Teflon (trade name by DuPont)
PU – Polyurethane
PVC – Polyvinyl Chloride
P/V – Peak-to-Valley ratio
QDC – Charge-to-Digital Converter
QE – Quantum Efficiency
RENO – Reactor Experiment for Neutrino Oscillation
RG (n) – Coaxial cable standard / type
RS232 – Recommended Standard 232 (for serial communication transmission of data)
RT – Rise Time (see also: FT)
R&D – Research and Development
SAGE – Soviet-American Gallium Experiment
SHV – Safe High Voltage (connector)
SiPM – Silicon-Photomultiplier
SK – Super-Kamiokande experiment
SM – Standard Model of particle physics
SMA – SubMiniature version A (coaxial connector)
SNEWS – Supernova Early Warning System
SNO – Sudbury Neutrino Observatory experiment
SPE – Single PE (see also: PE)
sPMT – small PMT (system); see also: PMT
SS – Scanning Station
SSB – Signal Switching Board
SSM – Solar Standard Model

SSS – Stainless Steel (lattice) Shell / Steel Support Structure
STEREO – Search for Sterile Reactor Neutrino Oscillations experiment
subVI – see: VI
SUSY – Super-Symmetry (Super Symmetric theory)
S/B – Signal-to-Background ratio
S/N – Signal-to-Noise ratio
T2K – Tokai to Kamioka experiment
TAO – Taishan Antineutrino Observatory (JUNO near detector)
TAUP – Biannual international conference on Topics in Astroparticle and Underground Physics
TG – Trigger Group
TNU – Terrestrial Neutrino Unit
TPC / IP – Transmission Control Protocol / Internet Protocol
TRG – Trigger unit
TS – Taishan NPP (see also: NPP)
TT – Top Tracker system
TTL – Transistor-Transistor Logic
TTS – Transit Time Spread
USB – Universal Serial Bus
UV – Ultra-Violet
UW – Underwater (box)
VI – Virtual Interface
VME – Versa Module Eurocard (bus)
V-A – Vector minus Axial theory of weak interaction
WLS – Wavelength Shifter
WP – Water Pool
YJ – Yangjiang NPP (see also: NPP)

Bibliography

[1] C. L. Cowan, F. Reines, F. B. Harrison, H. W. Kruse, and A. D. McGuire. Detection of the Free Neutrino: A Confirmation. *Science*, 124(3212):103 – 104, 1956. ISSN 0036-8075. doi: 10.1126/science.124.3212.103.

[2] F. Close. *NEUTRINO*. Oxford University Press, 2012. ISBN 9780199695997.

[3] B. T. Cleveland et al. Measurement of the Solar Electron Neutrino Flux with the Homestake Chlorine Detector. *The Astrophysical Journal*, 496(1):505 – 526, 1998. doi: 10.1086/305343.

[4] K. S. Hirata et al. (Kamiokande Collaboration). Observation of ^{8}B Solar Neutrinos in the Kamiokande-II Detector. *Phys. Rev. Lett.*, 63:16 – 19, 1989. doi: 10.1103/PhysRevLett.63.16.

[5] P. Anselmann et al. (GALLEX Collaboration). Solar Neutrinos Observed by GALLEX at Gran Sasso. *Phys. Lett. B*, 285(4):376 – 389, 1992. ISSN 0370-2693. doi: 10.1016/0370-2693(92)91521-A.

[6] J. N. Abdurashitov et al. (SAGE Collaboration). Measurement of the Solar Neutrino Capture Rate by SAGE and Implications for Neutrino Oscillations in Vacuum. *Phys. Rev. Lett.*, 83(23):4686 – 4689, 1999. doi: 10.1103/PhysRevLett.83.4686.

[7] Q. R. Ahmad et al. (SNO Collaboration). Measurement of the Rate of $\nu_e + d \rightarrow p + p + e^-$ Interactions Produced by ^{8}B Solar Neutrinos at the Sudbury Neutrino Observatory. *Phys. Rev. Lett.*, 87(7):071301, 2001. doi: 10.1103/PhysRevLett.87.071301.

[8] K. Eguchi et al. (KamLAND Collaboration). First Results from KamLAND: Evidence for Reactor Antineutrino Disappearance. *Phys. Rev. Lett.*, 90:021802, 2003. doi: 10.1103/PhysRevLett.90.021802.

[9] C. Arpesella et al. (Borexino Collaboration). First Real Time Detection of ^{7}Be Solar Neutrinos by Borexino. *Phys. Lett. B*, 658(4):101 – 108, 2008. doi: 10.1016/j.physletb.2007.09.054.

[10] S. Adrián-Martínez et al. (ANTARES Collaboration). Measurement of Atmospheric Neutrino Oscillations with the ANTARES Neutrino Telescope. *Phys. Lett. B*, 714 (2-5):224 – 230, 2012. doi: 10.1016/j.physletb.2012.07.002.

[11] M. G. Aartsen et al. (IceCube Collaboration). Evidence for High-Energy Extraterrestrial Neutrinos at the IceCube Detector. *Science*, 342(6161), 2013. ISSN 0036-8075. doi: 10.1126/science.1242856.

[12] T. Adam et al. (JUNO Collaboration). JUNO Conceptual Design Report. *arXiv e-prints*, art. arXiv:1508.07166, 2015.

[13] R. Acciarri et al. (DUNE Collaboration). Long-Baseline Neutrino Facility (LBNF) and Deep Underground Neutrino Experiment (DUNE) Conceptual Design Report Volume

1: The LBNF and DUNE Projects. *arXiv e-prints*, art. arXiv:1601.05471, 2016.

[14] M. G. Aartsen et al. (IceCube-Gen2 Collaboration). PINGU: A Vision for Neutrino and Particle Physics at the South Pole. *J. Phys. G*, 44(5):054006, 2017. doi: 10.1088/1361-6471/44/5/054006.

[15] K. Abe et al. (Hyper-Kamiokande Proto-Collaboration). Hyper-Kamiokande Design Report. *arXiv e-prints*, art. arXiv:1805.04163, 2018.

[16] N. Abgrall et al. (LEGEND Collaboration). The Large Enriched Germanium Experiment for Neutrinoless Double Beta Decay (LEGEND). *American Institute of Physics Conference Series*, 1894(1):020027, 2017. doi: 10.1063/1.5007652. Proceeding of Matrix Elements for the Double beta decay Experiments Conference (MEDEX'17): Prague, Czech Republic, May 29 - June 2, 2017.

[17] F. An et al. Neutrino Physics with JUNO. *J. Phys. G Nucl. Phys.*, 43(3):030401, 2016. doi: 10.1088/0954-3899/43/3/030401.

[18] R. B. Patterson. Prospects for Measurement of the Neutrino Mass Hierarchy. *Annual Review of Nuclear and Particle Science*, 65(1):177 – 192, 2015. doi: 10.1146/annurev-nucl-102014-021916.

[19] M. Tanabashi et al. (Particle Data Group). Review of Particle Physics. *Phys. Rev. D*, 98:030001, 2018. doi: 10.1103/PhysRevD.98.030001.

[20] M. K. Gaillard, P. D. Grannis, and F. J. Sciulli. The Standard Model of Particle Physics. *Rev. Mod. Phys.*, 71:96 – 111, 1999. doi: 10.1103/RevModPhys.71.S96.

[21] V. I. Borodulin, R. N. Rogalyov, and S. R. Slabospitsky. CORE 2.1 (COmpendium of RElations, Version 2.1). *arXiv e-prints*, art. hep-ph/9507456, 1995.

[22] M. Goldhaber, L. Grodzins, and A. W. Sunyar. Helicity of Neutrinos. *Phys. Rev.*, 109:1015 – 1017, 1958. doi: 10.1103/PhysRev.109.1015.

[23] E. C. G. Sudarshan and R. E. Marshak. Chirality Invariance and the Universal Fermi Interaction. *Phys. Rev.*, 109:1860 – 1862, 1958. doi: 10.1103/PhysRev.109.1860.2.

[24] Y. F. Li and Z. Z. Xing. Possible Capture of keV Sterile Neutrino Dark Matter on Radioactive β-decaying Nuclei. *Phys. Lett. B*, 695(1):205 – 210, 2011. ISSN 0370-2693. doi: 10.1016/j.physletb.2010.11.015.

[25] R. N. Mohapatra and G. Senjanović. Neutrino Mass and Spontaneous Parity Nonconservation. *Phys. Rev. Lett.*, 44:912 – 915, 1980. doi: 10.1103/PhysRevLett.44.912.

[26] J. Schechter and J. W. F. Valle. Neutrino Masses in SU(2) $\bigotimes$ U(1) Theories. *Phys. Rev. D*, 22:2227 – 2235, 1980. doi: 10.1103/PhysRevD.22.2227.

[27] T. Yanagida. Horizontal Symmetry and Masses of Neutrinos. *Progress of Theoretical Physics*, 64(3):1103 – 1105, 1980. ISSN 0033-068X. doi: 10.1143/PTP.64.1103.

[28] J. W. F. Valle. Neutrino Physics Overview. *Journal of Physics Conference Series*, 53: 473 – 505, 2006. doi: 10.1088/1742-6596/53/1/031. Lecture from Elementary Particle Physics Corfu Summer Institute (CORFU2005): Corfu, Greece, September 4-26, 2005.

[29] M. Aker et al. (KATRIN Collaboration). An Improved Upper Limit on the Neutrino Mass from a Direct Kinematic Method by KATRIN. *Phys. Rev. Lett.*, 123(22):221802,

2019. doi: 10.1103/PhysRevLett.123.221802.

[30] P. A. R. Ade et al. (Planck Collaboration). Planck 2013 Results. XVI. Cosmological Parameters. *Astronomy & Astrophysics*, 571:A16, 2014. doi: 10.1051/0004-6361/201321591.

[31] J. A. Formaggio and G. P. Zeller. From eV to EeV: Neutrino Cross Sections Across Energy Scales. *Rev. Mod. Phys.*, 84(3):1307 – 1341, 2012. doi: 10.1103/RevModPhys.84.1307.

[32] A. A. Aguilar-Arevalo et al. (MiniBooNE Collaboration). Search for Electron Neutrino Appearance at the $\Delta m^2 \sim 1\text{eV}^2$ Scale. *Phys. Rev. Lett.*, 98(23):231801, 2007. doi: 10.1103/PhysRevLett.98.231801.

[33] A. A. Aguilar-Arevalo et al. (MiniBooNE Collaboration). Significant Excess of Electron-Like Events in the MiniBooNE Short-Baseline Neutrino Experiment. *Phys. Rev. Lett.*, 121(22):221801, 2018. doi: 10.1103/PhysRevLett.121.221801.

[34] N. Allemandou et al. (STEREO Collaboration). The STEREO Experiment. *Journal of Instrumentation*, 13(7):P07009, 2018. doi: 10.1088/1748-0221/13/07/P07009.

[35] M. Agostini et al. (GERDA Collaboration). Background-Free Search for Neutrinoless Double-β Decay of ^{76}Ge with GERDA. *Nature*, 544(7648):47 – 52, 2017. doi: 10.1038/nature21717.

[36] J. B. Albert et al. (nEXO Collaboration). Sensitivity and Discovery Potential of the proposed nEXO Experiment to Neutrinoless Double-β Decay. *Phys. Rev. C*, 97(6):065503, 2018. doi: 10.1103/PhysRevC.97.065503.

[37] S. Mertens. Direct Neutrino Mass Experiments. *Journal of Physics Conference Series*, 718(2):022013, 2016. doi: 10.1088/1742-6596/718/2/022013. Proceeding of Prospects in Neutrino Physics (NuPhys2015): London, UK, December 16-18, 2015.

[38] A. Osipowicz et al. (KATRIN collaboration). KATRIN: A Next Generation Tritium Beta Decay Experiment with sub-eV Sensitivity for the Electron Neutrino Mass. Letter of Intent. *arXiv e-prints*, art. hep-ex/0109033, 2001.

[39] S. Mertens et al. (KATRIN Collaboration). Status of the KATRIN Experiment and Prospects to Search for keV-mass Sterile Neutrinos in Tritium β-decay. *Physics Procedia*, 61:267 – 273, 2015. ISSN 1875-3892. doi: 10.1016/j.phpro.2014.12.043. Proceeding of 13th International Conference on Topics in Astroparticle and Underground Physics (TAUP 2013): Asilomar (CA), USA, September 8-13, 2013.

[40] M. Galeazzi et al. (ECHo Collaboration). The Electron Capture Decay of 163-Ho to Measure the Electron Neutrino Mass with sub-eV Accuracy (and Beyond). *arXiv e-prints*, art. arXiv:1202.4763, 2012.

[41] K. Blaum et al. (ECHo Collaboration). The Electron Capture ^{163}Ho Experiment ECHo. *arXiv e-prints*, art. arXiv:1306.2655, 2013. Part of a White Paper for the Future of Neutrino Mass Measurements: Terrestrial, Astrophysical, and Cosmological Measurements in the Next Decade (NUMASS2013) Workshop: Milano, Italy, February 4-7, 2013.

[42] D. Ayres et al. (NOvA Collaboration). NOvA: Proposal to Build a 30 Kiloton Off-Axis Detector to Study $\nu_\mu \rightarrow \nu_e$ Oscillations in the Fermilab NuMI Beamline. *arXiv*

e-prints, art. hep-ex/0503053, 2005.

[43] M. A. Acero et al. (NOvA Collaboration). First Measurement of Neutrino Oscillation Parameters using Neutrinos and Antineutrinos by NOvA. *Phys. Rev. Lett.*, 123(15): 151803, 2019. doi: 10.1103/PhysRevLett.123.151803.

[44] R. Acciarri et al. (DUNE Collaboration). Long-Baseline Neutrino Facility (LBNF) and Deep Underground Neutrino Experiment (DUNE) Conceptual Design Report Volume 2: The Physics Program for DUNE at LBNF. *arXiv e-prints*, art. arXiv:1512.06148, 2015.

[45] M. G. Aartsen et al. (IceCube-PINGU Collaboration). Letter of Intent: The Precision IceCube Next Generation Upgrade (PINGU). *arXiv e-prints*, art. arXiv:1401.2046, 2014.

[46] J. H. Christenson, J. W. Cronin, V. L. Fitch, and R. Turlay. Evidence for the 2π Decay of the K_2^0 Meson. *Phys. Rev. Lett.*, 13:138 – 140, 1964. doi: 10.1103/PhysRevLett.13.138.

[47] B. Aubert et al. (BaBar Collaboration). Measurement of CP-Violating Asymmetries in B^0 Decays to CP Eigenstates. *Phys. Rev. Lett.*, 86(12):2515 – 2522, 2001. doi: 10.1103/PhysRevLett.86.2515.

[48] K. Abe et al. (Belle Collaboration). Observation of Large CP Violation in the Neutral B Meson System. *Phys. Rev. Lett.*, 87(9):091802, 2001. doi: 10.1103/PhysRevLett.87.091802.

[49] R. Aaij et al. (LHCb Collaboration). Observation of CP Violation in Charm Decays. *Phys. Rev. Lett.*, 122:211803, 2019. doi: 10.1103/PhysRevLett.122.211803.

[50] R. Aaij et al. (LHCb Collaboration). Observation of Several Sources of CP Violation in $B^+ \to \pi^+\pi^+\pi^-$ Decays. *Phys. Rev. Lett.*, 124:031801, 2020. doi: 10.1103/PhysRevLett.124.031801.

[51] K. Abe et al. (T2K Collaboration). Search for CP Violation in Neutrino and Antineutrino Oscillations by the T2K Experiment with 2.2×10^{21} Protons on Target. *Phys. Rev. Lett.*, 121(17):171802, 2018. doi: 10.1103/PhysRevLett.121.171802.

[52] K. Abe et al. (T2K Collaboration). Measurement of Neutrino and Antineutrino Oscillations by the T2K Experiment including a New Additional Sample of ν_e Interactions at the Far Detector. *Phys. Rev. D*, 96(9):092006, 2017. doi: 10.1103/PhysRevD.96.092006,10.1103/PhysRevD.98.019902. [Erratum: Phys. Rev.D98, no.1, 019902(2018)].

[53] R. Davis, D. S. Harmer, and K. C. Hoffman. Search for Neutrinos from the Sun. *Phys. Rev. Lett.*, 20:1205 – 1209, 1968. doi: 10.1103/PhysRevLett.20.1205.

[54] J. N. Bahcall, N. A. Bahcall, and G. Shaviv. Present Status of the Theoretical Predictions for the ^{37}Cl Solar-Neutrino Experiment. *Phys. Rev. Lett.*, 20:1209 – 1212, 1968. doi: 10.1103/PhysRevLett.20.1209.

[55] J. N. Bahcall, S. Basu, and M. H. Pinsonneault. How Uncertain are Solar Neutrino Predictions? *Phys. Lett. B*, 433(1-2):1 – 8, 1998. doi: 10.1016/S0370-2693(98)00657-1.

[56] J. N. Bahcall and R. Davis. Solar Neutrinos: A Scientific Puzzle. *Science*, 191(4224): 264 – 267, 1976. ISSN 0036-8075. doi: 10.1126/science.191.4224.264.

[57] J. N. Bahcall, W. F. Huebner, S. H. Lubow, P. D. Parker, and R. K. Ulrich. Standard Solar Models and the Uncertainties in Predicted Capture Rates of Solar Neutrinos. *Rev. Mod. Phys.*, 54:767 – 799, 1982. doi: 10.1103/RevModPhys.54.767.

[58] M. Altmann et al. (GNO Collaboration). GNO Solar Neutrino Observations: Results for GNO I. *Phys. Lett. B*, 490(1):16 – 26, 2000. ISSN 0370-2693. doi: 10.1016/S0370-2693(00)00915-1.

[59] J. M. Barnothy. Solar Neutrino Puzzle. *Nature*, 252:666 – 667, 1974. doi: 10.1038/252666b0.

[60] W. C. Haxton. The Solar Neutrino Puzzle. *Comments Nucl. Part. Phys.*, 16(2):95 – 108, 1986.

[61] Y. Fukuda et al. (Super-Kamiokande Collaboration). Evidence for Oscillation of Atmospheric Neutrinos. *Phys. Rev. Lett.*, 81(8):1562 – 1567, 1998. doi: 10.1103/PhysRevLett.81.1562.

[62] Y. Ashie et al. (Super-Kamiokande Collaboration). Evidence for an Oscillatory Signature in Atmospheric Neutrino Oscillations. *Phys. Rev. Lett.*, 93:101801, 2004. doi: 10.1103/PhysRevLett.93.101801.

[63] Q. R. Ahmad et al. (SNO Collaboration). Direct Evidence for Neutrino Flavor Transformation from Neutral-Current Interactions in the Sudbury Neutrino Observatory. *Phys. Rev. Lett.*, 89:011301, 2002. doi: 10.1103/PhysRevLett.89.011301.

[64] M. H. Ahn et al. (K2K Collaboration). Measurement of Neutrino Oscillation by the K2K eExperiment. *Phys. Rev. D*, 74(7):072003, 2006. doi: 10.1103/PhysRevD.74.072003.

[65] P. Adamson et al. (MINOS Collaboration). Measurement of Neutrino and Antineutrino Oscillations Using Beam and Atmospheric Data in MINOS. *Phys. Rev. Lett.*, 110(25):251801, 2013. doi: 10.1103/PhysRevLett.110.251801.

[66] Y. Abe et al. (Double Chooz Collaboration). Improved Measurements of the Neutrino Mixing Angle θ_{13} with the Double Chooz Detector. *Journal of High Energy Physics*, 10:86, 2014. doi: 10.1007/JHEP02(2015)074,10.1007/JHEP10(2014)086. [Erratum: JHEP02, 074(2015)].

[67] D. Adey et al. (Daya Bay Collaboration). Measurement of the Electron Antineutrino Oscillation with 1958 Days of Operation at Daya Bay. *Phys. Rev. Lett.*, 121(24):241805, 2018. doi: 10.1103/PhysRevLett.121.241805.

[68] J. K. Ahn et al. (RENO Collaboration). Observation of Reactor Electron Antineutrinos Disappearance in the RENO Experiment. *Phys. Rev. Lett.*, 108:191802, 2012. doi: 10.1103/PhysRevLett.108.191802.

[69] N. Agafonova et al. (OPERA Collaboration). Observation of a First ν_τ Candidate Event in the OPERA Experiment in the CNGS Beam. *Phys. Lett. B*, 691(3):138 – 145, 2010. ISSN 0370-2693. doi: 10.1016/j.physletb.2010.06.022.

[70] V. Gribov and B. Pontecorvo. Neutrino Astronomy and Lepton Charge. *Phys. Lett. B*, 28(7):493 – 496, 1969. ISSN 0370-2693. doi: 10.1016/0370-2693(69)90525-5.

[71] N. Cabibbo. Unitary Symmetry and Leptonic Decays. *Phys. Rev. Lett.*, 10:531 – 533,

1963. doi: 10.1103/PhysRevLett.10.531.

[72] M. Kobayashi and T. Maskawa. CP-Violation in the Renormalizable Theory of Weak Interaction. *Progress of Theoretical Physics*, 49(2):652 – 657, 1973. ISSN 0033-068X. doi: 10.1143/PTP.49.652.

[73] B. Pontecorvo. Inverse Beta Processes and Nonconservation of Lepton Charge. *Sov. Phys. JETP*, 7:172 – 173, 1958. [Zh. Eksp. Teor. Fiz.34,247(1957)].

[74] Z. Maki, M. Nakagawa, and S. Sakata. Remarks on the Unified Model of Elementary Particles. *Progress of Theoretical Physics*, 28(5):870 – 880, 1962. ISSN 0033-068X. doi: 10.1143/PTP.28.870.

[75] B. Pontecorvo. Neutrino Experiments and the Problem of Conservation of Leptonic Charge. *Sov. Phys. JETP*, 26:984 – 988, 1968. [Zh. Eksp. Teor. Fiz.53,1717(1967)].

[76] S. Antusch, C. Biggio, E. Fernández-Martínez, M. Belen Gavela, and J. López-Pavón. Unitarity of the Leptonic Mixing Matrix. *Journal of High Energy Physics*, 10:084, 2006. doi: 10.1088/1126-6708/2006/10/084.

[77] S. Antusch and O. Fischer. Non-Unitarity of the Leptonic Mixing Matrix: Present Bounds and Future Sensitivities. *Journal of High Energy Physics*, 10:094, 2014. doi: 10.1007/JHEP10(2014)094.

[78] A. Cabrera. Possible Precise Neutrino Unitarity? *arXiv e-prints*, art. arXiv:1911.03686, 2019. Proceeding of 2019 European Physical Society Conference on High Energy Physics (EPS-HEP2019): Ghent, Belgium, July 10-17, 2019.

[79] S. Eidelman et al. (Particle Data Group). Review of Particle Physics. *Phys. Lett. B*, 592:1, 2004.

[80] I. Esteban et al. NuFIT 4.1 (2019), 2019. URL `http://www.nu-fit.org`. Online available; last accessed: 7th August 2020.

[81] I. Esteban, M. C. Gonzalez-Garcia, A. Hernandez-Cabezudo, M. Maltoni, and T. Schwetz. Global Analysis of Three-Flavour Neutrino Oscillations: Synergies and Tensions in the Determination of θ_{23}, δ_{CP}, and the Mass Ordering (NuFIT 4.0). *Journal of High Energy Physics*, 01(1):106, 2019. doi: 10.1007/JHEP01(2019)106.

[82] L. Wolfenstein. Neutrino Oscillations in Matter. *Phys. Rev. D*, 17:2369 – 2374, 1978. doi: 10.1103/PhysRevD.17.2369.

[83] S. P. Mikheyev and A. Y. Smirnov. Resonant Amplification of ν Oscillations in Matter and Solar Neutrino Spectroscopy. *Il Nuovo Cimento C*, 9(1):17 – 26, 1986. ISSN 0390-5551. doi: 10.1007/BF02508049.

[84] M. A. Acero et al. (NOvA Collaboration). New Constraints on Oscillation Parameters from ν_e Appearance and ν_μ Disappearance in the NOvA Experiment. *Phys. Rev. D*, 98(3):032012, 2018. doi: 10.1103/PhysRevD.98.032012.

[85] Y. Hayato. Atmospheric Neutrino Results from Super-Kamiokande. 2018. doi: 10.5281/zenodo.1298567. Talk at XXVIII International Conference on Neutrino Physics and Astrophysics (NEUTRINO 2018): Heidelberg, Germany, June 4-9, 2018.

[86] P. F. de Salas, D. V. Forero, C. A. Ternes, M. Tórtola, and J. W. F. Valle. Status of Neutrino Oscillations 2018: 3σ Hint for Normal Mass Ordering and Improved CP

Sensitivity. *Phys. Lett. B*, 782:633 – 640, 2018. ISSN 0370-2693. doi: 10.1016/j.physletb.2018.06.019.

[87] F. Capozzi, E. Lisi, A. Marrone, and A. Palazzo. Current Unknowns in the Three Neutrino Framework. *Prog. Part. Nucl. Phys.*, 102:48 – 72, 2018. doi: 10.1016/j.ppnp.2018.05.005.

[88] S. Pascoli. A Portal to New Physics. *CERN Courier*, 56(6):34 – 39, 2016. URL `https://cerncourier.com/a/a-portal-to-new-physics/#`. Online available; last accessed: 7th August 2020.

[89] S. Choubey, S. T. Petcov, and M. Piai. Precision Neutrino Oscillation Physics with an Intermediate Baseline Reactor Neutrino Experiment. *Phys. Rev. D*, 68(11):113006, 2003. doi: 10.1103/PhysRevD.68.113006.

[90] L. Zhan, Y. Wang, J. Cao, and L. Wen. Determination of the Neutrino Mass Hierarchy at an Intermediate Baseline. *Phys. Rev. D*, 78:111103, 2008. doi: 10.1103/PhysRevD.78.111103.

[91] L. Zhan, Y. Wang, J. Cao, and L. Wen. Experimental Requirements to Determine the Neutrino Mass Hierarchy using Reactor Neutrinos. *Phys. Rev. D*, 79:073007, 2009. doi: 10.1103/PhysRevD.79.073007.

[92] Y.-F. Li, J. Cao, Y. Wang, and L. Zhan. Unambiguous Determination of the Neutrino Mass Hierarchy using Reactor Neutrinos. *Phys. Rev. D*, 88:013008, 2013. doi: 10.1103/PhysRevD.88.013008.

[93] P. Ghoshal and S. T. Petcov. Neutrino Mass Hierarchy Determination using Reactor Antineutrinos. *Journal of High Energy Physics*, 3:058, 2011. doi: 10.1007/JHEP03(2011)058.

[94] P. Lipari. Matter Effects in Long-Baseline Experiments, the Flavor Content of the Heaviest (or Lightest) Neutrino, and the Sign of Δm^2. *Phys. Rev. D*, 61:113004, 2000. doi: 10.1103/PhysRevD.61.113004.

[95] S. Palomares-Ruiz and J. Bernabéu. Atmospheric Neutrinos and ν-mass Hierarchy. *Nucl. Phys. B - Proceedings Supplements*, 138:398 – 401, 2005. ISSN 0920-5632. doi: 10.1016/j.nuclphysbps.2004.11.089. Proceeding of 8th International Workshop on Topics in Astroparticle and Underground Physics (TAUP 2003): Seattle (WA), USA, September 5-9, 2003.

[96] P. F. de Salas, S. Gariazzo, O. Mena, C. A. Ternes, and M. Tórtola. Neutrino Mass Ordering from Oscillations and Beyond: 2018 Status and Future Prospects. *Frontiers in Astronomy and Space Sciences*, 5:36, 2018. doi: 10.3389/fspas.2018.00036.

[97] X. Qian and P. Vogel. Neutrino Mass Hierarchy. *Prog. Part. Nucl. Phys.*, 83:1 – 30, 2015. doi: 10.1016/j.ppnp.2015.05.002.

[98] M. Blennow, P. Coloma, P. Huber, and T. Schwetz. Quantifying the Sensitivity of Oscillation Experiments to the Neutrino Mass Ordering. *Journal of High Energy Physics*, 03:028, 2014. doi: 10.1007/JHEP03(2014)028.

[99] M. Blennow and T. Schwetz. Determination of the Neutrino Mass Ordering by Combining PINGU and Daya Bay II. *Journal of High Energy Physics*, 09:089, 2013. doi: 10.1007/JHEP09(2013)089.

[100] M. G. Aartsen et al. (IceCube-Gen2 Collaboration and JUNO Collaboration Members). Combined Sensitivity to the Neutrino Mass Ordering with JUNO, the IceCube Upgrade, and PINGU. *Phys. Rev. D*, 101:032006, 2020. doi: 10.1103/PhysRevD.101.032006.

[101] X. N. Li. Daya Bay II: Jiangmen Underground Neutrino Observatory (JUNO). Talk at 9th Rencontres du Vietnam: Windows on the Universe: Guy Nhon, Vietnam, August 11-17, 2013, 2013. URL `http://vietnam.in2p3.fr/2013/Inauguration/transparencies/XiaoNanLi.pdf`. Slides online available; last accessed: 7th August 2020.

[102] F. P. An et al. (Daya Bay Collaboration). Observation of Electron-Antineutrino Disappearance at Daya Bay. *Phys. Rev. Lett.*, 108(17):171803, 2012. doi: 10.1103/PhysRevLett.108.171803.

[103] A. Garfagnini. Precision Measurements with JUNO: The Next Generation Reactor Neutrinos Experiment. Talk at International Workshop on Next Generation Nucleon Decay and Neutrino Detectors (NNN2018): Vancouver, Canada, November 1-3, 2018, 2018. URL `https://meetings.triumf.ca/indico/event/27/session/5/contribution/18`. Slides online available; last accessed: 7th August 2020.

[104] P. Vogel and J. F. Beacom. Angular Distribution of Neutron Inverse Beta Decay $\overline{\nu}_e + p \to e^+ + n$. *Phys. Rev. D*, 60:053003, 1999. doi: 10.1103/PhysRevD.60.053003.

[105] F. von Feilitzsch, A. A. Hahn, and K. Schreckenbach. Experimental Beta-Spectra from 239Pu and 235U Thermal Neutron Fission Products and their Correlated Antineutrino Spectra. *Phys. Lett. B*, 118(1):162 – 166, 1982. ISSN 0370-2693. doi: 10.1016/0370-2693(82)90622-0.

[106] K. Schreckenbach, G. Colvin, W. Gelletly, and F. von Feilitzsch. Determination of the Antineutrino Spectrum from 235U Thermal Neutron Fission Products up to 9.5 MeV. *Phys. Lett. B*, 160(4):325 – 330, 1985. ISSN 0370-2693. doi: 10.1016/0370-2693(85)91337-1.

[107] A. A. Hahn et al. Antineutrino Spectra from 241Pu and 239Pu Thermal Neutron Fission Products. *Phys. Lett. B*, 218(3):365 – 368, 1989. ISSN 0370-2693. doi: 10.1016/0370-2693(89)91598-0.

[108] P. Vogel, G. K. Schenter, F. M. Mann, and R. E. Schenter. Reactor Antineutrino Spectra and their Application to Antineutrino-Induced Reactions. II. *Phys. Rev. C*, 24:1543 – 1553, 1981. doi: 10.1103/PhysRevC.24.1543.

[109] P. Huber. Determination of Antineutrino Spectra from Nuclear Reactors. *Phys. Rev. C*, 84:024617, 2011. doi: 10.1103/PhysRevC.84.024617.

[110] Th. A. Mueller et al. Improved Predictions of Reactor Antineutrino Spectra. *Phys. Rev. C*, 83:054615, 2011. doi: 10.1103/PhysRevC.83.054615.

[111] P. Vogel, L. J. Wen, and C. Zhang. Neutrino Oscillation Studies with Reactors. *Nature Comm.*, 6:6935, 2015. doi: 10.1038/ncomms7935.

[112] L. Zhan. JUNO: A Next Generation Reactor Antineutrino Experiment. *Nuclear and Particle Physics Proceedings*, 273-275:1825 – 1829, 2016. ISSN 2405-6014. doi: 10.1016/j.nuclphysbps.2015.09.294. Proceeding of 37th International Conference on

High Energy Physics (ICHEP 2014): Valencia, Spain, July 2-9, 2014.

[113] F. Capozzi et al. Global Constraints on Absolute Neutrino Masses and their Ordering. *Phys. Rev. D*, 95(9):096014, 2017. doi: 10.1103/PhysRevD.95.096014.

[114] M. Grassi, A. Cabrera, and Y. Han. JUNO Energy Spectra. Internal JUNO Collaboration Document, 2018. DocDB #3497-v4.

[115] H. Minakata, H. Nunokawa, S. J. Parke, and R. Zukanovich Funchal. Determination of the Neutrino Mass Hierarchy via the Phase of the Disappearance Oscillation Probability with a Monochromatic $\overline{\nu}_e$ Source. *Phys. Rev. D*, 76:053004, 2007. doi: 10.1103/PhysRevD.76.053004.

[116] A. B. Balantekin et al. Neutrino Mass Hierarchy Determination and Other Physics Potential of Medium-Baseline Reactor Neutrino Oscillation Experiments. *arXiv e-prints*, art. arXiv:1307.7419, 2013. Proceeding of 2013 Community Summer Study on the Future of U.S. Particle Physics: Snowmass on the Mississippi (CSS2013): Minneapolis (MN), USA, July 29 - August 6, 2013.

[117] X. Qian et al. Mass Hierarchy Resolution in Reactor Anti-Neutrino Experiments: Parameter Degeneracies and Detector Energy Response. *Phys. Rev. D*, 87:033005, 2013. doi: 10.1103/PhysRevD.87.033005.

[118] J. Cao. Detection Methods at Reactor Neutrino Experiments. *Nucl. Instrum. and Meth. A*, 732:9 – 15, 2013. ISSN 0168-9002. doi: 10.1016/j.nima.2013.05.076. Proceeding of Vienna Conference on Instrumentation 2013 (VCI2013): Vienna, Austria, February 11-15, 2013.

[119] Y. Cheng. Physics Potential and Status of JUNO. 2018. URL `https://indico.ph.qmul.ac.uk/indico/contributionDisplay.py?contribId=16&confId=289`. Talk at Prospects in Neutrino Physics (NuPhys 2018): London, UK, December 19-21, 2018. Slides online available; last accessed: 7th August 2020.

[120] A. Gando et al. (KamLAND Collaboration). Reactor On-Off Antineutrino Measurement with KamLAND. *Phys. Rev. D*, 88(3):033001, 2013. doi: 10.1103/PhysRevD.88.033001.

[121] B. Aharmim et al. (SNO Collaboration). Combined Analysis of all Three Phases of Solar Neutrino Data from the Sudbury Neutrino Observatory. *Phys. Rev. C*, 88(2):025501, 2013. doi: 10.1103/PhysRevC.88.025501.

[122] A. Higuera. Results and Prospects from the Daya Bay Reactor Neutrino Experiment. *arXiv e-prints*, art. arXiv:1607.07324, 2016. doi: 10.1142/9789813148505_0020. Proceeding from the 7th Meeting on CPT and Lorentz Symmetry (CPT 16): Bloomington (IN), USA, June 20-24, 2016.

[123] Z.-Z. Xing. Towards Testing the Unitarity of the 3×3 Lepton Flavor Mixing Matrix in a Precision Reactor Antineutrino Oscillation Experiment. *Phys. Lett. B*, 718(4-5):1447 – 1453, 2013. doi: 10.1016/j.physletb.2012.12.062.

[124] X. Qian, C. Zhang, M. Diwan, and P. Vogel. Unitarity Tests of the Neutrino Mixing Matrix. *arXiv e-prints*, art. arXiv:1308.5700, 2013.

[125] J. N. Bahcall and M. H. Pinsonneault. What Do We (Not) Know Theoretically about Solar Neutrino Fluxes? *Phys. Rev. Lett.*, 92(12):121301, 2004. doi:

10.1103/PhysRevLett.92.121301.

[126] F. L. Villante, A. M. Serenelli, F. Delahaye, and M. H. Pinsonneault. The Chemical Composition of the Sun from Helioseismic and Solar Neutrino Data. *The Astrophysical Journal*, 787:13, 2014. doi: 10.1088/0004-637X/787/1/13.

[127] M. Bergemann and A. Serenelli. *Determination of Atmospheric Parameters of B-, A-, F- and G-Type Stars: Lectures from the School of Spectroscopic Data Analyses*, chapter Solar Abundance Problem, pages 245 – 258. GeoPlanet: Earth and Planetary Sciences. Springer International Publishing, Cham, 2014. doi: 10.1007/978-3-319-06956-2_21.

[128] S. Abe et al. (KamLAND Collaboration). Production of Radioactive Isotopes through Cosmic Muon Spallation in KamLAND. *Phys. Rev. C*, 81:025807, 2010. doi: 10.1103/PhysRevC.81.025807.

[129] G. Bellini et al. (Borexino Collaboration). Cosmogenic Backgrounds in Borexino at 3800 m water-equivalent Depth. *Journal of Cosmology and Astroparticle Physics*, 2013 (08):049 – 049, 2013. doi: 10.1088/1475-7516/2013/08/049.

[130] R. Jayawardhana. Coming Soon: A Supernova Near You. *Scientific American*, 309 (6):68 – 73, 2013. doi: 10.1038/scientificamerican1213-68. Now available under title: 'Physicists Eagerly Await Neutrinos from the Next Nearby Supernova [Excerpt]'. Online available; last accessed: 7th August 2020.

[131] K. Hirata et al. (Kamiokande Collaboration). Observation of a Neutrino Burst from the Supernova SN1987A. *Phys. Rev. Lett.*, 58:1490 – 1493, 1987. doi: 10.1103/PhysRevLett.58.1490.

[132] R. M. Bionta et al. Observation of a Neutrino Burst in Coincidence with Supernova 1987A in the Large Magellanic Cloud. *Phys. Rev. Lett.*, 58:1494 – 1496, 1987. doi: 10.1103/PhysRevLett.58.1494.

[133] E. N. Alekseev, L. N. Alekseeva, I. V. Krivosheina, and V. I. Volchenko. Detection of the Neutrino Signal from SN 1987A using the INR Baksan Underground Scintillation Telescope. In *European Southern Observatory Conference and Workshop Proceedings*, volume 26, pages 237 – 247, 1987.

[134] K. Bays et al. (Super-Kamiokande Collaboration). Supernova Relic Neutrino Search at Super-Kamiokande. *Phys. Rev. D*, 85:052007, 2012. doi: 10.1103/PhysRevD.85.052007.

[135] J. Sawatzki. *Towards the Detection of the Diffuse Supernova Neutrino Background in the Large Volume Scintillator Experiment JUNO*. PhD Thesis, Technische Universität München, Munich, 2020.

[136] K. Møller, A. M. Suliga, I. Tamborra, and P. B. Denton. Measuring the Supernova Unknowns at the Next-Generation Neutrino Telescopes Through the Diffuse Neutrino Background. *Journal of Cosmology and Astroparticle Physics*, 1805(05):066, 2018. doi: 10.1088/1475-7516/2018/05/066.

[137] T. Araki et al. (KamLAND Collaboration). Experimental Investigation of Geologically Produced Antineutrinos with KamLAND. *Nature*, 436:499 – 503, 2005. doi: 10.1038/nature03980.

[138] A. Gando et al. (KamLAND Collaboration). Partial Radiogenic Heat Model for Earth

Revealed by Geoneutrino Measurements. *Nature Geo.*, 4:647 – 651, 2011. doi: 10.1038/ngeo1205.

[139] G. Bellini et al. (Borexino Collaboration). Observation of Geo-Neutrinos. *Phys. Lett. B*, 687(4-5):299 – 304, 2010. doi: 10.1016/j.physletb.2010.03.051.

[140] M. Agostini et al. (Borexino Collaboration). Spectroscopy of Geo-Neutrinos from 2056 Days of Borexino Data. *Phys. Rev. D*, 92(3):031101, 2015. doi: 10.1103/PhysRevD.92.031101.

[141] J. Davies and D. Rhodri Davies. Earth's Surface Heat Flux. *Solid Earth*, 1:5 – 24, 2010. doi: 10.5194/se-1-5-2010.

[142] G. L. Fogli, E. Lisi, A. Palazzo, and A. M. Rotunno. Combined Analysis of KamLAND and Borexino Neutrino Signals from Th and U Decays in the Earth's Interior. *Phys. Rev. D*, 82(9):093006, 2010. doi: 10.1103/PhysRevD.82.093006.

[143] Y. Huang, V. Chubakov, F. Mantovani, R. L. Rudnick, and W. F. McDonough. A Reference Earth Model for the Heat-Producing Elements and Associated Geoneutrino Flux. *Geochemistry, Geophysics, Geosystems*, 14(6):2003 – 2029, 2013. doi: 10.1002/ggge.20129.

[144] V. Strati et al. Expected Geoneutrino Signal at JUNO. *Progress in Earth and Planetary Science*, 2(1):5, 2015. ISSN 2197-4284. doi: 10.1186/s40645-015-0037-6.

[145] A. D. Sakharov. Violation of CP Invariance, C Asymmetry, and Baryon Asymmetry of the Universe. *Pisma Zh. Eksp. Teor. Fiz.*, 5:32 – 35, 1967. doi: 10.1070/PU1991v034n05ABEH002497. [Usp. Fiz. Nauk161, no.5, 61(1991)].

[146] D. Griffiths. *Introduction to Elementary Particles*. Physics Textbook. Wiley, 2008. ISBN 9783527618477.

[147] K. S. Babu et al. Baryon Number Violation. *arXiv e-prints*, art. arXiv:1311.5285, 2013. Report at the 2013 Community Summer Study on the Future of U.S. Particle Physics: Snowmass on the Mississippi (CSS2013): Minneapolis (MN), USA, July 29 - August 6, 2013.

[148] K. Abe et al. (Super-Kamiokande Collaboration). Search for Proton Decay via $p \to \nu K^+$ using 260 kiloton·year Data of Super-Kamiokande. *Phys. Rev. D*, 90(7):072005, 2014. doi: 10.1103/PhysRevD.90.072005.

[149] T. Marrodán Undagoitia et al. Search for the Proton Decay $p \to K^+ \overline{\nu}$ in the Large Liquid Scintillator Low Energy Neutrino Astronomy Detector LENA. *Phys. Rev. D*, 72(7):075014, 2005. doi: 10.1103/PhysRevD.72.075014.

[150] W. V. Prestwich, M. A. Islam, and T. J. Kennett. A Determination of the Carbon Thermal Neutron Capture Cross Section. *Nuclear Science and Engineering*, 78(2):182 – 185, 1981. doi: 10.13182/NSE81-A20105.

[151] C. Genster et al. Muon Reconstruction with a Geometrical Model in JUNO. *Journal of Instrumentation*, 13(03):T03003, 2018. doi: 10.1088/1748-0221/13/03/t03003.

[152] B. S. Wonsak et al. Topological Track Reconstruction in Unsegmented, Large-Volume Liquid Scintillator Detectors. *Journal of Instrumentation*, 13(07):P07005, 2018. doi: 10.1088/1748-0221/13/07/p07005.

[153] H. Nunokawa, S. Parke, and R. Zukanovich Funchal. Another Possible Way to Determine the Neutrino Mass Hierarchy. *Phys. Rev. D*, 72(1):013009, 2005. doi: 10.1103/PhysRevD.72.013009.

[154] S.-F. Ge, K. Hagiwara, N. Okamura, and Y. Takaesu. Determination of Mass Hierarchy with Medium Baseline Reactor Neutrino Experiments. *Journal of High Energy Physics*, 05:131, 2013. doi: 10.1007/JHEP05(2013)131.

[155] K. Abe et al. (Hyper-Kamiokande Proto-Collaboration). Physics Potential of a Long Baseline Neutrino Oscillation Experiment Using J-PARC Neutrino Beam and Hyper-Kamiokande. *PTEP*, 2015:arXiv:1502.05199, 2015. doi: 10.1093/ptep/ptv061.

[156] S. K. Agarwalla, S. Prakash, and W. Wang. High-Precision Measurement of Atmospheric Mass-Squared Splitting with T2K and NOvA. *arXiv e-prints*, art. arXiv:1312.1477, 2013.

[157] F. P. An et al. (Daya Bay Collaboration). Measurement of Electron Antineutrino Oscillation Based on 1230 Days of Operation of the Daya Bay Experiment. *Phys. Rev. D*, 95(7):072006, 2017. doi: 10.1103/PhysRevD.95.072006.

[158] J. P. Ochoa-Ricoux. Latest Results from Daya Bay. 2018. doi: 10.5281/zenodo.1294112. Talk at XXVIII International Conference on Neutrino Physics and Astrophysics (NEUTRINO 2018): Heidelberg, Germany, June 4-9, 2018.

[159] L. Wen. Calibration and Energy Scale in JUNO. 2018. doi: 10.5281/zenodo.1314415. Talk at Energy Scale Calibration in Antineutrino Precision Experiments (ESCAPE 2018) Workshop: Heidelberg, Germany, June 1-2, 2018.

[160] H. Lu. The JUNO Veto Detector System. In *Proceedings of International Conference on Technology and Instrumentation in Particle Physics 2017 (TIPP 2017): Beijing, China, May 22-26, 2017*, pages 197 – 201, Singapore, 2018. Springer Singapore. ISBN 978-981-13-1316-5.

[161] Y. Heng, H. Lu, X. Ma, and X. Qian. Standard Slides about Detector Design for Conferences. Internal JUNO Collaboration Document, 2016. DocDB #1468-v16.

[162] C. Buck, B. Gramlich, and S. Wagner. Light Propagation and Fluorescence Quantum Yields in Liquid Scintillators. *Journal of Instrumentation*, 10(9):P09007, 2015. doi: 10.1088/1748-0221/10/09/P09007.

[163] I. B. Berlman. *Handbook of Fluorescence Spectra of Aromatic Molecules (Second Edition)*. Academic Press, 2nd edition, 1971. ISBN 978-0-12-092656-5. doi: 10.1016/B978-0-12-092656-5.50006-X.

[164] M. Wurm et al. Optical Scattering Lengths in Large Liquid-Scintillator Neutrino Detectors. *Review of Scientific Instruments*, 81(5):053301-053301-9, 2010. doi: 10.1063/1.3397322.

[165] M. Yeh et al. A New Water-Based Liquid Scintillator and Potential Applications. *Nucl. Instrum. and Meth. A*, 660(1):51 – 56, 2011. ISSN 0168-9002. doi: 10.1016/j.nima.2011.08.040.

[166] I. B. Nemchenok, V. I. Babin, V. B. Brudanin, O. I. Kochetov, and V. V. Timkin. Liquid Scintillator Based on Linear Alkylbenzene. *Phys. Part. Nucl. Lett.*, 8(2):129 – 135, 2011. ISSN 1531-8567. doi: 10.1134/S1547477111020099.

[167] H.-T. Chen et al. Aging of LAB-based Liquid Scintillator in Stainless Steel Containers. *Chinese Physics C*, 39(6):066002, 2015. doi: 10.1088/1674-1137/39/6/066002.

[168] H. M. O'Keeffe, E. O'Sullivan, and M. C. Chen. Scintillation Decay Time and Pulse Shape Discrimination in Oxygenated and Deoxygenated Solutions of Linear Alkylbenzene for the SNO+ Experiment. *Nucl. Instrum. and Meth. A*, 640(1):119 – 122, 2011. ISSN 0168-9002. doi: 10.1016/j.nima.2011.03.027.

[169] C. Genster. Status of the Jiangmen Underground Neutrino Observatory. 2018. URL `https://indico.jinr.ru/event/410/contributions/3354/`. Talk at New Trends in High Energy Physics 2018: Bečići, Montenegro, September 24-30, 2018. Slides online available; last accessed: 7th August 2020.

[170] S. Ajimura et al. Technical Design Report (TDR): Searching for a Sterile Neutrino at J-PARC MLF (E56, JSNS2). *arXiv e-prints*, art. arXiv:1705.08629, 2017.

[171] H.-L. Xiao et al. Study of Absorption and Re-emission Processes in a Ternary Liquid Scintillation System. *Chinese Physics C*, 34(11):1724 – 1728, 2010. doi: 10.1088/1674-1137/34/11/011.

[172] Y. Hotta. Hamamatsu Photonics K.K. - Latest Developement Status, 2017. URL `https://indico.mpp.mpg.de/event/5272/session/6/contribution/26/material/slides/0.pdf`. Talk at LIGHT-17 International Workshop: Castle Ringberg, Germany, October 16-20, 2017.

[173] Q. Sen et al. Status of the Large Area MCP-PMT in China. 2017. URL `https://indico.cern.ch/event/432527/contributions/1071941/`. Talk at the 38th International Conference on High Energy Physics (ICHEP2016): Chicago (IL), USA, August 3-10, 2016. Slides online available, last accessed: 7th August 2020.

[174] H.-B. Yang et al. Light Attenuation Length of High Quality Linear Alkyl Benzene as Liquid Scintillator Solvent for the JUNO Experiment. *Journal of Instrumentation*, 12 (11):T11004, 2017. doi: 10.1088/1748-0221/12/11/T11004.

[175] P. Lombardi et al. Distillation and Stripping Pilot Plants for the JUNO Neutrino Detector: Design, Operations and Reliability. *Nucl. Instrum. and Meth. A*, 925:6 – 17, 2019. doi: 10.1016/j.nima.2019.01.071.

[176] H. Th. J. Steiger. *Development of a Low Level Radioactive Liquid Scintillator and of the Detector Monitoring System for the JUNO Neutrino Experiment*. PhD Thesis, Technische Universität München, Munich, 2020.

[177] C. Guo, Y. P. Zhang, J. C. Liu, C. G. Yang, and P. Zhang. The Water System and Radon Measurement System of Jiangmen Underground Neutrino Observatory. *arXiv e-prints*, art. arXiv:1806.11105, 2018.

[178] Y. Zhang, C. Guo, J. Liu, P. Zhang, and C. Yang. The Study of Rn in the JUNO Prototype Water System. In *Proceedings of International Conference on Technology and Instrumentation in Particle Physics 2017 (TIPP 2017): Beijing, China, May 22-26, 2017*, pages 213 – 217, Singapore, 2018. Springer Singapore. ISBN 978-981-13-1316-5.

[179] Z. Qin. Status of the 20-in. PMT Instrumentation for the JUNO Experiment. In *Proceedings of International Conference on Technology and Instrumentation in Par-*

ticle Physics 2017 (TIPP 2017): Beijing, China, May 22-26, 2017, pages 285 – 293, Singapore, 2018. Springer Singapore. ISBN 978-981-13-1316-5.

[180] R. Wang, H. Lu, and C. Yang. Water Cherenkov Detector of the JUNO Veto System. 2018. doi: 10.5281/zenodo.1300733. Poster at XXVIII International Conference on Neutrino Physics and Astrophysics (NEUTRINO 2018): Heidelberg, Germany, June 4-9, 2018.

[181] H. Lu and E. Baussan. The Design of the JUNO Veto System. *Journal of Physics Conference Series*, 888:012088, 2017. doi: 10.1088/1742-6596/888/1/012088. Proceeding of XXVII International Conference on Neutrino Physics and Astrophysics (NEUTRINO 2016): London, UK, July 4-9, 2016.

[182] T. Adam et al. The OPERA Experiment Target Tracker. *Nucl. Instrum. and Meth. A*, 577:523 – 539, 2007. doi: 10.1016/j.nima.2007.04.147.

[183] J. P. Athayde Marcondes de André. The Top Tracker Detector of the JUNO Experiment. 2018. doi: 10.5281/zenodo.1300578. Poster at XXVIII International Conference on Neutrino Physics and Astrophysics (NEUTRINO 2018): Heidelberg, Germany, June 4-9, 2018.

[184] C. Guo. Status of the Jiangmen Underground Neutrino Observatory. *arXiv e-prints*, art. arXiv:1910.10343, 2019.

[185] T. Enqvist et al. OSIRIS Preliminary Design. Internal JUNO Collaboration Document, 2018. DocDB #3932-v2.

[186] C. Genster et al. OSIRIS Conceptual Design Report. Internal JUNO Collaboration Document, 2018. DocDB #3472-v4.

[187] X. Ding and C. Guo. Status of the JUNO Detector. 2020. URL `https://indico.cern.ch/event/846070/contributions/3693234/`. Talk at Lake Louise Winter Institute 2020: Chateau Lake Louise, Canada, February 9-15, 2020. Slides online available; last accessed: 7th August 2020.

[188] F. Kiel. *Design and Test of a Power Board for an intelligent PMT for the JUNO-Detector*. PhD Thesis, RWTH Aachen University, Aachen, 2019.

[189] C. Genster. *Software and Hardware Development for the Next-Generation Liquid Scintillator Detectors JUNO and OSIRIS*. PhD Thesis, RWTH Aachen University, Aachen, 2019.

[190] D. A. Dwyer and T. J. Langford. Spectral Structure of Electron Antineutrinos from Nuclear Reactors. *Phys. Rev. Lett.*, 114:012502, 2015. doi: 10.1103/PhysRevLett.114.012502.

[191] A. A. Sonzogni, M. Nino, and E. A. McCutchan. Revealing Fine Structure in the Antineutrino Spectra From a Nuclear Reactor. *Phys. Rev. C*, 98(1):014323, 2018. doi: 10.1103/PhysRevC.98.014323.

[192] L. Zhan. Proposal of a Near Detector for JUNO Experiment. 2018. doi: 10.5281/zenodo.1314423. Talk at Energy Scale Calibration in Antineutrino Precision Experiments (ESCAPE 2018) Workshop: Heidelberg, Germany, June 1-2, 2018.

[193] D. V. Forero, R. Hawkins, and P. Huber. The Benefits of a Near Detector for JUNO.

arXiv e-prints, art. arXiv:1710.07378, 2017.

[194] D. L. Danielson, A. C. Hayes, and G. T. Garvey. Reactor Neutrino Spectral Distortions Play Little Role in Mass Hierarchy Experiments. *Phys. Rev. D*, 99(3):036001, 2019. doi: 10.1103/PhysRevD.99.036001.

[195] H. de Kerret et al. (Double Chooz Collaboration). Double Chooz θ_{13} Measurement via Total Neutron Capture Detection. *Nature Physics*, 16(5):558 – 564, 2020. doi: 10.1038/s41567-020-0831-y.

[196] J. Cao and K.-B. Luk. An Overview of the Daya Bay Reactor Neutrino Experiment. *Nucl. Phys. B*, 908:62 – 73, 2016. doi: 10.1016/j.nuclphysb.2016.04.034.

[197] W. Beriguete et al. Production of a Gadolinium-Loaded Liquid Scintillator for the Daya Bay Reactor Neutrino Experiment. *Nucl. Instrum. and Meth. A*, 763:82 – 88, 2014. doi: 10.1016/j.nima.2014.05.119.

[198] F. P. An et al. (Daya Bay Collaboration). Measurement of the Reactor Antineutrino Flux and Spectrum at Daya Bay. *Phys. Rev. Lett.*, 116(6):061801, 2016. doi: 10.1103/PhysRevLett.116.061801,10.1103/PhysRevLett.118.099902. [Erratum: Phys. Rev. Lett. 118, no.9, 099902(2017)].

[199] S.-H. Seo et al. (RENO Collaboration). New Results from RENO and the 5 MeV Excess. *American Institute of Physics Conference Proceedings*, 1666:080002, 2015. doi: 10.1063/1.4915563. Proceeding of XXVI International Conference on Neutrino Physics and Astrophysics (NEUTRINO 2014): Boston (MA), USA, June 2-7, 2014.

[200] Abusleme, A. et al. (JUNO Collaboration). TAO Conceptual Design Report: A Precision Measurement of the Reactor Antineutrino Spectrum with Sub-percent Energy Resolution. *arXiv e-prints*, art. arXiv:2005.08745, 2020.

[201] L. J. Wen et al. A Quantitative Approach to Select PMTs for Large Detectors. *Nucl. Instrum. and Meth. A*, 947:162766, 2019. doi: 10.1016/j.nima.2019.162766.

[202] Hamamatsu Photonics K.K. *Photomultiplier Tubes - Basics and Applications*. Hamamatsu Photonics K.K., 4th edition, 2017. URL `https://www.hamamatsu.com/resources/pdf/etd/PMT_handbook_v4E.pdf`. Online available; last accessed: 7th August 2020.

[203] S. O. Flyckt and C. Marmonier. *Photomultiplier Tubes: Principles and Applications*. Photonis, Brive, 2nd edition, 2002. URL `https://cds.cern.ch/record/712713`.

[204] M. Breisch. Investigation of SiPM based Light Detectors for the Next Generation of Neutrino Experiments. Master Thesis, Eberhard Karls Universität Tübingen, Tübingen, 2019.

[205] H. Q. Zhang et al. Study on Relative Collection Efficiency of PMTs with Point Light. *arXiv e-prints*, art. arXiv:1810.04550, 2018.

[206] A. Yu. Barnyakov et al. Measurement of the Photoelectron Collection Efficiency in MCP-PMT. *Journal of Instrumentation*, 12(03):P03027, 2017. doi: 10.1088/1748-0221/12/03/p03027.

[207] Y. Abe et al. (Double Chooz Collaboration). Reactor ν_e Disappearance in the Double Chooz Experiment. *Phys. Rev. D*, 86(5):052008, 2012. doi: 10.1103/PhysRevD.86.

052008.

[208] F. P. An et al. (Daya Bay Collaboration). A Side-by-Side Comparison of Daya Bay Antineutrino Detectors. *Nuclear Instrum. and Meth. A*, 685:78 – 97, 2012. doi: 10.1016/j.nima.2012.05.030.

[209] J. K. Ahn et al. (RENO Collaboration). RENO: An Experiment for Neutrino Oscillation Parameter θ_{13} Using Reactor Neutrinos at Yonggwang. *arXiv e-prints*, art. arXiv:1003.1391, 2010.

[210] J. Boger et al. (SNO Collaboration). The Sudbury Neutrino Observatory. *Nucl. Instrum. and Meth. A*, 449(1):172 – 207, 2000. ISSN 0168-9002. doi: 10.1016/S0168-9002(99)01469-2.

[211] G. Alimonti et al. (Borexino Collaboration). The Borexino Detector at the Laboratori Nazionali del Gran Sasso. *Nucl. Instrum. and Meth. A*, 600(3):568 – 593, 2009. ISSN 0168-9002. doi: 10.1016/j.nima.2008.11.076.

[212] S. Fukuda et al. (Super-Kamiokande Collaboration). The Super-Kamiokande Detector. *Nucl. Instrum. and Meth. A*, 501(2):418 – 462, 2003. ISSN 0168-9002. doi: 10.1016/S0168-9002(03)00425-X.

[213] W. R. Leo. *Techniques for Nuclear and Particle Physics Experiments: A How-to Approach*. Springer Science & Business Media, 2nd edition, 2012. ISBN 9783642579202. doi: 10.1007/978-3-642-57920-2.

[214] Hamamatsu Photonics K.K. Photomultiplier Tubes and Assemblies for Scintillation Counting & High Energy Physics, 2017. URL `https://www.hamamatsu.com/resources/pdf/etd/High_energy_PMT_TPMZ0003E.pdf`. Online available; last accessed: 7th August 2020.

[215] SENSE. Photomultiplier Tubes (PMT), 2019. URL `https://www.sense-pro.org/lll-sensors/pmt`. Online available; last accessed: 7th August 2020.

[216] Hamamatsu Photonics K.K. Photomultiplier Tube R12860 Datasheet, 2019. URL `https://www.hamamatsu.com/resources/pdf/etd/LARGE_AREA_PMT_TPMH1376E.pdf`. Online available; last accessed: 7th August 2020.

[217] Hamamatsu Photonics K.K. Photomultiplier Tubes (PMTs) - About PMTs, 2019. URL `https://www.hamamatsu.com/eu/en/product/optical-sensors/pmt/about_pmts/index.html`. Online available; last accessed: 7th August 2020.

[218] D. Motta and S. Schönert. Optical Properties of Bialkali Photocathodes. *Nucl. Instrum. and Meth. A*, 539:217 – 235, 2005. doi: 10.1016/j.nima.2004.10.009.

[219] X.-C. Lei et al. Evaluation of New Large Area PMT with High Quantum Efficiency. *Chinese Physics C*, 40(2):026002, 2016. doi: 10.1088/1674-1137/40/2/026002.

[220] A. Kamiya. Hamamatsu Photonics K.K. - Photomultiplier Tubes: Recent Trends of PMTs for HEP & Scintillation Application, 2015. URL `http://www.lns.tohoku.ac.jp/workshop/c010/slides/011.pdf`. Online available; last accessed: 7th August 2020.

[221] HZC Photonics Technology Co. Ltd. Photomultiplier Tubes Product Manual, 2017. URL `http://www.hzcphotonics.com/products/ProductManual.pdf`. Online avail-

able; last accessed: 7th August 2020.

[222] B.-Z. Hu and J. Xu. The 3-inch PMTs of the JUNO Experiment. 2018. doi: 10.5281/zenodo.1286721. Poster at XXVIII International Conference on Neutrino Physics and Astrophysics (NEUTRINO 2018): Heidelberg, Germany, June 4-9, 2018.

[223] J. Xu et al. The 3-inch PMT System of JUNO Experiment, 2018. URL `https://pos.sissa.it/340/791/`. Poster at 39th International Conference on High Energy Physics (ICHEP2018): Seoul, Korea Rep., July 4-11, 2018.

[224] Northern Night Vision Technology Ltd. MCP, 2013. URL `http://en.nvt.com.cn/web-1101212-34.html`. Online available; last accessed: 7th August 2020.

[225] Z. Qin. The 20-inch PMT Instrumentation for the JUNO Experiment. 2018. doi: 10.5281/zenodo.1301074. Poster at XXVIII International Conference on Neutrino Physics and Astrophysics (NEUTRINO 2018): Heidelberg, Germany, June 4-9, 2018.

[226] Northern Night Vision Technology Ltd. MCP-PMT, 2013. URL `http://en.nvt.com.cn/web-1101212-35.html`. Online available; last accessed: 7th August 2020.

[227] S. Liu et al. Development of the Large Area MCP-PMT. In Y. Jiang, J. Yu, and B. Kippelen, editors, *7th International Symposium on Advanced Optical Manufacturing and Testing Technologies: Optoelectronics Materials and Devices for Sensing and Imaging*, volume 9284, pages 1 – 10. International Society for Optics and Photonics, SPIE, 2014. doi: 10.1117/12.2069902.

[228] Y. Wang et al. A New Design of Large Area MCP-PMT for the Next Generation Neutrino Experiment. *Nucl. Instrum. and Meth. A*, 695:113 – 117, 2012. doi: 10.1016/j.nima.2011.12.085. Proceeding of 6th International Conference on New Developments in Photodetection (NDIP11): Lyon, France, July 4-8, 2011.

[229] Y. Chang et al. The R&D of the 20in. MCP-PMTs for JUNO. *Nucl. Instrum. and Meth. A*, 824:143 – 144, 2016. ISSN 0168-9002. doi: 10.1016/j.nima.2015.10.106. Proceeding of Frontier Detectors for Frontier Physics: 13th Pisa Meeting on Advanced Detectors: Pisa, Italy, May 24-30, 2015.

[230] L. Wen and W. Wang. Characterization of the 20-inch Photomultiplier Tubes for the JUNO Central Detector. *Proceedings of Science*, page 301, 2018. URL `https://indico.cern.ch/event/686555/contributions/2973923/`. Talk at 39th International Conference on High Energy Physics (ICHEP2018): Seoul, Korea Rep., July 4-11, 2018. Slides online available, last accessed: 7th August 2020.

[231] Q. Sen. The Improvement of 20" MCP-PMT for Neutrino Detection. *Proceedings of Science*, page 662, 2019. doi: 10.22323/1.340.0662. URL `https://indico.cern.ch/event/686555/contributions/2972374/`. Talk at 39th International Conference on High Energy Physics (ICHEP2018): Seoul, Korea Rep., July 4-11, 2018. Slides online available, last accessed: 7th August 2020.

[232] F. Gao et al. Status of the 20-inch MCP-PMT Prototype Development for JUNO Experiment. *Journal of Physics Conference Series*, 888(1):012050, 2017. doi: 10.1088/1742-6596/888/1/012050. Proceeding of XXVII International Conference on Neutrino Physics and Astrophysics (NEUTRINO 2016): London, UK, July 4-9, 2016.

[233] L. Chen et al. Optimization of the Electron Collection Efficiency of a Large Area

MCP-PMT for the JUNO Experiment. *Nucl. Instrum. and Meth. A*, 827:124 – 130, 2016. ISSN 0168-9002. doi: 10.1016/j.nima.2016.04.100.

[234] F. Gao et al. The Status of the Batch Test of 20-inch MCP-PMT. In *Proceedings of International Conference on Technology and Instrumentation in Particle Physics 2017 (TIPP 2017): Beijing, China, May 22-26, 2017*, pages 233 – 236, Singapore, 2018. Springer Singapore. ISBN 978-981-13-1316-5.

[235] P. Lombardi. JUNO Detector: Design and Construction. *Journal of Instrumentation*, 15(04):C04028, 2020. doi: 10.1088/1748-0221/15/04/c04028. Proceeding of 15th Topical Seminar on Innovative Particle and Radiation Detectors (IPRD19): Siena, Italy, October 14-17, 2019.

[236] B. Clerbaux and Y. Yang. The Electronics Readout System of the JUNO Experiment. 2019. URL `https://indico.cern.ch/event/577856/contributions/3420148/`. Talk at European Physical Society Conference on High Energy Physics (EPS-HEP 2019): Ghent, Belgium, July 10-17, 2019. Slides online available; last accessed: 7th August, 2020.

[237] P.-A. Petitjean, B. Clerbaux, and Y. Yang. The Back-End Electronics System of the JUNO Experiment. *Proceedings of Science*, page 200, 2020. doi: 10.22323/1.364.0200. Proceeding of European Physical Society Conference on High Energy Physics (EPS-HEP 2019): Ghent, Belgium, July 10-17, 2019.

[238] Z. Qin. The 20-inch PMT System for the JUNO Experiment. *Proceedings of Science*, page 356, 2018. URL `https://indico.cern.ch/event/686555/contributions/2972208/`. Talk at 39th International Conference on High Energy Physics (ICHEP2018): Seoul, Korea Rep., July 4-11, 2018. Slides online available, last accessed: 7th August 2020.

[239] J. Xu. The JUNO Double Calorimetry System. *Proceedings of Science*, 369:117, 2020. doi: 10.22323/1.369.0117. Proceeding of 21st international workshop on neutrinos from accelerators (NuFact 2019): Daegu, Korea Rep., August 26-31, 2019.

[240] M. He. Double Calorimetry System in JUNO. *Radiation Detection Technology and Methods*, 1(2):21, 2017. ISSN 2509-9949. doi: 10.1007/s41605-017-0022-2.

[241] A. Cabrera. JUNO Stereo-Calorimetry. 2018. doi: 10.5281/zenodo.1314425. Talk at Energy Scale Calibration in Antineutrino Precision Experiments (ESCAPE 2018) Workshop: Heidelberg, Germany, June 1-2, 2018.

[242] H. T. .J. Steiger. Design and Status of JUNO. *arXiv e-prints*, art. arXiv:1912.02038, 2019. Proceeding of 16th International Conference on Topics in Astroparticle and Underground Physics (TAUP 2019): Toyama, Japan, September 9-13, 2019.

[243] N. Anphimov. Large Photocathode 20-inch PMT Testing Methods for the JUNO Experiment. *Journal of Instrumentation*, 12(6):C06017, 2017. doi: 10.1088/1748-0221/12/06/C06017. Proceeding of International Conference on Instrumentation for Colliding Beam Physics (INSTR17): Novosibirsk, Russia, February 27 - March 3, 2017.

[244] B. Asavapibhop. Earth Magnetic Field Compensation Coils System for JUNO, 2018. Poster at XXVIII International Conference on Neutrino Physics and Astrophysics (NEUTRINO 2018): Heidelberg, Germany, June 4-9, 2018.

[245] S. Dushman. Electron Emission from Metals as a Function of Temperature. *Phys. Rev.*, 21:623 – 636, 1923. doi: 10.1103/PhysRev.21.623.

[246] Y. T. Wei, M. Y. Guan, W. X. Xiong, Y. Y. Gan, and C. G. Yang. Consistency Test of PMT SPE Spectrum from Dark-Noise Pulses and LED Low-Intensity Light. *Radiation Detection Technology and Methods*, 2(1):11, 2018. ISSN 2509-9949. doi: 10.1007/s41605-018-0042-6.

[247] B. K. Lubsandorzhiev, P. G. Pokhil, R. V. Vasiljev, and A. G. Wright. Studies of Prepulses and Late Pulses in the 8" Electron Tubes Series of Photomultipliers. *Nucl. Instrum. and Meth. A*, 442(1):452 – 458, 2000. ISSN 0168-9002. doi: 10.1016/S0168-9002(99)01272-3.

[248] B. K. Lubsandorzhiev, R. V. Vasiliev, Y. E. Vyatchin, and B. A. J. Shaibonov. Photoelectron Backscattering in Vacuum Phototubes. *Nucl. Instrum. and Meth. A*, 567 (1):12 – 16, 2006. doi: 10.1016/j.nima.2006.05.047. Proceeding of 4th International Conference on New Developments in Photodetection (NDIP05): Beaune, France, June 19-24, 2005.

[249] G. A. Morton, H. M. Smith, and R. Wasserman. Afterpulses in Photomultipliers. *IEEE Transactions on Nuclear Science*, 14(1):443 – 448, 1967. ISSN 1558-1578. doi: 10.1109/TNS.1967.4324452.

[250] P. B. Coates. The Origins of Afterpulses in Photomultipliers. *Journal of Physics D: Applied Physics*, 6(10):1159 – 1166, 1973. doi: 10.1088/0022-3727/6/10/301.

[251] A. Yang et al. The Study of Linearity and Detection Efficiency for 20" Photomultiplier Tube. *Radiation Detection Technology and Methods*, 3(11), 2019. doi: 10.1007/s41605-018-0088-5.

[252] N. Anphimov. Testing Methods for 20-inches PMTs of the JUNO Experiment, 2017. URL `https://indico.inp.nsk.su/event/8/session/4/contribution/114/`. Poster at International Conference on Instrumentation for Colliding Beam Physics 2017 (INSTR17): Novosibirsk, Russia, February 27 - March 3, 2017. Online available; last accessed: 7th August 2020.

[253] M. Sisti. Radioactive Background Control for the JUNO Experimental Setup. 2018. doi: 10.5281/zenodo.1300598. Poster at XXVIII International Conference on Neutrino Physics and Astrophysics (NEUTRINO 2018): Heidelberg, Germany, June 4-9, 2018.

[254] H. Q. Zhang. A Note about Container System Calibration and PMT Performance Mass Test. Internal JUNO Collaboration Document, 2018. DocDB #4310-v1.

[255] H Q. Zhang. Visual Check of 20 inches PMTs for JUNO. Internal JUNO Collaboration Document, 2017. DocDB #2586-v1.

[256] J. Y. Guo. Visual Check of PMTs. Internal JUNO Collaboration Document, 2017. DocDB #2856-v1.

[257] J. Y. Guo. Visual Check Update. Internal JUNO Collaboration Document, 2019. DocDB #4865-v1.

[258] Z. Wang. Data Criteria of PMT Testing. Internal JUNO Collaboration Document, 2017. DocDB #2699-v2.

[259] Y. Chen. Measurements on the Afterpulse of the 20-inch Photomultiplier Tubes for the JUNO Experiment, 2020. Poster at XXIX International Conference on Neutrino Physics and Astrophysics (NEUTRINO 2020): Web-event, June 22-27, 2020.

[260] Y. Chen. PMT After Pulse Plan, Status and Results. Internal JUNO Collaboration Document, 2019. DocDB #4136-v1.

[261] A. Tietzsch and B. S. Wonsak. The PMT Mass Testing System for JUNO. 2018. doi: 10.5281/zenodo.1300494. Poster at XXVIII International Conference on Neutrino Physics and Astrophysics (NEUTRINO 2018): Heidelberg, Germany, June 4-9, 2018.

[262] C. R. Wuest et al. The IMB Photomultiplier Test Facility. *Nucl. Instrum. and Meth. A*, 239(3):467 – 486, 1985. ISSN 0168-9002. doi: 10.1016/0168-9002(85)90025-7.

[263] G. Ranucci et al. Characterization and Magnetic Shielding of the Large Cathode Area PMTs used for the Light Detection System of the Prototype of the Solar Neutrino Experiment Borexino. *Nucl. Instrum. and Meth. A*, 337(1):211 – 220, 1993. ISSN 0168-9002. doi: 10.1016/0168-9002(93)91156-H.

[264] A. Brigatti, A. Ianni, P. Lombardi, G. Ranucci, and O. Smirnov. The Photomultiplier Tube Testing Facility for the Borexino Experiment at LNGS. *Nucl. Instrum. Meth. A*, 537:521 – 536, 2005. doi: 10.1016/j.nima.2004.07.248.

[265] A. Baldini et al. The Photomultiplier Test Facility for the Reactor Neutrino Oscillation Experiment CHOOZ and the Measurements of 250 8-in. EMI 9356KA B53 Photomultipliers. *Nucl. Instrum. and Meth. A*, 372(1):207 – 221, 1996. ISSN 0168-9002. doi: 10.1016/0168-9002(95)01236-2.

[266] D. Barnhill et al. Testing of Photomultiplier Tubes for Use in the Surface Detector of the Pierre Auger Observatory. *Nucl. Instrum. and Meth. A*, 591(3):453 – 466, 2008. doi: 10.1016/j.nima.2008.01.088.

[267] X. Wang et al. Setup of a Photomultiplier Tube Test Bench for LHAASO-KM2A. *Chinese Physics C*, 40(8):086003, 2016. doi: 10.1088/1674-1137/40/8/086003.

[268] C. M. Mollo. Development and Performances of a High Statistics PMT Test Facility. *EPJ Web of Conferences*, 116:06010, 2016. doi: 10.1051/epjconf/201611606010.

[269] S. Aiello et al. Characterisation of the Hamamatsu Photomultipliers for the KM3NeT Neutrino Telescope. *Journal of Instrumentation*, 13(05):P05035, 2018. doi: 10.1088/1748-0221/13/05/p05035.

[270] N. Anphimov, H. Hu, and D. Korablev. PMT Uniformity in Magnetic Field from the 1st Test at Pan-Asia Testing Station. Internal JUNO Collaboration Document, 2016. DocDB #2585-v1.

[271] N. Anphimov, Z. Krumstein, and A. Olshevskiy. PMT Sampling Scanning Station FDR. Internal JUNO Collaboration Document, 2016. DocDB #1799-v1.

[272] W. H. Trzaska. Status of JUNO. 2018. URL `https://indico.ibs.re.kr/event/212/session/28/contribution/46`. Talk at 6th Symposium on Neutrinos and Dark Matter in Nuclear Physics (NDM 2018): Daejeon, Korea Rep., June 29 - July 4, 2018. Slides online available; last accessed: 7th August 2020.

[273] Z. Wang. FDR: General Issues and Test Results. Internal JUNO Collaboration Doc-

ument, 2018. DocDB #3130-v2.

[274] B. S. Wonsak. FDR: Status PMT Mass Testing Container. Internal JUNO Collaboration Document, 2018. DocDB #3118-v2.

[275] H. Q. Zhang et al. Tested Performance of JUNO 20" PMTs. *Journal of Physics Conference Series*, 1468(1):012197, 2020. doi: 10.1088/1742-6596/1468/1/012197. Proceeding of 16th International Conference on Topics in Astroparticle and Underground Physics (TAUP 2019): Toyama, Japan, September 9-13, 2019.

[276] M. Ashby, T. Davies, and S. Gorsse. The CES EduPack DB for Bulk Functional Materials. *Granta Teaching Resources*, pages 15 – 25, 01 2015.

[277] Ingersoll Rand Climate Control Technologies. ThermoKing Magnum®, 2007. URL `http://www.refrigerated-truck.com/PDF/Magnum%20brochure.pdf`. Online available; last accessed: 7th August 2020.

[278] DuPont. DuPont™ Tyvek®User Manual, 2002. URL `http://www.fibermark.com/sites/default/files/FMK_DuPontTyvekUsersManual_0.pdf`. Online available; last accessed: 7th August 2020.

[279] J. C. Arteaga Velázquez, C. Vazquez-Lopez, and A. Zepeda. Diffuse Reflectivity of Tyvek in Air and Water, and Anisotropical Effects. *Nucl. Phys. B - Proceedings Supplements*, 97:231 – 234, 2001. doi: 10.1016/S0920-5632(01)01271-3.

[280] A. Chavarria. A Study on the Reflective Properties of Tyvek in Air and Underwater. Bachelor Thesis, Duke University, Durham, 2007.

[281] D. S. Blum. Development of a PMT Testing Facility for the JUNO-Experiment. Master Thesis, Eberhard Karls Universität Tübingen, Tübingen, 2017.

[282] S. Reichert. Analysis of the Light Field of a Test Facility to Characterize the JUNO PMTs. Bachelor Thesis, Universität Hamburg, Hamburg, 2016.

[283] CAEN S.p.A. A7030 12/24/36/48 Channel 3 kV/1 mA (1.5W) Common Floating Return Boards, 2019. URL `https://www.caen.it/products/a7030/`. Online available; last accessed: 7th August 2020.

[284] CAEN S.p.A. SY5527 Universal Multichannel Power Supply Systema, 2019. URL `https://www.caen.it/products/sy5527/`. Online available; last accessed: 7th August 2020.

[285] CAEN S.p.A. R648 48 Channel Radiall to SHV connector Adapter (Max: 3kV - 19' Rack), 2019. URL `https://www.caen.it/products/r648/`. Online available; last accessed: 7th August 2020.

[286] CAEN S.p.A. VME8010 7U 21 Slot VME64 Low Cost Crate, 2019. URL `https://www.caen.it/products/vme8010/`. Online available; last accessed: 7th August 2020.

[287] CAEN S.p.A. V1742 32+2 Channel 12bit 5 GS/s Switched Capacitor Digitizer, 2019. URL `https://www.caen.it/products/v1742/`. Online available; last accessed: 7th August 2020.

[288] S. Ritt. DRS4 Chip Datasheet, 2009. URL `https://www.psi.ch/sites/default/files/import/drs/DocumentationEN/DRS4_rev09.pdf`. Online available; last ac-

cessed: 7th August 2020.

[289] CAEN S.p.A. 742 Digitizer Family, 2019. URL https://www.caen.it/subfamilies/742-digitizer-family/. Online available; last accessed: 7th August 2020.

[290] CAEN S.p.A. V895 16 Channel Leading Edge Discriminator, 2019. URL https://www.caen.it/products/v895/. Online available; last accessed: 7th August 2020.

[291] CAEN S.p.A. V830 32 Channel Latching Scaler, 2019. URL https://www.caen.it/products/v830/. Online available; last accessed: 7th August 2020.

[292] CAEN S.p.A. V2718 VME-PCI Optical Link Bridge, 2019. URL https://www.caen.it/products/v2718/. Online available; last accessed: 7th August 2020.

[293] CAEN S.p.A. A3818 PCI Express CONET2 Controller, 2019. URL https://www.caen.it/products/a3818/. Online available; last accessed: 7th August 2020.

[294] Keysight Technologies. 33512B Waveform Generator, 20 MHz, 2-Channel with Arb, 2019. URL https://www.keysight.com/de/pd-2155035-pn-33512B/waveform-generator-20-mhz-2-channel-with-arb. Online available; last accessed: 7th August 2020.

[295] CAEN S.p.A. V538A 8 Channel NIM-ECL/ECL-NIM Translator, 2019. URL https://www.caen.it/products/v538a/. Online available; last accessed: 7th August 2020.

[296] HVSys Company. Light Emmiting Diode Sources of Calibrated Short Light Flashes, 2013. URL http://hvsys.ru/images/data/news/10_small_1368803142.pdf. Online available; last accessed: 7th August 2020.

[297] NKT Photonics. PILAS Picosecond Pulsed Diode Lasers, 2019. URL https://www.nktphotonics.com/lasers-fibers/product/pilas-picosecond-pulsed-diode-lasers/. Online available; last accessed: 7th August 2020.

[298] Orangepip®. Kona328 Arduino UNO Compatible Development Board – Data Sheet, 2019. URL http://www.farnell.com/datasheets/2056033.pdf. Online available; last accessed: 7th August 2020.

[299] B. O. A. Kaiser. Commissioning of a Test Facility to Characterize JUNO Photomultipliers. Bachelor Thesis, Universität Hamburg, Hamburg, 2016.

[300] Arduino®. Arduino Mega 2560 Rev3 – Overview, Tech Specs and Documentation, 2019. URL https://store.arduino.cc/mega-2560-r3/. Online available; last accessed: 7th August 2020.

[301] Lapp Group. Lapp Kabel Product Information: UNITRONIC®LiYY Data transmission cable with colour code acc. to DIN 47100, 2020. URL https://products.lappgroup.com/online-catalogue/data-communication-systems/low-frequency-data-transmission-cables/din-colour-code/unitronic-liyy.html. Online available; last accessed: 7th August 2020.

[302] LD Didactic. 467 251 / 467 261 Compact Lab Spectrometer, 2010. URL https://www.ld-didactic.de/pdf/Spektrometer_de.pdf. Online available; last accessed: 7th August 2020.

[303] B. Caccianiga et al. A Multiplexed Optical-Fiber System for the PMT Calibration

of the Borexino Experiment. *Nucl. Instrum. and Meth. A*, 496:353 – 361, 2003. doi: 10.1016/S0168-9002(02)01762-X.

[304] Edmund Optics Inc. Absorptive ND Filters, 2018. URL `https://www.edmundoptics.de/document/download/354105`. Online available; last accessed: 7th August 2020.

[305] Thorlabs Inc. ND Filters: Unmounted, AR coated for 350-700 nm, 2018. URL `https://www.thorlabs.de/newgrouppage9.cfm?objectgroup_id=6271`. Online available; last accessed: 7th August 2020.

[306] N. Anphimov. Container's PTFE Wavelength Shifting Study. Internal JUNO Collaboration Document, 2017. DocDB #2839-v1.

[307] D. Meschede and C. Gerthsen. *Gerthsen Physik*. Springer-Lehrbuch. Springer, Berlin, 23rd edition, 2005. ISBN 9783540026228.

[308] L. Nozka et al. BRDF Profile of Tyvek and its Implementation in the Geant4 Simulation Toolkit. *Optics Express*, 19:4199 – 4209, 2011. doi: 10.1364/OE.19.004199.

[309] B. S. Wonsak and A. Tietzsch. Container 3 & 4 of the PMT Mass Testing. Internal JUNO Collaboration Document, 2018. DocDB #3652-v1.

[310] D. Korablev. Proposal for Introducing an Element of Accelerated Aging into Long Term Stability Test. Internal JUNO Collaboration Document, 2019. DocDB #4463-v3.

[311] Z. Wang, N. Anphimov, and D. Korablev. MCP PMT Long Term Performance Testing with Pan-Asia Container #3. Internal JUNO Collaboration Document, 2019. DocDB #4543-v1.

[312] D. Korablev. Container 3 Status. Internal JUNO Collaboration Document, 2019. DocDB #4919-v1.

[313] N. Anphimov, A. Rybnikov, and A. Sotnikov. Optimization of the Light Intensity for Photodetector Calibration. *Nucl. Instrum. and Meth. A*, 939:61 – 65, 2019. doi: 10.1016/j.nima.2019.05.070.

[314] CAEN S.p.A. V1751 4/8 Channel 10 bit 2/1 GS/s Digitizer, 2019. URL `https://www.caen.it/products/v1751/`. Online available; last accessed: 7th August 2020.

[315] CAEN S.p.A. V1730 16/8 Channel 14 bit 500 MS/s Digitizer, 2019. URL `https://www.caen.it/products/v1730/`. Online available; last accessed: 7th August 2020.

[316] National Instruments Corporation. LabVIEW, 2020. URL `https://www.ni.com/de-de/shop/labview.html`. Online available; last accessed: 7th August 2020.

[317] H.-P. Halvorsen. Introduction to LabVIEW, 2017. URL `https://www.halvorsen.blog/documents/tutorials/resources/Introduction%20to%20LabVIEW.pdf`. Online available; last accessed: 7th August 2020.

[318] B. Muthuswamy. Introduction to LabVIEW, 2004. URL `ftp://ftp.ni.com/pub/gdc/tut/intro-labview.pdf`. Online available; last accessed: 7th August 2020.

[319] T. R. Sterr. Aufbau eines PMT-Teststand Prototypen für das JUNO-Projekt. Bachelor Thesis, Eberhard Karls Universität Tübingen, Tübingen, 2016.

[320] T. R. Sterr. PMT Array Timing Calibration with a Pulsed Light Source. Master

Thesis, Eberhard Karls Universität Tübingen, Tübingen, 2018.

[321] CAEN S.p.A. *Technical Information Manual - MOD. V895 series 16 Channel Leading Edge Discriminators*. CAEN S.p.A., Viareggio, Italy, rev. 3 edition, 2009.

[322] CAEN S.p.A. *Technical Information Manual - MOD. V830 series 16 C. Latching Scalers*. CAEN S.p.A., Viareggio, Italy, rev. 4 edition, 2007.

[323] CAEN S.p.A. *User Manual UM4279 - V1742/VX1742: 32+2 Channel 12bit 5 GS/s Switched Capacitor Digitizer*. CAEN S.p.A., Viareggio, Italy, rev. 7 edition, 2017.

[324] National Oceanic and Atmospheric Administration. NCEI Magnetic Field Estimated Values, World Magnetic Model (WWM 2014-2019), 2019. URL `https://www.ngdc.noaa.gov/geomag/calculators/magcalc.shtml#igrfwmm`. Online available; last accessed: 7th August 2020.

[325] Y. Yoshizawa, S. Oguma, and K. Yamauchi. New Fe-Based Soft Magnetic Alloys composed of Ultrafine Grain Structure. *Journal of Applied Physics*, 64(10):6044 – 6046, 1988. doi: 10.1063/1.342149.

[326] Hitachi Metals Ltd. FINEMET® EMC Components: FM Shield™ MS-F / MS-FR Series: High Permeability, Thin and Flexible Magnetic Shielding Sheets, 2016. URL `https://www.hitachi-metals.co.jp/e/products/elec/tel/p02_21.html`. Online available; last accessed: 7th August 2020.

[327] CAEN S.p.A. *Technical Information Manual - MOD. V538 A Series: 8 Channel NIM-ECL / ECL-NIM Translator and Fan-Out*. CAEN S.p.A., Viareggio, Italy, rev. 3 edition, 2003.

[328] H. Q. Zhang. Tested Performance of JUNO 20" PMTs. 2018. doi: 10.5281/zenodo.1300500. Poster at XXVIII International Conference on Neutrino Physics and Astrophysics (NEUTRINO 2018): Heidelberg, Germany, June 4-9, 2018.

[329] I. N. Bronstein, K. A. Semendjajew, G. Musiol, and H. Mühlig. *Taschenbuch der Mathematik*. Verlag Harri Deutsch, Frankfurt am Main, 2008. ISBN 978-3-8171-2007-9. 7. überarbeitete und erweiterte Auflage.

[330] M. Friedel. Messmethoden Wichtiger Charakteristischer Parameter der JUNO-PMTs. Bachelor Thesis, Eberhard Karls Universität Tübingen, Tübingen, 2017.

[331] K. Levenberg. A Method for the Solution of Certain Non-Linear Problems in Least Squares. *Quarterly of Applied Mathematics*, 2(2):164 – 168, 1944. ISSN 0033569X, 15524485.

[332] D. W. Marquardt. An Algorithm for Least-Squares Estimation of Nonlinear Parameters. *Journal of the Society for Industrial and Applied Mathematics*, 11(2):431 – 441, 1963. doi: 10.1137/0111030.

[333] S. Jetter et al. PMT Waveform Modeling at the Daya Bay Experiment. *Chinese Physics C*, 36(8):733 – 741, 2012. doi: 10.1088/1674-1137/36/8/009.

[334] H. Q. Zhang et al. Comparison on PMT Waveform Reconstructions with JUNO Prototype. *Journal of Instrumentation*, 14(08):T08002, 2019. doi: 10.1088/1748-0221/14/08/T08002.

[335] E. H. Bellamy et al. Absolute Calibration and Monitoring of a Spectrometric Channel

Using a Photomultiplier. *Nucl. Instrum. and Meth. A*, 339(3):468 – 476, 1994. ISSN 0168-9002. doi: 10.1016/0168-9002(94)90183-X.

[336] I. Chirikov-Zorin et al. Method for Precise Analysis of the Metal Package Photomultiplier Single Photoelectron Spectra. *Nucl. Instrum. and Meth. A*, 456(3):310 – 324, 2001. ISSN 0168-9002. doi: 10.1016/S0168-9002(00)00593-3.

[337] P. Barrow et al. Qualification Tests of the R11410-21 Photomultiplier Tubes for the XENON1T Detector. *Journal of Instrumentation*, 12(1):P01024, 2017. doi: 10.1088/1748-0221/12/01/P01024.

[338] H. Q. Zhang et al. 20" MCP and Dynode PMT Gain Definition & Charge Response. 2020. (in prep.).

[339] J. L. Wiza. Microchannel Plate Detectors. *Nucl. Instrum. and Meth.*, 162(1):587 – 601, 1979. ISSN 0029-554X. doi: 10.1016/0029-554X(79)90734-1.

[340] L. Chen et al. The Gain and Time Characteristics of Microchannel Plates in Various Channel Geometries. *IEEE Transactions on Nuclear Science*, 64(4):1080 – 1086, 2017. doi: 10.1109/TNS.2017.2676010.

[341] Z. Qin, A. Olshevskiy, and W. Wang. Status of 20-inch PMT Instrumentation for the JUNO Experiment, 2020. Poster at XXIX International Conference on Neutrino Physics and Astrophysics (NEUTRINO 2020): Web-event, June 22-27, 2020.

[342] R. Zhao. The Delivery Status of JUNO 20" PMTs and their Performance, 2020. Poster at XXIX International Conference on Neutrino Physics and Astrophysics (NEUTRINO 2020): Web-event, June 22-27, 2020.

[343] H. Q. Zhang. Methods for Improving P/V and Resolution as well as Comparision of Results in Different System. Internal JUNO Collaboration Document, 2017. DocDB #2936-v1.

Danksagung / Acknowledgements

Zum Schluss möchte ich noch all denen DANKE sagen, die tatkräftig oder unterstützend dazu beitragen haben, dass ich diese Arbeit schreiben konnte.

Zuallererst gilt mein Dank natürlich Prof. Dr. Tobias Lachenmaier, der mir ermöglicht hat, diese Arbeit zu schreiben, für sein Vertrauen in mich, dieses Projekt zu übernehmen und zu realisieren, für die vielen Ratschläge und hilfreichen Diskussionen rund um die Container, aber auch für ein immer offenes Ohr und die vielen Gespräche zwischen Tür und Angel. Das Container-Projekt als Doktorarbeit machen zu können war - trotz aller Widrigkeiten - eine total coole Sache und ich habe echt super viel gelernt dabei.

Als nächstes möchte ich mich bei Dr. Björn Wonsak bedanken für die mega gute und produktive Zusammenarbeit über die letzten 5 Jahre, für deine Geduld, wenn es mal etwas länger gedauert hat, und für das wertvolle und immer aufbauende Feedback. Es hat wirklich großen Spaß gemacht, mit dir zusammen die Container aufzubauen.
Ein ebenso großes Danke an Tobias Sterr für deine unzähligen Löscheinsätze, wenn es bei den Containern mal wieder "gebrannt" hat, und für dein Durchhaltevermögen trotz all dem Kampf und Krampf bei der Softwareentwicklung. Du hast auf jeden Fall immer ein Bier bei mir gut!

Danke an die ganze Arbeitsgruppe Lachenmaier/Jochum für eine super angenehme und stets kollegliale und hilfreiche Arbeitsatmosphäre und natürlich auch für die zahlreichen Kuchen. Danke auch an Gaby und Günter und Torsten für die Hilfe bei allen großen und kleinen Fragen.
Herzlichen Dank auch an die Hamburger Neutrino-Gruppe für die freundliche Aufnahme, den Kaffee und das Kickern während der vielen Male, bei denen ich zu Besuch war (und mich dann trotzdem die meiste Zeit in die kleine Hütte vor eurem Institut verzogen habe).

Ein weiterer Dank gilt der Deutschen Forschungsgemeinschaft e.V., die diese Arbeit (speziell das Container-System) substanziell unterstützt und gefördert und damit überhaupt erst ermöglicht hat.

Mein Dank gilt auch der JUNO Forschergruppe, speziell Dr. Christoph Genster, Michaela Schever, Philipp Kampmann, Dr. Henning Rebber, David Meyhöfer, Willy

Depnering, Paul Hackspacher, Heike Enzmann, Dr. Hans Steiger und all den anderen, für die coole Zeit und die gemeinsamen Biere auf unseren Reisen nach China, Hongkong, Paris, Catania und den ganzen Meetings überall in Deutschland. War echt immer eine Gaudi, euch zu sehen.

Many thanks to the JUNO PMT Instrumentation Group, i.e. Haiqiong Zhang, Nikolay Anphimov, Alexander Olshevskij, Wei Wang, Zhimin Wang and Zhonghua Qin for the intense and very successful team work in the last years, the fruitful discussions over the time and all the help, which was very valuable for me. Working with you guys was really fun and I'm proud of all the milestones we have reached together.

Danke auch an alle Korrekturleser für die wertvollen Rückmeldungen zu dieser Arbeit. Außerdem danke noch an Dr. Tom Kaufmann, Dr. Tobias Mock (geb. Jammer) und Dr. Lukas Salfelder für die Kaffeerunden im 7. Stock und die Diskussionen über physikalische und nicht-physikalische Themen, die ich in den letzten 1.5 Jahren vermisst habe (ja, hat etwas länger gedauert bei mir).
Danke aber auch vor allem ans Büro für eine mega geile Zeit in den letzten Jahren: an Dr. Michael Gschwender (Hacking-Gott), Axel Müller (Kaffee-Meister), David Blum (FC Bayern des Magnetdarts), sowie den externen Büromitgliedern Andi Zschocke und Sebastian Rottenanger: für die vielen Gespräche über die kleinen und größeren Schwierigkeiten beim Promovieren, Weltpolitik und Enten, für die Erfindung einer neuen Sportart und für eine legendäre Party in einem Mensakeller in Würzburg, die ich sicher nicht vergessen werde :D.

Ein großes Danke an alle Freunde, die mich in den letzten Jahren in ganz verschiedenen Lebenslagen unterstützt haben, und natürlich an meine Familie: dafür, dass ihr nie dran gezweifelt habt, dass diese Arbeit noch fertig wird und immer wieder nachgefragt habt, obwohl das meistens in 30 Minuten "Gespräch" über Physik geendet hat – und auch, wenn ihr immer noch denkt, ich sei Theoretiker. Danke auch an dich, Papa, dass du immer an mich geglaubt hat; ich vermisse dich und hätte dir diese Arbeit so gerne noch gezeigt.

Und zuletzt, danke an dich, Carlo, dafür dass du mir jeden Tag zeigst, wofür sich das alles lohnt, und danke an dich, Lisa, für all das Aushalten und Mittragen und die stetige Unterstützung, die ich kaum in Worte fassen und die ich dir wahrscheinlich nie ganz zurückzahlen kann – ohne euch hätte ich das nicht geschafft.